N65-34635

AD711656

This document has been approved for public release and sale.

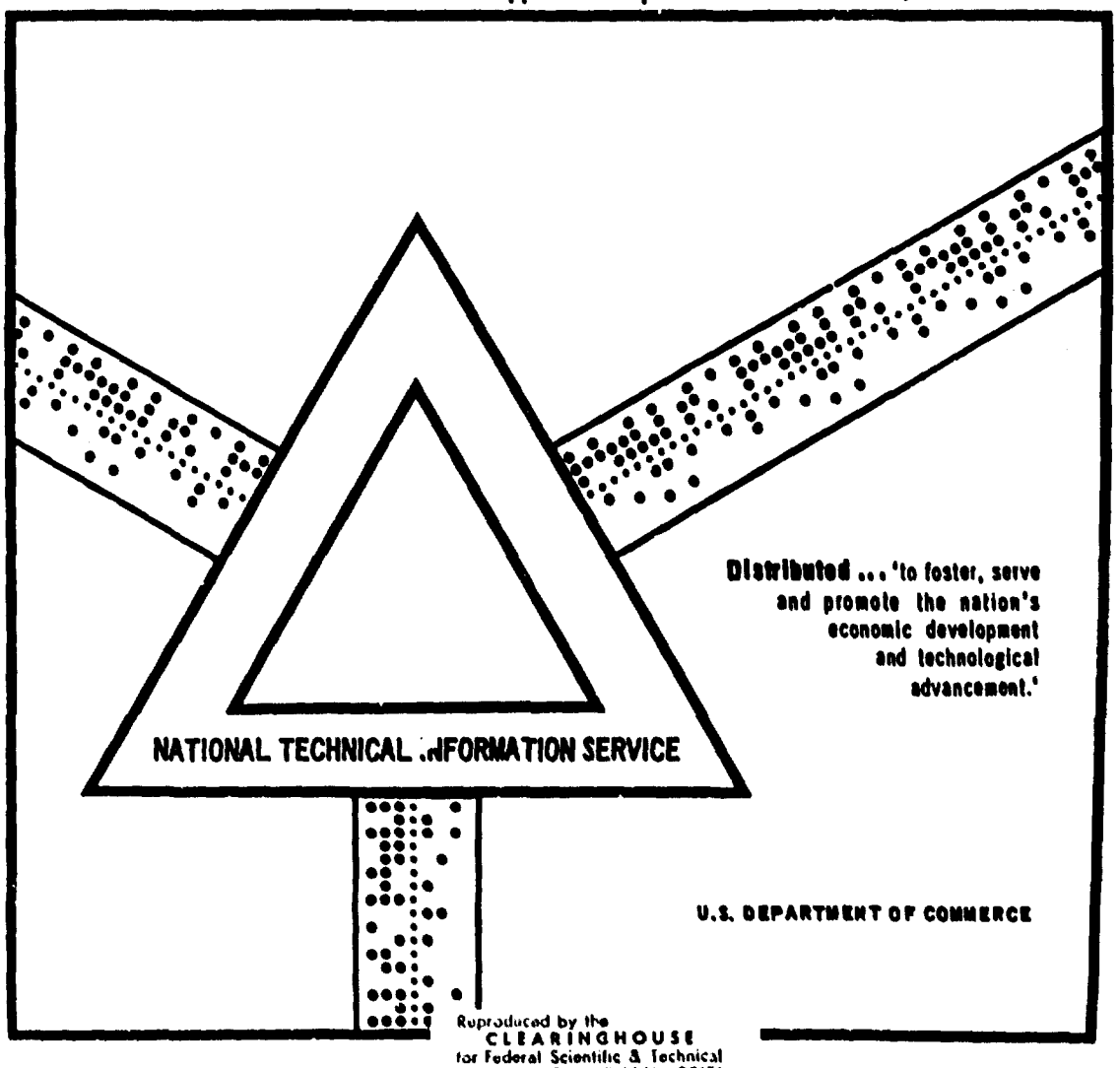

566

AGARDograph 97

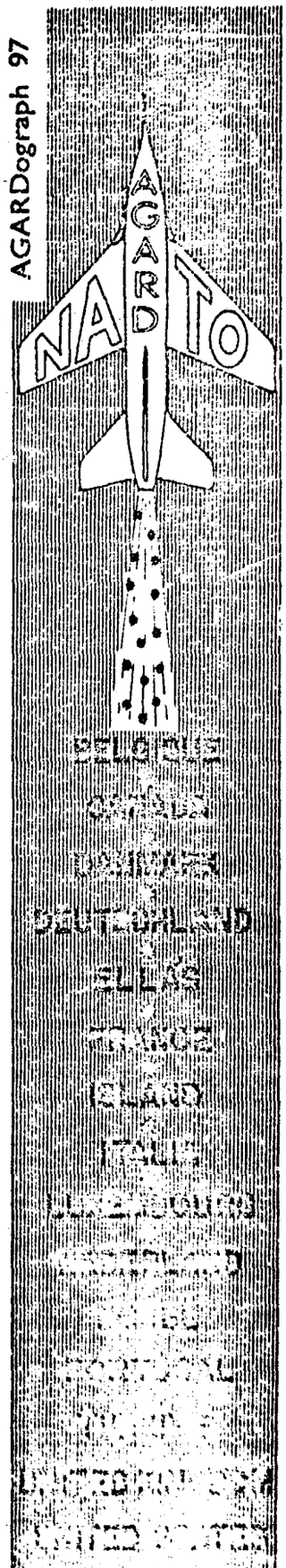

AGARDograph

RECENT DEVELOPMENTS IN BOUNDARY LAYER RESEARCH

PART I

MAY 1965

AGARDograph 97

NORTH ATLANTIC TREATY ORGANIZATION

ADVISORY GROUP FOR AEROSPACE RESEARCH AND DEVELOPMENT

(ORGANISATION DU TRAITE DE L'ATLANTIQUE NORD)

RECENT DEVELOPMENTS IN BOUNDARY LAYER RESEARCH

Published in Two Parts

P A R T I

Proceedings of a Specialists' Meeting, sponsored by the AGARD Fluid Dynamics Panel, held in Naples, Italy, 10-14 May 1965

Printed by Technical Editing and Reproduction Ltd
Harford House, 7–9 Charlotte St. London. W. 1.

FOREWORD

Boundary-layer conferences usually awake the interest of a large group of fluid dynamics people. This is because boundary layer research is not only of general scientific interest but the resulting knowledge is, to a large extent, of immediate use for practical developments of airplanes, vehicles and missiles. Therefore, the effort which is expended by fluid dynamics researchers is directed, on the one hand, towards a better understanding, mathematical formulation and accurate prediction of structure, stability and transition of boundary layers and, on the other hand, towards the practical elimination of adverse boundary layer effects on modern vehicle designs.

Since the first AGARD meeting on this subject in April 1960 in which progress and results were reported, many new investigations have been carried out by the "Specialists" in the NATO countries. The Fluid Dynamics Panel has decided, therefore, to hold this second symposium on "Recent Developments in Boundary Layer Research". The accumulated most interesting material for this meeting in Naples shows the timeliness and great desire for the conference.

H.H.Kurzweg
Chairman
Fluid Dynamics Panel

SUMMARY

This AGARDograph contains a collection of the papers presented at the AGARD Specialists' Meeting on "Recent Developments in Boundary Layer Research", held in Naples, Italy, 10-14 May 1965, under sponsorship of the AGARD Fluid Dynamics Panel.

The purpose of the Specialists' Meeting was to review and discuss in depth recent developments in selected areas of boundary layer research, to present a good cross-section of the state-of-the-art, to point out major problems, and to provide guidance for future research and development.

The collection of papers emphasizes the areas: Magneto-Fluid-Dynamic Boundary Layers; Turbulent Boundary Layers; Stability, Transition and Stabilization; Three-Dimensional Boundary Layers; and Interaction Effects at Hypersonic Speeds. Contributions have come from eight NATO countries.

SOMMAIRE

Cette AGARDographie réunit les exposés présentés à la Réunion des Specialistes de l'AGARD organisée à Naples, Italie, du 10 au 14 Mai 1965, par le Groupe de Travail de la Dynamique des Fluides, sur le thème: "Etat Actuel des Recherches Intéressant la Couche Limite".

Cette réunion avait pour but de passer en revue et de discuter en profondeur les progrès récents affectant certains aspects des recherches en couches limites, de présenter un tableau aussi complet que possible de l'état d'avancement dans ce domaine, de mettre en relief les problèmes majeurs, et de donner une direction aux recherches et développements futurs.

Les exposés rassemblés ici traitent en particulier des domaines suivants: Couches Limites en Magnéto-Dynamique des Fluides; Couches Limites Turbulentes; Stabilité et Stabilisation; Couches Limites Tri-dimensionnelles; Effets d'Interaction aux Vitesses Hypersoniques. Ces exposés représentent les contributions de huit pays de l'OTAN.

532.526

C O N T E N T S

Stability, Transition and Stabilization

Page

PART II

Three-Dimensional Boundary Layers

INTRODUCTION

The papers presented in this and related AGARDographs were prepared for a specialists' meeting on "Recent Developments in Boundary Layer Research" held at Naples, Italy during the period 10 to 14 May 1965. The meeting was organized by the Fluid Dynamics Panel of AGARD as one of a continuing series concerned with the scientific and technological aspects of fluid dynamics.

The previous AGARD meeting on boundary layers was held in London in 1960; the record of that meeting is preserved in the AGARDograph series. It is the practice of the Fluid Dynamics Panel to review at its annual executive session its program for the coming several years and to take such steps as seem required to develop in an orderly fashion that program. Accordingly, at Athens in August 1963, the panel decided to anticipate another boundary layer meeting five years after the London meeting, i.e., in the Spring of 1965. The Naples meeting is a result of that anticipation.

The Fluid Dynamics Panel uses a variety of procedures in setting up a specialists' meeting. The Naples meeting was preceded by a Round Table Discussion in Lisbon in September 1964. Individual Panel members and invited specialists presented survey papers on 10 topics which seemed of most current interest to NATO research workers in boundary layers. The purpose of the Round Table was to expose those topics of greatest mutual interest and thereby to select three or four topics for the anticipated specialists' meeting. It seemed to be agreed by the Panel members that the surveys were useful and accomplished their program. Thus there were selected the following four topics which led to the session structure of the Naples meeting:

Turbulent Boundary Layers
Stability, Transition and Stabilization
Three-Dimensional Boundary Layers
Interaction Effects at Hypersonic Speeds.

The first three of these topics relate to classical boundary layer phenomena; they have been the subject of investigations since the early days of boundary layer research and yet still provide a variety of problems, unsolved to some extent. Moreover, in technicological applications of boundary layer research to aeronautics and astronautics these topics are of great significance. The fourth topic has been of more recent origin, having first arisen in the early 1950's when hypersonic wind tunnels came into operation. It appears to be of fundamental interest because of the modifications of classical boundary layer concepts required by the interaction of the boundary layer and the essentially inviscid external flow and to be of technological interest in connection with high-speed flight at high altitudes.

There were some further results from the Lisbon Round Table Discussion. It was established that the topic "Separated Flows" was of sufficient interest to warrant a specialists' meeting of its own. Accordingly, a program committee headed by Professor J.J.Ginoux (Belgium) was appointed in order to prepare such a meeting for the Spring of 1966. In addition, the survey presented by Professor W.R.Sears (United States) at Lisbon on "Magneto-Fluid-Dynamic Boundary Layers" evoked such

interest that the Program Committee for the Naples meeting (excluding Professor Sears himself) considered it appropriate to request Professor Sears to give a more formal version thereof to the wider audience at Naples as a general invited lecture.

An examination of the program with its large number of papers will indicate the high level of activity in boundary layer research in the NATO countries. When the Program Committee was organizing the meeting, there was some sentiment expressed by the Panel members to have a shorter meeting than actually resulted. However, the present author for one feels that with authors and audience travelling large distances for a meeting and with a large number of submitted papers such as results when a topic of such general interest as boundary layer research is involved, it is worthwhile to have a full program of five days duration. It is hoped that after the meeting a consensus will exist to support this decision.

The program of the Naples meeting may also serve as a demonstration in 1965 of the apparently unending impact which Prandtl's paper in 1905 has had on a variety of fields of science and technology, clearly on fluid mechanics but on the chemical and electrical engineering sciences, and on applied mathematics as well. It is interesting to speculate on the extent to which Prandtl himself anticipated this impact and on directions that boundary layer research will take in the next 20 years. Could the developments of the last 20 years, since the end of World War II, have been foreseen?

In conclusion, the present author as Chairman of the Program Committee, gratefully acknowledges the cooperation and efforts of the other members of the Committee, Dr. P.Carriere (France), Prof.L.G.Napolitano (Italy), Prof.W.R.Sears (United States), and Prof.E.Truckenbrodt (Germany). Without their prompt and efficient collaboration it would not have been possible to put together the program in the short time available. Thanks are also due to other Panel members, Dr.W.J.Rainbird (Canada), Col.B.Marschner (United States), Dr.R.N.Cox and Mr.P.A.Hufton (United Kingdom) and perhaps others for their assistance. Special thanks are due to our host member of the Program Committee, Prof.Napolitano, who has had responsibilities far beyond the program itself. The present author is also indebted to the Chairman of the Fluid Dynamics Panel, Dr.H.H.Kurzweg, for his review of our activities and for his encouragement and suggestions. Finally, on behalf of the Program Committee there is sincerely acknowledged our debt to the Panel Executive, Lt.Col.S.C.Skemp, Jr., on whose competent shoulders rested the responsibility of tying down loose ends, informing and cajoling the authors, having the papers published in AGARDograph form, and handling the almost infinite details connected with the mechanics of the Naples meeting.

Paul A. Libby, Chairman of the Program Committee
Professor of Aerospace Engineering
University of California, San Diego

THE THREE-DIMENSIONAL STRUCTURE OF THE VISCOUS SUBLAYER

by

J. Sternberg

The Martin Company,
Baltimore, Maryland, U.S.A.

SUMMARY

A simplified form of a theory for the fluctuations in the viscous sublayer of a turbulent flow was given in a previous paper by the author. In this paper, the analysis is extended to include additional terms in the equations representing the convective effect of the mean flow on the fluctuation field. This makes it possible to obtain solutions for the elementary Fourier components at different wave numbers at all angles of obliquity to the flow direction. It is found that there is a strong effect of obliquity on the structure of the elementary components. Comparisons with available experimental data indicate that the energy-containing disturbances are strongly aligned with the flow direction.

SOMMAIRE

Au cours d'un exposé précédent, l'auteur présentait une forme simplifiée de théorie des fluctuations dans la sous-couche visqueuse d'un écoulement turbulent. Dans la communication présente, il étend son analyse pour inclure des termes supplémentaires dans les équations représentant l'effet de convection de l'écoulement moyen sur le champ de fluctuation. Ceci permet d'obtenir des solutions pour les parties composantes élémentaires de Fourier pour différents nombres d'ondes à tous les angles d'obliquité par rapport à la direction de l'écoulement. Il apparaît qu'un fort effet d'obliquité se fait sentir sur la structure des parties composantes élémentaires. En établissant des comparaisons avec les données expérimentales dont on dispose, on s'aperçoit que les perturbations détentrices d'énergie coincident fortement avec la direction de l'écoulement.

CONTENTS

LIST OF FIGURES

NOTATION

x	coordinate in direction of mean flow
y	coordinate normal to wall
z	coordinate transverse to flow
u, v, w	fluctuating velocities in the x, y, z direction
q	fluctuation velocity in the x, z plane
p	fluctuating pressure
p_θ	complex constant for Fourier component
f	frequency, c/s
β	$2\pi f$
λ	wave length
k	wave number, $k = 2\pi/\lambda$
U_w	convective disturbance velocity, $U_w = \beta/k_x$
θ	angle of obliquity to flow direction in x, z plane
g, h, k	complex velocity distribution functions
G, K	dimensionless distribution functions, $G = g/U_w$, $K = k/U_w$
$\bar{K}$	K for $A_2 = 1$ (Eqn. 13)
U_τ	friction velocity
δ	boundary layer thickness
δ_0	$\delta_0 = 0.69\,\delta$ for Grant's boundary layer
$\rho\overline{uv}$	turbulent shear stress
ϕ	phase angle between u and v
y^+	friction distance parameter, $y^+ = U_\tau y/\nu$
ν	kinematic viscosity, $= \mu/\rho$
ρ	density

Y	viscous region variable, $Y = \sqrt{\beta/2\nu}\, y$
$R_{nn}(x, 0, z)$	space correlations in the x , z direction
A_1, A_2	constants, Equations 12, 13

Subscripts

1	free stream flow
E	outer limit for variable Y
x, z	denotes x and z directions

THE THREE-DIMENSIONAL STRUCTURE OF THE VISCOUS SUBLAYER

J. Sternberg

1. INTRODUCTION

The viscous sublayer is defined as the region between the wall and the fully turbulent part of the flow. In terms of the friction distance parameter, $U_\tau y/\nu = y^+ \approx 60$, where U_τ is the friction velocity, y is the distance from the wall and ν is the kinematic viscosity. Perhaps the best characterization of the viscous sublayer is to describe it as a layer in which there is dissipation of the energy-containing eddies by direct viscous action.

If we regard a laminar flow as one in which the viscous shear stress $\mu dU/dy$ is greater than the turbulent shear stress $\rho\overline{uv}$, then there is in fact a "laminar" flow next to the wall, since at the wall the turbulent shear vanishes. Measurements show that the viscous and shear stresses are equal at $y^+ = 12$. On the other hand, the local turbulence level u'/U, where u' is the root-mean square value of the velocity fluctuation in the flow direction and U is the local mean velocity, rises to a maximum value at the wall. It is clear that any theory of the viscous sublayer must account for the measurements which show that the flow is highly disturbed all the way to the wall.

We hold to the view that the outer flow is the principal source of the energy-containing disturbances in the viscous sublayer. At any instant, the turbulent fluctuation field can be represented by a distribution of disturbance vorticity components throughout the boundary layer. In a turbulent boundary layer about half the energy is contained in eddies whose scale in the flow direction is more than twice the boundary layer thickness. Most of the fluctuation energy near the wall is induced by the large scale vorticity distributed further out in the boundary layer. Since vorticity travels with the fluid particles, the disturbance field near the wall is in effect swept downstream with the mean velocity of the turbulent outer flow. A theory for the viscous sublayer based on this approach has been recently proposed[1].

The magnitude of this convective velocity U_w for the disturbances is important. We have concluded that, for the larger scale motions containing most of the turbulent energy, the convective velocity is greater than the local mean velocity in the sublayer (see Ref. 1). There are three different types of experimental measurements that support this position.

(a) The data of Klebanoff[2] and others show that the energy-containing portion of the normalized energy spectra at different points in the fully turbulent part of the boundary layer are remarkably similar. This implies that for any particular frequency component of the turbulence, the convective velocity does

not vary significantly with position in the boundary layer. Otherwise turbulence scales, of the order of many boundary layer thicknesses, would have to vary in a special way across the boundary layer.

(b) Measurements of longitudinal correlations[2,3] show a systematic divergence from autocorrelation calculations (using the local mean velocity U for U_w) at large separations. Close to the wall the large scale motions appear to be travelling with a velocity substantially greater than the local mean velocity. In particular, analysis[1] of the data of Favre, at $y^+ = 35$ in the outer part of the sublayer, indicated that U_w was approximately equal to $0.78U_1$, where U_1 is the free stream velocity.

(c) Space-time correlation measurements of the wall pressure[4,5] indicate that the pressure pattern is convected downstream with a mean speed of about $0.82U_1$. The convective velocity decreases as the frequency increases, but in the frequency range of interest it is greater than the mean velocities in the sublayer.

For the purposes of the analysis, we have chosen to set $U_w/U_1 = 0.80$ for the energy-containing eddies. In the case of Klebanoff's boundary layer frequencies between $0 < f \lesssim 300$ c/s account for 80% of the $\overline{u^2}$ fluctuation energy. A frequency of 300 c/s corresponds to an eddy scale $L = U_w/f \approx \delta/2$. We then limit the condition $U_w = 0.8U$ to frequencies from 0 to 300 c/s. In fact there is no single value of the convective velocity. However, the solutions do not depend strongly on the specific choice of U_w as long as U_w is significantly greater than the local mean velocity U.

The purpose of the theory[1] was to represent the fluctuation field between the wall and the fully turbulent part of the flow. The mean flow in the viscous sublayer and the turbulent field outside the sublayer were assumed to be known from experiment. A simplified form of the linearized equations of motion for the fluctuations in a turbulent flow was used to describe the turbulent field between the wall and the fully turbulent part of the flow. The sublayer is the region where the viscous terms in the equation of motion are significant. The fluctuation field was made up of a superposition of Fourier components where the amplitude of each frequency component outside the sublayer was taken from experiment. It was found that the physical extent of the viscous region depends on the frequency of the turbulent component, varying inversely with $\sqrt{f}$. Low frequency components feel the wall much further out than high frequency components. This leads to a substantial change in the spectral distributions through the sublayer. Deep in the sublayer, the large scale motions make a much smaller contribution to the fluctuation field than outside the sublayer. Comparisons were made with the extensive hot-wire measurements of Klebanoff[2] and Laufer[6]. Figures 1(a) and 1(b) are taken from Reference 1. The calculated total extent of the sublayer and the qualitative change of the spectra deep inside the sublayer are in rough accord with the experiments. The thickness of the sublayer arises naturally in the theory. On the other hand the variation of u' in the outer part of the sublayer is not accounted for by the theory. It is interesting to note that although there is no theoretical distinction between an inner "laminar" layer and a "transition" zone, the rapid changes do primarily occur in the inner fraction of the sublayer. Other aspects of the fluctuation field were explored in Reference 1, but the use of the simplified equations limited the possible scope of the theory.

In this paper, the analysis is extended by retaining the previously neglected linear terms which represent the convective effect of the mean flow on the fluctuation field. Of particular importance we are now able to consider disturbances at high obliquity to the flow direction. The manipulation of the equations is straightforward, but difficulties arise in fixing the outer boundary condition for elementary components. Fundamental questions are involved and are discussed in the section on Boundary Conditions. To a considerable extent the difficulty reflects the limitations of the linear representation for a turbulent field. In view of the rather ambiguous nature of the outer boundary conditions, consideration will be restricted to those aspects of the sublayer structure that do not appear to be sensitive to a change in the outer boundary conditions. In particular, attention will be focussed on the question of the distribution of disturbance energy with obliquity in the sublayer. Townsend[7,8] and Grant[9] have studied the structure of the large scale motions in shear flows by comparing correlation measurements with what would be expected from the presence of hypothetical simple eddy structures. As Townsend notes, this procedure is neither simple nor unique and is fairly subjective. In this paper, we will examine the question of disturbance orientation anew using Fourier components which satisfy the dynamic equations near the wall.

2. EQUATIONS OF MOTION

The equations of motion for the fluctuation in a turbulent field can be considerably simplified close to the wall in a mean flow where the mean velocity $U = U(y)$ only, and $V = W = 0$, where U, V and W are the three components of the mean motion. If u, v, and w are the disturbance velocities, the components of the total velocity are $U + u$, v, and w, and the pressure is $P + p$. After linearization, the equations become

$$\frac{\partial u}{\partial t} + U\frac{\partial u}{\partial x} + v\frac{dU}{dy} = -\frac{1}{\rho}\frac{\partial p}{\partial x} + \nu\frac{\partial^2 u}{\partial y^2} \tag{1}$$

$$\frac{\partial v}{\partial t} + U\frac{\partial v}{\partial x} = -\frac{1}{\rho}\frac{\partial p}{\partial y} + \nu\frac{\partial^2 v}{\partial y^2} \tag{2}$$

$$\frac{\partial w}{\partial t} + U\frac{\partial w}{\partial x} = -\frac{1}{\rho}\frac{\partial p}{\partial z} + \nu\frac{\partial^2 w}{\partial y^2} \tag{3}$$

and the continuity equation

$$\frac{\partial u}{\partial x} + \frac{\partial v}{\partial y} + \frac{\partial w}{\partial z} = 0 . \tag{4}$$

Well away from the wall, the viscous terms are negligible for the large scale turbulent motions. In the immediate vicinity of the wall, the velocity gradients are greatly increased and the viscous terms may be of the same order as the other terms.

The form of an elementary oblique component of wave numbers k is shown in Figure 2. The total disturbance velocity in the x, z plane is q, periodic in the k direction with a wave length λ. Along any line perpendicular to the k direction

the phase, and hence q, is constant. In general q is not in the k direction but has a component normal to k. Then the wave length in the x direction is

$$\lambda_x = \lambda/\cos\theta .$$

In an experiment, the one-dimensional spectrum is measured. Thus the total $\overline{u^2}$ or $\overline{w^2}$ disturbance at a particular frequency or wave number k_x is made up of contributions from oblique components that satisfy the condition

$$k = k_x/\cos\theta .$$

This oblique component is carried downstream with the velocity U_w in the x direction. Introducing complex notation with $\beta = 2\pi f$, $k_x = 2\pi/\lambda_x$, and $k_z = 2\pi/\lambda_z$, the disturbance velocities can be represented as

$$u = \mathrm{Re}\{h(y)\ \exp[i(k_x x + k_z z - \beta t)]\}$$

$$w = \mathrm{Re}\{k(y)\ \exp[i(k_x x + k_z z - \beta t)]\}$$

$$v = \mathrm{Re}\{g(y)\ \exp[i(k_x x + k_z z - \beta t)]\}$$

$$\text{and} \quad p = \mathrm{Re}\{p(y)\ \exp[i(k_x x + k_z z - \beta t)]\} .$$

The functions $h(y)$, $k(y)$, $g(y)$, and $p(y)$ are complex. We proceed by substituting these expressions for u, v, w, and p in the equations of motion and the continuity equation (Eqns. 1-4). But first a simplification will be made.

The vertical velocity v is much smaller than q close to the wall. It follows that $\partial p/\partial k \gg \partial p/\partial y$ so that the pressure p is almost invariant with y close to the wall. Therefore, we set

$$\frac{\partial p}{\partial z} = \frac{\partial p}{\partial x}\tan\theta = \text{constant, and } p(y) = p_\theta \text{ a complex constant} .$$

It is then not necessary to solve Equation (2), but instead the velocity v can be found from the continuity equation. With $\partial p/\partial x$ and $\partial p/\partial z$ constant and $\partial p/\partial y \approx 0$, there will be three equations for the three unknowns u, v, and w.

In fact, the condition $\partial p/\partial y \approx 0$ is not valid as $\theta \to 90^\circ$. Without this simplification, a higher order set of equations must be used and it is much more trouble to obtain solutions. Solutions to the more complicated equations with $p = p(y)$ were obtained at a representative frequency and showed good agreement with the simpler equations up to $\theta = 85^\circ$.

The complication in solving these equations is due to the presence of v in Equation (1). This provides a coupling between Equations (1) and (3) and upsets the symmetry of the equations. Nevertheless, the problem can be reduced to the solution of two ordinary uncoupled differential equations.

If we substitute the complex expressions for u, v, and w in Equations (1) and (3), we obtain

$$-i\beta h(y) + ik_x U h(y) + g(y)\frac{dU}{dy} + i\frac{k_x}{\rho}p_\theta = \nu h''(y) \tag{5}$$

$$-i\beta k(y) + ik_x U k(y) + i\frac{k_z}{\rho}p_\theta = \nu k''(y)\,. \tag{6}$$

The spatial derivatives $\partial u/\partial x$, $\partial w/\partial z$ can be obtained by inspection of Figure 2. or from the u and w expressions and are

$$\frac{\partial u}{\partial x} = ik_x u\,, \quad \frac{\partial w}{\partial z} = ik_x w\tan\theta\,.$$

Then, substituting in the continuity equation, we have

$$h(y) = \frac{i}{k_x}g'(y) - \tan\theta\, k(y)\,. \tag{7}$$

Differentiating with respect to y, this becomes

$$h''(y) = \frac{i}{k_x}g'''(y) - k''(y)\tan\theta\,. \tag{8}$$

We substitute the expressions for h(y) and $h''(y)$ in Equation (5). Noting that the disturbance velocity $U_w = \beta/k_x$. Equation (5) can be written as

$$(U_w - U)g' + g\frac{dU}{dy} + i\frac{k_x}{\rho}p_\theta - \frac{i\nu}{k_x}g''' = -i\beta k(y)\tan\theta + ik_x U k(y)\tan\theta - \nu k''(y)\tan\theta\,. \tag{9}$$

But from Equation (6), the right-hand side of Equation (9)

$$= -i\frac{k_x}{\rho}p_\theta\tan^2\theta = \text{constant}\,.$$

Thus we can write Equations (5) and (6) as

$$(U_w - U)g' + g\frac{dU}{dy} + i\frac{k_x}{\rho}p_\theta[1 + \tan^2\theta] = \frac{i\nu g'''}{k_x} \tag{10}$$

$$(U_w - U)k(y) - \frac{p_\theta}{\rho}\tan\theta = \frac{i\nu}{k_x}k''\,. \tag{11}$$

The function h(y) is found from the continuity equation.

Equations (10) and (11) can be made dimensionless by introducing

$$Y = \sqrt{\beta/2\nu}\,y\,, \quad G = g/U_w\,, \quad K = k/U_w\,.$$

Then we have

$$\left[1 - \frac{U}{U_w}\right]\frac{dG}{dY} + G\,\frac{d(U/U_w)}{dY} + A_1 = \frac{i}{2}\frac{d^3G}{dY^3} \tag{12}$$

$$\left[1 - \frac{U}{U_w}\right]K + A_2 = \frac{i}{2}\frac{d^2K}{dY^2}\,. \tag{13}$$

The ratio of the constants is

$$\frac{A_2}{A_1} = \frac{i\sqrt{\beta/2\nu}}{k_x}\sin\theta\,\cos\theta\,.$$

The velocity distribution functions are then

$$h(y) = i\,\frac{\sqrt{\beta/2\nu}}{k_x}\,U_w[G' - \bar{K}\sin^2\theta]A_1$$

$$k(y) = i\,\frac{\sqrt{\beta/2\nu}}{k_x}\,U_w[\bar{K}\sin\theta\,\cos\theta]A_1$$

$$g(y) = U_w G A_1$$

$$\text{where} \quad K = i\bar{K}\sqrt{\beta/2\nu}\,\sin\theta\,\cos\theta\,.$$

The coefficients $(1 - U/U_w)$ and $d(U/U_w)/dY$ have been calculated for Klebanoff's boundary layer. The numerical solutions to these equations have been obtained using the digital computers of the Ballistic Research Laboratory.

3. BOUNDARY CONDITIONS

Several difficulties immediately arise in the determination of the boundary conditions for the elementary Fourier components.

In the simplified theory, Equations (12) and (13) become

$$\frac{dG}{dY} + A_1 = \frac{i}{2}\frac{d^3G}{dY^3} \tag{15}$$

$$K + A_2 = \frac{i}{2}\frac{d^2K}{dY^2}\,. \tag{16}$$

Each of the disturbance velocities u and w can be represented as the sum of an inviscid and a viscous component. The inviscid component is constant both inside and outside the viscous region. The viscous component then represents the effect of the wall friction.

First, for illustration, we will consider a two-dimensional disturbance, $\theta = 0^o$, and arbitrarily set $A_1 = 1$. Since $u = v = 0$ at $y = 0$, we have $G'(0) = G(0) = 0$ at $y = 0$. The third boundary condition can be stated as $G'' \to 0$ as $Y \to \infty$. Actually, the solution already satisfies the third condition for $Y < 5$ independently of f (Fig. 3(a)). The variation of the viscous term $|G'''|$ is shown in Figure 3(b). The viscous action is effectively confined to the region $0 < Y < 5$.

When the complete linearized equations are used, all "inviscid" disturbances are significantly altered by the mean flow and vary both inside the outside the principal viscous region. At the same time, the viscous region is smeared out. There is now some viscous action for $Y > 5$ due to the continued variation of the "inviscid" component which the viscous solution tends to smooth out.

The complete equations admit solutions which diverge exponentially at large values of the independent variable with a rapid increase of the viscous term. The solution with the desired viscous behavior (i.e. d^3G/dY^3 small at large Y) for a two-dimensional disturbance at a representative frequency $f = 70$, is also shown in Figures 3(a) and 3(b). While the distribution of $|G'''|$ is somewhat altered by the additional terms in the equations, the extent of the main viscous region is much the same. On the other hand, there is a large variation of $|G'|$ in the outer part of the viscous region. This is an important effect of the convective terms.

New features appear when we allow oblique disturbances, $\theta \neq 0^o$. Suppose we consider solutions to the "inviscid" equations

$$(1 - U/U_w)\frac{dG}{dY} + \frac{d(U/U_w)}{dY} G + A_1 = 0$$

$$\text{and} \quad (1 - U/U_w)K + A_2 = 0 \quad \text{with} \quad G(0) = 0,$$

$$G'(0) = -A_1, \quad \text{and} \quad K(0) = -A_2.$$

The inviscid variations of $\overline{u^2}$ and $\overline{w^2}$ given by these solutions are compared with the viscous variations given by Equations (12) and (13) in Figure 4. We somewhat arbitrarily set $Y = 4.4$ as the outer edge of the viscous region. (In the simplified theory, at $Y = 4.4$, u^2 is within 1% of the u^2 level outside the viscous region.) The disturbance velocity variations in the viscous region $Y < 4.4$ are due as much to the effect of the mean flow on the disturbance as to the effect of viscosity on the disturbance. However, only part of the viscous action can be attributed to the wall friction. The "inviscid" disturbance velocity variations due to the mean flow can be quite large and also induce compensatory viscous action. At an obliquity of $\theta = 80^o$, the wall friction itself appears to be a minor factor. These features become even more pronounced at still lower frequencies. Actually at high obliquity and low frequency the viscous terms in Equations (1,3) become small compared to the velocity terms.

Figures 3 and 4 would indicate that the edge of the region of viscous action can still be taken as $Y \approx 5$. However, it is clear that the behavior of these solutions at the edge of the viscous region differs from the behavior of the turbulent field at the edge of the sublayer (see Fig. 1(b)). Calculations for a range of frequencies at

$\theta = 80^{o}$ are shown in Figure 5. Experimentally, $\overline{u^2}$ and $\overline{w^2}$ vary very slowly at the edge of the sublayer, but this is certainly not the case for these linear solutions.

There is an even more important difficulty with the outer boundary conditions for the linear solutions. Basic to the approach of the theory, is the use of elementary Fourier components to connect a known turbulence field to the wall. A characteristic property of the turbulence in a shear flow is the correlation coefficient $\overline{uv}/u'v'$ of the turbulence. Townsend[7] has shown that a homogeneous turbulence subjected to a prolonged uniform strain approaches an equilibrium anisotropic structure and that an analogous equilibrium structure would be expected in an ordinary shear flow. The equilibrium structure depends on a balance between the effect of the sustained shearing action of the mean flow and some sort of nonlinear energy transfer between the fluctuating components. Now there is a direct connection between the correlation coefficient and the anisotropy of the turbulence[10]. Thus we cannot expect the correct value of the correlation coefficient to arise naturally from a linear theory. Instead, the experimental value would have to be put in as part of the outer boundary condition. Unfortunately solutions where u and v are forced to have the experimental phase angles at $Y = 4.4$, exhibit a rising rather than a vanishing viscous action near the end point. In effect, viscous action is being used to alter the phase angle between u and v instead of nonlinear inertia terms. However, it is of considerable interest to note that these solutions indicate that the phase angle between u and v at the edge of the viscous region has a strong effect on the velocity distribution in the viscous region.

This is illustrated in Figure 6 for a two-dimensional disturbance ($\theta = 0^{o}$). Two conditions are applied at the edge of the viscous region.

(a) $d\overline{u^2}/dy = 0$

(b) $\overline{uv}/u'v' = \cos\theta$ where θ is the phase angle between u and v.

Klebanoff's measurements indicate $\cos\theta = -0.54$ outside the sublayer[1] for $f = 70$. The velocity distribution in the outer part of the viscous region varies markedly with the phase angle although the outer boundary condition does not have much effect on the solutions for $0 < Y < 2$. Quite possibly the experimental increase in u' after entering the sublayer is related to the behavior exhibited by these solutions.

In summary, it appears that the linear theory is not capable of giving the correct transition at the outer edge of the sublayer. That is not to say that a useful approximation cannot be achieved by a suitable choice of boundary conditions. However, we will now confine our attention to those prominent features of the fluctuation field that are insensitive to the outer boundary conditions. For this purpose, we will use solutions for which the viscous effect becomes small at large Y.

4. THE EFFECT OF OBLIQUITY AT THE OUTER EDGE

4.1 The $\overline{u^2}$ and $\overline{w^2}$ components

The velocity components $\overline{u^2}$ and $\overline{w^2}$ are computed from the solutions to Equations (12) and (13) where

$$\overline{u^2} = \tfrac{1}{2}[h(y)h^*(y)] ,$$

$$\overline{w^2} = \tfrac{1}{2}[k(y)k^*(y)]$$

and the asterisk denotes the complex conjugate.

The ratio $\overline{u^2}/\overline{q^2}$ at $Y = 4.4$ as a function of θ and for a range of frequencies is shown in Figure 7, where $q^2 = u^2 + w^2$.

The most striking feature of these curves is the fact that $\overline{u^2}/\overline{q^2} \to 1$ at both $\theta = 0^\circ$, and $\theta = 90^\circ$. This result is a consequence of the fact that $A_2 = 0$ at $\theta = 0^\circ$ and 90° . If the disturbance velocity q were in the k direction, normal to the constant phase line, then the ratio $u^2/q^2 = \cos^2\theta$. Instead the effect of the mean flow is to reduce the w fluctuation as $\theta \to 90^\circ$. It is also apparent that the variation of $\overline{u^2}/\overline{q^2}$ with obliquity is weakly dependent on the frequency over the frequency range of interest.

The relative magnitude of the total $\overline{u^2}$ and $\overline{w^2}$ at the sublayer edge will then depend on the distribution of disturbance energy with both frequency and obliquity. If we assume that the disturbance energy at each wave number k is uniformly distributed with θ , then the relative area above and below the mean curve for $\overline{u^2}/\overline{q^2}$ gives the relative magnitude of $\overline{u^2}$ and $\overline{w^2}$. Under this assumption $\overline{u^2} \approx \overline{w^2}$ whereas experimentally Klebanoff finds $\overline{w^2}/\overline{u^2} \approx 0.5$ at the edge of the sublayer. According to Figure 7, the experimentally observed ratio implies some concentration of disturbances at either low or high obliquity. Consideration of the wall pressure field in the next section indicates that the large scale disturbances are concentrated at high obliquity.

4.2 The pressure field

The boundary layer wall pressure measurements of Willmarth[4] and Bull[5] transformed to the experimental conditions of Klebanoff are compared in Figure 8. There is good agreement for $f > 50$ ($\beta\delta^*/U_1 > 0.2$, where δ^* is the boundary layer displacement thickness). Willmarth attributes his rising spectra at low frequencies to extraneous large scale free stream disturbances rather than to the turbulence in the boundary layer. We might then conclude that in the absence of free stream disturbances, the pressure spectrum should decrease at low frequencies. Support for this position has been attributed to free flight measurements of Hodgson. Nevertheless, since we don't know whether extraneous disturbances were present in Klebanoff's experiments, some caution has to be exercised in using the spectra in Figure 8 for Klebanoff's experimental conditions below $f = 50$. The elementary solutions give the relative magnitude of the wall pressure field and the velocity components out in the flow where

$$\frac{p^2/\rho^2}{v^2} = \frac{U_\infty^2}{4}\cos^4\theta\left[\frac{|G''(0)|^2}{|G' - \bar{K}\sin^2\theta|^2}\right] . \qquad (17)$$

The relative magnitude of the pressure fluctuation falls off very rapidly at high obliquity because of the factor $\cos^4\theta$. As we have already discussed, $q^2 \to u^2$ as $\theta \to 90^\circ$, so $(p^2/\rho^2)/u^2 \to 0$ as $\theta \to 90^\circ$.

If we choose $y^+ \approx 60$ for the edge of the sublayer (i.e. $y/\delta = 0.02$ for Klebanoff), the corresponding values of Y are

$$Y = 2.3 \text{ at } f = 10$$

$$Y = 5.2 \text{ at } f = 50 .$$

Evaluating $\overline{u^2}$ at these end points, the ratio $(\overline{p^2}/\rho^2)\overline{u^2}$ as a function of θ is shown in Figure 9. At each frequency the experimental ratio can be calculated, using the u^2 spectrum just outside the sublayer. These values are marked on the curves. Clearly, agreement between theory and experiments requires disturbances concentrated at large obliquity. Any significant disturbance energy near $\theta = 0$ would lead to wide disagreement between theory and experiment.

Of course, the intercepts shown in Figure 9 are influenced to some extent by the selection of the end point for the calculation of $\overline{u^2}$. But $\overline{p^2}/\rho^2$ falls off so rapidly at high obliquity that an enormous change in $\overline{u^2}$, far beyond what appears possible, would be necessary to alter this result in any significant way. If we use the value of u^2 at the edge of the viscous region then the ratio $(\overline{p^2}/\rho^2)/\overline{u^2}$ increases with increasing frequency. This is illustrated in Figure 9 where we have added a curve at $f = 300$ which can be compared with the curve for $f = 50$ (i.e. $Y_s = 5.2$ for both frequencies).

Actually it is doubtful that the linear theory gives a satisfactory value for $\overline{p^2}$ where the ratio $(\overline{p^2}/\rho^2)/\overline{u^2}$ is very small. Under these circumstances, the pressure terms in the momentum equations are given by the small difference between large velocity terms. The neglected nonlinear terms in the equations of motion will then have a much stronger influence on the calculation of the pressure field than on the calculation of the velocity field. This probably means that the linear theory is not accurate at low frequencies and high obliquity, so that little weight should be given to specific values of obliquity at which theory and experiment coincide.

4.3 Space correlation measurements

Grant[9] has measured the nine components of the double velocity correlation in a boundary layer. One set of measurements was taken close to the wall in the outer region of the sublayer $y^+ = 30, 60$. These correlations should select the strongly aligned character of the disturbances and at the same time be consistent with the properties of the elementary solutions. A fairly direct comparison with the u and w velocity correlations in the x and z directions can be made. This is because the elementary solutions indicate that the ratio $\overline{w^2}/\overline{u^2}$ at the edge of the sublayer is primarily a function of obliquity and only has a weak dependence on the frequency. Grant's results for the u and w correlations in the x and z directions are reproduced in Figure 10. ($\delta_0 = 0.69\delta$, r the wire separation.)

These correlations indicate that the large scale components are at high obliquity. The covariance R_{11} for u, has a large correlation distance in the x direction, but a much smaller correlation distance in the z direction. Furthermore, the R_{33} correlation distance for w in the x direction is also considerably smaller than for R_{11} in the x direction. Therefore according to these correlations the large scale disturbances have a very small ratio, w/u. This is consistent with Figure 10 where $\overline{w^2}/\overline{u^2} \to 0$ as $\theta \to 90^\circ$.

Now the normalized $\overline{w^2}$ spectrum at the edge of the sublayer can be computed from the R_{33} correlation in the x direction where

$$F_{\overline{w^2}}(k_x) = \overline{w^2}\,\frac{2}{\pi}\int_0^\infty R_{33}(r,0,0)\cos k_x r\,dr\ .$$

This can be converted to a frequency spectrum using the assumption that $U_w = 0.8U_1$. The $\overline{u^2}$ spectra in different boundary layers can be roughly correlated using fU/δ as the dimensionless frequency and $(U/\delta)F(f)$ as the spectral function. In this way we have estimated the u^2 spectrum appropriate to Grant's boundary layer. Assuming that the integrated value of $w^2/u^2 \approx 0.5$ as for Klebanoff, we arrive at the u^2 and w^2 spectra shown in Figure 11 where the u^2 spectrum has been normalized.

A few points of comparison can be made with Klebanoff's $\overline{u^2}$ spectrum at the edge of the sublayer. For Grant's boundary layer an eddy scale $L \approx (1/2)\delta$ corresponds to $f = 200$ c/s where the frequency range $0 < f \leq 200$ includes 92% of the u^2 energy. Based on the previous discussion, we believe that $U_w = 0.8U_1$ is a reasonable approximation for $f < 200$ c/s. As anticipated, w^2/u^2 is very small at low frequencies.

The fluctuation velocity $\overline{w^2} = \overline{u^2}$ at $f = 265$ c/s, where $0 < f \leq 265$ c/s includes 95% of the u^2 energy, and 40% of w^2 energy. According to Figure 10 this cross over point is still at a fairly high obliquity. Most of the w^2 energy is found at high frequencies and lower obliquities. The comparative extent of the R_{33} covariance in the x and z direction appears to support this conclusion.

It appears then, that the pattern of the velocity covariances is consistent with a strong alignment of the energy containing disturbances in the flow direction.

The pressure velocity space correlation should also have a strong dependence on obliquity according to these solutions. The calculated variation of the correlation coefficient $\overline{pu}/p'u'$ with θ at $f = 70$, close to the wall, is shown in Figure 12. It is important to limit the calculation to the inner portion of the viscous region since the outer boundary condition affects the p, u correlation in the outer part of the viscous region. Near $\theta = 65^\circ$, the correlation coefficient changes sign.

Negative pressure-velocity correlations near the wall have been observed by Kawamura[11]. Spectral measurements indicated increasingly negative correlation coefficients with decreasing frequency. However more detailed measurements in the sublayer would provide a better basis for comparison with the calculations.

5. CONCLUSIONS

The structure of the turbulence field outside the sublayer leaves its footprint inside the sublayer and on the wall. This can be readily seen by examining the properties of the elementary Fourier components at different wave numbers and angles of obliquity. The relative magnitude of fluctuating quantities depends on the obliquity of the disturbance. At high obliquity, the convective action of the mean flow reduces the w^2 fluctuation associated with a Fourier component. As a result

as $\theta \to 90^{o}$, $\overline{w^2} \to 0$ and the ratio $\overline{w^2}/\overline{u^2} \to 0$. Also, the ratio of the pressure field p^2 in the sublayer to the velocity fluctuation at the edge of the sublayer decreases drastically at high obliquity. By $\theta = 80^{o}$, this ratio has already dropped two orders of magnitude below the value of the ratio at $\theta = 0^{o}$. As $\theta \to 90^{o}$, $p^2 \to 0$ . . A detailed comparison of these theoretical results with available experimental measurements indicates that the energy-containing eddies in the sublayer are strongly aligned with the flow direction.

Correlations of fluctuating quantities also depend on the obliquity. A particularly strong case is the variation of the correlation between p and u . The correlation coefficient $\overline{pu}/p'u'$ changes sign near $\theta = 65^{o}$ going from near +1 to near -1. Additional measurements in the sublayer are needed to compare with these calculations.

There appear to be inherent limitations to the linear representation. Experimentally, the variation of u^2 and w^2 is small just outside the sublayer. Further, we regard the correlation coefficient $\overline{uv}/u'v'$ as a fundamental property of a fully turbulent flow. Solutions with almost vanishing viscous action outside the sublayer, do not satisfy either of these conditions at the edge of the viscous region. On the other hand, the solutions in the inner part of the viscous region and the more dramatic effects of obliquity appear to be insensitive to the particular outer boundary conditions that are used.

Our view that the principal source of the energy-containing disturbances in the sublayer is the outer flow does not preclude the presence of other disturbances in the sublayer. The local flow of energy from the mean flow to the turbulence will modify the fluctuation field. Also Kline et al[12] have observed apparently self-excited longitudinal flow structures in the "laminar" sublayer. $y^{+} < 12$. However, the spacing of these disturbances is of the order of the sublayer thickness and it seems to us unlikely that they make any significant contributions to the energy-containing motions except very close to the wall.

REFERENCES

1. Sternberg, J. — J. Fluid Mech. Vol.13, 1962, p.241.
2. Klebanoff, P.W. — NACA Tech. Note No.3178, 1954.
3. Favre, A.J. — J. Fluid Mech. Vol.3, 1958, p.344.
4. Willmarth, W.W. — NASA Memo No.3-17-59-W, 1959.
5. Bull, M.K. — University of Southampton A.A.S.U. Report 234, 1963.
6. Laufer, J. — NACA Tech. Note No.2954, 1953.
7. Townsend, A.A. — *The Structure of Turbulent Shear Flow.* Cambridge University Press, 1956, p.101.
8. Townsend, A.A. — *Boundary Layer Research Symposium.* International Union of Theoretical and Applied Physics, Springer, Berlin, 1958.
9. Grant, H.L. — J. Fluid Mech., Vol.4, 1958, p.149.
10. Stewart, R.W. — Canadian Journal of Physics, Vol.34, 1956, p.722.
11. Kawamura, M. — J. Sci, Hiroshima University Ser. A, Vol.24, 1960, p.403.
12. Runstadler, P.W. et alii — Department of Mechanical Eng., Stanford University, Report MD-8, 1963.

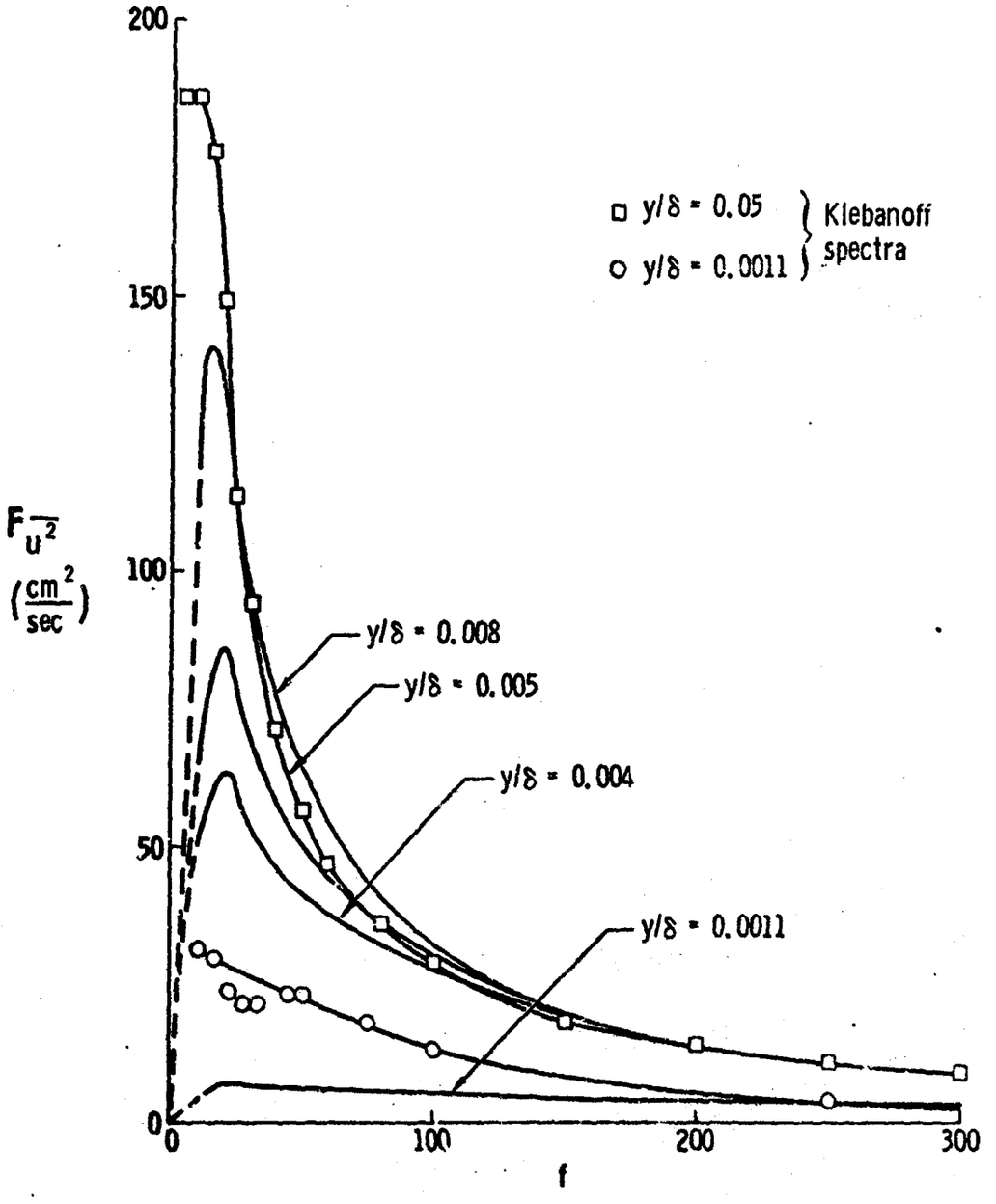

(a) Energy spectra in the sublayer

Fig. 1 Comparisons with simplified theory

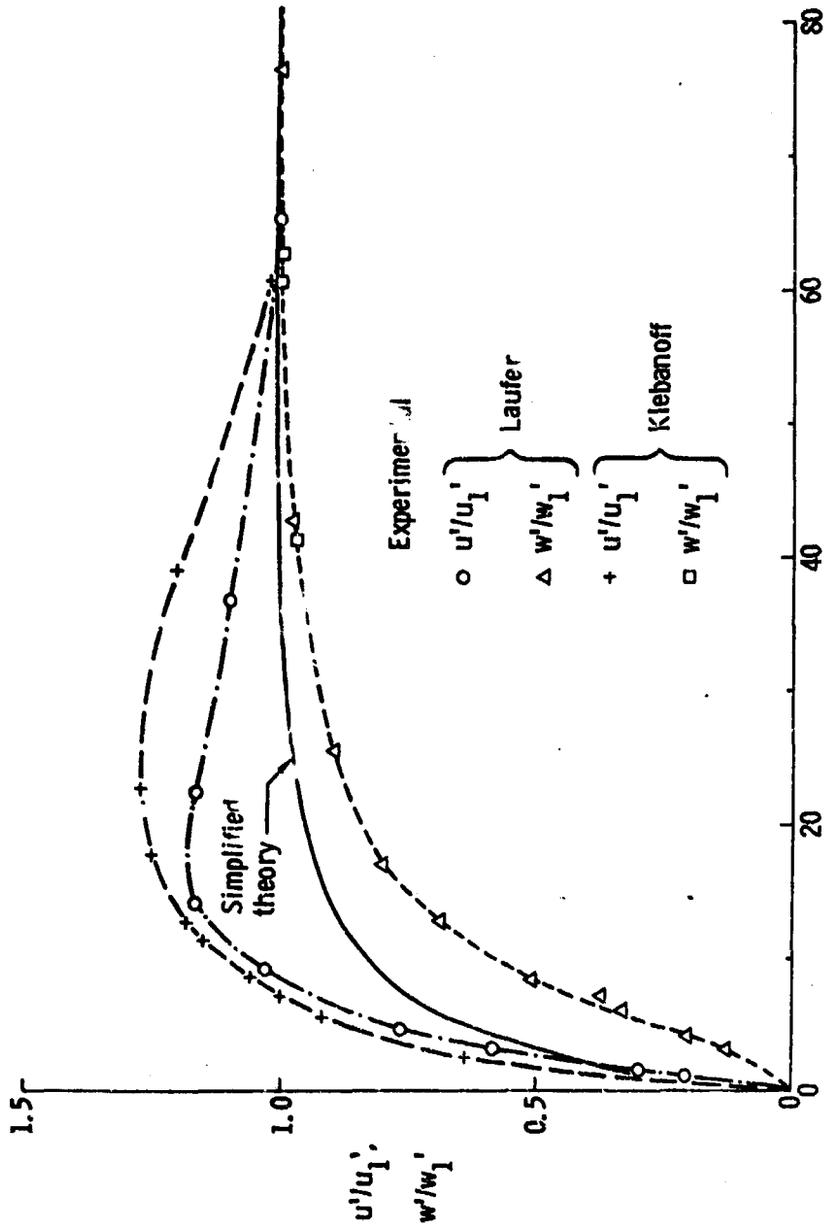

(b) Fluctuation levels across the sublayer

Fig. 1 Comparisons with simplified theory

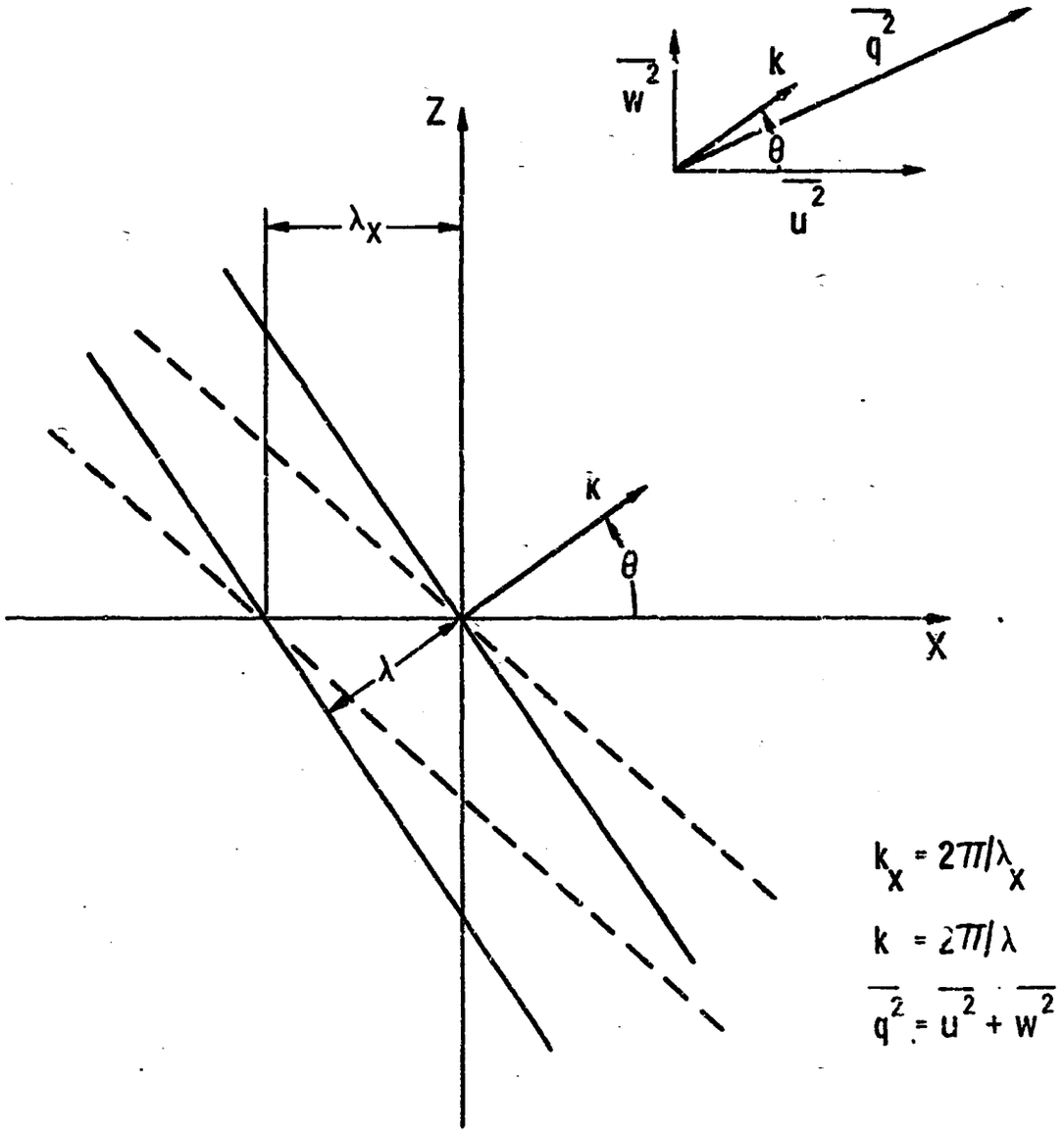

Fig. 2 Assumed form of Fourier components

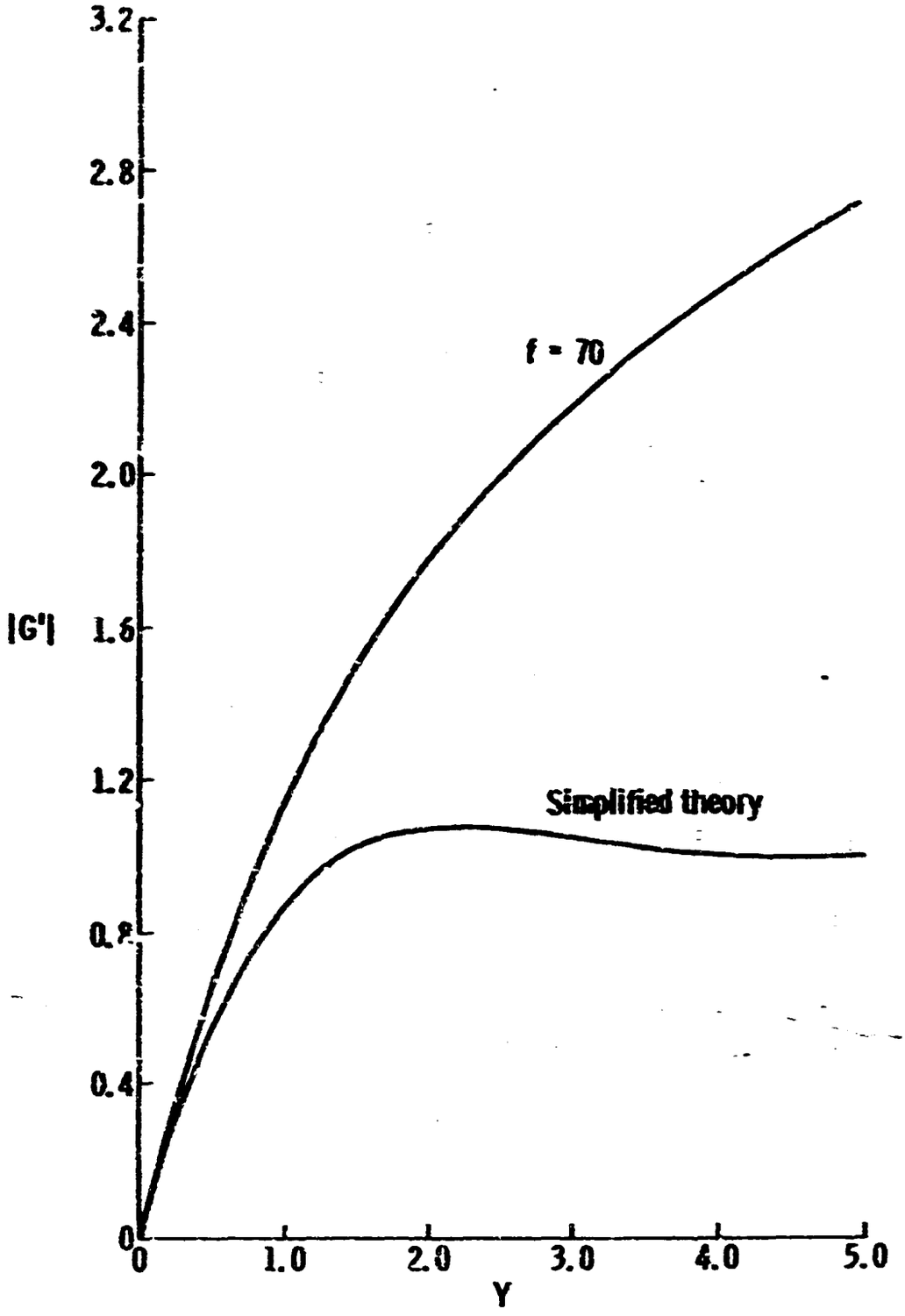

(a) Variation of disturbance velocity

Fig. 3 Two-dimensional component in viscous region

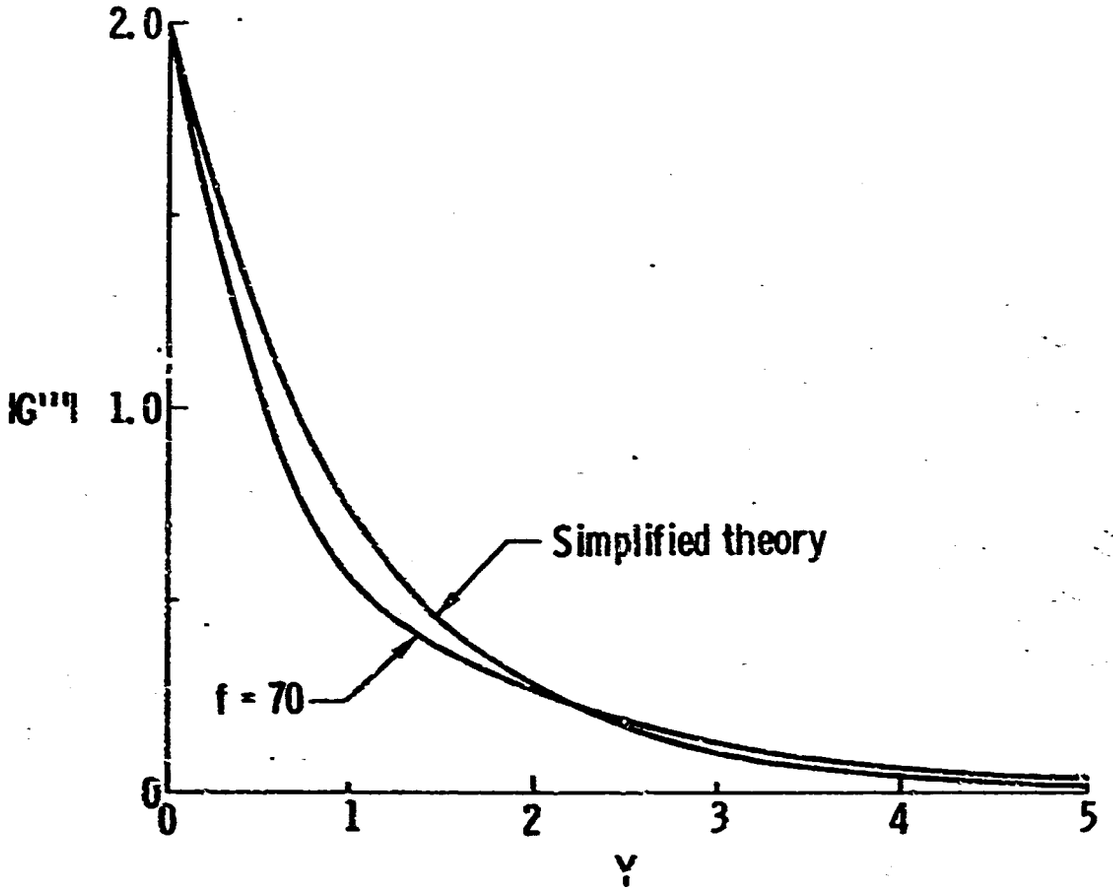

(b) Distribution of viscous term

Fig. 3 Two-dimensional component in viscous region

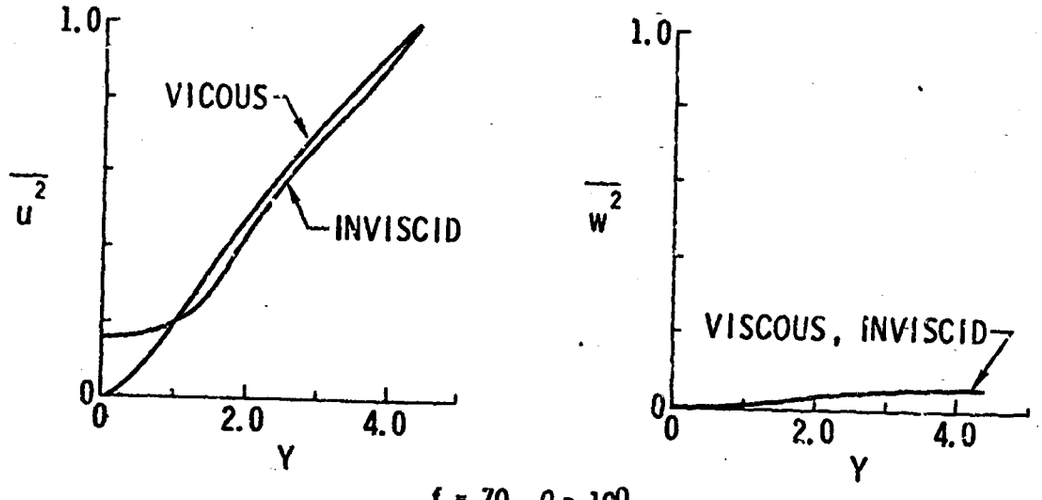

f = 70, $\theta = 10^0$

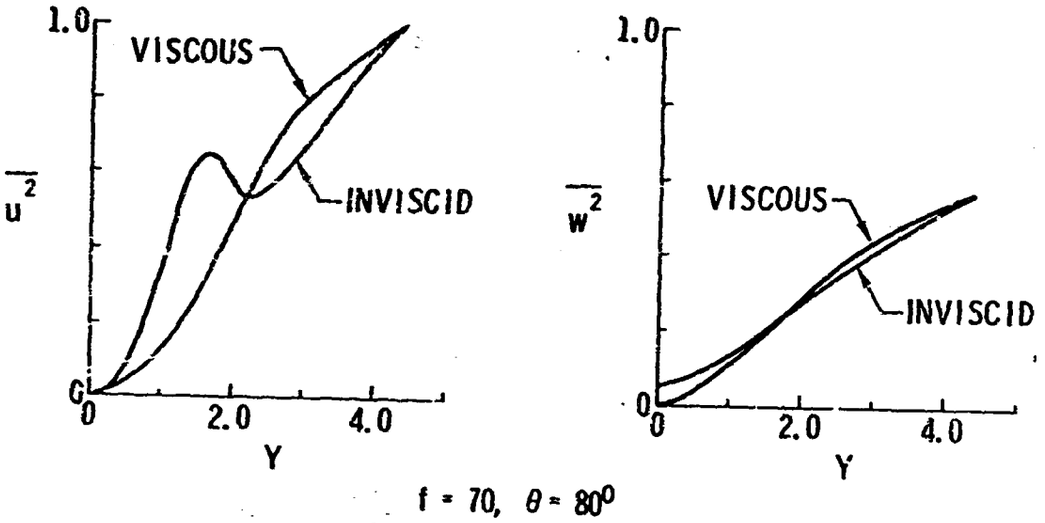

f = 70, $\theta = 80^0$

Fig. 4 Comparison of viscous and "inviscid" solutions

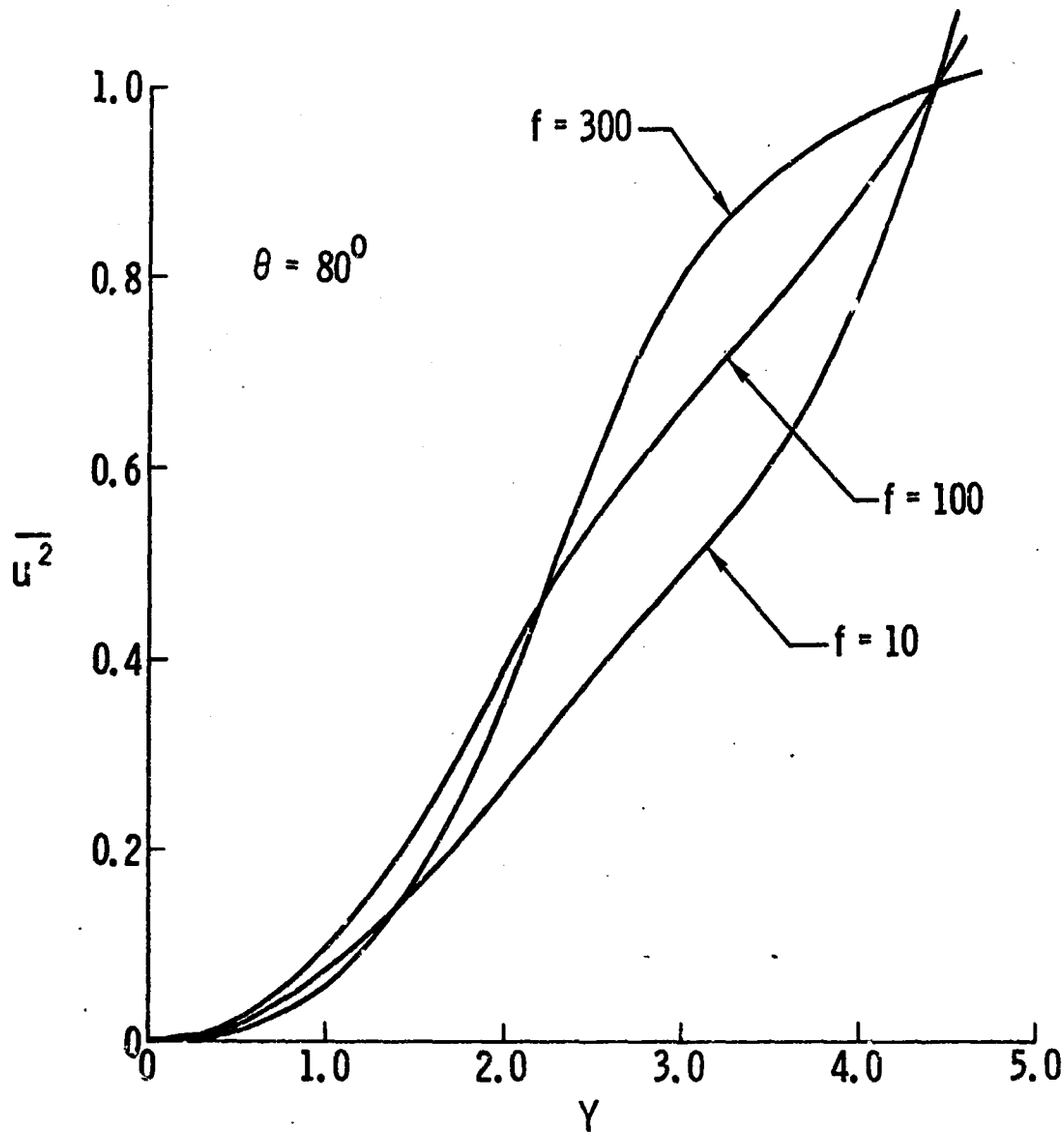

Fig. 5 Effect of frequency on velocity variation in viscous region

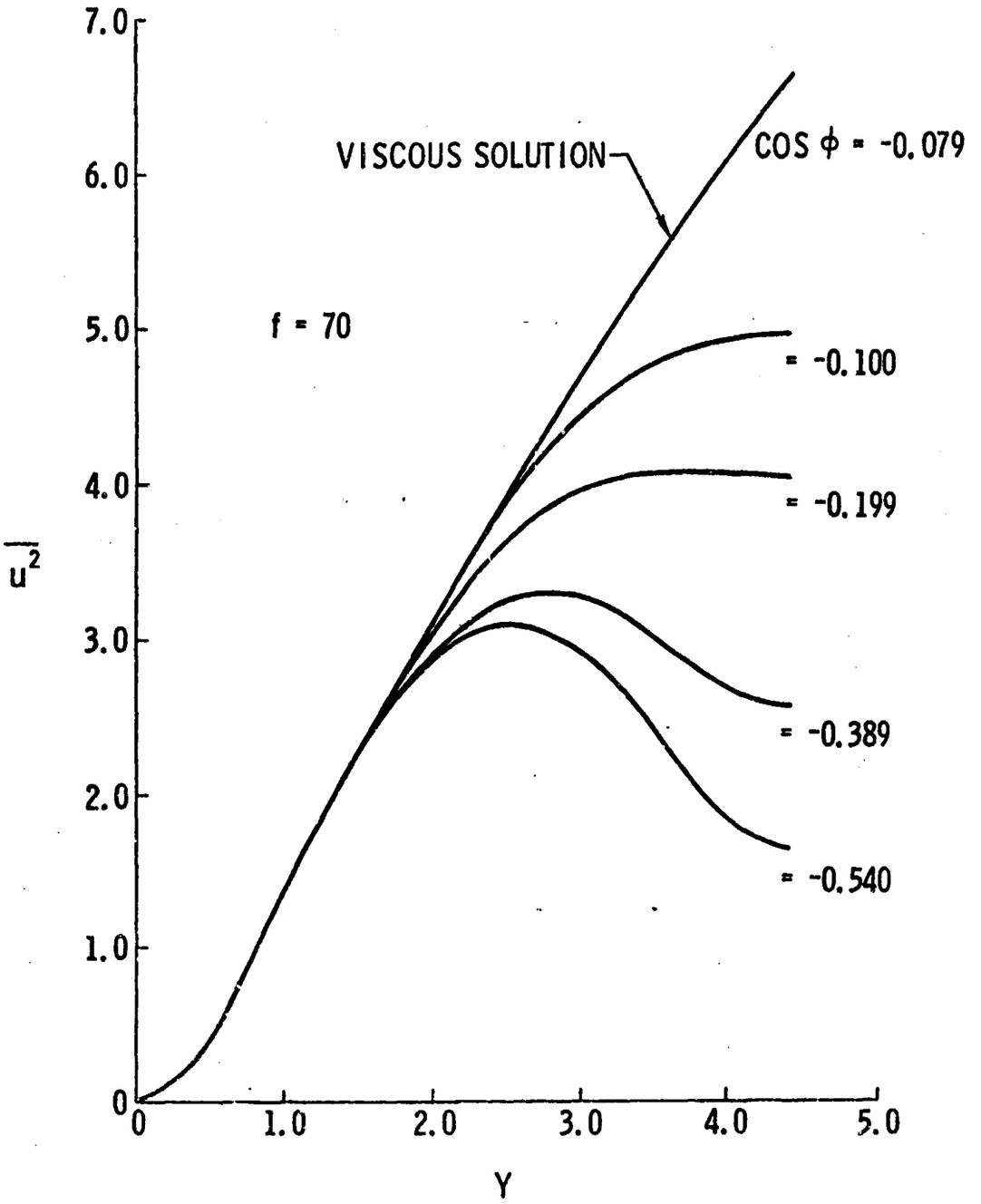

Fig.6 Effect of outer boundary conditions on velocity distribution

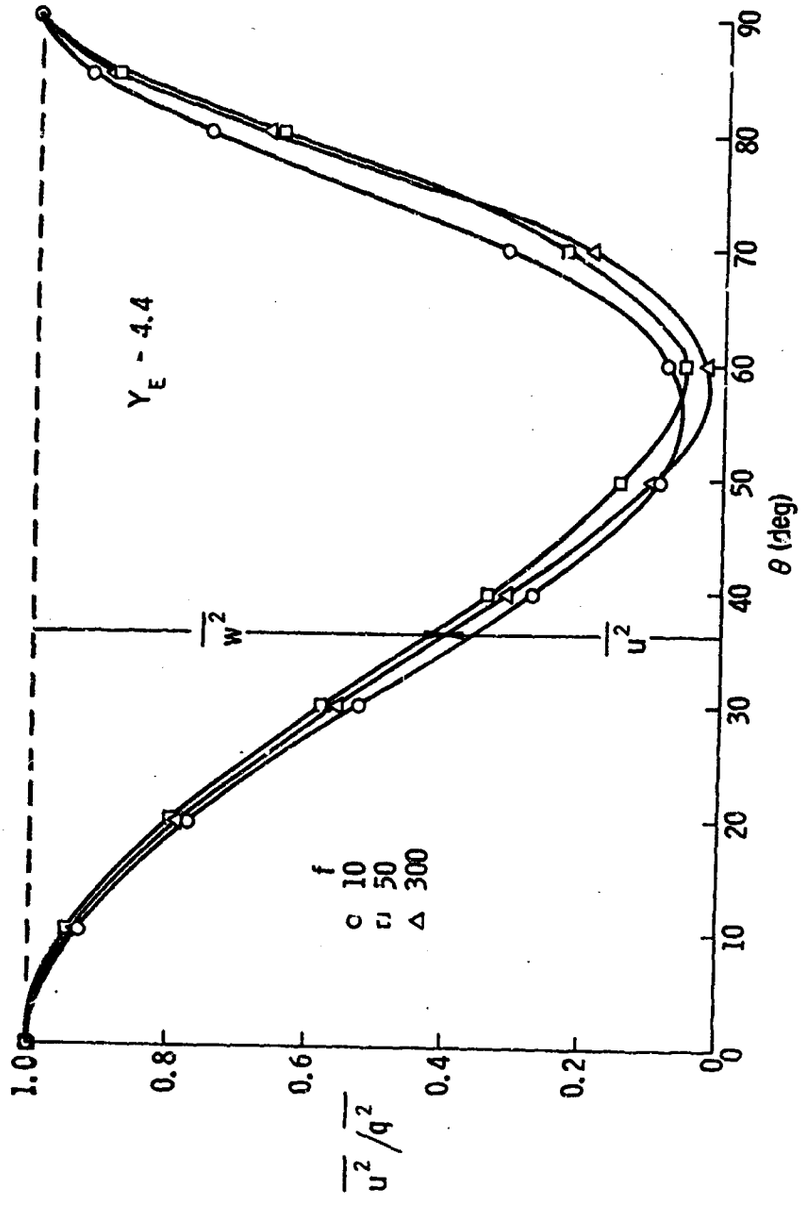

Fig.7 Velocity components at edge of viscous region

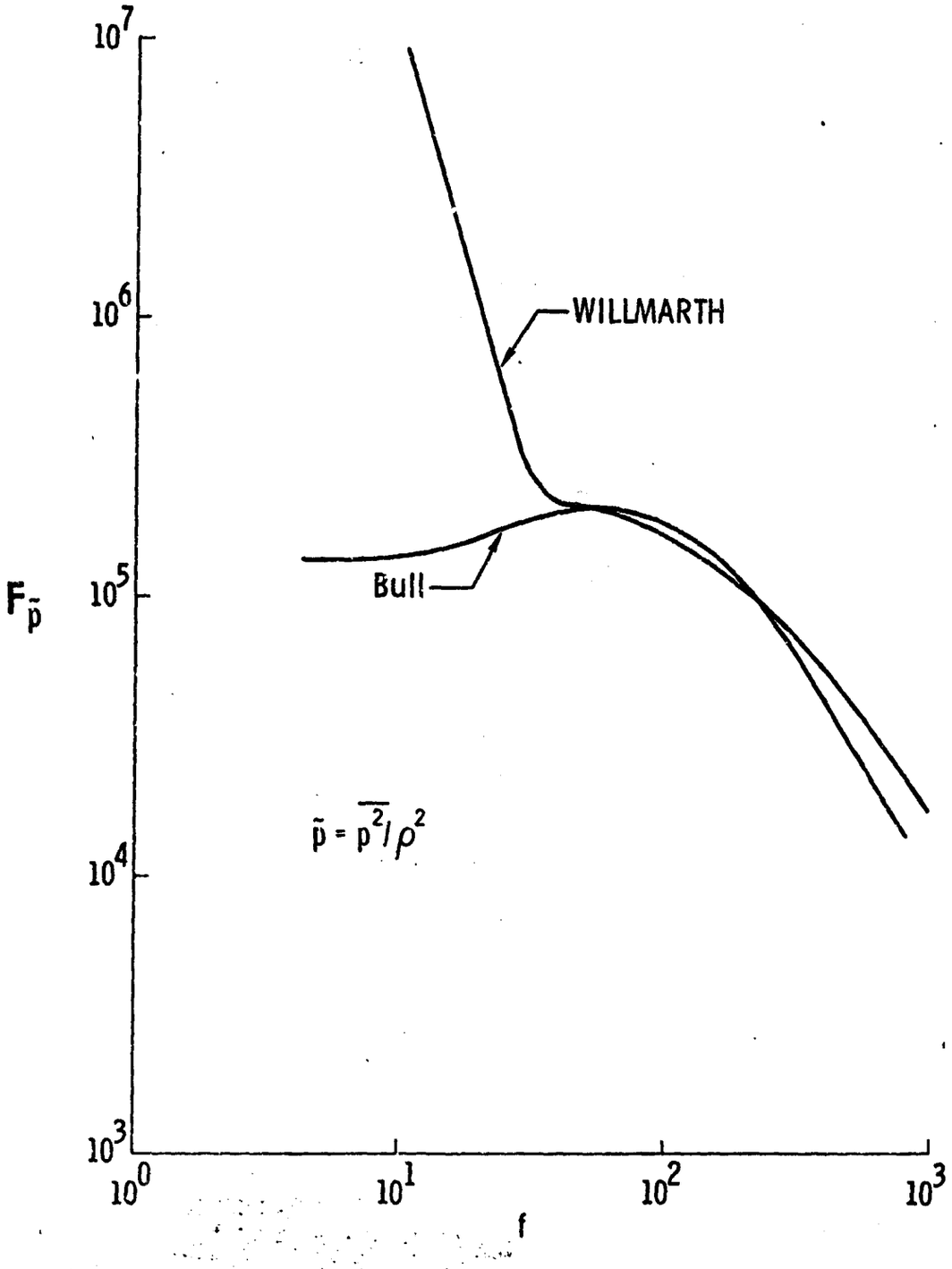

Fig. 8 Experimental data for wall pressure fluctuation spectra

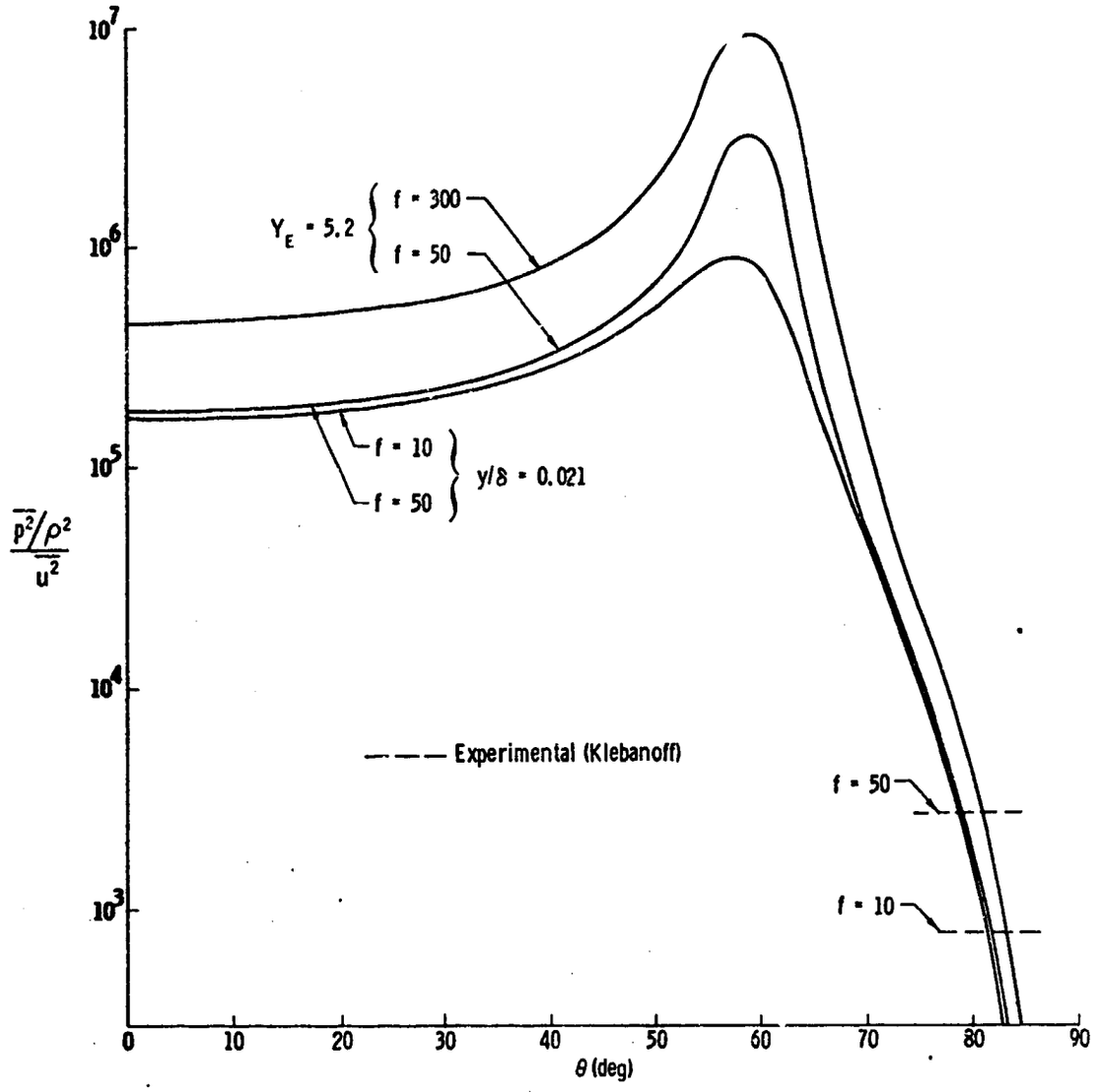

Fig. 9 Theory and experiment for relative magnitude of pressure and velocity fluctuations

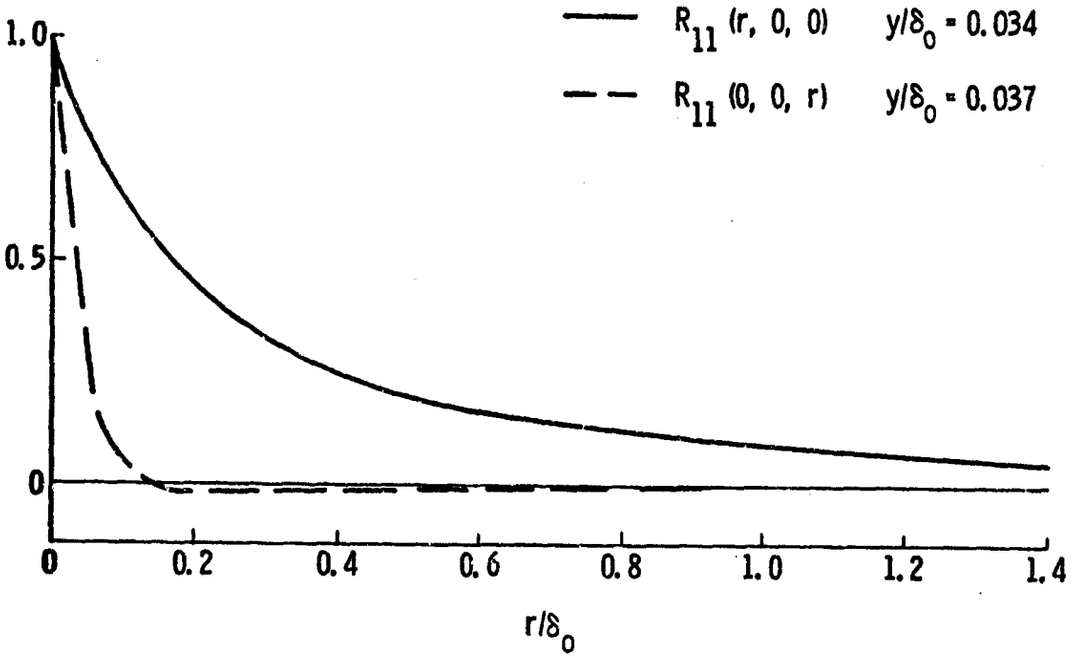

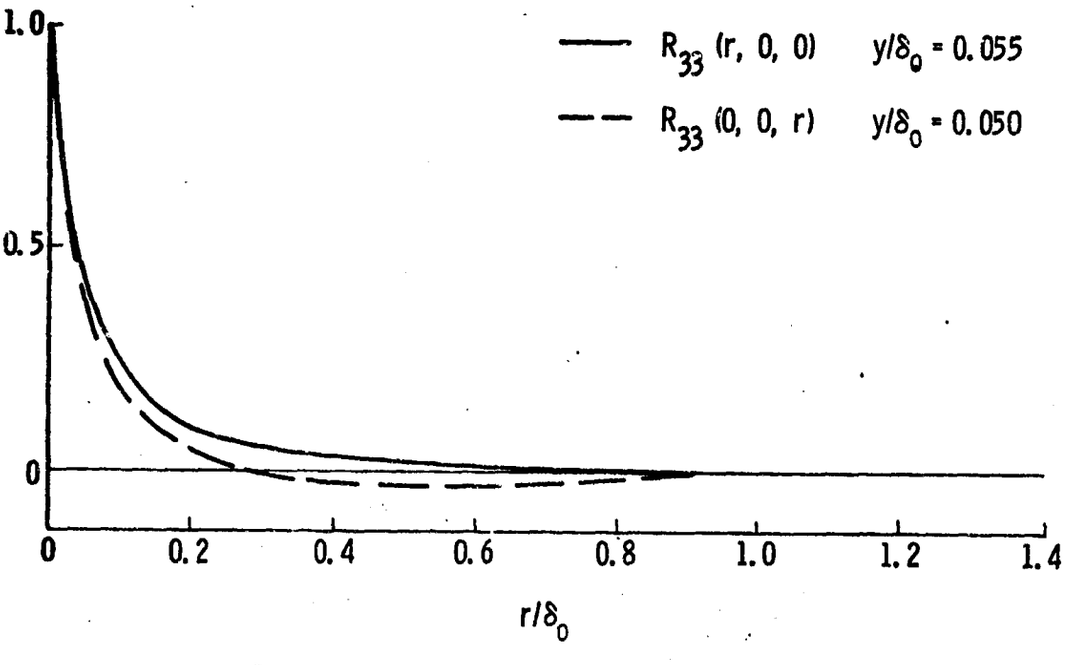

Fig. 10 Correlation measurements near the edge of the sublayer from Grant

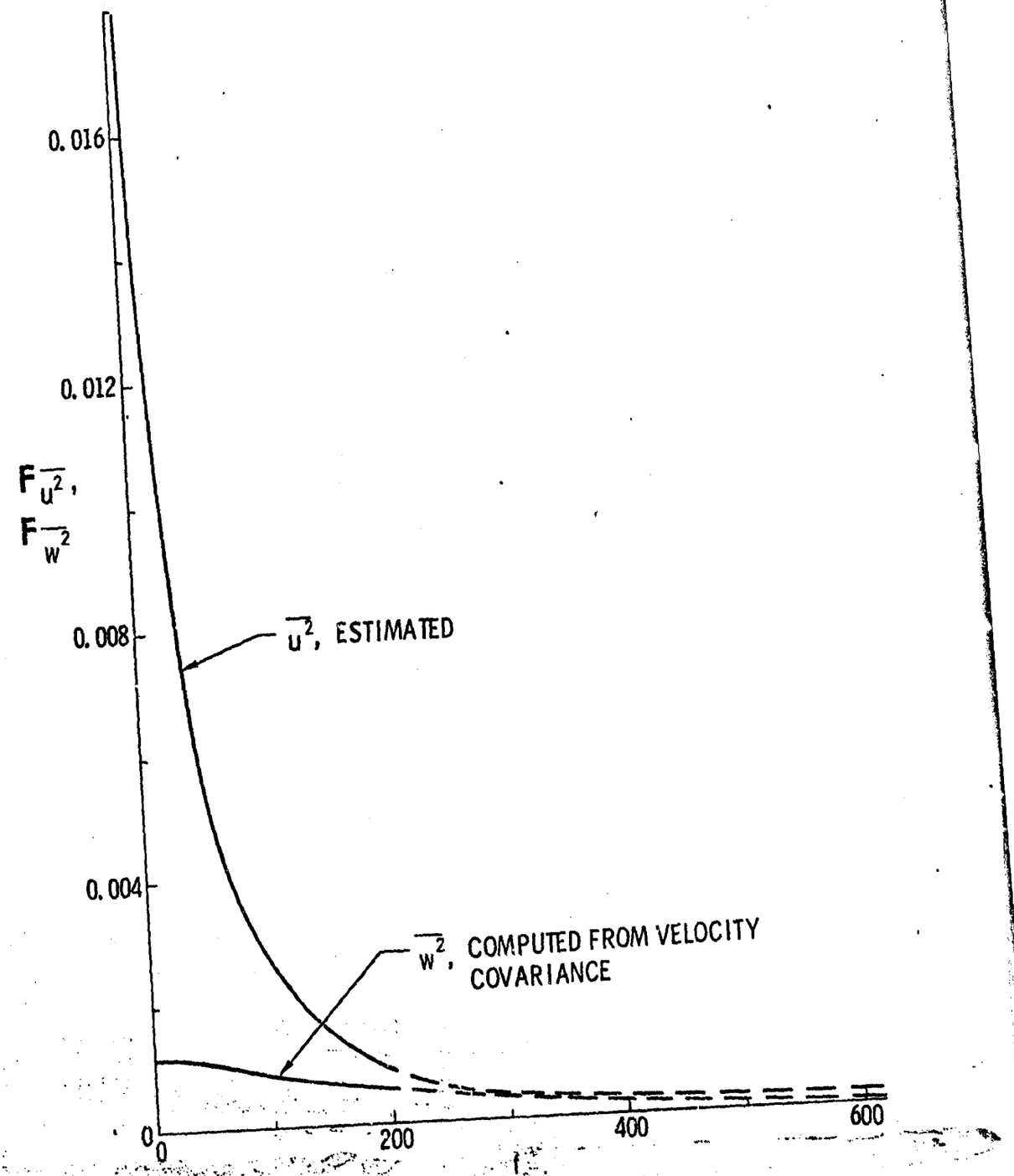

Fig. 11 Calculated spectra at edge of sublayer using Grant's correlation measurements

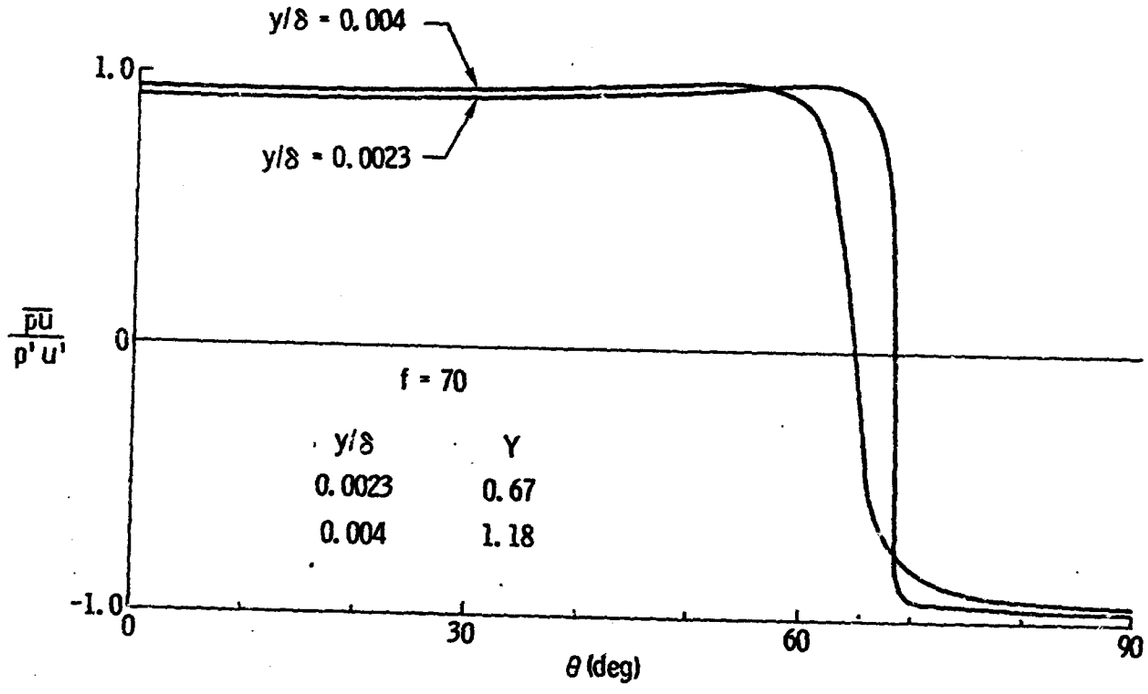

Fig. 12 Effect of obliquity on pressure velocity correlation

HEAT TRANSFER AND TEMPERATURE DISTRIBUTION IN TURBULENT BOUNDARY LAYERS AT SUPERSONIC AND HYPERSONIC FLOW

by

J.C. Rotta

Aerodynamische Versuchsanstalt Göttingen, Germany

SUMMARY

Theories to predict the rate of heat transfer and temperature distribution are reviewed. On the basis of these considerations, available experimental data are compared and turbulent Prandtl numbers are calculated from the experimental survey data. As far as turbulent boundary layers with zero heat transfer are concerned, the temperature distributions are in good agreement with predictions from Crocco's relation, and the integral of total energy is satisfied with a reasonable degree of accuracy. The turbulent Prandtl numbers are found in agreement with observations at subsonic and incompressible flow tests. When boundary layers with heat transfer are considered, remarkable differences are observed between boundary layers on nozzle walls and on a flat plate. The turbulent Prandtl numbers indicate extremely low turbulent heat transport rates in proximity of the wall when compared with the momentum transport. No evidence can be furnished that the Crocco relation provides a satisfactory approximation to the temperature distribution in supersonic turbulent boundary layers with heat transfer.

SOMMAIRE

L'auteur passe en revue les théories sur lesquelles sont basées les prédictions de taux de transfert de la chaleur et de répartition des températures. Il compare ensuite les données expérimentales existantes et calcule les nombres de Prandtl pour les couches turbulentes à partir des résultats de l'étude expérimentale. Pour les couches limites turbulentes à transfert de chaleur nulle, les répartitions de température correspondent bien aux prédictions basées sur la relation de Crocco, et l'intégrale de l'énergie totale bénéficie d'un degré d'exactitude raisonnable. Les nombres de Prandtl pour les couches turbulentes se révèlent concorder avec les observations effectuées au cours d'essais en écoulement subsonique et incompressible. Lorsque l'on considère des couches limites avec transfert de chaleur, on observe des différences remarquables entre les couches limites sur les parois de la tuyère et sur une plaque de surface plane. Les nombres de Prandtl pour les couches turbulentes indiquent des taux de transfert de chaleur extrêmement faibles au voisinage de la paroi, en comparaison du transfert de quantité de mouvement. On ne peut prouver que la relation de Crocco fournit une approximation satisfaisante pour la répartition des températures dans les couches limites turbulentes supersoniques, avec transfert de chaleur.

CONTENTS

LIST OF TABLES

LIST OF FIGURES

NOTATION

C_1, C_2	constants of integration, Equation (2.16)
c_f	local skin friction coefficient, Equation (2.2)
c_p	specific heat at constant pressure
h_s	total enthalpy, $h_s = c_p T + U^2/2$
Ma	Mach number
Pr	Prandtl number
q	heat flux perpendicular to wall (rate of heat transfer)
q_t	turbulent heat flux
R	radius of body of revolution
r	recovery factor, Equation (2.5)
St	Stanton number (heat transfer coefficient), Equation (2.1)
T	temperature
T_e	equilibrium wall temperature (zero heat transfer), Equation (2.5)
T_s	stagnation temperature (total temperature), $T_s = T + U^2/2c_p$
U	mean velocity parallel to the surface (x-direction)
V	mean velocity perpendicular to the surface (y-direction)
x, y	cartesian coordinates, x = distance from leading edge of plate, y = distance from surface
γ	ratio of specific heats
δ	total boundary layer thickness
δ_1	displacement thickness, Equation (2.9)
δ_2	momentum thickness, Equation (2.10)
δ_h	total enthalpy loss thickness, Equation (2.11)
μ	viscosity

ρ	density
σ_t	turbulent Prandtl number, Equation (4.1)
τ	shearing stress
τ_t	turbulent shearing stress

Subscripts

w	condition at the wall
∞	free stream condition

HEAT TRANSFER AND TEMPERATURE DISTRIBUTION IN TURBULENT BOUNDARY LAYERS AT SUPERSONIC AND HYPERSONIC FLOW

J.C. Rotta

1. INTRODUCTION

The knowledge of the boundary layer velocity and temperature distribution is required in order to determine the skin friction and the rate of heat transfer. Widely different assumptions with regard to the velocity profiles of supersonic turbulent boundary layers have been introduced with the various theories, while the estimation of the temperature distribution rests almost exceptionally on the relation to the velocity distribution, as is given by Crocco's solution of the energy equation. This relation has been accepted without major criticism by many investigators. However, recent investigations, made by Peterson[1] and Spalding and Chi[2], have shown again that the prediction of skin friction in boundary layers with heat transfer is afflicted with a considerable degree of uncertainty.

On the other hand, measurements of velocity and temperature profiles in turbulent boundary layers on cooled surfaces at supersonic speeds require a high effort and are time consuming and expensive. These are probably the reasons why relatively few experimental boundary layer investigations, which include temperature surveys, are reported in the literature. Unfortunately, some discrepancies have been observed among the available data and in comparison with theories. A. Walz[3], for instance, compared experimental temperature profiles with those calculated by the Crocco relation and found conflicting differences. Previous comparisons made by this author[4,5] with his theory suffer from shortcomings of the measurements.

It appears thus useful to inspect again the available information. Simple theoretical relationships for heat transfer and temperature distribution are reviewed and available experimental data are considered on the basis of these theories. Particular attention is paid to the temperature distributions in relation to the velocity distributions. No considerations about the velocity profiles (velocity as a function of wall distance) will be made here. Only flows are treated, for which the law of ideal gases is valid.

2. THEORY

2.1 Heat transfer coefficient

When the local rate of heat transfer q_w is non-dimensionally expressed by the heat transfer coefficient or Stanton number

$$St = \frac{q_w}{c_p \rho_\infty U_e (T_e - T_w)} \tag{2.1}$$

and the wall shearing stress τ_w is expressed by the local skin friction coefficient

$$c_f = \frac{\tau_w}{\rho_\infty U_\infty^2/2} \tag{2.2}$$

then from Reynolds' analogy follows

$$St = c_f/2 \tag{2.3}$$

which holds when the molecular and turbulent Prandtl number is equal to unity (see H. Schlichting[6]). A.P. Colburn[7] proposed for turbulent boundary layers in incompressible flow

$$\frac{2St}{c_f} = \frac{1}{Pr^{2/3}} . \tag{2.4}$$

The temperature recovery factor in the relation for the equilibrium temperature

$$T_e = T_\infty \left(1 + r \frac{\gamma - 1}{2} Ma_\infty^2\right) \tag{2.5}$$

is usually calculated from $r = \sqrt[3]{Pr}$.

Equations (2.3) and (2.4) are based on the assumption of constant pressure flow and constant wall temperature, T_w .

Using Newton's friction law and Fourier's law of heat conduction, the following relation is obtained.

$$\frac{2St}{c_f} = \frac{U_\infty (\partial T/\partial y)_w}{Pr(T_e - T_w)(\partial U/\partial y)_w} \tag{2.6}$$

which applies quite generally to any flow on smooth surfaces, when the condition of no slip holds.

Another relationship between heat transfer and skin friction, which is called after N.B. Cohen[3] "modified Reynolds analogy", can be derived by combination of von Kármán's momentum equation and the integrated differential equation of total energy. For

axisymmetric flow (boundary layer on the outer surface of the body), the momentum equation reads

$$\frac{d\delta_2}{dx} + \delta_2 \left[(2 + \delta_1/\delta_2) \frac{1}{U_\infty} \frac{dU_\infty}{dx} + \frac{1}{\rho_\infty} \frac{d\rho_\infty}{dx} + \frac{1}{R} \frac{dR}{dx} \right] = \frac{c_f}{2} , \tag{2.7}$$

and the integrated total energy equation (total enthalpy integral) is

$$\frac{d\delta_h}{dx} + \delta_h \left[\frac{1}{U_\infty} \frac{dU_\infty}{dx} + \frac{1}{\rho_\infty} \frac{d\rho_\infty}{dx} + \frac{1}{R} \frac{dR}{dx} + \frac{1}{h_{s\infty}} \frac{dh_{s\infty}}{dx} \right] = \frac{q_w}{\rho_\infty U_\infty h_{s\infty}} , \tag{2.8}$$

where

displacement thickness
$$\delta_1 = \int_0^\infty \left(1 - \frac{\rho U}{\rho_\infty U_\infty} \right) dy , \tag{2.9}$$

momentum loss thickness
$$\delta_2 = \int_0^\infty \frac{\rho U}{\rho_\infty U_\infty} \left(1 - \frac{U}{U_\infty} \right) dy , \tag{2.10}$$

energy loss thickness (enthalpy convection thickness)
$$\delta_h = \int_0^\infty \frac{\rho U}{\rho_\infty U_\infty} \left(1 - \frac{h_s}{h_{s\infty}} \right) dy . \tag{2.11}$$

Usually the flow is isoenergetic outside the boundary layer, such that the last term in the squared brackets of Equation (2.8) can be neglected. If one introduces

$$\frac{d\delta_h}{dx} = \left(\frac{\delta_h}{\delta_2} \right) \frac{d\delta_2}{dx} + \delta_2 \frac{d(\delta_h/\delta_2)}{dx} \tag{2.12}$$

into Equation (2.8) and eliminates $d\delta_2/dx$ and q_w using Equations (2.7) and (2.1) respectively, the following relation is then obtained (modified Reynolds analogy):

$$\frac{2St}{c_f} \frac{T_e - T_w}{T_{s\infty}} = \frac{\delta_h}{\delta_2} + \frac{2\delta_2}{c_f} \frac{d(\delta_h/\delta_2)}{dx} - \frac{2\delta_h}{c_f} (1 + \delta_1/\delta_2) \frac{1}{U_\infty} \frac{dU_\infty}{dx} . \tag{2.13}$$

For a boundary layer, which develops in a constant pressure field on a surface of constant temperature T_w, it is expected that both velocity and temperature profiles settle to self-preserving shapes and consequently, the ratio δ_h/δ_2 assumes a constant value. In this case, the modified Reynolds analogy of Equation (2.13) reduces to the simple form

$$\frac{2St}{c_f} = \frac{\delta_h}{\delta_2} \frac{T_{s\infty}}{T_e - T_w} . \tag{2.14}$$

The relations Equations (2.3) and (2.4) are designed to predict the heat transfer coefficient in a given flow. Equations (2.6), (2.13), and (2.14), however, can be applied only if the temperature distribution is known otherwise. These relations

can be used also to prove certain properties of experimentally determined temperature and velocity distributions. They will be used in this sense in the subsequent section.

2.2 Temperature distribution after Crocco

Crocco's relation for the temperature distribution is widely applied in laminar as well as turbulent boundary layer theory, and it is generally believed that it gives a good approximation to the actual temperature distribution. The necessary suppositions are the same as underlie the relations Equations (2.3), (2.4), and the reduced form Equation (2.14) of the modified Reynolds analogy, namely constant pressure and constant wall temperature T_w. In addition it is required that the molecular and the turbulent Prandtl number equal nearly unity. If the Prandtl numbers are exactly unity, the local temperature can be expressed as a function of local flow velocity and from the boundary layer equations one obtains

$$\frac{d^2T}{dU^2} + \frac{1}{c_p} = 0 . \tag{2.15}$$

Upon twofold integration this relation yields

$$T = -\frac{U^2}{2c_p} + C_1 U + C_2 \tag{2.16}$$

where C_1 and C_2 are constants of integration. Usually the constants of integration are determined from the boundary conditions

$$T = T_w \quad \text{at} \quad U = 0 ; \quad T = T_\infty \quad \text{at} \quad U = U_\infty .$$

Furthermore, the first term on the right hand side of Equation (2.16) is multiplied by the recovery factor r in order to compensate for the effect of the Prandtl numbers when differing from unity, thus Equation (2.16) can finally be written

$$\frac{T}{T_\infty} = \frac{T_w}{T_\infty} + \frac{T_e - T_w}{T_\infty}\frac{U}{U_\infty} - r\frac{\gamma - 1}{2} Ma_\infty^2 \left(\frac{U}{U_\infty}\right)^2 . \tag{2.17}$$

This is the relation for the temperature distribution most often used in boundary layer calculations. There are, however, some other possibilities to determine the constants of integration of Equation (2.16). The temperature distribution calculated from Equation (2.17) will be denoted as case 1 hereafter.

As the second possibility (case 2) the boundary condition $T = T_\infty$ at $U = U_\infty$ is dropped and instead of this, the constant C_1 is chosen as to bring the slope of the temperature distribution at the surface in agreement with given values of the rate of heat transfer and wall shearing stress

$$C_1 = \left(\frac{dT}{dU}\right)_w = Pr\frac{q_w}{c_p \tau_w} = Pr\frac{2St.}{c_f}\frac{T_e - T_w}{U_\infty} . \tag{2.18}$$

If in addition the first term on the right hand side of Equation (2.16) is multiplied by Pr, an exact solution for the temperature distribution within the sublayer is obtained, which is conditional only upon constancy of the shearing stress in that region. This condition is, however, fulfilled with a reasonable degree of accuracy in the sublayer. This relation can thus be used to predict the temperature distribution near the surface, when the rate of heat transfer and skin friction are known.

A similar temperature distribution results (case 3), if the constant C_1 is determined from the requirement that the calculated temperature distribution meets some experimental survey data nearest to the wall. This distribution may thus give a physically correct extrapolation of the experimental data to the wall, provided, of course, that the measurements are extended into the sublayer. From the slope of this curve at $U = 0$, the value of the ratio of $2St/c_f$ can be calculated, using Equation (2.18).

Finally, in case 4, the boundary condition $T = T_\infty$ at $U = U_\infty$ is satisfied, but $T = T_w$ at $U = 0$ is dropped. The remaining free constant can then be determined in such a way that the calculated temperature distribution agrees with experimental survey data of the outer part of the layer. The idea underlying this procedure is that the condition of constant pressure is fulfilled in the neighbourhood of the survey station, and that partially self-preserving boundary layer profiles exist in the outer part, but the pressure and also T_w may change further upstream. The solution may be interpreted also as a solution of Equation (2.17) with an apparent surface temperature T_{wa} differing from the actual surface temperature T_w. The conditions of the four versions of the Crocco solution are compiled in Table I.

3. COMPARISONS OF EXPERIMENTAL DATA WITH THE THEORY

3.1 Experimental data

The given relations are applied to available experiments. The data considered here are the experimental results of R.K. Lobb, E.M. Winkler, J. Persh[9, 10], E.M. Winkler, M.H. Cha[11, 12], F.K. Hill[13, 14], and G.J. Nothwang[15]. In all these tests, the Mach number distributions have been determined from the Pitot pressure surveys using the Rayleigh formula, and the total temperature distributions have been measured with total temperature probes.

The measurements of Reference [9], [10] have been performed in the turbulent boundary layer on the plane watercooled nozzle wall of the NOL 12 x 12 cm Hypersonic Tunnel. The free stream Mach numbers ranged from 5.0 to 8.2. In addition to the surveys, the temperature gradient in the nozzle wall perpendicular to the wetted surface has been measured, from which the rate of heat transfer could be determined. The measurements of References [11], [12] have been made on a liquid cooled flat plate, which was installed in the same NOL Hypersonic Tunnel, in which the aforementioned tests were carried out. The Mach number is about 5.2. Boundary layer surveys were taken at four different distances x from the leading edge of the plate for three different conditions of heat transfer. As with the measurements described before, heat transfer rates have been determined from measured wall temperature gradients.

F.K. Hill[13], investigated the turbulent boundary layer on the wall of a conical nozzle with 50 mm exit diameter. Nitrogen gas was used as flow medium, while the mentioned NOL-measurements were conducted in air flow. Only for one boundary layer profile, measured near the nozzle exit at a nominal Mach number of 9.07, were the given data sufficiently complete to be used for the purpose intended in this report. The ratio of specific heats is assumed $\gamma = 1.4$ for both air and nitrogen. The Prandtl number was put $Pr = 0.72$, although molecular nitrogen has a somewhat lower Prandtl number.

G.J. Nothwang[15] conducted measurements in the boundary layer with zero heat transfer on a flat steel plate, which was placed in the air stream of Mach number $Ma_\infty = 3.03$ through an 8 x 8-inch supersonic nozzle.

3.2 Heat transfer data

There are three different ways to determine the heat transfer coefficient from the measurements, namely determination from (i) the heat transfer measurements, (ii) the survey data of the sublayer (using the solution case 3 of Table I), and (iii) the modified Reynolds analogy, Equation (2.14). The latter relation is evaluated, after the momentum and energy loss thickness were calculated from the experimental survey data. The density ratio follows from the perfect gas law and constancy of pressure through the layer

$$\frac{\rho}{\rho_\infty} = \frac{T_\infty}{T} . \tag{3.1}$$

For an ideal gas, which is assumed from now on, the enthalpy values may be replaced by the corresponding temperatures. The results are compiled in Table II and III, and may be compared with each other and with the results using Colburn's version of Reynolds analogy.

The rates of heat transfer, determined from the survey data of the sublayer (column b in Table II and III) should be in agreement with the results of heat transfer measurements (column a). But marked discrepancies are observed. With the nozzle wall boundary layers, much lower rates of heat transfer are obtained from the wall slopes of the surveys. With two of the test series even negative values resulted, which are very unlikely to occur actually. In contrast with this, the heat transfer rates determined from the wall slope are in most of the cases of the flat plate experiments appreciably higher than those obtained from the wall temperature measurements, as follows from Table II. These observations raise some doubts with respect to the accuracy of the experiments.

On the other hand, the measured heat transfer rates (column a) are in good agreement with the values predicted from Colburn's version of Reynolds analogy (column d). They are on the average 3 p.c. higher for the flat plate boundary layers, whereas the measured heat transfer rates of the nozzle wall layers are on the average 2 p.c. below those resulting from Colburn's Reynolds analogy.

From a theoretical point of view, the interest exists, in the first place, in boundary layers on a flat plate with constant pressure and constant surface temperature, for which self-preserving velocity and temperature profiles are suggested from

theoretical arguments. If this condition is fulfilled, the rate of heat transfer calculated from the slope at the wall (case 3 of Table I, must agree with that from the modified Reynolds analogy Equation (2.14). The arguments for the existence of self-preserving profiles are strong enough that, in the case of discrepancies, the experiments are suspected rather than the theory. The equality of the two values is, however, a strong criterion, because it requires very accurate results for the whole profile. The heat transfer data, as determined from the sublayer survey data, are plotted versus the ratio $(\delta_h T_{s=})/(\delta_2 T_s)$ on Figure 1. It is seen that the said criterion is verified with reasonable accuracy only by a few of the flat plate profiles. The nozzle wall boundary layer profiles do not comply with this condition.

3.3 Boundary layers with zero heat transfer

When the temperature distributions calculated from the relations of Table I are compared with the experimental results, it should be kept in mind that the experimental data consist of two independent sets of measurements, viz. the Pitot surveys, from which the Mach number distributions are determined, and the stagnation temperature surveys. It appeared suitable for this reason to plot the local stagnation temperature ratio $T_s/T_{s\infty}$ versus the local Mach number ratio Ma/Ma_∞* . The measurement, conducted by G.J. Nothwang[15] in the turbulent layer on a flat plate at $Ma_\infty = 3$ is shown in Figure 2. The experimental data are slightly above the curve calculated from Equation (2.17), which appears to be reasonable. The value of the energy loss thickness δ_h is indeed not exactly zero, as is required by the total energy integral. It has a slightly negative value, viz. $(\delta_h T_{s=})/(\delta_2 T_s) = -0.043$. The NOL measurements include only one case, in which the heat transfer to the wall was zero. This case, labelled as No.1 in Table III, shows excellent agreement with the Crocco solution, case 1. Its value of $(\delta_h T_{s=})/(\delta_2 T_s)$ given in Table III column c, is small enough to be considered in fair agreement with the requirement. Other experimental (e.g. a test by Spivac quoted in Ref. [16]) and theoretical (see Ref. [17]) studies confirm that the actual temperature distribution does not differ greatly from the Crocco relation, case 1, and that the energy integral is fairly well satisfied.

3.4 Boundary layers with heat transfer on a flat plate

From the test arrangement, described in Reference [11] it is to be expected that the flow resembles very much that of a turbulent boundary layer on a semi-infinite flat plate in a uniform supersonic stream. The measurements represented on Figure 3 and 4 show excellent agreement with the Crocco solution, case 1, in the outer part of the layer. At smaller distances from the wall, systematic deviations from Crocco's solution, case 1, in the direction to higher temperatures occur with all measurements. The curves calculated from case 3 of Table I do not join the survey data smoothly, thus they do not provide an appropriate extrapolation of the survey data towards the wall. It must, however, be admitted that the measurements are extended not very deep into the sublayer. The curves, case 2, which are based on the experimental rate of heat transfer, cannot be reconciled with the survey data in proximity of the wall.

The discrepancies between survey data near the wall and the heat transfer measurements can hardly be explained with errors in the effective probe positions,

---

* The available space allows to reproduce only a few examples of the cited measurements here. More comparisons are given in Reference [19].

since relative shifts in probe positions up to 0.5 mm are required in order to remove the discrepancies. The probes used for Pitot pressure and local stagnation temperature were of similar geometry and had half-heights between 0.1 to 0.13 mm, thus they give little rise to suppose substantial errors in the effective probe positions.

3.5 Boundary layers with heat transfer on a nozzle wall

The boundary layers on a cooled nozzle wall are obviously not representative of boundary layers with heat transfer on a flat plate. The measured temperature distributions, represented on Figure 5, exhibit systematic deviations from the Crocco solution case 1, which increase with the rate of heat transfer, i.e. the ratio $(T_e - T_w)/T_e$. Furthermore, the rates of heat transfer, determined from the modified Reynolds analogy, Equation (2.14) and those determined from the sublayer survey data (case 3 of Table I) show differences which also increase with $(T_e - T_w)/T_e$, as is seen from Table III and Figure 1. These deviations are not incompatible with each other. They indicate that they must be caused essentially by the upstream history of the boundary layer on the nozzle wall. The most likely explanation for the observed behaviour of the temperature distributions will be that the thickness of the velocity boundary layer grows slowly under the influence of the falling pressure in the nozzle, the heat transfer, however, is high, such that great energy loss thicknesses and small momentum thicknesses are expected at the same time. This development, typical for the boundary layer on a supersonic nozzle wall, is confirmed by Hill's experiment, the results of which are shown on Figure 6.

It is perhaps interesting to notice that the Crocco solution, case 4 of Table I, represents a fair approximation to measured temperature distribution of the outer part of the layer in most of the cases. The corresponding apparent wall temperatures T_{wa} are, however, considerably lower than the measured wall temperatures. In order to approximate the outer part of Hill's measurements, even a negative value of the apparent surface temperature T_{wa} is required, which has, of course, no real physical meaning.

The temperature distributions calculated from the Crocco solution, case 3 of Table I, join the experimental survey data quite smoothly within the sublayer region (which extends to about $Ma/Ma_\infty = 0.25$), thus providing a good extrapolation of the survey data towards the wall. They show, however, much lower rates of heat transfer than obtained from the heat transfer measurements. In general, the survey data cannot be reconciled with the heat transfer rates determined from wall temperature measurements.

The flattened Pitot tube, used for the surveys of Reference [10], had a half-height of 0.125 mm and the flattened stagnation temperature probe had a half-height of 0.48 mm, such that a shift of a few tenths of a millimeter in the effective positions of temperature probe relative to those of the Pitot probe cannot be excluded. At some of the boundary layers, actually relative shifts of 0.2 to 0.3 mm are sufficient to remove the discrepancies between survey data and the distribution calculated from case 2 of Table I. In other cases, however, greater shifts are necessary. For the measurement at $Ma_\infty = 8.2$ (not shown here) a shift of 0.8 to 1 mm is required to bring the survey data of the sublayer in agreement with the calculated curve of case 2. It thus appears doubtful that errors in probe positioning alone are responsible for the observed differences. The most striking phenomenon is that the discrepancies are in the opposite direction to those of the flat plate boundary layers. No plausible explanation can be suggested.

4. TURBULENT PRANDTL NUMBERS

In order to supplement the comparisons and the preceding discussion, the turbulent Prandtl number as defined by

$$\sigma_t = c_p \frac{\tau_t}{q_t} \frac{\partial T/\partial y}{\partial U/\partial y} , \tag{4.1}$$

has been determined for some of the surveys. This magnitude, which is the ratio of the coefficients for turbulent momentum and heat exchange, gives some insight into the turbulent mixing processes.

The distributions of shearing stress and heat flux can be calculated with the assumption of self-preserving velocity and temperature profiles from the equations for continuity, momentum and total energy of mean flow quantities. After some algebraic calculations, the following relations are obtained:

$$\left.\begin{aligned} \tau &= -\frac{c_f}{2\delta_2}\left(U\int_0^y \rho U\, dy' - \int_0^y \rho U^2\, dy'\right) + c_1 , \\ q &= -\frac{c_f}{2\delta_2} c_p \left(T_s \int_0^y \rho U\, dy' - \int_0^y \rho U T_s\, dy'\right) - U\tau + c_2 \end{aligned}\right\} \tag{4.2}$$

from which the shearing stress and heat flux can be calculated by simple quadratures. The constants of integration, c_1 and c_2, are to be determined from the boundary conditions $\tau = 0$, $q = 0$ for $y = \delta$. The portions produced by the turbulent mixing process are determined from

$$\left.\begin{aligned} \tau_t &= \tau - \mu \frac{\partial U}{\partial y} , \\ q_t &= q - \frac{\mu}{Pr} c_p \frac{\partial T}{\partial y} . \end{aligned}\right\} \tag{4.3}$$

Only boundary layers on the flat plate have been considered. As the only exception the nozzle wall boundary layer with zero heat transfer of Reference [10] is included. On Figure 7 the distributions of the turbulent Prandtl number for the boundary layers with zero heat transfer are plotted as a function of y/δ, and on Figure 8 the σ_t values for the boundary layer on the flat plate at $Ma_\infty = 5.2$ and $(T_e - T_w)/T_e \simeq 0.35$ are given. Although a smoothing procedure was applied to the experimental data before the calculations were carried out, the results show a considerable scatter. The distribution of σ_t after H. Ludwieg[18], which had been obtained from the equilibrium temperature distributions in turbulent pipe flow at high subsonic speeds, is indicated by a dashed curve, where the pipe radius is replaced by the boundary layer thickness δ.

For the boundary layers with zero heat transfer, σ_t is on the average below unity, however σ_t is greater than from Ludwieg's results in the outer part of the layer. Nearer to the wall the flat plate measurements yield lower turbulent Prandtl numbers than Ludwieg's experiments. The results of the nozzle wall layer are - on the average

and in particular close to the wall - higher than the flat plate results. This may perhaps be caused by neglecting the slight pressure gradient in the analysis. The rapid increase of σ_t above unity in the vicinity of the wall has probably no real meaning. All in all the agreement with Ludwieg's results is quite good.

The turbulent Prandtl numbers of the flat plate boundary layers with heat transfer are in most cases lower than unity in the outer region of the layer, but show a very pronounced tendency to rise towards the wall. At the middle of the layer σ_t exceeds already unity and assumes extraordinarily high values in proximity of the wall, thus indicating an extremely low heat transport compared with the momentum transport. This is in gross contradiction to our previous experience from turbulent flow at subsonic speeds. The author is not aware of any other case of turbulent flow, where σ_t exceeds the value of unity. In view of the other deficiencies in the experimental data, which have been mentioned above, the result will be considered with some reservation, as long as it is not confirmed by other experiments.

The turbulent Prandtl numbers for x = 216 mm are remarkably higher than those for the downstream stations. It might be suspected that fully turbulent flow is not established at x = 216 mm. But this is not confirmed by the boundary layers with lower heat transfer.

5. CONCLUSIONS

The most important results of the above investigations may be summarized as follows:

1. The measured temperature distributions in turbulent boundary layers with zero heat transfer satisfy the requirement of vanishing energy loss thickness with sufficient accuracy. The Crocco relation provides a good approximation to the actual temperature distribution. The turbulent Prandtl numbers are in fair agreement with observations at subsonic speeds.

2. The available temperature distributions of flat plate boundary layers with heat transfer are found only in moderate or poor agreement with the modified Reynolds analogy. The measured temperature distributions display unexpected deviations from the Crocco solution. The turbulent Prandtl numbers are greater than unity through the inner half of the layer, and extremely low turbulent heat transport rates are indicated near the wall.

3. The temperature distributions of boundary layers on nozzle walls are not representative of those on flat plates. Obviously the temperature distributions on nozzle walls are severely affected by the upstream history. The measured temperature distributions differ greatly from the Crocco relation. This is an indication that Crocco's relation cannot be applied to boundary layers with pressure gradients.

4. For the boundary layers with heat transfer (on both nozzle wall and flat plate) remarkable discrepancies are observed between measured heat transfer rates and the heat transfer, determined from the sublayer survey data. The measured heat transfer rates are found, however, in agreement with Colburn's version of Reynolds analogy.

5. There is no evidence that the Crocco relation provides a satisfactory approximation to the temperature distribution in supersonic turbulent boundary layers with heat transfer.

The considerations revealed a number of gaps in our knowledge. In addition, obvious shortcomings of the available experimental results shed doubts on the reliability of the conclusions drawn. In order to obtain a more complete and firm picture of the mechanism of turbulent heat transfer, further measurements of temperature distributions over a range of Mach numbers and wall temperatures are needed.

REFERENCES

1. Peterson, J.B., Jr. — *A comparison of experimental and theoretical results for the compressible turbulent-boundary-layer skin friction with zero pressure gradient.* NASA TN D-1795 (1963)

2. Spalding, D.B., Chi, S.W. — *The drag of a compressible turbulent boundary layer on a smooth flat plate with and without heat transfer.* J. Fluid Mech. Vol.18 (1964), p.117-143

3. Walz, A. — *Compressible turbulent boundary layers.* Colloqu. Int. CNRS No.108 Mécanique de la turbulence, Marseille 1961, p.299-352

4. Rotta, J.C. — *Ueber den Einfluss der Machschen Zahl und des Wärmeübergangs auf das Wandgesetz turbulenter Strömung.* Z. Flugwiss. Vol.7 (1959), p.264-274

5. Rotta, J.C. — *Turbulent boundary layers with heat transfer in compressible flow.* AGARD Rep.281 (1960)

6. Schlichting, H. — *Boundary Layer Theory.* McGraw-Hill Book Comp., Inc., New York-Toronto-London. Verl. G. Braun, Karlsruhe, IV. Ed. 1960, 3rd Printing 1962

7. Colburn, A.P. — *A method of correlating forced convection heat-transfer data and a comparison with fluid friction.* Trans. AICHE Vol.29 (1933), p.174-210. Reprinted Int. J. Heat Mass Transfer Vol.7, 1359-1384, 1964

8. Cohen, N.B. — *A method for computing turbulent heat transfer in the presence of a streamwise pressure gradient for bodies in high-speed flow.* NASA MEMO 1-2-59L (1959)

9. Lobb, R.K. et alii — *Experimental investigation of turbulent boundary layers in hypersonic flow.* J. Aero. Sci. Vol.22 (1955), p.1-9

10. Lobb, R.K. et alii — *Experimental investigation of turbulent boundary layers in hypersonic flow.* U.S. Naval Ord. Lab., White Oak, Md., NAVORD Rep. 3880 (1955)

11. Winkler, E.M. Cha, M.H. — *Investigation of flat plate hypersonic turbulent boundary layers with heat transfer at a Mach number of 5.2 (U).* U.S. Naval Ord. Lab., White Oak, Md., NAVORD Rep. 6631 (1959)

12. Winkler, E.M. — *Investigation of flat plate hypersonic turbulent boundary layers with heat transfer.* Trans. ASME, J. Appl. Mech. Vol. 28 (1961), p. 323-329

13. Hill, F.K. — *Boundary-layer measurements in hypersonic flow.* J. Aero. Sci. Vol. 23 (1956), p. 35-42

14. Hill, F.K. — *Turbulent boundary layer measurements at Mach numbers from 8 to 10.* Phys. Fluids Vol. 2 (1959), p. 668-680

15. Nothwang, G.J. — *An evaluation of four experimental methods for measuring mean properties of a supersonic turbulent boundary layer.* NACA TN 3721 (1956)

16. Schubauer, G.B. Tchen, C.M. — *Turbulent Flow In: High Speed Aerodynamics and Jet Propulsion. Vol.V: Turbulent Flows and Heat Transfer.* Princeton N.J. 1959, p. 75-195

17. Rotta, J.C. — *Temperaturverteilungen in der turbulenten Grenzschicht an der ebenen Platte.* Int. J. Heat Mass Transfer Vol. 7 (1964), p. 215-228

18. Ludwieg, H. — *Bestimmung des Verhältnisses der Austauschkoeffizienten für Wärme und Impuls bei turbulenten Grenzschichten.* Z. Flugwiss. Vol. 4 (1956), p. 73-81

19. Rotta, J.C. — *A review of experimental temperature distributions in supersonic and hypersonic turbulent boundary layers with heat transfer.* Aerodynamische Versuchsanstalt Göttingen, Bericht Nr. 64 A 10

TABLE I

Temperature distribution based on Crocco's solution

Case	T/T_∞	Condition for C_2	Condition for C_1	Applicable to	Presented in Fig. 2 to 6
1	$\frac{T_w}{T_\infty} + \frac{T_e - T_w}{T_\infty}\frac{U}{U_\infty} - r\frac{\gamma-1}{2}Ma_\infty^2\left(\frac{U}{U_\infty}\right)^2$		$T = T_\infty$ at $U = U_\infty$	whole layer	———
2	$\frac{T_w}{T_\infty} + Pr\frac{2St}{c_f}\frac{T_e - T_w}{T_\infty}\frac{U}{U_\infty} - Pr\frac{\gamma-1}{2}Ma_\infty^2\left(\frac{U}{U_\infty}\right)^2$	$T = T_w$ at $U = 0$	exp. rate of heat transfer	sublayer	——··——
3	$\frac{T_w}{T_\infty} + C_1\frac{U}{T_\infty} - Pr\frac{\gamma-1}{2}Ma_\infty^2\left(\frac{U}{U_\infty}\right)^2$		survey data of sublayer	sublayer	— — — —
4	$\frac{T_e}{T_\infty} + C_1\frac{U-U_\infty}{T_\infty} - r\frac{\gamma-1}{2}Ma_\infty^2\left(\frac{U}{U_\infty}\right)^2$	$T = T_\infty$ at $U = U_\infty$	survey data of outer part	outer part of the layer	——·——

TABLE II

Heat transfer data of turbulent boundary layers on a flat plate determined from Reference 11

x mm	Ma_∞	$\frac{T_e - T_w}{T_e}$	$\frac{2\,St(T_e - T_w)}{c_f T_w}$ a	b	c	d	Fig.
216	5.21	0.126	0.184	0.260	0.649	0.173	
216	5.14	0.044	-	-0.089	0.829	0.051	
292.5	5.20	0.084	0.109	0.079	0.434	0.108	
368.5	5.26	0.062	0.084	0.123	0.569	0.111	
445	5.29	0.078	0.103	0.018	0.214	0.100	
216	4.98	0.183	0.287	0.436	0.371	0.256	3
216	5.18	0.189	-	-	0.625	0.284	
292.5	5.20	0.179	0.257	0.646	0.485	0.268	
368.5	5.24	0.156	0.237	0.356	0.413	0.222	
445	5.24	0.163	0.245	0.260	0.351	0.236	
216	5.17	0.331	0.603	1.01	0.711	0.60	4
292.5	5.16	0.360	0.710	1.44	0.645	0.690	
292.5	5.10	0.370	-	-	0.626	0.722	
368.5	5.20	0.384	-	-	0.632	0.684	
368.5	5.11	0.357	0.806	1.53	0.750	0.767	
445	5.12	0.340	0.657	0.83	0.542	0.639	

a heat transfer measurements

b from wall slope of temperature profile, case 3 of Table I

c modified Reynolds analogy, Eq. (2.14)

d Reynolds' analogy after Colburn, Eqs. (2.4) and (2.5)

TABLE III

Heat transfer data of turbulent boundary layers on a nozzle wall determined from References 10 and 13

No.	Ma_∞	$\frac{T_e - T_w}{T_e}$	$\frac{2\,St(T_e - T_w)}{c_f T_w}$ a	b	c	d	Fig.
1	4.93		-	-	0.119	- 0.016	
2	5.01	0.224	0.344	0.140	0.729	0.348	
3	5.03	0.374	0.754	0.430	1.35	0.728	
4	5.06	0.420	-	0.447	1.56	0.879	
5	5.75	0.108	0.147	- 0.168	0.474	0.147	
6	5.79	0.238	0.386	- 0.063	0.900	0.384	5
7	5.82	0.379	0.732	0.400	1.51	0.748	
8	6.83	0.326	0.579	0.728	1.14	0.591	
9	6.78	0.438	0.966	0.845	1.62	0.956	
10	6.83	0.444	0.958	0.505	1.89	0.977	
11	6.78	0.499	1.18	0.684	2.04	1.23	
12	7.67	0.488	-	0.553	2.20	1.17	
13	8.18	0.495	1.13	0.331	2.51	1.20	
14	9.07	0.438	-	0.296	2 82	1.12	6

a heat transfer measurements

b from wall slope of temperature profile, case 3 of Table I

c modified Reynolds analogy, Eq. (2.14)

d Reynolds' analogy after Colburn, Eqs. (2.4) and (2.5)

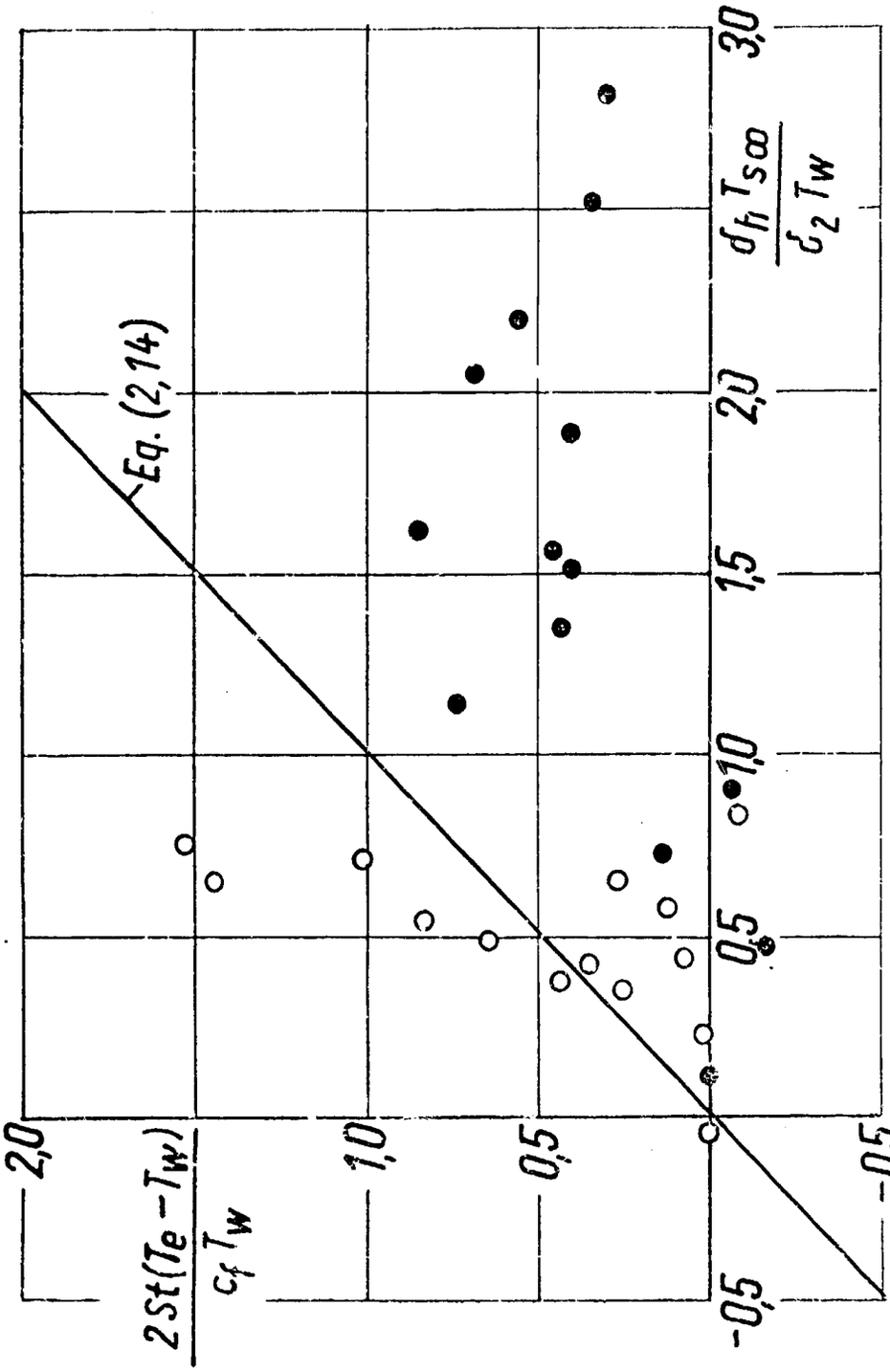

Fig. 1 Dimensionless heat transfer rates, as determined from sublayer survey data, versus the thickness ratio $(\delta_h T_{s\infty})/(\delta_2 T_w)$

● nozzle wall data; ○ flat plate data

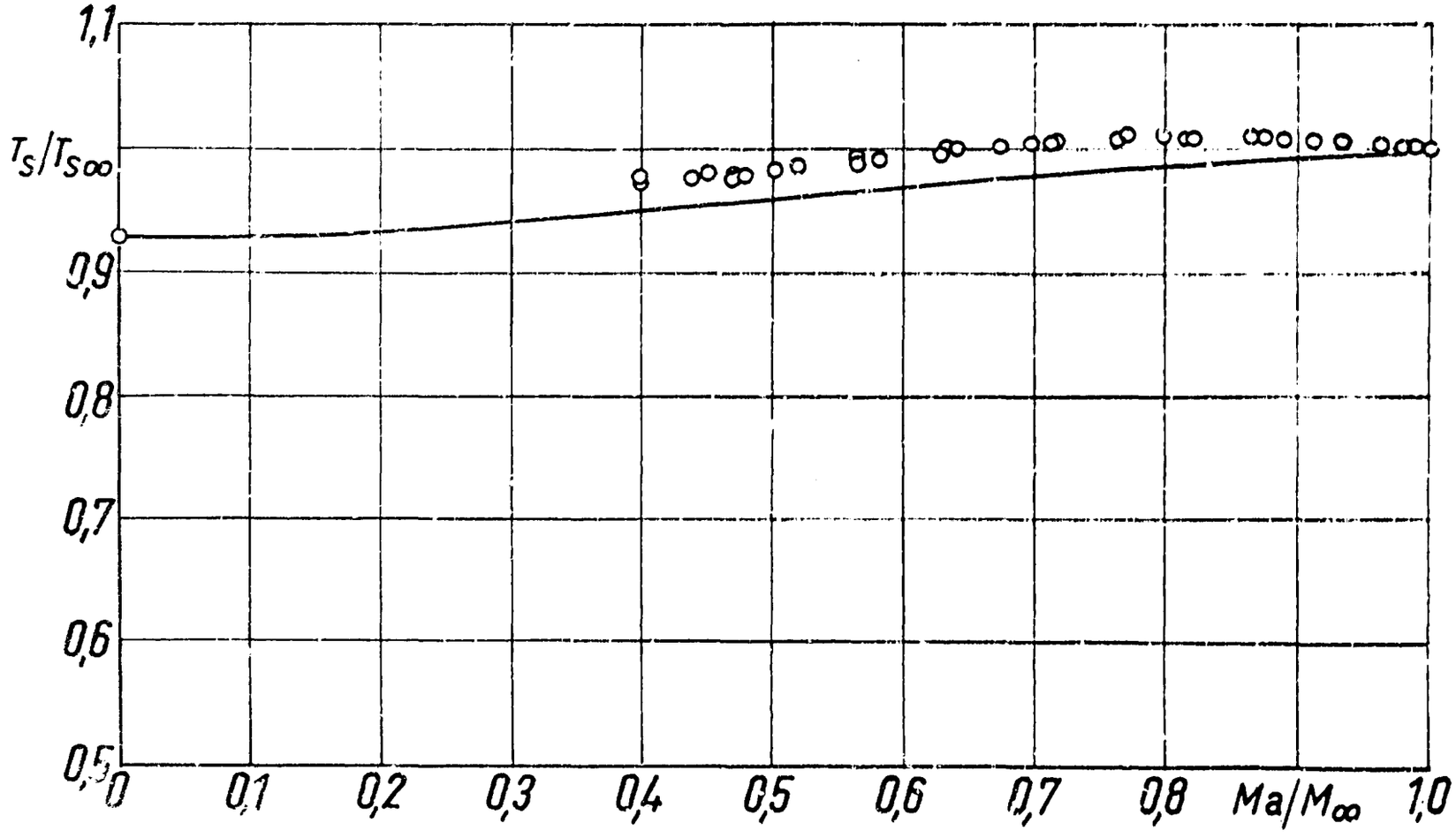

Fig. 2 Local stagnation temperature in the turbulent boundary layer on a flat plate with zero heat transfer, $Ma_\infty = 3.03$, Reference [15]

——— Crocco solution, case 1, $T_w/T_\infty = 2.63$

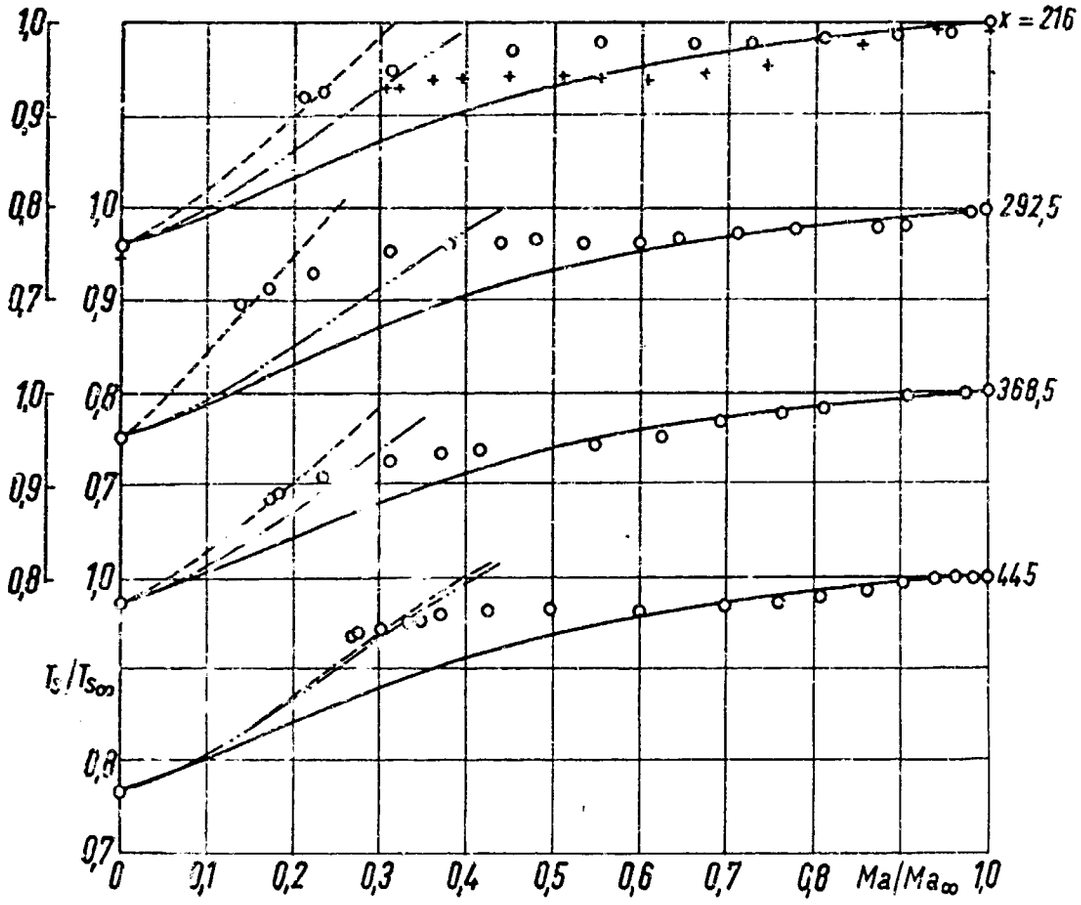

Fig. 3 Local stagnation temperature in the turbulent boundary layer on a cooled flat plate, $Ma_\infty \sim 5.2$, $(T_e - T_w)/T_e \sim 0.17$, Reference [11]

x mm	Ma_∞	$\frac{T_e - T_w}{T_e}$	Symb.	Crocco solution, Table I: Case 1 T_w/T_∞	Case 2 $\frac{2St(T_e - T_w)}{c_f T_w}$	Case 3 $\frac{2St(T_e - T_w)}{c_f T_w}$
216	4.98	0.183	o	4.51	0.287	0.436
216	5.18	0.169	+	-	-	-
262.5	5.20	0.179	o	4.81	0.257	0.646
368.5	5.24	0.156	o	5.02	0.237	0.336
445	5.24	0.163	o	4.97	0.245	0.260

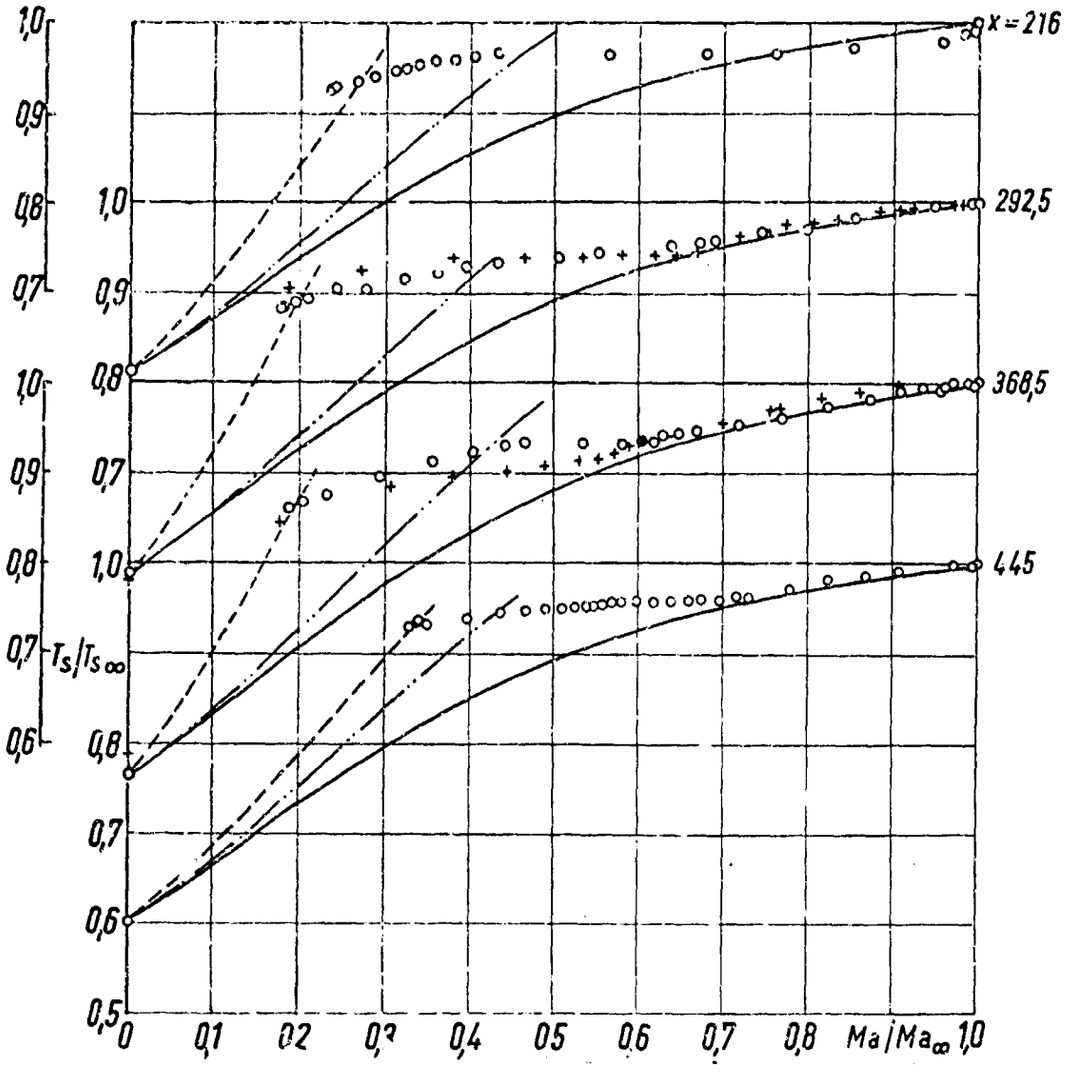

Fig. 4 Local stagnation temperature in the turbulent boundary layer on a cooled flat plate. $Ma_\infty \sim 5.1$, $(T_e - T_w)/T_e \sim 0.35$, Reference [11]

x mm	Ma_∞	$\frac{T_e - T_w}{T_e}$	Syn.b.	Crocco solution, Table I Case 1 T_w/T_∞	Case 2 $\frac{2St(T_e - T_w)}{c_f T_w}$	Case 3 $\frac{2St(T_e - T_w)}{c_f T_w}$
216	5.17	0.331	o	3.89	0.603	1.01
292.5	5.16	0.360	o	3.70	0.710	1.44
292.5	5.20	0.370	+		-	-
368.5	5.20	0.384	+	-	-	-
368.5	5.11	0.357	o	3.51	0.806	1.533
445	5.12	0.340	o	3.76	0.65	0.833

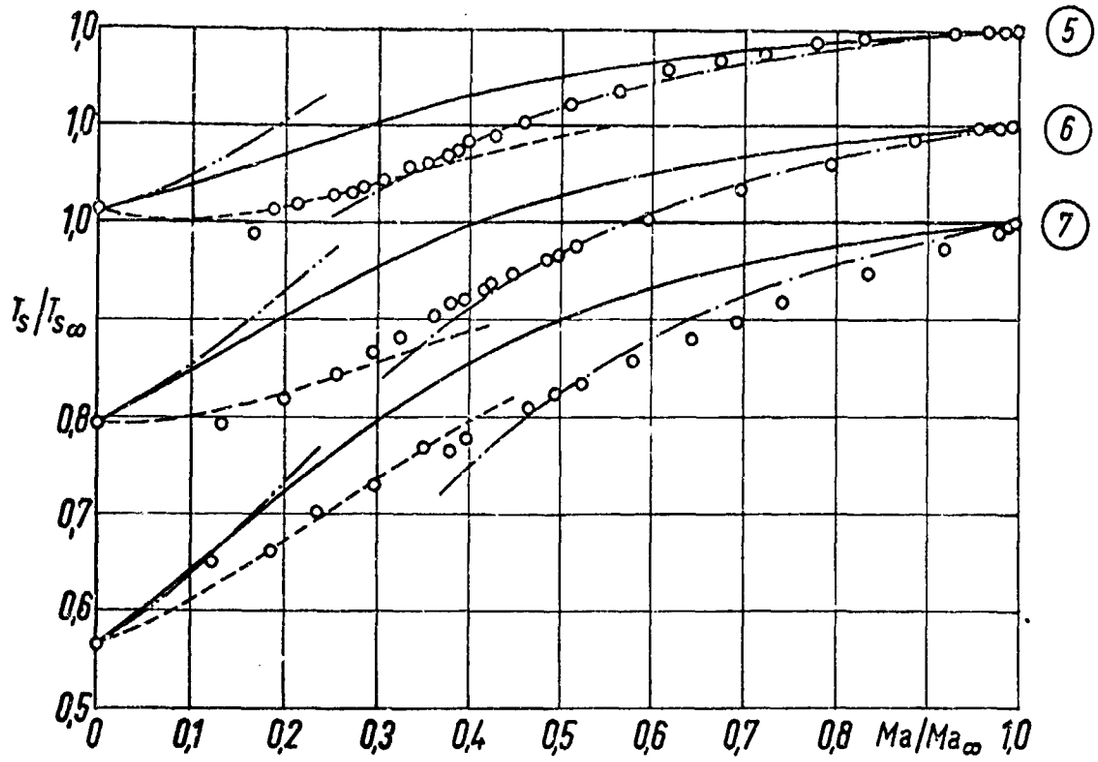

Fig. 5 Local stagnation temperature in the turbulent boundary layer on a cooled plane nozzle wall, $Ma_\infty \sim 5.8$, Reference [10]

Crocco solution, Table I

No	Ma_∞	$\frac{T_e - T_w}{T_e}$	Case 1 T_w/T_∞	Case 2 $\frac{2St(T_e - T_w)}{c_f T_w}$	Case 3 $\frac{2St(T_e - T_w)}{c_f T_w}$	Case 4 T_{wa}/T_∞
			———	—·—·—	— — —	—·—
5	5.75	0.108	6.19	0.147	-0.168	4.99
6	5.79	0.238	5.35	0.386	-0.063	3.50
7	5.82	0.379	4.41	0.732	0.40	2.46

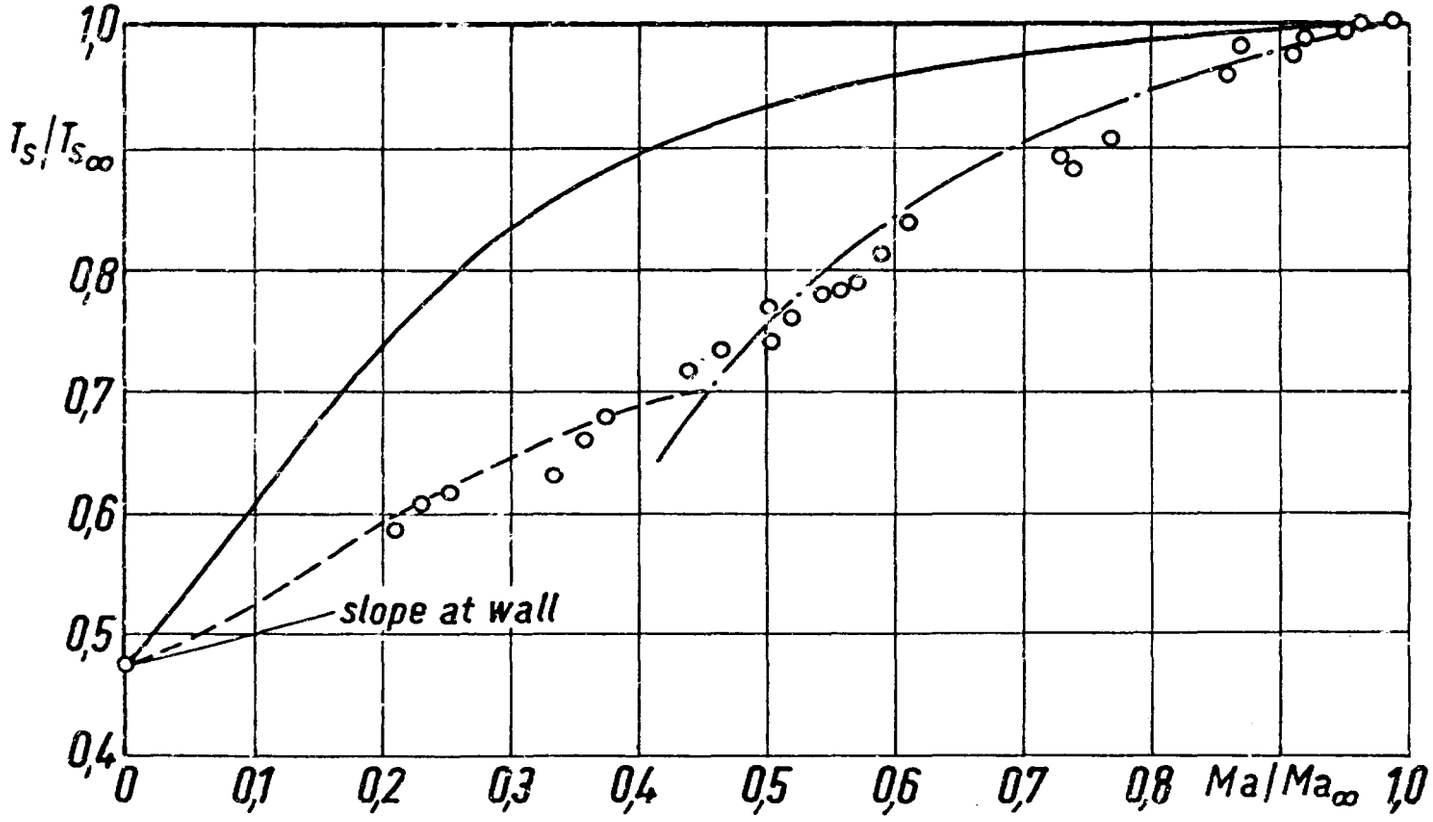

Fig.6 Local stagnation temperature in the turbulent boundary layer on a conical nozzle wall. $Ma_\infty = 9.07$. $(T_e - T_w)/T_e = 0.438$, Reference [13]

Crocco solution, Table I:

——— Case 1, $T_w/T_\infty = 8.28$; ——— Case 3, $2St(T_e - T_w)/c_f T_w = 0.296$;

—·— Case 4, $T_{wa}/T_\infty = -2.63$

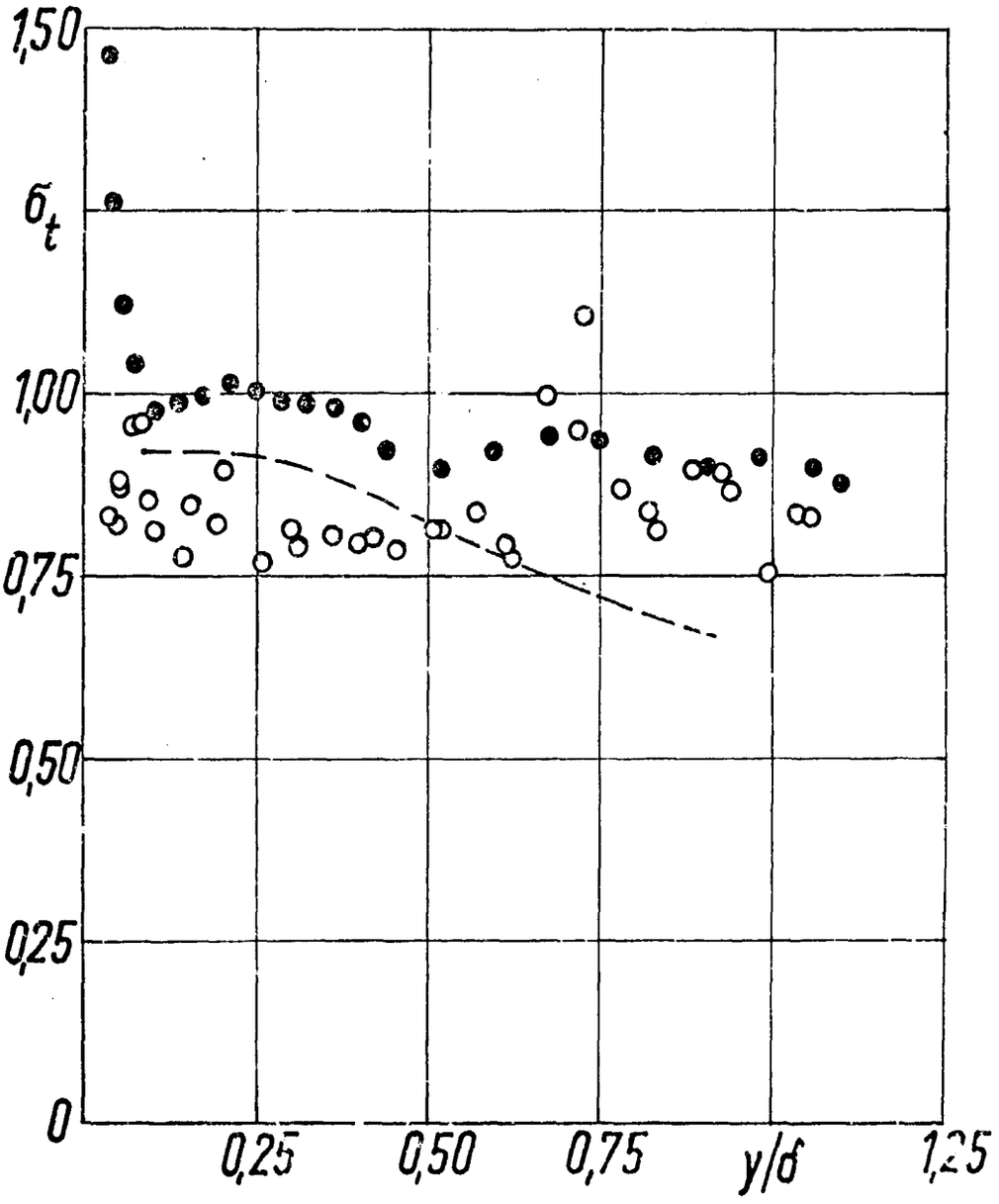

Fig.7 Turbulent Prandtl numbers of boundary layers with zero heat transfer

○ flat plate, $Ma_\infty = 3.03$, Ref. [15]

● nozzle wall, $Ma_\infty = 4.03$, Ref. [10]

— — — subsonic pipe flow, H. Ludwieg [18]

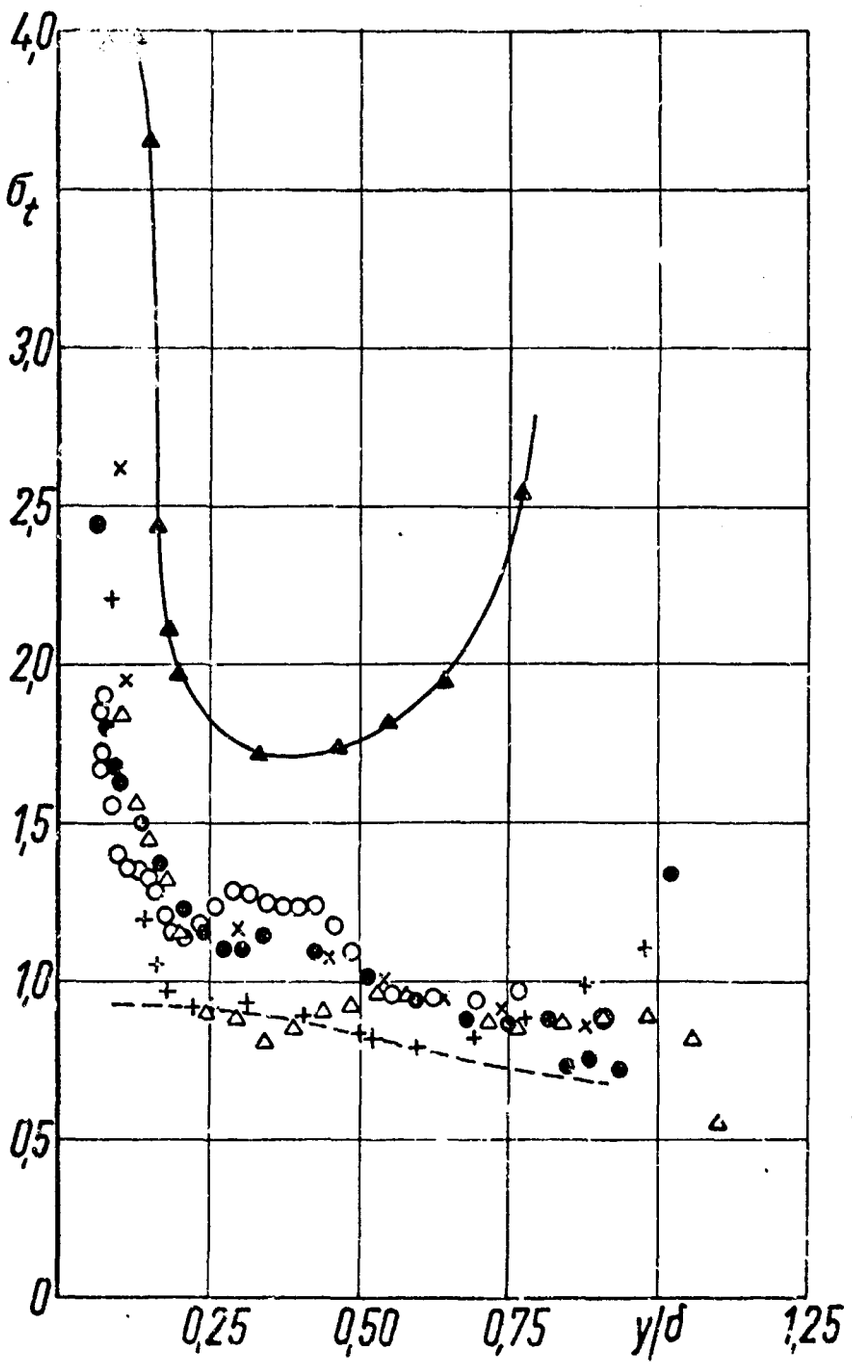

Fig. 8 Turbulent Prandtl numbers of boundary layers on a cooled flat plate, $Ma_\infty \sim 5.1$, $(T_e - T_w)/T_e \sim 0.55$, Reference [11]

▲ x = 216 mm

+ ● } x = 368.5 mm

× △ } x = 292.5 mm

○ x = 445 mm

——— subsonic pipe flow, H. Ludwieg [18]

QUELQUES RESULTATS SUR LES CARACTERISTIQUES THERMIQUES DES COUCHES LIMITES TURBULENTES A TEMPERATURE ELEVEE

par

R. Michel et P. Mentré

ONERA, Châtillon-sous-Bagneux (Seine), France

SOMMAIRE

Analyse des couches limites turbulentes à des températures suffisamment élevées pour permettre la dissociation.

Dans une première partie la répartition des enthalpies et la concentration à l'intérieur de la couche limite d'une plaque plane sont étudiées au moyen d'une combinaison des équations locales de la couche limite dans l'hypothèse d'un gaz parfait puis pour un gaz réel figé ou à l'équilibre. On en déduit le rapport du transfert de chaleur au frottement de la paroi.

Dans la seconde partie de l'étude les résultats obtenus sont utilisés pour le calcul du transfert de chaleur sur des avant-corps arrondis en faisant appel à l'intégration de l'équation globale de l'énergie.

SUMMARY

This paper is devoted to the analysis of turbulent boundary-layers at temperatures sufficiently high for dissociation to occur.

In the first part the enthalpy distributions and the concentration in a flat plate boundary-layer are studied by means of a combination of the local boundary-layer equations in the cases of the perfect gas and of the real gas either frozen or at equilibrium. The ratio of the heat flux to the wall friction is thus deduced.

The results obtained are used in the second part to calculate the heat transfer on rounded fore-bodies by integration of the global energy equation.

TABLE DES MATIERES

LISTE DES TABLEAUX

LISTE DES FIGURES

NOTATION

x, y	coordonnées longitudinale et normale
r	rayon transversal de la paroi
j	courant plan $j = 0$; courant de révolution $j = 1$
u, v	composantes de la vitesse
u_e	vitesse extérieure
w	vitesse réduite, u/u_e
p	pression, p_i pression d'arrêt
T	température
ρ	masse volumique
h	enthalpie, h_i enthalpie d'arrêt
h_f	enthalpie de paroi athermane
h_A^0	chaleur de formation des atomes
C_A	concentration massique des atomes
C_{pf}	chaleur spécifique "figée" $C_{pf} = C_A C_{pA} + (1 - C_A) C_{pA2}$
μ, ϵ	viscosité et viscosité turbulente
λ, χ	conductibilité et conductibilité turbulente
D, D_t	diffusion et diffusion turbulente

nombres de Prandtl, de Lewis, de Schmidt, laminaires, mixtes, turbulents:

$$\mathcal{P} = \frac{\mu C_{pf}}{\lambda} ; \qquad \mathcal{L} = \frac{\rho D C_{pf}}{\lambda} ; \qquad S = \frac{\mathcal{P}}{\mathcal{L}}$$

$$\mathcal{P}_m = \frac{(\mu + \epsilon) C_{pf}}{\lambda + \chi} ; \qquad \mathcal{L}_m = \frac{\rho (D + D_t) C_{pf}}{\lambda + \chi} ; \qquad S_m = \frac{\mathcal{P}_m}{\mathcal{L}_m}$$

$$\mathcal{P}_t = \frac{\epsilon C_{pf}}{\chi} ; \qquad \mathcal{L}_t = \frac{\rho D_t C_{pf}}{\chi} ; \qquad S_t = \frac{\mathcal{P}_t}{\mathcal{L}_t}$$

τ frottement interne

ϕ flux de chaleur

Q_A flux massique de diffusion

w_A taux massique de formation chimique des atomes

C_f coefficient de frottement $\tau_p \Big/ \frac{\rho_e}{2} u_e^2$

C_h coefficient de flux de chaleur $\dfrac{\phi_p}{\rho_e u_e (h_p - h_f)}$

s facteur d'analogie $C_h \Big/ \dfrac{C_f}{2}$

r factor de récupération $(h_f - h_e)/(h_{ie} - h_e)$

δ, δ_1, δ_2, Δ, épaisseur, de déplacement, de quantité de mouvement, d'énergie

$$\delta_1 = \int_0^\delta \left(1 - \frac{\rho}{\rho_e} w\right) dy \; ; \qquad \delta_{1I} = \int_0^\delta (1 - w)\, dy$$

$$\delta_2 = \int_0^\delta \frac{\rho}{\rho_e} w(1 - w)\, dy \; ; \qquad \delta_{2I} = \int_0^\delta w(1 - w).\, dy$$

$$\Delta = \int_0^\delta \frac{\rho}{\rho_e} w \left(1 - \frac{h_i}{h_{ie}}\right) dy$$

H$_I$ paramètre de forme δ_{1I}/δ_{2I}

f et g fonctions C_f/C_{fI} (formule 18)

Indices

A atomes, A_2 molécules

e écoulement amont non perturbé

i conditions d'arrêt

e extérieur à la couche limite

p conditions à la paroi

I incompressible

QUELQUES RESULTATS SUR LES CARACTERISTIQUES THERMIQUES DES COUCHES LIMITES TURBULENTES A TEMPERATURE ELEVEE

R. Michel et P. Mentré

INTRODUCTION

Le problème des transferts de chaleur en régime turbulent, peut se trouver posé d'une façon très critique dans certains cas de vol hypersonique, comme par exemple, celui de la rentrée d'un engin spatial dans l'atmosphère terrestre; l'expérience montre en effet qu'une transition prématurée peut donner lieu à une couche limite turbulente à une faible distance en aval du point d'arrêt des avant-corps arrondis.

On se propose ici, afin d'aboutir à une estimation raisonnable des transferts de chaleur qui sont alors enregistrés à la paroi, d'effectuer une analyse des propriétés thermiques des couches limites turbulentes à température élevée. Une attention spéciale doit être prêtée aux effets de gaz réel, le cas envisagé étant celui de la dissociation d'un gaz diatomique.

Une première phase de l'étude est consacrée à l'analyse des propriétés d'une couche limite turbulente en écoulement uniforme; on y propose un traitement séparé du problème thermique et du problème dynamique.

Moyennant l'hypothèse d'existence de relations exprimant dans la couche limite l'enthalpie et la concentration en fonction de la vitesse, une combinaison des équations locales est d'abord effectuée; elle conduit à l'établissement d'équations différentielles ordinaires dont la résolution doit fournir les relations cherchées; la solution fait appel à l'hypothèse d'une distribution du frottement interne distinguant une loi laminaire et une loi turbulente de paroi, et une région turbulente externe dans laquelle le frottement évolue pour rejoindre la valeur nulle de l'écoulement extérieur. Les résultats concernent, pour le gaz parfait, puis pour un gaz réel figé et à l'équilibre, les profils d'enthalpie et de concentration; des relations explicites sont proposées, qui font intervenir des fonctions tabulées de la vitesse. On en déduit dans les trois cas le rapport du transfert de chaleur au frottement de la paroi.

La détermination du frottement de paroi est basée sur le concept d'enthalpie de référence; la référence proposée est la valeur moyenne par rapport à la vitesse, d'une fonction combinée de l'enthalpie et de la concentration.

Dans le cas d'un gradient de pression, le calcul du transfert de chaleur à la paroi fait appel à l'intégration de l'équation globale de l'énergie. L'application en est effectuée à un avant corps hémisphérique pour lequel sont présentés en gaz parfait

les résultats relatifs à différentes positions de la transition. En gaz réel, le transfert de chaleur est calculé pour un gaz à l'équilibre et pour un gaz figé; on met en relief dans le second cas l'influence du pouvoir catalytique de la paroi.

1. EQUATIONS ET DEFINITIONS GENERALES

1.1 Hypothèses

On se propose d'examiner la forme que prennent les équations de la couche limite pour un gaz en cours de dissociation, l'application prévue étant la dissociation de l'air, considéré en première approximation comme un gaz formé d'atomes et de molécules dont les propriétés sont les propriétés moyennes de l'oxygène et de l'azote, compte tenu de leurs concentrations. Les hypothèses les plus fréquentes et qui sont retenues ici sont les suivantes:

les effets du rayonnement sont négligeables,

l'écoulement moyen est stationnaire,

l'épaisseur de la couche limite est faible devant les rayons de courbure de la paroi,

la diffusion thermique étant négligée, on se limite au cas d'une diffusion binaire,

on se limite aux cas du courant plan et du courant de révolution,

la différence entre l'enthalpie spécifique des atomes et celle des molécules est supposée constante et égale à la chaleur de formation h_A^0 .

1.2 Equations Locales de la Couche Limite

Le système des quatre équations locales de la couche limite, valable en laminaire, et en turbulent pour les caractéristiques moyennes est le suivant:

équation des quantités de mouvement:
$$\rho u \frac{\partial u}{\partial x} + \rho v \frac{\partial u}{\partial y} = \frac{\partial \tau}{\partial y} + \frac{dp}{dx} \qquad (1a)$$

équation de l'énergie:
$$\rho u \frac{\partial h_i}{\partial x} + \rho v \frac{\partial h_i}{\partial y} = \frac{\partial}{\partial y} (u\tau - \phi) \qquad (1b)$$

équation de continuité du mélange:
$$\frac{\partial (\rho u r^j)}{\partial x} + \frac{\partial (\rho v r^j)}{\partial y} = 0 \qquad (1c)$$

équation de conservation des atomes:
$$\rho u \frac{\rho C_A}{\partial x} + \rho v \frac{\partial C_A}{\partial y} = \dot{w}_A - \frac{\partial Q_A}{\partial y} \qquad (1d)$$

C_A est la concentration massique des atomes; $\dot{w}_A$ est le taux massique de formation chimique des atomes par unité de volume; τ, ϕ et Q_A sont le frottement, le flux de chaleur, le flux de diffusion massique, par unité de surface au sein de la couche limite. On les exprime en fonction des gradients de la vitesse, de la température et de la concentration, en faisant intervenir dans le cas turbulent les coefficients apparents de viscosité, de conductibilité et de diffusion ϵ, χ et D_t :

$$\tau = (\mu + \epsilon)\frac{\partial u}{\partial y}, \quad \phi = -(\lambda + \chi)\frac{\partial T}{\partial y} + Q_A h_A^0, \quad Q_A = -\rho(D + D_t)\frac{\partial C_A}{\partial y}. \qquad (2)$$

Les conditions aux limites concernent à la frontière extérieure de la couche limite u, h et C_A qui doivent rejoindre les valeurs u_e, h_e, C_{Ae}, supposées connues.

A la paroi, la température prend une valeur T_p supposée connue. La concentration et la diffusion dépendent du pouvoir catalytique de la paroi; deux cas extrêmes sont généralement considérés:

une paroi non catalytique, constituée d'un matériau ne donnant lieu à aucun phénomène de catalyse, donne la condition d'un flux de diffusion nul à la paroi:

$$(\partial C_A/\partial y)_p = 0$$

une paroi totalement catalytique donne lieu à une catalyse amenant le gaz au voisinage de la paroi à l'équilibre; on a pour une paroi froide

$$C_{Ap} = 0 .$$

Deux cas extrêmes sont également considérés en ce qui concerne l'état du gaz dans la couche limite:

gaz à l'équilibre: les vitesses de réaction chimique sont partout très grandes devant la vitesse de diffusion; les concentrations se déterminent en fonction des enthalpies par la loi d'action de masse;

gaz figé: les vitesses de réaction chimique sont au contraire faibles devant la vitesse de diffusion et le terme $\dot{w}_A$ de l'équation de conservation des atomes est négligé;

dans le cas général, le terme de cinétique chimique $\dot{w}_A$ dépend d'une façon très complexe des températures et des concentrations; la grande difficulté est que sa présence interdit pratiquement toute solution de similitude, même approchée.

2. ETUDE DES COUCHES LIMITES SANS GRADIENT DE PRESSION

2.1 Principe et Plan de l'Etude Envisagée

Le principe d'étude qu'on envisage d'appliquer pour aboutir aux caractéristiques principales de la couche limite consiste à dissocier le problème dynamique du problème thermique, et a en déterminer séparément les solutions.

Une première démarche, va nous conduire à combiner les équations locales de la couche limite de façon à aboutir à une loi d'évolution de l'enthalpie et la concentration en fonction de la vitesse dans la couche limite. Utilisée avec succès pour la plaque plane laminaire en gaz parfait, cette technique sera d'abord étendue à la plaque plane turbulente en gaz parfait; un traitement tout à fait analogue pourra ensuite être appliqué au gaz figé et au gaz à l'équilibre. Un résultat pratique essentiel sera dans les trois cas la détermination du rapport du transfert

de chaleur au frottement de la paroi; il s'obtiendra très simplement à partir des dérivées à la paroi de l'enthalpie et de la concentration par rapport à la vitesse.

Une seconde démarche serait en laminaire de traiter l'équation locale de quantité de mouvement de façon à déterminer l'évolution du frottement de paroi en fonction des données qui sont essentiellement le nombre de Mach extérieur et la température de paroi. En turbulent, une telle évolution ne pourra être établie, qu'à partir de relations empiriques, basées sur le concept d'enthalpie de référence.

2.2 Recherche de Relations $h(u)$ et $C_A(u)$

2.2.0 L'intérêt de ces relations apparaît immédiatement lorsqu'on exprime en dérivation par rapport à u les rapports ϕ/τ et Q_A/τ du flux de chaleur et du flux de diffusion au frottement; introduisant pour commodité les nombre caractéristiques mixtes de Prandtl, de Lewis et de Schmidt, $\mathcal{P}_m$, $\mathcal{L}_m$, et $S_m = \mathcal{P}_m/\mathcal{L}_m$, on obtient pour une abscisse fixée:

$$\frac{\phi}{\tau} = -\frac{1}{\mathcal{P}_m}\left[\frac{\partial h}{\partial u} + (\mathcal{L}_m - 1)h_A^0 \frac{\partial C_A}{\partial u}\right], \quad \frac{Q_A}{\tau} = -\frac{1}{\mathcal{P}_m}\frac{\partial C_A}{\partial u}. \tag{3}$$

Ecrite à la paroi, la relation pour ϕ/τ permettra par exemple de déterminer les conditions relatives au flux de chaleur nul de la paroi athermane:

$$\left(\frac{\partial h}{\partial u}\right)_p = h_A^0 \left[(1 - \mathcal{L}) \frac{\partial C_A}{\partial u}\right]_p. \tag{4}$$

La relation donnera encore le rapport ϕ_p/τ_p à la paroi; il sera commode pour un nombre de Lewis égal à l'unité et spécialement en gaz parfait d'en déduire le facteur d'analogie:

$$s = \frac{1}{\mathcal{P}_p (h_f - h_p)}\left(\frac{\partial h}{\partial u}\right)_p.$$

2.2.1 *Etablissement des Equations Différentielles Nécessaires*

On envisage d'établir des relations entre la concentration et l'enthalpie en fonction de la vitesse, ce qui impose de discuter d'abord des conditions sous lesquelles ces relations peuvent effectivement exister.

Au sens strict, il ne pourra exister de relations $h(u)$ et $C_A(u)$ indépendantes de l'abscisse que s'il existe des profiles u/u_e, h/h_e, C_A/C_{Ae}, eux mêmes indépendants de l'abscisse c'est-à-dire semblables. Compte tenu des connaissances actuelles, on ne peut donc espérer en turbulent que des solutions approchées, comparables aux solutions de similitude locale établies dans certains cas pour le laminaire. En laminaire comme en turbulent, il convient de plus que la distribution de la vitesse extérieure se prête à l'hypothèse envisagée. Les relations pour h et C_A ne seront ici recherchées que dans le cas d'une vitesse extérieure uniforme (plaque plane).

L'existence de relations $h(u)$ et $C_A(u)$ n'est enfin possible que si la concentration et l'enthalpie de paroi sont constantes; cette condition ne peut être satisfaite pour une paroi semi-catalytique, cas dans lequel il n'est encore possible d'envisager que des solutions approchées. La complexité du terme de cinétique chimique, limite enfin l'application aux cas de l'équilibre et du figeage qui seront seuls examinés.

On se propose donc d'établir pour la plaque plane des équations différentielles obtenues en combinant les équations locales, ceci grâce à l'utilisation des nombres ρ_m et $\mathcal{L}_m$, dans le cas général laminaire ou turbulent. Après division respectivement par $\partial u/\partial y$, $\partial h_i/\partial y$, $\partial C_A/\partial y$, les équations locales (1a) (1b) (1c) s'écrivent pour la plaque plane:

$$\rho u \left(\frac{v}{u} - m_u \right) = \frac{\partial \tau}{\partial u} \tag{5a}$$

$$\rho u \left(\frac{v}{u} - m_{hi} \right) = \frac{\partial}{\partial h_i} (u\tau - \phi) \tag{5b}$$

$$\rho u \left(\frac{v}{u} - m_{C_A} \right) = \frac{\partial Q_A}{\partial C_A} + \frac{\dot{w}_A}{\partial C_A/\partial y} . \tag{5c}$$

m_u, m_{hi}, m_{CA} sont les pentes des lignes de niveau de $u(x,y)$, $h_i(x,y)$, $C_A(x,y)$; nous admettons qu'il existe deux relations $h_i(u)$ et $C_A(u)$; il en résulte que $m_u = m_{hi} = m_{CA}$.

Compte tenu des expressions (3) pour ϕ/τ et Q_A/τ, la combinaison de (5a) et (5b), et celle de (5a) et (5c) conduit aux deux équations .

$$\left[\frac{h'}{\rho_m} + \frac{\mathcal{L}_m - 1}{\rho_m} h_A^0 C_A' \right]' + \frac{\tau'}{\tau} \left[h' \frac{1 - \rho_m}{\rho_m} + \frac{\mathcal{L}_m - 1}{\rho_m} h_A^0 C_A' \right] + u_e^2 = 0 \tag{6a}$$

$$\left(\frac{C_A'}{\rho_m} \right)' + \frac{\tau'}{\tau} \frac{1 - S_m}{S_m} C_A' + (\mu + \epsilon) \frac{u_e^2}{\tau^2} \dot{w}_A = 0 . \tag{6b}$$

l'accent signifiant une dérivation par rapport à $w = u/u_e$.

Il s'agit bien là d'équations différentielles pour l'enthalpie et la concentration en fonction de la vitesse; y interviennent comme inconnues auxiliaires, la distribution du frottement, et celles du nombre de Prandtl et du nombre de Lewis mixtes.

2.2.2 *Cas où* $\mathcal{L}_m = 1$. *Relation Enthalpie - Vitesse en Gaz Parfait*

2.2.2.1 *Solution Générale; Rappel des Résultats du Laminaire*

Il est commode, pour discuter les hypothèses qu'on va devoir introduire sur la distribution du frottement, aussi bien que pour établir un mode général de résolution utilisé ensuite en gaz réel, d'examiner d'abord le cas d'un nombre de Lewis mixte

égal à l'unité. L'équation différentielle pour l'enthalpie prend alors exactement la forme de l'équation établie et résolue par Crocco[1] et van Driest[2] dans le cas de la plaque plane laminaire en gaz parfait. Conservant le nombre de Prandtl mixte, on suivra le même développement.

Pour $\Sigma_m = 1$, l'équation (6a) s'écrit:

$$\left(\frac{h'}{\rho_m}\right)' + (1 - \rho_m)\frac{\tau'}{\tau} + u_e^2 = 0 \qquad (7)$$

équation différentielle linéaire du second ordre dont l'intégration est effectuée à partir de la paroi ($w = u/u_e = 0$) où l'enthalpie h_p est donnée, τ'/τ étant tout d'abord supposé connu:

la double intégration fait intervenir les expressions:

$$\left.\begin{aligned} G &= \int_0^w \exp\left(\int_{\tau_p}^{\tau} (1 - \rho_m)\frac{\partial\tau}{\tau}\right) dw \\ I &= \int_0^w \rho_m \exp\left(\int_{\tau_p}^{\tau} (\rho_m - 1)\frac{\partial\tau}{\tau}\right) dw \qquad I_e = \int_0^1 \text{------} dw \\ J &= \int_0^w G\,\rho_m \exp\left(\int_{\tau_p}^{\tau} (\rho_m - 1)\frac{\partial\tau}{\tau}\right) dw \qquad J_e = \int_0^1 \text{------} dw \end{aligned}\right\} \qquad (8)$$

la distribution d'enthalpie s'obtient d'abord sous la forme:

$$h = h_p + \left(\frac{h'}{\rho}\right)_p I - u_e^2 J$$

écrite à la frontière ($h = h_e$), la relation donne la pente à l'origine:

$$h_p' = \frac{\rho_p}{I_e}(h_e - h_p + u_e^2 J_e)$$

pour une distribution fixée de ρ_m et de τ/τ_p , on en déduit la facteur de récupération et la facteur d'analogie:

$$r = 2J_e \quad (9a) \qquad\qquad s = 1/I_e \quad (9b)$$

la forme finale de la relation enthalpie-vitesse est alors:

$$h = h_p + (h_e - h_p)\theta^I + u_e^2\theta^{II}, \qquad \theta^I = \frac{I}{I_e}; \qquad \theta^{II} = \frac{I}{I_e}J_e - J. \qquad (10)$$

La distribution d'enthalpie est ainsi obtenue à partir de fonctions I, J, θ^I, θ^{II}, qui seront déterminées en fonction de la vitesse réduite w, dès que seront connues les distributions du nombre de Prandtl et du frottement.

Ces fonctions ont été calculées en laminaire par van Driest, pour différentes valeurs d'un nombre de Prandtl supposé constant dans la couche limite. La propriété utilisée est que la distribution de τ/τ_p en fonction de u/u_e est très peu influencée par la compressibilité; celle donnée en incompressible par la solution de Blasius est retenue pour calculer les fonctions I, J, θ^I, θ^{II} qui sont ainsi des fonctions de w et de P calculées et tabulées[2]. On les utilisera dans la suite.

2.2.2.2 Schéma Utilisé pour la Distribution de τ et P_m en Turbulent

La difficulté évidente du problème turbulent est de connaître d'une façon même approchée la distribution du frottement et du nombre de Prandtl dans la couche limite.

Les résultats expérimentaux de l'incompressible apportent des renseignements sur leur comportement au voisinage de la paroi. On admet très généralement le frottement constant et le nombre de Prandtl égal à la valeur laminaire dans le film laminaire. Le frottement demeure encore sensiblement constant dans la région turbulente de paroi, P_m étant le plus souvent supposé constant et égal à une certaine valeur turbulente P_t.

L'incertitude la plus grave porte sur la région turbulente externe, et sur la façon dont le frottement rejoint une valeur nulle à l'extérieur de la couche limite; l'hypothèse faite par certains[3,4], d'un nombre de Prandtl turbulent égal à l'unité, élude en fait la question, en rendant la solution indépendante de la distribution du frottement comme le montre clairement la solution générale.

On se propose ici, pour aboutir à la relation h(u) de la plaque plane turbulente d'utiliser un schéma amélioré, donnant une évolution vraisemblable du frottement turbulent dans la région externe, et permettant d'utiliser un nombre de Prandtl turbulent différent de l'unité. Ce schéma distingue (Fig.1) dans la couche limite turbulente, trois régions dont les caractéristiques sont les suivantes:

film laminaire ..... $0 < w < w_L$ ..... $P_m = P$ ..... τ constant

région turbulente de paroi .... $w_L < w < w_0$ ..... $P_m = P_t$ ..... τ constant

région turbulente externe ..... $w_0 < 1 < 1$ ..... $P_m = P_t$ ..... τ variable et τ_p à 0.

Pour déterminer les frontières de ces domaines, il n'est d'autre recours que de faire appel à des connaissances expérimentales provenant essentiellement de l'incompressible. L'idée qui va nous guider pour les étendre au cas compressible est basée sur l'observation expérimentale que la forme générale des profils de vitesses turbulents est peu influencée par la compressibilité; on étendra donc les résultats de l'incompressible en utilisant des paramètres liés à la forme du profil des vitesses et particulièrement le paramètre de forme H_i.

En ce qui concerne ainsi la vitesse à la frontière du film laminaire, les résultats de l'incompressible montrent qu'elle est fonction du coefficient de frottement, dont dépend également pour la plaque plane le paramètre de forme. On a, d'après Clauser[5] et Rotta[6]:

$$w_L = 11,5\sqrt{C_f/2} \qquad H_I = 1/1 - 6,1\sqrt{C_f/2}\ .$$

Ces deux relations seront combinées pour admettre d'une façon générale:

$$w_L = 1,884(H_I - 1)/H_I$$

H_I étant le paramètre de forme "incompressible" de la couche limite.

Pour traiter la couche externe, on utilisera un schéma qui consiste, en négligeant en première approximation le film laminaire et la loi turbulent de paroi, à admettre que la couche limite turbulente externe est composée d'une région à viscosité ϵ constante, pour laquelle la vitesse en $y = 0$ est finie et précisément égale à la limite w_0 définie ci-dessus.

A cette condition limite près, et dans l'hypothèse de profils de vitesse semblables, on trouve facilement que l'équation du mouvement peut être mise sous une forme identique à celle de Blasius ou à celle de Crocco pour la couche limite laminaire de la plaque plane. Clauser donne ainsi les profils de vitesse correspondant à différentes valeurs de w_0 [5]. Reprenant les solutions des équations écrites sous la forme de Crocco, nous avons calculé pour différents w_0 les distributions du frottement τ/τ_p en fonction de $w = u/u_e$; trois exemples sont donnés Figure 1.

Clauser avait observé que les profils de vitesse obtenus à différentes valeurs de w_0 s'écartaient peu du profil de Blasius lorsqu'on les représentait à l'aide de la variable $V = (w - w_0)/(1 - w_0)$; portées Figure 1 en fonction de V, les distributions du frottement (c'est-à-dire de $\epsilon\,\partial u/\partial y$) diffèrent quelque peu de la distribution de frottement laminaire. On négligera cet écart pour admettre dans ce qui suit, que la distribution du frottement dans la couche limite turbulente externe est donnée par la solution laminaire, lorsqu'on représente la variation de τ/τ_p en fonction de V.

On utilisera enfin pour déterminer w_0, les résultats expérimentaux relatifs à la fonction de dissipation, laquelle fait intervenir l'intégrale du frottement par rapport à la vitesse. Avec notre schéma on trouve facilement que

$$\int_0^1 \frac{\tau}{\tau_p}\,dw = w_0 + (1 - w_0)\int_0^1 \frac{\tau}{\tau_p}\,dV = w_0 + 0,786(1 - w_0)\ .$$

L'expérience montre d'autre part que l'intégrale précédente est une fonction du paramètre de forme pour laquelle sont disponibles en incompressible d'assez nombreux résultats. On choisira d'utiliser ici la fonction de dissipation proposée par Tani [7] sur la base des profils d'équilibre de Clauser et de la loi de frottement de Ludwieg et Tillmann.

La variation des vitesses aux frontières des régions considérées en fonction du paramètre de forme, est ainsi représentée Figure 1. La valeur $H_I = 1$ correspond à un coefficient de frottement nul, donc à un nombre de Reynolds infini; la vitesse à la frontière du film laminaire y est nulle alors que w_0 est égal à l'unité; w_L est une fonction croissante de H_I alors que w_0 diminue quand H_I augmente;

la vitesse à la frontière du film laminaire rejoint ainsi w_0 pour un paramètre de forme de 1,35, valeur qui représente la limite supérieure d'application du schéma proposé (il lui correspond en incompressible un nombre de Reynolds de l'ordre de 10^6).

Aux valeurs supérieures de H_I, il semble qu'on doive utiliser un schéma à deux regions, l'une étant le film laminaire, l'autre la région turbulente à frottement variable et nombre de Prandtl P_t ; il est suggéré afin de satisfaire à l'évolution expérimentale de la fonction de dissipation de choisir pour leur frontière la vitesse w_0.

2.2.2.3 Relation Enthalpie-Vitesse pour la Plaque Plane Turbulente

L'introduction des hypothèses précédentes sur τ et sur P_m dans la solution générale donnée par les formules (9) et (10) conduit pour la relation enthalpie-vitesse de la plaque plane turbulente aux résultats suivants:

dans le film laminaire, l'enthalpie est une fonction du second degré de la vitesse pour laquelle les fonctions I et J ont la forme

$$I = P w \qquad J = P \frac{w^2}{2} \tag{11a}$$

dans la région turbulente de paroi, l'enthalpie est encore une fonction du second degré pour laquelle:

$$I = P w_L + P_t (w - w_L) \qquad J = P \frac{w_L^2}{2} + P_t \left(\frac{w^2}{2} - \frac{w_L^2}{2} \right) . \tag{11b}$$

dans la région turbulente externe, les fonctions I et J ont les formes:

$$I = P w_L + P_t (w_0 - w_L) + (1 - w_0)\, I(V, P_t)$$

$$J = (P - P_t) \frac{w_L^2}{2} + P_t \frac{w_0^2}{2} + w_0 (1 - w_0)\, I(V, P_t) + (1 - w_0)^2 J(V, P_t) \tag{11c}$$

$I(V, P_t)$ et $J(V, P_t)$ étant pour la variable $V = (w - w_0)/(1 - w_0)$ les fonctions de la solution laminaire prises à un nombre de Prandtl égal au nombre de Prandtl turbulent P_t.

Le résultat dépend ainsi de la valeur du paramètre de forme du profil des vitesses, et de celle d'un nombre de Prandtl turbulent supposé constant, mais qui peut être choisi au mieux des connaissances expérimentales. Les résultats expérimentaux relatifs au nombre de Prandtl turbulent lui-même sont malheureusement encore actuellement des plus incertains; on dispose par contre de résultats plus sûrs pour le facteur de récupération de la paroi athermane dont aucune variation systématique avec le nombre de Reynolds et le nombre de Mach n'est décelée par l'expérience. L'évolution du facteur de récupération $r = 2J_c$ correspondant au traitement proposé ici, est présentée Figure 2 pour trois valeurs de P_t ; il est clair qu'un nombre de Prandtl de l'ordre de 0,90 ne donne lieu dans le domaine considéré qu'à une variation négligeable du facteur de récupération. Un nombre de Prandtl de 0,89 donne exactement même valeur de r aux deux limites $H_I = 1$ et $H_I = 1,35$ du domaine considéré, le facteur de récupération conservant très sensiblement cette valeur quand le paramètre de forme varie. Ce résultat a été jugé suffisamment proche des résultats

expérimentaux disponibles pour qu'un nombre de Prandtl turbulent de 0,89 soit retenu dans la solution.

Sont également représentées Figure 2 les variations du facteur d'analogie $s = 1/I_e$ pour les nombres de Prandtl $P_t = 1$ et $P_t = 0,89$.

En résumé, il est donc proposé d'utiliser pour la relation entre l'enthalpie et la vitesse d'une couche limite turbulente de plaque plane une formule identique à celle de la couche limite laminaire.

$$h = h_p + (h_p - h_e)\theta^I + u_e^2 \theta^{II}$$

θ^I et θ^{II} résultant des formules établies précédemment pour les fonctions I et J avec un nombre de Prandtl turbulent de 0,89.

Les fonctions I(V) et J(V) nécessaires sont données Table 1, le nombre de Prandtl étant pris égal à 0,725. Les fonctions θ^I et θ^{II} sont également tabulées pour 3 valeurs du paramètre de forme, auxquelles correspondraient dans un profil de vitesse en puissance les valeurs 9, 7 et 5,7 de l'exposant $n = 2/H_i - 1$.

Une comparaison des distributions de l'enthalpie d'arrêt obtenues avec le traitement proposé, et des résultats expérimentaux de Northwang et Kistler regroupés par Coles[8] est enfin représentée Figure 3 pour la paroi athermane.

2.2.3 *Cas où* $C_m \neq 1$. *Relations en Gaz Réel*

2.2.3.1 *Résultats pour le Gaz Figé*

La disparition du terme de cinétique chimique apporte pour le gaz figé une simplification qui rend possible une résolution immédiate du système des équations générales (6a) et (6b). On observe alors que l'équation (6a) prend exactement la forme (7) écrite pour le cas du gaz parfait, lorsqu'on y fait apparaître la nouvelle variable,

$$\bar{h} = h - h_A^0 C_A = h_{A2}$$

$\bar{h}$ est simplement l'enthalpie des molécules, sensiblement proportionnelle à la température.

Le système des équations (6a) et (6b) devient ainsi:

$$\left(\frac{\bar{h}'}{\rho_m}\right)' + \frac{\tau'}{\tau}\frac{\bar{h}'}{\rho_m}(1 - P_m) + u_e^2 = 0 \qquad (12a)$$

$$\left(\frac{C_A'}{\rho_m}\right)' + \frac{\tau'}{\tau}\frac{1 - S_m}{S_m} C_A' = 0 \qquad (12b)$$

On retiendra dans leur intégration les distributions du frottement et du nombre de Prandtl du schéma établi précédemment.

La distribution de l'enthalpie des molécules est ainsi

$$h = h_p + (h_p - h_e)\theta^I + u_e^2 \theta^{II} \qquad (13a)$$

θ^I et θ^{II} étant exactement les fonctions introduites pour le gaz parfait et données Table 1.

La distribution des concentrations fait intervenir l'intégrale

$$K = \int_0^w S_m \exp\left(\int_{\tau_p}^{\tau} (S_m - 1)\frac{d\tau}{\tau}\right) dw \; ; \qquad K_e = \int_0^1 \text{------} \; dw$$

expression identique à l'intégrale I (Formule 8) le nombre de Prandtl $\mathcal{P}_m$ s'y trouvant remplacé simplement par le nombre de Schmidt S_m. On obtient ainsi:

$$C_A = C_{Ae} + (C_{Ae} - C_{Ap})\theta^{III} \quad \text{avec} \quad \theta^{III} = K/K_e \qquad (13b)$$

les dérivées à l'origine sont respectivement:

$$\bar{h}'_p = \frac{\mathcal{P}_p}{I_e}(\bar{h}_e - \bar{h}_p + u_e^2 J_e) \; ; \qquad C'_{Ap} = \frac{S_p}{I_e}(C_{Ae} - C_{Ap})$$

le rapport du flux de chaleur au frottement à la paroi est donné par:

$$-u_e \frac{\phi_p}{\tau_p} = \frac{1}{I_e}\left[\bar{h}_e - \bar{h}_p + u_e^2 J_e + h_A^0 (C_{Ae} - C_{Ap})\frac{I_e}{K_e}\right] \qquad (14)$$

Le résultat dépend encore du paramètre de forme, du nombre de Prandtl turbulent pour lequel on prendra toujours $\mathcal{P}_t = 0,89$, et d'un nombre de Lewis turbulent supposé constant mais dont la valeur peut encore être choisie au mieux des connaissances expérimentales. Comme pour le nombre de Prandtl, ces connaissances sont des plus incertaines, l'opinion prévalant généralement que le nombre de Lewis turbulent est voisin de l'unité. Un nombre de Lewis laminaire $\mathcal{L} = 1,4$ et un nombre de Lewis turbulent $\mathcal{L}_t = 1$ ont été choisis dans les applications présentées.

On trouvera dans cette hypothèse, les valeurs des fonctions θ^{III} nécessaires à la détermination des distributions de la concentration (Table 1).

On observera que la condition concernant la dérivée de la concentration à la paroi conduit pour la paroi non catalytique à une concentration constante dans toute la couche limite et égale à la concentration extérieure. L'annulation du terme $C_{Ae} - C_{Ap}$, entraînera une diminution importante de ϕ_p/τ_p, et en fin de compte du flux de chaleur, par rapport au cas de la paroi catalytique.

Pour la paroi catalytique froide ($C_{Ap} = 0$) on aura simplement:

$$C_A/C_{Ae} = \theta^{III} .$$

2.2.3.2 Résultats pour le Gaz à l'Equilibre

Pour le gaz à l'équilibre, le problème est de résoudre l'équation différentielle (6a) dans laquelle la concentration est une fonction de l'enthalpie donnée par la loi d'action de masse du gaz considéré; cette résolution devra faire appel dans le cas général à des techniques numériques qui seront appliquées pour des conditions aux limites à préciser.

Cependant, une solution explicite peut être obtenue avec les schémas adoptés pour les distributions de τ et de $\mathcal{L}_m$ lorsque le nombre de Lewis turbulent est supposé égal à l'unité. Introduisant alors la variable

$$\tilde{h} = h + (\mathcal{L}_m - 1)\, h_A^0 C_A \tag{15}$$

on trouve en effet que l'équation (6a) prend encore, et dans les trois domaines, la forme:

$$\left(\frac{\tilde{h}'}{\rho_m}\right)' + \frac{\tau'}{\tau}(1 - \rho_m)\frac{\tilde{h}'}{\rho_m} + u_e^2 = 0$$

la solution est encore: (pour un nombre de Lewis laminaire voisin de 1)

$$\tilde{h} = \tilde{h}_p + (\tilde{h}_e - \tilde{h}_p)\theta^I + u_e^2 \theta^{II} \tag{16}$$

θ^I et θ^{II} étant toujours les fonctions de la Table 1.

le rapport du flux de chaleur au frottement à la paroi est donné par:

$$-u_e \frac{\phi_p}{\tau_p} = \frac{\tilde{h}'_p}{\rho_p} = \frac{1}{I_e}(\tilde{h}_e - \tilde{h}_p + u_e^2 J_e) \tag{17}$$

On observera que la variable $\tilde{h}$ se confond avec l'enthalpie à la frontière extérieure et dans la partie turbulente de la couche limite. Elle se confond encore avec l'enthalpie à la paroi dans le cas d'une paroi froide ($C_{Ap} = 0$). Le film laminaire excepté, la distribution de l'enthalpie est donc la même qu'en gaz parfait.

Il est encore intéressant pour se comparer au cas du figeage, d'exprimer ϕ_p/τ_p en fonction de l'enthalpie des molécules $\bar{h}$; on obtiendra aisément pour une paroi froide,

$$-u_e \frac{\phi_p}{\tau_p} = \frac{1}{I_e}[\bar{h}_e - \bar{h}_p + u_e^2 J_e] + h_A^0 \frac{C_{Ae}}{I_e}$$

alors que pour le gas figé, avec une paroi catalytique

$$-u_e \frac{\phi_p}{\tau_p} = \frac{1}{I_e}[\bar{h}_e - \bar{h}_p + u_e^2 J_e] + h_A^0 \frac{C_{Ae}}{K_e}$$

Les fonctions I et K et leurs valeurs extérieures étant assez peu différentes, on trouvera des transferts de chaleur du même ordre à l'équilibre et en gaz figé à paroi catalytique.

2.3 Concept d'Enthalpie de Référence - Frottement et Transfert de Chaleur à la Paroi

2.3.1 *Coefficient de Frottement*

Les relations qui précèdent donnant dans les différents cas le rapport du flux de chaleur au frottement de paroi, il reste à déterminer les lois qui régissent l'évolution du coefficient de frottement avec le nombre de Reynolds et avec la vitesse de l'écoulement extérieur et la température de la paroi. On appliquera dans ce but le concept d'enthalpie de référence, d'après lequel on peut utiliser en compressible la loi d'évolution du coefficient de frottement avec le nombre de Reynolds de l'abscisse, de l'écoulement incompressible, à condition de prendre pour la masse volumique et la viscosité des valeurs de référence ρ^* et μ^* correspondant à une certaine enthalpie h^* à choisir à partir des conditions aux limites.

Appliqué à la plaque plane laminaire, le concept conduit aux résultats:

$$\frac{C_f}{2} = \frac{\tau_p}{\rho_e u_e^2} = \frac{0,332\ f}{\left(\frac{\rho_e u_e x}{\mu_e}\right)^{1/2}} = \frac{0,2205\ g}{\frac{\rho_e u_e \delta_2}{\mu_e}} ; \qquad g = f^2 = \frac{\rho^* \mu^*}{\rho_e \mu_e} \tag{18a}$$

Appliqué à la plaque plane turbulente, en choisissant pour l'incompressible la relation en puissance proposée[9], il donne:

$$\frac{C_f}{2} = \frac{0,0184\ f}{\left(\frac{\rho_e u_e x}{\mu_e}\right)^{1/6}} = \frac{0,0086\ g}{\left(\frac{\rho_e u_e \delta_2}{\mu_e}\right)^{1/5}} ; \qquad g = f^{5/5} = \frac{\rho^*}{\rho_e}\left(\frac{\mu^*}{\mu_e^*}\right)^{1/5} \tag{18b}$$

on aboutit ainsi en gaz parfait à des résultats remarquablement en accord avec les solutions exactes en laminaire, avec l'expérience en turbulent.

2.3.2 *Justification et Estimation de l'Enthalpie de Référence en Laminaire*

Bien que la notion d'enthalpie de référence ait été introduite à l'origine de façon empirique, une justification et une estimation théorique peuvent en être données pour la plaque plane laminaire.

On a montré en effet[10] qu'une solution approchée à $\rho\mu$ constant de l'équation de Crocco conduisait au même résultat:

$$\frac{C_f}{2} = \frac{0,332}{R_x^{1/2}}\left(\frac{\rho^*\mu^*}{\rho_e\mu_e}\right)^{1/2}$$

Imposant à cette solution approchée de satisfaire à l'équation globale des quantités de mouvement, on trouve alors que la valeur moyenne du produit $\rho\mu$ est donnée par l'intégrale:

$$\rho^*\mu^* = \int_0^1 \frac{\rho\mu(1 - w)w}{\tau/\tau_p} \cdot dw$$

Faisant enfin l'hypothèse d'une évolution linéaire de $\rho\mu$ en fonction de h on détermine l'enthalpie de référence qui s'exprime finalement en fonction des conditions aux limites par la relation linéaire:

$$h^* - h_e = a(h_p - h_e) + b\,\frac{u_e^2}{2}$$

a et b étant des coefficients numériques faisant intervenir des intégrales où figurent les fonctions θ^I et θ^{II} de la distribution d'enthalpie; ils dépendent de la valeur choisie pour le nombre de Prandtl et sont donnés[10]. On a montré que cette solution approchée donne pour C_f des résultats pratiquement confondus avec ceux de Crocco et van Driest.

Une autre détermination, proposée par Monaghan[11], consiste à prendre la valeur moyenne de l'enthalpie par rapport à la vitesse dans la couche limite; l'enthalpie de référence a toujours la même forme, avec des coefficients a et b quelque peu différents; elle conduit encore à des coefficients de frottement très proches de ceux de la solution exacte; cette coincidence est encore un argument que nous invoquerons pour le choix de l'enthalpie de référence en turbulent.

2.3.3 *Enthalpie de Référence en Turbulent*

Faute de disposer d'une équation locale qui permette comme celle de Crocco de comparer les frottements du compressible et de l'incompressible, on admettra donc en turbulent que l'enthalpie de référence est donnée en gaz parfait par la valeur moyenne de l'enthalpie; son expression sera:

$$h^* - h_e = a(h_p - h_e) + b\,\frac{u_e^2}{2} \quad \text{avec} \quad \begin{cases} a = \int_0^1 (1 - \theta^I)\ .\ dw \\ b = \int_0^1 2\,\theta^{II}\ .\ dw \end{cases} \tag{19}$$

a et b sont maintenant des fonctions des conditions aux limites introduites pour θ^I et θ^{II}, c'est-à-dire de w_0, w_L ou encore de H_I, le tableau ci-dessous en précise les valeurs pour $\mathcal{P} = 0,725$ et $\mathcal{P}_t = 0,89$:

n	5	5,71	7	9	11
H_I	1,4	1,35	1,286	1,222	1,182
a	0,535	0,535	0,533	0,529	0,526
b	0,139	0,139	0,139	0,139	0,139

a et b varient très peu avec la forme du profil des vitesses; ils sont très proches des valeur $a = 0,540$ et $b = 0,137$ obtenues pour l'enthalpie moyenne en laminaire au nombre de Prandtl $\mathcal{P} = 0,725$ considéré.

Dans le cas du gaz réel, la variable intervenant dans l'équation de l'énergie n'est plus l'enthalpie, mais une combinaison $\tilde{h}$ de l'enthalpie et de la concentration

(on démontre facilement que dans l'hypothèse $\mathcal{L}_t = 1$, la variable $\tilde{h}$ peut être également utilisée pour le gaz figé, la solution étant alors en $\tilde{h}$, identique à celle de l'équilibre). Les fonctions f et g faisant intervenir également par ρ^* et μ^* une combinaison de la concentration et de la température, il est suggéré d'appliquer le concept de référence à la variable $\tilde{h}$; ρ^*, μ^*, f et g seront ainsi déterminés à une valeur de référence $\tilde{h}^*$ donnée très exactement par la même formule qu'en gaz parfait,

$$\tilde{h}^* - \tilde{h}_e = a(\tilde{h}_p - \tilde{h}_e) + b u_e^2$$

a et b étant les coefficients du tableau, donnés précédemment.

2.3.4 *Transfer de Chaleur à la Paroi*

Il est immédiat, à partir des expressions obtenues dans les différents cas pour ϕ_p/τ_p et de celles qui donnent le coefficient de frottement en fonction du nombre de Reynolds, de déterminer les relations qui expriment le transfert de chaleur à la paroi.

En fonction du nombre de Reynolds de l'abscisse on obtient:

$$\frac{-\phi_p}{\rho_e u_e h_{ie}} = \frac{A}{\left(\frac{\rho_e u_e x}{\mu_e}\right)^{1/6}} \qquad \text{avec} \qquad A = 0{,}0184\ f\left(\frac{-u_e\phi_p}{h_{ie}\tau_p}\right) \tag{20}$$

Il sera utile également de disposer d'une relation exprimant le flux de chaleur en fonction du nombre de Reynolds de l'épaisseur d'énergie. Introduisant l'expression précédente dans l'équation globale de l'énergie, $\phi_p = -\rho_e u_e h_{ie}\, d\Delta/dx$, on obtient après intégration:

$$\frac{-\phi_p}{\rho_e u_e h_{ie}} = \frac{B}{\left(\frac{\rho_e u_e \Delta}{\mu_e}\right)^{1/5}} \qquad \text{avec} \qquad B = 0{,}0086\ g\left(\frac{-u_e\phi_p}{h_{ie}\tau_p}\right)^{6/5} \tag{21}$$

Il sera commode en gaz parfait de faire intervenir le facteur d'analogie en exprimant notamment le coefficient B sous la forme:

$$B = 0{,}0086\ g\left(s\,\frac{h_f - h_p}{h_{ie}}\right)^{6/5}$$

2.4 Exemple d'Application Numérique du Traitement Proposé

On a effectué, à titre de première application numérique, le calcul des caractéristiques d'une couche limite supposée turbulente, se développant depuis l'origine, à l'intrados d'une plaque à bord d'attaque arrondi précédé d'une onde de choc normale détachée, et placée sous une incidence de 15°. L'altitude étant fixée à 60 km, on a fait varier la vitesse de vol U_0 jusqu'à des valeurs assez élevées pour que soit en cours localement, à la frontière de la couche limite une dissociation avancée. La pression sur la face inférieure a été déterminée par la loi newtonienne.

La température de paroi a été prise égale à 1,000°K. On a fait l'hypothèse d'un paramètre de forme H_i de 1,286 (n = 7).

Les résultats obtenus, dont des exemples sont donnés Figure 4 concernent les profils d'enthalpie de concentration et de température et l'évolution avec la vitesse de vol du transfert de chaleur à la paroi.

Les hypothèses utilisées pour appliquer à l'air, le traitement établi pour un gaz diatomique ont été les suivantes:

l'écoulement extérieur étant supposé à l'équilibre, la concentration a été déterminée à partir des concentrations en atomes de l'oxygène et de l'azote; celles-ci ont été reliées au facteur de compressibilité Z de l'air à l'équilibre dans l'hypothèse d'une dissociation de l'oxygène d'étendant de $Z = 1$ à $Z = 1,2$ et d'une dissociation de l'azote couvrant le domaine $1,2 < Z < 2$.

l'enthalpie de formation des atomes a été obtenue en pondérant les valeurs relatives à l'azote et à l'oxygène, compte tenu de leurs concentrations dans l'écoulement extérieur.

à l'équilibre, on a négligé la différence entre l'enthalpie et la variable $\tilde{h}$ dans le film laminaire.

la viscosité a été exprimée en fonction de la température par la loi de Sutherland.

La Figure 4 montre que le cas de l'équilibre et celui du figeage avec paroi catalytique conduisent à des profils d'enthalpie et de concentration relativement peu différents, résultat lié à des conditions aux limites identiques. Par contre, le cas du figeage avec paroi non catalytique, pour lequel la concentration est constante et égale à C_{Ae} donne lieu, pour des températures identiques, à des enthalpies très nettement supérieures à celles de la paroi catalytique.

La même différence essentielle est enregistrée pour le flux de chaleur à la paroi; des valeurs nettement plus faibles sont obtenues comme il était attendu dans le cas de la paroi non catalytique.

3. TRANSFERT DE CHALEUR TURBULENT DANS UN GRADIENT DE PRESSION

3.1 Méthode Approchée de Résolution de l'Equation Globale de l'Energie

On a déjà établi en gaz parfait une méthode de calcul approché du transfert de chaleur à la paroi, valable dans des gradients de pression modérés et plus spécialement dans des gradients négatifs, méthode appliquée au calcul des transferts de chaleur turbulents autour d'un avant corps arrondi[12]. On étendra simplement cette technique au cas du gaz réel en utilisant les résultats obtenus précédemment pour la plaque plane.

La méthode est basée sur l'intégration de l'équation globale de l'énergie, considérée comme une équation différentielle pour l'épaisseur d'énergie:

$$\frac{-\phi_p}{\rho_e u_e h_{ie}} = \frac{d\Delta}{dx} + \Delta \frac{d}{dx} \left[\log_e (\rho_e u_e r^j)\right] . \qquad (23)$$

L'hypothèse faite est que les profils de vitesse et de température s'écartent assez peu de ceux d'une plaque plane, pour qu'on puisse utiliser dans l'équation globale, l'expression établie pour la plaque plane entre le flux de chaleur et le nombre de Reynolds de l'épaisseur d'énergie, soit:

$$\frac{-\phi_p}{\rho_e u_e h_{ie}} = \frac{B}{\left(\frac{\rho_e u_e \Delta}{\mu_e}\right)^{1/5}} \qquad \text{avec} \qquad B = 0{,}0086\, g \left(\frac{-u_e \phi_p}{h_{ie} \tau_p}\right)^{6/5} \qquad (21)$$

ϕ_p/τ_p étant donné selon le cas considéré par la Formule (9b), (14) ou (17) et g s'obtenant à partir du concept d'enthalpie de référence.

Intégrée à partir d'un point x_1 où Δ est supposée connue, l'équation donne d'abord l'épaisseur d'énergie sous la forme

$$(\Delta \rho_e u_e r^j)^{6/5} = \frac{(\Delta \rho_e u_e r^j)^{6/5}}{\text{en } x_1} + \frac{6}{5} \int_{x_1}^{x} B \rho_e \mu_e^{1/5} u_e r^{6j/5} \, dx \qquad (24)$$

On en déduit immédiatement le flux de chaleur en utilisant à nouveau l'hypothèse[21]. On obtient notamment, lorsque l'origine de la couche limite turbulente coïncide avec celle des abscisses:

$$\frac{\phi_p}{h_{ie}} = \frac{B \rho_e \mu_e^{1/5} u_e r^{j/5}}{\left[\frac{6}{5} \int_0^x B \rho_e \mu_e^{1/5} u_e r^{6j/5} \, dx\right]^{1/6}} \qquad (25)$$

3.2 Application au Transfer de Chaleur d'un Avant-Corps Hémisphérique

3.2.1 Cas du Gaz Parfait. Influence de la Transition

La méthode intégrale avait été appliquée en gaz parfait à un avant-corps hémisphérique, l'origine de la couche limite turbulente étant supposée coïncider avec le point d'arrêt[12]. Nous apportons quelques résultats complémentaires, en tenant compte d'un développement laminaire précédant une transition pour laquelle sont choisies plusieurs positions. Les conditions, précisées Figure 5, correspondent au cas pour lequel avait été effectuées[13] une étude théorique en couche limite laminaire et des mesures au tube à choc.

L'hypothèse faite est celle d'une transition ponctuelle, au cours de laquelle est pourtant assurée la continuité de l'épaisseur d'énergie; l'épaisseur d'énergie turbulente est ainsi calculée à partir de la valeur obtenue en laminaire au point de transition supposé; il lui correspond une origine fictive où elle est nulle et le flux de chaleur infini. Le transfert de chaleur se déduisant en laminaire et en turbulent de l'épaisseur d'énergie par des lois différentes, subit une discontinuité au point de transition.

On a représenté Figure 5 les résultats relatifs à un rayon du nez de 0,2 m; le nombre de Reynolds R_1 formé avec les conditions du point d'arrêt étant alors 3.10^6. Le flux de chaleur est rapporté au flux laminaire du point d'arrêt, calculé par la formule de Fay et Riddell*. Le calcul confirme que le flux de chaleur turbulent passe par un maximum qui peut largement dépasser le flux laminaire du point d'arrêt; on observera que la valeur de ce maximum dépend sensiblement de la position de la transition et qu'une transition produite à quelque distance, donne lieu à des transferts de chaleur plus importants qu'une transition à l'origine.

3.2.2 Cas du Gaz Réel

La méthode intégrale a été appliquée au même corps et pour les mêmes conditions de température et de pression du point d'arrêt, la couche limite étant supposée turbulente depuis l'origine.

Les hypothèses du calcul ont été les mêmes que celles utilisées en 2,4 pour la plaque plane en incidence, le paramètre de forme étant encore supposé égal à 1,286 (n = 7) et le gaz à la frontière de la couche limite considéré comme à l'équilibre.

Les profils h(u), T(u) et $C_A(u)$ sont donnés Figure 6 en deux abscisses respectivement voisines du point d'arrêt et de l'épaule. On y a également représenté l'évolution du transfert de chaleur à la paroi pour une couche limite à l'équilibre et pour une couche limite figée. Les conclusions à tirer de l'examen de ces résultats sont identiques à celles relatives aux calculs effectués précédemment pour la plaque; on note toujours une diminution très importante du flux de chaleur à la paroi, dans le cas "non catalytique".

4. CONCLUSIONS

On a montré qu'il est possible, à partir d'une hypothèse d'existence de relations entre l'enthalpie, la concentration et la vitesse, d'aboutir pour la plaque plane turbulente à des formes explicites pour les distributions de l'enthalpie et de la concentration dans la couche limite et pour le rapport du flux de chaleur au frottement de la paroi; des fonctions tabulées de la vitesse permettent de déterminer ces distributions pour un gaz parfait et pour un gaz diatomique en cours de dissociation dans le cas de l'équilibre et dans celui du figeage; limité ici aux parois totalement catalytique et non catalytique, le traitement doit pouvoir être appliqué aux cas intermédiaires, à titre de solution approchée de similitude locale.

On peut estimer le transfert de chaleur en présence d'un gradient de pression par intégration de l'équation globale de l'énergie en y utilisant la relation établie pour la plaque plane entre le coefficient de flux de chaleur et le nombre de Reynolds de l'épaisseur d'énergie. L'application à un avant-corps hémisphérique a montré les effets du gaz réel et spécialement celui du pouvoir catalytique de la paroi.

Il reste pour améliorer la méthode, à examiner l'influence des gradients de pression sur les relations enthalpie, concentration-vitesse et sur le rapport du flux

---

* On notera que Λ/R est proportionnel à $R^{1/2}$ en laminaire, à $R^{1/6}$ en turbulent. $\phi/\phi_{F,R}$ indépendant de R en laminaire, est proportionnel à $R^{1/3}$ en turbulent.

de chaleur au frottement. Une première approche effectuée pour le gaz parfait[12] est à poursuivre en gaz réel.

REFERENCES

1. Crocco, L. — *Lo Strato Limite Laminaire Nei Gaz.* Monographie Scientifiche di Aeronautica, Rome 1946.

2. van Driest, E.R. — *Investigation of Laminar Boundary Layer in Compressible Fluids Using the Crocco Method.* NACA TN 2597, 1952.

3. Dorrance, W.H. — *Viscous Hypersonic Flow.* McGraw-Hill, 1962.

4. Lapine, U.V. — *Couche Limite Turbulente dans un Gaz Dissocié.* Journal Tekhitcheskoï Fiziki. Vol.32, No.4, 1962, Trad. SDIT 6309.

5. Clauser, F.H. — *The Turbulent Boundary Layer.* Advances in Applied Mechanics Vol.IV, 1956.

6. Rotta, J. — *Uber die Théorie der Turbulenten Grenzschicht.* Mitt. Max Planck. Inst. Göttingen, Vol.1, 1950.

7. Tani, I. — *Energy Dissipation in Turbulent Boundary Layers.* Jour. Aer. Sc. June 1956.

8. Coles, D.E. — *The Turbulent Boundary Layer in a Compressible Fluid.* Rand Corporation, R. 403, PR, 1962.

9. Michel, R. — *Calcul Pratique de la Couche Limite Turbulente Compressible.* ONERA TN 49, 1959.

10. Michel, R. Kretschmar, G. — *Détermination Théorique d'une Enthalpie de Référence pour la Couche Limite Laminaire de la Plaque Plane.* La Recherche Aérospatiale No.94, 1963.

11. Monaghan, R.J. — *Behaviour of the Boundary Layer at Supersonic Speeds.* I.A.S. Preprint 557, 1955.

12. Michel, R. Ngo Duc Lam — *Frottement et Flux de Chaleur Turbulents en Ecoulements Bi et Tridimensionnels.* XIème Congrès de Mécanique Appliquée, Munich 1964, et TP ONERA No.151, 1964.

13. Kemp, N.H. et alii — *Laminar Heat Transfer Around Blunt Nose Bodies in Dissociated Air.* Jour. Aero. Sc. 7, 1959.

V	I (V)	J (V)
0	0	0
0,10	0,0290	0,00444
0,20	0,1180	0,0178
0,30	0,2672	0,0400
0,40	0,3564	0,0713
0,50	0,4462	0,1116
0,60	0,5366	0,1613
0,70	0,6278	0,2202
0,80	0,7213	0,2896
0,85	0,7690	0,3293
0,90	0,8121	0,3705
0,94	0,8590	0,4066
0,97	0,9027	0,4413
1	0,9290	0,4731

TABLE 1(a)

Fonctions laminaires pour $\mathcal{P} = 0,89$

W	$n = 5,71$ $H_I = 1,35$			$n = 7$ $H_I = 1,226$			$n = 9$ $H_I = 1,222$		
	θ^I	θ^{II}	θ^{III}	θ^I	θ^{II}	θ^{III}	θ^I	θ^{II}	θ^{III}
0	0	0	0	0	0	0	0	0	0
0,10	0,0870	0,0350	0,0704	0,0862	0,0349	0,0663	0,0853	0,0347	0,0663
0,20	0,1740	0,0628	0,1408	0,1723	0,0625	0,1365	0,1706	0,0621	0,1325
0,30	0,2611	0,0834	0,2111	0,2585	0,0829	0,2048	0,2559	0,0822	0,1988
0,33							0,2815	0,0869	0,2127
0,40	0,3431	0,0967	0,2815	0,3447	0,0961	0,2731	0,3542	0,0970	0,2924
0,47	0,4090	0,1017	0,3308						
0,50	0,4405	0,1028	0,3670	0,4505	0,1033	0,3904	0,4596	0,1040	0,4123
0,555				0,5086	0,1035	0,4550			
0,60	0,5485	0,1014	0,4875	0,5560	0,1016	0,5075	0,5643	0,1020	0,5262
0,635							0,6010	0,0993	0,5661
0,70	0,6550	0,0910	0,6090	0,6625	0,0911	0,6250	0,6690	0,0911	0,6405
0,80	0,7635	0,0714	0,7320	0,7690	0,0715	0,7435	0,7745	0,0712	0,7545
0,85	0,8180	0,0583	0,7945	0,8230	0,0581	0,8030	0,8270	0,0579	0,8118
0,90	0,8740	0,0424	0,8580	0,8725	0,0425	0,8645	0,8808	0,0421	0,8705
0,94	0,9215	0,0280	0,9110	0,9230	0,0279	0,9145	0,9250	0,0273	0,9188
0,98	0,9765	0,0110	0,9665	0,9710	0,0107	0,9680	0,9725	0,0105	0,9700
1	1	0	1	1	0	1	1	0	1
	Ie	Je	Ke	Ie	Je	Ke	Ie	Je	Ke
	0,8341	0,4444	0,7352	0,8414	0,4470	0,7585	0,8498	0,4438	0,7814

TABLE 1(b)

Fonctions turbulentes pour les profils d'enthalpie et de concentration
($\mathcal{P} = 0,725$; $\mathcal{P}_t = 0,89$; $\mathcal{L} = 1,4$; $\mathcal{L}_t = 1$)

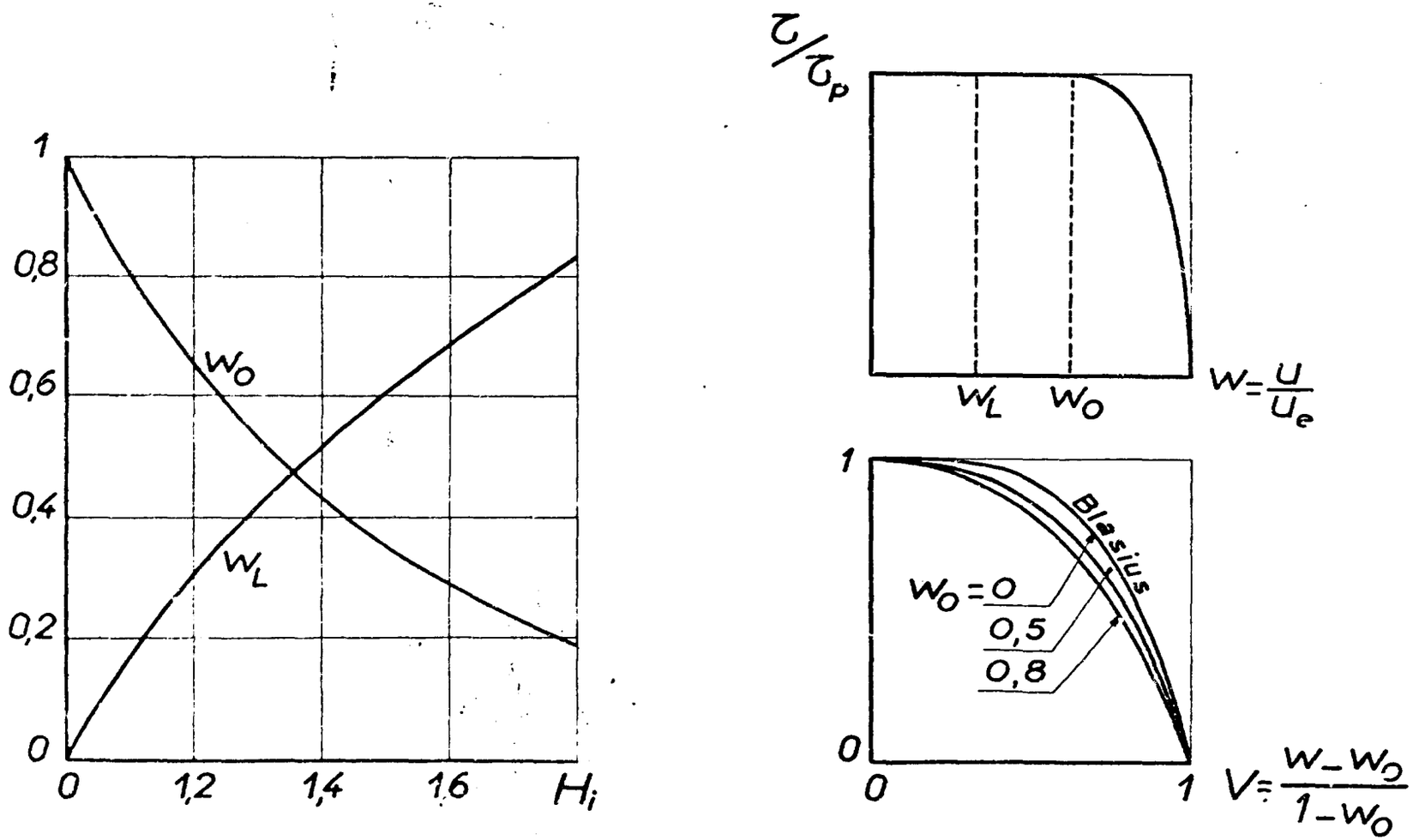

Fig. 1 Schéma de distribution du frottement pour la plaque plane turbulente et frontières des domaines considérés

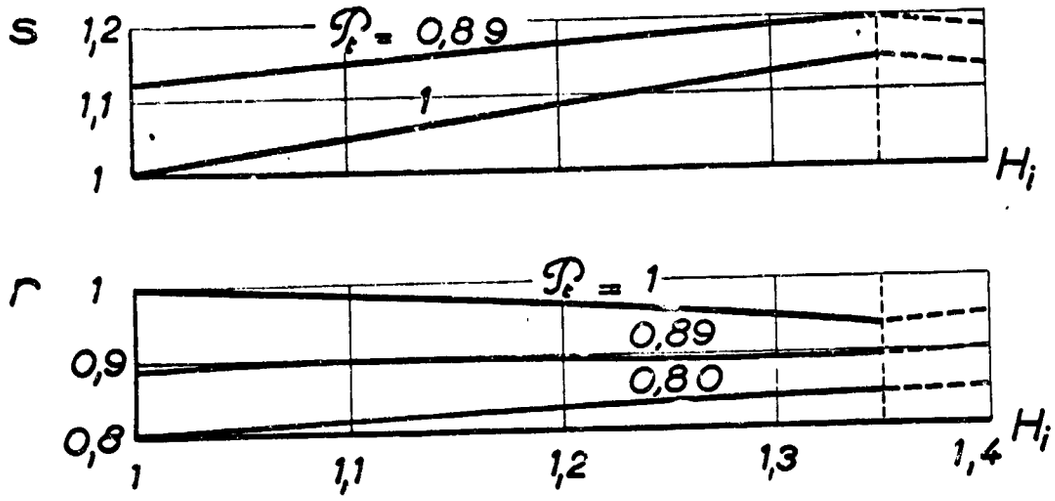

Fig.2 Facteurs de récupération et d'anal[illegible]ie (gaz parfait, $\gamma = 1,4$)

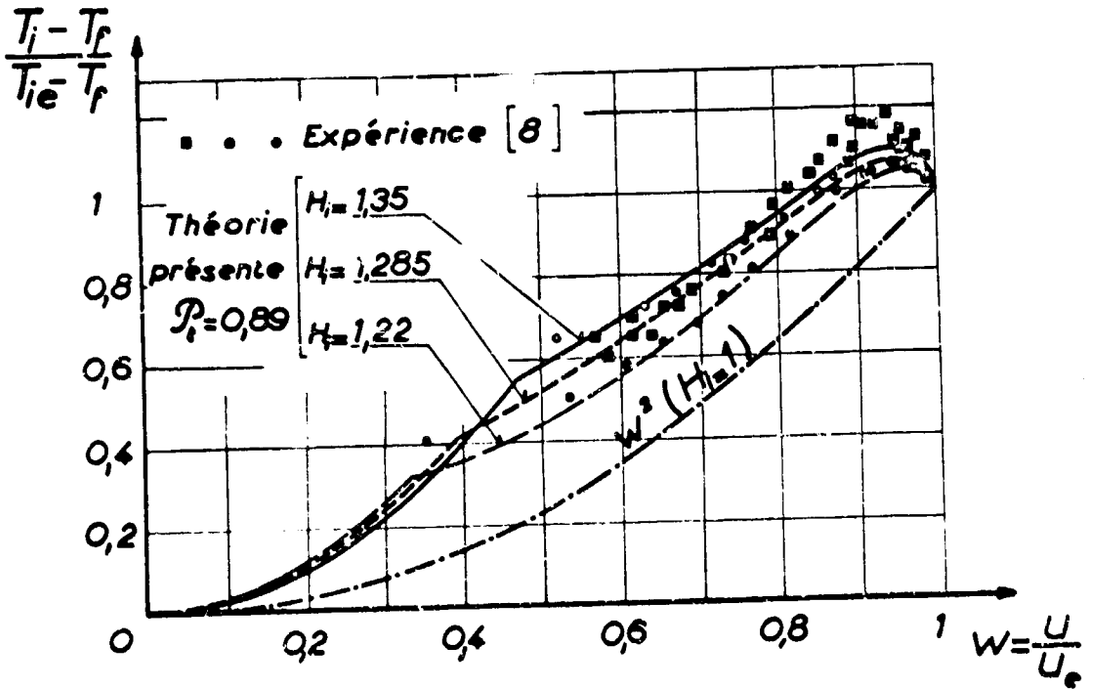

Fig.3 Distribution des températures d'arrêt pour la plaque plane athermane turbulente en gaz parfait

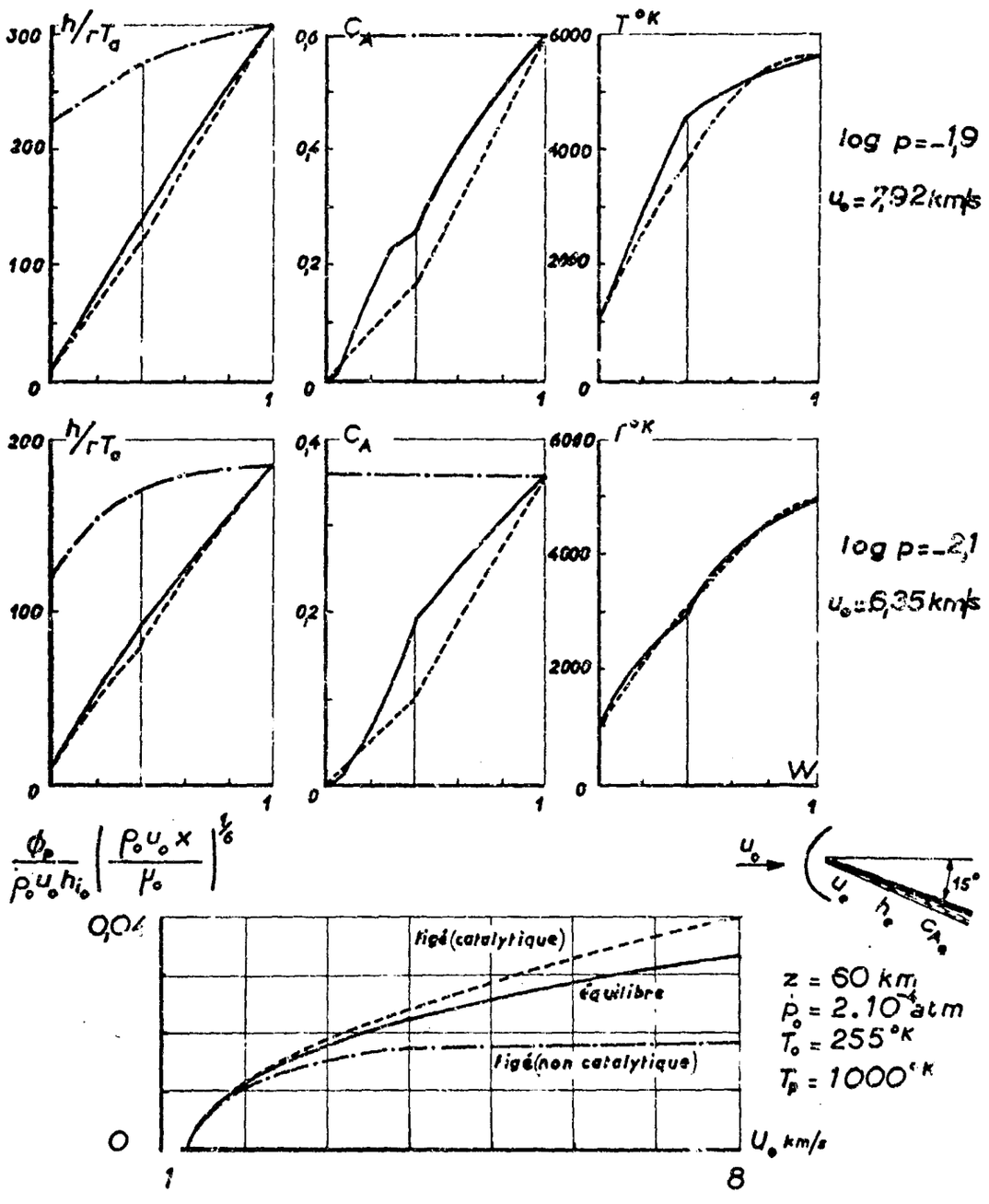

Fig. 4 Plaque plane – transferts de chaleur et profils de couche limite en gaz réel

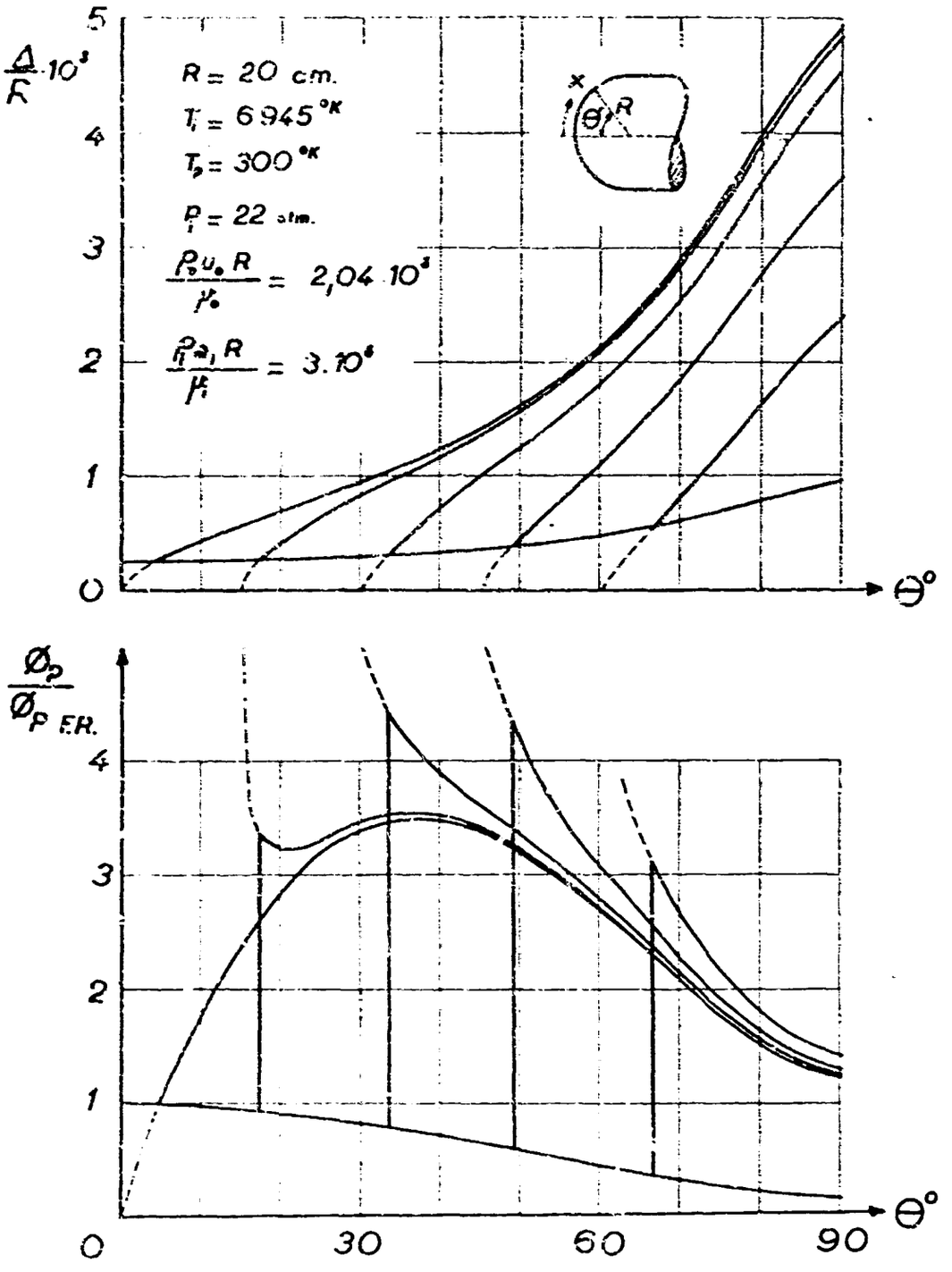

Fig.5 Epaisseur d'énergie et transfert de chaleur pour différentes transitions sur l'hémisphère (gaz parfait $\gamma = 1,4$)

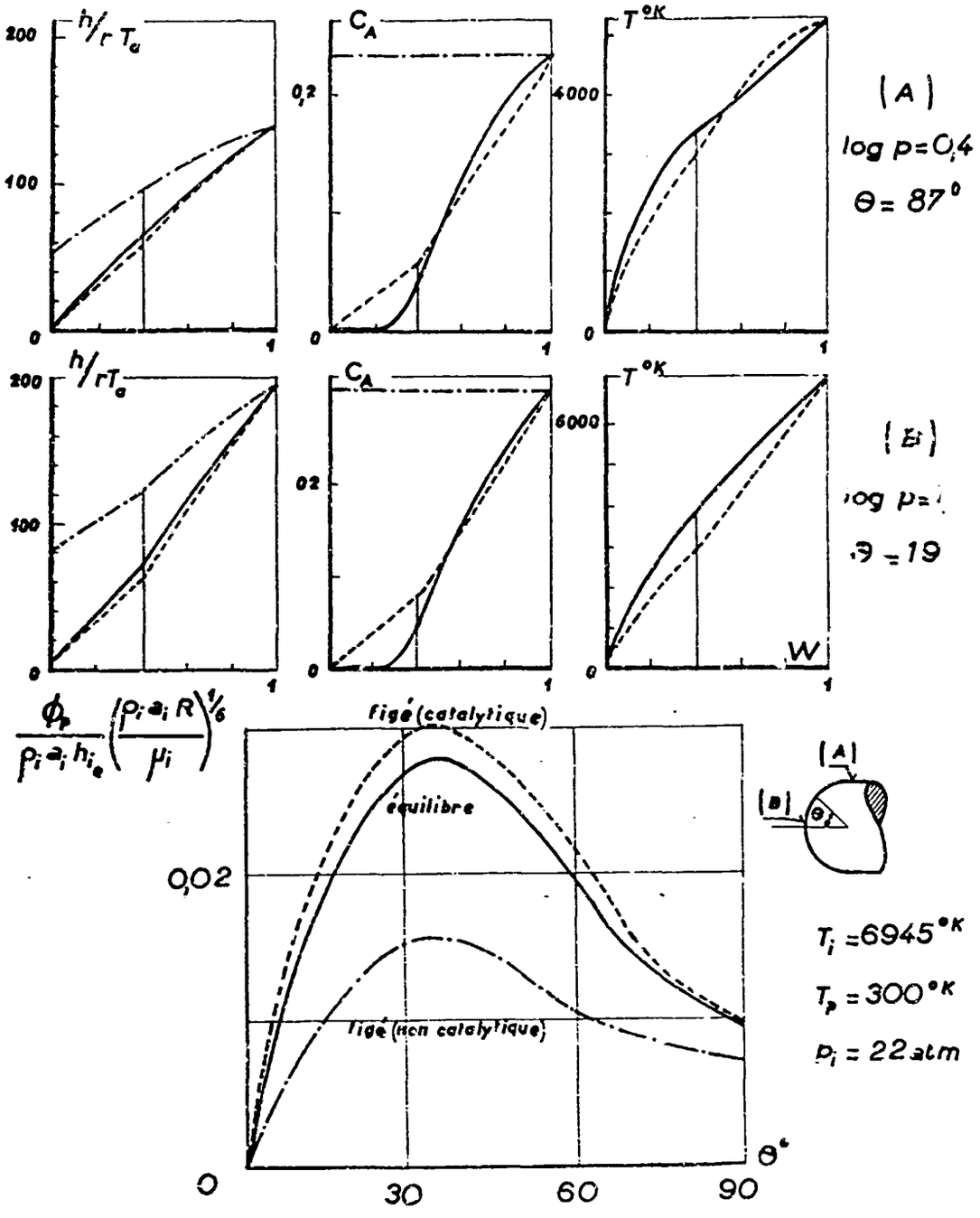

Fig.6 Profils de couche limite et flux de chaleur sur l'hémisphère en gaz réel

MEASUREMENTS OF TURBULENT SKIN FRICTION AT HIGH REYNOLDS NUMBERS AT MACH NUMBERS OF 0.2 AND 2.2

by

K.G. Winter, K.G. Smith, L. Gaudet

Royal Aircraft Establishment, Bedford, U.K.

SUMMARY

The measurements, taken on the sidewall of the R.A.E. 8 ft x 8 ft Wind Tunnel, consist of surface shearing stress using a large force balance together with velocity and temperature distributions through the boundary layer. The maximum effective length Reynolds numbers obtained are 2.2×10^8 at $M = 0.2$ and 1.1×10^8 at $M = 2.2$. The results agree moderately well with the empirical correlation proposed by Spalding and Chi. The variation of skin friction with Reynolds number is however less than given by most of the accepted formulae.

SOMMAIRE

Les mesures, effectuées sur la paroi latérale de la soufflerie de 8 ft x 8 ft du Royal Aircraft Establishment, portaient sur les efforts de cisaillement des surfaces. On a utilisé une balance à forces de grandes dimensions et les répartitions des vitesses et des températures dans la couche limite. Les nombres de Reynolds de la longueur effectifs maximums ont été de 2.2×10^8 pour $M = 0.2$ et de 1.1×10^8 pour $M = 2.2$. Ces résultats correspondent plus ou moins à la corrélation empirique proposée par Spalding et Chi. La variation du frottement de surface en fonction du nombre de Reynolds est cependant inférieure à celle que donnent la plupart des formules courantes.

CONTENTS

LIST OF FIGURES

NOTATION

A	defined by $C_F = ARe_x^{-1/N}$
c_f	local skin friction coefficient
C_F	mean skin friction coefficient
F_c, F_{R_δ}, F_{R_x}	parameters defined in Reference 6
M	free stream Mach number
N	(-1/N) is exponent in mean skin friction power law
Re	unit Reynolds number (per foot)
Re_x	streamwise length Reynolds number
Re_{δ_2}	momentum thickness Reynolds number
T	temperature
u	velocity
u_τ	friction velocity
x	streamwise length
y	distance normal to wall
μ	viscosity
ν	kinematic viscosity
ρ	density
δ_1	displacement thickness $= \int_0^\delta \left(1 - \frac{\rho u}{\rho_\delta u_\delta}\right) dy$
δ_2	momentum thickness $= \int_0^\delta \frac{\rho u}{\rho_\delta u_\delta}\left(1 - \frac{u}{u_\delta}\right) dy$

$$\delta_1^{(u)} = \int_0^{\delta} \left(1 - \frac{u}{u_\delta}\right) dy$$

$$\delta_2^{(u)} = \int_0^{\delta} \frac{u}{u_\delta} \left(1 - \frac{u}{u_\delta}\right) dy$$

$$H_{12} = \delta_1/\delta_2$$

$$H_{12}^{(u)} = \delta_1^{(u)}/\delta_2^{(u)}$$

Subscripts

s refers to sublayer conditions (Ref. 4)

w refers to wall conditions

δ refers to conditions at edge of boundary layer

Superscript

$\star$ refers to intermediate temperature conditions $T^\star = 0.28T_\delta + 0.72T_w$

MEASUREMENTS OF TURBULENT SKIN FRICTION AT HIGH REYNOLDS NUMBERS AT MACH NUMBERS OF 0.2 AND 2.2

K.G. Winter, K.G. Smith, L. Gaudet

1. INTRODUCTION

As aircraft fly faster and further so there is a tendency for the percentage payload to diminish. It therefore becomes more essential to be able to estimate drag accurately either by extrapolation from wind tunnel experiments or by direct calculation. In either case more data is needed on the variation of skin friction with Reynolds number extending up to flight Reynolds numbers which increase as aircraft become longer and more slender. For example the flight Reynolds number based on the length of the Concord is of the order of 350 million.

The sidewall of the R.A.E. 8 ft x 8 ft Wind Tunnel gives an effective run of some 40 ft at subsonic speeds and 30 ft at supersonic speeds and enables Reynolds numbers of about 200 million to be obtained in virtually incompressible flow*, and of 100 million in supersonic flow. The experiments discussed in this paper were made at Mach numbers of 0.2 and 2.2. They form part of a more extensive continuing programme for which the highest Mach number is 2.8 and which includes measurements at other intermediate Mach numbers.

The experiments consist of direct measurements of surface shear using a force balance together with explorations of velocity and temperature profiles in the boundary layer on the tunnel sidewall.

2. DESCRIPTION OF WIND TUNNEL AND APPARATUS

Figure 1 shows the general arrangement of the working section and contraction cone of the tunnel, which is of closed return circuit and operates continuously. The tunnel cooler is situated at the maximum section and since it is 16 ft long with the air flowing through a large number of tubes (1¼ in internal diameter) can be regarded as an effective honeycomb. Downstream of the cooler two slots are provided for screens (not at present fitted), and there is a further row of slots to enable part of the total flow round the circuit to bypass the working section under some conditions of running. The settling chamber is square with corner fillets and the geometrical contraction ratio to the working section is about 15.6:1. The working section has rigid parallel sidewalls with flexible roof and floor operated by hydraulic jacks. All walls in the working section are coated with a layer of epoxy resin giving a good surface finish which has not been measured but which can be assumed to be of the order of 10 μin .

* Higher values than this could be obtained at higher subsonic speeds.

The measurements were made on the port sidewall in the small aperture, of 18 in diameter, shown in Figure 1 upstream of the main windows.

The balance used for the surface shear measurements is sketched in Figure 2. The airswept surface of the floating plate is 14.5 in diameter. It has a surface finish of better than 8 μin . The use of a plate of large surface area enables the force on the plate to be measured by normal strain gauge techniques. The gauges are mounted on three parallel flexures 0.025 in thick, 0.35 in wide and 1 in long. The flexures carry the floating plate and are supported from the rear plate of the balance housing. The housing fits into the tunnel sidewall and leaks are prevented by 'O' rings in appropriate places. Steps on the surface between sidewall and housing, and housing and floating plate do not exceed 0.001 in . The clearances at the edge of the floating plate, and shown in Figure 2, are such that the balance flexures cannot be overstrained either by axial load or normal pressure load. Twelve pressure tappings are provided round the gap to enable buoyancy corrections to be determined. In calculating the buoyancy force the pressure has been taken as constant over the depth of the edge of the plate ('ab' in Fig. 2). Any pressure difference between the free surface and the balance cavity will be carried by viscous forces on the surfaces along 'bc'.

The balance was calibrated in situ in the tunnel using weights supported on a thread attached to the centre of the floating plate and passing over a large diameter balanced pulley. Because of changes of temperature in the tunnel when running there will generally be temperature differences between the floating plate and the backplate. The resulting differential expansion will give rise to spurious stresses within the flexures. Provided individual sensitivities of the flexures are used, the total force should still be given by the sum of the forces in each flexure, since the apparent forces due to differential temperature will cancel. It was found, however, that the apparent force recorded was sensitive to differential temperature. It is presumed that this is due to small misalignments of the gauges so that they are sensitive to transverse stresses (in direction Z in Fig. 2) which will be high because of the large stiffness of the flexures in this direction. Allowance was made for this effect by suitable calibration against an effective temperature difference, which to first order, is proportional to the difference between the apparent load in the single flexure (3) and the sum of the apparent loads in (1) and (2). It should be remarked that the existence of a temperature difference between the back plate and the floating plate does not imply that there is any significant aerodynamic heat transfer. The air space provides good insulation and the flexures are of too small cross-sectional area to conduct much heat.

The rake used for the boundary layer surveys is shown in Figure 3. It has 49 pitot tubes and 8 static tubes. Near the wall the pitot tubes were 0.020 in o.d. and 0.010 in i.d., and were mounted in five columns in order to avoid mutual interference in an array of densely packed tubes. Further from the wall the size is increased to 0.039 in o.d. and 0.024 in i.d. Static tubes are either side of the main column to avoid interference. The measured static pressures have not in fact been used in the analysis. For $M = 0.2$ velocities were obtained from pitot pressure and wall static pressure (corrected for hole size); for $M = 2.2$ static pressure was derived via the Mach number given by the normal shock formula applied to total pressure and pitot pressure readings outside the boundary layer. The tubes were connected to a bank of capsule manometers with a least count of 0.005 in Hg. The same strut was also utilised to carry temperature probes (as a separate experiment) and is shown so modified in

Figure 4 together with a sketch showing the details of a probe. The probes were calibrated against the tunnel instruments which measure stagnation temperature. The recovery factor was found to depend upon Reynolds number but little upon Mach number. This dependence was taken into account in determining temperature profiles.

3. RESULTS AND DISCUSSION

3.1 General

The Mach number distribution along the tunnel sidewall is shown in Figure 5 with the test station and effective origin of the turbulent boundary layers indicated. Because, particularly at $M = 2.2$, the development takes place in a favourable pressure gradient and in the presence of transverse gradients, the question must be asked as to whether the profiles studied can be considered to be typical for a flat plate or whether there is some distortion. Using their high Reynolds number data Smith and Walker[1] followed the approach suggested by Coles[2] and devised a semi-empirical law which they put forward tentatively. They tabulate the variation with Reynolds number of a number of boundary layer parameters. Of these the variation of shape parameter H_{12} with the momentum thickness Reynolds number should be a fairly critical criterion for judging whether there is any profile distortion. Furthermore Walz[3] implies that if the shape parameter is based on 'velocity' values of momentum and displacement thickness there is only a very weak dependence upon Mach number. Accordingly $H_{12}^{(u)} = \delta^{(u)}$ is plotted in Figure 6 against momentum thickness Reynolds number. Except for the lower Reynolds numbers where the data is inaccurate, and where at $M = 0.2$ there is some anomalous behaviour as will be shown later, the data follows closely the suggestion of Smith and Walker. Their own data, as they point out, is at variance with the line at lower Reynolds number. It is for this reason that they make their suggestions only tentatively.

3.2 Velocity Profiles

The measured velocity profiles are shown in law of the wall form in Figure 7(a) and 7(b) using the measured value of c_f to define u_τ. The profile for the lowest Reynolds number at $M = 0.2$ for which a point was plotted in Figure 6 is omitted. For reference the 'law of the wall' lines according to Coles[4]* are drawn for each profile. At $M = 0.2$ the measurements lie above this line for nearly all Reynolds numbers. For the lowest Reynolds number plotted ($R_\theta = 0.47 \times 10^6$ per foot) where the accuracy is marginal the data is so far above as to suggest that there is some error. There is a general tendency for the curves to become increasingly flatter than the reference line as Reynolds number increases. At $M = 2.2$ (Fig.7 (b)) the accuracy of measurement is better and the data shows less scatter. The curves again become flatter as Reynolds number increases.

3.3 Momentum Thickness and Local Skin Friction Coefficient

The variation of the momentum thickness, calculated from the profiles, with unit Reynolds number is shown in Figure 8. At $M = 0.2$ the variation is not monotonic; though some of this can be attributed to lack of accuracy in pressure measurement

* Coles suggests that the Howarth transformation for y should be used.

repeat points confirm the general shape. It must be assumed that there is some factor, at present undetermined, other than unit Reynolds number which affects transition. The variation of the measured local skin friction with unit Reynolds number is given in Figure 9. The faired curves through the data have been assumed for subsequent analysis. The many points plotted are samples obtained at various times during a period of about six months. Much of the data was acquired incidentally during the course of other tests, this being possible as the balance produced no flow disturbance and was sited far enough upstream not to be influenced by the presence of a model. The readings during any particular test showed considerable fluctuation, mostly fairly consistently about a mean, but with occasional excursions to high values, and attempts were made to obtain readings over the full range of fluctuation. Some of the fluctuations were considered genuine but some probably arise from structural vibrations and are aggravated by lack of damping in the balance.

The two sets of measurements are combined in Figure 10 in which c_f is plotted against the momentum thickness Reynolds number $Re_{\delta 2}$. Values of c_f are taken from the mean curves of Figure 9 at the unit Reynolds numbers at which the boundary layer surveys were made. The data from Figure 10 are replotted in three ways in Figures 11 (a), (b) and (c). In Figure 11(a) the intermediate temperature hypothesis of Eckert[5] is used. Three datum curves are shown, those due to Kármán-Schoenherr, Prandtl-Schlichting (commonly used in the U.K.) and the Smith and Walker evaluation compatible with the shape parameter relationship in Figure 6. The latter line follows the trend of the experimental points at $M = 0.2$ but predicts c_f consistently higher by about 0.07×10^{-3}. The Prandtl-Schlichting curve is too steep but agrees with the data at high Reynolds number. The Kármán-Schoenherr line is in best agreement but also gives somewhat greater variation of c_f with $Re_{\delta 2}$ than indicated by the measurements. The intermediate temperature hypothesis fails to correlate the data at $M = 2.2$ with that at $M = 0.2$. The correlation proposed by Coles[4] using his sublayer concept is shown in Figure 11(b) together with his proposed incompressible relationship. This relationship is a fair fit to the data at $M = 0.2$ but fails to correlate the data at $M = 2.2$, though Coles has shown this to conform with a body of other data supersonic speeds though at lower Reynolds number. Finally in Figure 11(c) the empirical factors, and 'incompressible line' of Spalding and Chi[6] are used. The fit is very much better than in either Figure 11(a) or (b). The data do however suggest a less rapid variation with Reynolds number than proposed and a smaller value of either F_c or F_{R_δ} for $M = 2.2$.

3.4 Effective Origin of Boundary Layer

From the curves of c_f against $Re_{\delta 2}$ the effective origin of the boundary layers has been determined in the following way.

By definition

$$c_f = \frac{2dRe_{\delta 2}}{dRe_x}$$

hence for a set of points $s = 1$ to n as in Figure 10

$$Re_{xs} = Re_{x1} + 2\int_{(Re_{\delta 2})_1}^{(Re_{\delta 2})_s} \frac{1}{c_f}\, dRe_{\delta 2}$$

and Re_{xs} for any point s is determined apart from the starting value Re_{x1}.

Now if a power law variation of mean skin friction is assumed, i.e.

$$C_F = ARe_x^{-1/N}$$

then

$$c_f = \frac{\partial}{\partial x}(C_F x) = ARe_x^{-1/N} - A\frac{x}{N}Re_x^{(-1/N)-1}\frac{\partial Re_x}{\partial x} = ARe_x^{-1/N}(1 - 1/N)$$

also

$$C_F = \frac{2Re_{\delta 2}}{Re_x}$$

Therefore

$$\frac{Re_{\delta 2}}{c_f} = \frac{1}{2}\frac{C_F Re_x}{c_f}$$

$$= \frac{1}{2}\frac{Re_x}{1 - 1/N}$$

Thus if $Re_{\delta 2}/c_f$ is plotted against $Re_{xs} - Re_{x1}$ and a straight line is obtained, Re_{x1} and N can be determined. The data of Figure 10 plotted in this fashion are shown in Figure 12, where it can be seen that an extremely good fit to a straight line is obtained. The straight lines drawn were found by a 'least squares fit' and give values of N of 7.866 and 7.464 respectively at $M = 0.2$ and 2.2. Knowing the values of unit Reynolds number, the effective length x can be obtained from Re_x, and is plotted against Re_x in Figure 13. The anomalous behaviour at the lower Reynolds numbers at $M = 0.2$ is shown in these plots as an apparent reversal of transition position with increasing Reynolds number. At $M = 2.2$ possibly because of the larger favourable gradients x is virtually independent of Reynolds number.

3.5 Skin Friction as a Function of Length Reynolds Number

Following the procedure outlined in the previous paragraph curves for the variation of local skin friction coefficient c_f and mean coefficient C_F with length Reynolds number Re_x are plotted in Figures 14(a) and (b). The derived points are compared with a power law in which the mean value of N for $M = 0.2$ and 2.2 i.e. $N = 7.665$ is taken, with the value of A obtained by a least squares procedure applied to the measured skin friction coefficient C_F. The multiplier for c_f is $(1 - 1/N)$ times that for C_F. As would be anticipated from Figure 12 the fit is good.

The results are replotted in terms of intermediate temperature in Figure 15(a) and according to Spalding and Chi in Figure 15(b). In Figure 15(a) the conclusion of the previous comparison Figure 11(a) that the variation with Reynolds number predicted by the Prandtl-Schlichting formula is too great is reiterated. Because of this the formula in intermediate temperature terms predicts C_F at $M = 2.2$ to within 3% over the Reynolds number range of the experiment even though the intermediate temperature hypothesis in Eckert's form is not fulfilled. The final figure 15(b) shows that the method of Spalding and Chi, which was shown to give the best fit to the basic data, agrees quite well with c_f on an Re_x basis with the same reservations as mentioned previously. For C_F the data virtually all lie below the prediction and as in the other comparisons have less variation with Re_x than predicted. However, for Re_x of around 10^8, c_f and C_F as measured are closely predicted for both test Mach numbers.

Also shown on Figure 15(b) are the high Reynolds number results from Moore and Harkness[7] which have been reanalysed using the method of the previous paragraph. The data, for which M varies from 2.897 to 2.669, was first corrected (by the intermediate temperature method) to $M = 2.80$. They do not confirm the trend of the present experiments in that the variation of both c_f and C_F with Reynolds number is greater than predicted by Spalding and Chi. One salient difference in the experimental procedures is the omission by Moore and Harkness of measurements of temperature distribution and the assumption in calculating δ_2 of constant total temperature. The effects of this assumption will be examined in further analysis of the present experimental results.

4. CONCLUDING REMARKS

There is a long history of measurements of skin friction in incompressible flow on which have been built the various current empirical relationships. It would be presumptuous to draw any firm conclusions on the basis of this single experiment which conflict with this vast body of data. Nevertheless it is felt that the smaller variation of skin friction with Reynolds number shown by the present data should not be disregarded. It is admitted that this variation could be modified by different assumptions in deriving Re_x but the authors feel that Figure 12 is very convincing. It could be that the various accepted formulae for skin friction are biased by the data available at low Reynolds numbers, and that of necessity this involves the use of artificial stimulation of turbulence with some consequent distortion of the boundary layers. No such stimulation is used in this experiment. It is significant that the measurements are in fair agreement with deductions from the results of Smith and Walker at higher Reynolds numbers where the effect of their trip might be expected to have diminished.

The same arguments can be used to explain why the results at $M = 2.2$ are in rather better agreement with the statistical analysis of Spalding and Chi. In effect their parameter F_{Rx} reduces the Reynolds number of measurements at supersonic speeds to a lower 'incompressible' value. In this way the compressibility parameters are tailored to produce a fit to a possibly erroneous incompressible relationship.

Finally a word should be said about the effect of assumed temperature distribution on boundary layer parameters. A very limited analysis only has so far been undertaken. It was found that at $M = 2.2$ there could be up to 3% difference in momentum thickness calculated using constant total temperature compared with using the measured temperature distribution. The further implications of this are still being examined.

REFERENCES

1. Smith, D.W. Walker, J.H. — *Skin-friction Measurements in Incompressible Flow.* NACA TN.4231 March, 1958 (Superseded by NASA T.R. R-26 1959).

2. Coles, D. — *Measurements in the Boundary Layer on a Smooth Flat Plate in Supersonic Flow. I. The Problem of the Turbulent Boundary Layer.* California Institute of Technology, Jet Propulsion Laboratory Rep.20-69 June, 1953.

3. Walz, A. — Bietrag zur Naeherungstheorie kompressibler turbulenter Grenzschichten, II. Berechnung der universellen Funktionen und Beispiele. DVL Rep.136 October, 1960. English translation available as Library of Congress AID Rep.T-63/110 August, 1963.

4. Coles, D. — *The Turbulent Boundary Layer in a Compressible Fluid.* USA Rand Rep.R-403-PR September, 1962.

5. Eckert, E.R.G. — *Survey on Heat Transfer at High Speeds.* WADC Tech. Rep.54-70 April, 1954.

6. Spalding, D.B. Chi, S.W. — *The Drag of a Compressible Turbulent Boundary Layer on a Smooth Flat Plate With and Without Heat Transfer.* J. Fluid Mechanics Vol.18 pp.117-143, 1964.

7. Moore, D.R. Harkness, J. — *Experimental Investigations of the Compressible Turbulent Boundary Layer at Very High Reynolds Numbers* $M = 2.8$. AIAA Paper No.64-592 August, 1964.

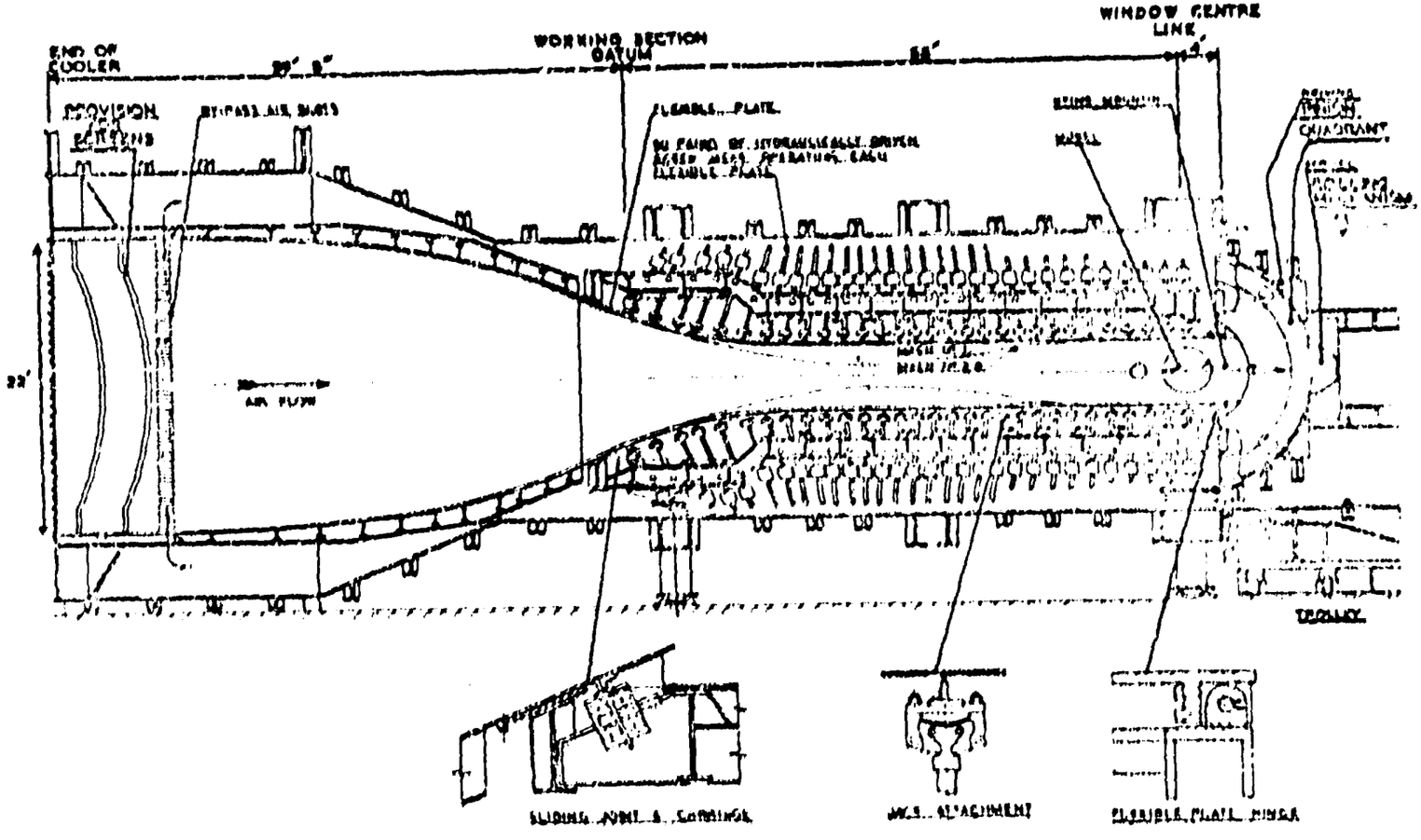

Fig. 1 General arrangement of working section and contraction, 8 ft x 8 ft wind tunnel

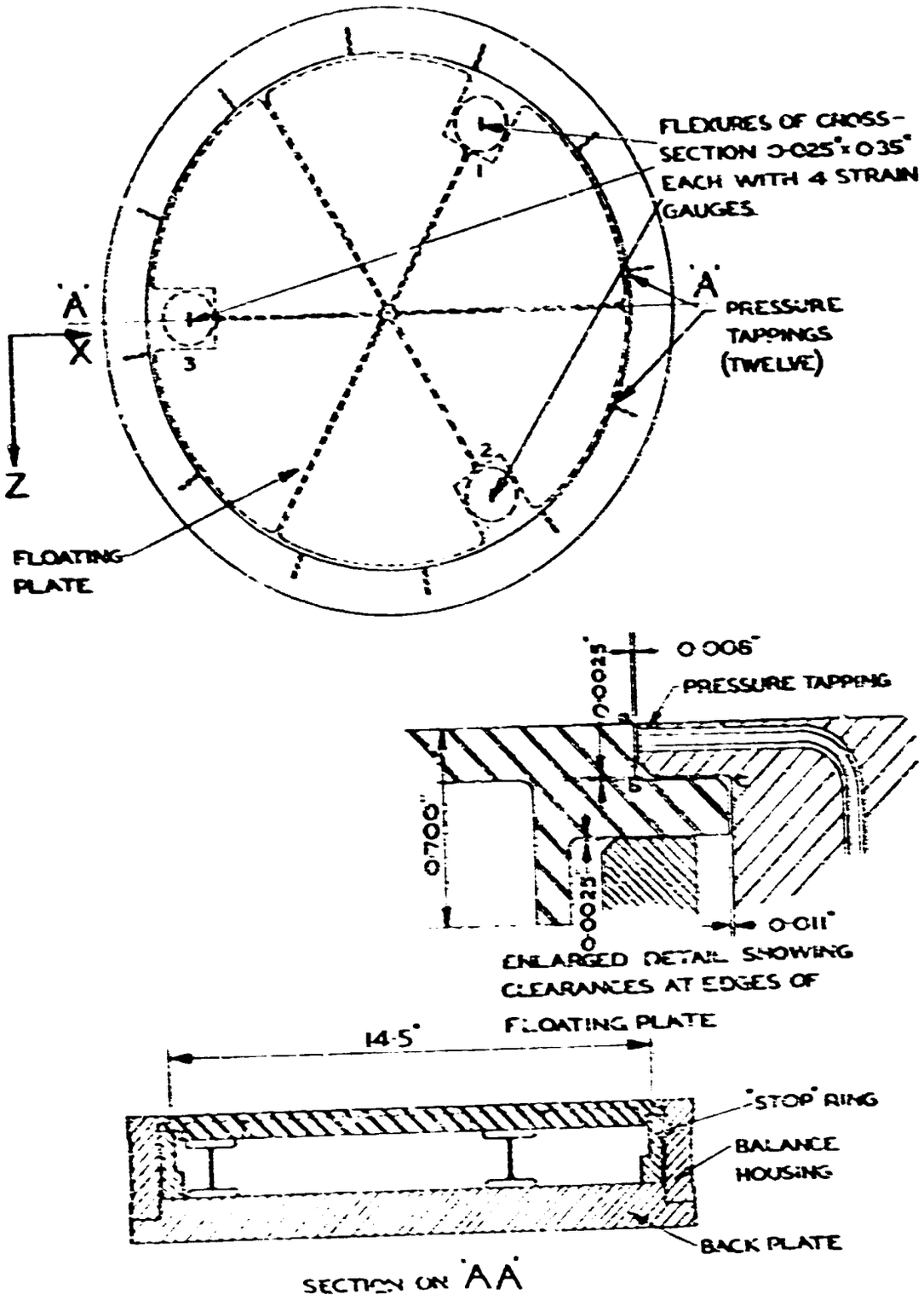

Fig. 2 Details of skin friction balance

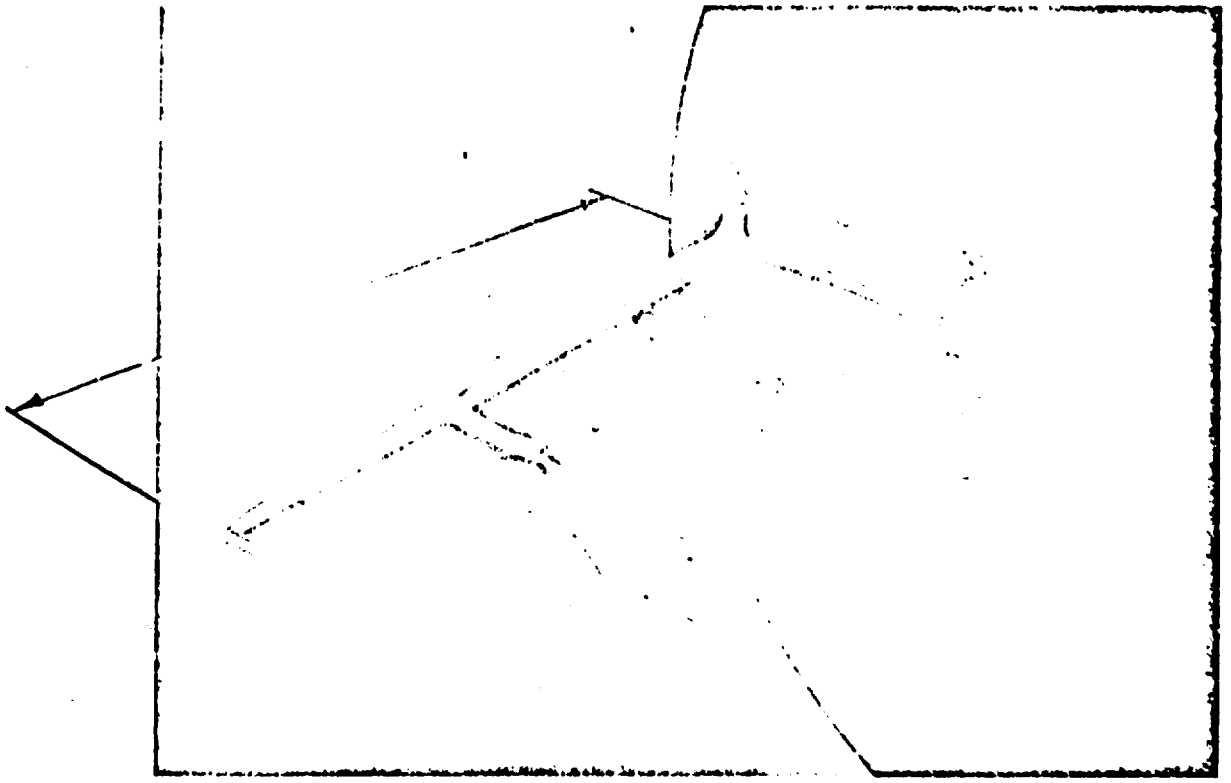

Fig. 3 Boundary layer rake

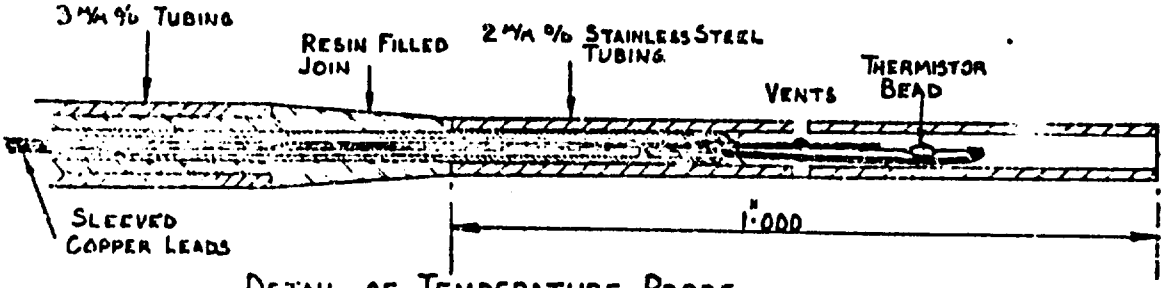

Detail of Temperature Probe.

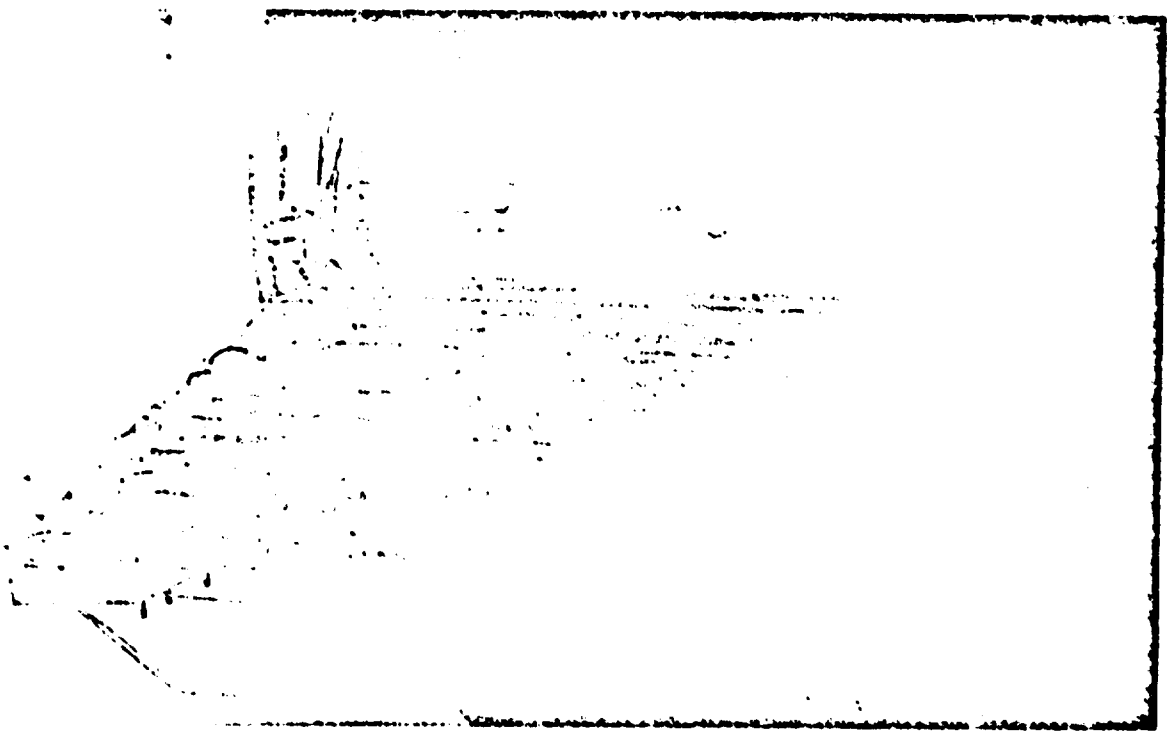

Fig. 4 Rake with temperature probes

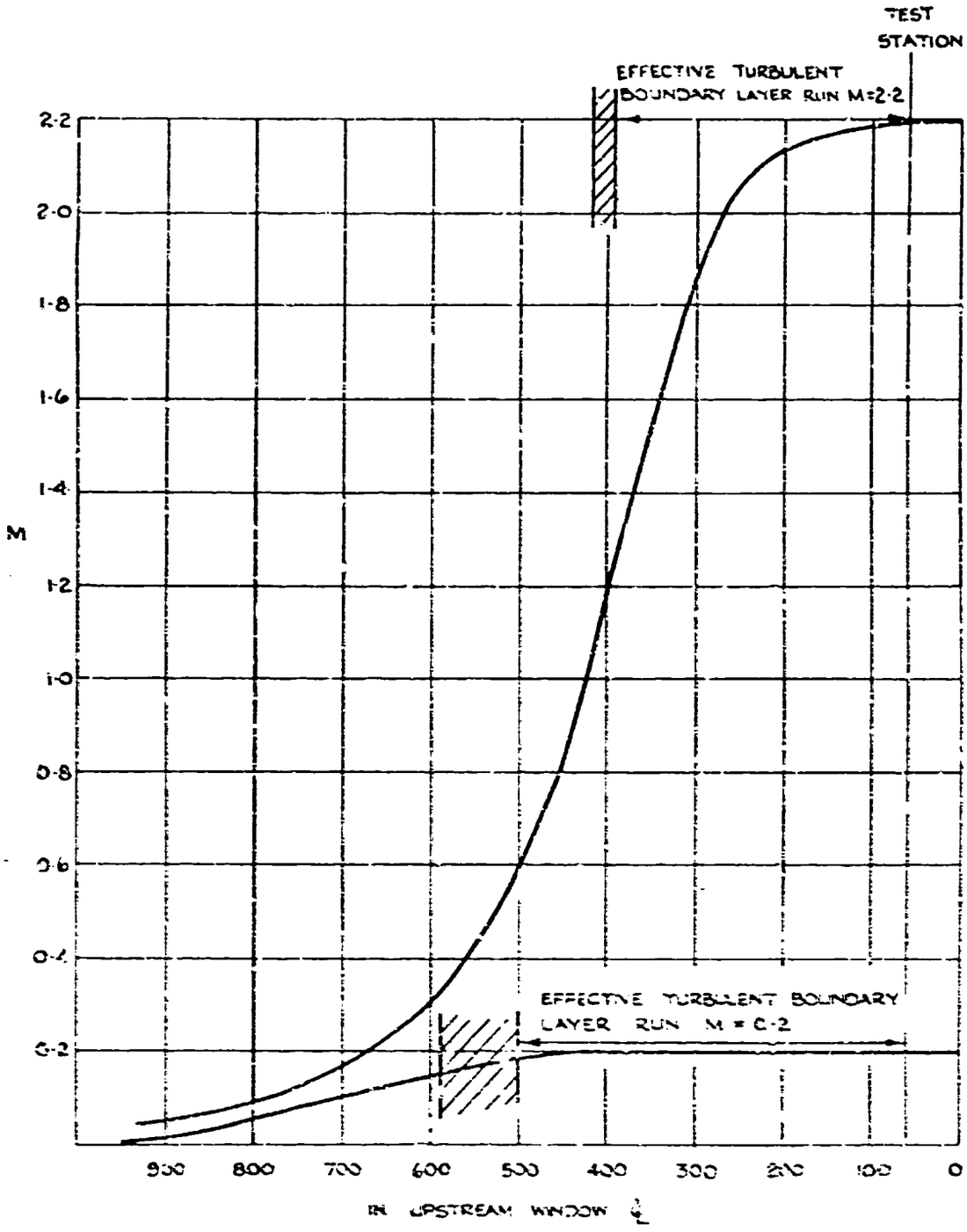

Fig.5 Mach number distribution along turn 1 sidewall

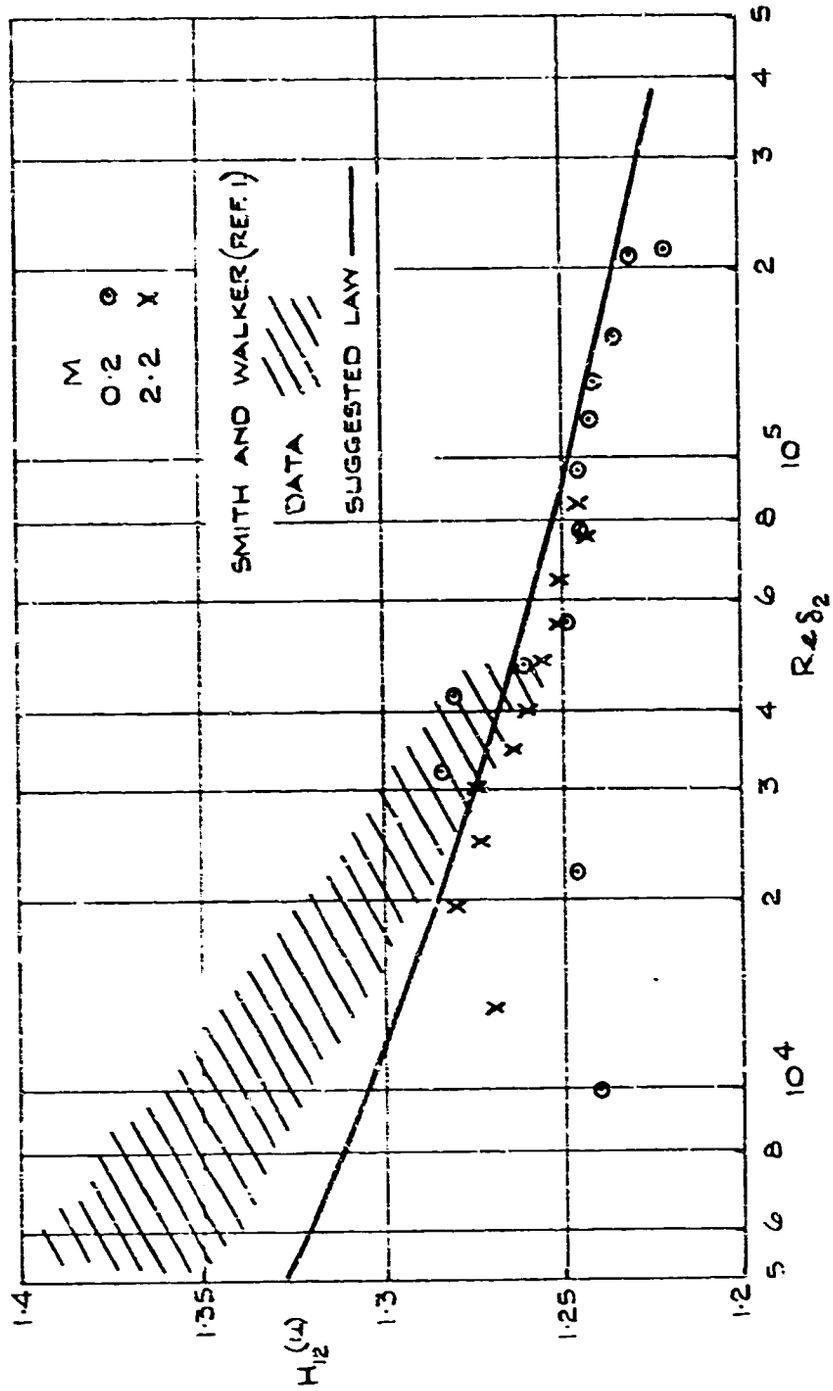

Fig. 6 Dependence of 'velocity' shape parameter on momentum [illegible] Reynolds number

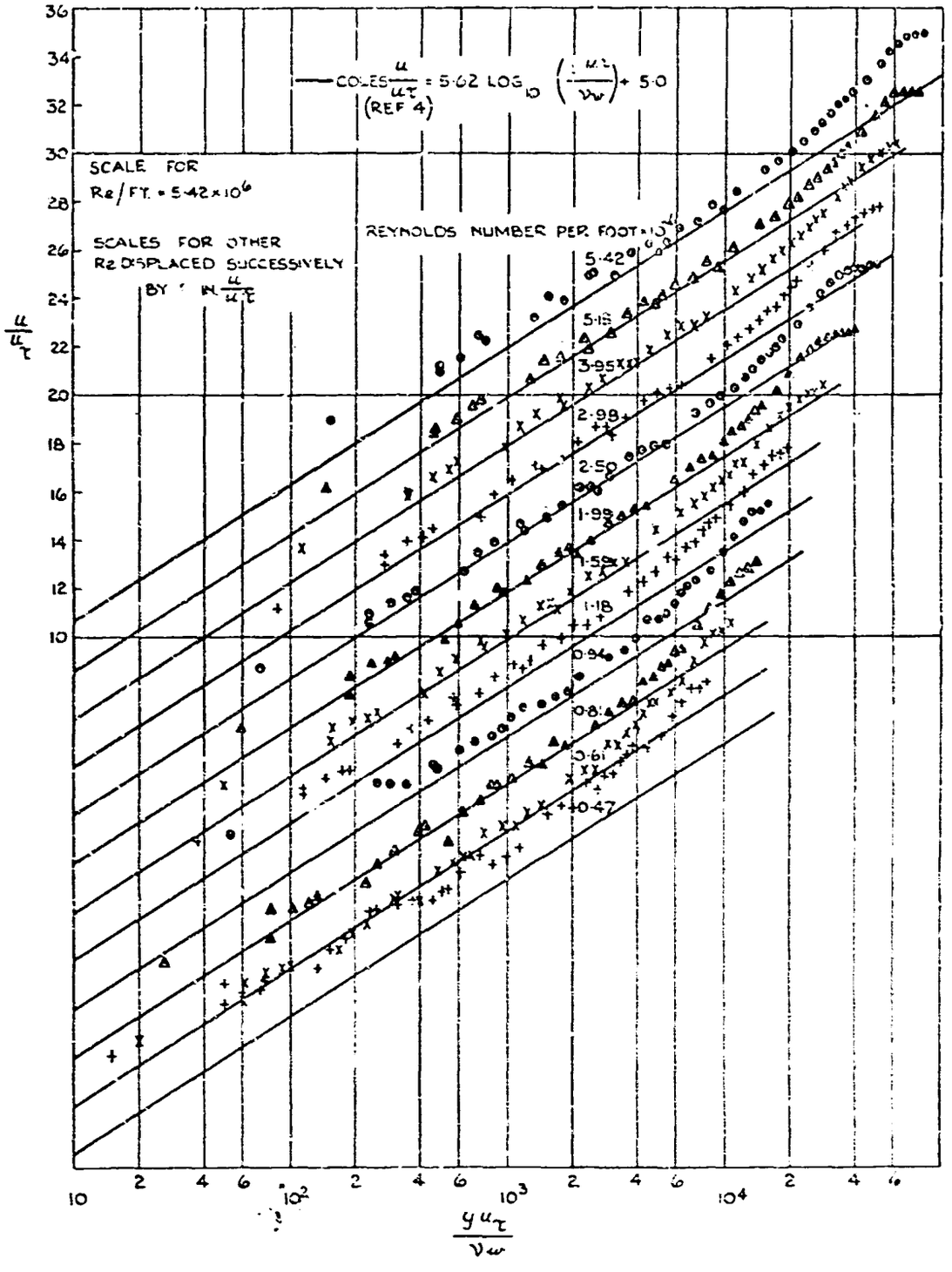

Fig.7(a) Logarithmic velocity profiles. M = 0.2

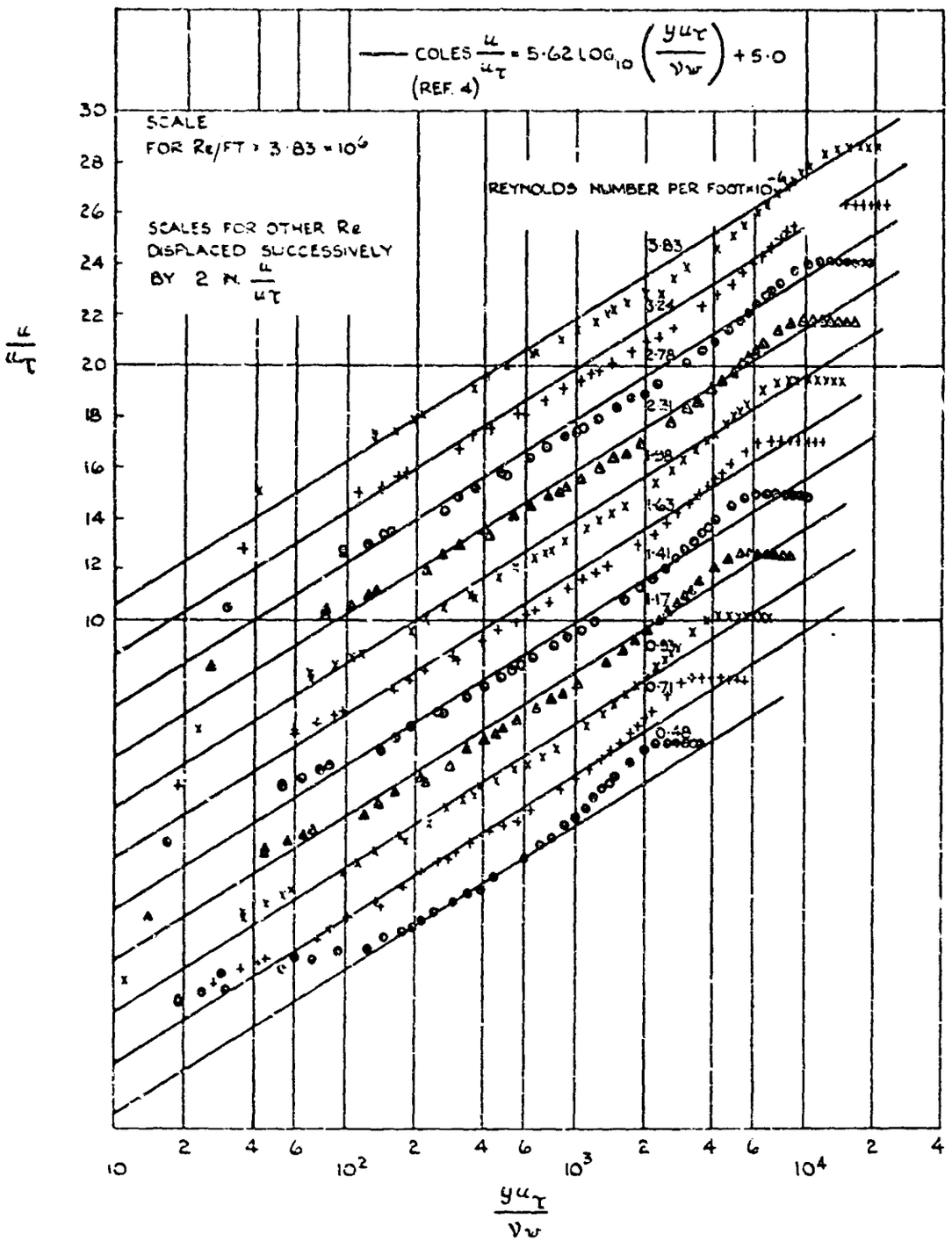

Fig.7(b) Logarithmic velocity profiles. M = 2.2

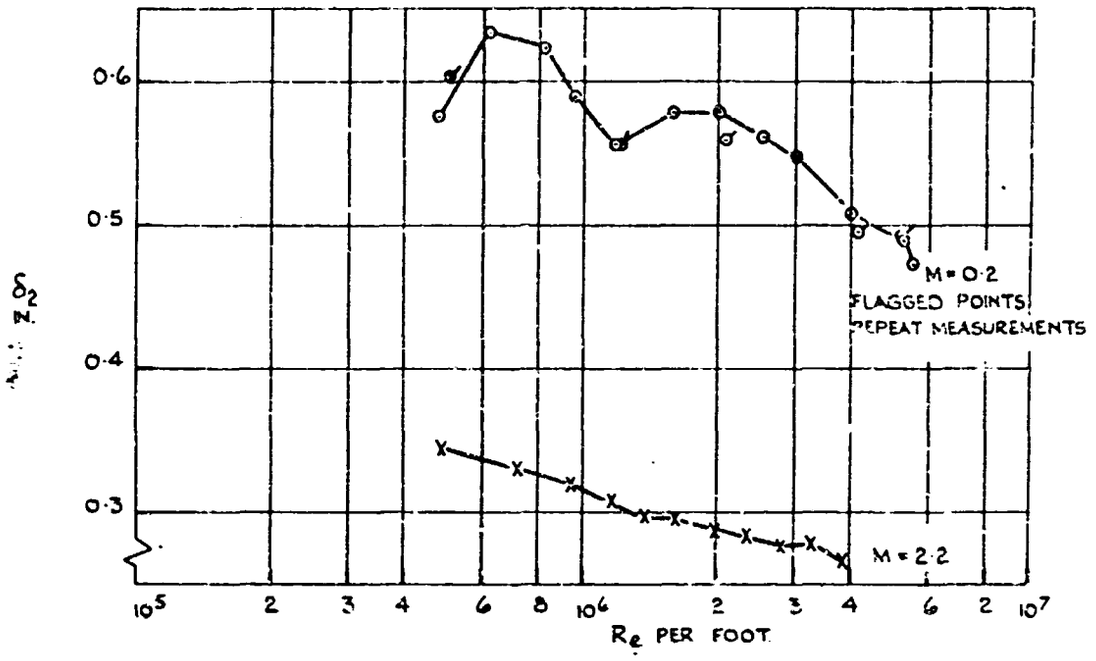

Fig. 8 Momentum thickness variation with unit Reynolds number

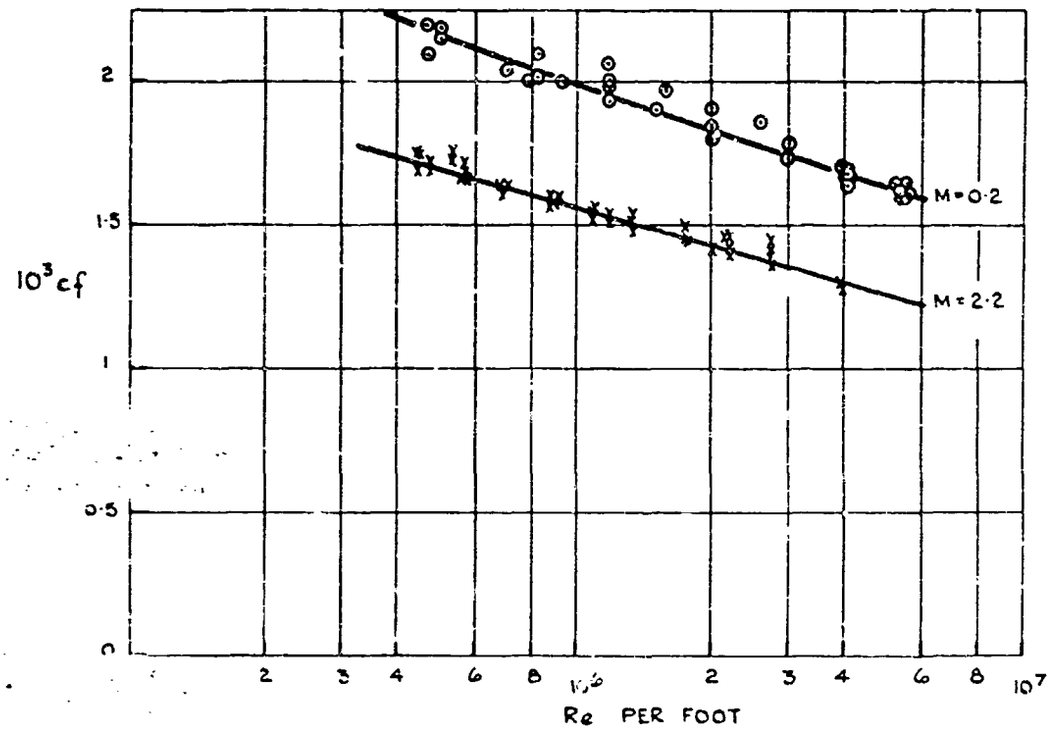

Fig.9 Local skin friction variation with unit Reynolds number

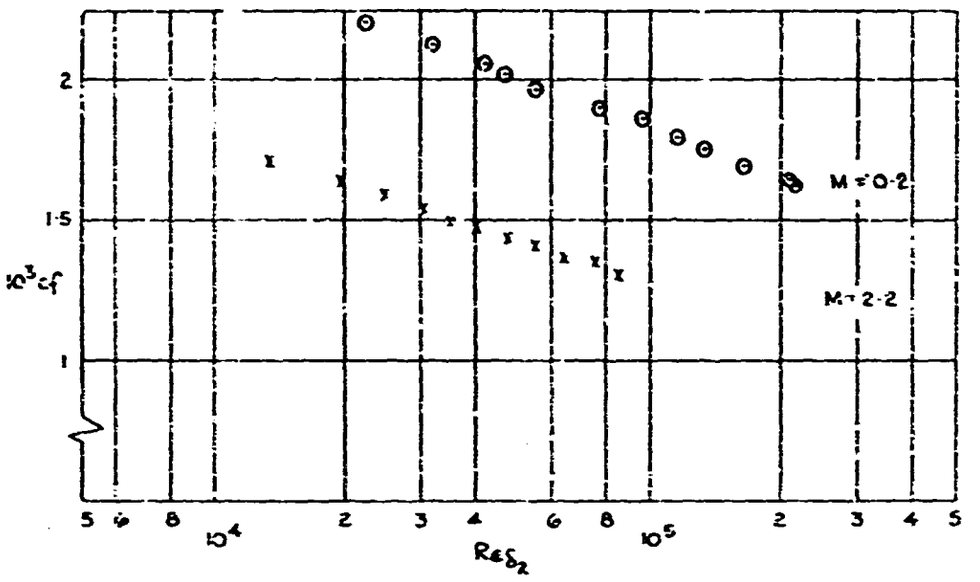

Fig. 10 Local skin friction coefficient as a function of momentum thickness Reynolds number

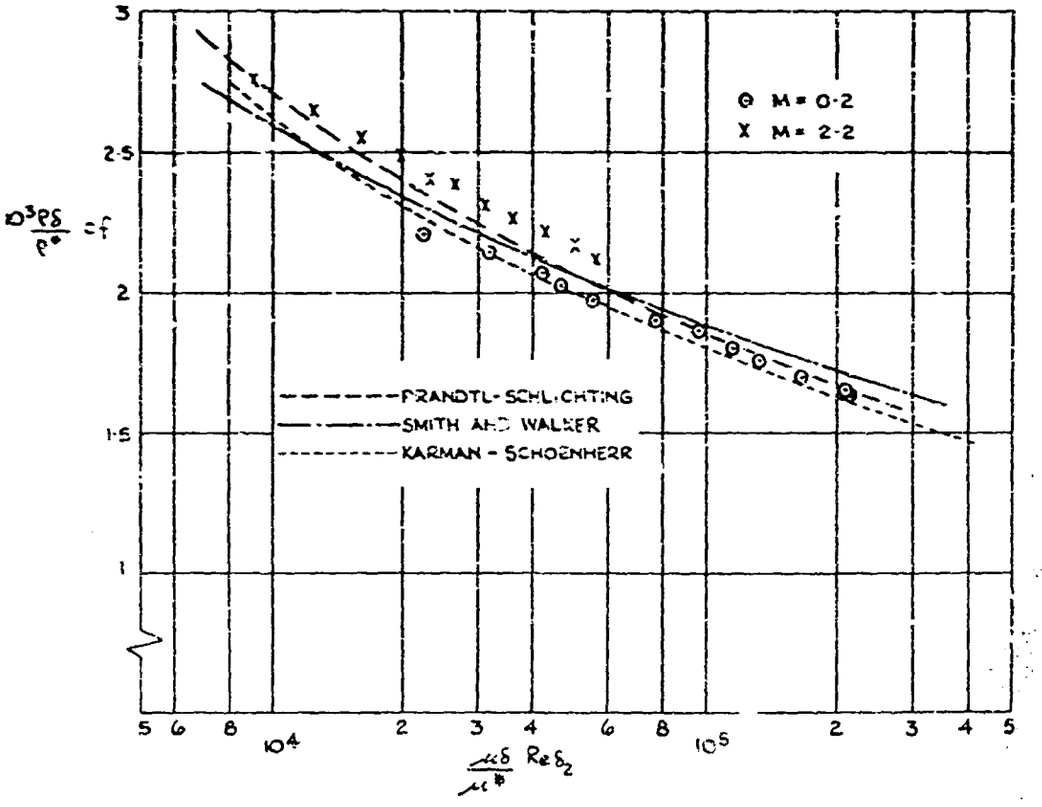

Fig. 11(a) Local skin friction coefficient related to momentum thickness Reynolds number in intermediate temperature form

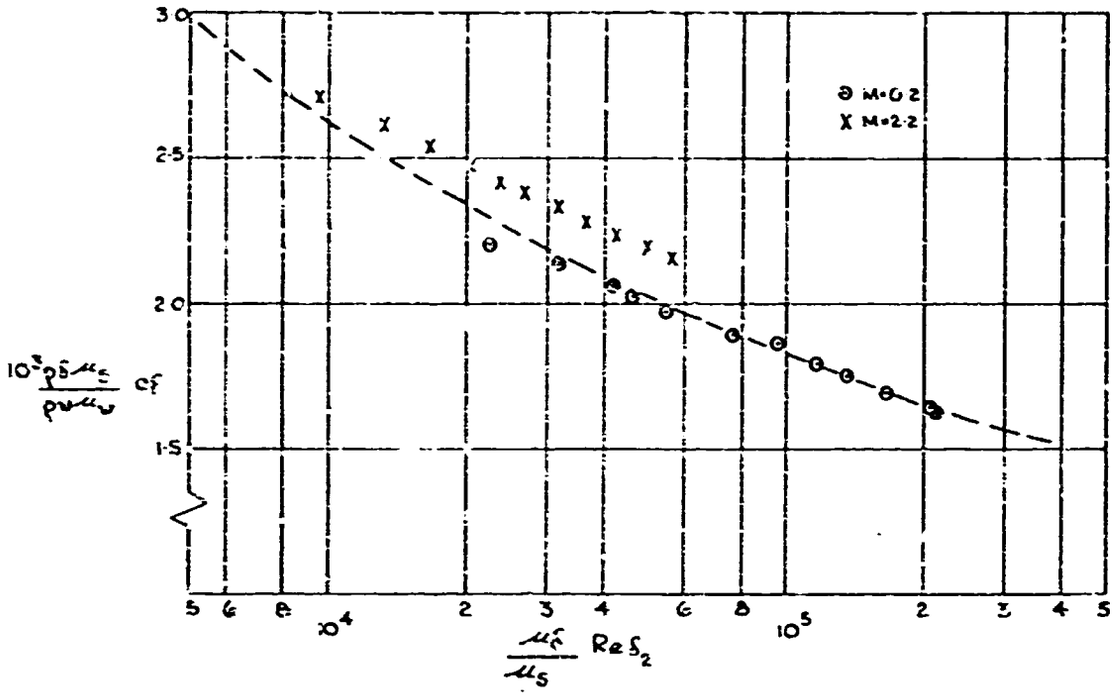

Fig. 11(b) Local skin friction coefficient related to momentum thickness Reynolds number according to Coles (Ref. 4)

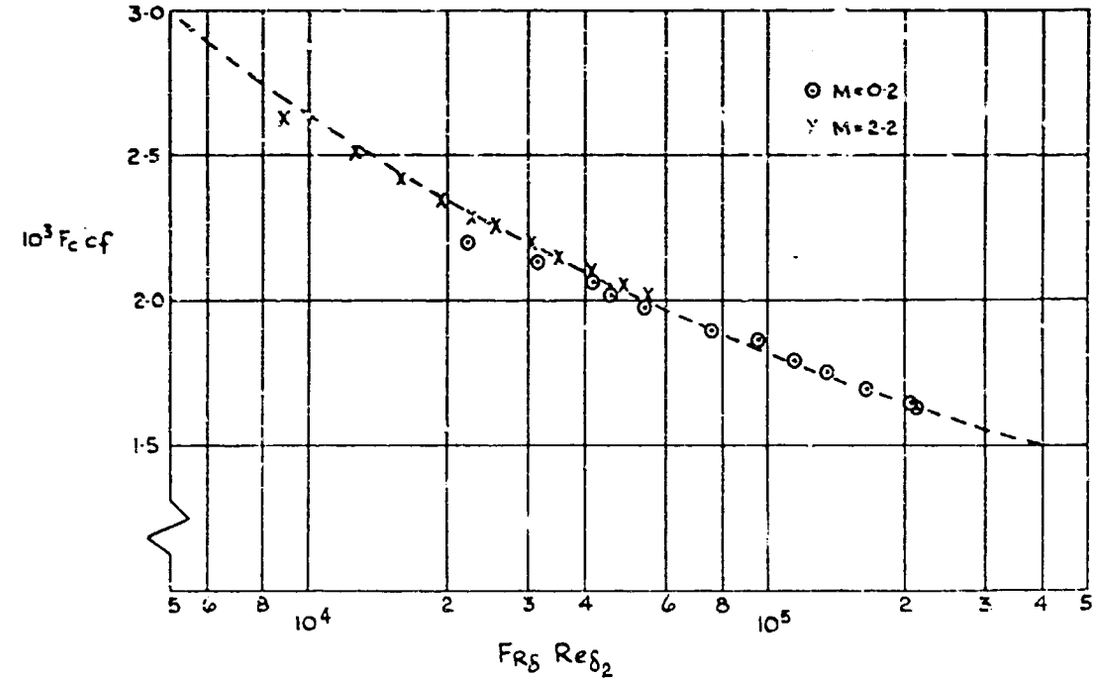

Fig. 11(c) Local skin friction coefficient related to momentum thickness Reynolds number according to Spalding and Chi (Ref. 6)

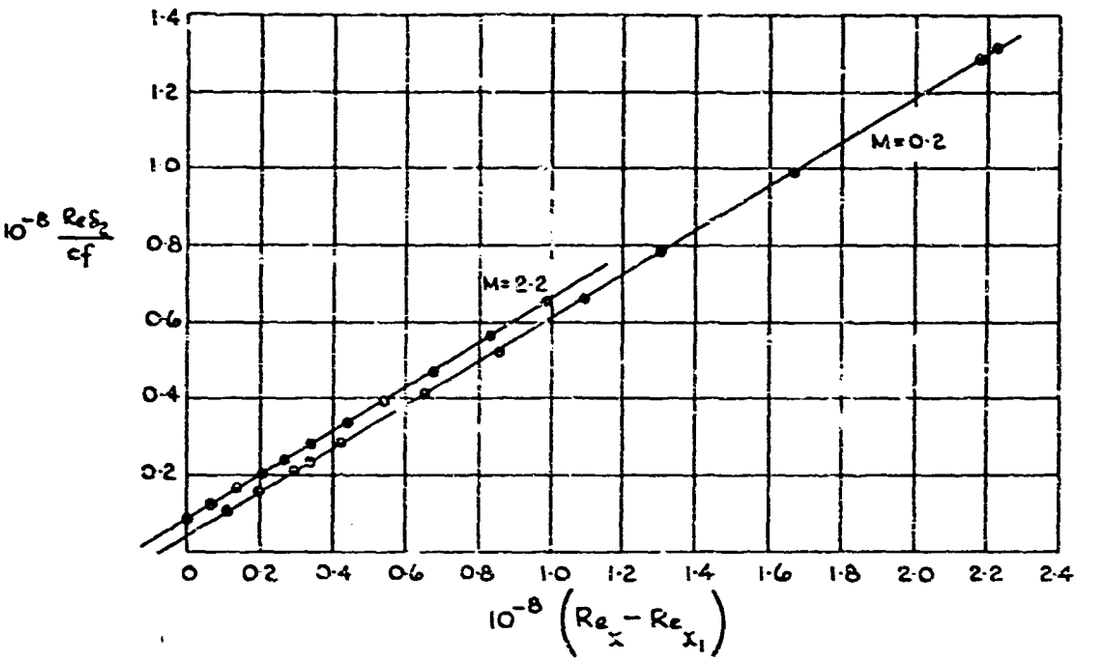

Fig. 12 Derivation of Re_x

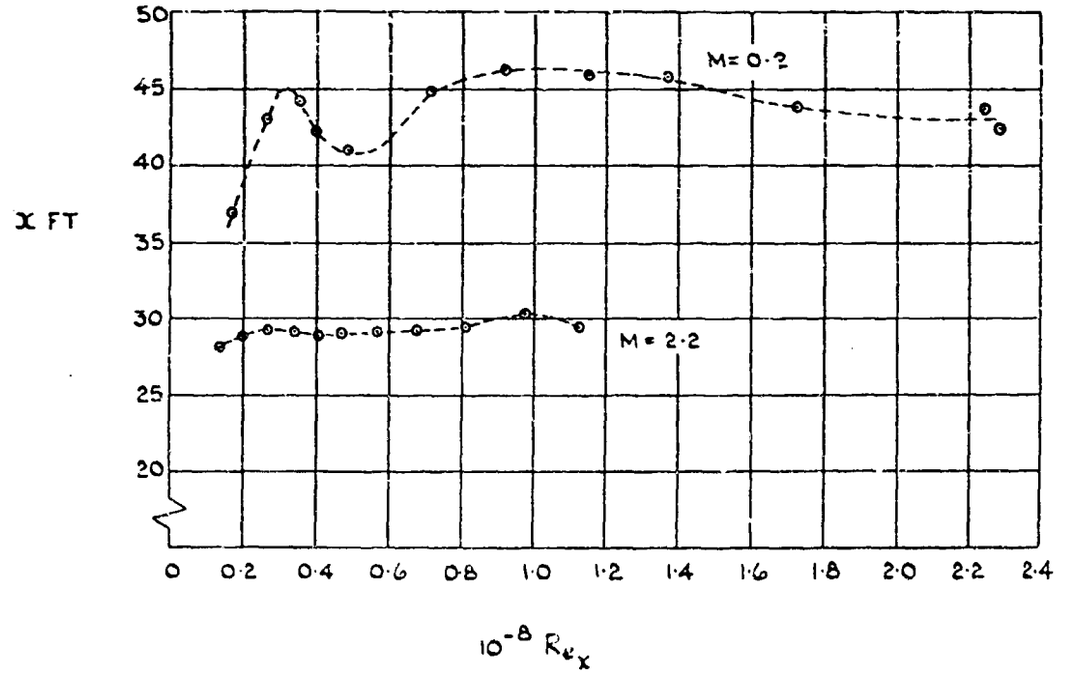

Fig. 13 Effective run of turbulent boundary layer

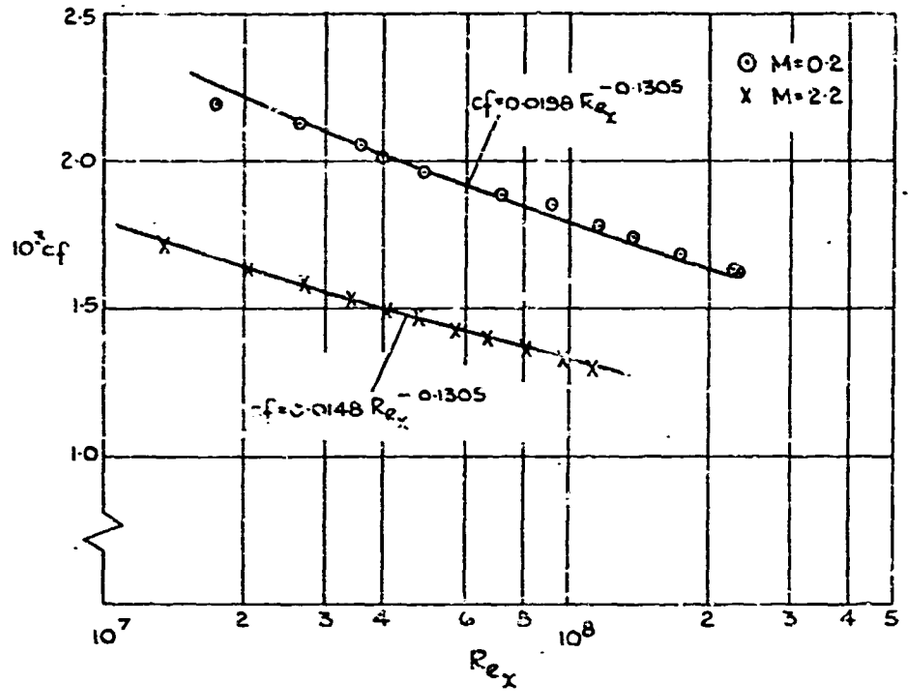

(a) Local coefficient

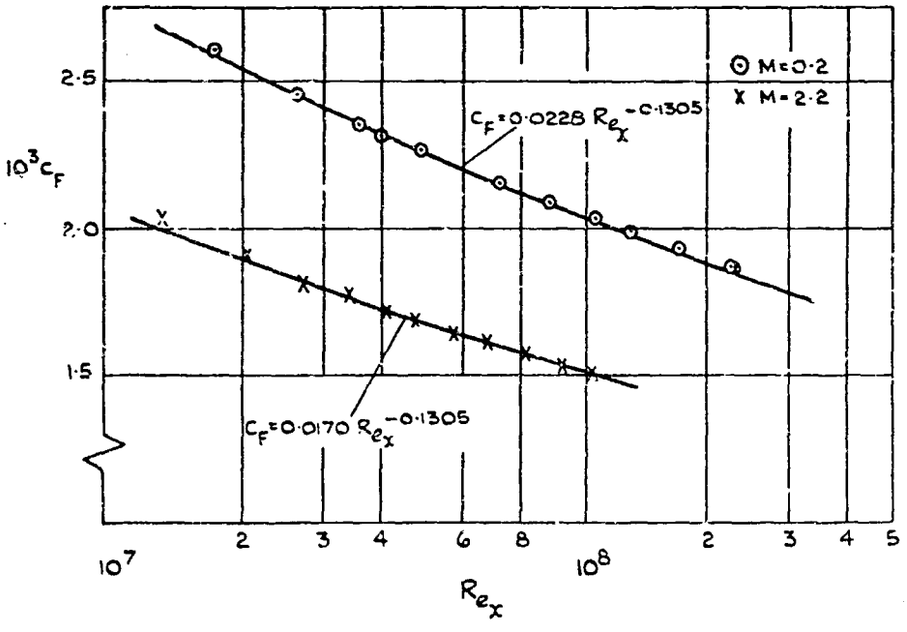

(b) Mean coefficient

Fig. 14 Dependence of skin friction on streamwise length Reynolds number

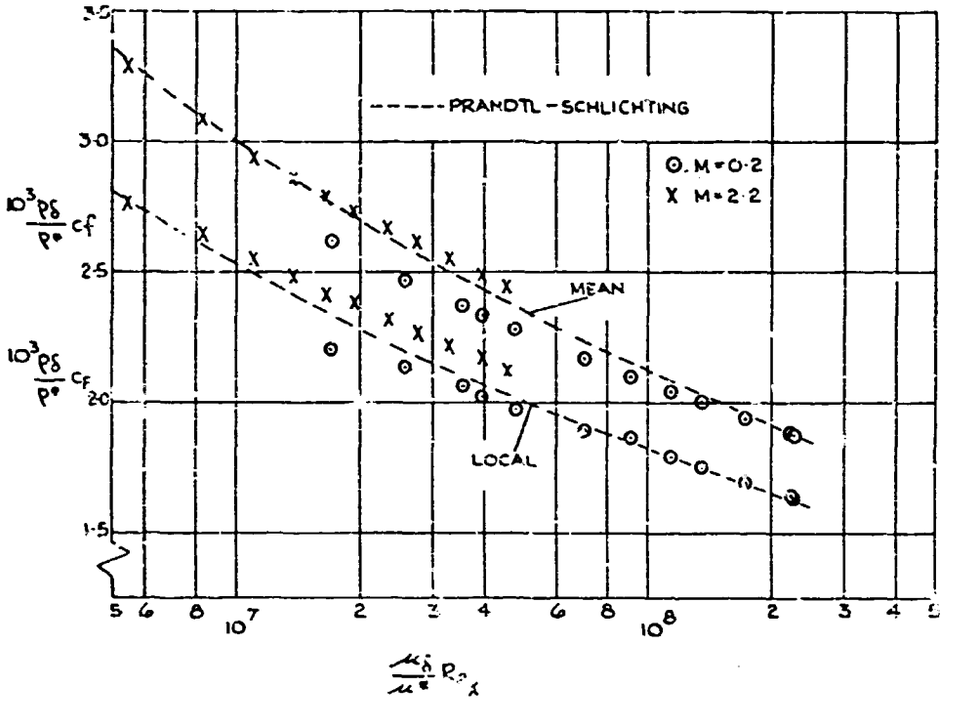

Fig. 15(a) Skin friction – Reynolds number relation in intermediate temperature form

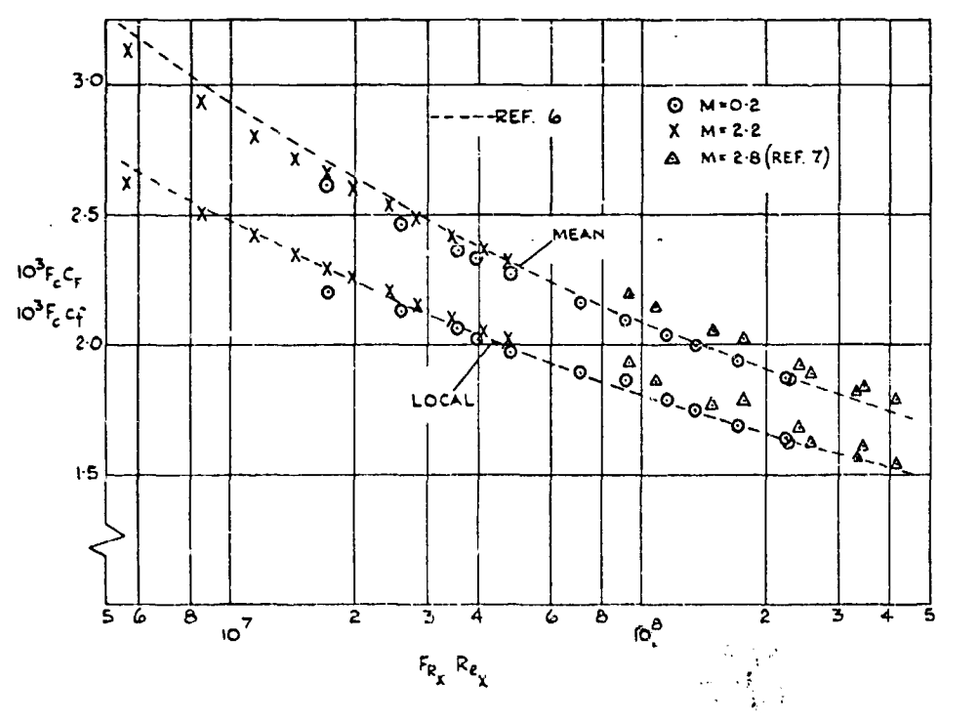

Fig. 15(b) Skin friction – Reynolds number relation according to Spalding and Chi

THE TURBULENT WALL JET IN A MOVING STREAM

by

C.I. Harris

von Kármán Institute for Fluid Dynamics,
Rhode-Saint-Gènese, Belgium.

SUMMARY

The two-dimensional incompressible turbulent wall jet on a plane surface beneath a moving stream of arbitrary pressure gradient has been treated analytically by integral methods. The solution has been programmed for the IBM 1620 digital computer and the results thereby obtained compared with experimental data.

SOMMAIRE

Le jet pariétal turbulent incompressible bi-dimensionnel sur une surface plane et en présence d'un écoulement à gradient de pression arbitraire a été traité analytiquement par des méthodes intégrales. La solution a été programmée pour le calculateur digital IBM 1620 et les résultats ainsi obtenus comparés avec les mesures expérimentales.

CONTENTS

LIST OF FIGURES

NOTATION

b	slot width
c_f	skin friction coefficients $c_f = \tau_w / \frac{1}{2}\rho V_j^2$
C_i	constants
e	base of natural logarithm = 2.718
E_d	energy dissipation per unit time
H	total energy
k	constant in Equation (19), $k = \log_e 2 = 0.693$
K_i	constants
l	Prandtl's mixing length
L	constant appearing in Equation (12), $L = 0.01575$
p	static pressure
$P(\eta)$	velocity distribution function in inner layer (Eqn. (21))
$Q(\zeta)$	velocity distribution function in outer layer (Eqn. (21))
Re_s	slot Reynolds number $Re_s = V_j b/\nu$
r	$= \delta_m/b$
s	$= \delta_{m/2}/b$
t	$= u_m/V_j$
$T(\zeta)$	shear stress function
U	x-directional velocity component at the edge of the shear layer $U = u(y \geq \delta)$
u	x-direction velocity component at distance y from the surface
u_m	u at $y = \delta_m$
V_j	slot discharge velocity
x	distance measured along surface from slot exit
x_o	distance from slot exit to end of core region

y distance measured normal to surface

a_i variable coefficients (Eqn.(17))

δ total height of wall jet

δ_m distance from surface to peak velocity point ($u = u_m$)

$\delta_{m/2}$ distance to half-maximum velocity point [$u = \frac{1}{2}(u_m - U)$]

ϵ exponent appearing in Equation (12), $\epsilon = 0.182$

κ Prandtl's mixing length constant, $\kappa = 0.0684$

$\kappa_1 = \kappa^2(2.25)^2 = 0.0236$

λ external velocity ratio $\lambda = U/V_j$

ν kinematic viscosity, $\nu = \mu/\rho$

μ viscosity

η non-dimensional coordinate in the inner layer

ρ density

τ shearing stress

τ_m shearing stress at peak velocity point $y = \delta_m$

τ_w shearing stress at the surface $y = 0$

ξ non-dimensional coordinate along the surface $\xi = x/b$

ζ non-dimensional coordinate in the outer layer

$$= \frac{y - \delta_m}{\delta_{m/2} - \delta_m}$$

THE TURBULENT WALL JET IN A MOVING STREAM

G.L. Harris

1. INTRODUCTION

The quantitative understanding of the flow in a two-dimensional jet discharged tangentially along a plane surface beneath an external moving stream is fundamental to the study of blowing boundary layer and circulation control systems, and wall jet-type ejectors.

In the following pages, an approximate analytical solution of this problem which is based on mean flow momentum and energy considerations is developed. The numerical results thereby obtained are compared with experimental measurements made in the present study and by other investigators.

2. ANALYTICAL DEVELOPMENT

2.1 Model of the Flow

The assumed structure of the flow in a two-dimensional incompressible turbulent wall jet on a plane surface beneath an external stream is shown schematically in Figure 1. A number of distinct regions of the flow exist which are as follows.

2.1.1 *The Upstream Boundary Layer Region*

Due to the presence of the external stream, a boundary layer forms upstream of the slot exit as shown in the figure which may in some cases interfere with the jet flow. In the present analysis, it is considered that the slot velocity and the slot width are sufficiently large so that the momentum deficit of the upstream boundary layer at the slot lip is negligible with respect to the momentum of the jet. In view of these conditions, it is assumed that the boundary layer is completely absorbed by the jet immediately downstream of the slot exit and that it in no way interferes with the flow development downstream of the slot.

2.1.2 *The Potential Core Region*

Downstream of the slot exit there appears for a relatively short distance (on the order of 10 slot widths) a potential core region in which the velocity is equal to the slot velocity V_j. The fluid in the core region has not had sufficient time to mix with the surrounding fluid and therefore retains its original velocity. As the distance from the slot increases, the mixing process penetrates more deeply into the core region until at the point $x = x_0$, (called the starting length), the potential

core region disappears entirely, and the peak velocity begins to decrease for $x > x_0$.

In order to compute the jet development downstream of the point $x = x_0$, it is necessary to know the initial conditions $\delta_m(x_0) = \delta_{m0}$, and $\delta(x_0) = \delta_0$ (Fig. 1). These quantities depend too heavily on the details of individual slot designs to merit involved computation, so that mean values will be selected from existing experimental data and will be assumed valid for all wall jets.

2.1.3 *The Inner Layer* ($0 < y < \delta_m$)

The inner layer resembles a normal turbulent boundary layer or channel flow. Defining the non-dimensional coordinate in this region $\eta = y/\delta_m$, the velocity is assumed to be given by

$$\frac{u}{u_m} = P(\eta) \tag{1}$$

where $P(\eta)$ is a universal function.

2.1.4 *The Outer Layer* ($\delta_m < y < \infty$)

The outer layer will be assumed to possess many of the characteristics of a plane turbulent free jet discharging into a moving stream. Defining the non-dimensional coordinate in the outer layer as

$$\zeta = \frac{y - \delta_m}{\delta_{m/2} - \delta_m} \tag{2}$$

the velocity distribution in this region is assumed to be of the form

$$\frac{u - U}{u_m - U} = Q(\zeta) \tag{3}$$

where $Q(\zeta)$, like $P(\eta)$, is a universal function.

2.2 Flow Similarity

Defining universal non-dimensional velocity profiles in the inner and outer layers of the wall jet for $x > x_0$ is of course tantamount to assuming that flow similarity is achieved independently in each layer everywhere downstream of x_0 . This is not strictly true in general.

It may be seen from the available experimental data that the shape of the non-dimensional velocity profile in the inner layer of a wall jet flow in fact depends somewhat on the existing conditions external to the shear layer. Strictly speaking therefore, $P(\eta)$ is not universal and the similarity assumption for the inner layer is invalid. On the other hand, the thickness of the inner layer is always very much smaller than the overall height of the wall jet. Furthermore, the variations in $P(\eta)$ are confined within fairly well defined limits. Little error is therefore likely to accrue from selecting a single mean representative form of $P(\eta)$ and calling it universal.

In the outer layer, there exists for some distance downstream of the starting length a transitional region in which the non-dimensional velocity profiles adjust to attain the stable form $Q(\zeta)$. The transitional distance is usually sufficiently small[2] so it is reasonable to postulate that flow similarity is attained immediately downstream of the starting length.

2.3 The Existence of a Finite Shearing Stress at $y = \delta_m$

In the case of a plane turbulent free jet, the shearing stress vanishes at the peak velocity point. This same condition exists at the axis of symmetry of a plane turbulent channel flow and at the edge of a turbulent boundary layer. In the first two cases, this condition is required by symmetry, while in the latter it results from the requirement that beyond the edge of the boundary layer, the flow is inviscid and hence no shearing stress can exist.

At first inspection, it would appear that the shearing stress would also vanish at the peak velocity point of a turbulent wall jet, since the derivative $\partial u/\partial y$ at that point vanishes, and according to Prandtl's mixing length theory[1]

$$\frac{\tau}{\rho} = l^2 \left|\frac{\partial u}{\partial y}\right| \frac{\partial u}{\partial y}$$

so should the shearing stress.

If this were in fact true, one could assume that the outer layer of the turbulent wall jet behaves exactly as a plane turbulent free jet, and that the inner layer is in every way identical to a normal turbulent boundary layer or channel flow, since there would be no stress interaction at their respective extremities. Solutions could then be obtained for each case and matched at the point $y = \delta_m$.

A number of investigators[2,3,4] have exploited this approach in dealing analytically with certain particular cases of wall jet flows.

In reality however, the shearing stress at the peak velocity point is not zero, and in general is not small. The stress results from the asymmetric turbulent fluid transport across the $y = \delta_m$ boundary which gives rise to a net Reynold's stress $\rho\overline{u'v'}$ at $y = \delta_m$ which is not zero since the velocity distribution about the peak velocity point is not symmetrical. Hot wire anemometer measurements[5] indicate that in the case of a wall jet in still air ($U = 0$) on a flat surface, the shearing stress at $y = \delta_m$ is equal and opposite to the wall shearing stress ($\tau_m = -\tau_w$).

A rigorous theoretical treatment of this phenomenon would require detailed information as to the complex behavior of a turbulent shear flow in the vicinity of an inflection point. This problem has thus far escaped mathematical treatment and is beyond the scope of the present study.

Rather than ignore the existence of this stress, a first approximation to its behavior will be employed in the subsequent analytical treatment, which is obtained from the following phenomenological considerations.

The turbulent shearing stress at the maximum point of a plane turbulent wall jet is in general negative[5]. $\tau(y)$ must therefore pass through zero at some point in the inner layer. In the case of a wall jet in still air, as mentioned previously, $\tau_m = -\tau_w$. Since in a plane turbulent free jet the shearing stresses are negative and in a turbulent boundary layer or channel flow they are positive it appears that when combined in a wall jet flow, the outer (jet) layer impresses its influence across the inner layer thereby overcoming the effect of the positive slope of the velocity profile in this region (which would normally create the positive shearing stress in the inner layer) and imposes a negative shearing stress over part of the inner layer. The magnitude of this influence would appear to depend on the shear stress level in the outer layer, which according to Prandtl's hypothesis is

$$\tau(y > \delta_m) \simeq (\delta - \delta_m)^2 \left|\frac{\partial u}{\partial y}\right| \frac{\partial u}{\partial y} .$$

The average slope of the velocity profile in the outer layer may be approximately taken as

$$\left(\frac{\partial u}{\partial y}\right)_{av} = \frac{u_m - U}{\delta - \delta_m}$$

so that

$$\tau_m \simeq \tau_{av} \simeq (u_m - U)^2 .$$

It has been already noted that for a plane wall jet in still air ($U = 0$), $\tau_m = -\tau_w$. It is also observed that when $u_m = U$, $\tau_m = 0$ since the flow degenerates to that of a normal turbulent boundary layer where the shear stress must vanish at the edge. Imposing these conditions, i.e.

$$\tau_m = -\tau_w \quad \text{when} \quad U = 0$$

$$\tau_m = 0 \quad \text{when} \quad U = u_m$$

the shear stress at the peak velocity point becomes

$$\tau_m = -\tau_w \left(\frac{u_m - U}{u_m}\right)^2 . \tag{4}$$

2.4 Shearing Stress in the Outer Layer

As mentioned previously, the outer layer of a turbulent wall jet behaves in a manner which is similar to a turbulent free jet under the same conditions. In a plane turbulent free jet, however, the shear stress at the point $y = \delta_m$ is zero, which is not the case for the wall jet. It is observed experimentally that the influence of the shearing stress at $y = \delta_m$ on the overall shear stress distribution in the outer layer is relatively small. It is assumed therefore that its influence may be taken into consideration by simply linearly adding a function $\tau_m T(\zeta)$ to the corresponding free jet shear stress distribution, i.e.

$$\tau(\zeta)\Big]_{\substack{\text{wall}\\\text{jet}}} = \tau(\zeta)\Big]_{\substack{\text{free}\\\text{jet}}} + \tau_m T(\zeta) \ . \tag{5}$$

The shearing stress distribution across a turbulent free jet is given by Prandtl's mixing length relationship

$$\frac{\tau}{\rho} = l^2 \left|\frac{\partial u}{\partial y}\right| \frac{\partial u}{\partial y} \tag{6}$$

where, within the context of the present wall jet nomenclature

$$\begin{aligned} l &\simeq (\delta - \delta_m) \\ &= \kappa(\delta - \delta_m) \end{aligned} \tag{7}$$

where $\kappa = 0.0684$ (Ref.7).

The edge of a plane turbulent free jet may be defined approximately by the relationship

$$\frac{\delta - \delta_m}{\delta_{m/2} - \delta_m} = 2.25 \ . \tag{8}$$

Substituting Equations (7) and (8) in Equation (6) gives, for the plane free jet,

$$\frac{\tau}{\rho} = \kappa_1 \left|\frac{\partial u}{\partial \zeta}\right| \frac{\partial u}{\partial \zeta} \tag{9}$$

where $\kappa_1 = \kappa^2(2.25)^2 = 0.0236$.

From Equation (5) then

$$\frac{\tau}{\rho} = \kappa_1 \left|\frac{\partial u}{\partial \zeta}\right| \frac{\partial u}{\partial \zeta} + \frac{\tau_m}{\rho} T(\zeta) \ . \tag{10}$$

Substituting the universal velocity profile in the outer layer (Eqn.(3)) gives

$$\frac{\tau}{\rho} = \kappa_1 (u_m - U)^2 \left|Q'(\zeta)\right| Q'(\zeta) + \frac{\tau_m}{\rho} T(\zeta) \tag{11}$$

where the primes denote differentiation with respect to ζ.

2.3 The Wall Shearing Stress

According to Reference 5 the relationship

$$\tau_w = \frac{L \rho u_m^2}{\left(\frac{u_m \delta_m}{\nu}\right)^{\epsilon}} \tag{12}$$

describes the wall shearing stress with good accuracy when $L = 0.01575$ and $\epsilon = 0.1820$.

2.6 The Integral Equations

2.6.1 *Momentum Integral in the Inner Layer* ($0 < y < \delta_m$)

Consider a control volume of elemental width dx and height δ_m located within the inner layer as shown in Figure 2(a). Balancing the x-direction momentum flux per unit time through the volume against the pressure and shearing forces exerted upon its boundaries, the following expression for momentum conservation is obtained

$$\rho u_m \frac{d}{dx}\int_0^{\delta_m} u\,dy - \frac{d}{dx}\int_0^{\delta_m} \rho u^2\,dy = \tau_w - \tau_m - p\frac{d\delta_m}{dx} + \frac{d}{dx}\delta_m p .$$

Substituting the assumed velocity profile (Eqn.(1)) into the above expression, and noting that at the edge of the wall jet (where the flow is inviscid) Bernoulli's equation

$$\frac{dp}{dx} = -\rho u \frac{dU}{dx} \tag{13}$$

relates the local velocity to the local static pressure (which is constant across the jet), one obtains

$$C_1 u_m \frac{d}{dx}\delta_m u_m - C_2 \frac{d}{dx}\delta_m u_m^2 = \frac{\tau_w}{\rho} - \frac{\tau_m}{\rho} - \delta_m U \frac{dU}{dx}$$

where $C_1 = \int_0^1 P(\eta)d\eta$ and $C_2 = \int_0^1 P^2(\eta)d\eta$.

Expanding the above relationship, and making the required substitutions from Equations (4) and (12) gives

$$(C_1 - 2C_2)u_m\delta_m \frac{du_m}{dx} + (C_1 - C_2)u_m^2 \frac{d\delta_m}{dx} = \frac{L\{u_m^2 + (u_m - U)^2\}}{\left(\frac{u_m\delta_m}{\nu}\right)^{\epsilon}} - \delta_m U \frac{dU}{dx} . \tag{14}$$

2.6.2 *Momentum Integral in the Outer Layer* ($\delta_m < y < \infty$)

Consider another control volume of elemental width dx, but of height $(\delta - \delta_m)$ located in the outer layer as shown in Figure 2(b). The principle of momentum conservation in this layer gives

$$\rho U \frac{d}{dx}\int_0^{\delta_m} u\,dy + \rho U \frac{d}{dx}\int_{\delta_m}^{\infty} u\,dy - \rho u_m \frac{d}{dx}\int_0^{\delta_m} u\,dy - \frac{d}{dx}\int_{\delta_m}^{\infty} \rho u^2 dy$$

$$= \tau_m - p\frac{d\delta}{dx} + p\frac{d\delta_m}{dx} + \frac{d}{dx}(\delta - \delta_m)p$$

which upon substitution of Equations (2), (3), (4), (12) and (13) becomes, after expanding, and simplifying,

$$\left\{K_1U + 2K_2(u_m - U) + C_1 \frac{\delta_m}{\delta_{m/2} - \delta_m}(u_m - U)\right\}(\delta_{m/2} - \delta_m)\frac{du_m}{dx} +$$

$$+ \{K_1U + K_2(u_m - U)\}(u_m - U)\frac{d\delta_{m/2}}{dx} - \{K_1U + K_2(u_m - U) - C_1u_m\}(u_m - U)\frac{d\delta_m}{dx}$$

$$= (\delta_{m/2} - \delta_m)\{2(K_2 - K_2)(u_m - U) + K_1U\}\frac{dU}{dx} + \frac{L(u_m - U)^2}{\left(\frac{u_m\delta_m}{\nu}\right)^{\epsilon}} \qquad (15)$$

where $K_1 = \int_0^\infty Q(\zeta)\,d\zeta$ and $K_2 = \int_0^\infty Q^2(\zeta)\,d\zeta$.

2.6.3 Energy Integral in the Outer Layer

Referring to the control volume of Figure 2(c) the net flux of total energy per unit time of the mean motion passing through the volume must equal the energy dissipated within the volume per unit time. The energy dissipation integral is written[1]

$$E_d = \int_{\delta_m}^\infty \tau\frac{\partial u}{\partial y}\,dy = \int_0^\infty \tau\frac{\partial u}{\partial \zeta}\,d\zeta .$$

If $H(y) = p + 1/2\,\rho u^2$ is the total mean flow energy at any point in the outer layer and

$$H_m = H(y = \delta_m)$$

and

$$H_e = H(y > \delta) ,$$

then the principle of conservation of energy requires that,

$$H_e\frac{d}{dx}\int_0^\infty u\,dy - H_m\frac{d}{dx}\int_0^{\delta_m} u\,dy - \frac{d}{dx}\int_{\delta_m}^\infty H(y)\,dy = \int_{\delta_m}^\infty \tau\frac{\partial u}{\partial y}\,dy$$

which becomes, upon expansion and substitution,

$$\left.\begin{aligned}&\{C_1\delta_m(u_m^2 - U^2) + (2K_1U^2 + 6K_2(u_m - U)U + 3K_3(u_m - U)^2\}(\delta_{m/2} - \delta_m)\frac{du_m}{dx} +\\ &+ \{2K_1(u_m - U)U^2 + 3K_2(u_m - U)^2U + K_3(u_m - U)^3\}\frac{d\delta_{m/2}}{dx} +\\ &+ \{C_1u_m(u_m^2 - U^2) + 2K_1(u_m - U)U^2 + 3K_2(u_m - U)^2U + K_3(u_m - U)^3\}\frac{d\delta_m}{dx} =\end{aligned}\right| \qquad (16)$$

$$= (\delta_{m/2} - \delta_m)\{2U^2K_2 + 2(3K_2 - 2K_1)(u_m - U)U + 3(K_3 - K_2)(u_m - U)^2\}\frac{dU}{dx} - \left.\begin{array}{l}\\ \\ \\ \end{array}\right. \quad (16)$$

$$- 2(u_m - U)^3\left\{\kappa_1 K_4 - LK_5\left(\frac{u_m\delta_m}{\nu}\right)^{-\epsilon}\right\} \quad \left.\begin{array}{l}\\ \\ \\ \end{array}\right.$$

where

$$K_3 = \int_0^\infty Q^3(\zeta)\, d\zeta$$

$$K_4 = \int_0^\infty |Q'(\zeta)|\, Q'^2(\zeta)\, d\zeta$$

$$K_5 = \int_0^\infty Q'(\zeta)\, T(\zeta)\, d\zeta$$

2.6.4 Non-dimensional Form of the Equations

It is convenient to non-dimensionalize the equations by introducing the variables

$$t = u_m/V_j \qquad r = \delta_m/b \qquad s = \delta_{m/2}/b$$

$$\lambda = U/V_j \qquad c_f = \frac{\tau_w}{\frac{1}{2}\rho V_j^2} \qquad Re_s = \frac{V_j b}{\nu}$$

Equations (14), (15) and (16) become respectively

$$\left.\begin{array}{l} \alpha_1 t' + \alpha_2 s' + \alpha_3 r' = \alpha_4 \\ \alpha_5 t' + \alpha_6 s' + \alpha_7 r' = \alpha_8 \\ \alpha_9 t' + \alpha_{10} s' + \alpha_{11} r' = \alpha_{12} \end{array}\right\} \quad (17)$$

and the skin friction coefficient becomes

$$c_f = 2Lt^2(Re_s rt)^{-\epsilon}. \quad (18)$$

In Equation (17), the primes denote differentiation with respect to ξ, and the variable coefficients α_i are as follows

$$\left.\begin{array}{l} \alpha_1 = rt(C_1 - 2C_2) \\ \alpha_2 = 0 \\ \alpha_3 = t^2(C_1 - C_2) \\ \alpha_4 = L\{t^2 + (t - \lambda)^2\}(Re_s rt)^{-\epsilon} - r\lambda\lambda' \\ \alpha_5 = \{K_1\lambda + 2K_2(t - \lambda)\}(s - r) + C_1 r(t - \lambda) \end{array}\right. \quad (19)$$

$$
\left.
\begin{aligned}
\alpha_6 &= (t-\lambda)\{K_1\lambda + K_2(t-\lambda)\} \\
\alpha_7 &= -(t-\lambda)\{K_1\lambda + K_2(t-\lambda) - C_1 t\} \\
\alpha_8 &= \{K_1\lambda + 2(K_2 - K_1)(t-\lambda)\}(s-r)\lambda' + L(t-\lambda)^2(Re_s rt)^{-\epsilon} \\
\alpha_9 &= C_1 r(t^2 - \lambda^2) + (s-r)\{2K_1\lambda^2 + 6K_2(t-\lambda)\lambda + 3K_3(t-\lambda)^2 \\
\alpha_{10} &= \{2K_1\lambda^2 + 3K_2(t-\lambda)\lambda + K_3(t-\lambda)^2\}(t-\lambda) \\
\alpha_{11} &= (t^2 - \lambda^2)C_1 t - \{2K_1\lambda^2 + 3K_2(t-\lambda)\lambda + K_3(t-\lambda)^2\}(t-\lambda) \\
\alpha_{12} &= (s-r)\{3(K_3 - K_2)(t-\lambda)^2 + 2\{3K_2 - 2K_1)(t-\lambda)\lambda + 2K_1\lambda^2\}\lambda' - \\
&\qquad - 2(t-\lambda)^3\{\kappa_1 K_4 - LK_5(Re_s rt)^{-\epsilon}\} .
\end{aligned}
\right\} \quad (19)
$$

Equations (17) may be solved simultaneously to give

$$
\left.
\begin{aligned}
t' &= \frac{\alpha_{14}(\alpha_6\alpha_{12} - \alpha_8\alpha_{10}) - \alpha_{16}(\alpha_5\alpha_{11} - \alpha_7\alpha_{10})}{\alpha_{15}(\alpha_6\alpha_{11} - \alpha_7\alpha_{10}) - \alpha_{14}(\alpha_5\alpha_{10} - \alpha_6\alpha_9)} \\
r' &= \frac{\alpha_{16} + \alpha_{15}t'}{\alpha_{14}} \\
s' &= \frac{\alpha_8 - \alpha_5 t' - \alpha_7 r'}{\alpha_6}
\end{aligned}
\right\} \quad (20)
$$

where

$$
\begin{aligned}
\alpha_{14} &= \alpha_2\alpha_7 - \alpha_3\alpha_6 \\
\alpha_{15} &= \alpha_1\alpha_6 - \alpha_2\alpha_5 \\
\alpha_{16} &= \alpha_2\alpha_8 - \alpha_4\alpha_6 .
\end{aligned}
$$

The universal functions $P(\eta)$ and $Q(\zeta)$ selected to describe the velocity profiles in the inner and outer layers are

$$
\left.
\begin{aligned}
P(\eta) &= \eta^{1/10} \\
Q(\zeta) &= e^{-k\zeta^2} .
\end{aligned}
\right\} \quad (21)
$$

These functions are compared with experimental data in Figures (3) and (4).

Using expression (21), the integrals appearing throughout the analytical development may be evaluated as

$$
\begin{aligned}
C_1 &= 0.909 & K_2 &= 0.7523 \\
C_2 &= 0.833 & K_3 &= 0.6145 \\
K_1 &= 1.062 & K_4 &= 0.308 \\
& & K_5 &= -0.10
\end{aligned}
$$

where K_5 which corresponds to the integral of the unknown shear stress correction function $T(\zeta)$ in the outer layer has been evaluated experimentally.

The representative initial conditions selected from experimental data are

$$\xi_0 = 12.0$$

$$r_0 = 0.235$$

$$s_0 = 1.30$$

If the initial conditions are known beforehand, they should of course replace the above values.

The IBM Fortran program for the simultaneous solution of Equations (20) is presented in the Appendix for those who might be interested in making similar calculations.

3. EXPERIMENTAL INVESTIGATION

An experimental investigation was carried out to verify the analytical results obtained in the last section.

The experiments were performed in the VKI low speed two dimensional wind tunnel L-2B at stream Reynolds numbers based on test section height ranging nominally between 2 and 5 x 10^5 and slot Reynolds numbers between 5 and 8 x 10^3.

The object of the experiments was to measure by means of pitot tube exploration the development of a turbulent wall jet along a flat surface in both zero and adverse pressure gradient.

The jet was issued tangentially along the flat upper wall of the test section through a slot which completely spanned the tunnel test section and the air was supplied from a high pressure reservoir.

The adverse pressure gradient in the tunnel was produced by installing a curved surface on the wall of the tunnel opposite the test wall. The general arrangement is shown schematically in Figure 5.

4. DISCUSSION OF RESULTS

The analytical method of Section 2 will be compared with experimental results obtained not only in the present study, but also with measurements made by other investigators under different conditions.

Figures 6 and 7 demonstrate the validity of the theory in the case of a plane turbulent wall jet in still air ($\lambda = U/V_j = 0$). It is noted that under these conditions the growth of both the half-maximum velocity point $s = \delta_{m/2}/b$ and the maximum velocity point itself $r = \delta_m/b$ is linear.

Figures 8 and 9 contain data for the case of a wall jet in a moving stream with zero pressure gradient ($\lambda' = 0$). It is observed that while the growth of the peak velocity point r is still linear, this is no longer true for the half-maximum velocity point s.

Figures 10, 11 and 12 show the experimental and theoretical jet development in adverse pressure gradients ($\lambda' < 0$). The variations of λ along the test surface are also included in the figures. Even under these conditions, the growth of r is still effectively linear.

Figures 13, 14 and 15 show the measured and predicted variations of the skin friction coefficient $c_f = \tau_w / \frac{1}{2} \rho V_j^2$ with distance from the slot for wall jets in still air, and in moving streams with $\lambda' = 0$ and $\lambda' < 0$.

5. CONCLUSIONS

An approximate method for computing the development of a plane turbulent wall jet under an external stream of arbitrary pressure gradient has been developed. The analytical results compare favorably with experimental measurements obtained at VKI and by other investigators under varying conditions. The computer program presented in the Appendix permits the rapid computation of the jet development (i.e. peak velocity decay and growth of the peak velocity and half-peak velocity points) and the skin friction. It has been demonstrated that the wall jet velocity profile exhibits downstream similarity, so that all of the jet properties at any point on the surface may be obtained once these parameters have been computed.

REFERENCES

1. Schlichting, H. — *Boundary Layer Theory*. McGraw-Hill, New York, 1956.

2. Patel, R.P. — *Self-preserving Two-dimensional Turbulent Jets and Wall Jets in a Moving Stream*. McGill University, Dept. of Mech. Eng., 1962.

3. Myers, G.E. et alii — *The Plane Turbulent Wall Jet, Part 1*. Stanford University, Dept. of Mech. Eng., Tech. Report 1, June 1961.

4. Glauert, M.B. — *The Wall Jet*. Jour. Fluid Mechanics, Vol. 1, 1956, p. 625.

5. Bradshaw, P. Gee, M.T. — *Turbulent Wall Jets With and Without an External Stream*. ARC ... and M 3252, 1962.

6. Gartshore, I. — *Jets and Wall Jets in Uniform Streaming Flow*. McGill University, Dept. of Mech. Eng., Report 64-4.

7. Förthmann, E. — *Turbulent Jet Expansion*. NACA TM 789, 1936.

APPENDIX: DIGITAL COMPUTER PROGRAM

```
C     INCOMPRESSIBLE TURBULENT WALL JET IN ARBITRARY PRESSURE GRADIEN.,
C
C     KSI=DISTANCE FROM SLOT=X/B
C     LAMBDA=VELOCITY RATIO=U/VJ
C     R=HEIGHT OF POINT OF MAXIMUM VELOCITY=DM/B
C     S=HEIGHT OF POINT OF 1/2 MAX.VELOCITY
C     T=VELOCITY RATIO=UM/VJ
C
C
    1 ACCEPT TAPE 3,S,R,T,C1,C2,C3,ELLE,EPS,HK1,RE,DX,X,XF,K,H1
    3 FORMAT(9F5.4,F6.0,3F3.0,I2,F5.4)
      ACCEPT TAPE 30,UK,DK,TK,UM,DM,TM,UN,DN,TN,HKA,A,SIG,SI
   30 FORMAT(10F5.4,F7.4,F8.0,F2.0)
      ACCEPT TAPE 33,H2,H3,H4,T1,T2,T3,T4
   33 FORMAT(3F5.4,4E14.8)
      H=0.
      CP=0.
      M=1
    2 EL=T1+T2*X+T3*X*X+T4*X**3
      ELP=T2+2.*T3*X+3.*T4*X*X
      IF(M-1)10,10,13
   13 B1=S-R
      B2=T-EL
      B3=B2**2
      B4=B2*(T+EL)
      A42=ELLE/(RE*R*T)**EPS
      EC=EL*EL
      DL=2.*EL*B2
      DR=2.*R*B2
      PH=0.
      TH=0.
      IF(SI)31,32,31
   31 PH=B1/(SIG+SI*S)
      TH=R/(2.*SIG+SI*R)
   32 G=B3*DK+DL*UK+2.5*EC
      B=B3*UM+DL*DM+EC*TM
      W=UN*B2*B3+EL*B3*(2.*DN+UM)+EC*B2*(TN+2.*DM)+EC*EL*TM
      A1=R*T*(C1-2.*C2)+4.*C3*R*T*TH+PH*DR*DK+2.*UK*R*PH*EL
      D1=G*R/B1
      A2=D1*PH*(1.-SI*PH)
      A3=T*T*(C1-C2+4.*C3*TH-2.*C3*SI*TH**2)-PH*D1
      A4=(PH*DR*(DK-UK)+R*EL*(2.*PH*UK-5.*PH-1.))*ELP+A42*(T*T+HK1*B3)
      A5=B1*(2.*B2*DK+UK*EL-2.*PH*(B2*UM+EL*DM))+C1*R*B2
      A6=B2*(B2*DK+EL*UK)-B*PH*(2.-SI*PH)
      A7=-B2*(DK*B2+UK*EL-C1*T)-PH*(G-2.*B)
      A8=ELP*B1*(2.*B2*(DK-UK)+UK*EL-2.*PH*(B2*(UM-DM)+EL*(DM-TM)))
      A8=A8+A42*HK1*B3
      A9=3.*B3*(TK-2.*UN*PH)+2.*UK*EC-DL*(2.*PH*(2.*DN+UM)-3.*DK)
      A9=C1*R*(T*T-EC-2.*PH*G)+(A9-2.*PH*EC*(TN+2.*DM))*B1
      A10=B2*B3*TK+3.*EL*DK*B3+UK*EL*DL-4.*W*PH+2.*W*SI*PH**2
      A11=-C1*T*(2.*PH*G-B4)-TK*B2*B3-3.*DK*EL*B3-DL*EL*UK+4.*W*PH
      A12=3.*B3*(TK-DK-2.*UN*PH)+DL*(3.*DK-2.*UK)+2.*PH*B3*(2.*DN+UM)
      A12=A12+2.*(EC*UK-PH*EC*(TN+2.*DM)+PH*DL*(TN+2.*DM)+3.*PH*EC*TM)
      A13=-2.*B2*B3*(HKA*(H1-SI*A*PH*H2-SI*A*PH*EL*H3/B2)-A42*H4*HK1)
      A12=B1*A12*ELP+A13
      H=A42*2.*T*T
      CP=2.*(2.*C1*T*T*TH+PH*G)
      A14=A2*A7-A3*A6
      A15=A1*A6-A2*A5
      A16=A2*A8-A4*A6
      TP=A15*(A6*A11-A7*A10)-A14*(A5*A10-A6*A9)
      TP=(A14*(A6*A12-A8*A10)-A16*(A6*A11-A7*A10))/TP
      RP=(A16+A15*TP)/A14
      SP=(A8-A5*TP-A7*RP)/A6
      S=S+SP*DX
      T=T+TP*DX
      R=R+RP*DX
      K=K+1
      IF(K-10)9,11,10
   11 K=0
   10 PRINT 14,X,EL,S,T,R,H,CP
   14 FORMAT(F6.1,F9.5,3F11.5,2E16.8)
    9 M=2
      X=X+DX
      IF(X-XF)7,7,1
      END
```

NOTE: 1. -If the 1620 has to print the results for every value of ξ, κ has to be > 10.0.
If the 1620 has to print the results only every tenth ξ, κ has to be < 9 and equal to the unit digit of ξ_o.
2. -A00, A01, A02, A03 are the coefficients of the polynomial expansion for λ.
3. -$\Delta\xi$ is a step in the step by step solution.

SYMBOLS		SYMBOLS		SYMBOLS	
PROGRAM	ANALYSIS	PROGRAM	ANALYSIS	PROGRAM	ANALYSIS
S	S_o	UK	K_1=1.062	H2	1.0
R	R_o	DK	K_2=0.7523	H3	1.0
T	T_o	TK	K_3=0.6145	H4	K_5= -0.10
C1	C_1=0.909	UM	1.0	T1	A A00
C2	C_2=0.833	DM	1.0	T2	A01
C3	C_3=1.0	TM	1.0	T3	A02
ELLE	L=0.01575	UN	1.0	T4	A03 .
EPS	ε=0.182	DN	1.0		See Note 2
HKI	χ=1.0	TN	1.0		
RE	R_{es}	HKA	κ=0.0238		
DX	$\Delta\xi$	A	1.0		
X	ξ Initial	SIG	1.0		
XF	ξ Final	SI	0.0		
K	See Note 1				
H1	K_4=0.308				

PROGRAM AAN

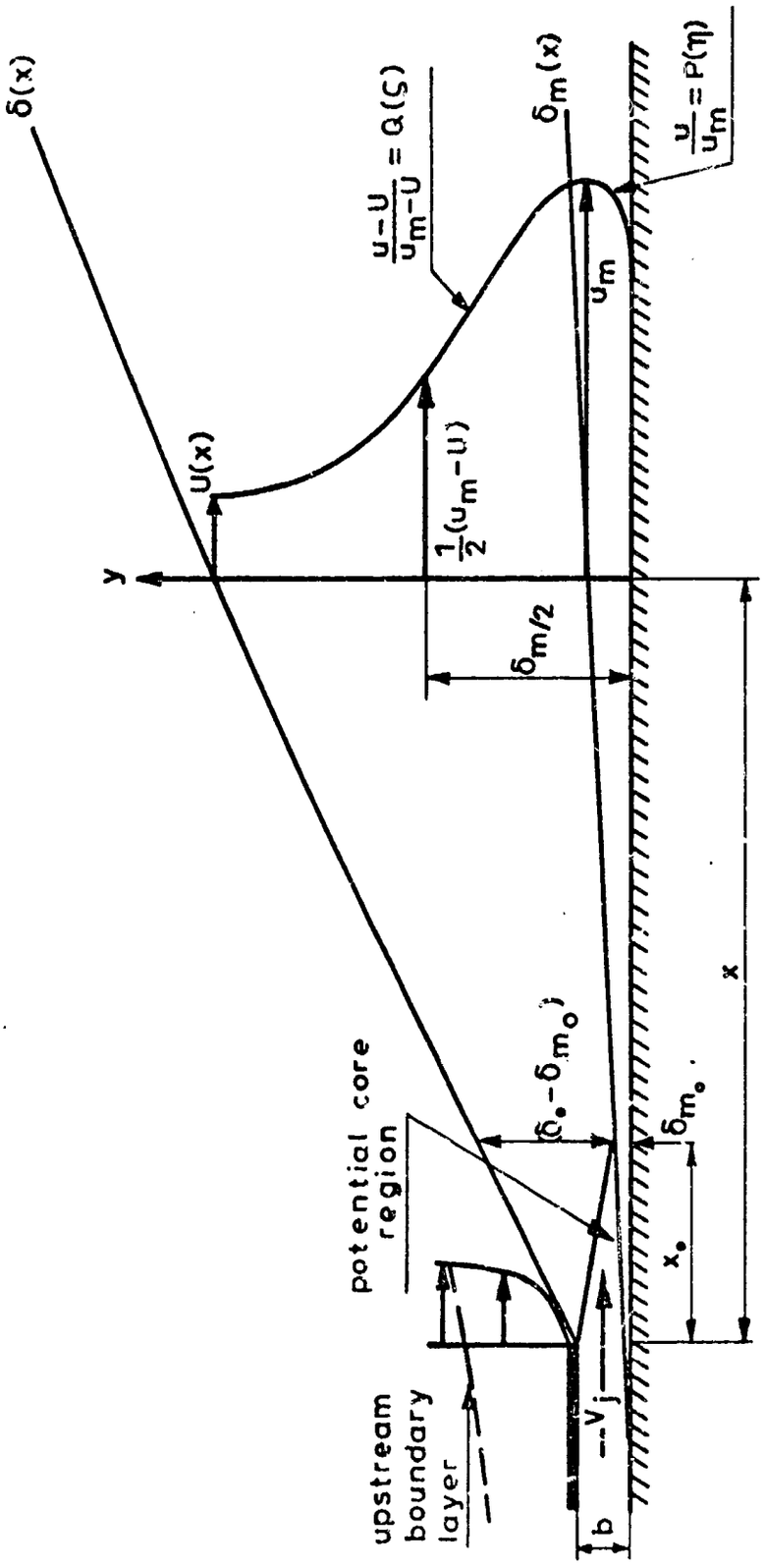

Fig. 1 The flow in a plane two-dimensional wall jet in a moving stream

MOMENTUM CONSERVATION IN THE INNER LAYER

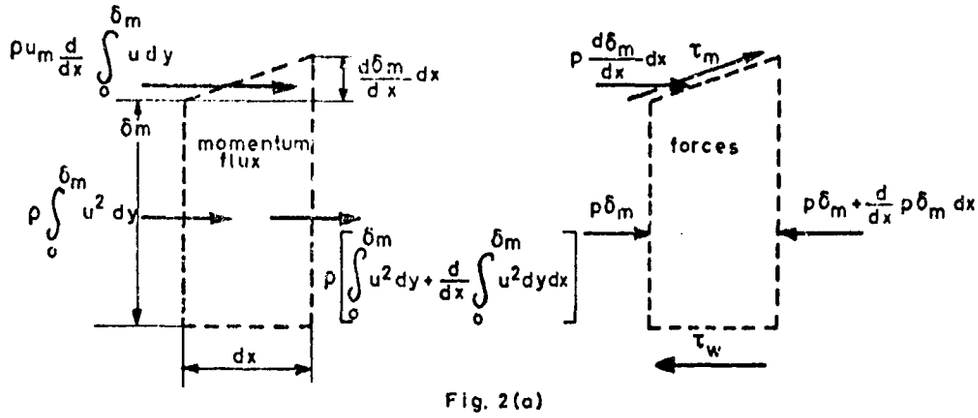

Fig. 2(a)

MOMENTUM CONSERVATION IN THE OUTER LAYER

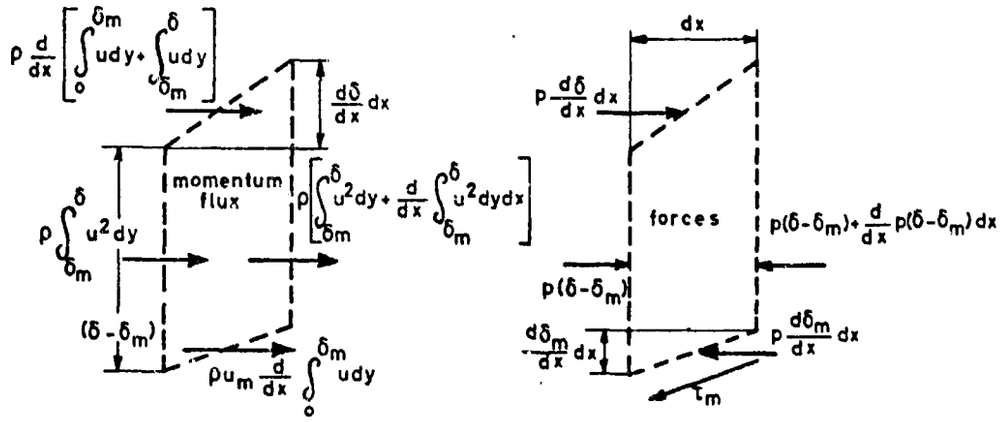

Fig. 2(b)

ENERGY CONSERVATION IN THE OUTER LAYER

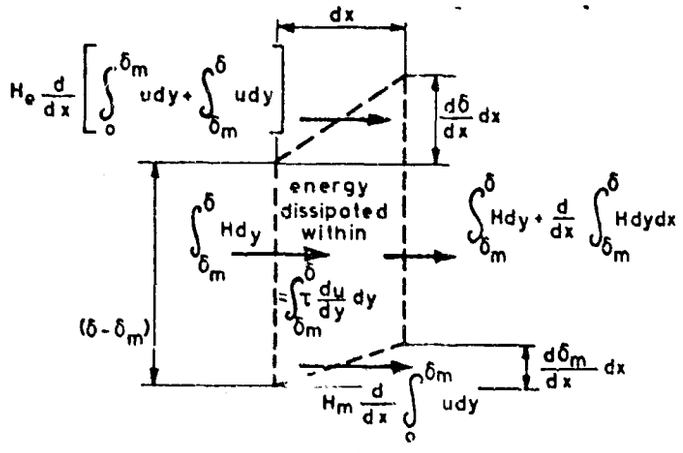

Fig. 2 (c)

Fig. 2 Momentum and energy conservation across jet

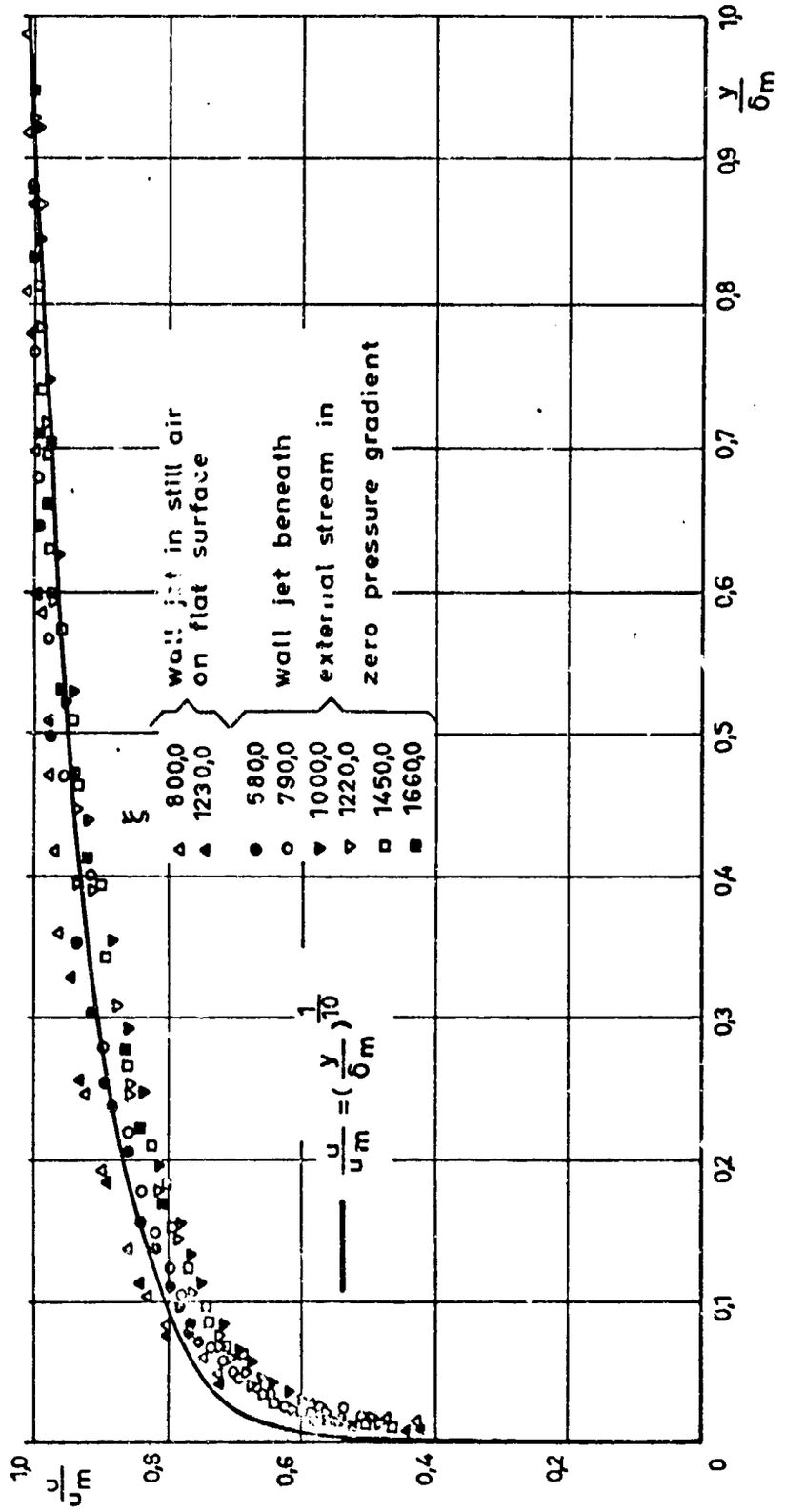

Fig.3 Non-dimensional velocity profiles in inner layer on flat surface, measurements of Bradshaw and Gee[5]

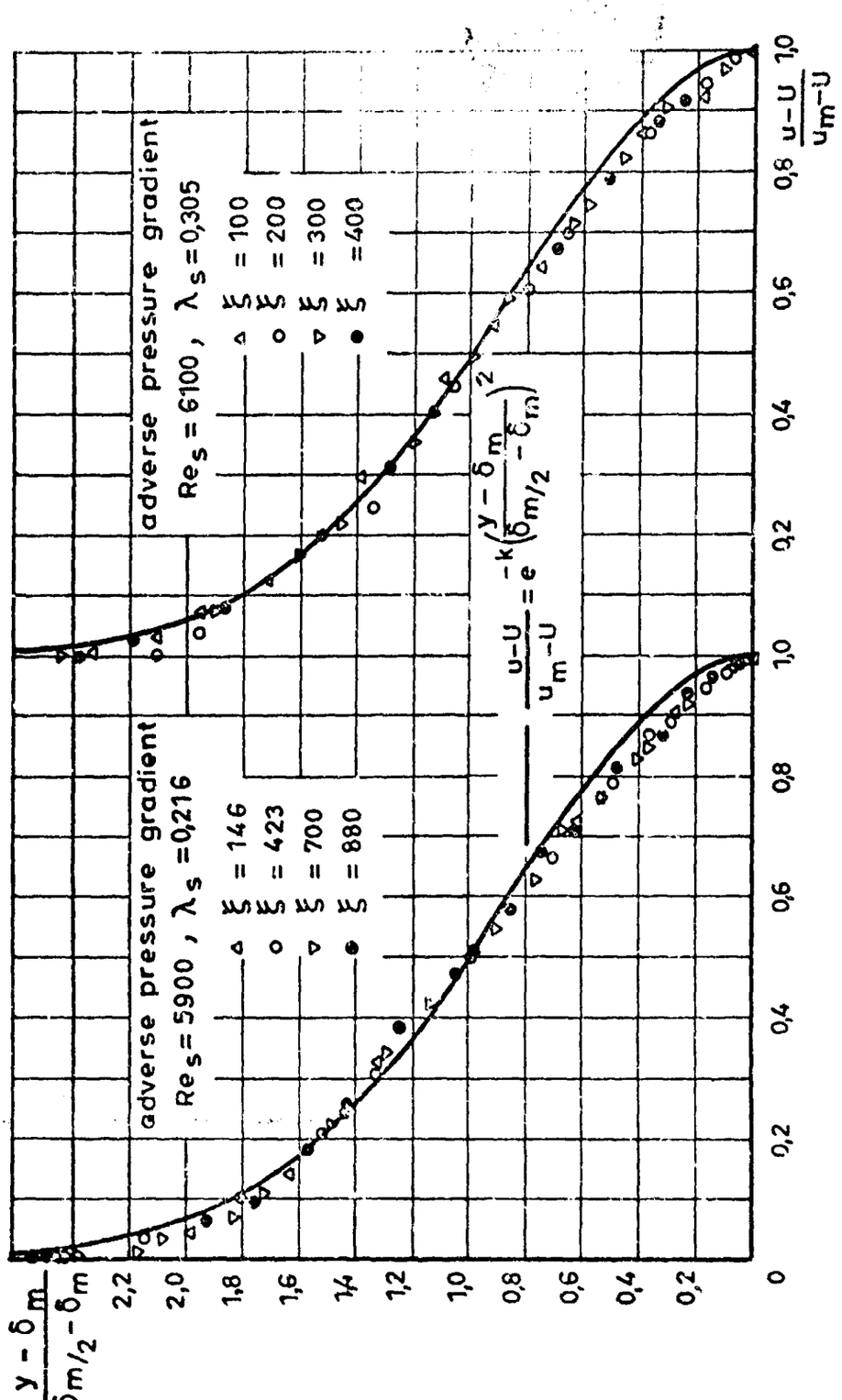

Fig. 4 Non-dimensional velocity profiles in outer layer, present measurements, flat plate

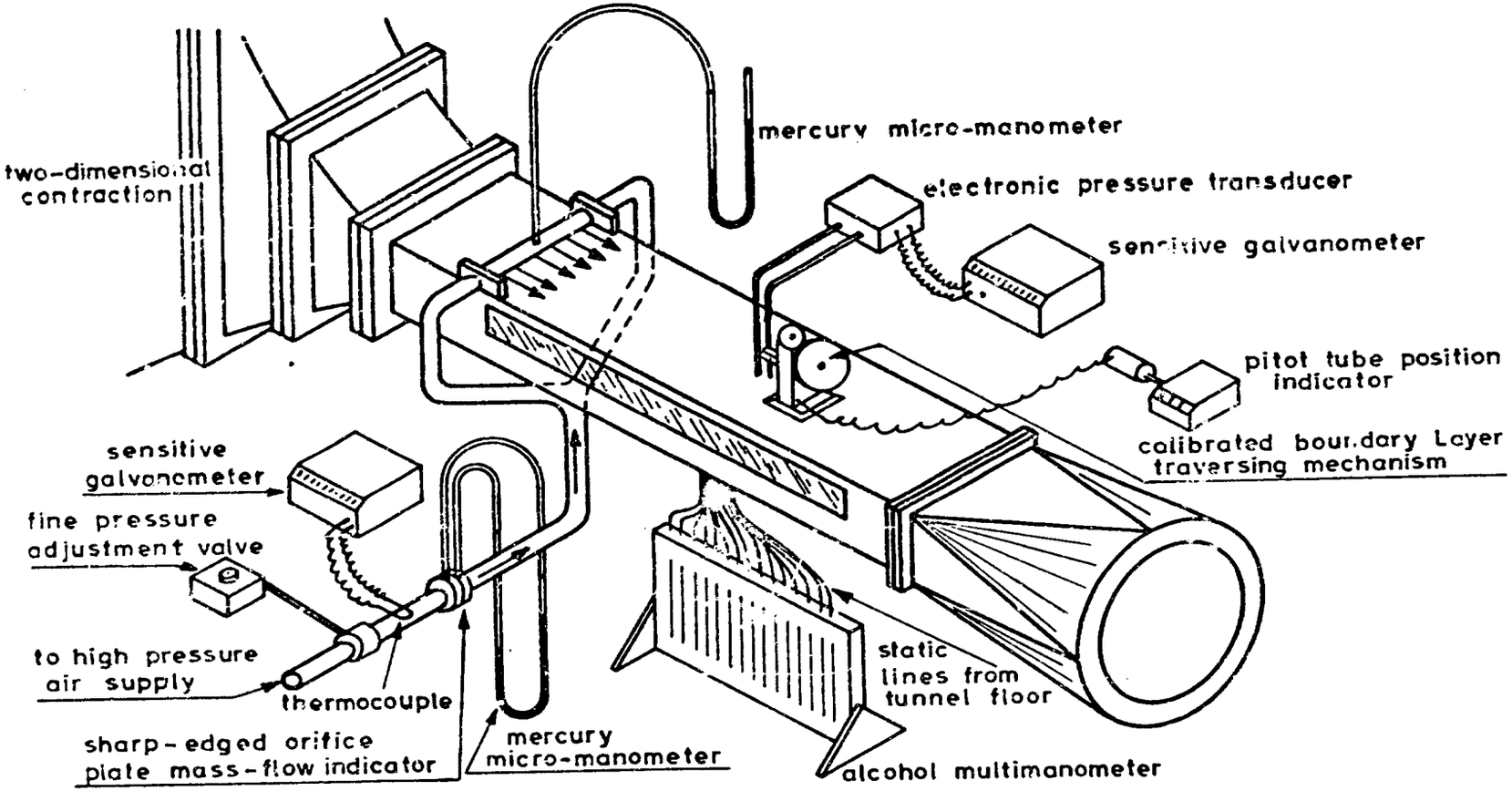

Fig.5 Sketch of general arrangement of tunnel and instrumentation

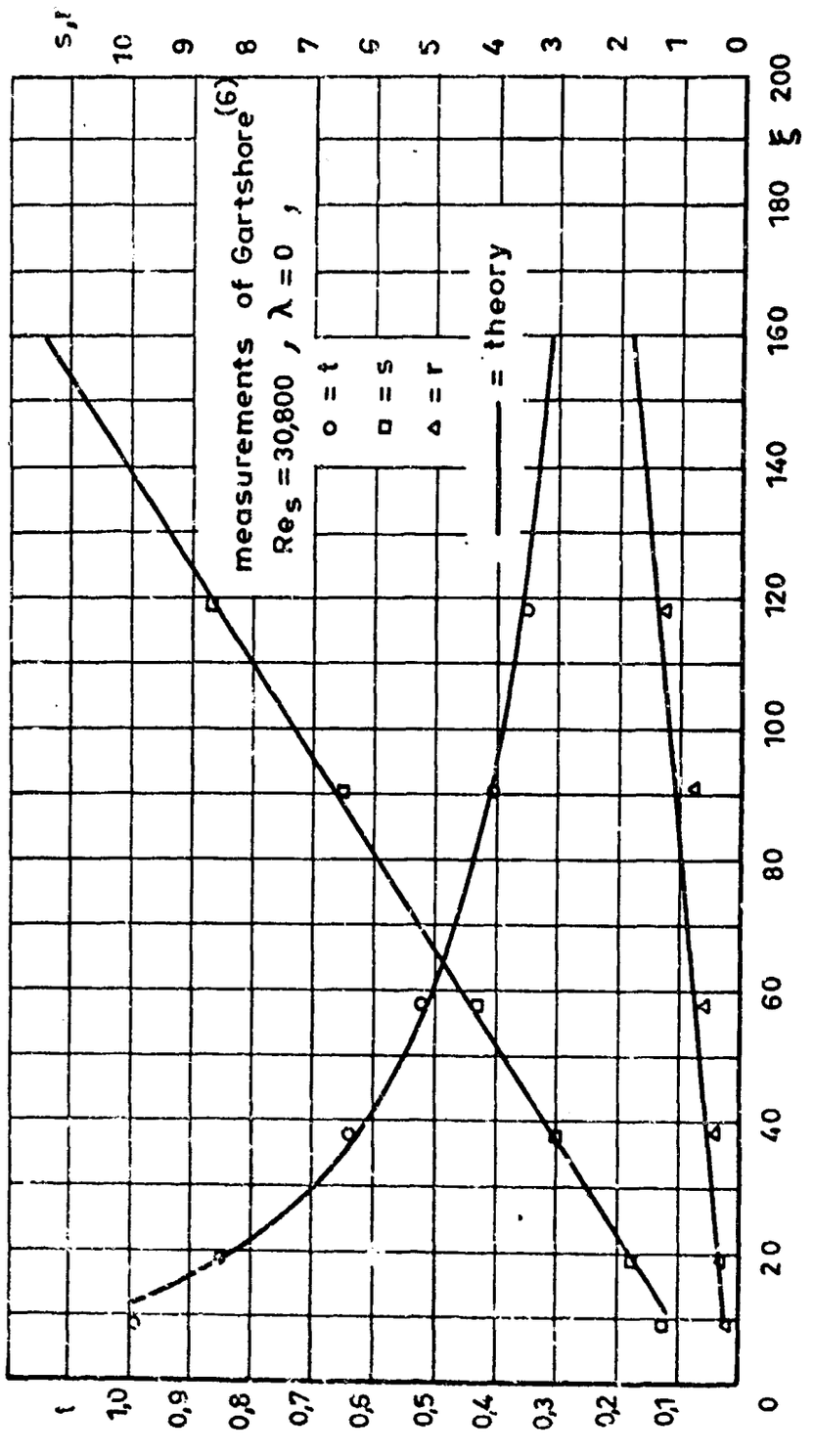

Fig.6 Jet development on flat surface in still air

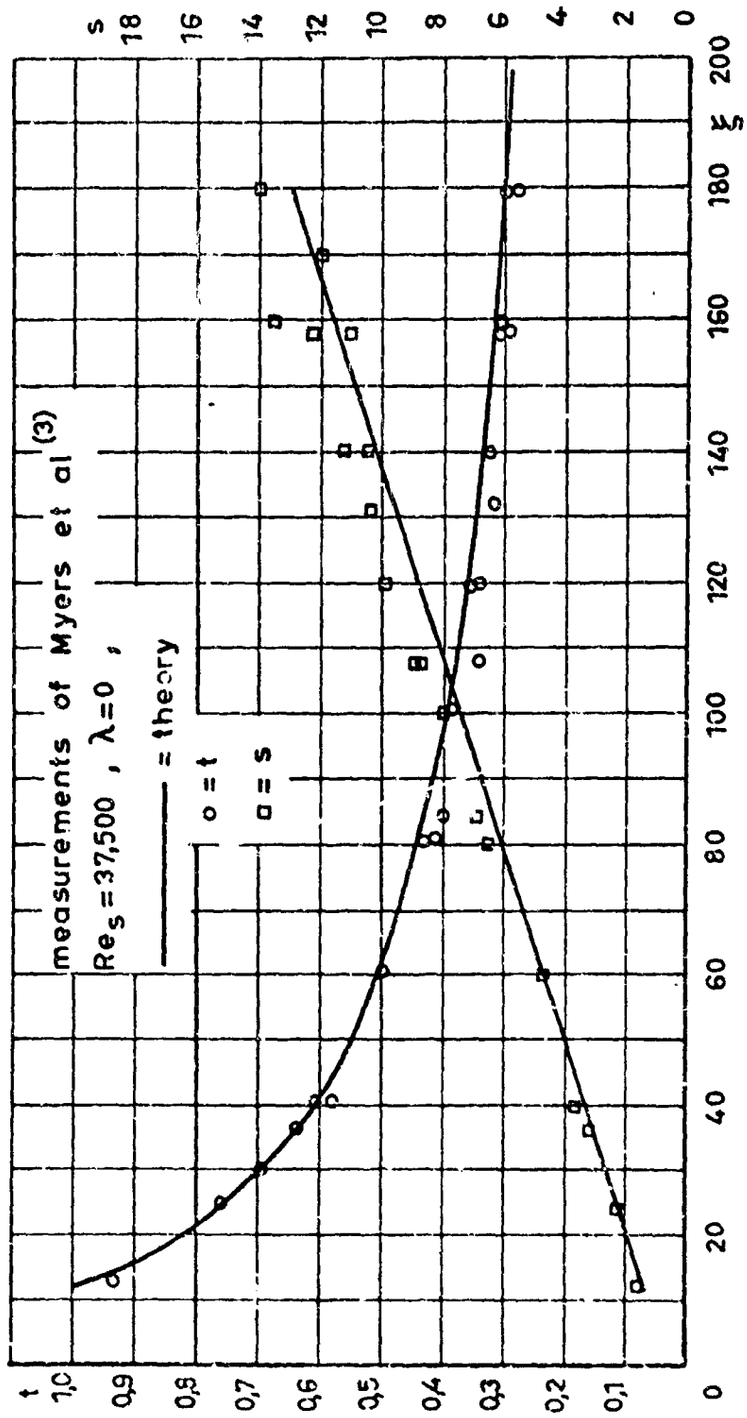

Fig.7 Jet development on flat plate in still air

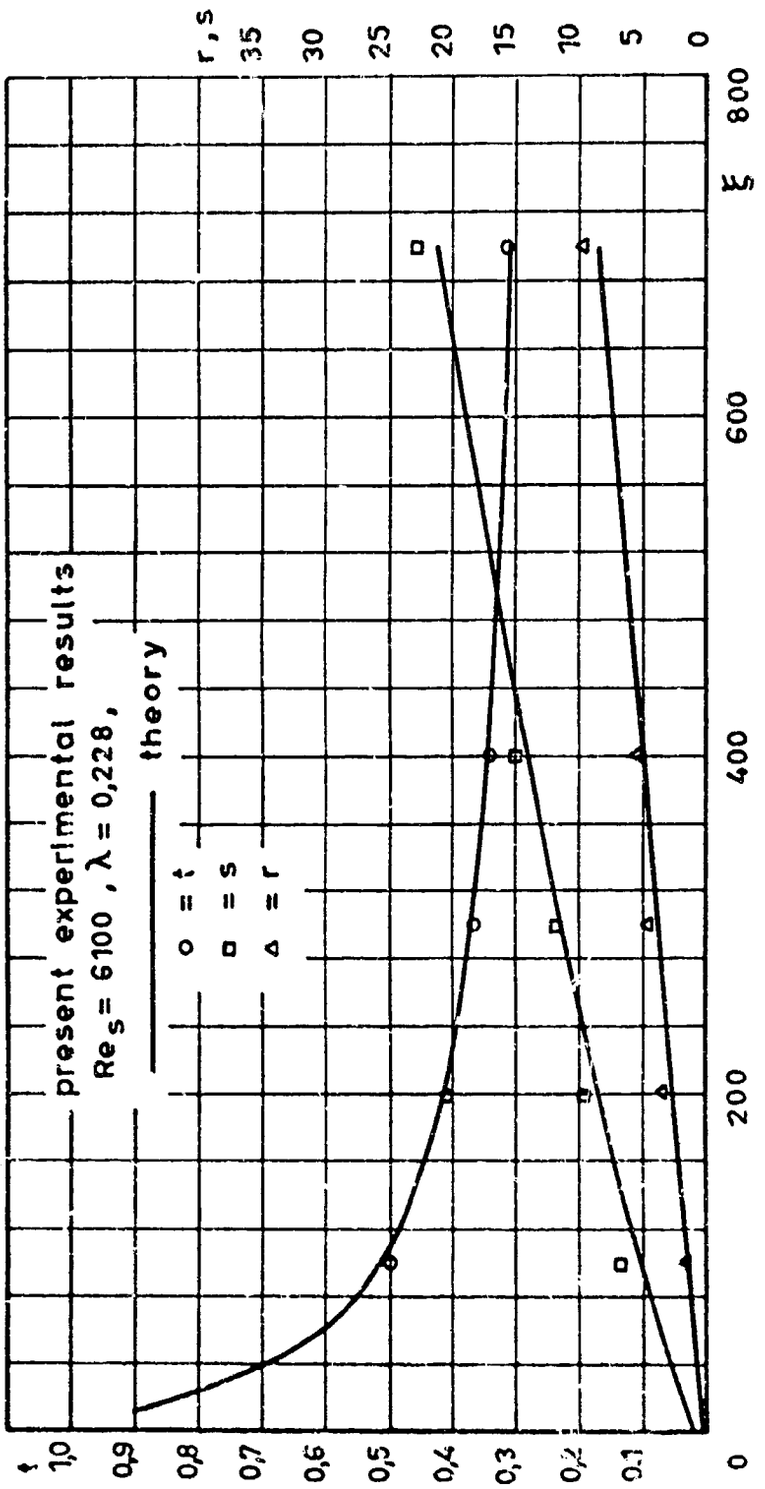

Fig.8 Jet development on flat surface in zero pressure gradient

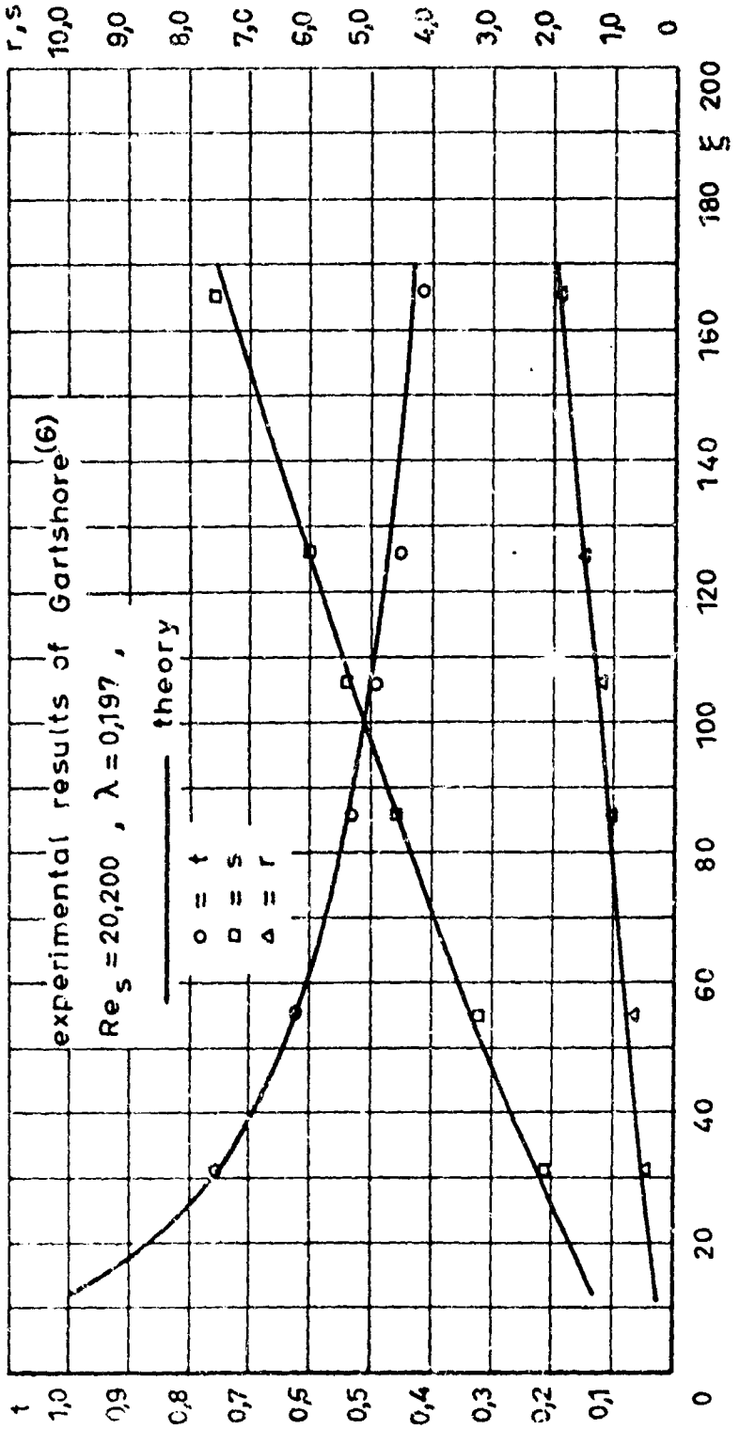

Fig.9 Jet development on flat surface in moving stream of zero pressure gradient

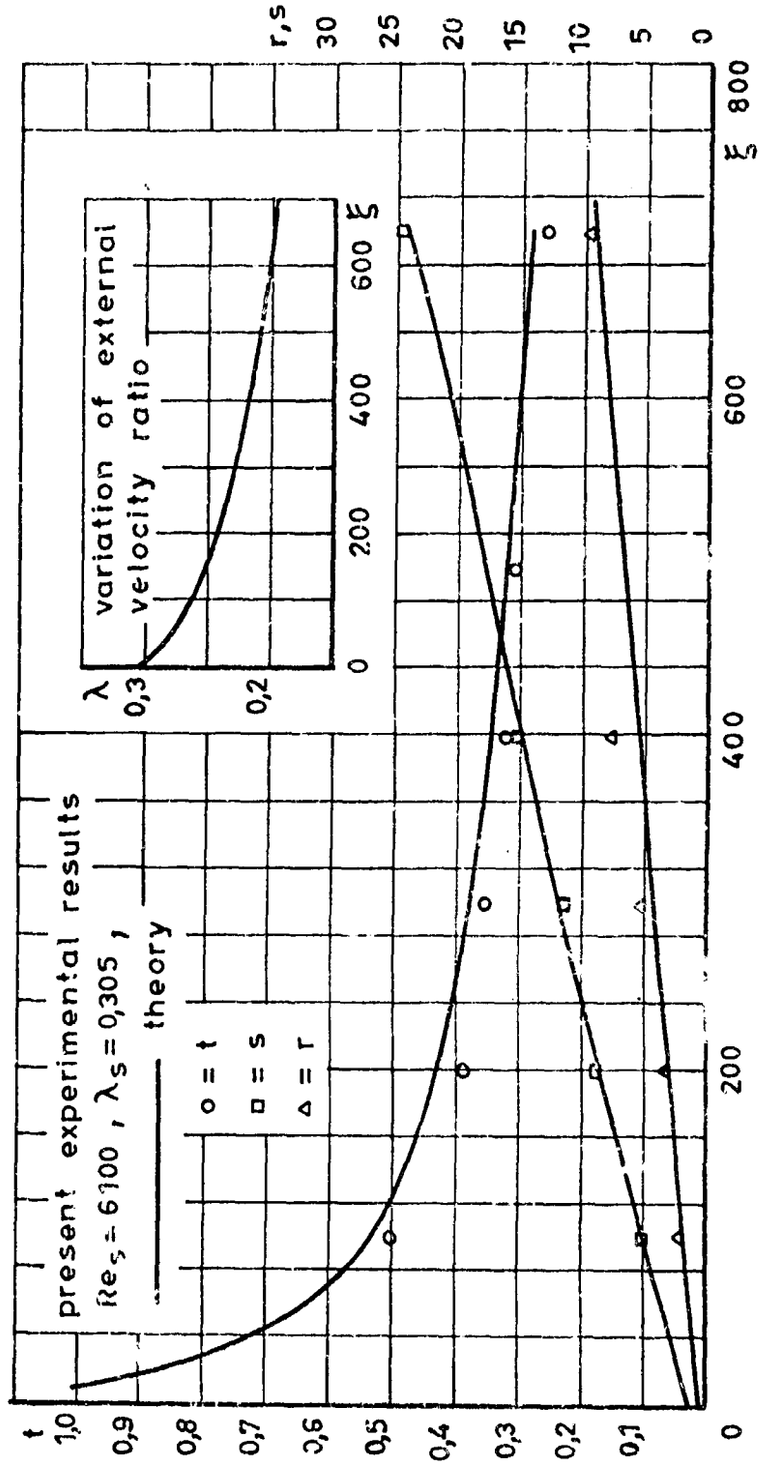

Fig.10 Jet development on flat plate in adverse pressure gradient

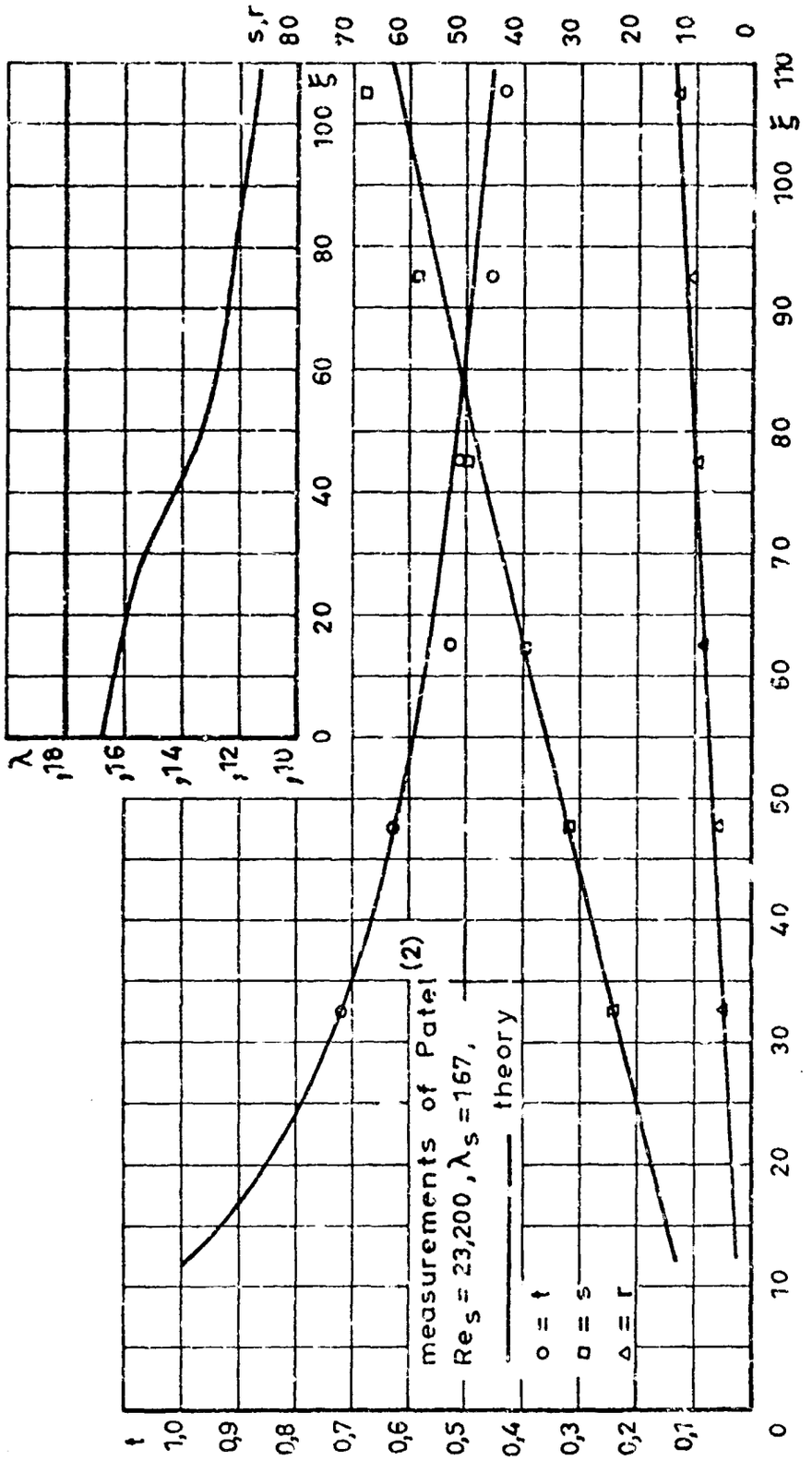

Fig.11 Jet development on flat plate in adverse pressure gradient

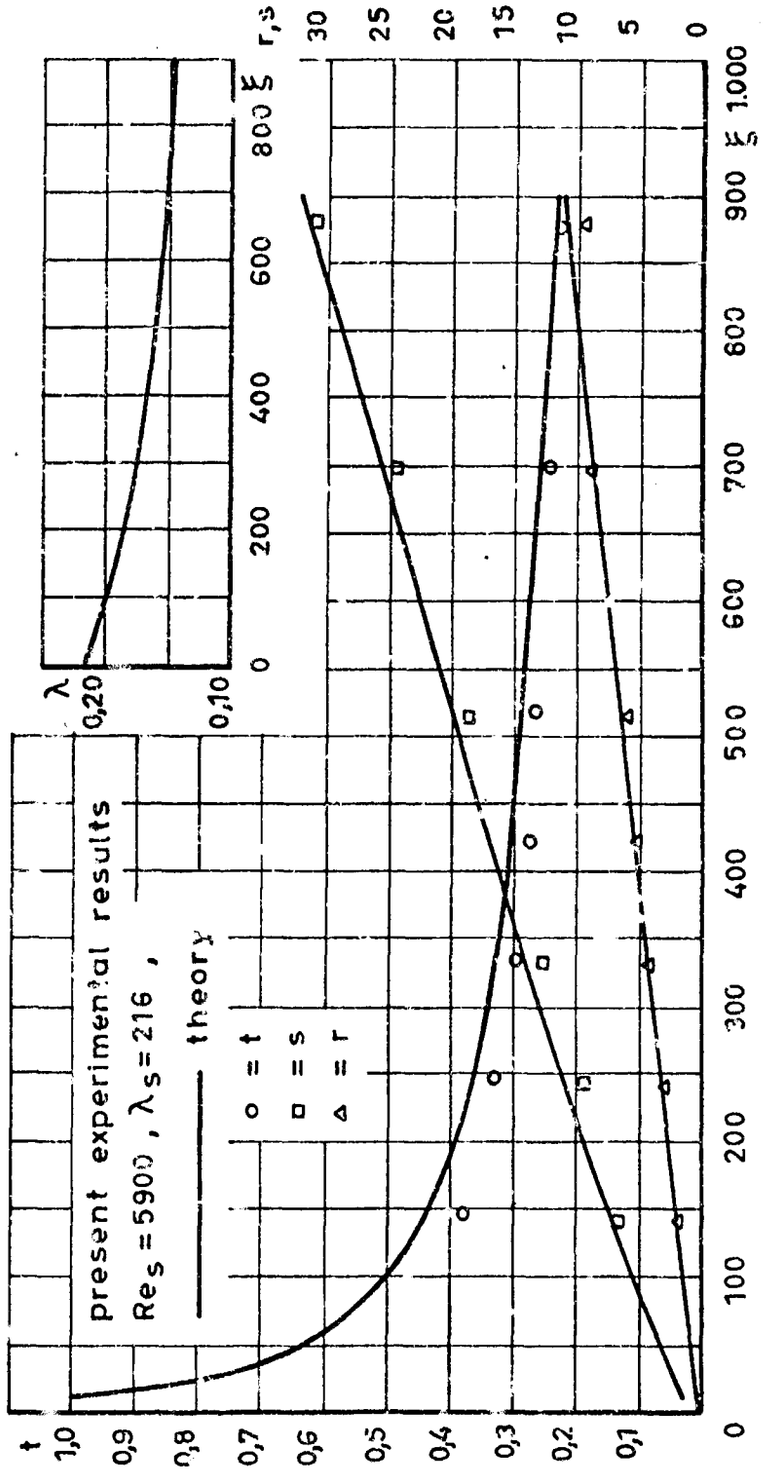

Fig.12 Jet development on flat plate in adverse pressure gradient

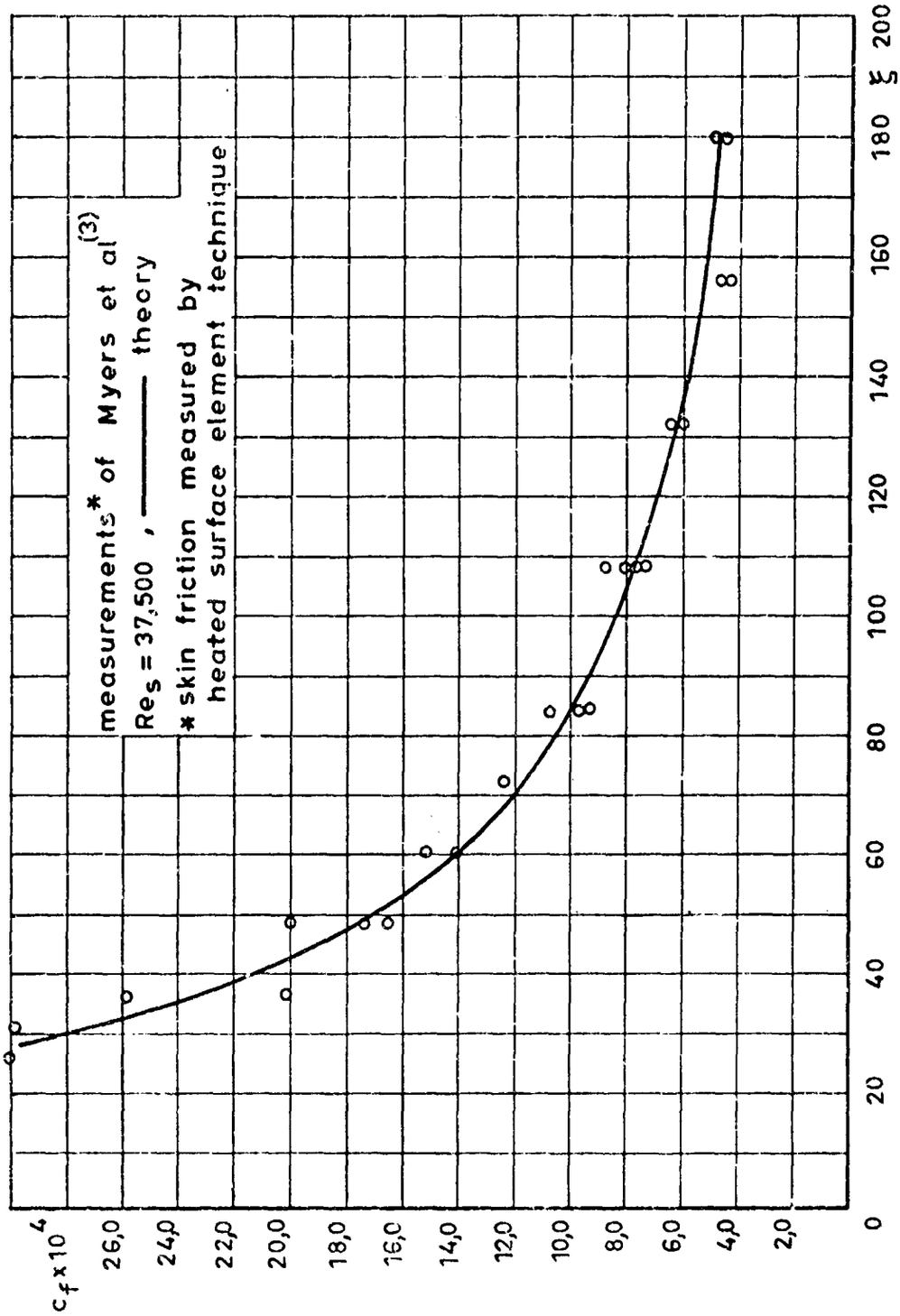

Fig.13 The skin friction generation of a wall jet on a flat surface in still air

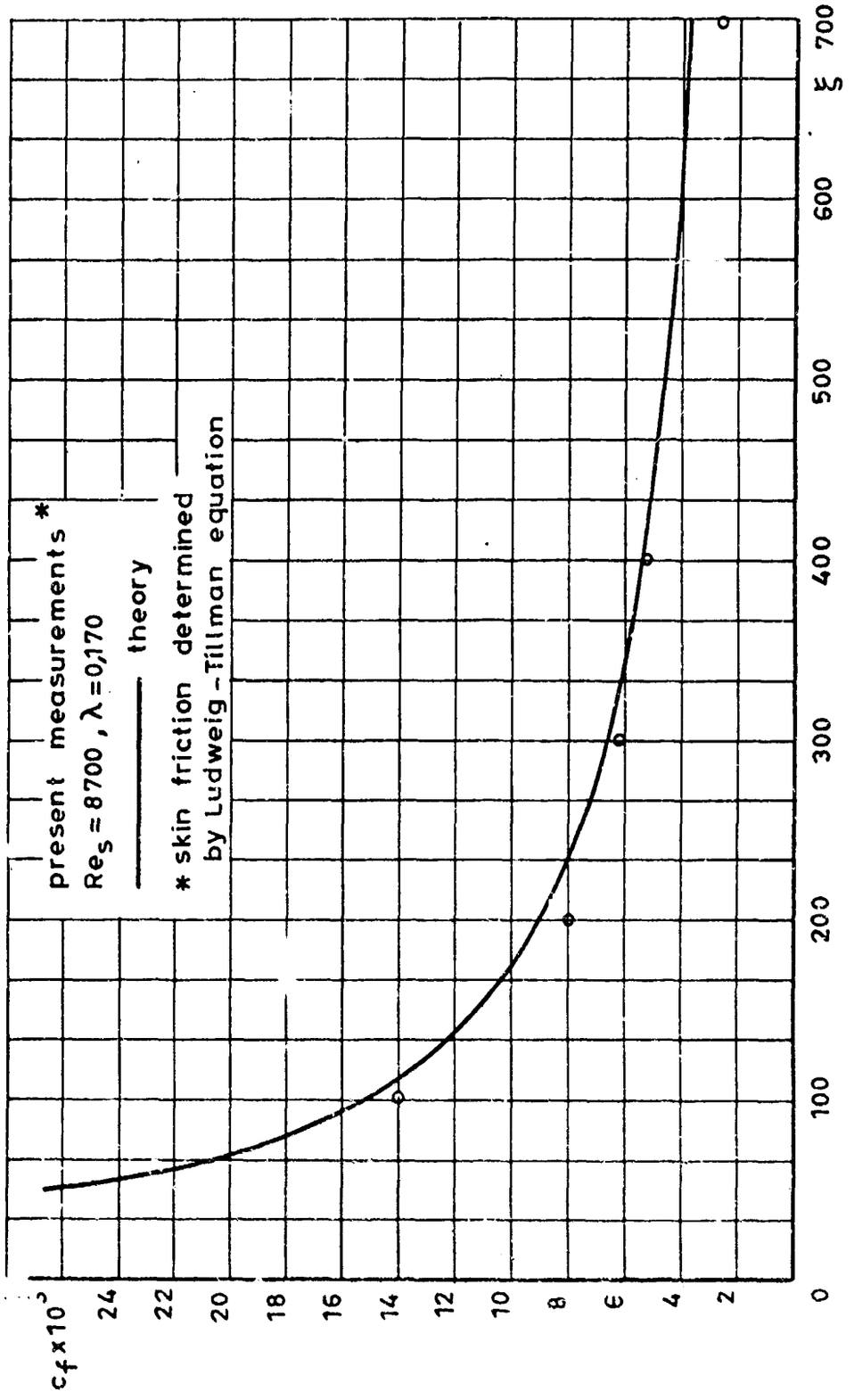

Fig. 14 Skin friction of jet on flat plate in moving stream of zero pressure gradient

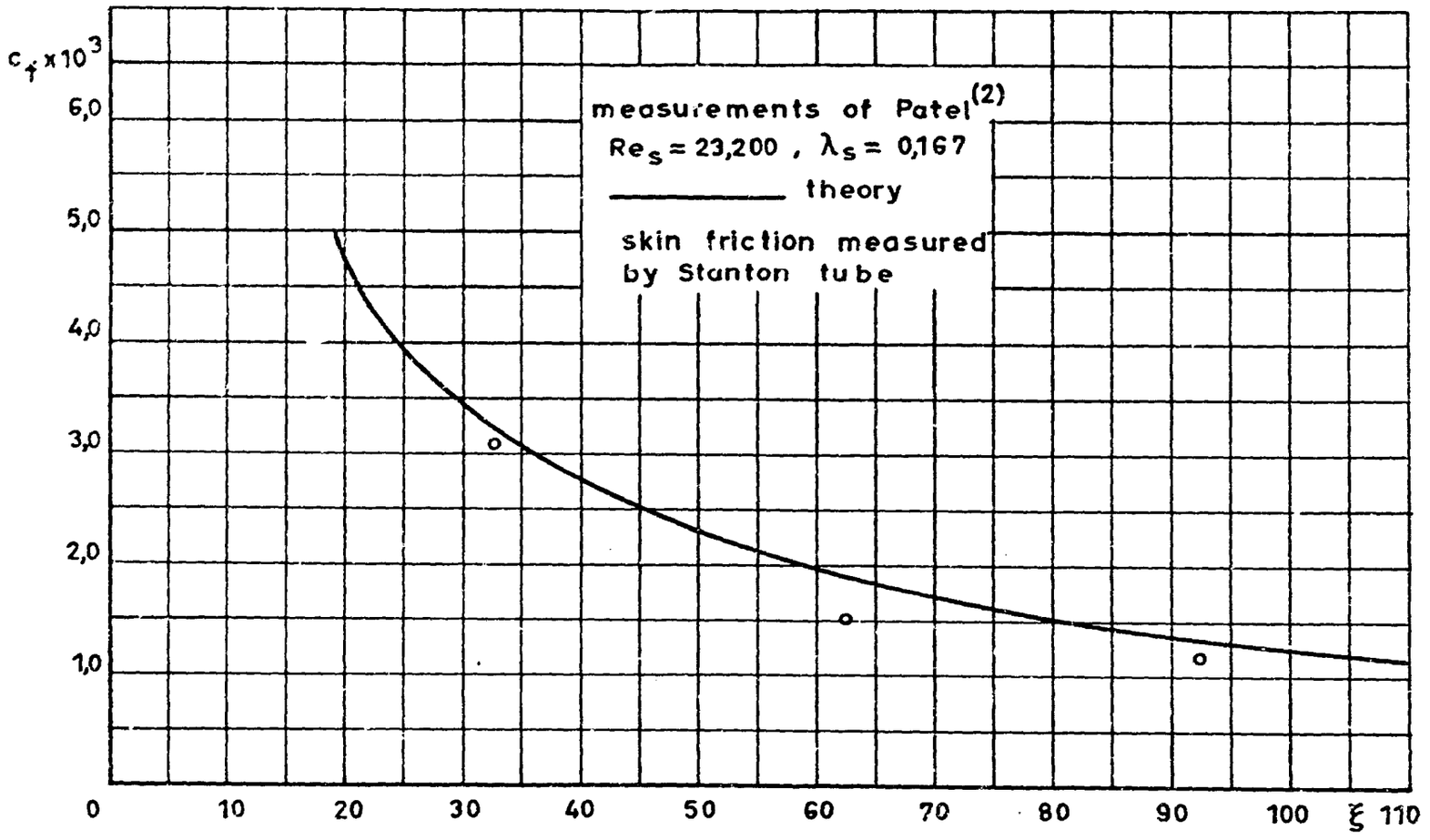

Fig. 15 The skin friction generation of a wall jet on a flat plate in "tailored" adverse pressure gradient

THE CALCULATION OF SHAPE-FACTOR DEVELOPMENT IN INCOMPRESSIBLE TURBULENT BOUNDARY LAYERS WITH OR WITHOUT TRANSPIRATION

by

B.G.J. Thompson

Cambridge University Engineering Laboratory,
Cambridge, England.

SUMMARY

The predictions of shape-factor development given by existing auxiliary equations are shown to vary widely and are in some cases very inaccurate. Head's entrainment equation is the most generally satisfactory.

A new entrainment equation is described and is shown to give improved agreement with experiment, especially in equilibrium conditions. An important feature of this new approach is the use of an explicit term to account for the effects of small three-dimensional flows that appear to be present in measured layers, as indicated by the disagreement between measured growth of momentum thickness and the predictions of the two-dimensional momentum equation even far from separation.

Finally, the entrainment methods are shown to be distinctly superior, in conditions of distributed suction or blowing, to the method of Pechau.

SOMMAIRE

On montre que les prévisions concernant l'évolution d'un facteur de forme obtenues au moyen des équations auxiliaires existantes varient très considérablement et qu'elles sont dans certains cas très inexactes. L'équation d'entraînement de Head est la plus généralement satisfaisante.

Une nouvelle équation d'entraînement est décrite et on montre qu'elle permet de réaliser un meilleur accord avec les résultats d'expérimentation et plus particulièrement dans les conditions d'équilibre. Une caractéristique importante de cette nouvelle méthode consiste dans l'emploi d'un terme explicite pour tenir compte des effets de petits écoulements tri-dimensionnels qui semblent se présenter dans les couches mesurées, comme l'indique le désaccord qui existe entre l'amplification mesurée de l'épaisseur de quantité de mouvement et les prévisions pour l'équation de la quantité de mouvement bi-dimensionnelle même loin du décollement.

Enfin, il est prouvé que les méthodes d'entraînement sont nettement supérieures à la méthode Pechau lorsqu'il y a une aspiration ou une injection distribuée.

CONTENTS

LIST OF FIGURES

NOTATION

c	aerofoil chord length
c_f	local skin-friction coefficient
F	entrainment function of Head
H, H_1	profile shape-factors: $H = \frac{\delta^*}{\theta}$; $H_1 = \frac{\delta - \delta^*}{\theta}$
$k(x)$	term in the momentum integral equation representing the departure from two-dimensional conditions
Q	volume flux in the boundary layer
Q_t	volume flux of turbulent fluid in the boundary layer
R	local radius of curvature of the surface (in the x-y plane)
R_θ, R_c	Reynolds numbers: $R_\theta = \frac{U_1\theta}{\nu}$; $R_c = \frac{U_1 c}{\nu}$
t	turbulent flux thickness $\left(= \int_0^\infty \frac{\gamma u_t}{U_1}\, dy \right)$
t_{12}	spanwise turbulence flux thickness $\left(= \int_0^\infty \frac{\gamma w_t}{U_1}\, dy \right)$
$\frac{t}{\theta}$, $\frac{t_{12}}{\theta_{12}}$	shape-factors appearing in the new entrainment equation
u, v, w	components of velocity in the boundary layer in the x, y, z directions respectively
U_1	component of velocity in the free stream in the x-direction
U_{ref}	reference value of U_1, shown in Figure 21
u_t, w_t	mean velocity components of turbulent fluid over "time turbulent", in the x, z directions respectively
u_p	mean velocity of irrotational fluid over "time potential"
v_0	local transpiration velocity at the surface (positive for injection)
v_e, $\overline{v_{et}}$, v_{et}	entrainment velocities

x, y, z	localised rectangular Cartesian coordinates; x is measured longitudinally along the surface; y is the distance perpendicular to the surface, and z is the spanwise distance
Y	height of turbulence front above surface
α_1	universal constant in Equation (6)
α_e, α, β	entrainment coefficients used in the new auxiliary equations
γ	intermittency factor (ratio of "time turbulent" to total time)
δ, δ_1	boundary layer thicknesses; $\delta_1 = y$ at $\frac{u}{U_1} = 1.00$, used by the present author; $\delta = y$ at $\frac{u}{U_1} = 0.995$, used by Head
δ_u, δ_e	velocity defect and length scales, respectively, of the flow at or near to the turbulence front
δ^*	displacement thickness $\left(= \int_0^\infty \left(1 - \frac{u}{U_1}\right) dy \right)$
$\frac{\Delta u}{U_1}$	velocity defect parameter
θ	momentum loss thickness $\left(= \int_0^\infty \frac{u}{U_1}\left(1 - \frac{u}{U_1}\right) dy \right)$
θ_{12}	spanwise momentum loss thickness $\left(= \int_0^\infty \frac{w}{U_1}\left(1 - \frac{u}{U_1}\right) dy \right)$
ν	kinematic viscosity

THE CALCULATION OF SHAPE-FACTOR DEVELOPMENT IN INCOMPRESSIBLE TURBULENT BOUNDARY LAYERS WITH OR WITHOUT TRANSPIRATION

B.G.J. Thompson

1. INTRODUCTION

A recent review[1] by the present author has shown that, in most cases, the existing measurements of nominally two-dimensional turbulent boundary layers are affected by the presence of small three-dimensional flows, as indicated by the disagreement (even far from separation) found between the measured developments of momentum thickness (θ) and those calculated from step-by-step solutions of the two-dimensional momentum integral equation using measured H values and values of skin-friction[13] similar to those obtained from the law of Ludwieg and Tillmann[14]. The more important examples are shown here as Figures 1, 2 and 3.

The construction of a satisfactory shape-factor equation is in principle a difficult problem due to the absence of a satisfactory (known) general relationship between the turbulent shear stress and the mean velocity distribution. The results of the momentum calculations show that this problem is further complicated, at present, by the necessity of using data obtained in three-dimensional layers which are not properly specified by the measured boundary conditions, as the latter are appropriate only to the strictly two-dimensional flow assumed. However, when auxiliary equations are tested against experiment, the calculations of H development can be made using the *measured* development of momentum thickness in each case as this provides an additional boundary condition accounting to some extent for the influence of the cross-flows on the shape-factor growth. Comparisons, on this basis, have been made[1] between the predictions of several of the better known auxiliary equations (from Refs. 2 to 6) and experiment. Some typical examples are shown here in Figures 4 to 10, for the measured layers of References 7 to 12.

The different equations usually predict widely differing H developments in any given pressure distribution and are often inaccurate. The results obtained from the entrainment equation of Head[2] are, however, generally much better than the remainder especially for the equilibrium layers of Clauser[7] shown in Figures 4 and 5; also for the layer of Schubauer and Spangenberg[9] shown in Figure 7. The agreement with experiment is still unsatisfactory in some cases, however, particularly those shown in Figures 5 and 6, and so an improved equation has been developed and is described in the following sections.

The new auxiliary equation was developed from Head's original approach but uses a revised physical picture of the turbulent boundary layer and of the entrainment process. By incorporating an explicit allowance for the cross-flow this has resulted in an

equation giving rather better agreement with experiment except for one layer, and so, by equating the cross-flow term to zero it may be used for calculations of shape-factor development in two-dimensional conditions with more confidence than the earlier equations which have not taken account of three-dimensional effects.

The entrainment approach was chosen not only because of the superiority of Head's original equation but also because of the belief that the entrainment relationships, obtained for layers on solid surfaces, would be very little affected by transpiration, whereas the direct effect of the suction or injection on the whole of the shear-stress distribution through the layer might make the energy equation, for example, more difficult to extend to such physical situations.

Encouraging results, using the entrainment equations, have been obtained on a provisional basis for layers with distributed suction or injection and are described at the end of this paper.

2. THE ENTRAINMENT EQUATION OF HEAD

Head[2] equated the rate of increase of quantity flow (Q) in the boundary layer to the entrainment velocity (v_e), and assumed that the entrainment was controlled by the largest turbulent eddies characterised by the scales U_1, $\delta - \delta^*$, and a shape-factor $H_1 = \dfrac{\delta - \delta^*}{\theta}$.

Hence,

$$\frac{dQ}{dx} = \frac{d[U_1(\delta - \delta^*)]}{dx} = v_e = F(H_1) \qquad (1)$$

where $\delta = y$ at $u/U_1 = 0.995$. Equation (1) was used in calculations in the form,

$$\frac{dR_{\theta}H_1}{dx} = \frac{U_1}{\nu} F(H_1) . \qquad (2)$$

The single-curve relationship $F(H_1)$ is somewhat arbitrarily drawn between the data of References 8 and 10, and can be more logically derived by assuming that v_e is proportional to some scale velocity defect of the outer region; in addition the original approach suffers from the difficulty of defining the boundary layer thickness δ. Consequently, at Dr. Head's suggestion, a revised entrainment approach was adopted where the turbulent boundary layer was no longer considered as purely a region of defect of mean velocity.

3. THE NEW ENTRAINMENT EQUATION

3.1 The basic physical model

The investigations of Corrsin and Kistler[15] and others, show that the turbulent layer consists of a body of turbulent fluid, adjacent to the wall, possessing both mean and fluctuating vorticity and separated, at any instant, from the external potential flow by an apparently continuous interface (or turbulence front) that is strongly distorted in three-dimensions by the action of the largest scales of the underlying turbulence.

The turbulence front is continuously propagating into the external flow, converting potential fluid to a rotational state and enabling the transfer of mean-flow kinetic energy to the retarded turbulent region to occur. This appears to be the essential mechanism by which the layer grows and, together with the clearly defined extent of the fully turbulent flow (see Fig.11), provided the main physical reasons for developing the new auxiliary equation by equating the rate of increase of flux ( ) of turbulent fluid to the mean entrainment rate $\overline{v_{et}}$. Now, if u_t is the average velocity of the turbulent fluid taken over "time turbulent" and u_p is the average velocity of the irrotational fluid over "time potential",

$$u = \gamma u_t + (1 - \gamma)u_p \tag{3}$$

where γ is the fraction of the time for which the flow is turbulent at a particular position and is called the "intermittency factor". Hence,

$$Q_t = \int_c^\infty \gamma u_t dy = U_1 t \tag{4}$$

where t is the "turbulence flux thickness", and the basic equation therefore becomes,

$$\frac{dQ_t}{dx} = \frac{dU_1 t}{dx} = \nu \frac{dR_\theta(t/\sigma)}{dx} = \overline{v_{et}}. \tag{5}$$

3.2 The velocity-defect hypothesis for entrainment

The local rate of vorticity diffusion per unit area of the interface will depend solely on local conditions and, in the mean for all times at which the turbulence front is at height Y, this rate (v_{eY}) will depend only on the average velocity defect scale ($\delta u(Y)$) provided the overall Reynolds number of the flow is not too small.

That is,

$$\frac{v_e}{\delta u} = \alpha_1 \quad \text{(a universal constant)}. \tag{6}$$

The overall entrainment rate ($\overline{v_{et}}$) will depend[16] on the way in which the larger scales of the turbulence govern the shape of the interface (and hence the "area" over which v_{ev} may be assumed to act) and the probability distribution of Y. If, therefore, there is an overall similarity of the flow as in equilibrium layers a simple relationship might be expected of the form

$$\overline{v_{et}} = \alpha_e \Delta u \tag{7}$$

where Δu is some suitable scale of velocity defect to the turbulent region, and α_e is a universal constant called the "entrainment coefficient". This does not rule out, a priori, the possibility that α_e should be insensitive to departures from similarity and the new equation was used initially in the form, from (5) and (7),

$$\frac{dR_\theta(t/\theta)}{dx} = \alpha_e \frac{\Delta u}{U_1} \frac{U_1}{\nu} . \tag{8}$$

In the absence of more detailed measurements it was necessary to assume that

(a) $u_p = U_1$,

(b) γ was a universal function of y/δ_1 given by the measurements of Klebanoff[17] for zero pressure gradient, where $\delta_1 = y$ at $u/U_1 = 1.00$.

The velocity-defect parameter was chosen as

$$\frac{\Delta u}{U_1} = 1 - \left[\gamma \frac{u_t}{U_1}\right]_{MAX} . \tag{9}$$

This is shown, together with other features of the new approach, in Figure 12. The shape factors

$$\frac{\Delta u}{U_1}, \quad \text{and} \quad (t/\theta) = \int_0^\infty \left(\frac{u}{U_1} - 1 + \gamma\right) d(y/\theta)$$

were found as functions of H and R_θ , using a new two-parameter velocity profile family[13] similar to Coles family[18] in many respects, and these relationships are shown in Figures 13 and 14.

3.3 Results of calculations using the new equations

It was found that with a value of $\alpha_e = 0.09$, Equation (8) gave good agreement with the equilibrium layers but this value of α_e was much too large for the other layers. Therefore it was assumed that $\theta \dfrac{d(t/\theta)}{dx}$ could be used as a measure of the departure from similarity and, for simplicity in computation, it was assumed also that

$$\alpha_e = \alpha + \beta\theta \frac{d(t/\theta)}{dx} . \tag{10}$$

Equation (8) thus took the form

$$\frac{d(t/\theta)}{dx} = \frac{\alpha \dfrac{U_1}{\nu} \dfrac{\Delta u}{U_1} - (t/\theta) \dfrac{dR_\theta}{dx}}{R_\theta \left(1 - \beta \dfrac{\Delta u}{U_1}\right)} \tag{11}$$

where by trial and error it was found that $\alpha = 0.09$, $\beta = 1.0$ gave better agreement than Head's equation for the layers on flat walls, except for layer "D" of Schubauer and Spangenberg[9] where Head's excellent result could not be matched, unfortunately. For layers developing along *convex* curved surfaces the entrainment was too large, however, resulting in values of H that were too small and separations that were delayed.

3.4 The additional effect of wall curvature on entrainment

The additional streamline curvature (in the x-y plane) imposed due to convex wall curvature may be expected to reduce the intensity of turbulent mixing and to decrease the entrainment. The largest scales of the turbulence will be affected most strongly and so it was assumed that α depended upon δ_1/R, where δ_1 is the boundary layer thickness for $u/U_1 = 1.00$ defined by a relationship of the form

$$\delta_1/\theta = f(H, R_\theta) \tag{12}$$

obtained from the new profile family[13].

Equation (11) was solved for $\alpha(\delta_1/R)$ using the data of References 10 and 12 and one layer from Reference 11. On recalculation for the H developments in these and in two additional layers from Reference 11, good agreement with experiment was now obtained. The extent of this improvement may be gauged from the typical example shown in Figure 15.

Although, at this stage, the overall agreement with experiment was very satisfactory, except for Schubauer and Spangenberg "D" it was not certain that the influence of the cross-flows in the measured layers had been eliminated and so an explicit allowance for these was added to give the final equation suitable for use in two-dimensional conditions.

3.5 The inclusion of a term to allow for the effects of cross-flow

The only available measure of the magnitude of the cross-flow in nominally two-dimensional layers is the difference (k(x)), locally, between the measured rate of change of momentum thickness (used in dimensionless form as R_θ) and that calculated from the two-dimensional form of the momentum equation as described in the Introduction.

That is,

$$k(x) = \frac{d\left[R_{\theta_{EXPT}} - R_{\theta_{2\text{-}D}}\right]}{dx}. \tag{13}$$

The inclusion of the cross-flow term in the momentum integral equation gives, neglecting the Reynolds stress terms,

$$\frac{\partial R_\theta}{\partial x} = \frac{c_f}{2}\frac{U_1}{\nu} - (H+1)\frac{R_\theta}{U_1}\frac{dU_1}{dx} - \frac{U_1}{\nu}\frac{\partial \theta_{12}}{\partial z} \tag{14}$$

and thus

$$k(x) = -\frac{U_1}{\nu}\frac{\partial \theta_{12}}{\partial x} \tag{15}$$

where

$$\theta_{12} = \int_0^\infty \frac{w}{U_1}\left(1 - \frac{u}{U_1}\right) dy \,. \tag{16}$$

The corresponding form of the entrainment equation is

$$\frac{1}{\nu}\frac{\partial U_1 t}{\partial x} + \frac{1}{\nu}\frac{\partial U_1 t_{12}}{\partial z} = \alpha_e \frac{\Delta u}{U_1}\frac{U_1}{\nu} \tag{17}$$

where the spanwise flux

$$U_1 t_{12} = \int_0^\infty \gamma w_t dy \tag{18}$$

and γw_t is the overall time mean value of the spanwise (z) component of velocity within the turbulent fluid.

Now,

$$\frac{1}{\nu}\frac{\partial U_1 t_{12}}{\partial z} = \frac{U_1 \theta_{12}}{\nu}\frac{\partial (t_{12}/\theta_{12})}{\partial z} + \frac{\theta_{12}}{\nu}\frac{t_{12}}{\theta_{12}}\frac{\partial U_1}{\partial z} + \frac{U_1}{\nu}\frac{\partial \theta_{12}}{\partial z}\frac{t_{12}}{\theta_{12}} \,. \tag{19}$$

Hence, assuming that the measurements have been made at or near a plane of symmetry of the flow the third term on the right-hand side predominates and the entrainment equation becomes, from (15), (17) and (19),

$$\frac{\partial R_\theta (t/\theta)}{\partial x} = \alpha_e \frac{\Delta u}{U_1}\frac{U_1}{\nu} + k(x)\frac{t_{12}}{\theta_{12}} \,. \tag{20}$$

The form of the spanwise velocity profile cannot be determined in general for the nominally two-dimensional layers and so it was assumed that the effects of spanwise pressure gradients predominated over those due to divergence or convergence of the external streamlines. A cross-flow profile family was accordingly constructed from the new two-parameter streamwise profile family[13] and the triangular polar model of Johnston[19]. This gave a relationship for t_{12}/θ_{12}, which was closely approximated by

$$\frac{t_{12}}{\theta_{12}} = \frac{H}{H - 1} \tag{21}$$

where the cross flow had been assumed to occur entirely within the fully turbulent region ($w = \gamma w_t$).

The new Equation (20) was solved for α_e, using Equation (21) and the measured developments of References 7, 8, 9, 10, 11 and 12, and the resulting correlations were approximated by

$$\alpha_e = \alpha + \beta\theta \frac{\partial(t/\theta)}{\partial x} \tag{22}$$

where

$$\alpha = 0.02 + 0.02194 \left(\frac{\delta_1}{R} + 0.001\right)^{-0.16794} \tag{23}$$

$$\beta = 1.0 \quad \text{for} \quad \theta \frac{\partial(t/\theta)}{\partial x} \geq -0.003 \tag{24}$$

and

$$\beta = 2.0 \quad \text{for} \quad \theta \frac{\partial(t/\theta)}{\partial x} < -0.003 \,. \tag{25}$$

3.6 The new auxiliary equation

Combining Equations (20), (21) and (22) the new auxiliary equation, in the form suitable for calculations, becomes

$$\frac{\partial(t/\theta)}{\partial x} = \frac{\alpha \left(\frac{\delta_1}{R}\right) \frac{U_1}{\nu} \frac{\Delta u}{U_1} - (t/\theta) \frac{\partial R_\theta}{\partial x} + \left(\frac{H}{H-1}\right) k(x)}{R_\theta \left(1 - \beta \frac{\Delta u}{U_1}\right)} . \tag{26}$$

This was used, together with Equations (23), (24), (25) and the charts for t/θ, $\Delta u/U_1$ and δ_1/θ, to give the predictions for H shown in Figures 4 to 10 and labelled "NEW EQUATION".

Starting values of H and R_θ, and distributions of $k(x)$, R_θ, U_1/ν, $\partial R_\theta/\partial x$ were obtained from experiment.

3.7 The results of the calculations

The new equation gives better results than the existing equations, except for Schubauer and Spangenberg "D" (Fig.7). The improvement in agreement with the equilibrium layers of Clauser (Figs.4 and 5) is very satisfactory. However, for Newman's aerofoil layer (Fig.6) dH/dx is underestimated near to separation because $k(x)$ has been calculated from the momentum equation without allowing for the measured normal-stress terms (see Fig.3); otherwise agreement with experiment is excellent.

3.8 Discussion

Figures 16 and 17 compare the results given by the new equation with and without its cross-flow term. The addition of a cross-flow term to the equation should, intuitively, result in a lowering of H in the *divergent* flow conditions of Clauser I (Fig.16) and correspondingly, an increase of H would be expected for the convergent flow conditions of Clauser II (Fig.17). In fact, the observed effect on the predicted H development is in the opposite direction, with H values being *raised* for Clauser I and *lowered* for Clauser II. Therefore, when attempting to derive an auxiliary equation from the present data or to use it to seek agreement with the present measurements of

H development, these results show that the use of the measured momentum thickness alone, *without* the inclusion of an explicit cross-flow term leads to an overestimate of the effect of the cross-flow term on the H development, although the conclusions drawn in Section 1, regarding the usefulness of the earlier auxiliary equations, do not depend critically on the use of measured $R_\theta(x)$ (see Ref.1).

The present assumptions for the form of the cross-flow profile underestimate the true value of t_{12}/θ_{12} and the use of a profile based upon the assumption of a local radial flow as attempted by Rotta[20] and Norbury[21] should be tried. Re-analysis of the existing data assuming that measurements were made in a plane of symmetry might offer further improvements[16].

More detailed measurements of γ, u_t, and u_p are needed to establish the new physical model on a firmer basis, particularly as regards the influence of wall curvature.

The energy equation, or any alternative having a clear physical significance, would almost certainly have given an equally trustworthy equation for solid surface two-dimensional layers, provided a proper numerical analysis of the data had been made and three-dimensional flows had been accounted for. Purely empirical equations, however, are unlikely to be as satisfactory in this respect even if they predict the present measurements accurately, and they would be more difficult to extend to new physical situations. The question will remain open, however, until measurements have been made in accurately two-dimensional conditions or in layers where the three-dimensional flow is properly determined.

4. SHAPE-FACTOR CALCULATIONS FOR LAYERS WITH DISTRIBUTED SUCTION OR INJECTION

4.1 The equations

Equations (2) and (26) become

$$\frac{dH_1R_\theta}{dx} = \left[F(H_1) + \frac{v_0}{U_1}\right]\frac{U_1}{\nu} \tag{27}$$

and

$$\frac{d(t/\theta)}{dx} = \frac{\alpha\left(\frac{\delta_1}{R}\right)\frac{\Delta u}{U_1} + \frac{v_0}{U_1}\frac{U_1}{\nu} - (t/\theta)\frac{dR_\theta}{dx} + \left(\frac{H}{H-1}\right)k(x)}{R_\theta\left(1 - \beta\frac{\Delta u}{U_1}\right)} \tag{28}$$

where it is assumed that the entrainment functions $F(H_1)$, $\alpha(\delta_1/R)$ and β are unaffected by transpiration provided that suction rates are not high enough to produce a reversion towards laminar flow. Figures 18 and 19 show the curves used with Equation (27) and it is seen that the solid surface profile shape-factor relationship is only satisfactory for injection profiles[22,24]. The solid surface values of t/θ, $\Delta u/U_1$ have been used in Equation (28), provisionally, although the new profile family can now account for the effects of transpiration and the full relationships will be available soon.

4.2 Results of calculations

A typical result for the injection layers of Mickley and Davis[22] is shown in Figure 20, where the good agreement obtained using the entrainment equations may be contrasted with the poor result given by the equation of Pechau[23].

Figure 21 shows that the entrainment approach gives reasonably good results with suction especially when the correct shape-factor relationship is used. Pechau's results are again unsatisfactory.

The $k(x)$ values of these layers were found to be negligible using a new skin friction relationship (which accounts for the direct effects of transpiration on the inner profile) in the calculations of momentum thickness development. (See Figs.22 and 23).

5. CONCLUSIONS

(i) Existing shape-factor equations give widely differing results in any given pressure distribution and are sometimes very inaccurate. Head's equation is rather better than the remainder.

(ii) Auxiliary equations for predicting H in two-dimensional conditions can only be satisfactorily derived on the basis of the present experiments if direct account is taken of the cross-flows that appear to be present in most measured boundary layers.

(iii) A new form of entrainment equation has been evolved and shown to give improved agreement with experiment except for one layer measured by Schubauer and Spangenberg[9].

(iv) The physical basis of the new approach needs to be more firmly established, by additional measurements of intermittency and by measurement of comparative velocities in the fully turbulent and potential flow regimes.

(v) The entrainment equations give much better agreement with H development in layers with transpiration than does the published method of Pechau.

(vi) There remains an urgent need for measurements in accurately two-dimensional or in known three-dimensional conditions.

6. ACKNOWLEDGEMENTS

The author gratefully acknowledges the guidance and advice of Dr.M.R. Head, who supervised the present investigation whilst the author was a research student at Cambridge University. Thanks are also due to Miss Susan Gray for assistance in the numerical work.

REFERENCES

1. Thompson, B.G.J. — *A critical review of existing methods of calculating the turbulent boundary layer.* Aeronautical Research Council 26,109, FM3492, August 1964.

2. Head, M.R. — *Entrainment in the turbulent boundary layer.* Aeronautical Research Council R & M 3152, 1960.

3. Spence, D.A. — *The development of turbulent boundary layers.* J. Aero. Sci., Vol.23, 1956, pp.3-15.

4. Rubert, K.F.; Persh, J. — *A procedure for calculating the development of turbulent boundary layers under the influence of adverse pressure gradients.* NACA TN 2478, 1951.

5. Maskell, E.C. — *Approximate calculation of the turbulent boundary layer in two-dimensional incompressible flow.* RAE Rep. No. Aero. 2443, 1951; also Aeronautical Research Council 14,654.

6. Truckenbrodt, E. — *Ein Quadraturverfahren zur Berechnung der laminaren und turbulenten Reibungsschicht bei ebener und rotationssymmetrischer Strömung.* Ing-Archiv. Vol.20, 1952, pp.211-228.

   Read in translation as: *A method of quadrature for calculation of the laminar and turbulent boundary layer in the case of plane and rotationally-symmetrical flow.* NACA TM 1379, 1955.

7. Clauser, F.H. — *Turbulent boundary layers in adverse pressure gradients.* J. Aero. Sci., Vol.21, No 2, 1954, pp.91-108.

8. Newman, B.G. — *Some contributions to the study of the turbulent boundary layer.* Aust. Dept. Supply Rep. No.ACA – 53, 1951.

9. Schubauer, G.B.; Spangenberg, W.G. — *Forced mixing in boundary layers.* J. Fluid Mech., Vol.8, 1960, pp.10-32.

10. Schubauer, G.B.; Klebanoff, P.S. — *Investigation of separation of the turbulent boundary layer.* NACA TN 2133, 1950; also NACA Report 1030, 1951.

11. von Doenhoff, A.E.; Tetervin, N. — *Determination of general relations for the behaviour of turbulent boundary layers.* NACA Report 772, 1943.

12. Schmidbauer, H. — *Turbulente Reibungsschicht an erhaben gekrümmten Flächen.* Luftfahrtforschung, Vol.13, 1936, pp.160-162: (read in a private translation) also NACA TM 791, 1936.

13. Thompson, B.G.J. — Profile family report. Unpublished.

14. Ludwieg, H.; Tillmann, W. — *Untersuchungen über die Wandschub-spannung in Turbulenten Reibungsschichten.* Ing. Archiv. Vol.17, 1949, pp.288-299, translated as: *Investigations of the wall shearing stress in turbulent boundary layers.* NACA TM 1285, 1950, also Aeronautical Research Council 14,800.

15. Corrsin, S.; Kistler, A.L. — *The free-stream boundaries of turbulent flows.* NACA Report 1244, 1955, (formerly NACA TN 3133).

16. Thompson, B.G.J. — Unpublished Ph.D. Dissertation, Cambridge University, November 1963.

17. Klebanoff, P.S. — *Characteristics of turbulence in a boundary layer with zero pressure gradient.* NACA Report 1247, 1955, (formerly NACA TN 3178, 1954).

18. Coles, D. — *The law of the wake in the turbulent boundary layer.* J. Fluid Mech., Vol.1, 1956, pp.191-226.

19. Johnston, J.P. — *The turbulent boundary layer at a plane of symmetry in a three-dimensional flow.* Trans. ASME, Ser. D., Journal Basic Eng., Vol.82, 1960, pp.622-628.

20. Rotta, J.C. — *Über die Theorie der turbulenten Grenzschichten.* Ström. Forsch. Nr.1, 1950. Read in translation as, *On the theory of the turbulent boundary layer.* NACA TM 1344, 1953.

21. Norbury, J.F. — *An approximate method for the calculation of turbulent boundary layers in diffusers.* Aero. Quart., Vol.8, 1957, pp.58-77.

22. Mickley, H.S.; Davis, R.S. — *Momentum transfer for flow over a flat plate with blowing.* NACA TN 4017, 1957.

23. Pechau, W. — *Calculation of the turbulent boundary layer with continuously distributed suction.* AGARD Report 259, 1960.

24. Mugalev, V.P. — *Izvestiya Vysshikh Uchebriykh Zavendenii.* MVO. SSR., seriya "Aviatsionnaya Teknika", No.3, 1959, pp.72-79, read in translation as, *Experimental investigation of a presonic turbulent boundary layer, on a plate, with air admission.*

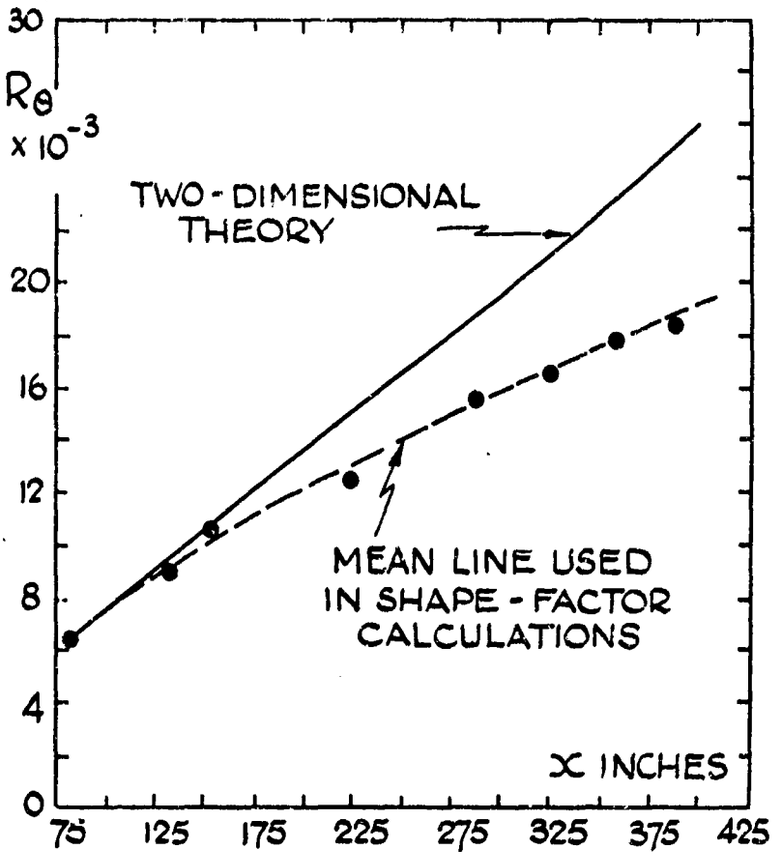

Fig. 1 Comparisons of momentum calculations with experiment. Clauser Series I

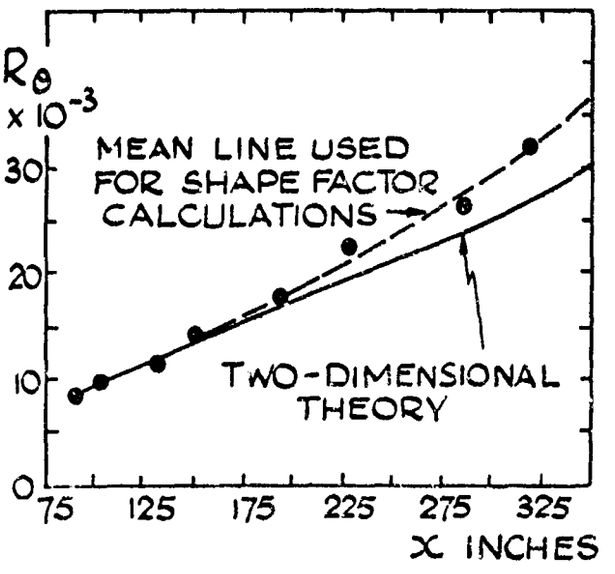

Fig. 2 Comparisons of momentum calculations with experiment. Clauser Series II

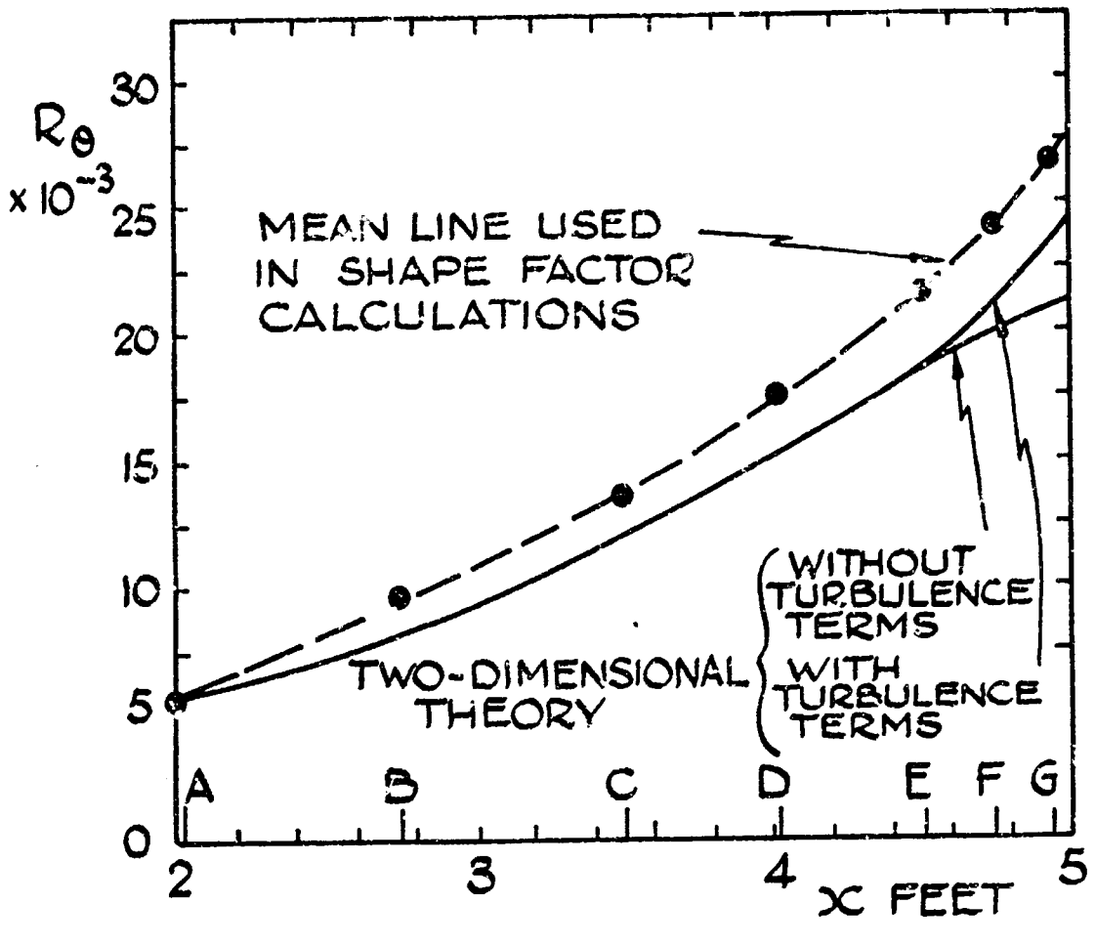

Fig.3 Comparisons of momentum calculations with experiment. Newman Series II

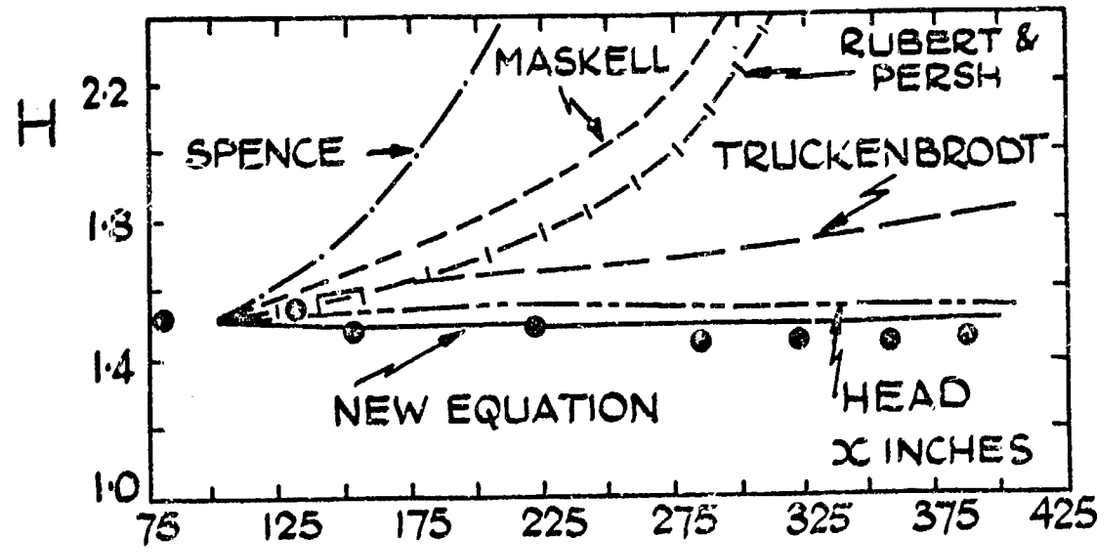

Fig.4 Comparisons of shape-factor predictions. Clauser Series I

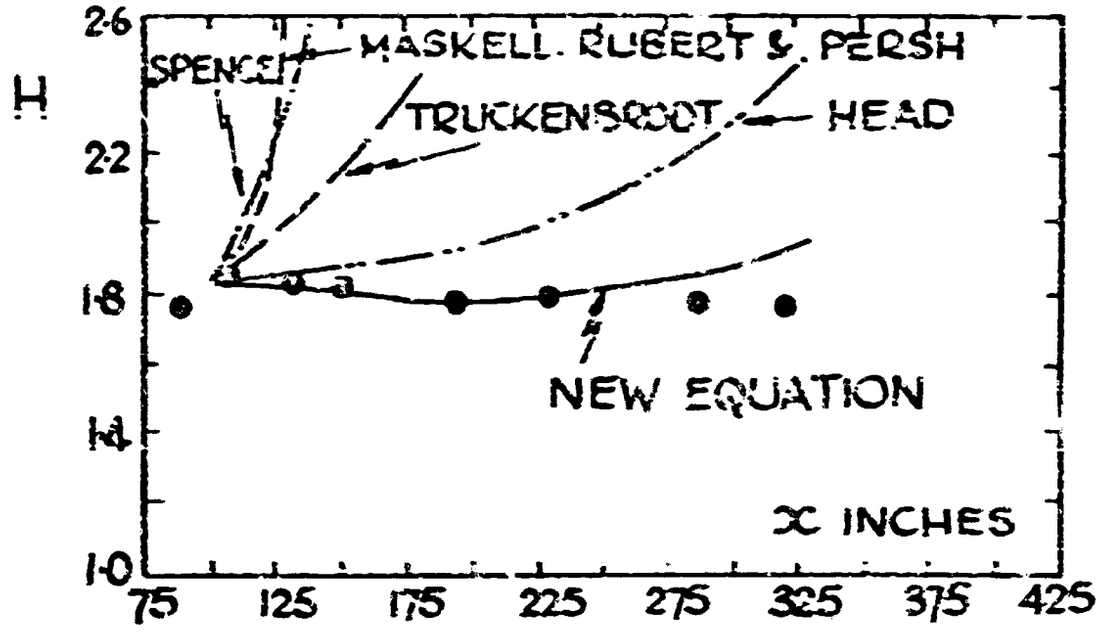

Fig.5 Comparisons of shape-factor predictions. Clauser Series II

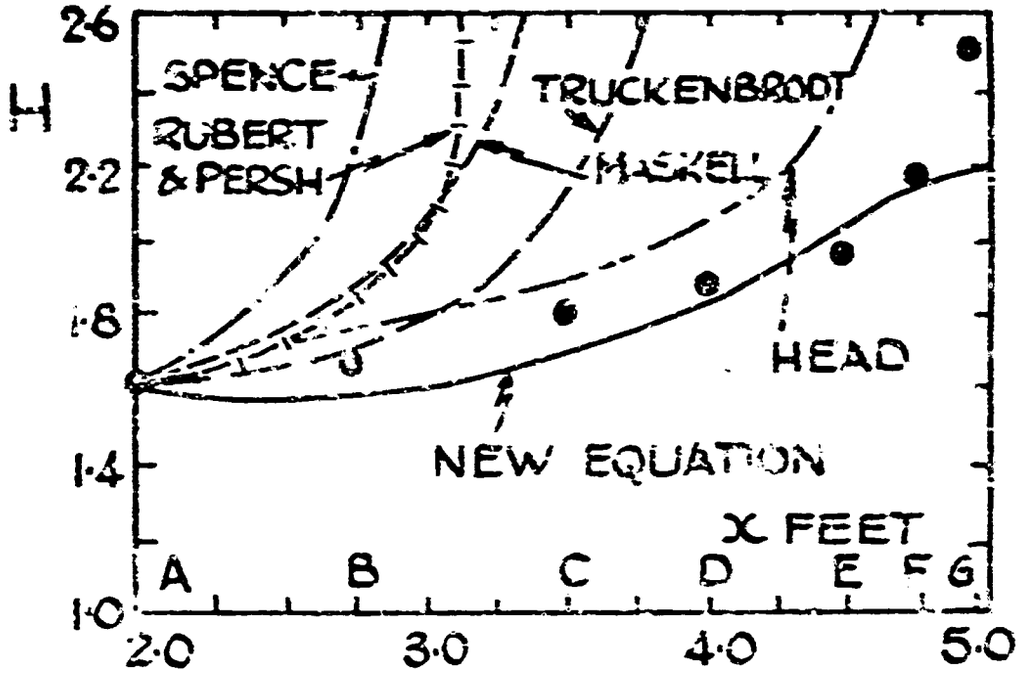

Fig.6 Comparisons of shape-factor predictions. Newman Series II

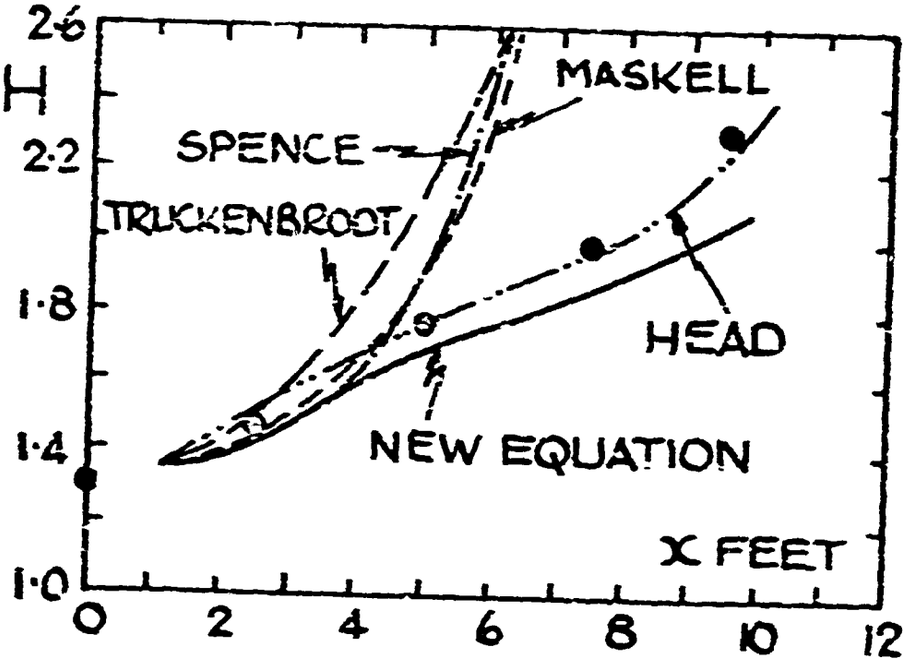

Fig. 7 Further comparisons of shape-factor predictions. Schubauer and Spangenberg [7]

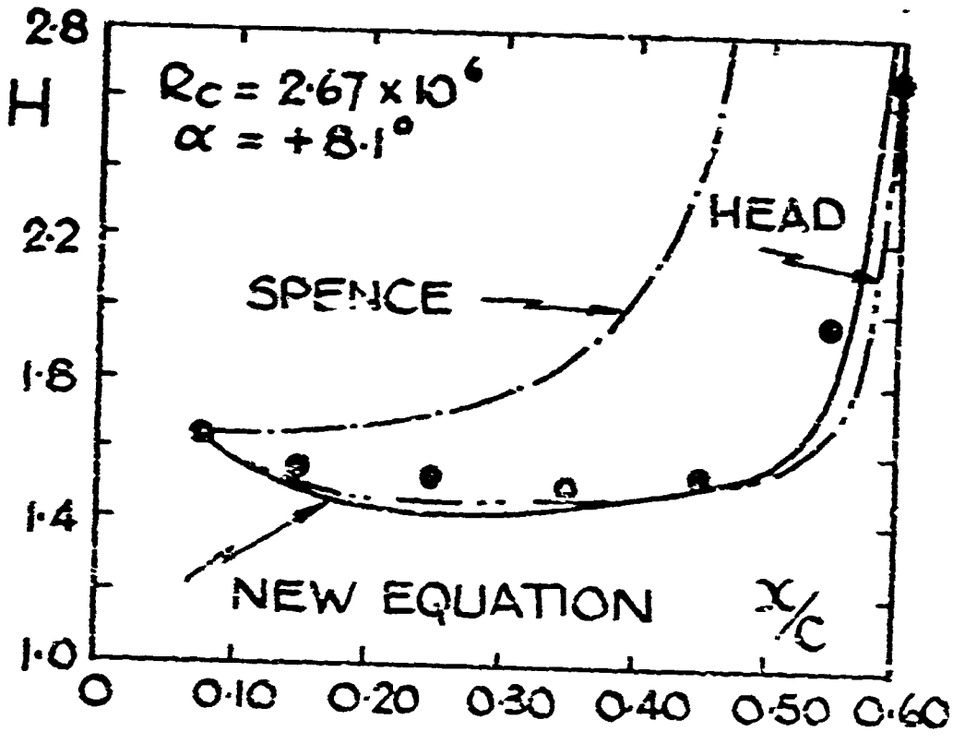

Fig. 8 Further comparisons of shape-factor predictions. van Ingen, Boerstoel and Peterson (NACA 65(212) - 222 aerofoil)

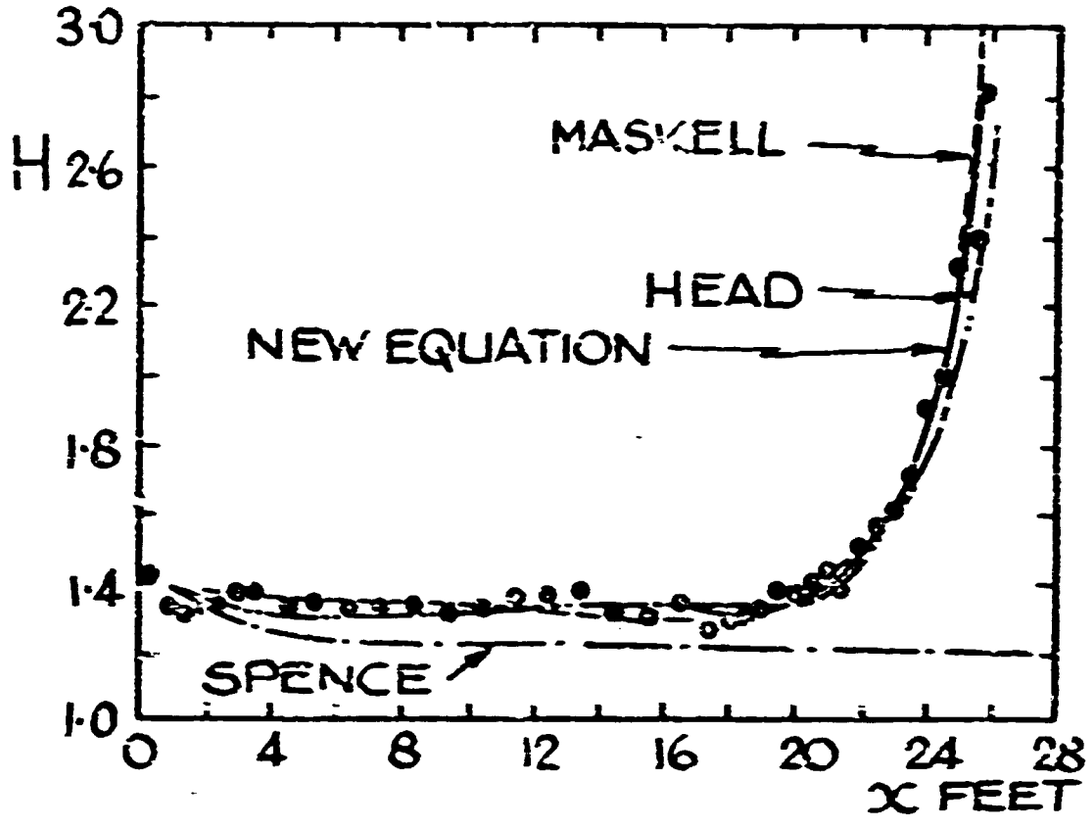

Fig.9 Further comparisons of shape-factor predictions. Schubauer and Klebanoff

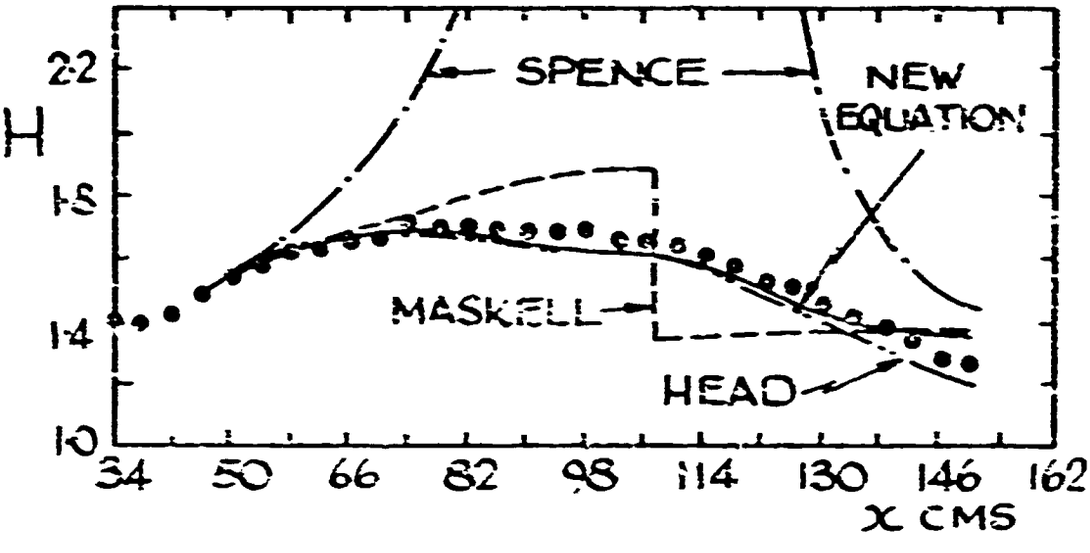

Fig.10 Further comparisons of shape-factor predictions. Schmidbauer

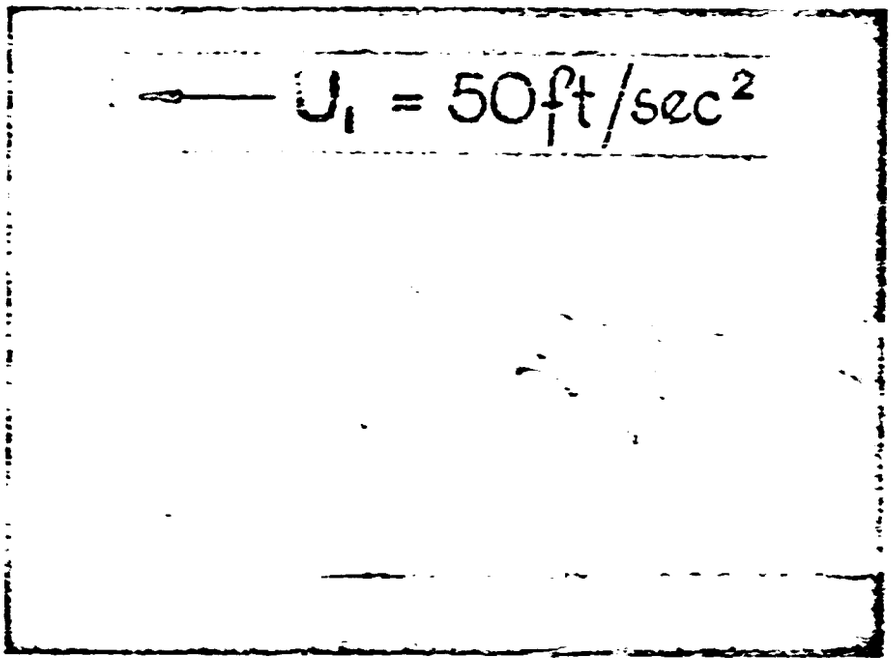

Fig. 11 Smoke photograph showing intermittency in the zero pressure gradient boundary layer ($R_x = 6000$)

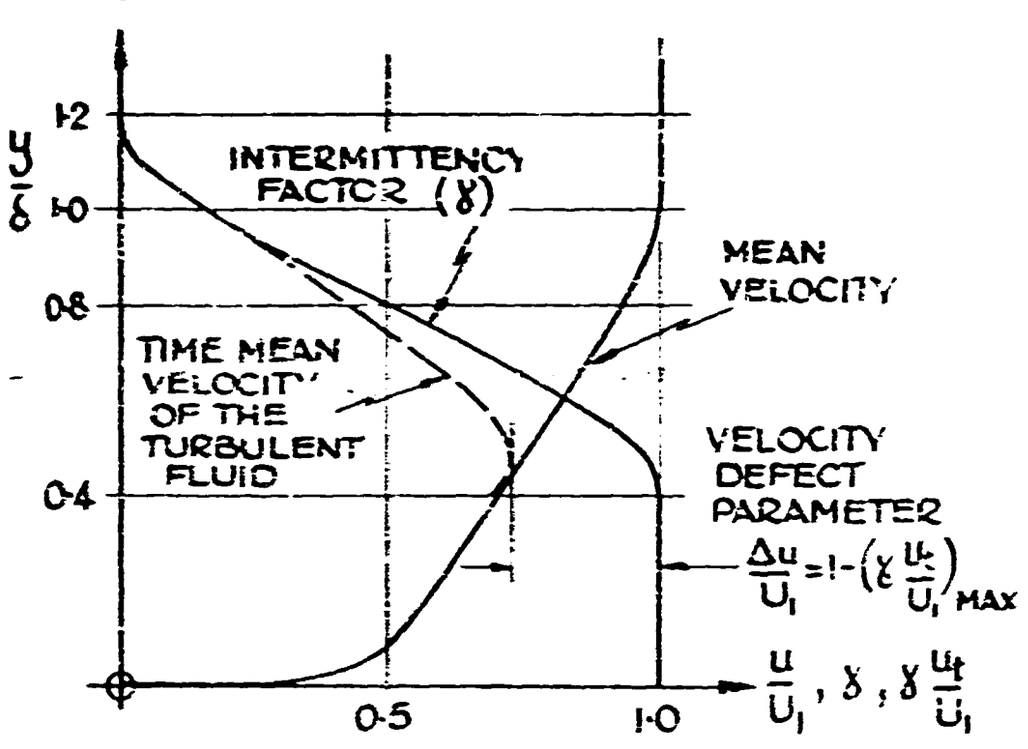

Fig. 12 Explanation of terms used in the new entrainment approach

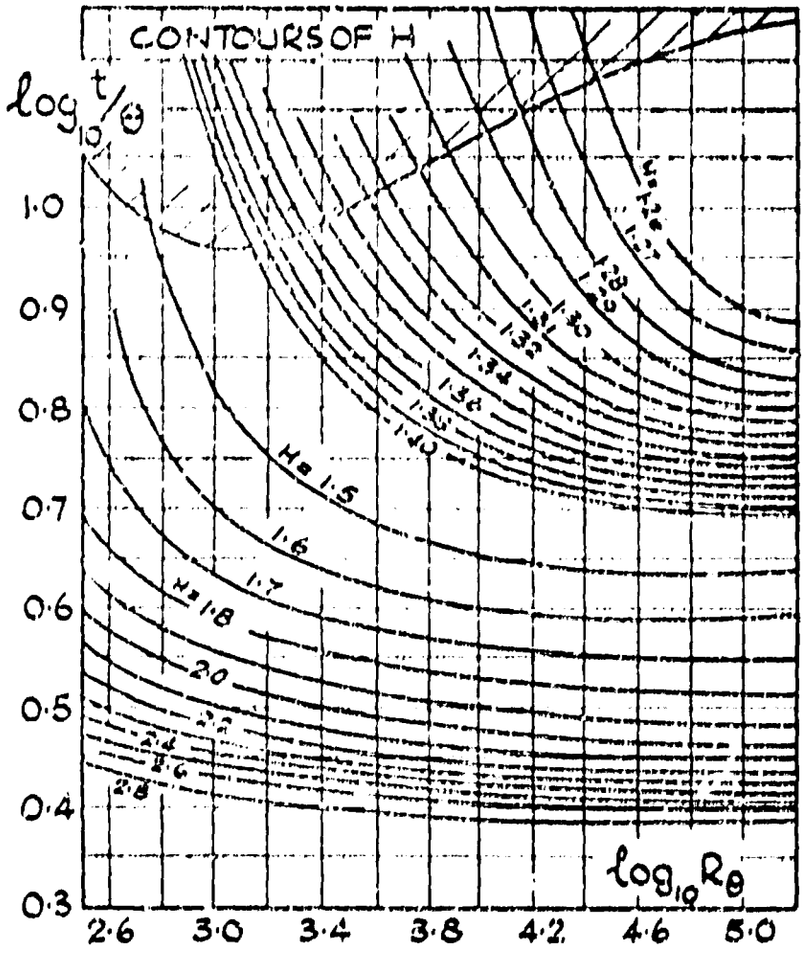

Fig. 13 Shape-factor relationships for use in the new entrainment equation. Turbulence flux thickness parameter

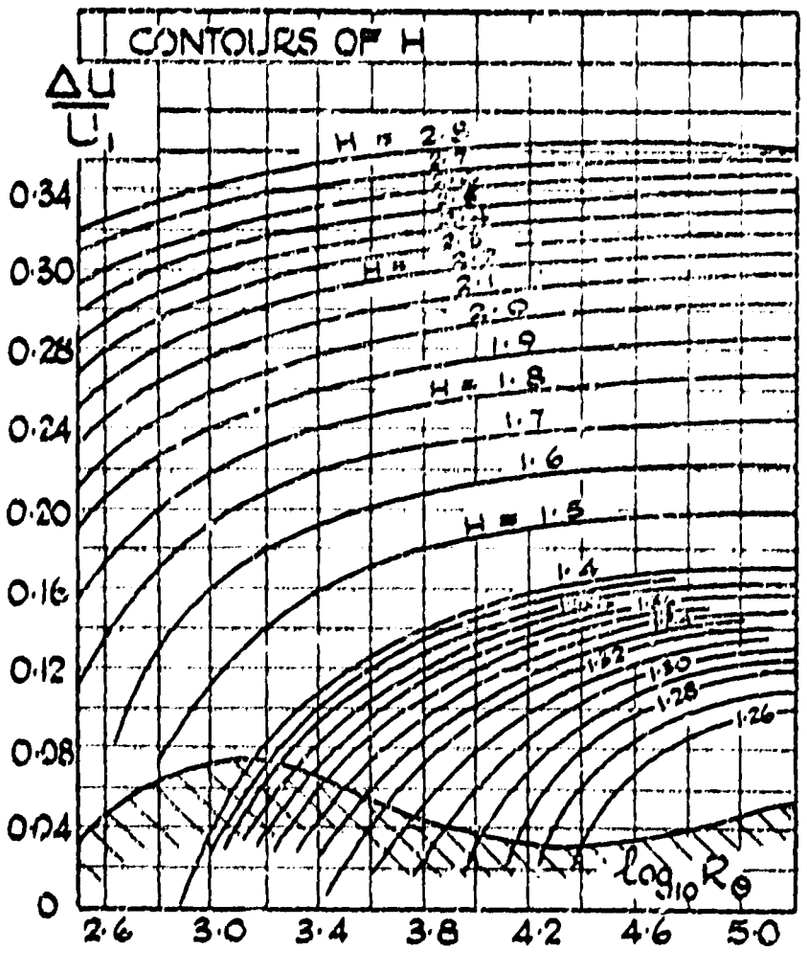

Fig. 14 Shape-factor relationships for use in the new entrainment equation. Velocity-defect parameter

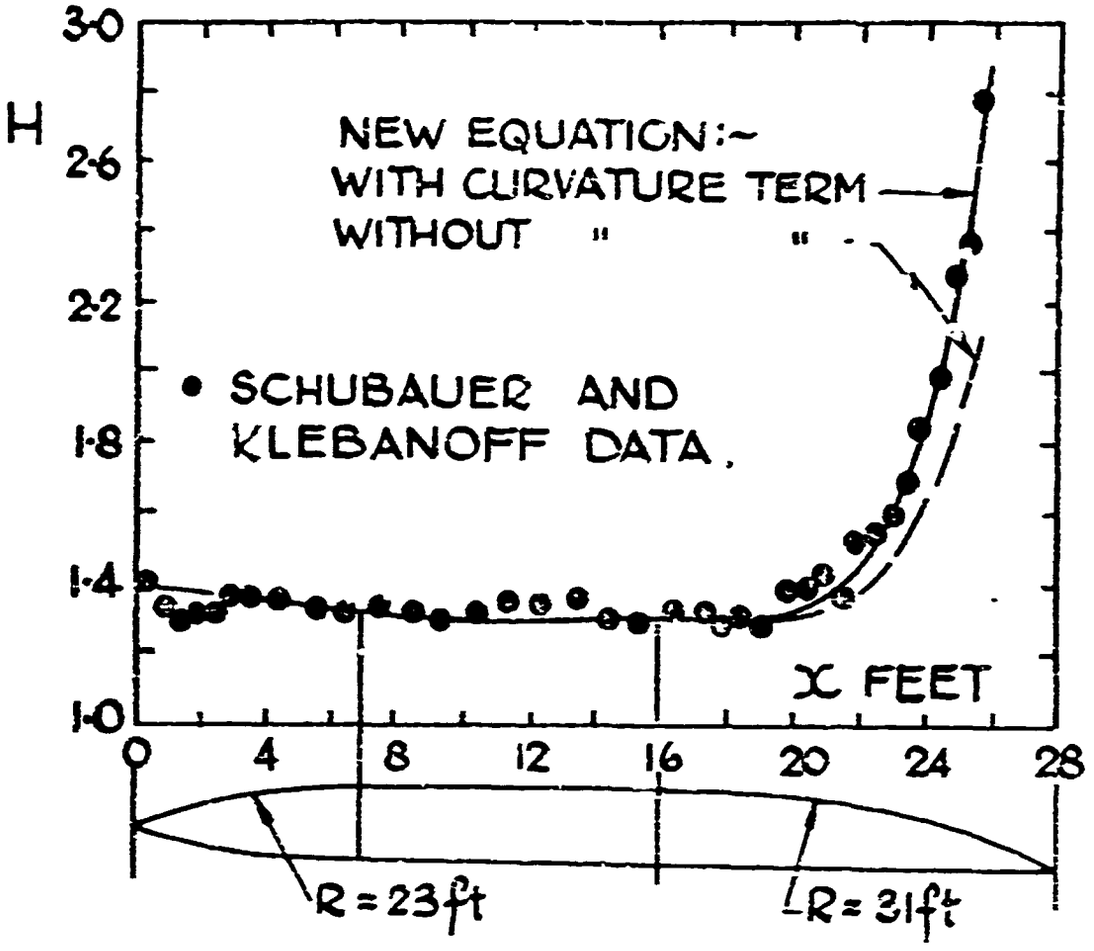

Fig. 15 Example of the effect of the curvature term on shape-factor prediction

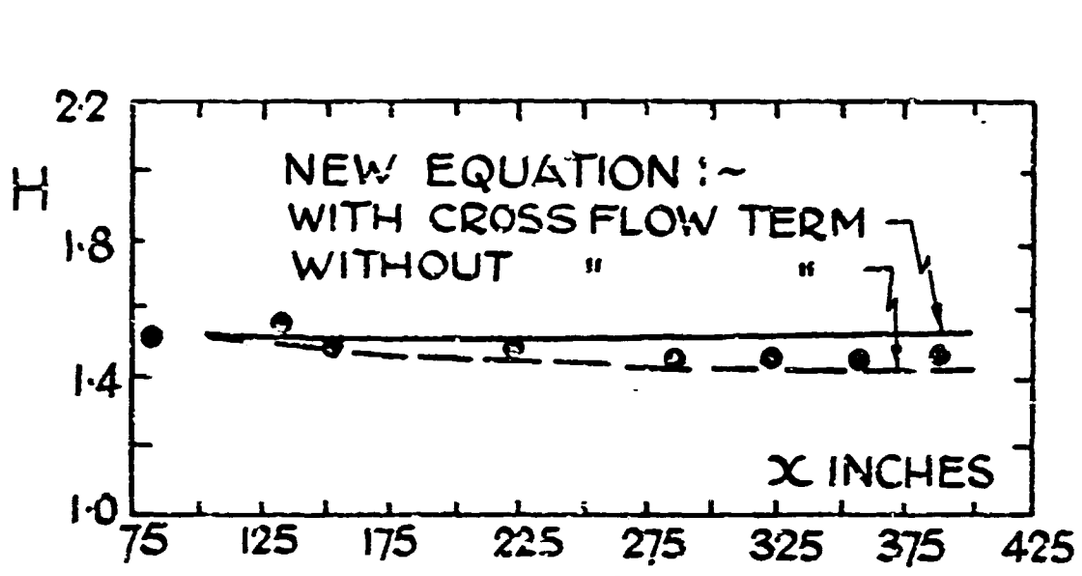

Fig. 16 The effect of the cross-flow term on shape-factor prediction. Clauser Series I

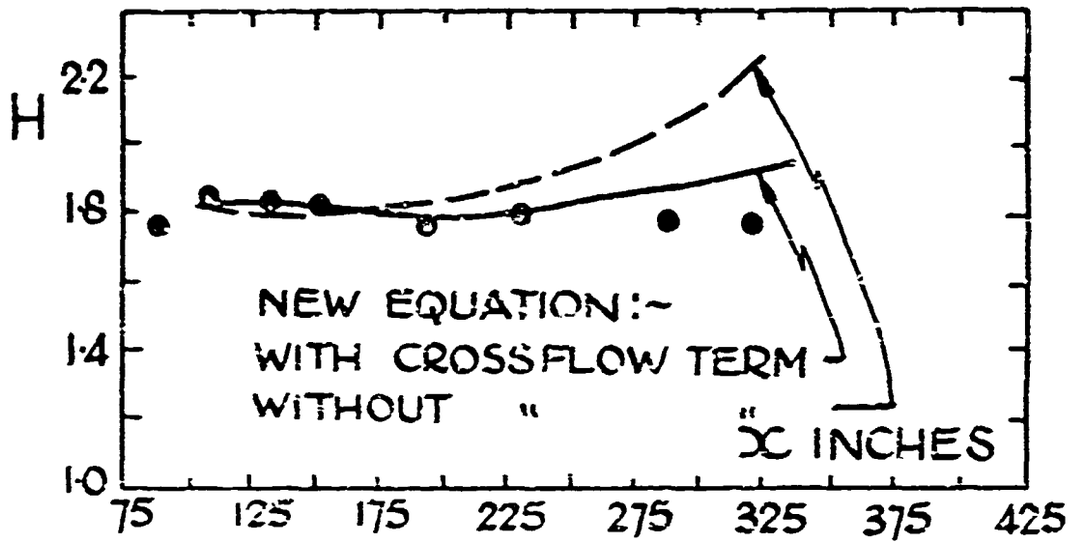

Fig. 17 The effect of the cross-flow term on shape-factor prediction. Clauser Series II

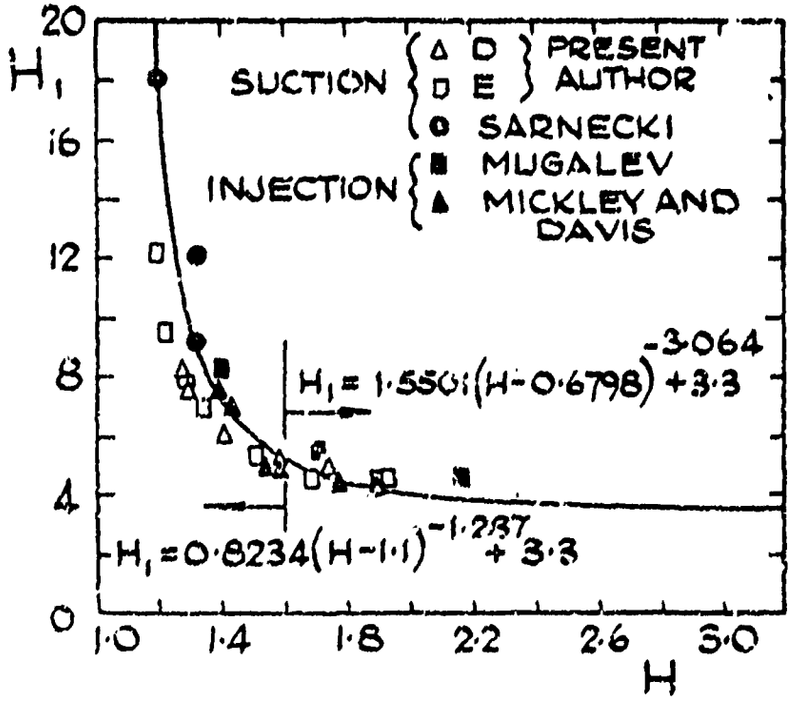

Fig. 18 Head's shape-factor relationship extended for transpired layers

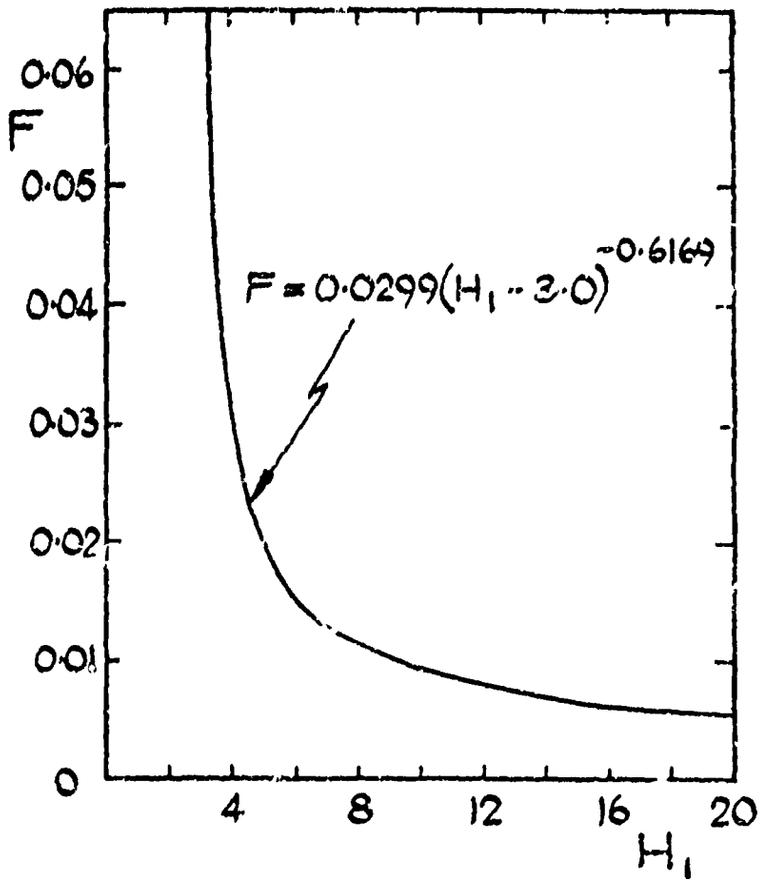

Fig. 19 Head's entrainment relationship extended for transpired layers

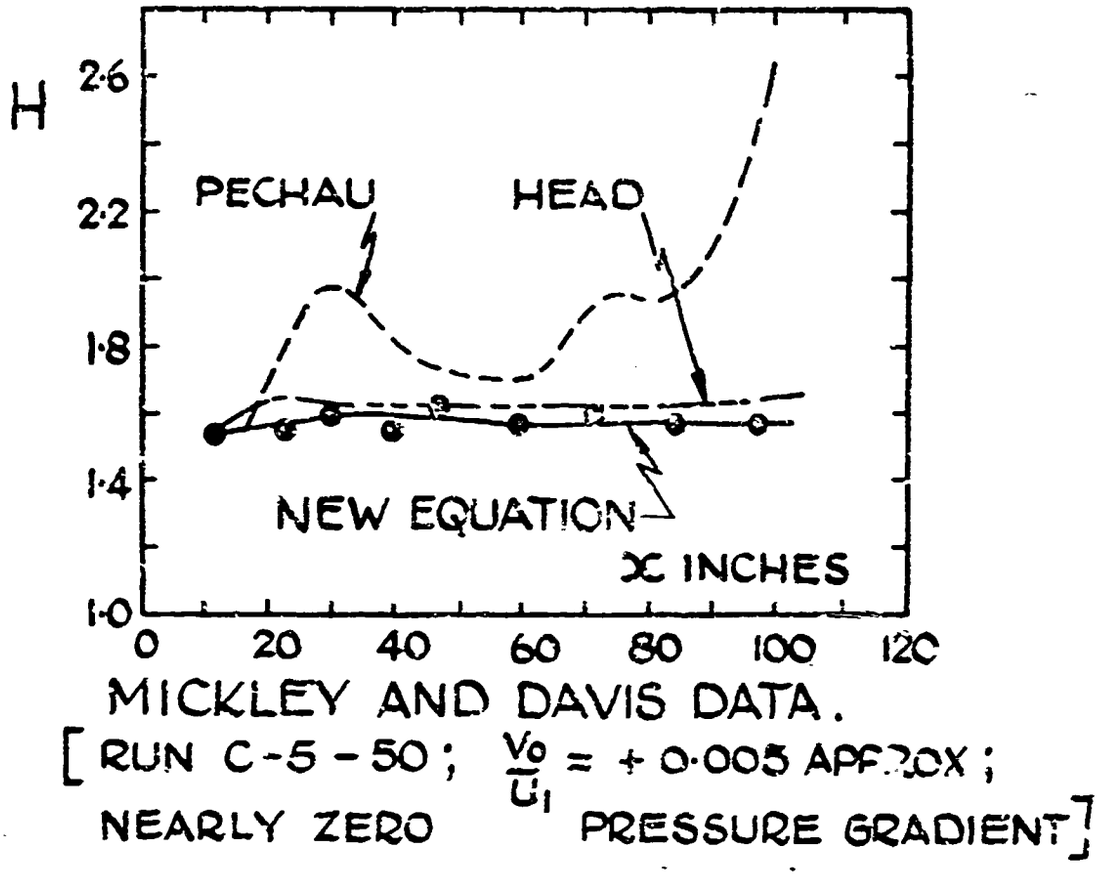

Fig. 20 Comparison of shape-factor predictions for a layer with injection

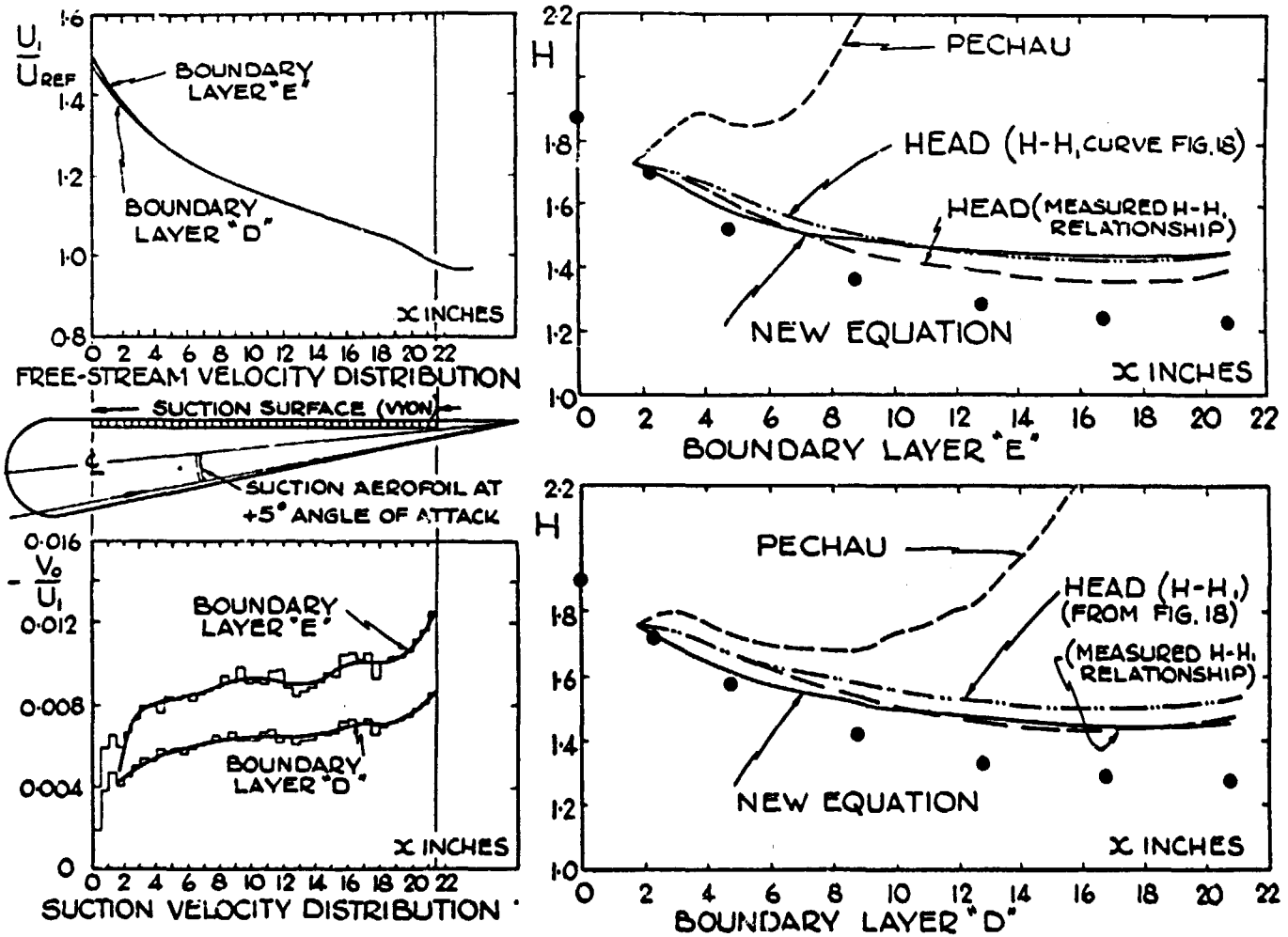

Fig. 21 Shape-factor developments with distributed suction

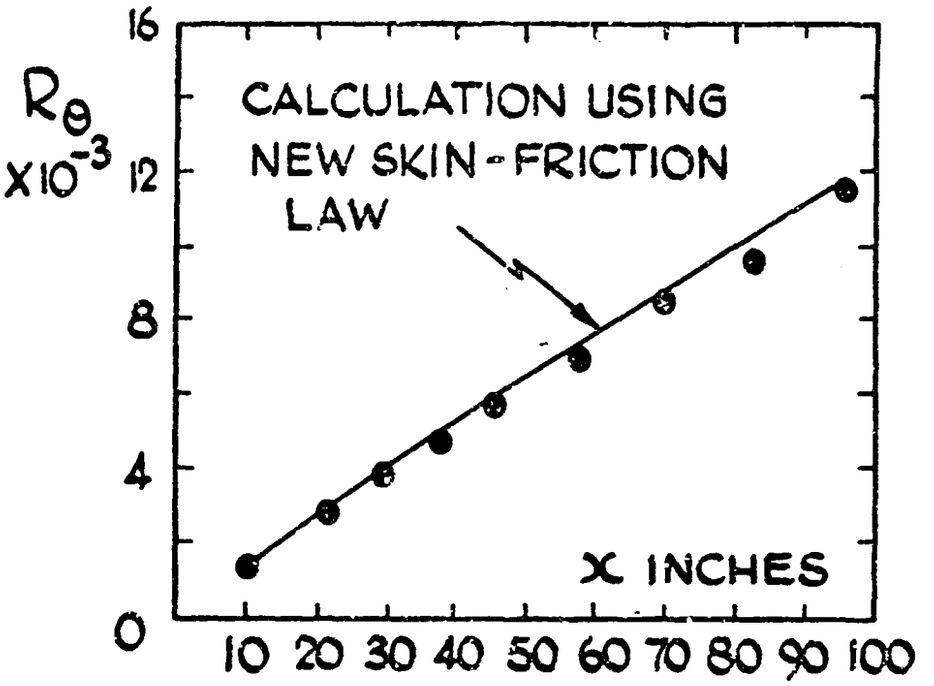

Fig. 22 Momentum thickness developments in injection layer of Mickley and Davis. Run C - 5 - 50 , $v_0/U_1 = + 0.005$

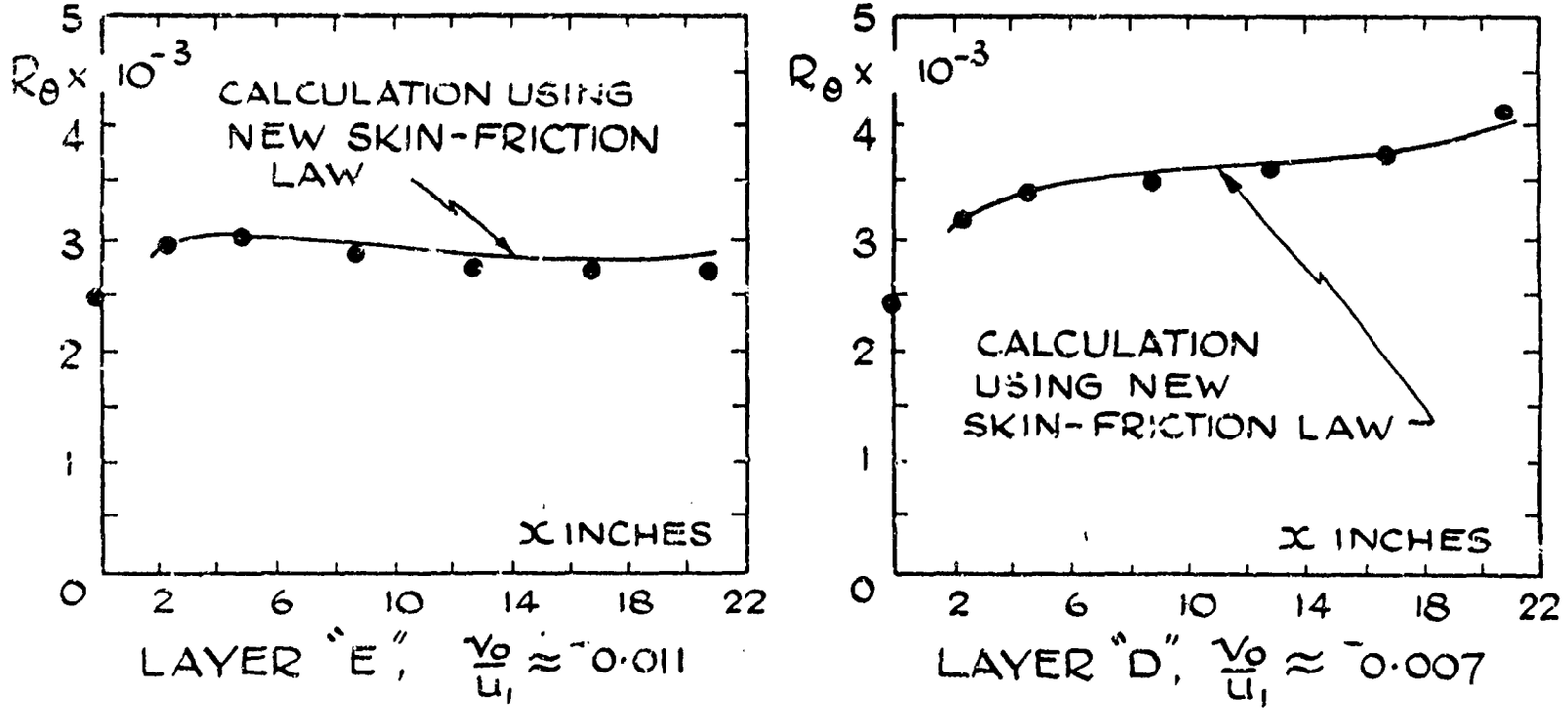

Fig. 23 Momentum growth in boundary layers with suction (experiment as in Fig. 21)

THE KINETIC-ENERGY-DEFICIT EQUATION OF THE TURBULENT BOUNDARY LAYER

by

D.B. Spalding

Mechanical Engineering Department,
Imperial College of Science and Technology,
London, S.W.7.

SUMMARY

It is shown that formal relations exist between the "entrainment function", appearing in the theory of Head (1960) and others, and the "dissipation integral" appearing in the theories of Rotta (1950), Truckenbrodt (1951) and others. Use of the relations, and of knowledge of free turbulent flows, permits improved expressions to be recommended for the dissipation integral, valid for near-flat-plate flows, for nearly-separating boundary layers, and for flows for which the velocity profiles exhibit maxima. The relations also indicate a non-arbitrary definition of the outer "edge" of the boundary layer for use with the entrainment function. Further research will be needed to verify and improve the recommendations which have been made and to extend them to situations of greater complexity; some suggestions are made concerning these extensions.

SOMMAIRE

L'auteur de cet exposé montre l'existence de relations formelles entre la "fonction d'entraînement", apparaissant dans la théorie de Head (1960) et dans d'autres théories, et "l'intégrale de dissipation", apparaissant dans les théories de Rotta (1950), de Truckenbrodt (1951) etc. En utilisant ces relations et les données que l'on possède sur les écoulements libres turbulents, on peut recommander, pour l'intégrale de dissipation, des expressions améliorées, valables pour des écoulements sur plaques presque planes, pour des couches limites proches du décollement, et pour des écoulements où les profils de vitesse présentent des maxima. Ces relations conduisent aussi à une définition non arbitraire du "bord" externe de la couche limite, à utiliser avec la "fonction d'entraînement". Un complément de recherches s'imposera pour confirmer et améliorer les recommandations qui ont été formulées, et pour étendre leur application à des situations d'une plus grande complexité; l'auteur exprime quelques suggestions concernant cette dernière possibilité.

CONTENTS

LIST OF FIGURES

Page

NOTATION

		Equations of First Mention
C	constant in entrainment law	(2.4-18)
H	displacement thickness divided by momentum thickness	(2.1-21)
H_1	another shape factor	(2.1-22)
$H_{1,0}$	value of H_1 at blow-off from the wall ($z_E = 0$)	(2.4-4)
H_3	kinetic-energy thickness divided by momentum thickness	(2.1-23)
$H_{3,0}$	value of H_3 at blow-off from the wall ($z_E = 0$)	(2.4-4)
I_0, I_1, I_2, I_3	various integrals involving the velocity and density profiles	(2.1-16 to 19)
l'	the logarithm of the boundary layer thickness divided by the length scale of the turbulence in the near-wall region	(3.1-1)
m	mass-transfer rate through the wall into the boundary layer, divided by $\rho_G u_G$	(2.1-14)
m_G	rate of transfer of mass from the mainstream into the boundary layer, divided by $\rho_G u_G$	(2.1-15)
R_G, R_m, R_2, R_3, R_x	various Reynolds numbers	(2.1-24 to 28)
s	non-dimensional shear stress	(2.1-13)
s_S	value of s at the wall ($\equiv c_f/2$ in conventional notation)	(2.1-30)
$\bar{s}$	average value of s on a velocity basis	(2.1-20)
u	velocity of fluid along the wall (ft/s)	(2.1-1)
v	velocity of fluid normal to and away from the wall (ft/s)	(2.1-1)
w	width of stream (ft)	(2.1-1)

		Equations of First Mention
x	distance along wall in mainstream direction (ft)	(2.1-1)
X	a property of the boundary layer which influences the value of $\bar{s}$	Section 4.21
y	distance from wall in direction towards the fluid	
y_G	value of y at the outer "edge" of the boundary layer (ft)	(2.1-3)
z	non-dimensional velocity u/u_G	(2.1-11)
μ	dynamic viscosity of fluid (lb/ft s)	(2.2-2)
ξ	dimensionless distance from the wall y/y_G	(2.1-12)
ρ	fluid density (lb/ft^3)	(2.1-1)
τ	shear stress in fluid times constant in Newton's Second Law of Motion ($lb/ft\ s^2$)	(2.1-2)

Subscripts

G	appertaining to conditions in the main stream
S	appertaining to conditions in the fluid close to the wall

THE KINETIC-ENERGY-DEFICIT EQUATION OF THE TURBULENT BOUNDARY LAYER

D.B. Spalding

1. INTRODUCTION

1.1 The problem considered

Since the 1920's, theories of the boundary layer based on the integral momentum-deficit equation (von Kármán, 1921) have been in common use. In the early 1950's* several authors (Rotta, 1950; Truckenbrodt, 1951; Tetervin and Lin, 1951; Rubert and Persh, 1951) proposed the use, in addition, of the integral kinetic-energy-deficit equation, more commonly† called "the energy equation". In the form advocated by Truckenbrodt, the method has become widely known, partly through the textbook of Schlichting (1960).

The status of the kinetic-energy equation is the same as that of the momentum equation: being derived rigorously from the partial differential equations of motion and continuity, the equation itself is a firm foundation for any theory of the boundary layer. If predictions based on it are in error, the cause must lie with auxiliary assumptions and not with the equation.

Nevertheless, methods based on the energy equation have not been especially successful for the turbulent boundary layer; Thompson's (1963, 1964) review of most available methods showed that only that of Head (1960) provided even tolerable predictions over the whole range of conditions tested. Head's method did not employ the kinetic-energy equation at all, but was based on the integral mass-conservation equation, conjoined with an "entrainment law". The present author has shown that this starting point permits the prediction of many features of the properties and behaviour of the turbulent boundary layer (Spalding, 1964).

All theories which employ the integral equations mentioned above, in place of the partial differential equations, necessarily involve assumptions about the shape of the velocity profile ($u \sim y$ relation). This requirement presents little difficulty in practice, because, for turbulent flow, the velocity profiles can be satisfactorily regarded as belonging to a single-parameter family. The analytical expressions contain

---

*The equation was derived earlier by Wieghardt (1945).

†Although the word "deficit" can be dropped without loss, it is unwise to delete the qualification "kinetic", lest the equation should be confused with the quite separate one, involving enthalpies, which is based on the First Law of Thermodynamics.

a certain degree of arbitrariness; but considerable changes in analytical form prove to cause but small changes in the resulting predictions. However, it must be admitted that the method based on the mass-conservation equation contains *more arbitrariness* than the others: for it alone necessitates the prescription of a definite outer limit to the boundary layer, which cannot be detected by measurements.

Two questions therefore arise:- (i) Why, nevertheless, have methods based on the kinetic-energy equation proved less successful than those based on the mass-conservation equation? And: (ii) is it possible to devise a new method which combines the advantages of both but lacks the disadvantages? It is these questions which will be discussed in the present paper. Provisional answers will be suggested, but final ones must await the execution of more research, some of which is suggested in the paper.

1.2 Outline of the present paper

Section 2 of this paper presents the mathematical basis of the argument. The derivation of the integral equations in Section 2.1 is conventional and can probably be skipped by most readers. Section 2.4 contains the most important theoretical results; these are Equation (2.4-3) which connects the shear-stress integral with the entrainment function, and Equation (2.4-4) which provides a non-arbitrary definition of the outer edge of the boundary layer.

Section 3 surveys the information, theoretical and experimental, which exists concerning the shear-stress integral. Although this information proves to be scanty, it suffices to demonstrate the inadequacies of earlier proposals for its form and to suggest a recommendation which has better prospects of success and a wider range of application. This recommendation is contained in Section 3.4.6.

Section 4 discusses the question of which of the two methods, after necessary amendment, will be the more convenient to use; the tentative conclusion is in favour of the method based on the kinetic-energy method. Thereafter some of the outstanding questions of turbulent-boundary-layer research are brought under review, and some suggestions are made for means of tackling them.

2. MATHEMATICAL DEVELOPMENT

2.1 The integral equations

The *partial differential equations* governing the steady two-dimensional converging or diverging flow of a fluid along a surface are as follows:.

Mass conservation:

$$\frac{\partial}{\partial x}(\rho w u) + \frac{\partial}{\partial y}(\rho w v) = 0 \qquad (2.1\text{-}1)$$

Momentum:

$$\rho u \frac{\partial u}{\partial x} + \rho v \frac{\partial u}{\partial y} = \rho_G u_G \frac{du_G}{dx} + \frac{\partial \tau}{\partial y} \qquad (2.1\text{-}2)$$

where: x is the distance in the mainstream direction along the surface
y is the distance from and normal to the surface
w is the width separating imaginary "stream-planes" which are normal to the surface*.

The *integral mass-conservation equation* is obtained from (2.1-1) by direct integration in the y direction from the wall to the (arbitrarily specified) outer limit of the boundary layer, a distance y_G from the wall, where $u = u_G$ and $\rho = \rho_G$. These results:

$$\frac{1}{w}\frac{d}{dx}\left\{w\int_0^{y_G}\rho u\,dy\right\} = \rho_S v_S - \rho_G v_G + \rho_G u_G\frac{dy_G}{dx}. \qquad (2.1\text{-}3)$$

Here subscripts S denotes conditions at the surface (wall) which may be porous (v_S not necessarily equal to zero). The final term on the right-hand side arises because y_G will ordinarily vary with x.

The *integral momentum-deficit equation* is obtained from (2.1-1) and (2.1-2) as follows. The rule for differentiation by parts permits (2.1-2) to be re-written thus:

$$\left\{\frac{\partial}{\partial x}(\rho u^2) - u\frac{\partial(\rho u)}{\partial x}\right\} + \left\{\frac{\partial}{\partial y}(\rho u v) - u\frac{\partial(\rho v)}{\partial y}\right\} = \rho_G u_G\frac{du_G}{dx} + \frac{\partial \tau}{\partial y}. \qquad (2.1\text{-}4)$$

But (2.1-1) implies (since w depends on x alone):

$$w\left\{\frac{\partial(\rho u)}{\partial x} + \frac{\partial(\rho v)}{\partial y}\right\} + \rho u\frac{dw}{dx} = 0. \qquad (2.1\text{-}5)$$

Combination of Equations (2.1-4) and (2.1-5), together with integration with respect to y yields:

$$\frac{1}{w}\frac{d}{dx}\left\{w\int_0^{y_G}\rho u^2 dy\right\} + \rho_G v_G u_G = \rho_G u_G\frac{du_G}{dx}y_G - \tau_S + \rho_G u_G^2\frac{dy_G}{dx} \qquad (2.1\text{-}6)$$

where we have put u equal to zero at the wall and τ equal to zero in the main stream.

Finally, Equation (2.1-3) is multiplied through by u_G and Equation (2.1-6) is subtracted from it with the result:

$$\boxed{\frac{1}{w}\frac{d}{dx}\left\{w\int_0^{y_G}\rho u(u_G - u)dy\right\} + \frac{du_G}{dx}\int_0^{y_G}(\rho_G u_G - \rho u)dy = \rho_S v_S u_G + \tau_S} \qquad (2.1\text{-}7)$$

---

*dw/dx thus measures the extent to which the flow diverges. w is independent of y. If the flow is constrained so that all streamlines are parallel to a single plane, w is a constant which can be eliminated from the equations.

The *integral kinetic-energy-deficit equation* is obtained by multiplying Equation (2.1-2) by u and then applying the rule for differentiation by parts. There results:

$$\left\{\frac{\partial}{\partial x}\left(\frac{\rho u^3}{2}\right) - \frac{u^2}{2}\frac{\partial(\rho u)}{\partial x}\right\} + \left\{\frac{\partial}{\partial y}\left(\rho v \frac{u^2}{2}\right) - \frac{u^2}{2}\frac{\partial(\rho v)}{\partial y}\right\} = u\rho_G u_G \frac{du_G}{dx} + \left\{\frac{\partial}{\partial y}(\tau u) - \tau\frac{\partial u}{\partial y}\right\} \tag{2.1-8}$$

Integration with respect to y now yields, in view of Equation (2.1-5) and the fact that u_S equals zero:

$$\frac{1}{w}\frac{d}{dx}\left\{w\int_0^{y_G}\rho\frac{u^3}{2}\,dy\right\} + \rho_G v_G\frac{u_G^2}{2} = \rho_G u_G\frac{du_G}{dx}\int_0^{y_G}u\,dy - \int_0^{y_G}\tau\frac{\partial u}{\partial y}\,dy + \rho_G\frac{u_G^3}{2}\frac{dy_G}{dx}. \tag{2.1-9}$$

Finally, this equation is subtracted from the equation formed by multiplying each term of (2.1-3) by $u_G^2/2$. There results:

$$\boxed{\frac{1}{w}\frac{d}{dx}\left\{w\int_0^{y_G}\rho u\left(\frac{u_G}{2} - \frac{u^2}{2}\right)dy\right\} - u_G\frac{du_G}{dx}\int_0^{y_G}(\rho_G - \rho)u\,dy = \rho_S v_S\frac{u_G^2}{2} + \int_0^{y_G}\tau\frac{\partial u}{\partial y}\,dy.} \tag{2.1-10}$$

We now express the equation in *dimensionless forms* in accordance with the practice of the author's earlier paper (Spalding, 1964). The following definitions are used:-

Variables:

$$z \equiv u/u_G \tag{2.1-11}$$

$$\xi \equiv y/y_G \tag{2.1-12}$$

$$s \equiv \tau/(\rho_G u_G^2) \tag{2.1-13}$$

$$m \equiv \rho_S v_S/(\rho_G u_G) \tag{2.1-14}$$

$$m_G \equiv \frac{\rho_G v_G - \rho_G u_G dy_G/dx}{\rho_G u_G} \tag{2.1-15}$$

Integrals:

$$I_0 \equiv \int_0^1 z\,d\xi \tag{2.1-16}$$

$$I_1 \equiv \int_0^1 (\rho/\rho_G)z\,d\xi \tag{2.1-17}$$

$$I_2 \equiv \int_0^1 (\rho/\rho_G)z^2\,d\xi \tag{2.1-18}$$

$$I_3 \equiv \int_0^1 (\rho/\rho_G) z^3 d\xi \qquad (2.1\text{-}19)$$

$$\bar{s} \equiv \int_0^1 s \frac{\partial z}{\partial \xi} d\xi \qquad (2.1\text{-}20)$$

Shape factors:

$$H \equiv (1 - I_1)/(I_1 - I_2) \qquad (2.1\text{-}21)$$

$$H_1 \equiv I_1/(I_1 - I_2) \qquad (2.1\text{-}22)$$

$$H_3 \equiv (I_1 - I_3)/(I_1 - I_2) \qquad (2.1\text{-}23)$$

Reynolds numbers:

$$R_G \equiv \rho_G u_G y_G/\mu_{ref} \qquad (2.1\text{-}24)$$

$$R_m \equiv I_1 R_G \qquad (2.1\text{-}25)$$

$$R_2 \equiv (I_1 - I_2) R_G \qquad (2.1\text{-}26)$$

$$R_3 \equiv (I_1 - I_3) R_G \qquad (2.1\text{-}27)$$

$$R_x \equiv (1/\mu_{ref}) \int_0^x \rho_G u_G dx \qquad (2.1\text{-}28)$$

Here μ_{ref} is a reference value of the fluid viscosity, for example, the viscosity in the stagnation state of the main stream.

Substitution of the above definitions in the three integral equations yields:

Mass:

$$\frac{dR_m}{dR_x} + R_m \frac{d(\log_e w)}{dR_x} = m - m_G \qquad (2.1\text{-}29)$$

Momentum:

$$\frac{dR_2}{dR_x} + R_2 \frac{d(\log_e w)}{dR_x} + (1 + H) R_2 \frac{d(\log_e u_G)}{dR_x} = m + s_S \qquad (2.1\text{-}30)$$

Kinetic-energy:

$$\frac{dR_3}{dR_x} + P_3 \frac{d(\log_e w)}{dR_x} + 2\left\{\frac{(I_0 - I_1)}{(I_1 - I_3)}\right\} R_3 \frac{d(\log_e u_G)}{dR_x} = m + 2\bar{s} \qquad (2.1\text{-}31)$$

Of course, other forms are possible. For example, we might eliminate all but one of R_m, R_2 and R_3; H could be expressed in terms of I_1 and I_2; and new equations could be derived by combination of the above three.

2.2 The "kinetic-energy method"

By the "kinetic-energy method" we here mean the method of predicting boundary layer behaviour which is based on the simultaneous solution of the integral kinetic-energy-deficit Equation (2.1-31) *and* of the integral momentum-deficit Equation (2.1-30). To bring out the special nature of the method, and to facilitate later comparison with the method based on the mass-conservation equation, we shall re-write the kinetic-energy

equation in terms of the shape factor H_3. From Equations (2.1-31) and (2.1-30) and the definition of H_3, we can derive:

$$R_2 \frac{dH_3}{dR_x} = 2\bar{s} - m(H_3 - 1) - H_3 s_S + \left\{H - 1 - \frac{(I_0 - I_1)}{(I_1 - I_2)}\right\} H_3 R_2 \frac{d(\log_e u_G)}{dR_x} \quad (2.2\text{-}1)$$

This equation, together with the momentum equation, permits the development of the boundary layer to be predicted, provided that it is possible to relate all the quantities appearing on the right-hand side to the two dependent variables of the differential equations, R_2 and H_3, and to the independent variable R_x. There are various ways in which these relations can be obtained; thus the assumption that the velocity profile belongs to a one-parameter family, together with a related assumption about the density, may link H, I_0, I_1 and I_2 to H_3; s_S may be connected with R_2 and H by way of the Ludwieg-Tillmann drag law (Ludwieg and Tillmann, 1949); and m and $d(\log_e u_G)/dR_x$ may be specified in terms of R_x. Only $\bar{s}$ requires special treatment, some examples of which will be discussed in Section 3; for the time being we shall merely suppose that $\bar{s}$ can also be expressed as a function of R_2, H_3 and of other locally determined properties.

Before proceeding further, it will be useful to discuss various implications of Equation (2.2-1), namely:-

(i) It is possible to contrive experimental conditions such that the shape of the velocity profile varies but slowly. Then the left-hand side of Equation (2.2-1) can be placed equal to zero, and the equation ceases to be a differential equation at all. Boundary layers of this kind have been studied by Clauser (1954), among others; they are often called "equilibrium boundary layers".

(ii) The quantity H_3, which appears in the coefficients of m and of s, is plotted in Figure 1 versus the more familiar shape factor H boundary layers possessing the velocity profile of the author's earlier paper (Spalding, 1964), i.e., one comprising a logarithmic "wall" component and a sinusoidal "wake" component (see Eqn. (3.3-1) overleaf). The parameter l', lies between 7 and 12 for common values of the Reynolds number. The curves are valid for the uniform-density boundary layers on which the majority of experiments have been carried out. For such boundary layers, the quantities I_0 and I_1 are equal; the coefficient of $R_2 d(\log_e u_G)/dR_x$ is therefore equal to $(H - 1)H_3$. This quantity is also plotted in Figure 1 for the family of velocity profiles just mentioned.

(iii) For an equilibrium boundary layer on an impermeable ($m = 0$) wall in the absence of pressure gradient, Equation (2.1-1) implies:

$$\bar{s} = (H_3/2)s_S . \quad (2.2\text{-}2)$$

Since for such boundary layers H is around 1.3 and so (Fig. 1) H_3 is around 1.8, $\bar{s}$ is slightly less than s_S; in other words the average shear stress in the boundary

layer is slightly less than the shear stress at the wall. This result is in accordance with experimental information, for example that of Klebanoff (1954) which is illustrated in Figure 2. It should be noted that it is the average of s with respect to *velocity* that is in question (see Eqn. (2.1-20)), not that with respect to distance.

(iv) A turbulent boundary layer may be "blown away" from a wall, in the absence of a pressure gradient, if the wall is porous and m is large enough. The experiments of Hacker (1958) suggest that m must lie between 0.02 and 0.04 for this to occur; this finding accords with the fact that the velocity of entrainment into a free turbulent mixing layer from a fluid at rest is about 0.03 times the velocity of the entraining fluid (Reichardt, 1942; Liepmann and Laufer, 1947). Since, under this condition, all terms in Equation (2.2-1) are zero except those containing $\bar{s}$ and m, and since also H_3 must be about 1.5 (for a sinusoidal velocity profile, we deduce that $\bar{s}$ must be about 0.0075 for the "blown away" boundary layer).

(v) A similar condition of incipient separation of the boundary layer from the wall can, in principle at least, be caused by an adverse pressure gradient on an impermeable wall. The corresponding value of the quantity $R_2 d(\log_e u_G)/dR_x$ is therefore (with $\bar{s} = 0.0075$, and with $H = 4$ and $H_3 = 1.5$ for the sinusoidal profile) about -0.0033. This is not necessarily the greatest adverse pressure gradient which the boundary layer can sustain, but is almost certainly is of the order of magnitude of that which will precipitate separation.

(vi) These considerations are, of course, not sufficient for the complete determination of the $\bar{s}$ function. However, we have seen two conditions which the function must satisfy (paragraphs (iii) and (iv)); and the experimental study of equilibrium boundary layers with adverse pressure gradients and/or blowing through the wall would clearly permit values of $\bar{s}$ to be deduced.

2.3 The "mass-conservation method"

We shall now present the method of Head (1960), as developed by the present writer, in a similar manner. The two equations which are used in this method are (2.1-29) and (2.1-30). Leaving the latter as it is, we shall re-write the former so as to make H_1 the dependent variable. From Equations (2.1-30), (2.1-29) and the definition of H_1, we derive:

$$R_2 \frac{dH_1}{dR_x} = -m_G - m(H_1 - 1) - H_1 s_S + (1 + H)H_1 R_2 \frac{d(\log_e u_G)}{dR_x} . \qquad (2.3\text{-}1)$$

This equation, which is the counterpart to Equation (2.2-1) of the kinetic-energy method, forms with the momentum equation an adequate foundation for the prediction of boundary layer development, provided that the quantities appearing on the right-hand side can be expressed in terms of R_2, H_1 and R_x. Here, once a reasonable family of velocity profiles has been selected, the sole uncertainty pertains to the quantity $-m_G$, the entrainment function; Head (1960) determined this empirically as a function of H_1; the present author (Spalding, 1964) expressed $-m_G$ in terms of a different property of the velocity profile, z_E, which will be discussed below (Sections 2.4, 3.1 and 3.3), and used knowledge of free turbulent flows for its determination.

Equation (2.3-1) is similar in form to Equation (2.2-1), thus:

(i) For equilibrium boundary layers ($dH_1/dR_x = 0$), the equation ceases to be a differential one.

(ii) The quantities H_1 and $(1 + H)H_1$, appearing in the equation, are plotted versus H in Figure 3, l' again being the parameter, and the velocity-profile assumption being that of the author's earlier paper (Eqn.3.3-1) below. The curves are valid for uniform-density flows.

(iii) For equilibrium boundary layers on an impermeable wall in the absence of a pressure gradient, Equation (2.3-1) implies:

$$- m_G = H_1 s_S . \qquad (2.3\text{-}2)$$

Evidently, since s_S is of the order of 0.001 for such flows while H_1 is of the order of 10, the dimensionless entrainment rate $- m_G$ will be about 0.01.

(iv) When the boundary layer is "blown away" by mass transfer through a porous wall, in the absence of pressure gradient, we have (since both s_S and $d(\log_e u_G)/dR_x$ are zero):

$$- m_G = (H_1 - 1)m . \qquad (2.3\text{-}3)$$

If the value of 0.03 is accepted as the corresponding mass-transfer rate, and H_1 is taken as 4 under this condition (see Fig.3), we deduce that $- m_G$ is equal to 0.09. This is probably the maximum rate of entrainment into a boundary layer which does not exhibit reverse flow or a velocity maximum. It should be noted, however, that both H_1 and $- m_G$ depend on the arbitrary choice of the outer limit of the boundary layer; in deriving the values of Figure 3, this limit was taken as the point where the tangent of the sinusoidal velocity profile is horizontal.

(v) If we consider incipient separation of an equilibrium boundary layer from an impermeable wall with a pressure gradient, and suppose $- m_G$ to have the value of 0.09, as just calculated, we deduce that $R_2 d(\log_e u_G)/dR_x$ must have the value of $- 0.0045$. This is of the same order as the value obtained by consideration of the kinetic-energy equation; the difference in value, which can be regarded as minor for present purposes, presumably results from the arbitrary choice of outer limit, referred to in the immediately preceding paragraph.

(vi) We have now learned that $- m_G$ is likely to vary between 0.01 for equilibrium boundary layers on a flat plate and about 0.09 for a separating boundary layer. Complete information about the entrainment function must be obtained, however, in other ways, for example from experiment.

2.4 Relation between the dissipation integral and the entrainment rate

The quantity $\bar{s}$ in the kinetic-energy method is similar in nature to the quantity $- m_G$ in the mass-conservation method: both must, at the present time, be determined empirically. However, if one of the quantities is known, the other can be deduced, as follows:

Equation (2.2-1) and (2.3-1) must be valid simultaneously. By division, therefore, we deduce:

$$2\bar{s} - m(H_3 - 1) - H_3 s_S + \left\{H - 1 - \frac{(I_0 - I_1)}{(I_1 - I_2)}\right\} H_3 R_2 \frac{d(\log_e u_G)}{dR_x}$$

$$= \frac{dH_3}{dH_1}\left[- m_G - m(H_1 - 1) - H_1 s_S + (1 + H) H_1 R_2 \frac{d(\log_e u_G)}{dR_x}\right] . \tag{2.4-1}$$

Here dH_3/dH_1 is a quantity which can be evaluated by reference to the prescribed family of velocity profiles.

Let us now *assume* that the quantities $\bar{s}$, $-m_G$ and s_S depend on only the velocity profile, the local mass-transfer rate through the wall m, and the Reynolds number R_2; i.e. we suppose that the pressure gradient has no *direct* influence on any of these quantities. It follows that the coefficient of $d(\log_e u_G)/dR_x$ in Equation (2.4-1) must be zero, i.e., that:

$$\left\{H - 1 - \frac{(I_0 - I_1)}{(I_1 - I_2)} H_3\right\} = \frac{dH_3}{dH_1} (1 + H) H_1 . \tag{2.4-2}$$

Let us now restrict consideration to the case of uniform density, so that I_0 and I_1 are equal. Then substitution of (2.4-2) into (2.4-1) yields*:

$$\frac{2}{(H - 1)H_3} \bar{s} - \frac{1}{H_1(H + 1)} (- m_G) + \left\{\frac{(H_1 - 1)}{(H + 1)H_1} - \frac{(H_3 - 1)}{(H - 1)H_3}\right\} m - \frac{2}{(H + 1)(H - 1)} s_S = 0 . \tag{2.4-3}$$

Equation (2.4-3) permits the dissipation integral $\bar{s}$ to be calculated if the velocity-profile family and the entrainment law are known; alternatively the entrainment rate can be calculated if $\bar{s}$ and the velocity profile are known.

It should be remarked that Equation (2.4-2) is a conditions which the velocity-profile family *must* satisfy if $\bar{s}$, m_G, etc., are to be independent of pressure gradient. This equation permits the removal of the arbitrariness concerning the definition of entrainment. Instead of defining H_1 by way of Equation (2.1-22), which contains the integral I_1 having an arbitrary upper limit, we can define H_1 via Equation (2.4-2), which may be re-written:

---

*Equation (2.4-3) may be derived in an alternative manner, viz. by considering equilibrium boundary layers for which the left-hand sides of Equations (2.2-1) and (2.3-1) vanish, and then eliminating the pressure-gradient term. The use of the equation as generally valid follows again from the assumption that all the quantities in the equation depend on the velocity profile, m and R_2 alone.

$$H_1 = H_{1,0}\exp\left\{\int_{H_{3,0}}^{H_3} \frac{(H+1)}{\left[H - 1 - \frac{(I_0 - I_1)}{(I_1 - I_2)}\right]} \frac{1}{H_3}\, dH_3\right\}. \qquad (2.4\text{-}4)$$

The following points should be noted about this result:

(a) The quantity $H_{1,0}$ is the value of H_1 for some arbitrary condition, for example that of incipient boundary layer separation, where H_3 equals $H_{3,0}$. For this case s_S equals zero. If we put s_S equal to zero in Equation (2.4-3) and then postulate that $\bar{s}$ and $(-m_G)$ have the same values, regardless of whether the separation is caused by blowing or by a pressure gradient, we deduce that the coefficient of m in this equation must be zero. Hence:

$$H_{1,0} = \frac{H_{3,0}(H_0 - 1)}{1 + H_0 - 2H_{3,0}} \qquad (2.4\text{-}5)$$

where H_0 is, of course, the value of H at separation.

(b) Although, if Equations (2.4-4) and (2.4-5) are used, the definition (2.1-22) must be abandoned, there is no objection to other uses of the quantity I_1. For example, the quantities $I_0 - I_1$ and $I_1 - I_2$, since their integrands vanish at the outer limit of the boundary layer, are not affected by the arbitrary specification of the position of this limit.

(c) If a one-parameter family of profiles is used, for example the power-law family, there is no doubt about the significance of the quadrature of Equation (2.4-4). If, however, as in the author's earlier work, a two-parameter family is used, one of them must be kept constant in the integration; this should be the one which varies the more slowly. If z_E and l' are the quantities in question (see Figs. 1 and 3, and Sections 3.1 and 3.3 below), l' should be regarded as a constant in the integration.

In order to make the above conclusions more concrete, a simple example will now be considered, namely that for which the fluid density is uniform and the velocity profile is the linear one shown in Figure 4 and represented by:

$$\left.\begin{aligned} \xi = 0: &\quad z = 0 \\ 0 \leqslant \xi \leqslant 1: &\quad z = z_E + (1 - z_E)\xi \\ \xi > 1: &\quad z = 1 \end{aligned}\right\}. \qquad (2.4\text{-}6)$$

It is easy to show that, for this case:

$$I_0 = I_1 = \tfrac{1}{2}(1 + z_E) \qquad (2.4\text{-}7)$$

$$I_2 = \tfrac{1}{3}(1 + z_E + z_E^2) \qquad (2.4\text{-}8)$$

$$I_3 = \tfrac{1}{4}(1 + z_E + z_E^2 + z_E^3) \qquad (2.4\text{-}9)$$

and so: $$H = 3/(1 + 2z_E) \qquad (2.4\text{-}10)$$

$$H_3 = 1.5(1 + z_E)^2/(1 + 2z_E) \; . \qquad (2.4\text{-}11)$$

These equations have been derived from Equations (2.1-16, 17, 18, 19, 21) and (2.1-23). No use has, however, so far been made of Equation (2.1-22).

At the point of incipient separation, characterised by $z_E = 0$, we easily deduce that H equals 3 and H_3 equals 1.5. Equation (2.4-5) then yields the value 3 for $H_{1,0}$. Substitution in Equation (2.4-4) leads, after straightforward algebra, to:

$$H_1 = \frac{3(1 + z_E)}{(1 - z_E)(1 + 2z_E)} \; . \qquad (2.4\text{-}12)$$

By coincidence, this expression is the same as would have been obtained by the use of the equation which we have abandoned, namely (2.1-22). However, this would not generally be the case; it is not so, for example, for the profile: $z = z_E + 0.5(1 - z_E)(1 - \cos\pi\xi)$. Nor is it true for the profiles according to Equation (3.3-1) below, the corresponding shape factors of which have been plotted in Figures 1 and 2, and which is used extensively later in this paper.

Figure 5 displays the values of H, H_3 and H_1 graphically for the linear profile.

Let us now return to the consideration of the relation between $\bar{s}$ and $-m_G$, inserting into Equation (2.4-3) the expression valid for the linear velocity profile. We obtain:

$$\boxed{\bar{s} = \frac{(1 + z_E)(1 - z_E)^2}{4(2 + z_E)}(-m_G) + z_E \frac{(3 + 8z_E + 5z_E^2 + 2z_E^3)}{4(1 + 2z_E)(2 + z_E)} m + \frac{3(1 + z_E)^2}{4(2 + z_E)} s_S \; .}$$

(2.4-13)

The coefficients of $-m_G$, m and s_S, appearing in this equation, are plotted versus z_E in Figure 6. Since the quantity z_E is less familiar and more "artificial" than the quantity H, we also plot the contents of Figures 5 and 6 versus H in Figures 7 and 8.

A few remarks about Equation (2.4-13) may be helpful at the present stage. These are:

(a) When z_E tends to unity the entrainment term vanishes; there results:

$$z_E \to 1 : \quad \bar{s} \to m/2 + s_S \; . \qquad (2.4\text{-}14)$$

This result is easily understood if we recollect that, if the Couette-flow assumptions were made, the local dimensionless shear stress in the boundary layer, s, would be given by

$$s = s_S + mz \,. \qquad (2.4\text{-}15)$$

Figure 9 illustrates this. The z-based average of s is clearly $m/2 + s_S$.

(b) When z_E tends to zero, the mass-transfer term vanishes. Under these conditions (incipient separation) s_S is also zero. Hence:

$$z_E \to 0 : \quad \bar{s} \to -m_G/8 \,. \qquad (2.4\text{-}16)$$

There is, therefore, a close numerical connection between the two empirical functions which appear respectively in the kinetic-energy and the mass-conservation equations.

(c) An approximate form of Equation (2.4-13), which fits the extreme values just mentioned and does not give large errors even for intermediate values of z_E is:

$$0 \leqslant z_E \leqslant 1 : \quad \bar{s} \simeq -m_G(1 - z_E)^2/8 + z_E m/2 + s_S \,. \qquad (2.4\text{-}17)$$

(d) Experience with many free turbulent flows, together with the more detailed studies of the author's earlier paper (Spalding, 1964), suggest that the entrainment law has some such form as, for $z_E < 1$:

$$-m_G \simeq C(1 - z_E) \qquad (2.4\text{-}18)$$

where C is a constant equal to, say, 0.08. If this is the case, an approximate equation for the dissipation integral $\bar{s}$ would be:

$$0 \leqslant z_E \leqslant 1 : \quad \bar{s} \simeq 0.01(1 - z_E)^3 + z_E m/2 + s_S \,. \qquad (2.4\text{-}19)$$

The first term on the right-hand side can be interpreted as being associated with the free-turbulence portion of the velocity profile, i.e., the so-called "wake" component; the second and third terms can be regarded as arising by reason of processes occurring very close to the wall.

(e) Of course, z_E may exceed unity, as in the case of the "wall-jet", and in flows associated with film-cooling devices and blown flaps. Let us consider the extreme case in which z_E tends to infinity, i.e. that in which the main stream has a very much lower velocity than the fluid in the boundary layer. Equation (2.4-13) now yields:

$$z_E \to \infty : \quad \bar{s}/z_E^3 \to (-m_G/z_E)/4 + (m/z_E)/4 + 3(s_S/z_E^2) \,. \qquad (2.4\text{-}20)$$

Experimental data on entrainment into such boundary layers suggest (Spalding, 1964) that $(-m_G/z_E)$ is approximately equal to 0.03; s_S/z_E^2 under such conditions is around 0.001, when m is zero and less when m is positive. We might therefore expect $\bar{s}/z_E^3$ to have the value of about 0.0075.

2.5 Closure

In the present section it has been shown that there are close connections between the dissipation integral of the kinetic-energy method and the entrainment function of the mass-conservation method. We have also seen how to eliminate the arbitrariness which has beset the latter method in respect of the outer limit of the boundary layer.

The last two equations in the section, developed by consideration of a linear velocity profile (Fig. 4) and simple forms of entrainment law, have already provided suggestions for the way in which the dissipation integral should depend on the wall shear stress, the mass-transfer rate through the wall, and the magnitude of the "wake" component of the velocity profile. The importance of the $\bar{s}$ - function is such as to demand a more comprehensive treatment. This is provided in Section 3, at the end of which we return to the derivation of the $\bar{s}$ - function from entrainment data.

3. SURVEY OF INFORMATION ABOUT THE DISSIPATION INTEGRAL

3.1 Earlier theoretical proposals for boundary layers

(a) Rotta (1950, 1952, 1961) was among the first to suggest how $\bar{s}$ might be related to the velocity profile. He supposed the velocity profile, in the absence of mass transfer, to have the form:

$$z = z_E\{(1 + 1/l')\xi\} + (1 - z_E)\xi^{l'+1} . \qquad (3.1\text{-}1)$$

This profile is a more general version of that of Equation (2.4-6) and Figure 4, to which it reduces for l' equal to infinity. l' is equal to $0.4z_E s_S^{-\frac{1}{2}}$ and, for a smooth wall, to $\log_e(7.7y_0 u_0 s_S^{\frac{1}{2}}/\nu)$. The proposal was made for flows of uniform density.

Rotta's expression for $\bar{s}$ was:

$$\bar{s} = s_S\{1 + 0.30(1 - z_E)\} - 5.55s_S^{\frac{3}{2}} + 0.0736s_S^{\frac{1}{2}}(1 - z_E)^2 . \qquad (3.1\text{-}2)$$

The wall shear-stress factor s_S, it is implied above, is equal to $0.16z_E^2/(l')^2$, and l' can be related to the momentum-thickness Reynolds number R_2 by:

$$l' = \log_e\left[\frac{3.08\,R_2\,z_E/l'}{\frac{1}{6} + z_E\left(\frac{1}{6} - \frac{1}{2l'}\right) + z_E^2\left\{\frac{1}{3} - \frac{3}{2l'} + \frac{2}{(l')^2}\right\}}\right] . \qquad (3.1\text{-}3)$$

Here the denominator in the square bracket is the expression for $I_1 - I_2$ which corresponds to Equation (3.1-1).

We shall discuss the correctness of Rotta's proposal for $\bar{s}$ later. Here it is merely appropriate to note its implications that:-

(i) At $z_E = 1$, $\bar{s}$ is equal to $s_S(1 - 5.55s_S^{\frac{1}{2}})$, i.e. slightly less than s_S. This is in qualitative accordance with experimental information (Fig. 2).

(ii) At $z_E = 0$, since the wall shear-stress s_S equals zero under this condition, $\bar{s}$ is equal to zero.

(iii) As may be determined by differentiation, $\bar{s}$ does not vary rapidly with z_E when z_E is in the neighbourhood of unity and l' lies in its usual range (7 to 12).

(b) Truckenbrodt (1951) examined the implications of Rotta's proposal and decided that the variations of $\bar{s}$ with shape factor were small enough to be ignored. He therefore recommended the use of the following relation:

$$\bar{s} = 0.0056 R_2^{-1/6} . \qquad (3.1\text{-}4)$$

For the evaluation of s_S, the wall shear stress, Truckenbrodt advocated the use of the Ludwieg-Tillmann relation, namely:

$$s_S = 0.123 \times 10^{-0.678H} R_2^{-0.268} . \qquad (3.1\text{-}5)$$

It may be verified that these recommendations lead to the approximate equality of $\bar{s}$ and s_S under conditions appropriate to an equilibrium boundary layer on an impermeable flat plate. Under adverse-pressure-gradient conditions (large H), s_S goes to zero while $\bar{s}$ is unaffected.

Most experimental data are valid for R_2 between 10^3 and 10^4. Equation (3.1-4) therefore implies that $\bar{s}$ lies between 0.00177 and 0.001209. If we take the values of H_3 and H for the uniform-density separating boundary layer with a sinusoidal velocity profile (Fig.1), namely 1.5 and 4, the argument of sub-section 2.2 can be employed to show that Truckenbrodt's $\bar{s}$ recommendation implies that separation would occur for values of $R_2 d(\log_e u_G)/dR_x$ between - 0.000786 and - 0.000537, for an equilibrium boundary layer on an impermeable wall; these values are appreciably lower than (about one eighth of) those which prevail in practice. "Blow-off" as a result of mass transfer in the absence of pressure gradient would occur, it may be similarly argued, at values of m between 0.00709 and 0.00483; these values are appreciably lower than those in the already-mentioned experiments of Hacker (1953).

(c) Rubert and Persh (1951) deduced an expression for $\bar{s}$ by evaluating all the other terms in Equation (2.2-1) from various experimental measurements. In principle, of course, this method is a very reliable one; in practice, however, the credibility of the results is influenced by limitations on the accuracy and range of the experiments, by assumptions made about velocity profiles, and by other factors.

Rubert and Persh expressed their recommendations in the form of a graph, reproduced here as Figure 10; since they also recommended the Ludwieg-Tillmann formula (Eqn.3.1-5) for the wall shear stress, the ordinate of the graph can be recognised to be:

$$0.123(\bar{s}/s_S)\left[(3H - 1)^2/\{H(3H - 0.9) - 0.1\}\right] .$$

The function of H appearing in the square brackets does not vary greatly within the practical range; it may be seen from Figure 10, therefore, that, according to Rubert and Persh, the main factor causing $\bar{s}$ to differ from s_S is the pressure gradient $R_2 d(\log_e u_G)/dR_x$. It is a consequence of the recommendation that the dissipation integral is zero whenever the shear stress at the wall is zero.

Since the pressure gradient is held to influence the value of the dissipation integral, Rubert and Persh clearly do not regard the shape of the velocity distribution as being fixed when the velocity distribution is fixed. They would therefore presumably dissent from the hypothesis which led to Equation (2.1-4).

A proposal of Tani (1956) has similar implications to these of Rubert and Persh; it will therefore not be discussed separately.

(d) *Other related recommendations.* Although Hudimoto (1951) did not explicitly calculate the dissipation integral, the shear-stress distribution which he recommended is worthy of citation here. This was:

$$s = \{z_E f_1(\xi) + (1 - z_E) f_2(\xi)\}^2 \qquad (3.1\text{-}6)$$

where f_1 and f_2 are functions of the dimensionless wall distance $\xi (= y/y_G)$, and z_E represents, as in Equations (2.4-6) and (3.1-1) the relative magnitudes of wall-law and wake-law components of the velocity profile. Obviously, when $z_E = 1$ (roughly speaking, the flat-plate case), s is equal to f_1^2; when $z_E = 0$ (the separating boundary layer), s is equal to f_2^2.

The latter case ($z_E = 0$) deserves particular study. Hudimoto's proposals reduce to:

$$s = 0.0734 \xi (1 - \xi)^2 \qquad (3.1\text{-}7)$$

and

$$z = \xi^{3/2}(2.5 - 1.5\xi) . \qquad (3.1\text{-}8)$$

From these two results it is easy to calculate that $\bar{s}$ must be equal to 0.00715. This, of course, is appreciably greater than Truckenbrodt's values for this condition (between 0.00177 and 0.001209), greater still than Rotta's and Rubert and Persh's values (which were zero), and of the order of magnitude deduced in sub-sections 2.2 and 2.4 for the separating boundary layer.

3.2 Some other theoretically based expressions for $\bar{s}$

(a) *Expressions derived from the theory of free turbulent flows.* Rotta (1950), Ross and Robertson (1951), Hudimoto (1951), Coles (1956) and Spalding (1964) have all implicitly or explicitly postulated that the outer part of a boundary layer obeys similar laws to those governing free-turbulent flows: the plane mixing layer, the two-dimensional wake, or the two-dimensional jet. Let us therefore summarise the information which exists concerning the dissipation integral for such flows.

Tollmien (1926) made use of the Prandtl mixing-length hypothesis, and the assumption that the mixing-length was constant across the width of the layer, to calculate velocity and shear-stress distributions in the free turbulent mixing layer formed at the edge of a stream which enters a reservoir of fluid at rest. The variation of s versus z obtained by Tollmien is plotted in Figure 11 (curve 1); here an experimentally-based constant has been incorporated ($a = 0.09$, in the notation of Abramovich (1963), who summarises available information); and the quantity z is interpreted as the ratio of the local velocity u to the free-stream velocity u_G, as for boundary layers. The corresponding value of $\bar{s}$ is 0.008. The flow pattern is akin to that of a separating boundary layer.

Tollmien made a similar analysis of the two-dimensional jet emerging into a stagnant fluid. His resulting $s \sim z$ relation, (with the empirical constant $a \sim 0.11$, quoted

by Abramovich (1963), is shown as curve 2 in Figure 11. In the definitions of s and z, the local velocity on the jet axis is substituted for u_G. The corresponding value of $\bar{s}$ is 0.0145. Thus the shear stresses are nearly twice as great as these appearing in the free mixing layer, when both are normalised with respect to the greatest dynamic pressure which is present at the section.

Schlichting (1930) used the Prandtl mixing-length theory in a similar manner to predict the velocity distribution in the wake, far downstream of a rod held transversely to a stream of otherwise uniform velocity. Incorporation into this theory of a necessary constant deduced from Schlichting's experimental data, and interpretation of u_G as the maximum *velocity difference* which is present in the stream, yields the curve shown as curve 3 in Figure 11; the corresponding value of $\bar{s}$ is 0.044. This is three times as great as the value appropriate to the two-dimensional jet, and five times as great as the value appropriate to the plane mixing layer. The reason for the differences is not known; it may be connected with the fact that, in contrast to the two previous cases, the velocity differences which are responsible for the shear stress are differences imposed on a general stream velocity of much greater magnitude.

(b) *The constant-eddy-viscosity hypothesis*. Clauser (1954), has deduced, from measurements made on turbulent boundary layers, that the eddy viscosity (≡ shear stress divided by product of density and velocity gradient) can be taken as equal, in the outer regions of the layer, to a constant times the product of fluid density, mainstream velocity and displacement thickness. Clauser reported a constant of 0.018, but a later examination of the experimental data by Mellor and Gibson (1965) led to 0.016. Let us accept the latter; then:

$$s = 0.016 \frac{\partial z}{\partial \xi} (1 - I_1) \qquad (3.2\text{-}1)$$

Let us now suppose, for the sake of simplicity, that the velocity profile is given by Equation (2.4-6) and Figure 4; the average dimensionless shear stress in the infinitely thin region adjacent to the wall will be taken as $(s_S + mz_E/2)$; in the remainder of the region s will be given by Equation (3.2-1). Figure 12 illustrates the corresponding $s \sim z$ relation.

Now I_1 is given by Equation (2.4-7). It is easy therefore to deduce that:

$$\bar{s} = (s_S + mz_E/2)z_E + 0.008(1 - z_E)^3 . \qquad (3.2\text{-}2)$$

Obviously, according to this equation, $\bar{s}$ and s_S are equal when z_E equals unity, i.e. when the "wake component" of the boundary layer is absent; when z_E equals zero, on the other hand, as for a separating boundary layer, $\bar{s}$ is equal to 0.008.

Equation (3.2-2) is quite remarkably similar to Equation (2.4-19), which was derived, it may be remembered, from the assumption of a particular entrainment law.

In the special case in which z_E equals zero, Equation (3.2-1) yields: $s = \bar{s} = 0.008$. This is the case of the free turbulent mixing layer already referred to; the corresponding (horizontal) $s \sim z$ line has been added to Figure 11, as curve 4. It is interesting to note that the area beneath it is precisely the same as that beneath curve 1, which is Tollmien's version of the shear-stress distribution in a free mixing layer.

3.3 Experimental data for $\bar{s}$

(a) *The investigation of Schubauer and Klebanoff (1951).* The most comprehensive of the few experimental studies of the shear-stress distribution in turbulent boundary layers is that of Schubauer and Klebanoff (1951) who made their measurements on a single flow past a smooth convex wall. The authors reported velocity distributions at various stations along the wall, and also distributions of shear-stress measured by means of hot wires.

The experimental data can be replotted so as to yield plots of s versus z for various stations. A few such plots are shown in Figure 13; the re-plotting procedure has eliminated the rather considerable scatter which characterises the original data. The curves may be compared with that of Figure 2, which was valid for a uniform-pressure boundary layer; in contrast to these, those of Figure 13 exhibit "humps" which may be regarded as rounded-off versions of the distribution shown in Figure 12.

If it is assumed that the velocity profiles can be described by particular algebraic expressions, the constants in these expressions which are appropriate to each profile can be deduced from the measured values of, say, the shape factor H and the momentum-thickness Reynolds number R_2. The Schubauer/Klebanoff profiles have been processed in this way, that value of z_E being obtained for each profile which accords with the assumption of the author's earlier paper (Spadling, 1964), namely that:

$$z = z_E\{1 + (\log_e \xi)/l'\} + \tfrac{1}{2}(1 - z_E)(1 - \cos\pi\xi) \qquad (3.3\text{-}1)$$

where, since the wall is smooth,

$$l' = \log_e \left\{ \frac{7.7 R_2 s_S^{\frac{1}{2}}}{(I_1 - I_2)} \right\} \qquad (3.3\text{-}2)$$

The values of $\bar{s}$ appropriate to each station have been determined by measurement of the areas beneath curves such as these of Figure 13. The resulting values have been smoothed and then plotted, together with the values of the wall shear stress s_S, versus z_E in Figure 14. It is evident that, as z_E decreases (as occurs with increasing x when the pressure gradient is unfavourable), $\bar{s}$ increases while s_S decreases. At high z_E, it appears likely that s_S will exceed $\bar{s}$, as was found to be true for Figure 2, the points for which are added to Figure 14 for comparison. The values of momentum-thickness Reynolds number corresponding to a few of the points are indicated on the graph; the value of l' was close to 10 throughout.

In order to provide a means of comparison with the $\bar{s}$ functions which have been mooted above, a broken curve is provided which corresponds to Equation (3.2-2), based, it will be recalled on the constant-eddy-viscosity hypothesis, with empirical additions; the experimental values of s_S are employed, and m is naturally put equal to zero. It will be seen that Equation (3.2-2) predicts values of $\bar{s}$ which are of the right order of magnitude; however, the experimental values of $\bar{s}$ exceed those predicted by Equation (3.2-2) over most of the range.

Also shown on Figure 14, as horizontal chain-dotted lines, are the values of $\bar{s}$ which correspond to the recommendation of Truckenbrodt (1951), expressed by

Equation (3.1-4); momentum-thickness Reynolds numbers are 2×10^4 (upper line) and 7.5×10^4 (lower line), which are about the extreme values of the Schubauer/Klebanoff data. It is quite clear that Equation (3.1-4) agrees with the experimental data only where z_E has a high value; at moderate and low values of z_E, such as tend to occur when the pressure gradient is adverse, Equation (3.1-4) greatly under-estimates the value of the dissipation integral.

(b) *The investigation of Sandborn and Slogar (1955).* These authors made measurements of the velocity and shear-stress profiles on one smooth impermeable wall of a two-dimensional diffuser. Their data have been treated in the same way as these of Schubauer and Klebanoff. Figure 15 displays the $s \sim z$ distributions for the four stations which were investigated; and Figure 16 displays the $\bar{s} \sim z_E$ and $s_S - z_E$ curves.

The conclusions to be drawn from Figures 15 and 16 are similar to those drawn from Figures 13 and 14; the quantitative differences can in part be attributed to the lower Reynolds numbers; l' lay between 8 and 9. The $s \sim z$ curves exhibit "humps" for the smaller values of z_E. The prediction of Equation (3.2-2) gives fairly good agreement with the data, but tends to underestimate $\bar{s}$ for z_E less than 0.8. The Truckenbrodt prediction also gives fairly good agreement in the region of the experiments; there are no data in the low $- z_E$ region where discrepancies might be expected.

The Sandborn - Slogar data in Figure 16 also illustrate the difficulty of estimating the form of the $\bar{s}(z_E, R_2)$ function from experimental data covering only a limited range, and in the absence of theoretical guidance. By themselves, these data would give no hint that $\bar{s}$ will rise to high values as z_E tends to zero; they might be regarded as demonstrating the validity of Equation (3.1-4). However, the existence of the Schubauer/Klebanoff data, together with the theoretically based Equation (3.2-2), make it reasonable to suppose that, had Sandborn and Slogar continued their experiments to lower values of z_E, $\bar{s}$ would have begun to rise.

(c) *Shape factors and velocity profiles for the equilibrium boundary layer on a flat plate.* Further information concerning the dissipation integral may be obtained from knowledge of the velocity profiles which prevail on smooth and rough impermeable plates in the absence of pressure gradient. As shown in the author's earlier paper, he data collected by Schultz-Grunow (1940) and Hama (1947) imply that, for such boundary layers:

$$1 - z_E = 2.342 s_S^{\frac{1}{2}} . \qquad (3.3\text{-}3)$$

This result is valid when the velocity profile is supposed to obey Equation (3.3-1).

Now l' is defined, in general, by:

$$l' = 0.4 z_E (s_S + m z_E)^{-\frac{1}{2}} . \qquad (3.3\text{-}4)$$

Since m is equal to zero for an impermeable wall, we may deduce from Equations (3.3-3) and (3.3-4) that, for an equilibrium impermeable-flat-plate boundary layer:

$$l' = 0.94 z_E / (1 - z_E) . \qquad (3.3\text{-}5)$$

Now it is a matter of mere algebra to show that the velocity profile of Equation (3.3-1), together with the assumption that the density is uniform and with the definitions of I_1, I_2, and II_3, imples that:

$$I_1 = 0.5 + z_E(0.5 - 1/l') \tag{3.3-6}$$

$$I_2 = 0.375 + z_E(0.25 - 0.411/l') + z_E^2\{0.375 - 1.589/l' + 2/(l')^2\} \tag{3.3-7}$$

and

$$I_3 = 0.3125 + z_E(0.1875 - 0.1567/l') + z_E^2\{0.1875 - 2.0804/l' + 4.116/(l')^2\} + z_E^3\{0.3125 - 1.3433/l' + 1.8843/(l')^2 - 6/(l')^3\} . \tag{3.3-8}$$

Substitution of Equation (3.3-5) into these relations, and neglect of terms embodying higher powers of $(1 - z_E)$ yields, by way of Equation (2.1-23):

$$z_E \simeq 1 : \quad H_3 \simeq 2 - 2.9(1 - z_E) . \tag{3.3-9}$$

Now Equation (2.2-2) is valid for an equilibrium boundary layer on an impermeable wall; combination with Equation (3.3-9) yields:

$$z_E \simeq 1 : \quad \bar{s}/s_S \simeq 1 - 1.45(1 - z_E) . \tag{3.3-10}$$

Finally, with the aid of Equation (3.3-3), we deduce:

$$\bar{s} = 0.182(1 - z_E)^2 - 0.264(1 - z_E)^3 . \tag{3.3-11}$$

Figure 17 displays a plot of $\bar{s}$ according to Equation (3.3-11), together with one of s_S according to Equation (3.3-3). Also shown are the previously cited experimental data of Klebanoff (1954) and of Sandborn and Slogar (1955). The former points lie very close to their respective curves; this is a confirmation of the validity of the analysis and of the accuracy of the experimental data. Only the upstream data points of the Sandborn/Slogar data coincide with the equilibrium curves; this accords with our expectations, since only at the entrance to the diffuser, which was preceded by a uniform-pressure region, are the assumptions underlying Equation (3.3-11) likely to be valid.

Values of l' are marked along the horizontal axis of Figure 17. If the wall is smooth, these may be related to the momentum-thickness Reynolds number R_2 by means of Equation (3.3-2); this may be re-written, when Equation (3.3-3) is obeyed, as:

$$z_E \simeq 1 : \quad R_2 = 0.477 \frac{(l' - 2.585)}{(l' + 0.94)} e^{l'} . \tag{3.3-12}$$

(d) *Measurements of shear stresses in wall jets.* The families of velocity profiles represented by Equations (2.4-6), (3.1-1) and (3.3-1) are flexible enough to describe the flows which are found downstream of slots through which fluid is injected into the

boundary layer along the surface, or which result when a jet of fluid impinges on and is deflected by the surface. If there exists a finite main-stream velocity, smaller in magnitude than that of the fluid emerging from the jet, the appropriate value of z_E is usually greater than unity. If the bulk of the fluid is at rest, z_E takes an infinite value.

As will be recognised from the foregoing survey, none of the previous users of the kinetic-energy method has been concerned with such flows. However, as was argued in the author's earlier paper (Spalding, 1964) there is some advantage in having a *unified* theory which will apply to flows having velocity maxima, such as those mentioned above, as well as to the flows more conventionally dealt with. It is therefore desirable to collect the information which is available on the behaviour of the dissipation integral $\bar{s}$ when z_E exceeds unity.

Three sets of experimental data are available, all for the case in which the main "stream" is at rest ($z_E \rightarrow \infty$). Mathieu (1961) measured the shear stress by means of a hot-wire instrument in the flow downstream of the point of impingement of an inclined two-dimensional jet on a plane smooth wall. Bradshaw and Gee (1962) used a similar technique for the flow caused by injection of air through a slot placed flush with a plane wall. Schwartz and Cosart (1961) employed a similar flow, but deduced the shear-stress distribution by application of the integral momentum equation to various parts of the flow. Each of these authors of course also measured the velocity profile.

Figure 18 contains *sketches* of velocity and shear-stress profiles representative of the findings of all three investigations. The shape of the velocity profile requires little comment. The shear-stress profile exhibits the interesting feature, not encountered in more conventional boundary-layer flows, of a change of sign; this occurs near to, but not usually precisely at, the location of the velocity maximum.

Figure 19 shows curves, deduced from the measurements reported in the papers of Mathieu (1961), Bradshaw and Gee (1962) and Schwartz and Cosart (1961), of $\tau/\rho u_{max}^2$ versus u/u_{max}, u_{max} being defined as the greatest velocity which is present at the section of measurement. All three curves are qualitatively similar to each other; they differ from those encountered earlier (e.g. in Figs. 12 and 15) in exhibiting two values of shear-stress for every velocity, a feature that is easily explained by reference to Figure 18.

Now the dissipation integral appearing in the integral kinetic-energy-dificit Equation (2.1-10) is $\int_0^{y_G} \tau(\partial u/\partial y)dy$. This quantity is proportional no longer to the area *beneath* the curve representing a plot of τ versus u(s versus z in the dimensionless form used above) but to the area *enclosed* by this curve. The areas are, for the three curves of Figure 19; $0.0128\rho u_{max}^3$ for Mathieu, $0.0155\rho u_{max}^3$ for Bradshaw and Gee, and $0.0134\rho u_{max}^3$ for Schwartz and Cosart. We may continue to use the dimensionless dissipation integral $\bar{s}$ if we presume, as is surely permissible, that the mainstream velocity u_G is finite and thus capable of use for normalisation, but sufficiently small not to modify the flow. Then we deduce that:

$$\bar{s}\left(\frac{u_G}{u_{max}}\right)^3 = 0.0128,\ 0.0155 \quad \text{or} \quad 0.0134 \qquad (3.3\text{-}13)$$

according to which investigation is considered.

It remains to relate z_E to u_G/u_{max}. This may be done by suitable manipulation of Equation (3.3-1), which has been shown (Spalding, 1964) to describe the velocity profiles of wall jets fairly well; for the Reynolds-number range in which the above-mentioned experiments lie, it will be sufficiently accurate simply to extract the result:

$$l' = 9.94 : \quad \frac{u_{max}}{u_G} z_E = 0.7544 . \tag{3.3-14}$$

The result of our study of the three experimental investigations is thus:

$$\left.\begin{aligned} \bar{s}/z_E^3 &= 0.00563 \text{ for Mathieu} \\ &\quad 0.00682 \text{ for Bradshaw and Gee} \\ &\quad 0.0059 \text{ for Schwartz and Cosart} \end{aligned}\right\} . \tag{3.3-15}$$

3.4 A preliminary recommendation about the dissipation integral

3.4.1 A resumé of information about the $\bar{s}$-function

Let us now review the main facts which have been established concerning the $\bar{s}$-function. These are:

(i) If it is supposed, as was done explicitly in Section 2.4 and implicitly since then, that the shear-stress distribution depends only on the velocity distribution, and if further it is assumed that the velocity distribution is described by some such expression as Rotta's (Eqn. (3.1-1)), or Spalding's (Eqn. (3.3-1)), we might suppose that $\bar{s}$ is a function of two arguments, namely z_E and l'. Further thought, however, reveals that the dimensionless mass-transfer rate m may appear as an additional parameter; for, though the description of the velocity profile in terms of z_E and l may be sufficiently accurate for the evaluation of integrals such as I_1, I_2, etc., the presence of mass transfer is likely to influence the relation between shear-stress and velocity in the thin region close to the wall. Figures 9 and 12 may be held to make this suggestion plausible, but the author's earlier paper (Spalding, 1964) should be consulted for more rigorous justification. We therefore conclude that our task is to establish a three-argument function;

$$\bar{s} = \bar{s}(z_E, l', m) . \tag{3.4-1}$$

(ii) When z_E equals zero, as is the case for a boundary layer separating under the influence of pressure gradient or blowing, we expect that $\bar{s}$ will have the value which obtains in a free turbulent mixing layer, namely 0.008 approximately. The grounds of this expectation lie in Section 3.2(a) and 3.2(b).

(iii) For an impermeable (m = 0) flat plate having an equilibrium boundary layer, for which l' obeys Equation (3.3-5), $\bar{s}$ is given by Equation (3.3-11). The experiments on which this equation is based are valid for z_E - values between say 0.85 and 0.95.

(iv) For a wall-jet ($z_E \to \infty$) on an impermeable wall, with l' in the neighbourhood of 10, $\bar{s}$ is approximately equal to $0.006z_E^3$, as shown by Equation (3.3-15) which sums up the measurements of Mathieu, of Bradshaw and Gee, and of Schwarz and Cosart.

(v) The data of Klebanoff (1954), Schubauer and Klebanoff (1951), and Sandborn and Slogar (1955), provide a few measurements of $\bar{s}$ for z_E values between 0 and 1 and l' in the neighbourhood of 10 with m again equal to zero. The facts were presented in Sections 3.3(a) and 3.3(b).

(vi) If the Reynolds number were so high that the stress at the wall tended to zero ($l' \to \infty$), there is some reason to expect that $\bar{s}$ would be equal to about $0.008(1 - z_E)^3$ when z_E is less than unity, and $0.008(z_E - 1)^3$ when z_E is greater than unity. This expectation rests primarily on theoretical ideas about the free turbulent mixing layer between two streams both of which are in motion, as summarised for example by Abramovich (1963).

3.4.2 The probable qualitative form of the $\bar{s}$ function for $m = 0$

The data summarised above are but a flimsy foundation for the delineation of a three-argument function. Nevertheless, they permit us to prepare the sketch of the $\bar{s}$-function which is shown in Figure 20 for the case of an impermeable wall. The broken curve represents a possible relation for infinite l'; the others have been constrained to pass through the same point at $z_E = 0$, to have similar tendencies at large z_E, and to pass through points obeying Equation (3.3-11).

One fact is made very clear by this diagram: that it is not possible to neglect the influence of either z_E or l' on the value of $\bar{s}$; both variables exert significant influences. The reason is no doubt that $\bar{s}$ is influenced both by happenings in the outer region of the boundary layer, for which z_E is a major characteristic, and by events closer to the wall which are measured by l'. We therefore cannot expect a formulation of the $\bar{s}$ function to be satisfactory unless it expresses both these influences.

3.4.3 The unacceptability of previous theoretical proposals

(a) Figure 21 represents the $\bar{s}(z_E, l')$ function which is based on Rotta's (1950) proposal, already given as Equation (3.1-2), with s_S replaced by $0.16z_E^2/(l')^2$ in accordance with Equation (3.3-4). Evidently this proposal disagrees seriously with the expectation expressed by Figure 20 at low and moderate values of z_E; it implies a zero $\bar{s}$ at $z_E = 0$ instead of a large one. Equation (3.3-4) therefore appears to be unacceptable as a description of the $\bar{s}$-function, even for $m = 0$.

(b) Figure 22 represents the $\bar{s}(z_E, l')$ function corresponding to Truckenbrodt's (1951) proposal already presented as Equation (3.1-4). The relation between R_2, z_E and l' is that which corresponds to the velocity profile of Equation (3.3-1) on a smooth wall. We see that s_S is influenced but little by z_E, an implication which is in conflict with Figure 20. It appears necessary to conclude that Equation (3.1-4) cannot serve as a reliable description of the $\bar{s}(z_E, l')$ function.

(c) The recommendation for $\bar{s}$ made by Rubert and Persh (1951), expressed above by Figure 10, cannot be reduced to a function of z_E and l' alone, because of the

postulated influence of the pressure gradient. However, this recommendation can also be rejected on the grounds that, like Rotta's, it implies a zero $\bar{s}$ when z_E is zero. This is shown by Figure 23, which represents the Rubert/Persh recommendation for *zero* pressure gradient; those for finite pressure gradients are qualitatively similar.

(d) It is not easy to deduce a dissipation integral from the proposal of Hudimoto (1951), given in Equation (3.1-6), because s is not expressible explicitly in terms of z. We may however, note that, as pointed out in Section 3.1, this proposal implies that $\bar{s}$ equals 0.00715 when z_E equals 1, which is in fair agreement with the expectation expressed by Figure 20. It may be concluded therefore that a shear-stress integral based on Hudimoto's proposal might be acceptable; however, for this to be useful, it would be necessary to compute the $\bar{s}$-integral numerically and then to devise approximate analytical formulae. This has not been done.

In summary, it can therefore be said that none of the previous theoretical proposals for the $\bar{s}$-function seems likely to solve our problem. The first three disagree strongly with experimental evidence and with theoretical expectation at low z_E, while the fourth is only implicit, and difficult to use. None of the proposals is valid for the case of the porous wall; and none is applicable to values of z_E greater than unity. Figure 20 is indeed already probably more reliable than the previous recommendations, even though its curves have been drawn freehand so as to correspond to a few known facts.

3.4.4 The constant-eddy-viscosity hypothesis

Although Equation (3.3-2) was based on the idealised velocity profile of Figure 4 and on the idealised $s \sim z$ relation of Figure 12, it may nevertheless be instructive to work out the corresponding $\bar{s}(z_E, l')$ function for $m = 0$ in detail, by replacing s_S by $0.16z_E^2/(l')^2$. The result is shown in Figure 24. Also plotted on this diagram are the experimental data of Klebanoff (1954) and Schubauer and Klebanoff (1951), for which l' had a value of about 10, and of Sandborn and Slogar (1955), for which l' was about 8. The curves are continued into the region for which z_E exceeds unity, but with the second term of Equation (3.2-2) written as $0.008(z_E - 1)^3$ because of the change of sign of the shear-stress; for the counterpart to Figure 12, for z_E in excess of unity, is the $s \sim z$ curve shown in Figure 25. Thus Figure 24 expresses the relation, for $m = 0$:

$$\bar{s} = z_E^3 \left\{ \frac{0.16}{(l')^2} + \frac{m}{2z_E} \right\} + 0.008|1 - z_E|^3 . \qquad (3.4\text{-}2)$$

Figure 24 fits fairly well the main facts listed in Section 3.4.1. When z_E equals zero, $\bar{s}$ is equal to 0.008; when z_E tends to infinity, $\bar{s}$ becomes proportional to z_E^3, the proportionality constant being 0.0064, for l' equal to 10, and when, for the equilibrium flat-plate boundary layer, l' is related to z_E by Equation (3.3-5), Equation (3.4-2) reduces to:

$$\bar{s} = 0.182(1 - z_E)^2 - 0.173(1 - z_E)^3 . \qquad (3.4\text{-}3)$$

These implications are in good agreement with the facts enumerated in Section 3.4.1 as (ii), (iv) and (iii) respectively. It is true that the coefficient of the second term on the right of Equation (3.4-3) is appreciably lower than that of Equation (3.3-11); but this term is in any case not of great importance.

When the implications of Equation (3.4-2) are compared with the experimental data plotted on Figure 24 it is seen that, for the values of l' in question, the equation predicts values of z_E which are rather too low in the moderate $-z_E$ range. It is therefore not possible to say that Equation (3.4-2) is entirely satisfactory as a dissipation-integral expression, but it is certainly an improvement on the earlier recommendations. It agrees well with data for separating boundary layers, for the equilibrium flat plate and for the wall jet; and it expresses the influence of m (though whether rightly or wrongly we do not yet know).

3.4.5 Deduction of the dissipation integral from an entrainment law

In Section 2 of the present paper, it was shown that there exist parallels and relationships between the "kinetic-energy method" and the "mass-conservation method". Indeed, in Equation (2.4-3), a connection was provided between the empirical functions of the two methods, namely the dissipation integral $\bar{s}$ of the first method and the entrainment function m_G of the second method.

Now there is reason to believe that the entrainment function, relating as it does to events at the outer edge of the boundary layer, should not be influenced by the values of s_S and m, which exert their influence on the part of the boundary layer close to the wall. It seems quite possible therefore that m_G may depend on z_E alone.

In the author's earlier paper (Spalding, 1964), a provisional recommendation was made for the relation between m_G and z_E. Further examination of experimental data, though not yet sufficiently comprehensive, has suggested that the recommendations over-estimated the entrainment rate; it appears that a better, but still provisional, recommendation is:

$$\left.\begin{aligned} z_E \leq 1 : \quad -m_G &= 0.06 - 0.05 z_E \\ z_E \geq 1 : \quad -m_G &= 0.03 z_E - 0.02 \end{aligned}\right\} . \qquad (3.4\text{-}4)$$

This recommendation is made for use with the velocity-profile family of Equation (3.3-1), the outer boundary of the layer being defined, when the shape factor H_1 is calculated, by the point where ξ equals 1. Since, as already mentioned, this definition does not satisfy Equation (2.4-4), some improvement remains to be made.

Equation (2.4-3) can be re-arranged as:

$$\bar{s} = (-m_G + m)\frac{(H-1)H_1}{2(H+1)H_1} + (s_S + m)\frac{H_1}{H+1} - \frac{m}{2} . \qquad (3.4\text{-}5)$$

We shall now examine some of the properties of the $\bar{s}$-function given by this equation when the shape factors correspond to Equation (3.3-1) and the entrainment function is given by Equation (3.4-4). Attention will be restricted to the case in which m is equal to zero.

When z_E is zero, Equation (3.4-5) leads to:

$$z_E = 0 : \quad \bar{s} = 0.00676 \qquad (3.4\text{-}6)$$

regardless of the value of l'. This result may be thought sufficiently close to our previous estimate for this condition, based on data for the free turbulent mixing layer, of about 0.008.

When z_E *tends to infinity,* Equation (3.4-5) reduces (for $m = 0$) to:

$$z_E \to \infty : \quad \frac{\bar{s}}{z_E^3} = \frac{\left\{0.3125 - \frac{1.923}{l'} + \frac{1.88}{(l')^2} - \frac{6}{(l')^3}\right\}}{\left(1 - \frac{2}{l'}\right)} \left(\frac{-m_G}{z_E}\right) + \\ + \frac{\left\{0.3125 - \frac{1.923}{l'} + \frac{1.88}{(l')^2} - \frac{6}{(l')^3}\right\}}{\left\{0.375 - \frac{1.589}{l'} + \frac{2}{(l')^2}\right\}} \times \frac{0.16}{(l')^2} . \tag{3.4-7}$$

If l' is given the typical value of 10, and $-m_G/z_E$ is taken as 0.03 in accordance with Equation (3.4-4), $\bar{s}/z_E^3$ becomes equal to 0.0059. This value may be regarded as sufficiently close to the experimental values cited in Equation (3.3-15).

Figure 26 contains values of $\bar{s}$, calculated in accordance with Equation (3.4-5) and the other already-stated assumptions* for various values of l'. Also plotted are the experimental data of Klebanoff (1954), Schubauer and Klebanoff (1951) and Sandborn and Slogar (1955). The following observations may be made:

(i) The curves have the same general form as those sketched in Figure 20 and as those calculated from Equation (3.4-2) and plotted in Figure 24.

(ii) The curves pass very close to the points corresponding to Equation (3.3-11) which represents experimental data for the equilibrium flat plate.

(iii) The agreement with the other experimental data is rather better than that displayed on Figure 24, but still not entirely satisfactory.

We may conclude that Equation (3.4-5) forms an acceptable basis for the derivation of the $\bar{s}$-function and that, since the entrainment function employed is still only provisional, it may ultimately yield reliable values for $\bar{s}$. The equation gives complete information about the effects of z_E, l' and m on the dissipation integral, but no test has so far been provided of the effect of the latter.

---

* Parts of the curves for $l' = 7$ and $l' = 8$ on Figure 26 are broken. The broken curves bridge a region where the curves according to Equations (3.4-5) and (3.4-4) suddenly exhibit large positive and negative values of the ordinate. These large values result from the fact that the shape factors are extremely sensitive to profile shape when z_E is slightly greater than unity. Since the velocity-profile assumption has been made without special attention to this region, it is the author's opinion that the broken curves are more to be trusted than those which precisly obey the equations.

3.4.6 Provisional recommendation

It would of course be premature to suppose that the problem of the $\bar{s}$ - function is now solved. In the author's view little more has been done than to find the direction in which part of the truth probably lies. As a stimulus to further research, however, it may be helpful to make the following recommendations for $\bar{s}$. These are:

(i) *When a simple formula is desired,* $\bar{s}$ should be calculated from Equation (3.4-2). This tends to underestimate $\bar{s}$ for values of z_E around 0.5, and perhaps to overestimate $\bar{s}$ for z_E slightly greater than unity. However its qualitative correctness seems assured.

(ii) *More accurate calculations* for $\bar{s}$ can be made by way of Equation (3.4-5) and the associated Equations (3.3-4), (3.3-6), (3.3-7), (3.3-8) and (3.4-4). The latter equation, i.e. the entrainment law, is no more than provisional; and the values of H_1 which satisfy the condition (2.4-4) and the velocity profile (3.3-1) remain to be worked out. The potential of Equation (3.4-5) is therefore probably greater than that of Equation (3.4-2) although its achievement is only marginally better at present.

4. DISCUSSION OF RESULTS

4.1 Comparison of the "kinetic-energy" and "mass-conservation" methods

4.1.1 Advantages of the "mass-conservation" method

As mentioned in Section 1.1, of all methods of calculating the rate of growth of turbulent boundary layers available until now, only that of Head (1960) yields uniformly tolerable results. The first advantage of the method employing the entrainment concept is therefore that it gives good predictions of boundary layer development. As shown by the present writer (Spalding, 1964), the method can be applied to the whole range of two-dimensional problems, including those involving wall jets; and there is every prospect of its being successfully extended to three-dimensional flows also.

Possibly the reason for the success of the method lies in the fact that the entrainment function is a fairly simple one, the form of which is easy to guess. Thus, Head supposed that the dimensionless entrainment rate was a function of H alone, and determined it by analysis of experimental data. The present writer started independently from the postulate, derived from knowledge of free turbulent flows, that $-m_G$ was more or less proportional to $|1 - z_E|$, the absolute magnitude of the wake or jet component of the velocity profile. Because the *ideas* of "entrainment" and of "mass flow rate of boundary layer fluid" are easy ones to grasp, first guesses about the entrainment function turned out to be quite good.

4.1.2 Disadvantages of the "mass-conservation" method

Despite its success, the "mass-conservation" method suffers from three main disadvantages. The first concerns the location of the outer boundary of the layer, separating the entrained fluid from that which is deemed to be outside the layer.

In Head's paper, and the earlier one of the present writer (Spalding, 1964), this boundary was arbitrarily fixed; although the present paper provides (in Section 2.4) a means for the removal of this arbitrariness, the argument supporting it possesses subtleties which may limit its acceptability.

The second disadvantage is that, whereas it was easy to guess the form of the entrainment function for uniform-density flow, this is by no means the case for flows in which, perhaps because of kinetic heating, density variations arise. The reasons are that there is little experimental information about the effects of such variations on free turbulent flows; and that no theoretical clue exists even as to the *direction* of the effect of a density variation on entrainment.

The second disadvantage can be removed by the execution of a suitable experimental programme: the third disadvantage, by contrast is irremediable. This is the inapplicability of the concept of entrainment to flows within ducts, for example diffusers, which are sufficiently long for the boundary layers on opposite walls of the duct to make contact on the duct axis. Here can be no entrainment, by symmetry; yet the wake component of the velocity profile may well be large in such a case.

4.1.3 Disadvantages of the "kinetic-energy" method

Is the method employing the dissipation integral any better? Here we must repeat the remark made in Section 1.1: methods based on the integral kinetic-energy-dificit equation have not been especially successful, particularly when the pressure gradient is adverse. The reason appears to be that the $\bar{s}$ – function, being as much dependent on events near the wall as on those in the fully turbulent part of tne layer, has a more complex structure than has the m_G – function; its form is harder to guess; and the early guesses have been wrong.

Nevertheless, the new light which has been thrown on the dissipation integral by the present paper may be held to have changed the situation. Indeed, although it has been necessary to draw aid from entrainment data, a new $\bar{s}$ – expression has been found which seems bound to lead to predictions of boundary layer growth which are as successful as those based on the mass-conservation equation.

4.1.4. Advantages of the "kinetic-energy" method

First we note that this method does not possess any of the flaws which had to be recorded in Section 4.1.2. The arbitrariness of the outer boundary does not arise at all; there exists at least a reasonable hypothesis (described in Section 4.2.2), concerning the way in which density variations will influence the dissipation integral; and $\bar{s}$ can be expected to be the same function of z_E, l' and m when the boundary layers "join up" in a duct as when only one boundary layer is present. The last of these points is the most important, in the author's view.

The method posesses, however, further possibilities, scarcely exploited until now. For example, the dissipation-integral expression can reasonably be made to apply to three-dimensional flows by postulating that the eddy viscosity is proportional to the maximum velocity difference across the shear layer, regardless of direction, and not solely to the component of that velocity in the direction of the shear stress. Another extention which requires little ingenuity is that which takes account of

small-radius-of-curvature effects, as when an axially symmetrical boundary layer is formed on a pencil-like surface. Further, the knowledge which has been gained so far renders it possible at least to speculate intelligently about the way in which $\bar{s}$ would be influenced by velocity profiles more complex than those considered so far, for example, profiles exhibiting reverse flows, or more than one velocity maximum.

4.1.5 A tentative recommendation

The author's present opinion is that it will ultimately be preferable to use the "kinetic-energy" method rather than the "mass-conservation" method. Of course, for some time it may be necessary, when developing the $\bar{s}$ - function, to draw on the store of knowledge about entrainment, and, in any case, the formal relations which have been proved to exist between the two methods reduce the importance of the choice. However, it seems probably that the greater directness with which the dissipation integral can be connected with density-variation, radius-of-curvature and other effects, and the conceptual difficulty which attaches to the entrainment concept in some circumstances, will make it easier to work in terms of $\bar{s}$ and H_3 rather than m_G and H_1. If this should come about, it should not be forgotten that the role of the entrainment-based theory, though perhaps brief, was a valuable one.

4.2 Some problems for research

In an earlier paper (Spalding, 1964), the present author drew attention to the questions which arose from the achievement of a unified theory based on the entrainment principle. One of these questions, incidentally, has been resolved by the present paper, that of the relation of the "mass-conservation" and "kinetic-energy" equations. Most of the other questions remain open, but some can now be conveniently recast in terms of the shear-stress integral in place of the entrainment function.

4.2.1 The determination of the $\bar{s}$ function

The recommendations for $\bar{s}$ made in Section 3.4.6 are merely provisional and require comprehensive experimental verification and amendment. There are two main methods: (i) the measurement of shear-stress and velocity profiles in boundary layers and wall jets with the aid of hot-wire instruments; and (ii) the measurement of successive velocity profiles and the deduction therefrom, by way of the integral kinetic-energy-deficit equation, of the value of $\bar{s}$. Since several velocity-profile studies have been published, the second method can be immediately applied to them; however, as has been shown by Thompson (1964), uncertainties concerning two-dimensionality beset most experiments.

An important question which requires an early answer is: Does $\bar{s}$ indeed depend only on the local velocity distribution, as postulated in the present paper? If the answer is negative, it should be said, the results of the present paper do not become valueless: all that is needed is to enlarge the $\bar{s}$ function so that it becomes: $\bar{s}(z_E, l', m, X)$ where X stands for some property of the boundary layers which depends, say, on the rate of change of profile shape.

It is quite likely that the quantity $R_2 dz_E/dR_X$ will prove to be an X, i.e., will influence the value of $\bar{s}$. This possibility can be investigated by measuring $\bar{s}$ in two or more profiles, having the same z_E, l' and m, which are situated in different

boundary layers; thus, one might be an equilibrium layer of the Clauser (1954) type, another might be present on an aerofoil surface, and yet another might involve constancy of pressure along the surface with variation of profile shape resulting from discontinuities in the degree of roughness of the surface. The inclusion of the influence of this or any other X in the computer programme embodying the theory is a perfectly straightforward matter; all that is needed is a systematic series of experiments designed to establish the influence of the X quantitatively.

One crucial and related experiment would be the measurement of $\bar{s}$ in two separating ($z_E = 0$) boundary layers, one on an impermeable wall with an adverse pressure gradient, the other in a unform stream with mass transfer through the wall. In Sections 2.2 and 2.3 it has been regarded as probably that the $\bar{s}$ values are the same. Is this so? And if not, what are the magnitude and cause of the difference? The answers to these questions will have important implications for the future development of the theory.

4.2.2 *Extension to situations having non-uniform density*

As has been mentioned, it is possible to make reasonable proposals about the way in which $\bar{s}$ is influenced by the non-uniformity of density which arises in problems involving, for example: the injection of a light-gas coolant into a boundary layer, flow at high Mach number or combustion of a fuel jet near a wall. The proposals would be founded on the assumptions:

(i) That the velocity profile can still be described by Equation (3.3-1), although the relation between l' and s_S would be modified in accordance with some theory of compressibility effects in a Couette flow, for example that of Spalding and Chi (1964).

(ii) That, z_E, l' and m being fixed, the shear stress at any point is proportional to a definite function of velocity *and to the local density*. The function of velocity will be more or less complicated according to the extent of our knowledge; for example, if the simple hypotheses of Section 3.2(b) were adopted, we might take it as a constant equal to $0.008(1 - z_E)^2 u_G^2$.

(iii) That the density at any point in the profile is deducible from the thermodynamic properties of the fluid together with profile assumptions and differential equations expressing conservation principles.

Some progress could be made theoretically, simply by working out the implications of these proposals quantitatively and in detail. This is probably worth doing. However, before long it will certainly be necessary to carry out experiments to check both the assumptions and the implications. There is much work of this kind to do because no studies have been made for compressible flows in the detail of, say, that of Schubauer and Klebanoff (1951) for subsonic flows. Yet there are more quantities to be measured when the density varies; and most of the measurements are more difficult to make.

4.2.3 *A short list of further problems*

In Section 4.1.4 it has already been mentioned that the theory can probably be extended to three-dimensional flows, to flows in which the distance from the symmetry

axis is not large compared with the boundary layer thickness, and to flows with more complex velocity profiles than have so far been considered. It will be profitable, in the present author's opinion, to investigate each of these lines.

Another situation which requires study is that in which transverse body forces act on the boundary layer. There are two main types of force, those associated with curvature of the body surface in the stream direction, and those concerned with density variations in a gravitational field; the first occurs, for example, when a jet is blown over a flap to prevent boundary layer separation; the second occurs predominately in the earth's atmosphere where the direction and magnitude of the temperature gradient can vary the shear stresses in the flow by several orders of magnitude. At present, there is no knowledge of the quantitative relationships governing these effects; but their importance is such as to make detailed study desirable.

Finally one might add the problem of laminarisation, i.e. the disappearance of turbulence in the downstream region of an initially turbulent boundary layer under the influence of a favourable pressure gradient. This process, which is of practical importance in rocket nozzles for example, could be brought within the scope of the present theory if the $\bar{s}$-function were extended so as to possess a term proportional to the fluid viscosity. If the assumptions of Section 3.2(b) are made, but the extra effect of viscosity is added, it is not hard to show that Equation (3.2-2) should be extended, so as to become:

$$\bar{s} = (s_S + mz_E/2)z_E + 0.008(1 - z_E)^3 + \frac{(1 - z_E)}{2HR_2} . \qquad (4.2\text{-}1)$$

If an additional modification is made to the $s_S(z_E, l')$ relationship, which causes it to reduce to the appropriate form at low Reynolds number, we should possess a theory which permits calculation of the transition for turbulent to laminar flow; indeed it might serve for transition from laminar to turbulent flow also.

4.3 Conclusions

The main results of the study here reported appear to be:

(i) Formal relations exist between the entrainment function of the mass-conservation method and the dissipation integral of the kinetic-energy method.

(ii) Use of these relations has permitted *both* methods to be improved: the arbitrariness of the outer boundary of the layer can now be discarded from the entrainment function; and a dissipation-integral expression has been discovered which agrees better than previous expressions with experimental data for boundary layers nearing separation, and which extends into the region, not previously charted, of flows exhibiting velocity maxima.

(iii) Many research problems remain; however, the prospects of a major extension of the scope of the theory are bright.

5. ACKNOWLEDGEMENTS

The author's thanks are due to Miss M.P. Steele, Mr. P. Dale and Mr. G.N. Pustintsev for assistance in the preparation of the manuscript and diagrams.

REFERENCES

Abramovich, G.N. — *The theory of turbulent jets.* M.I.T. Press, Cambridge, Mass., U.S.A., (1963).

Bradshaw, P.
Gee, M.T. — *Turublent wall jets with and without an external stream.* Aeronautical Research Council, R. and M. No.3252, H.M.S.O., London, (1962).

Clauser, F.H. — *Turbulent boundary layers in adverse pressure gradients.* J. Aero Sci., Vol.21, No.2, (1954), pp.91-108.

Coles, D. — *The law of the wake in the turbulent boundary layer.* J. Fluid Mech., Vol.1, (1956), pp.191-226.

Hacker, D.S. — *Interferometric investigation of the stability of a turbulent boundary layer with mass addition.* ASME Paper 58-A-249, (1958).

Hama, F.R. — *Turbulent boundary layer along a flat plate.* Rep. Institute Sci. and Tech., Univ. of Tokyo, Vol.1, quoted by D. Ross (1953), pp.13-16, 49-50, (1947).

Head, M.R. — *Entrainment in the turbulent boundary layer.* Aeronautical Research Council, R & M No.3152, H.M.S.O., London, (1960).

Hudimoto, B. — *Momentum equations of the boundary layer and their application to the turbulent boundary layer.* Mem. Fac. Engng. Kyoto University, Vol.13, (1951), pp.162-173.

von Kármán, T. — *Über laminare und turbulente Reibung.* ZAMM, Vol.1 (Transl. as NACA Tech. Memo. 1092), (1921), p.233.

Klebanoff, P.S. — *Characteristics of turbulence in a boundary layer with zero pressure gradient.* NACA Rep. 1247, (1955), pp.1135-1153.

Liepmann, H.W.
Laufer, J. — *Investigations of free turbulent mixing.* NACA Tech. Note 1257, (1947).

Ludwieg, H.
Tillmann, W.

Untersuchungen uber die Wandschub-spannung in Turbulenten Reibungsschichten. Ing. Archiv. Vol.17, pp.288-299, (1949). Transl. as *Investigations of the wall shearing stress in turbulent boundary layers.* NACA TM 1285, 1950, also Aeronautical Research Council 14800.

Mathieu, J.

Contribution a l'étude aérothermique d'un jet plan évoluant en présence d'une paroi. Publications Scientifiques et Techniques du Ministère de l'Air, No.374, (1961).

Mellor, G.L.
Gibson, D.M.

Equilibrium turbulent boundary layers. Princeton University, Dept. Aerospace and Mech. Sci., FLD No.13, (1963).

Reichardt, H.

Gesetzmässigkeit der freien Turbulenz. VDI Forschungsheft 414, 3nd Ed. 1951, (1942).

Ross, D.
Robertson, J.M.

A superposition analysis of the turbulent boundary layer in an adverse pressure gradient. J. Appl. Mech., Vol.18, (1951), pp.95-100.

Rotta, J.

Uber die Theorie der turbulenten Grenzschichten Strom. Forsch. Nr.1. Transl. as *On the theory of the turbulent boundary layer.* NACA TM 1344, 1953, (1950).

Rotta, J.

Schubspannungsverteilung und Energiedissipation bie turbulenten Grenzschichten. Ing. Arch. Vol.20, (1952), pp.195-207.

Rotta, J.

Incompressible turbulent boundary layers. Colloques Internationaux du Centre National de la Recherche Scientifique, Marseilles, No.108, (1961), pp.255-285.

Rubert, K.F.
Persh, J.

A procedure for calculating the development of turbulent boundary layers under the influence of adverse pressure gradients. NACA TN 2478, (1951).

Sandborn, V.A.
Slogar, R.J.

Study of the momentum distribution of turbulent boundary layers in adverse pressure gradients. NACA TN 3264, (1955).

Schlichting, H.

Uber das ebene Windschatten-problem. Thesis, Göttingen. Also Ing. Arch., Vol.1, (1930), pp.537-571.

Schlichting, H.

Boundary layer theory. Fourth edition. McGraw Hill, New York, (1960).

Schubauer, G.B.
Klebanoff, P.S.

Investigation of separation of the turbulent boundary layer. NACA Rep.1030, (1951).

Schultz-Grunow, G. — *Neues Reibungswiderstandsgesetz für glatte Platten.* Luftfahrtforschung, Vol.17, pp.239-246, (1940), transl. as *New frictional resistance law for smooth plates.* NACA TM 986 (1941).

Schwartz, W.H.
Cosart, W.P. — *The two-dimensional turbulent wall jet.* J. Fluid Mech. Vol.10, (1961), pp.481-495.

Spalding, D.B. — *A unified theory of friction, heat transfer and mass transfer in the turbulent boundary layer and wall jet.* Mech. Eng. Dept. Imperial College, and Aeronautical Research Council 25023, (1964).

Spalding, D.B. — *Some suggestions for research in the field of turbulent boundary layers.* Mech. Eng. Dept. Imperial College, and Aeronautical Research Council 25988, (1964).

Spalding, D.B.
Chi, S.W. — *The drag of compressible turbulent boundary layer on a smooth flat plate with and without heat transfer.* J. Fluid Mech. Vol.18, (1964), pp.114-143.

Tani, I. — *Energy dissipation in turbulent boundary layers.* J. Aero. Sci. Vol.23, (1956), pp.606-607.

Tetervin, N.
Lin, C.C. — *A general integral form of the boundary layer equation for incompressible flow with an application to the calculation of the separation point of turbulent boundary layers.* NACA Rep.1046, (1951).

Thompson, B.G.J. — *Calculations of turbulent boundary layers.* Two volumes. Cambridge Ph.D. Thesis, (1963).

Thompson, B.G.J. — *A critical review of existing methods of calculating the turbulent boundary layer.* Aeronautical Research Council 26109, (1964).

Tollmien, W. — *Berechnung turbulenten Ausbreitungsvorgänge.* ZAMM Vol.6, pp.468-478. (Transl. as NACA Tech. Memo. 1085), (1926).

Truckenbrodt, E. — *Ein Quadraturverfahren zur Berechnung der laminaren und turbulenten Reibungschicht bei ebener und rotations symmetrischer Strömung.* Ing. Arch. Vol.20, (1952), p.211.

Wieghardt, K. — *On an energy equation for the calculation of laminar boundary layers.* Habilitation paper, Göttingen. Referred to by W. Tollmien in AVA Monographs B 1.15, British Ministry of Aircraft Production Rep. & Transl. No.1001, March, 1948, (1945).

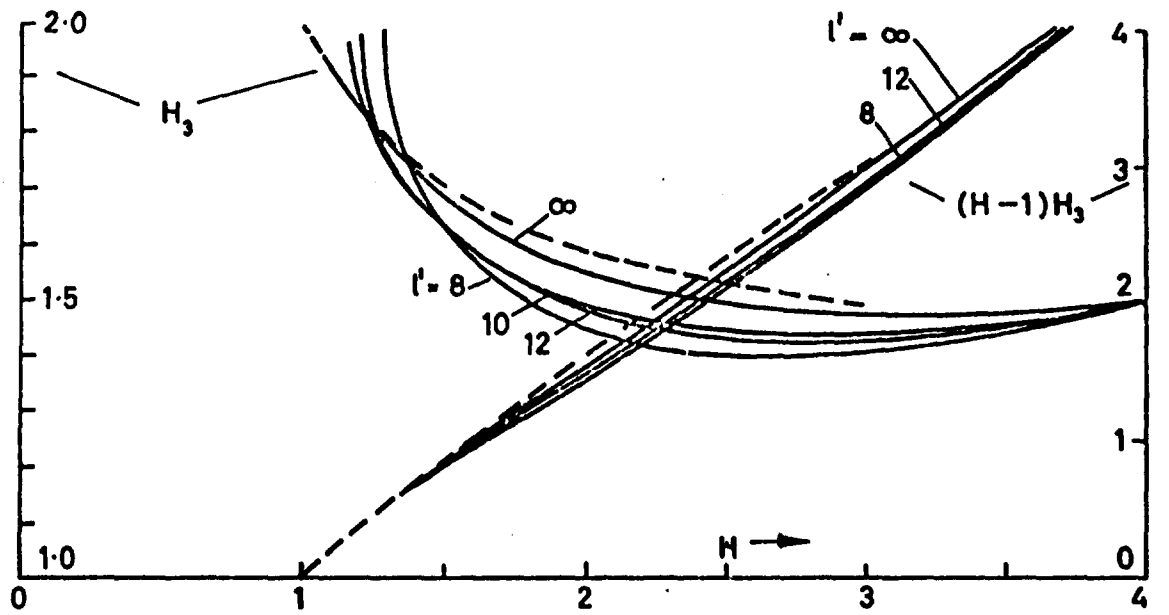

Fig. 1 Relations between shape factors H and H_3 for boundary layers having uniform density and the velocity profile
$z = z_E\{1 + (\log_e \xi)/l'\} + \frac{1}{\pi}(1 - z_E)(1 - \cos\pi\xi)$
The dotted curves correspond to the family of velocity profile: $z = \xi^n$

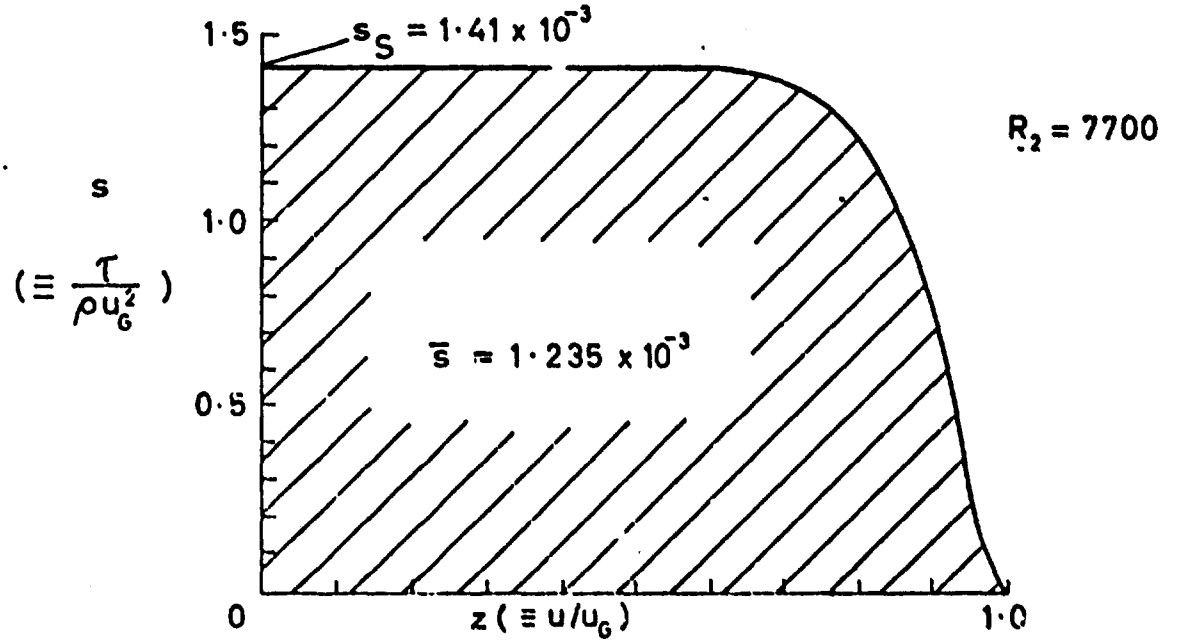

Fig. 2 Variation of shear stress with velocity for an equilibrium-flat-plate boundary layer, (experimental measurements of Klebanoff, 1955)

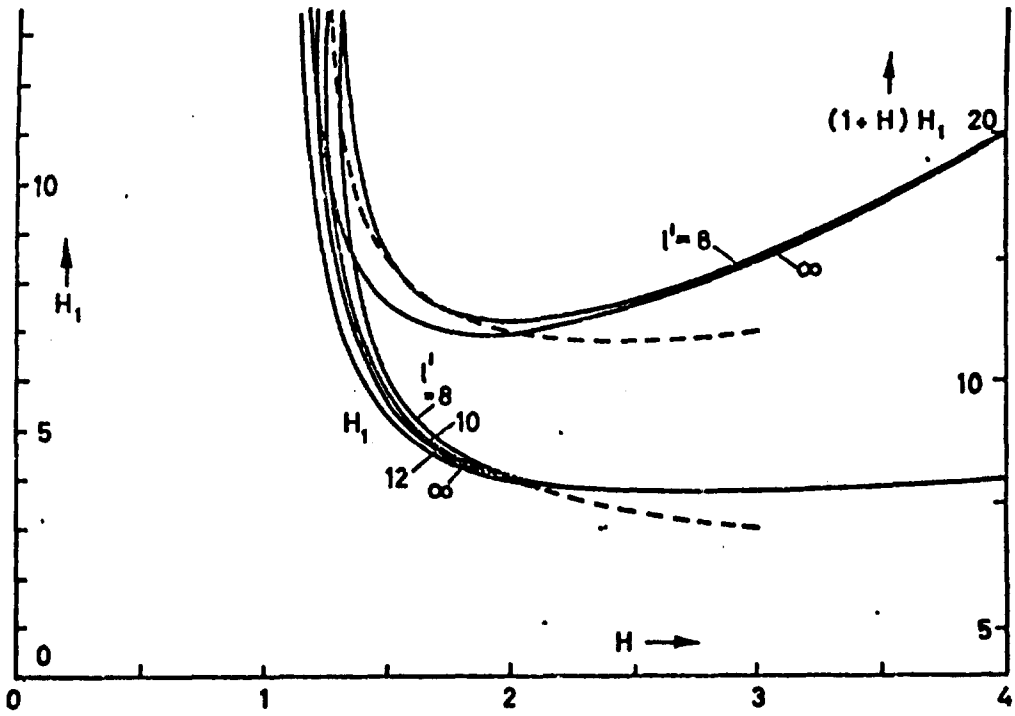

Fig. 3 Relation between shape factors H and H_1 for boundary layers having uniform density and the velocity profile

$$z = z_E\{1 + (\log_e \xi)/l'\} + \tfrac{1}{\pi}(1 - z_E)(1 - \cos\pi\xi)$$

The dotted curves correspond to the family of velocity profile: $z = \xi^n$

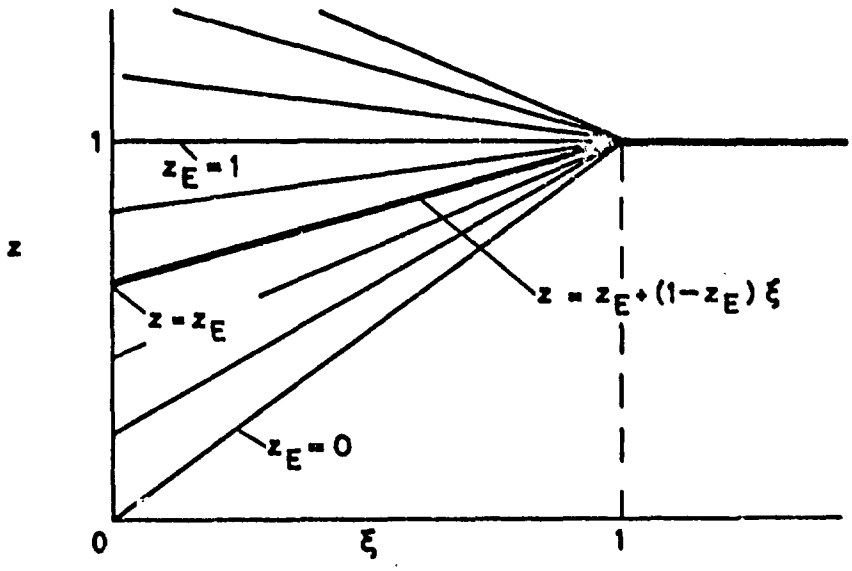

Fig. 4 The linear velocity profile described by Equation (2.4-6)

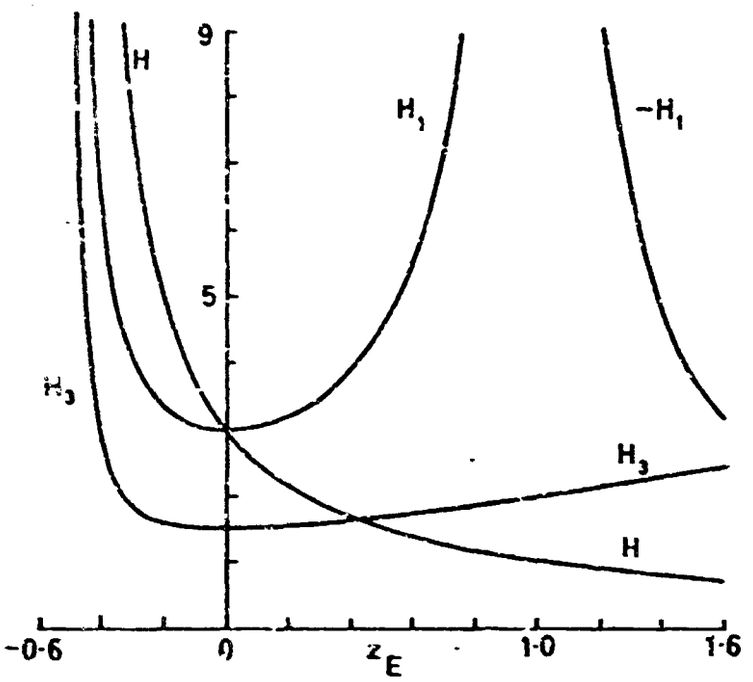

Fig. 5 Shape factors of the linear velocity profiles described by Equation (2.4-6) and represented in Figure 4. Note that H_1 changes sign at $z_E = 1$

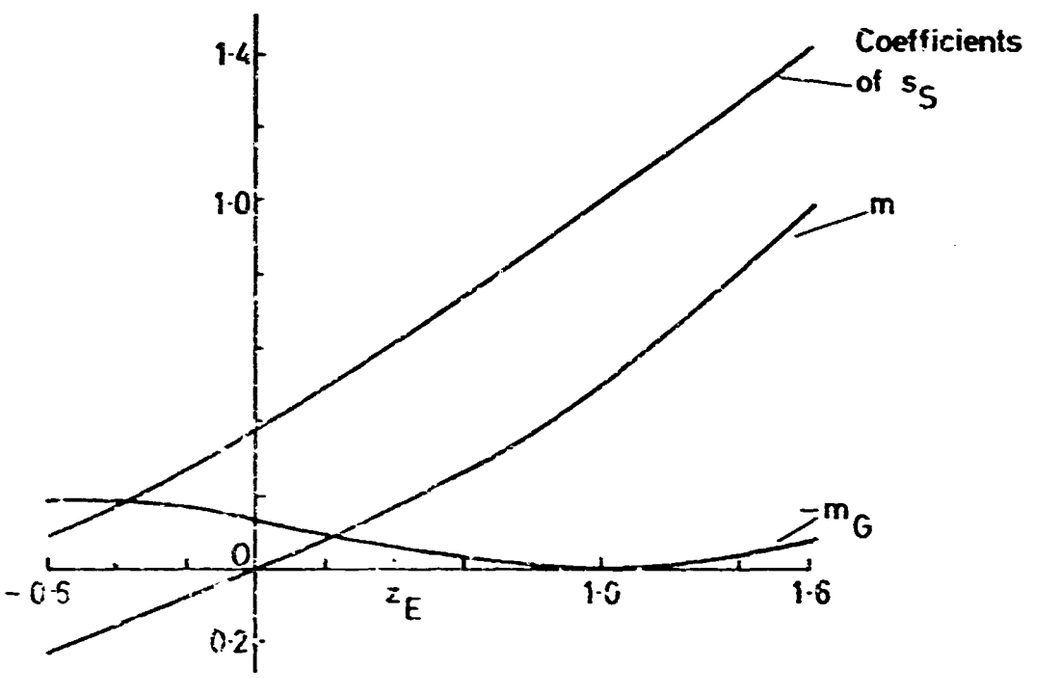

Fig. 6 Coefficients of $-m_G$, m and s_S in the expression for $\bar{s}$, Equation (2.4-13), based on the linear velocity profile

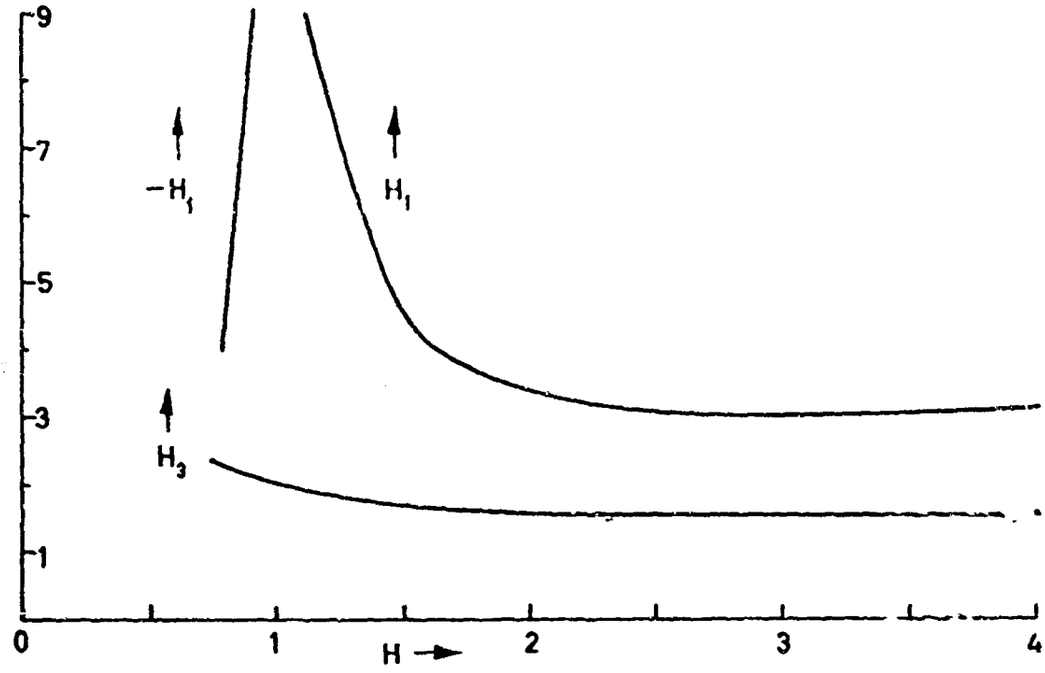

Fig.7 Relation between shape factors for the linear velocity profile. (Replot data of Fig. 5)

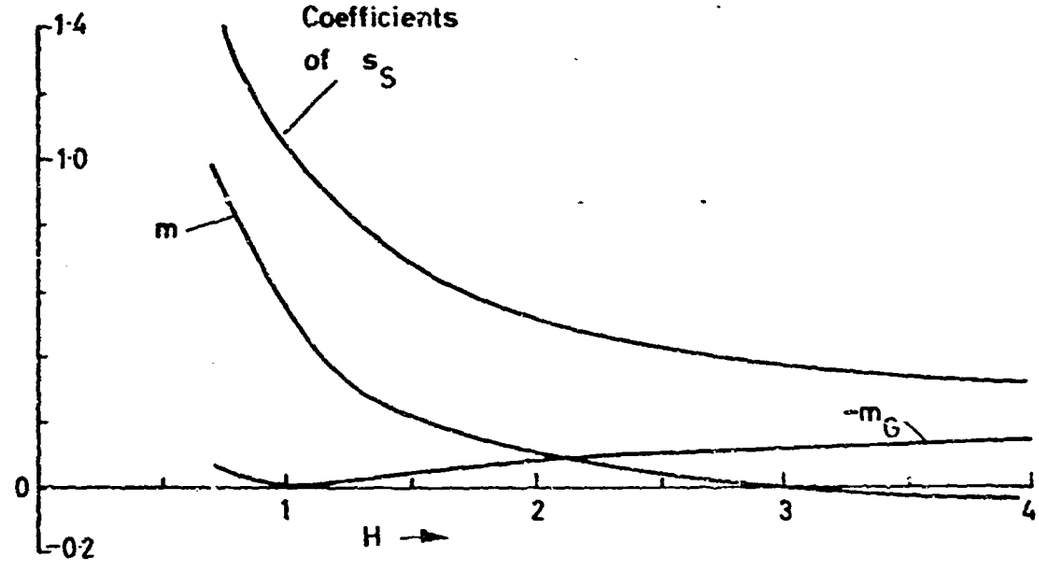

Fig.8 Coefficients of $-m_G$, m and s_S in the expression for $\bar{s}$, Equation (2.4-13). (Replot of data of Fig.6)

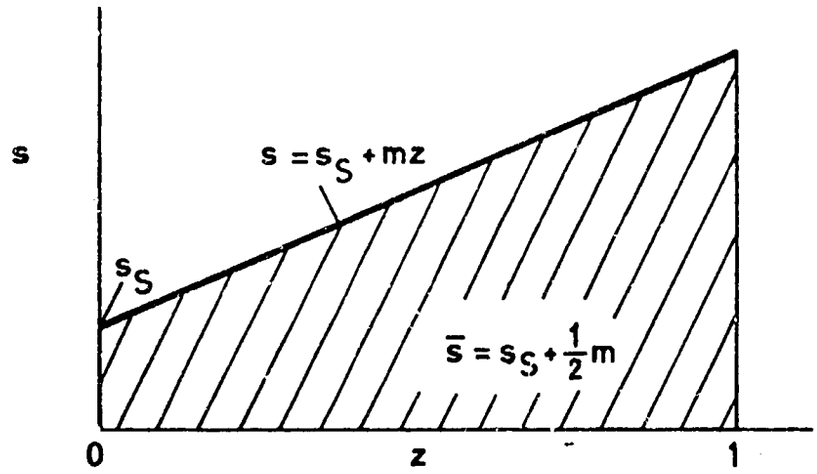

Fig. 9 Shear stress distribution in a Couette flow with mass transfer through the wall (where z = 0) at dimensionless rate m

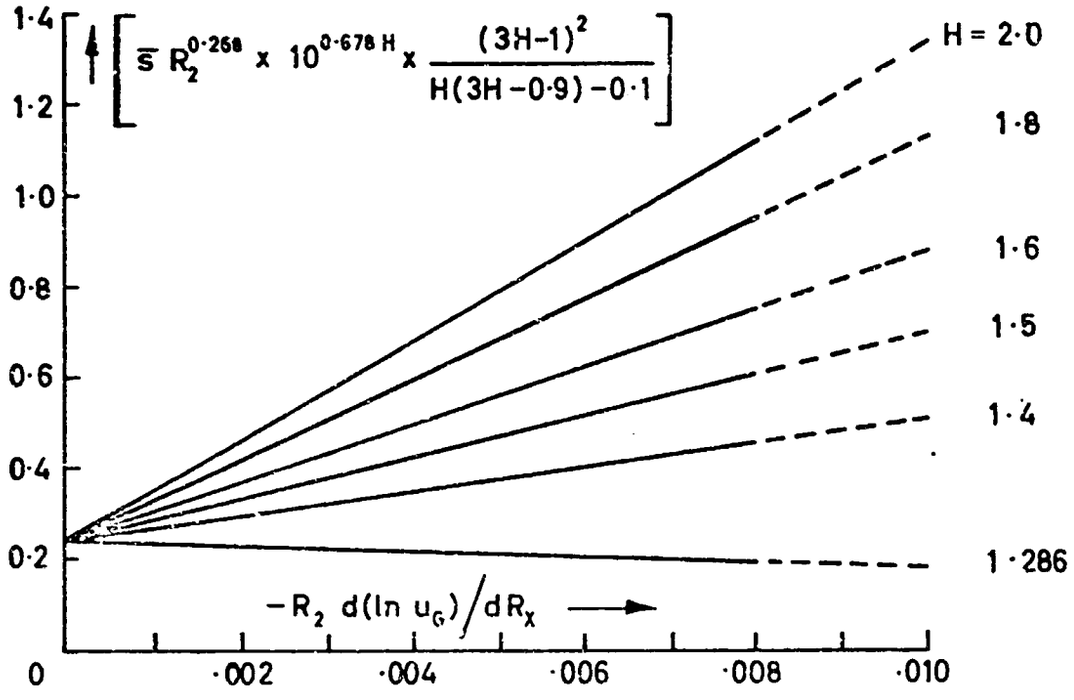

Fig. 10 Recommendation for $\bar{s}$ made by Rubert and Persh (1951)

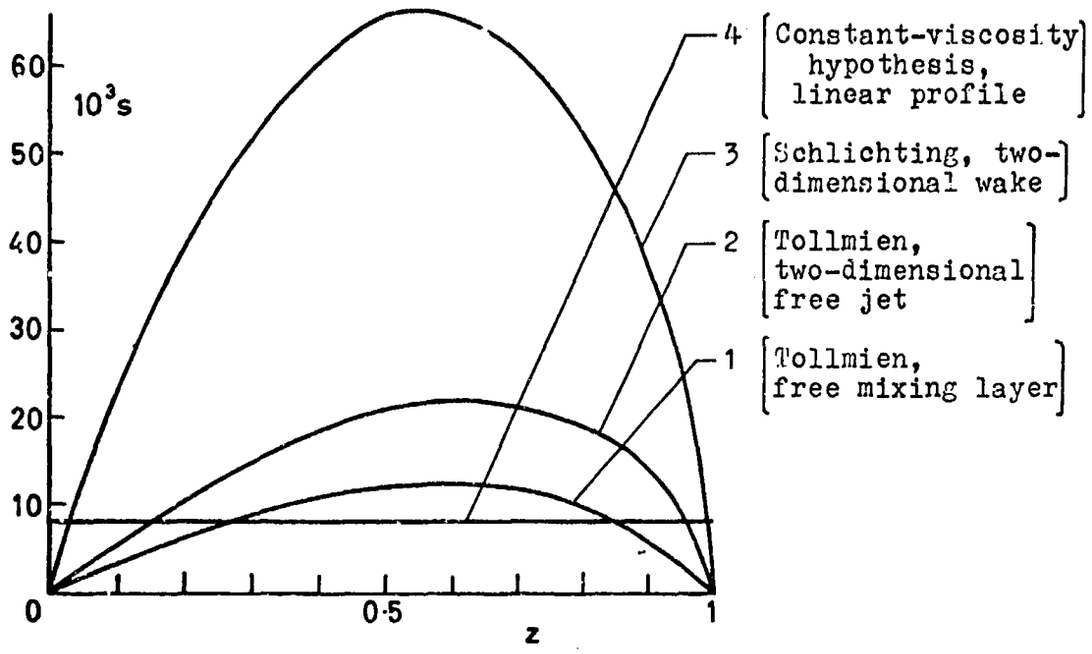

Fig. 11 Some theoretically based shear stress distributions in free turbulent flows, each embodying one empirical constant

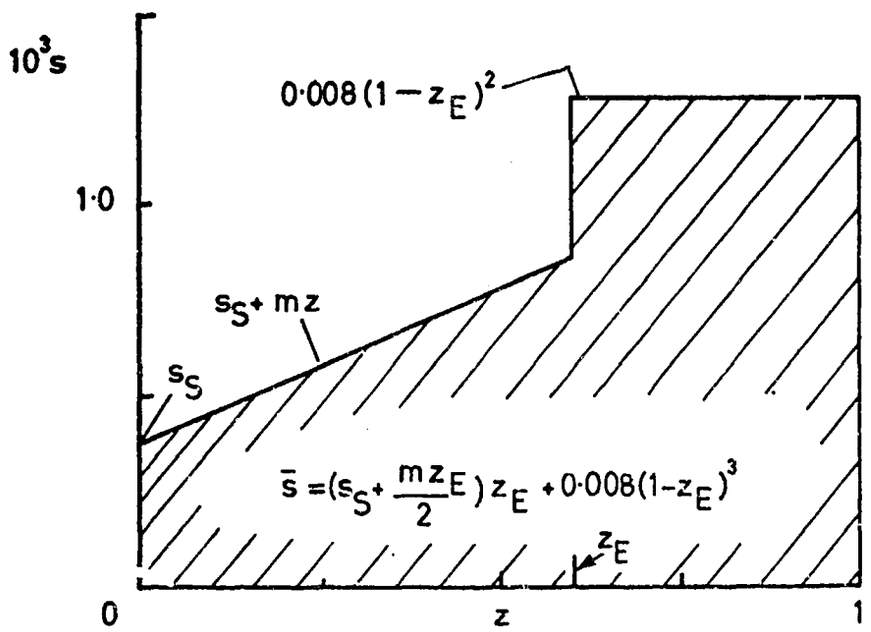

Fig. 12 Shear stress distribution corresponding to the linear velocity profile of Figure 4 and the Clauser/Mellor/Gibson constant-viscosity hypothesis

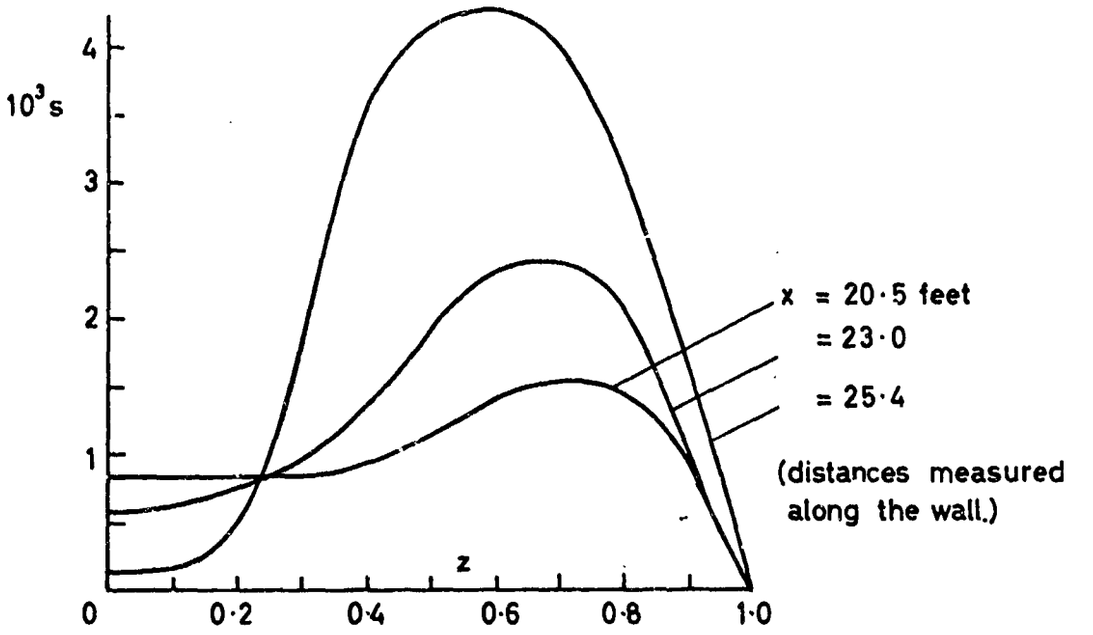

Fig. 13 Some $s \sim z$ distributions deduced from the measurements of Schubauer and Klebanoff (1951)

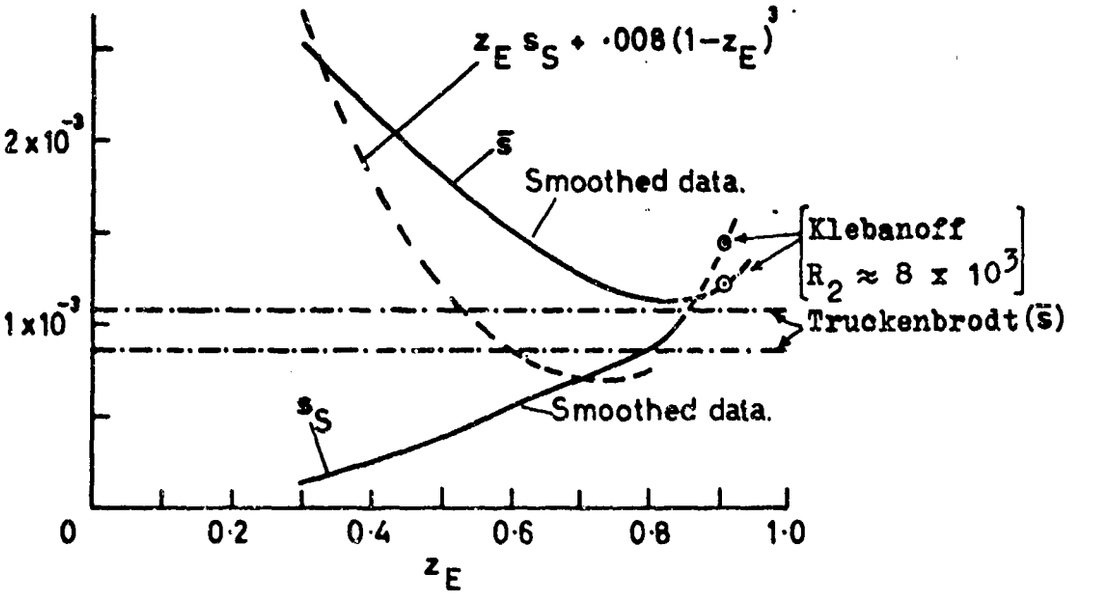

Fig. 14 Smoothed data for $\bar{s}$ and s_S deduced from the measurements of Schubauer and Klebanoff (1954) and some theoretically based curves for comparison

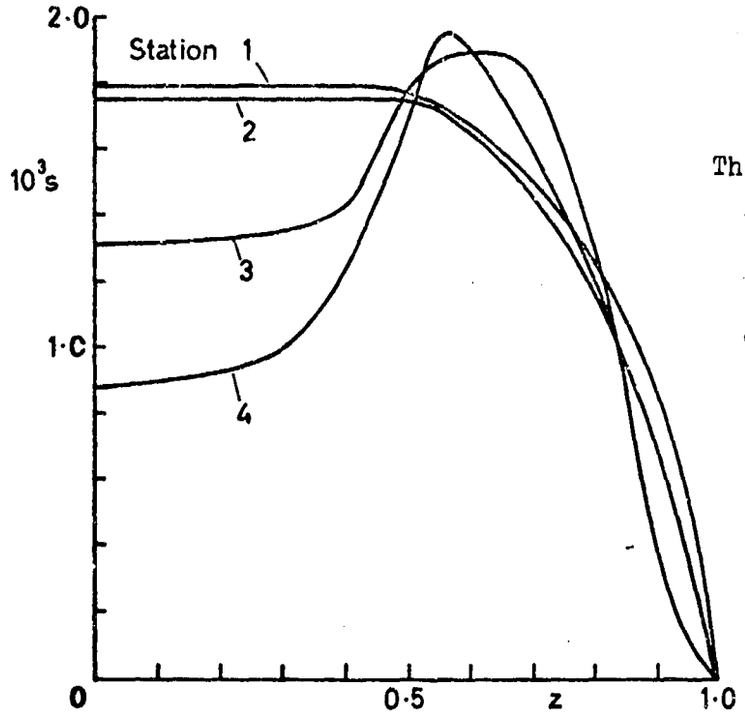

The numbers 1,2,3 and 4 signify the station, the higher numbers corresponding to downstream positions

Fig. 15 The $s \sim z$ distributions deduced from the measurements of Sandborn and Slogar (1955)

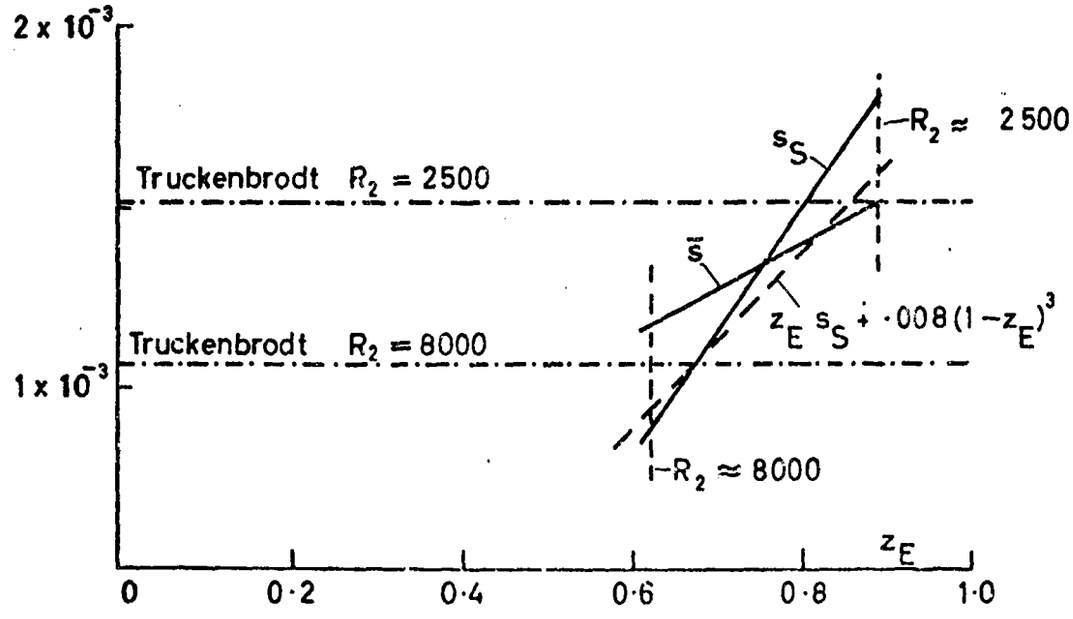

Fig. 16 Data for $\bar{s}$ and s_S deduced from Sandborn and Slogar (1955). With some theoretically based curves for comparison

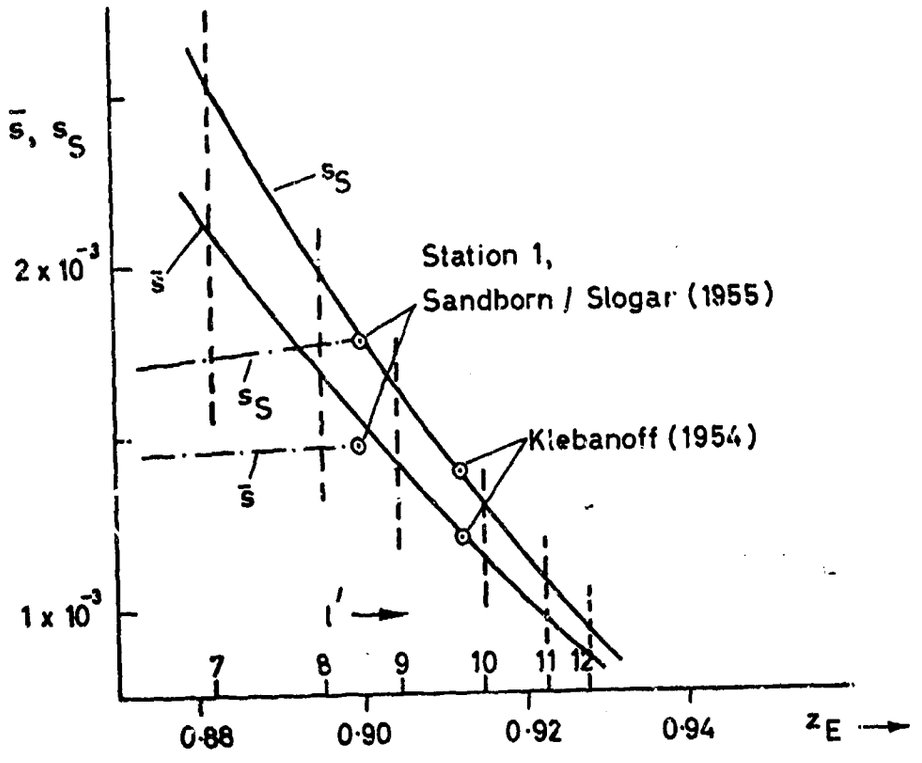

Fig. 17 Variations of $\bar{s}$ and s_S with z_E for equilibrium boundary layers on impermeable flat plates. The curves represent Equations (3.3-11) and (3.3-3). Chain-dotted lines represent data of Sandborn and Slogar (1955), from Figure 16

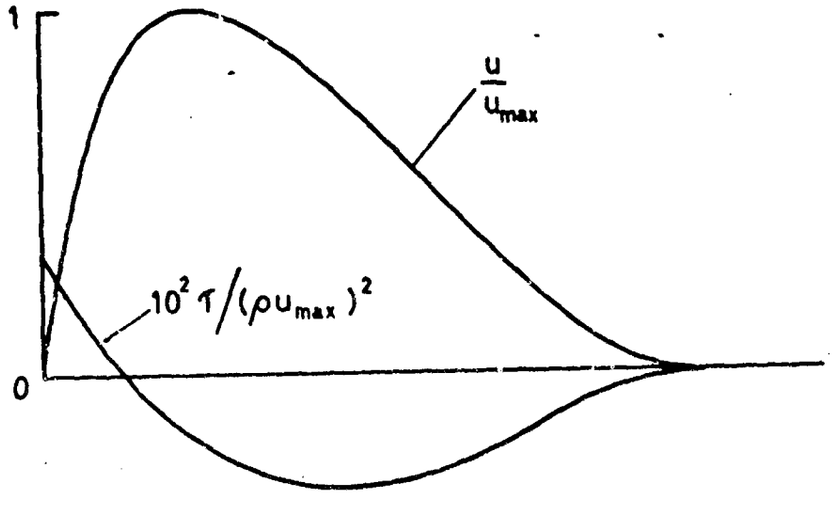

Fig. 18 Sketch of velocity and shear stress profiles across a wall jet

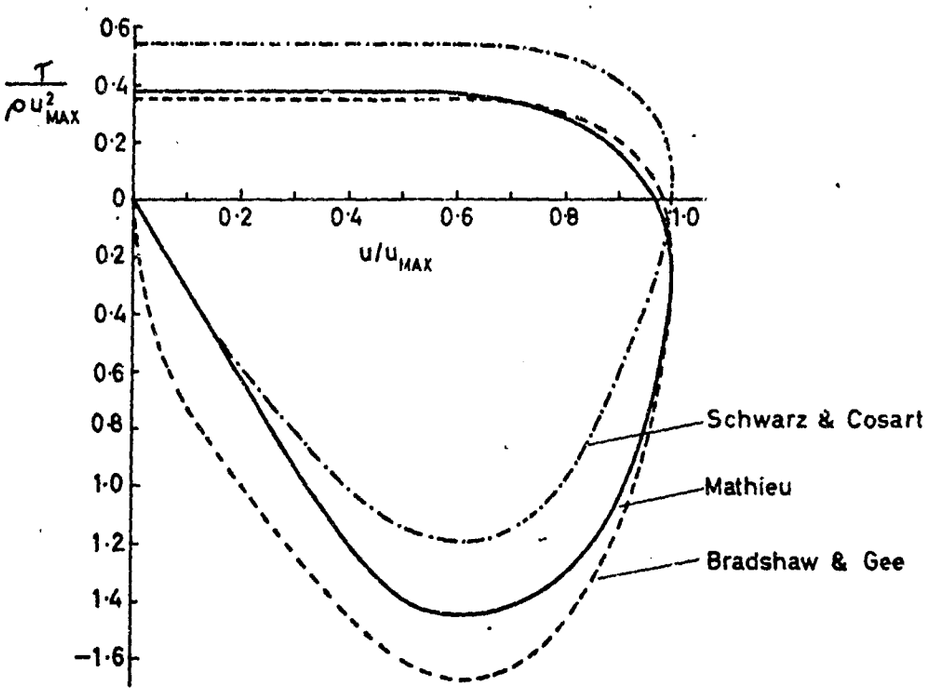

Fig. 19 Shear stress versus velocity for wall jets

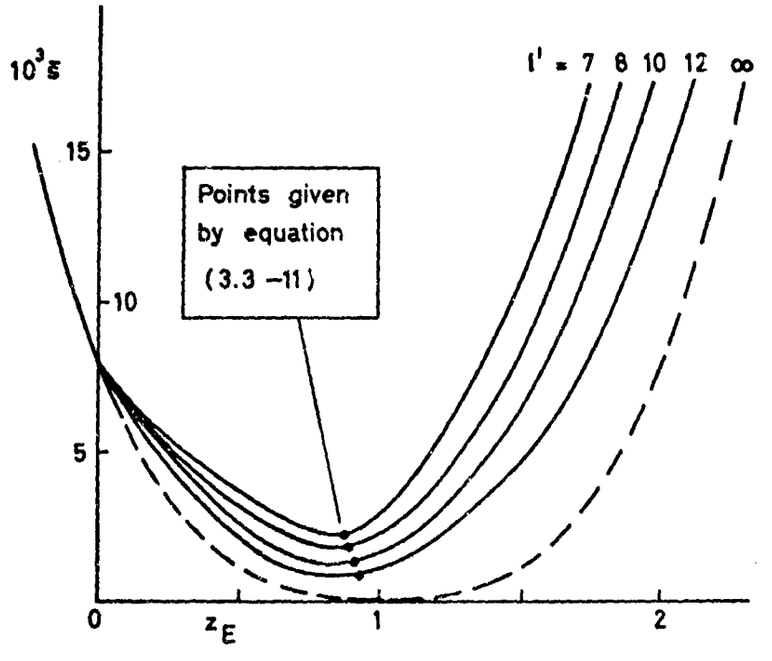

Fig. 20 A sketch of the probable shape of the $\bar{s}(z_E, l')$ function for $m = 0$. Compare Figures 14, 16 and 17, which contain experimental data

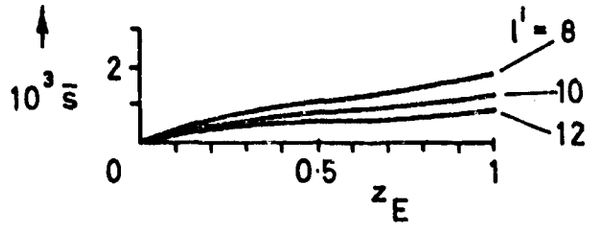

Fig. 21 The $\bar{s}(z_E, l')$ function for an impermeable wall which corresponds to the proposal of Rotta (1950)

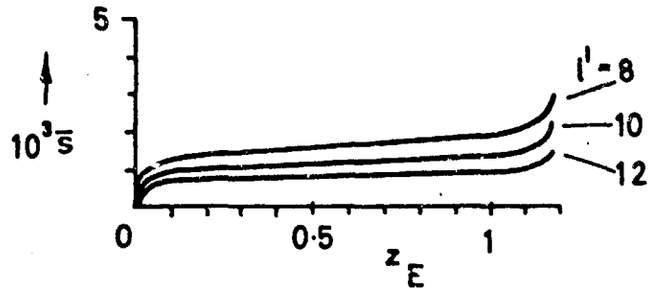

Fig. 22 The $\bar{s}(z_E, l')$ function for an impermeable wall which corresponds to the proposal of Truckenbrodt (1951)

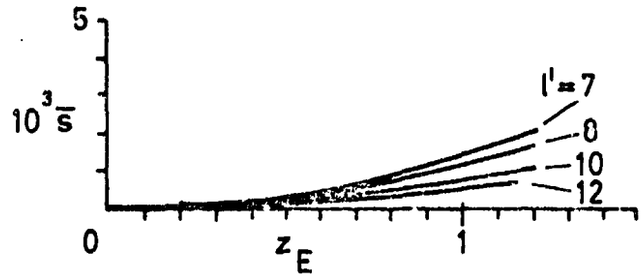

Fig. 23 The $\bar{s}(z_E, l')$ function for an impermeable wall which corresponds to the proposal of Rubert and Persh (1951); the pressure gradient is taken as zero

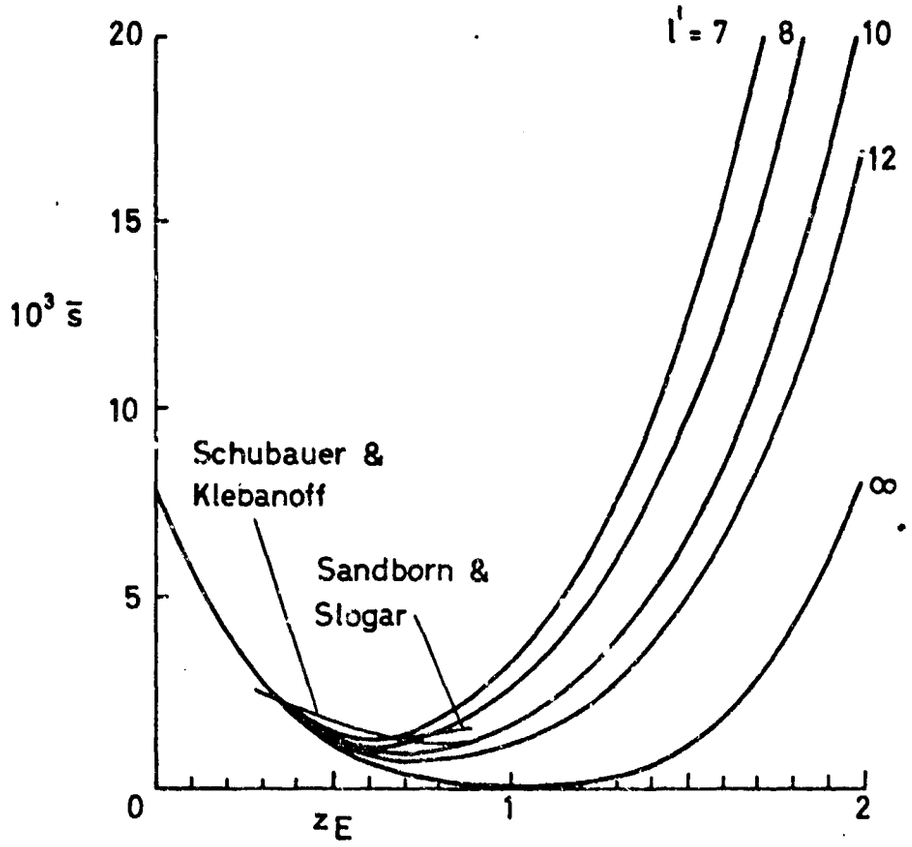

Fig. 24 The $\bar{s}(z_E, l')$ function for an impermeable wall corresponding to the constant-eddy-viscosity hypothesis, expressed by Equation (3.4-2)

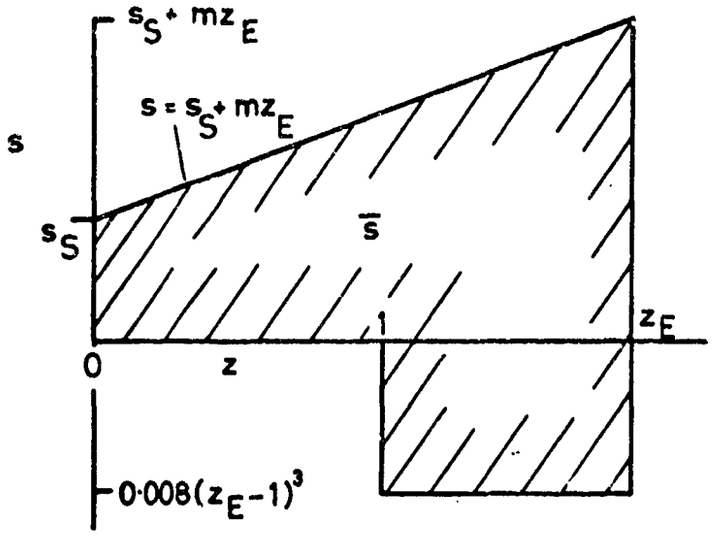

Fig. 25 The $s \sim z$ relation corresponding to the constant-viscosity hypothesis and the linear velocity profile of Equation (2.4-6). This diagram is the $z_E < 1$ counterpart of Figure 12, which was valid for $z_E < 1$

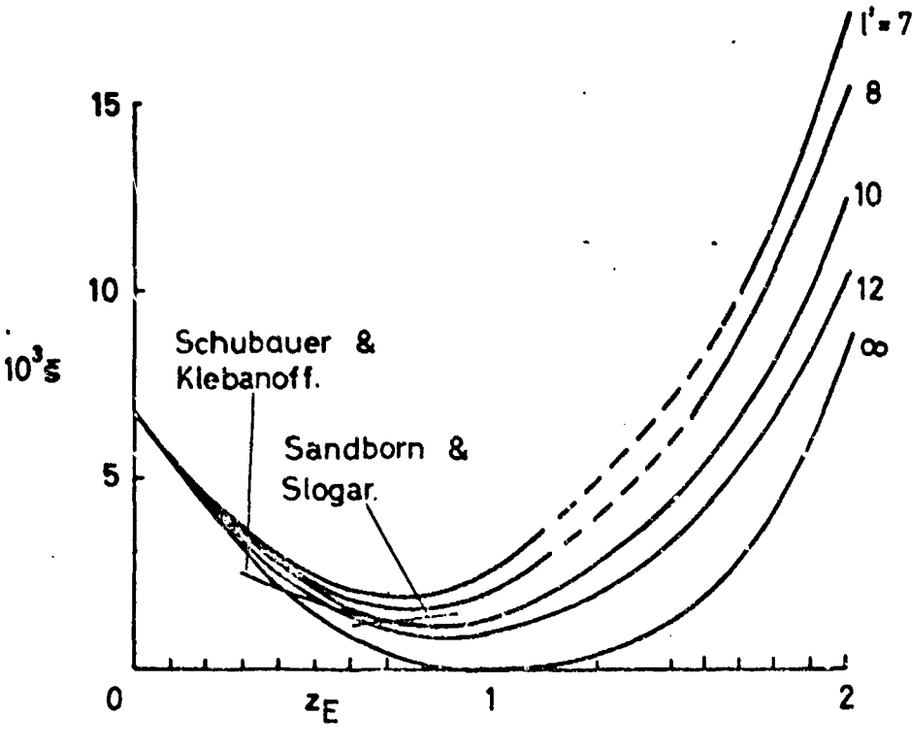

Fig. 26 The $\bar{s}(z_E, l')$ function for an impermeable wall deduced from Equation (3.4-5) and the entrainment law of Equation (3.4-4)

TURBULENT-BOUNDARY-LAYER BEHAVIOUR AND THE AUXILIARY EQUATION

by

John F. Nash

National Physical Laboratory,
Teddington, Middlesex, England

SUMMARY

In addition to the Kármán momentum-integral equation, two further equations are required for the purposes of calculating the development of the incompressible turbulent boundary layer - a "skin-friction law" and an "auxiliary equation". The problem of deriving a satisfactory form of auxiliary equation is a major one. Indeed, despite the effort devoted to this equation for many years, few derived forms of auxiliary equation can be relied upon to account for the boundary-layer development in more than a restricted number of cases.

As a contribution to the elucidation of the problem an examination is made of several sets of experimental data covering different types of pressure distribution. Among the data certain basic types of boundary-layer behaviour can be distinguished. The equilibrium boundary-layer may be regarded as a datum condition and the other types of behaviour are discussed in the context of tendencies towards, or departures from, equilibrium.

Simple forms of auxiliary equation are postulated and an examination is made of the extent to which they can be reconciled, even qualitatively, with the observed types of boundary-layer behaviour. It is shown that several forms of the equation must be rejected as inadequate. The most economical form which appears to be capable of describing all the various trends of the data is a second-order differential equation involving the shape factor. A limited number of comparisons with experiment indicate that values can be ascribed to the free constants in the equation which lead to quantitatively acceptable predictions.

SOMMAIRE

Pour le calcul du développement de la couche limite turbulente incompressible, il faut avoir non seulement l'équation de Kármán de quantité de mouvement mais deux autres équations, celle de la "loi de frottement de surface" et "l'équation auxiliaire". La recherche d'une forme satisfaisante de l'équation auxiliaire pose un problème majeur, et les travaux qui y ont été consacrés depuis des années n'ont abouti qu'à un petit nombre d'équations auxiliaires expliquant de manière satisfaisante le développement de la couche limite en dehors d'un nombre limité de cas particuliers.

Pour essayer de résoudre ce problème, divers systèmes de résultats expérimentaux, obtenus pour différents types de distribution de la pression, ont été étudiés. On a pu ainsi dégager plusieurs cas types de comportement de la couche limite. La couche limite à l'état d'équilibre peut être considérée comme base de comparaison, les autres types de comportement étant envisagés du point de vue de leur tendance à l'équilibre ou à l'altération de cet équilibre.

On propose quelques formes simples d'équations auxiliaires en examinant jusqu'à quel point elles peuvent être mises d'accord, même qualitativement, avec les types de comportement de la couche limite fournis par l'expérience. Certaines d'entre elles, inapplicables, doivent être rejetées. La forme la plus économique, qui semble tenir compte des divers aspects des données, est une équation différentielle du second degré mettant en jeu un facteur forme. Quelques comparaisons établies avec les résultats d'expérience montrent qu'il est possible de donner aux constantes libres de l'équation des valeurs permettant des prédictions satisfaisantes du point de vue quantitatif.

CONTENTS

LIST OF FIGURES

NOTATION

x,y	orthogonal coordinates, x measured along the surface
ρ	fluid density
ν	kinematic pressure
p	static pressure
u	velocity in the x-direction
u_e	velocity at the edge of the boundary layer
u_τ	friction velocity $(u_\tau^2 = \tau_w/\rho)$
τ_w	wall shear stress
C_f	local skin-friction coefficient $C_f = \frac{\tau_w}{\frac{1}{2}\rho u_e^2}$
δ	boundary-layer thickness
δ^*	displacement thickness
θ	momentum thickness
Re_θ	Reynolds number based on θ
H	"geometric" shape factor $(H = \delta^*/\theta)$
G	shape factor based on the velocity-defect profile, $\left[G = \left(\frac{2}{C_f}\right)^{\frac{1}{2}}\left(1 - \frac{1}{H}\right)\right]$
$\hat{G}$	value of G if the boundary-layer were in equilibrium at the local value of Π
Π	pressure-gradient parameter $\left(\Pi = \frac{\delta^*}{\tau_w}\frac{dp}{dx}\right)$
l	length scale
$\bar{x}$	nondimensional distance parameter

$$\left(\bar{x} = \int_{x_1}^{x} \frac{dx}{l}, \text{ with } l \text{ generally equal to } \delta^*\right)$$

α, β, λ constants in equation (22).

$f, f_1, f_2, \bar{f}, \bar{\bar{f}}, F, H_1, H_2, \phi, \psi$ and Ψ denote arbitrary functions.

The suffix o denotes initial values.

TURBULENT-BOUNDARY-LAYER BEHAVIOUR AND THE AUXILIARY EQUATION

John F. Nash

1. INTRODUCTION

The purpose of this paper is to discuss the two-dimensional, incompressible turbulent boundary-layer developing on a smooth, plane, unpermeable wall in an adverse pressure gradient.

Basic to most methods of treating the incompressible turbulent boundary-layer is the Kármán momentum-integral equation which expresses the rate of change of momentum-defect in terms of the pressure gradient and the wall shear stress:-

$$\frac{d}{dx}(\rho u_e^2 \theta) = \delta^* \frac{dp}{dx} + \tau_w . \qquad (1)$$

If the pressure p (or the velocity, u_e, at the edge of the boundary-layer) is given as a function of x, Equation (1) contains three unknowns: the momentum thickness, θ, the displacement thickness, δ^*, and the local wall shear stress, τ_w. Thus, for the purposes of calculating the development of the boundary layer, two further equations involving these quantities are required. Using the conventional nomenclature, these are referred to as the "skin-friction law", and the "auxiliary equation" or "shape-factor equation".

As usually formulated, skin-friction laws relate the local wall shear stress to a Reynolds number based on a length scale typical of the boundary-layer thickness and a parameter (such as H, $= \delta^*/\theta$) which describes the shape of the velocity profile. A brief review of some skin-friction laws in current use was made in Reference 1.

The auxiliary equation essentially describes the effect of pressure gradients on the shape of the mean velocity profile. Attempts have been made for more than thirty years to derive a satisfactory form of auxiliary equation but recent reviews of this problem[2, 3] have shown that few forms of this equation can be relied upon to account for the boundary-layer development faithfully in more than a limited number of cases.

In the next Section a brief discussion will be made of the principal forms of auxiliary equation to be found in the literature. The point will be made that most of these were originally based on data relating to only one type of boundary-layer development. As a contribution to the general work in this field an examination is made in Section 3 of the various types of boundary-layer behaviour which can be distinguished from an analysis of existing experimental data. Finally, in Section 4

simple forms of auxiliary equation will be discussed in relation to these types of boundary-layer behaviour, and an attempt will be made to find an equation which will account for them at least qualitatively.

2. REVIEW OF EXISTING AUXILIARY EQUATIONS

2.1 Most published forms of the auxiliary equation (e.g. see Ref.2) are formulated on the assumption that the mean velocity profiles in the turbulent boundary layer reduce to a two-parameter family, i.e. that they can be described adequately by a thickness parameter and a single "shape factor". Thus the auxiliary equation takes the form of an expression relating the shape factor and, usually, its derivatives to the Reynolds number and the pressure gradient.

Basically, there are two types of shape factor in general use. One type is a parameter based simply on the geometry of the velocity profile; the other type involves the wall shear stress in addition. Most of the auxiliary equations found in the literature are formulated in terms of the geometric type of shape factor. In some cases this is the ratio, H, of displacement to momentum thickness; in others the shape factor is based on such ratios as

$$\left(\frac{u}{u_e}\right)_{y=\theta} \quad \text{or} \quad \frac{\delta - \delta^*}{\theta} .$$

There is no essential difference between any of these geometric shape factors and, in the light of the assumption that the velocity profiles form a two-parameter family, they can all be related to one another (at least in principle). Accordingly, our remarks will refer explicitly to auxiliary equations based on H but they can be taken to apply to equations involving other geometric shape factors also.

This interchangeability of shape factors does not extend to those which involve the wall shear stress. Among these are Clauser's parameter, G, which is based on the velocity-defect profile[4], and Coles' wake-component coefficient[5] which is also used by Spalding[6]. Reference to shape factors of this category will be left to another Section.

2.2 Despite the confusing variety of auxiliary equations in current use, only two basic types can be distinguished. The first is represented by the method of Buri[7] and is a direct analogue of the Polhausen method for the laminar boundary-layer and the numerous later methods which owe their inspiration to the Polhausen approach (e.g. see Ref.8). Buri postulated that the shape factor, H, was a function of the Reynolds number and the pressure gradient:-

$$H = f_1\left(Re_\theta, \frac{\theta}{u_e}\frac{du_e}{dx}\right) . \qquad (2)$$

This form of the auxiliary equation has never commanded much attention, largely as a result of Prandtl's criticism[9] that it ignored the effects of the upstream history of the boundary layer. In the light of more recent knowledge it would be fairer to say

that it is valid so long as the layer is in local equilibrium at each streamwise station. More will be said about this point later in the paper.

2.3 The second form of the auxiliary equation is represented by some thirteen methods listed by Rotta[2] to which must be added recent methods such as Head's[10]. This form can be written

$$\theta \frac{dH}{dx} = f_2\left(H, Re_\theta, \frac{\theta}{u_e}\frac{du_e}{dx}\right). \qquad (3)$$

By virtue of its being a differential equation of the first order in H, Equation (3) requires the specification of an initial value of H with which to start the calculation. Thus in broad terms Equation (3) contains a mechanism by which the upstream history can be taken into account in so far as it affects the velocity profile. Consequently, as far as this auxiliary equation is concerned, two boundary layers with the same initial velocity profile subsequently subjected to the same pressure distribution will develop alike whether or not their previous history was the same. No provision is made for the possibility that their initial shear-stress distributions could be dissimilar. The distribution of shear stress across the boundary-layer is, of course, related not to the local velocities in the layer but, via the equation of motion, to their derivative with respect to x. Therefore some estimate of the effect of the initial shear distribution could be made by specifying, in addition to H, the initial value of dH/dx, say. Equation (3) would then need to be replaced by a second-order differential equation in H. So far as is known to the author, no attempt to do this has been reported.

It is not intended, here, to give a detailed discussion of the merits or demerits of the various auxiliary equations grouped under Equation (3). Useful work has already been done in this respect by Rotta[2] and Thompson[3]. Their work has shown that the confidence with which the state of the art has been viewed in many of the text books could not be substantiated and that many of the auxiliary equations have a severely limited validity of application. Essentially they are correlations of experimental data whether or not some physical concept - for instance the kinetic energy or moment - of - moment equations (e.g. see Ref.12), or the entrainment equation (Refs.6,10,11) - has been invoked as the basis for the correlation. Consequently much depends on the range of types of boundary-layer development which has been examined in the correlation. Nearly all the auxiliary equations in the literature have been derived from an analysis of boundary-layers of a single type, namely, where the shape factor H increases with distance downstream. This is typical of boundary-layers growing on aerofoils or in diffusers. Bearing this in mind it is not difficult to see why these methods are of doubtful validity when applied to either equilibrium boundary layers (where H is approximately constant) or boundary-layers where H is decreasing with x (see Refs.2,3). Even when applied to the same sort of boundary-layer development as the ones on which they were originally based, some auxiliary equations have exhibited limitations such as an unlikely sensitivity to initial conditions[13]. In this respect, however, it must be pointed out that there is little experimental data to elucidate the question of the extent to which initial conditions affect the boundary-layer development at appreciable distances downstream.

3. TYPES OF BOUNDARY-LAYER BEHAVIOUR

3.1 The equilibrium boundary-layer

The first type of boundary-layer behaviour which we shall discuss, and the most important from a fundamental standpoint, is the equilibrium boundary-layer. This topic has received considerable attention in recent years. The early experimental work of Clauser[4, 14] and the analysis of Rotta[15] served to demonstrate that equilibrium boundary-layers in non-zero pressure gradients could exist (at least in an approximate form) on a smooth surface. Their work has been added to by a number of theoretical treatments, among which those of Townsend[16] and Mellor and Gibson[17] are important in the present context, and by the recent experiments of Bradshaw[18].

The particular aspect of equilibrium boundary-layers which is of prime importance in our present work is the observation that a certain type of streamwise pressure distribution can support a boundary-layer growth characterised by similarity of the velocity-defect profiles. The pressure distribution is one of constant "severity" in so far as the ratio of pressure-gradient forces to skin-friction forces acting on an element dx of boundary-layer is the same at each streamwise station. The appropriate pressure-gradient parameter which expresses this ratio is Π (e.g. see Ref. 2) where

$$\Pi = \frac{\delta^*}{\tau_w}\frac{dp}{dx} \tag{4}$$

and Π is independent of x for an equilibrium boundary-layer. For a particular value of this pressure-gradient parameter, the velocity-defect profile in the boundary-layer has a given shape independent of Reynolds number:-

$$\frac{u_e - u}{u_\tau} = f\left(\frac{y}{\delta}\right). \tag{5}$$

Clauser[4] has suggested that a convenient "shape factor" for describing the velocity-defect profile could be defined by

$$\frac{\int_0^1 f^2 d\left(\frac{y}{\delta}\right)}{\int_0^1 f d\left(\frac{y}{\delta}\right)}. \tag{6}$$

G can also be related to the geometric shape factor H by

$$G = \left(\frac{2}{C_f}\right)^{\frac{1}{2}}\left(1 - \frac{1}{H}\right). \tag{7}$$

The value of G is about 6.5 for the flat-plate case and tends to infinity for the equilibrium boundary-layer with zero wall shear stress[19].

Thus for equilibrium boundary-layers G is a unique function of Π. Some relevant experimental data is shown in Figure 1 along with the relation between G and Π indicated by the theories of Townsend[16] and Mellor and Gibson[17]. The former is restricted to values of Π greater than about 2; the latter makes no such restriction but states that no equilibrium boundary-layer can exist for values of Π less than -0.5. Over the common range Mellor and Gibson predict higher values of G than are given by Townsend's theory. Judging by the experiment of Bradshaw[18] and Clauser's "Boundary-layer I"[5], Townsend's theory seems the more accurate. Clauser's "Boundary-layer II" has a measured value of G higher than that predicted by either theory if one takes the value of Π indicated in Reference 14, namely 7. However Mellor and Gibson found from an examination of Clauser's data that the actual value varied between about 6 and 13 over the course of development of the layer. Thus it would seem that the value of 7 is to be taken only as a guide and the discrepancy indicated in Figure 1 is of little significance. For small values of Π, Mellor and Gibson's theory appears to predict values of G which agree satisfactorily with experiment.

For the purposes of our later calculations a relation between G and Π will be required covering the whole range of Π. An empirical curve has therefore been drawn in Figure 1 representing a synthesis of experiment and theory. This curve is given by the function

$$G = 6.1(\Pi + 1.81)^{\frac{1}{2}} - 1.7 . \qquad (8)$$

3.2 Tendency towards equilibrium

If the pressure distribution appropriate to a particular equilibrium boundary-layer is set up but the initial value of G is not the equilibrium value, one of two things can happen. If the boundary-layer has "downstream stability" (see Ref. 2) the value of G will approach the equilibrium value $\hat{G}$, say, as the layer progresses downstream; if it is "unstable" the value of G will diverge from the equilibrium value. The only direct experimental evidence there is concerning the approach to equilibrium relates to the flat plate case. Tillmann[20] and Klebanoff and Diehl[21] carried out tests to observe the downstream behaviour of constant-pressure boundary-layers which had been disturbed initially giving a value of G higher than 6.5. Recently one of Bradshaw's experiments[18] consisted of setting up an equilibrium boundary-layer and subsequently (i.e., downstream of some x-position) removing the pressure gradient so that the layer could return to the flat-plate type.

It might be supposed that, at least some distance downstream of the disturbing agency, the return to equilibrium would exhibit some universality independent of the particular form of the disturbance. For instance, the rate of change of G might be uniquely related to the amount, $G - \hat{G}$, say, by which G was out of equilibrium. Such considerations lead us to inquire whether an expression of the form

$$l \frac{dG}{dx} = f(G - \hat{G}) \qquad (9)$$

has any general validity. In Equation (9) $\hat{G}$ is the particular equilibrium value of G (6.5 for the flat-plate case) and l is some length scale typical of the boundary-layer thickness. Integration of Equation (9) yields an expression for G :-

$$G - \hat{G} = F(\bar{x}) \tag{10}$$

where

$$\bar{x} = \int_{x_0}^{x} \frac{dx}{l} \tag{11}$$

and x_0 is an arbitrary constant. Three sets of experimental data are shown in Figure 2 in the form of a plot of G against $\bar{x}$, using δ^* for l, and choosing x_0 such that all the curves pass through the point "A". Figure 2 indicates little evidence that a universal function of the form of Equations (9) or (10) exists; now does it seem likely that a better correlation could be achieved by using some other length scale in Equation (11).

The failure of this exercise casts considerable doubt on the suggestion that boundary layers with the same initial velocity profile will develop in the same way if subjected to the same pressure distribution downstream of the initial station. It will be recalled that this assertion is implicit in nearly all the auxiliary equations appearing in the literature (see Section 2 above).

Before passing to the next topic it is instructive to note from Figure 2 how long it can take for a disturbance to die out. The data of Klebanoff and Diehl, and Bradshaw indicate that G is unlikely to approach the equilibrium value closely for a distance of hundreds of times the displacement thickness. This observation strongly supports the comments of Coles in Appendix A of Reference 22.

3.3 Departures from equilibrium

The equilibrium boundary-layer develops in a pressure gradient of constant severity (see Section 3.1 above). The parameter Π (Eqn. (4)) is constant with respect to x and the shape factor G is also constant. On the other hand, if the severity of the pressure gradient changes, the boundary-layer will cease to be in equilibrium and both Π and G will be functions of x. In a sense Π can be regarded as the independent and G the dependent variable, or, to use Clauser's "black-box" terminology[14], there is a certain response in G to a given input function $\Pi(x)$.

The severity of the pressure gradient can either increase ($d\Pi/dx > 0$) or decrease ($d\Pi/dx < 0$). We shall now proceed to examine experimental data relating to each of these possibilities.

An increasingly "severe" pressure gradient is typical of the boundary-layer developing on an aerofoil surface or in a diffuser. The actual pressure gradient dp/dx may be constant but due to the increase in δ^* and the decrease in τ_w with increasing x, the value of Π increases with x, reaching infinity at a separation point (zero τ_w). Some experimental results obtained under such conditions are shown in Figure 3* as a plot of G against Π. Since Π is increasing with x each curve represents a trajectory whose sense is indicated by the arrow head.

---

* To reduce the data to this form one requires values of the wall shear stress. These were found using the skin-friction law derived in Reference 1.

One of the important features of the data in Figure 3 is the fact that the curves lie close to the curve $\hat{G}(\Pi)$ which represents the locus of all possible equilibrium boundary-layers. [This curve has been drawn according to Eqn.(8).] The significance of a trajectory which coincides with the curve $\hat{G}(\Pi)$ is not, of course, that the boundary-layer is in equilibrium[1] but that the variation in shape factor is the same as if the layer were passing through each possible equilibrium state. This situation might be referred to as "local equilibrium" at each streamwise station. To illustrate the point further Figure 4 shows the variations in H corresponding to the spread of the data in Figure 3 about the curve $\hat{G}(\Pi)$. The dotted curves represent the loci of points for which H is the given percentage above or below the value corresponding to "local equilibrium" at a Reynolds number (Re_θ) of 10^4. It will be noted that the data lie within about 5 or 10 percent of the "equilibrium" values of H. One might expect a boundary-layer trajectory to remain close to the $\hat{G}(\Pi)$ curves so long as the value of Π was increasing very slowly. However this does not seem to be a necessary condition. The curve in Figure 3 derived from Schubauer and Klebanoff's data[23] is close to the "local equilibrium" condition although a typical value of $\delta^* d\Pi/dx$ is 0.3 (when $\Pi = 8$).

To turn to the case where the severity of the pressure gradient is decreasing, Figure 5 shows some experimental data presented in a similar way to that in Figure 3. The data of Ludwieg and Tillmann[24] relate to the case where Π first increases with x and subsequently decreases. Bradshaw's boundary layer[18] is initially in equilibrium with $\Pi = 5.5$; subsequently Π falls to zero.

Compared with the data in Figure 3, that in Figure 5 gives a quite different picture. Whereas for $d\Pi/dx > 0$ the trajectories were confined to a narrow corridor about the curve $\hat{G}(\Pi)$, in the present case the trajectories diverge markedly from the equilibrium locus. This is most evident in the cases where Π is initially increasing with x; the subsequent reduction of Π is accompanied by little sympathetic response in G. The impression is gained that some kind of "inertia" effect is causing G to continue increasing even after $d\Pi/dx$ has decreased to zero and is increasing negatively. Even in the case of the boundary-layer initially in equilibrium there is a "sluggish" response of G to the decrease in Π to zero. Nor is Π changing particularly rapidly. The maximum value of $-\delta^* d\Pi/dx$ in the case of Bradshaw's test was about 0.25; this may be compared with the value quoted above for the data of Schubauer and Klebanoff which lay close to the conditions of "local equilibrium".

3.4 Summary

Before proceeding to the next Section it will be useful to list the main points which have emerged from this study of the data:-

1. The equilibrium boundary-layer is specified by values of $G(= \hat{G})$ and Π which are independent of x. From a synthesis of experimental data and theory the function $\hat{G}(\Pi)$ can be defined fairly precisely.

---

[1] For instance, the shear-stress distribution would be expected to differ considerably from that in an equilibrium boundary-layer.

2. The rate at which an initially-disturbed, flat-plate boundary-layer tends to equilibrium is not determined solely by the initial value of the shape factor and the boundary-layer thickness. This would appear to indicate that in more general cases also knowledge of the pressure distribution downstream of some initial station together with the initial value of the shape factor is insufficient information from which to compute the boundary-layer growth.

3. Boundary-layers in pressure gradients of increasing "severity" ($d\Pi/dx > 0$) remain close to the conditions of "local equilibrium"; i.e. $G \simeq \hat{G}(\Pi)$. This appears to be true even if Π is changing quite rapidly.

4. Boundary-layers in pressure gradients of decreasing "severity" ($d\Pi/dx < 0$) depart markedly from the condition of "local equilibrium". This is particularly so in the case where $d\Pi/dx$ is initially positive but subsequently changes sign, suggestive of some kind of "inertia" effect.

4. THE AUXILIARY EQUATION

4.1 We return now to the problem of the auxiliary equation. Stated briefly the problem is one of finding some algebraic or differential equation involving the shape factor which exhibits a response to various changes of pressure gradient which is similar to that observed in the experimental data. It was seen in the previous Section that certain basic trends can be distinguished in the data and that these trends can be interpreted in the context of tendencies towards, or departures from, a condition of "local equilibrium". It would seem that this way of examining the data is an important one which can make many of the observed trends meaningful and coherent. Moreover it is likely to facilitate the process of deriving a satisfactory auxiliary equation.

With the object of making maximum use of this concept of variations about an equilibrium state, G is selected as the appropriate shape factor, and Π becomes the corresponding pressure-gradient parameter. A fundamental requirement of our auxiliary equation is that a solution must exist of the form

$$\left.\begin{aligned} G &= \text{constant} \\ \Pi &= \text{constant} \end{aligned}\right\}.$$

4.2 One possibility is the algebraic auxiliary equation:-

$$G = \hat{G}(\Pi) . \tag{12}$$

Clearly this equation satisfies the conditions for equilibrium boundary-layers. Moreover, as was seen in Section 3.3 above, it is a reasonably good approximation in the case of boundary-layers of the "aerofoil" or "diffuser" type, (i.e. for which $d\Pi/dx > 0$). If a given form for Equation (12) is assumed - Equation (8) for example - together with a suitable skin-friction law, the geometric shape factor, H , can be expressed as a function of Re_θ and the local pressure gradient:-

$$H = H\left(Re_\theta , \frac{\theta}{u_e}\frac{du_e}{dx}\right) \tag{13}$$

which is identical to Equation (2). If the necessary calculations are performed one does not arrive at an expression of the same detailed form as Buri's, namely

$$H = H\left(\frac{\theta Re_\theta^{\frac{1}{4}}}{u_e}\frac{du_e}{dx}\right) \tag{14}$$

but one more nearly of the form

$$H = H_1(Re_\theta) + H_2\left(\frac{\theta}{u_e}\frac{du_e}{dx}\right). \tag{15}$$

Nevertheless, in so far as Equation (13) represents his fundamental assumption Buri's work appears to be confirmed.

On the other hand Equation (12) is incapable of describing the return to equilibrium following a perturbation - indeed perturbations from equilibrium are themselves inadmissible - nor can it account for the type of observed behaviour illustrated in Figure 5 for pressure gradients of decreasing "severity".

4.3 If Equation (15) is equivalent to Buri's approach, an auxiliary equation corresponding to that of most other investigators (see Eqn.(3)) would be of the form

$$\frac{dG}{d\bar{x}} = \Phi(\Pi, G) \tag{16}$$

with $\bar{x}$ as a non-dimensional distance defined, say, by

$$d\bar{x} = \frac{1}{\delta^*}dx . \tag{17}$$

A form similar to this has been suggested by Rotta[2]. If the function Φ in Equation (16) is of a form which vanishes for $G = \hat{G}(\Pi)$ the equilibrium case would be taken into account. Thus we might postulate some expression like

$$\frac{dG}{d\bar{x}} = \phi(\Pi) . \ (G - \hat{G})^n . \tag{18}$$

Equation (18) also goes some way to accounting for a return to equilibrium following some disturbance, with ϕ and n determining the degree of downstream stability. However the remarks in Section 2.2. should serve to show that no combination of values of $\phi(0)$ and n can lead to an expression which can account *quantitatively* for all the data in Figure 2. This is because the experimental results indicate different degrees of stability for the same value of G.

Passing to the cases where Π is a function of x this problem of fitting either Equation (16) or Equation (18) to the data becomes even more difficult. Figures 3 and 5 show that, at any given value of Π, the data are not even consistent as far as the *sign* of stability is concerned, at least so long as the "stability" is interpreted in the sense of Equations (16) or (18). Furthermore Equations (16) or (18)

contain no mechanism for taking into account the apparent "inertia" effect suggested by the data in Figure 5.

It soon becomes clear that an auxiliary equation of the form of Equation (16) is inadequate in describing the different types of behaviour which we have distinguished in the experimental data. The best that could be done with Equation (16) is to make it strongly stable about the "local equilibrium" condition. In this way the advantages of the simple form, Equation (15), would be retained, in that the equation would predict values of G close to $\hat{G}$ which is correct for the "aerofoil type" boundary-layers, and also in that the approach to equilibrium following an initial perturbation would be accounted for at least qualitatively. It is possible that this provides the explanation for the partial success of some of the auxiliary equations in the form of Equation (3), that of Reference 10 for example.

4.4 Some of the disadvantages of Equation (16) can be minimised by the use of an auxiliary equation formed by a combination of Equations (15) and (16). In a fairly general form this could be written as

$$\frac{dG}{d\bar{x}} = \Psi\left(\Pi, \frac{d\Pi}{d\bar{x}}, G\right). \tag{19}$$

However, this equation still cannot account for the different rates of approach to equilibrium exhibited by the data in Figure 2, nor for the apparent inertia effect suggested by the data in Figure 5. For these reasons it will not be considered further in this paper.

4.5 The two effects which it has not been found possible to account for - the return to equilibrium and the inertia effect - appear to demand that the auxiliary equation be of the second order in G. Starting with the former, it was seen in Section 3.2 that Equation (9) was inadequate because the behaviour of a flat-plate boundary-layer following a disturbance did not depend solely on the initial value of G. This point was mentioned in Section 2.3 also, and it was suggested that there were good grounds for expecting that the first derivative of the shape factor might be a necessary additional starting condition. Accordingly, we postulate that the approach to equilibrium can be described by

$$\frac{dG}{d\bar{x}} = \tilde{f}\left[\left(\frac{dG}{d\bar{x}}\right)_0, G - \hat{G}\right] \tag{20}$$

where the suffix o denotes an initial condition. Differentiating Equation (20) throughout with respect to $\bar{x}$ and eliminating $(dG/d\bar{x})_0$ between this new equation and Equation (20) leads to an expression of the form

$$\frac{d^2G}{d\bar{x}^2} = \bar{\tilde{f}}\left[\frac{d}{d\bar{x}}(G - \hat{G}), G - \hat{G}\right] \tag{21}$$

since $\hat{G}$ is assumed constant.

To give the function $\bar{f}$ some definite form we suggest

$$\frac{d^2G}{d\bar{x}^2} = \lambda\left\{\frac{d}{d\bar{x}}(G - \hat{G})\right\}^{\alpha}(G - \hat{G})^{\beta} . \qquad (22)$$

By a suitable choice of the constants λ, α and β, Equation (22) can, in fact, be fitted satisfactorily to the experimental data relating to the approach to constant-pressure equilibrium. But what is more important, however, Equation (22) also appears to be capable of describing, at least qualitatively, each of the other types of boundary-layer behaviour discussed in Section 3. In these latter cases, of course, $\hat{G}$ is not constant but is a function of x by way of its relations with $\Pi(x)$. Thus in the sense of Equation (22) $\hat{G}$ can be regarded as equivalent to a pressure-gradient parameter.

By trial and error the values of the coefficients λ, α and β in Equation (22) have been assessed to give satisfactory agreement with two or more sets of boundary layer data from each class discussed in Section 3. When a comparison is made with more data it may be necessary to modify these assessments, but the provisional values obtained are as follows:-

$$\left.\begin{aligned} &\frac{d}{d\bar{x}}(G - \hat{G}) > 0 :- \\ &\qquad \lambda = -0.25 , \ \alpha = 3 , \ \beta = -2 \\ &\frac{d}{d\bar{x}}(G - \hat{G}) < 0 :- \\ &\qquad \lambda = 5 , \ \alpha = 2 , \ \beta = -2 \end{aligned}\right\} . \qquad (23)$$

The distinction between the values of λ and α, depending on the sign of $d(G - \hat{G})/d\bar{x}$, is of prime importance in describing the different type of response of G according to whether $d\Pi/dx$ is positive or negative.

Since β is negative, Equation (22) is singular at $G = \hat{G}$. This behaviour has only local repercussions but it is an embarrassment for a number of reasons and it is suggested that the term $(G - \hat{G})^{-2}$ in Equation (22) be replaced by

$$\{(G - \hat{G})^2 + a^2\}^{-1}$$

where a is some small number. Insufficient experience of the equation has been gained so far to estimate the precise significance of the value of a but in the calculations it has been taken as 0.1.

Some comparisons between the new auxiliary equation and experimental data are shown in Figures 6 to 11. In this exercise the measured variation of Π and δ^* with x have been assumed as data and the variation of G with x has been calculated using Equation (22). In Figures 6 to 11 the solid curve represents the predicted values of G, the dots showing the intervals in the computation. The measured values of G are shown as square data points. In each case suitable initial values of G and dG/dx have had to be assumed in the calculations.

In Figures 6 and 7 two boundary-layers of the "aerofoil" type are considered. Equation (22) strongly portrays the tendency of boundary-layers of this type to remain close to the "local equilibrium" condition. The initial conditions need to be chosen fairly critically if the precise small departure from "local equilibrium" is to be correctly represented. If the initial values of G and dG/dx had been appreciably higher the predicted values of G would soon have coincided with the $\hat{G}$-curves. As it is, the small departure from "local equilibrium" is somewhat exaggerated. The significance of this sensitivity to initial conditions needs to be examined more carefully, but allowing for this the comparisons in Figures 6 and 7 can be regarded as satisfactory.

Figure 8 shows Sandborn's data[25] relating to his "zero suction" conditions. The pressure distribution is of the same general form as that considered in Figures 6 and 7 but the initial value of G is higher than the local value of $\hat{G}$. Again the agreement between the predicted and the measured values of G is very encouraging.

Figure 9 shows one of the sets of data obtained by Ludwieg and Tillmann[24]. This boundary-layer was subjected to a pressure gradient of initially increasing, and subsequently decreasing, "severity". Over the first part, with Π increasing, the value of G remains close to $\hat{G}$, as was the case in Figures 6 and 7. For larger values of x, where Π and, consequently, $\hat{G}$ are decreasing, G continues to increase - exhibiting the apparent "inertia" effect. The predicted variation of G with x is seen to represent these different types of behaviour adequately.

Another case in which Π decreases with increasing x is illustrated in Figure 10. This shows the data from Bradshaw's experiment in which a boundary-layer initially in equilibrium at a value of Π of about 5.5 is subsequently subjected to constant pressure. Π falls rapidly to zero but G responds only slowly and would take a distance of several hundreds of times the displacement thickness to approach the new equilibrium state closely. The predicted variation of G follows the observed behaviour very well.

For values of x greater than about 65 in, $\Pi = 0$, and the data in Figure 10 correspond to the case of a perturbed flat-plate boundary-layer. Figure 11 shows another set of data relating to this class of boundary-layers, namely the results of Klebanoff and Diehl for the 0.25 in rod (Ref. 21). Again the agreement between the measured and the predicted variation of G with x is very satisfactory.

These comparisons between calculations based on Equation (22) and experimental data are far from exhaustive. Nevertheless they serve to show that the proposed form of auxiliary equation can be fitted to a range of different types of boundary-layer development, and that it is probably the most economical one which can be. There is scope for a considerable amount of further work. Comparisons must be made with a far greater number of sets of data before Equation (22) can be used with confidence in making boundary-layer predictions. When further comparisons have been made it may, of course, be necessary to modify the values of the constants to give the best overall agreement.

5. CONCLUDING REMARKS

5.1 A review, in broad terms, of existing forms of the auxiliary equation, used in the calculation of the incompressible turbulent boundary layer in two dimensions, reveals two basic types. One is an algebraic equation involving the shape factor (Buri); the other is the familiar first-order differential equation on which attention has been concentrated for more than thirty years.

5.2 From an analysis of the experimental data certain fundamental types of boundary-layer behaviour can be distinguished. These are

(a) The equilibrium boundary-layer which is characterised by a pressure gradient of constant "severity" and similarity of the velocity-defect profiles.

(b) The return to equilibrium conditions following an initial perturbation.

(c) The departure from equilibrium when the "severity" of the pressure gradient is changing with x. Two possibilities can be considered, according to whether the "severity" of the pressure gradient is increasing or decreasing with x.

5.3 A synthesis of experiment and theory relating to equilibrium boundary-layers enables a relation to be defined fairly accurately between a shape factor G (based on the velocity-defect profile) and a pressure-gradient parameter

$$\Pi \left(= \frac{\delta^*}{\tau_w} \frac{dp}{dx} \right).$$

The function $G = \hat{G}(\Pi)$ thus represents all possible equilibrium boundary layers.

5.4 At least in the particular case of $\Pi = 0$, the rate at which the shape factor G approaches the equilibrium value $\hat{G}$, following an initial perturbation, is not solely determined by the initial value of G and the scale of the boundary-layer. From this it can be deduced that, in the general case also, knowledge of the initial velocity profile together with the subsequent pressure distribution is insufficient information from which to compute the development of the boundary-layer.

5.5 If the pressure-gradient parameter Π is a function of x the "response" of G takes alternative forms depending on the sign of $d\Pi/dx$. In cases where Π is continuously increasing G remains close to the value $\hat{G}$ corresponding to an equilibrium boundary-layer at the local value of Π. This situation might be referred to as "local equilibrium" at each streamwise station. On the other hand, if Π is decreasing with increasing x, G departs markedly from the "local equilibrium" condition. This type of behaviour appears to be accentuated when Π decreases subsequent to an initial increase, i.e. when $d\Pi/dx$ is first positive and then negative. Under such conditions G can continue increasing although the local value of $\hat{G}$ is decreasing with increasing x. By analogy with dynamical systems one might attribute this to a kind of "inertia" effect.

5.6 The main points which emerge from the examination of experimental data are used as a basis for evaluating various possible forms of auxiliary equation. It is seen that for an important class of boundary-layers - including typical ones on aerofoils or in diffusers - the assumption of "local equilibrium" could lead to predictions of H which are accurate to better than 10 percent under most conditions. This assumption is equivalent to the type of algebraic auxiliary equation proposed by Buri.

The use of an algebraic auxiliary equation implies that the upstream history of the boundary-layer has no significant influence on the shape factor except by way of its effect on the thickness of the layer. To take direct account of the effect of upstream history one requires a differential equation. But in view of the comment in 5.4, above, it would seem that a first-order auxiliary equation involving one initial condition (the initial value of the shape factor) must be inadequate. This goes some way to explaining why the use of a first-order equation is only marginally more effective in describing the various types of boundary-layer behaviour than the algebraic auxiliary equation mentioned in the previous paragraph.

The use of a second-order differential equation offers considerably more promise of success. Two initial conditions are required, and these may be regarded as specifying information about the initial velocity profile and shear-stress profile. The demand for an additional starting condition thus has a strong physical justification.

A tentative proposal is made as to a suitable form for a second-order auxiliary equation. It would seem that this new auxiliary equation is capable of describing all the types of boundary-layer behaviour listed above at least qualitatively, and a limited number of comparisons with experiment indicate that acceptable quantitative agreement can be obtained also.

The work described in this paper is at an interim stage. Further comparisons between the auxiliary equation proposed and experimental data will probably require some adjustment of the constants in the equation to maintain the best overall agreement. But in any event it is thought that the results which have already been obtained are of sufficient interest to merit presentation at this stage. Furthermore it is hoped that the paper will stimulate discussion of the more general points raised, and of their relevance and possible repercussions on the current work of other investigators.

ACKNOWLEDGEMENTS

The author is indebted to Prof. J.C. Rotta, of the Aerodynamische Versuchsanstalt Göttingen, for making available certain unpublished A.V.A. material.

The author also wished to acknowledge fruitful discussions with Mr. P. Bradshaw, of the Aerodynamics Division NPL, and Dr. B.G.J. Thompson, of the Engineering Laboratory, Cambridge University, during the course of this work.

The work described above has been carried out as part of the research programme of the National Physical Laboratory, and this paper is published by permission of the Director of the Laboratory.

REFERENCES

1. Nash, J.F. — *A note on skin-friction laws for the incompressible turbulent boundary layer.* NPL Aero Rep.1135. December 1964.

2. Rotta, J.C. — *Turbulent boundary-layers in incompressible flow.* "Progress in Aeronautical Sciences", Vol.II. Pergamon Press. 1962.

3. Thompson, B.G.J. — *A critical review of existing methods of calculating the turbulent boundary-layer.* ARC 26, 109. August 1964.

4. Clauser, F.H. — *Turbulent boundary-layers in adverse pressure gradients.* J. Aero. Sci. Vol.21, No.2. February 1954.

5. Coles, D. — *The law of the wake in the turbulent boundary-layer.* J. Fluid Mech., Vol.1, Part 2. July 1956, p.191.

6. Spalding, D.B. — *A unified theory of friction, heat transfer and mass transfer in the turbulent boundary-layer and wall jet.* ARC 25, 925. March 1964.

7. Buri, A. — *Eine Berechnungsgrundlage für die turbulente Grenzschicht bei beschleunigter und verzögerter Grundströmung.* Diss. eidgen. tech. Hochsch., Zurich 652. 1931. (Transl. as RTP Translation 2073).

8. Curle, N. — *The laminar boundary-layer equations.* "Oxford Mathematical Monographs". Clarendon Press. 1962.

9. Prandtl, L. — *The mechanics of viscous fluids. Turbulent friction layers in accelerated and retarded flows.* Vol.3 of "Aerodynamic Theory", W.F. Durand (Ed.). Julius Springer (Berlin). 1935.

10. Head, M.R. — *Entrainment in the turbulent boundary-layer.* ARC R & M 3152. September 1958.

11. Thompson, B.G.J. — *The calculation of turbulent boundary-layers.* Ph.D. Dissertation, Cambridge University. November 1963.

12. Tetervin, N.
Lin, C.C. — *A general integral form of the boundary-layer equation for incompressible flow with an application to the calculation of the separation point of turbulent boundary layers.* NACA Rep.1046. 1951.

13. - — *Incompressible aerodynamics.* Edited by B. Thwaites, Clarendon Press. 1960, p.89.

14. Clauser, F.H. — *The turbulent boundary-layer.* "Advances in applied mechanics", Vol.4. Academic Press. 1956, p.1.

15. Rotta, J.C. — *Beitrag zur Berechnung der turbulenten Grenzschichten.* Ing.-Arch. Heft 19. S.31. 1951.

16. Townsend, A.A. — *Equilibrium layers and wall turbulence.* J. Fluid Mech. Vol.11, Part 1. August 1961, p.97.

17. Mellor, G.L.; Gibson, D.M. — *Equilibrium turbulent boundary-layers.* Princeton Univ. M.E. Dept. Rep. FLD 13. November 1963.

18. Bradshaw, P. — (Unpublished work).

19. Townsend, A.A. — *The development of turbulent boundary-layers with negligible wall stress.* J. Fluid Mech., Vol.8, Part 1. May 1960, p.143.

20. Tillmann, W. — *Untersuchungen über Besonderheiten bei turbulenten Reibungsschichten an Platten.* Z.W.B., Kaiser-Wilhelm Inst., Göttingen. U & M 6627. 1945. (Transl. as ARC 9732).

21. Klebanoff, P.S.; Diehl, Z.W. — *Some features of artificially thickened fully developed turbulent boundary-layers with zero pressure gradient.* NACA Rep.1110. 1952.

22. Coles, D.E. — *The turbulent boundary-layer in a compressible fluid.* RAND Corp. Rep.R-403-PR. September 1962.

23. Schubauer, G.B.; Klebanoff, P.S. — *Investigation of separation of the turbulent boundary-layer.* NACA Rep.1030. 1951.

24. Ludwieg, H.; Tillmann, W. — *Untersuchungen über die Wandschubspannung in turbulenten Reibungsschichten.* Ing.-Arch. Heft. 17, S.288. 1949. (Transl. as NACA TM 1285).

25. Sandborn, V.A. — *Preliminary experimental investigation of low speed turbulent boundary-layers in adverse pressure gradients.* NACA TN 3031. October 1953.

26. Smith, D.W.; Walker, J.H. — *Skin-friction measurements in incompressible flow.* NASA TR R-26. 1959.

27. Newman, B.G. — *Some contributions to the study of the turbulent boundary-layer near separation.* Dept. of Supply (Australia). Rep.ACA-53. March 1951.

28. Schubauer, G.B.; Spangenberg, W.G. — *Forced mixing in boundary-layers.* J. Fluid Mech., Vol.8, Part 1, May 1960, p.10.

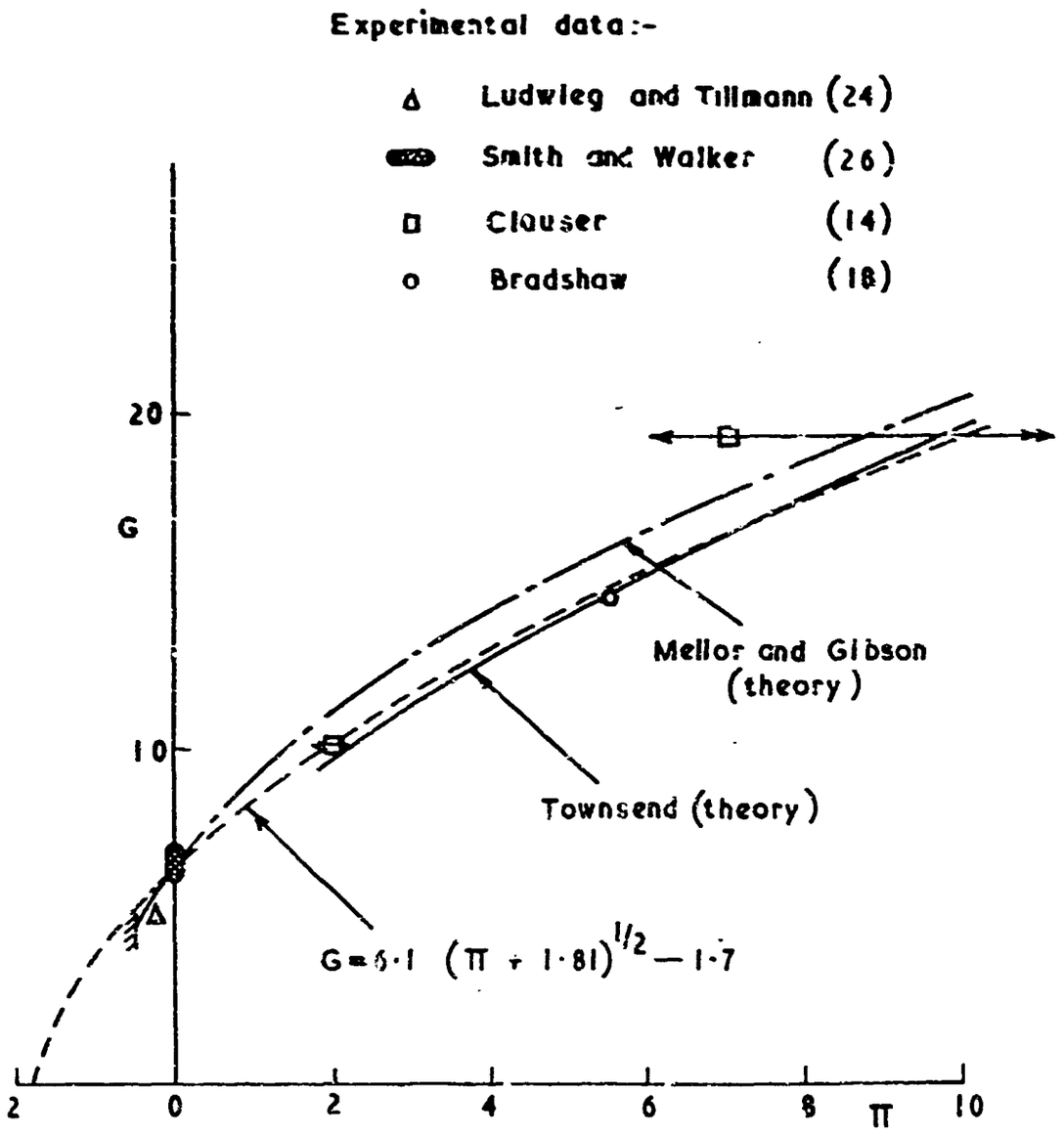

Fig. 1 Equilibrium boundary-layer - comparison between theory and experiment

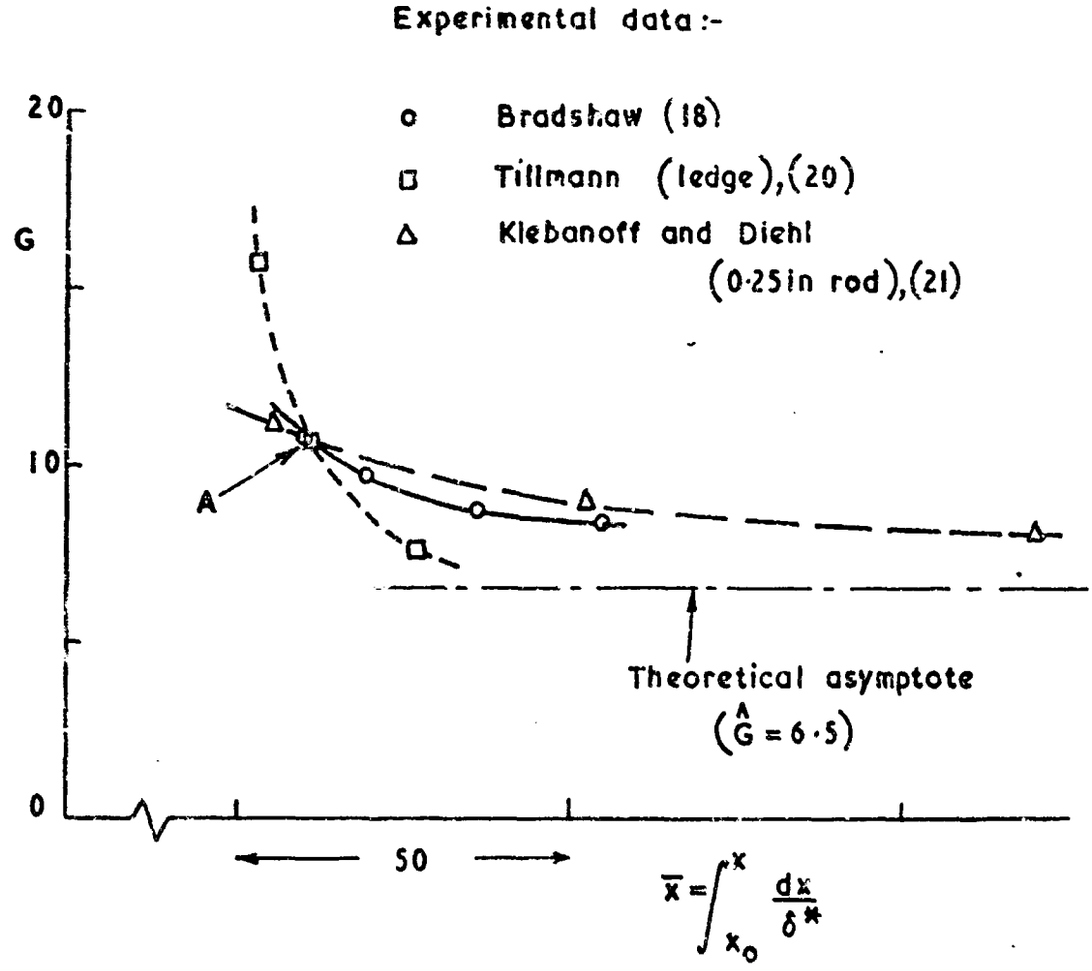

Fig. 2 Return to equilibrium ($\Pi = 0$) following a perturbation

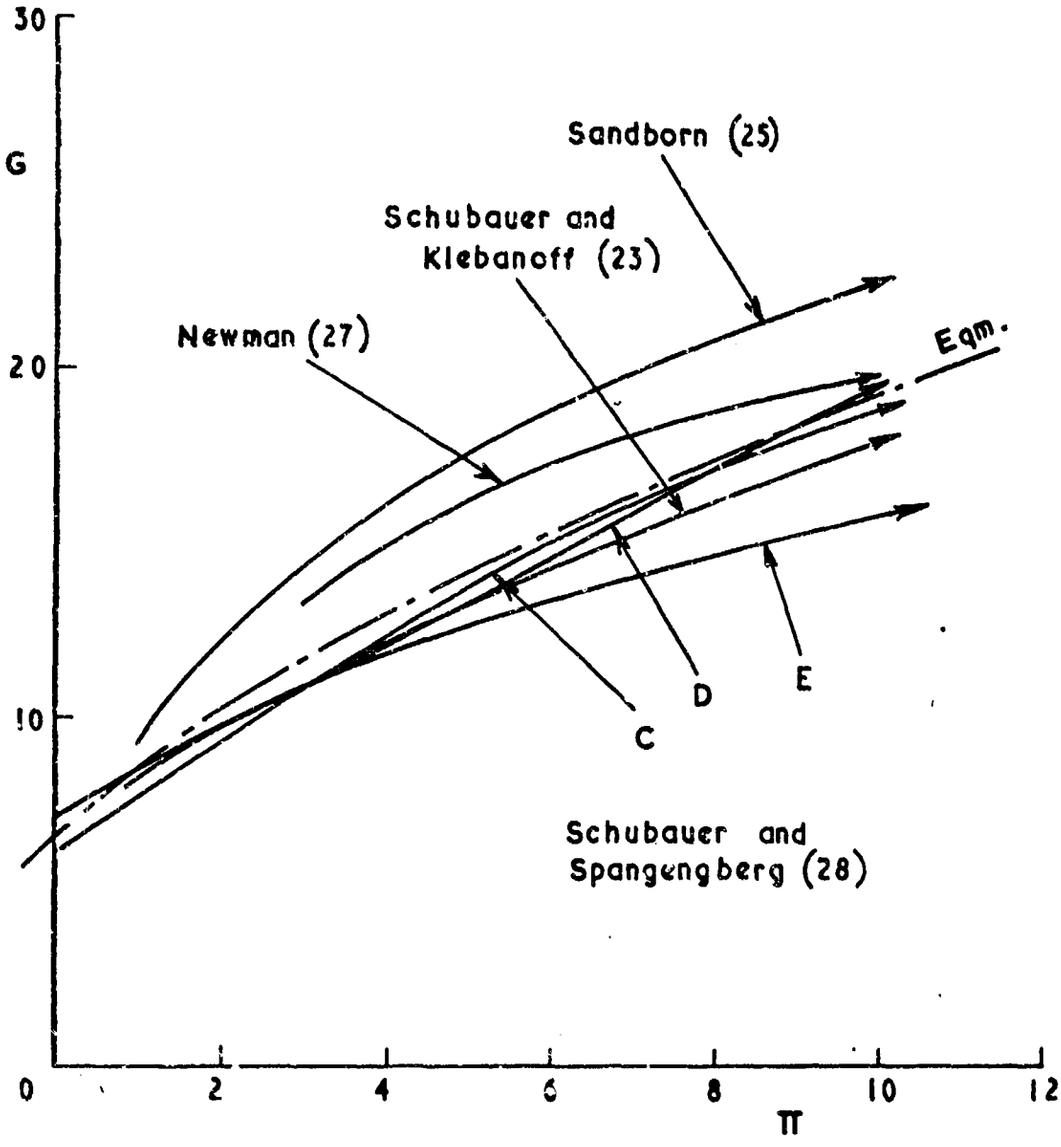

Fig. 3 Turbulent boundary-layer trajectories - augmentation of pressure gradient

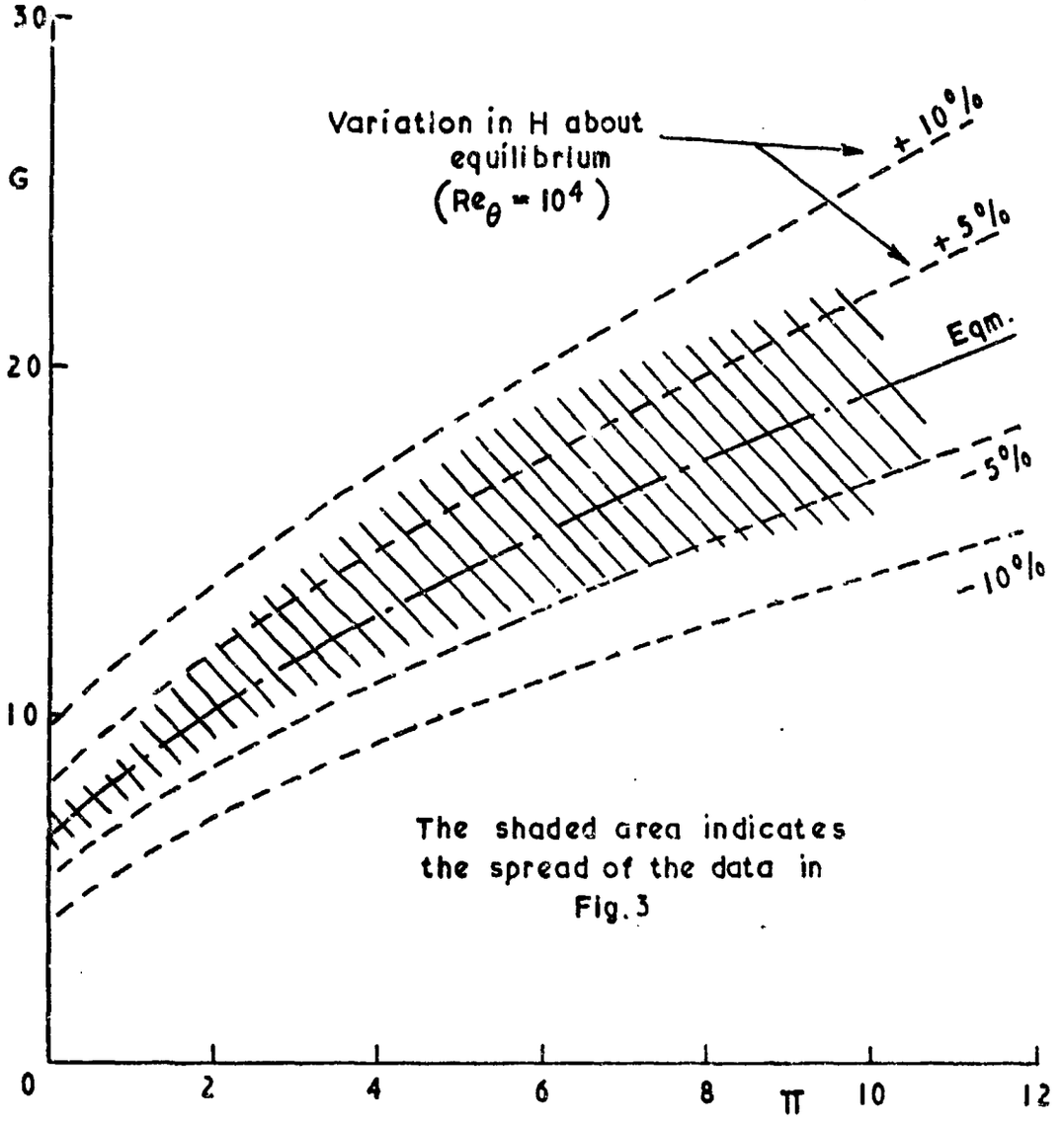

Fig. 4 Proximity to "local equilibrium" in boundary-layers with increasing pressure gradients

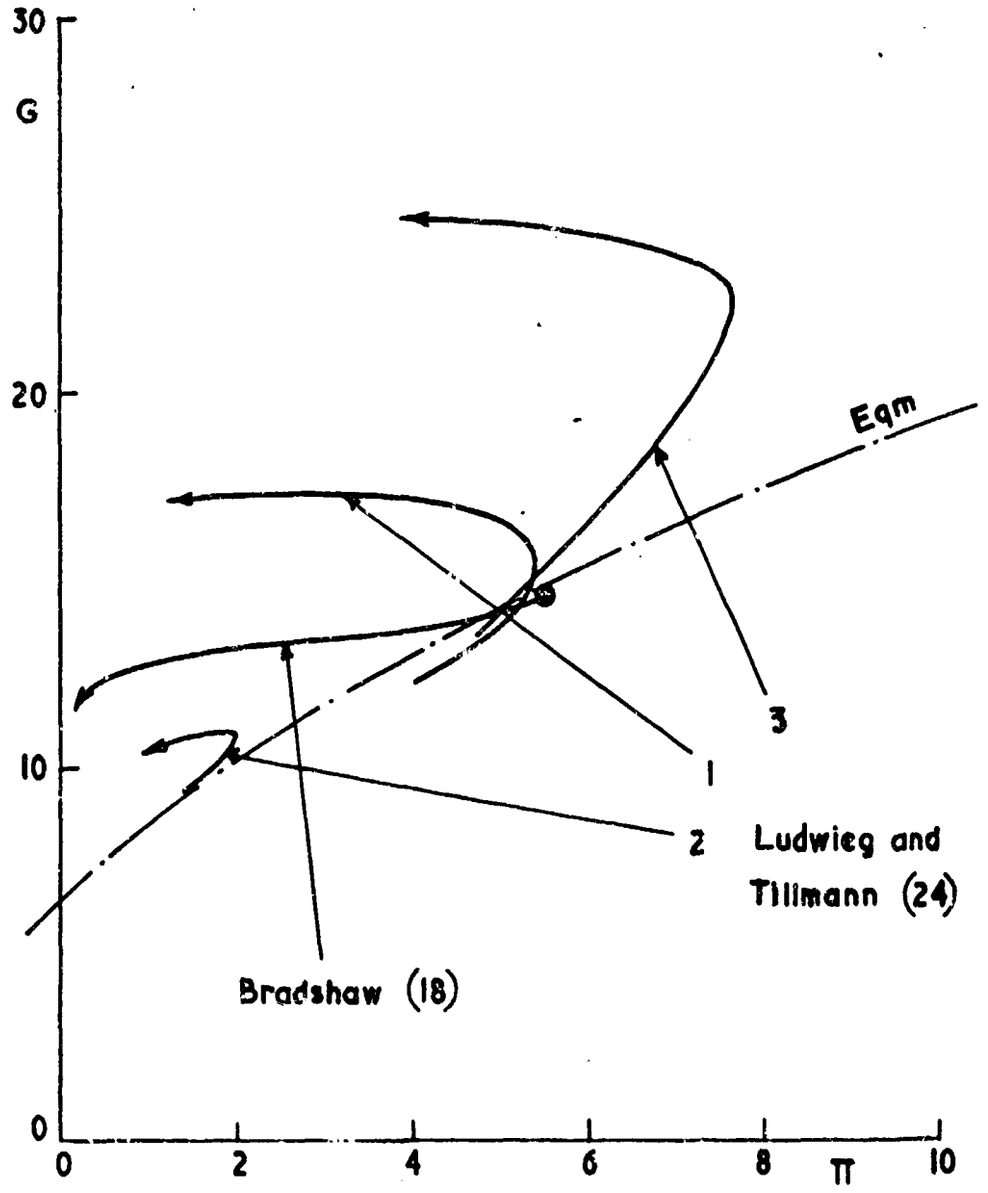

Fig. 5 Turbulent boundary-layer trajectories - alleviation of pressure gradient

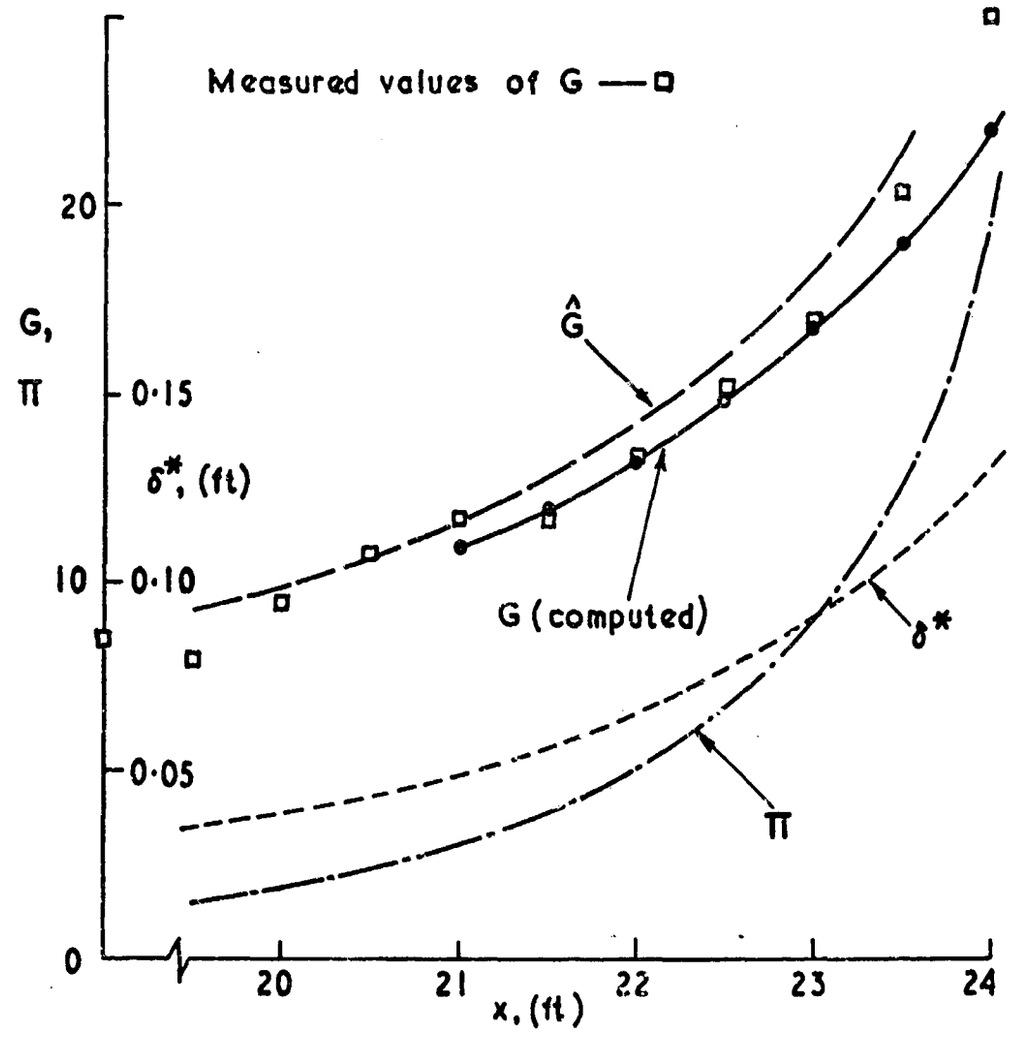

Fig.6 Comparison between new auxiliary equation and experiment: Schubauer and Klebanoff, (Ref.23)

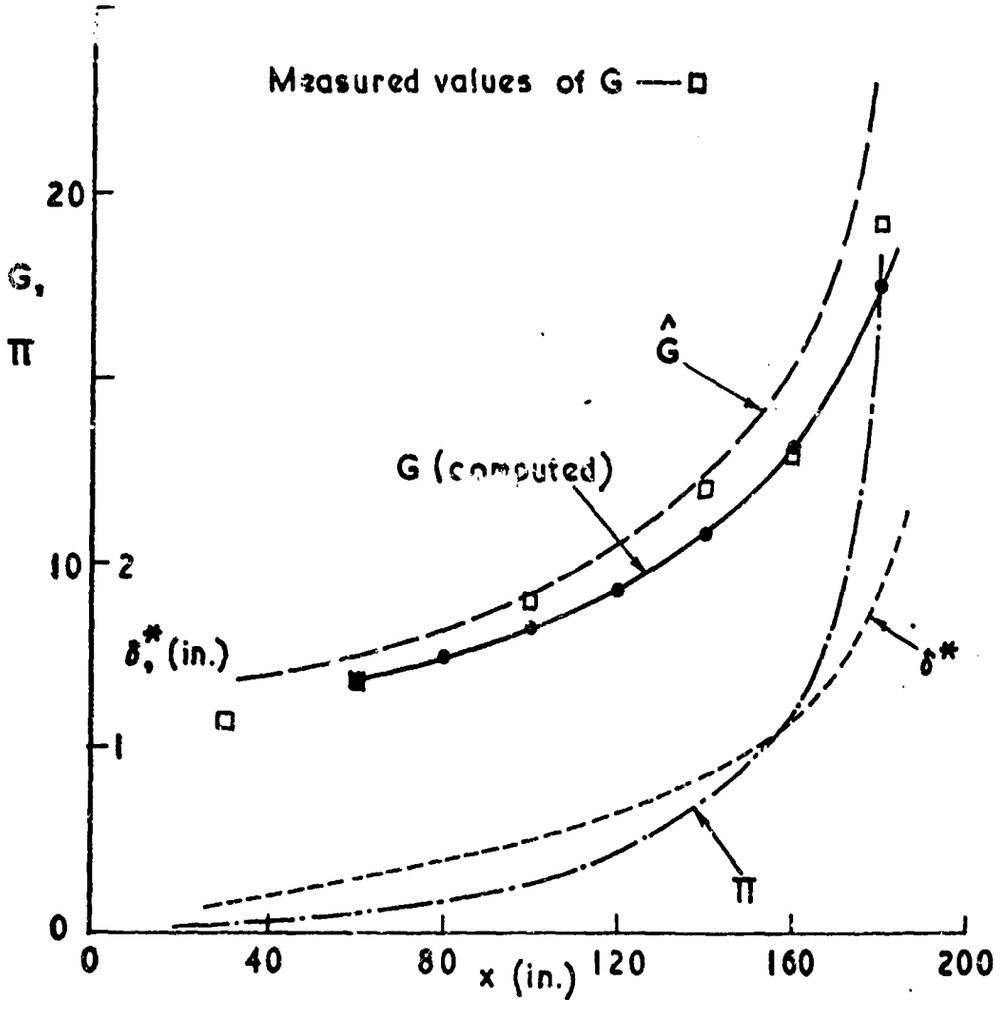

Fig. 7 Comparison between new auxiliary equation and experiment: Schubauer and Spangenberg (E), (Ref. 28)

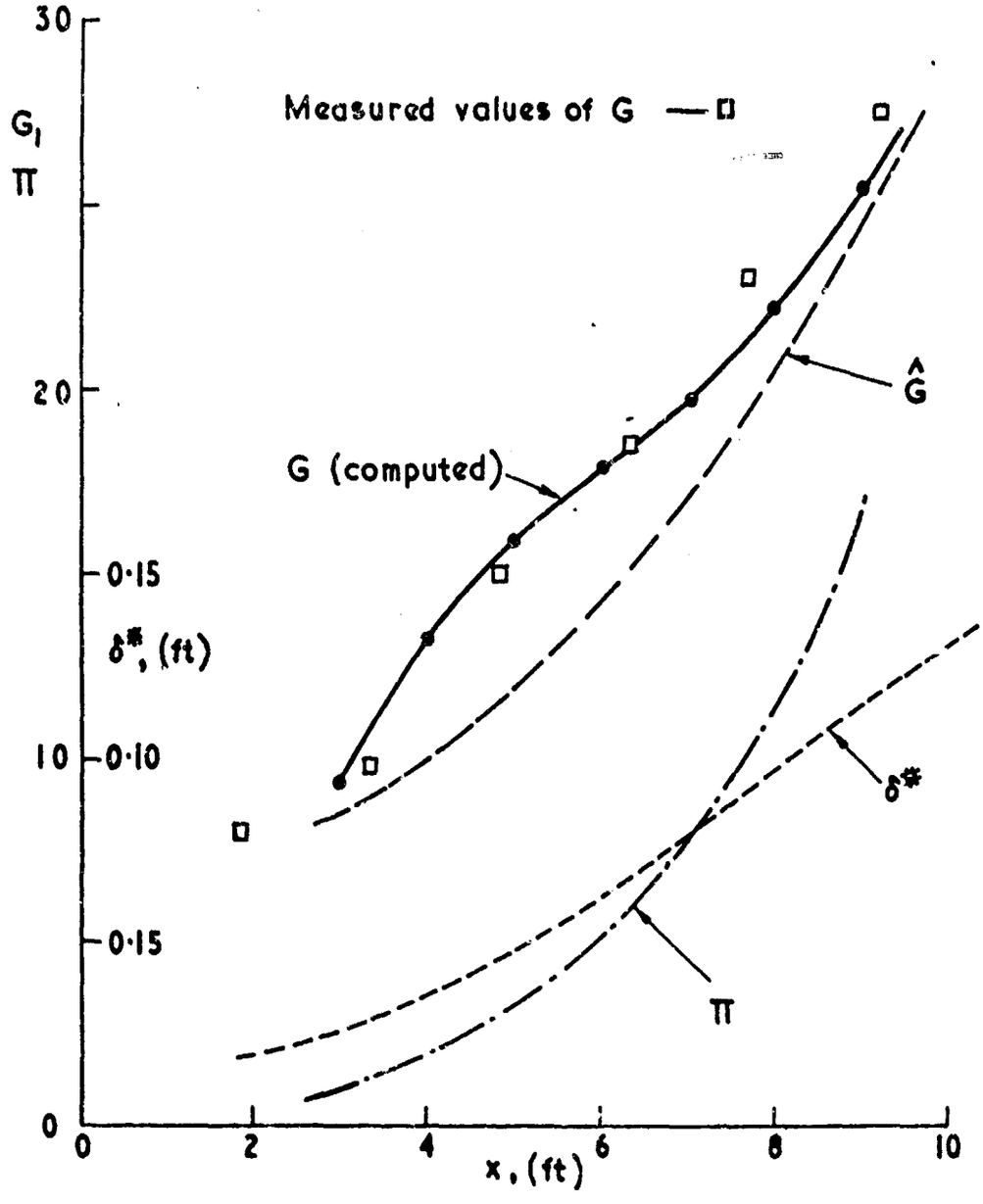

Fig.8 Comparison between new auxiliary equation and experiment: Sandborn, (Ref.25)

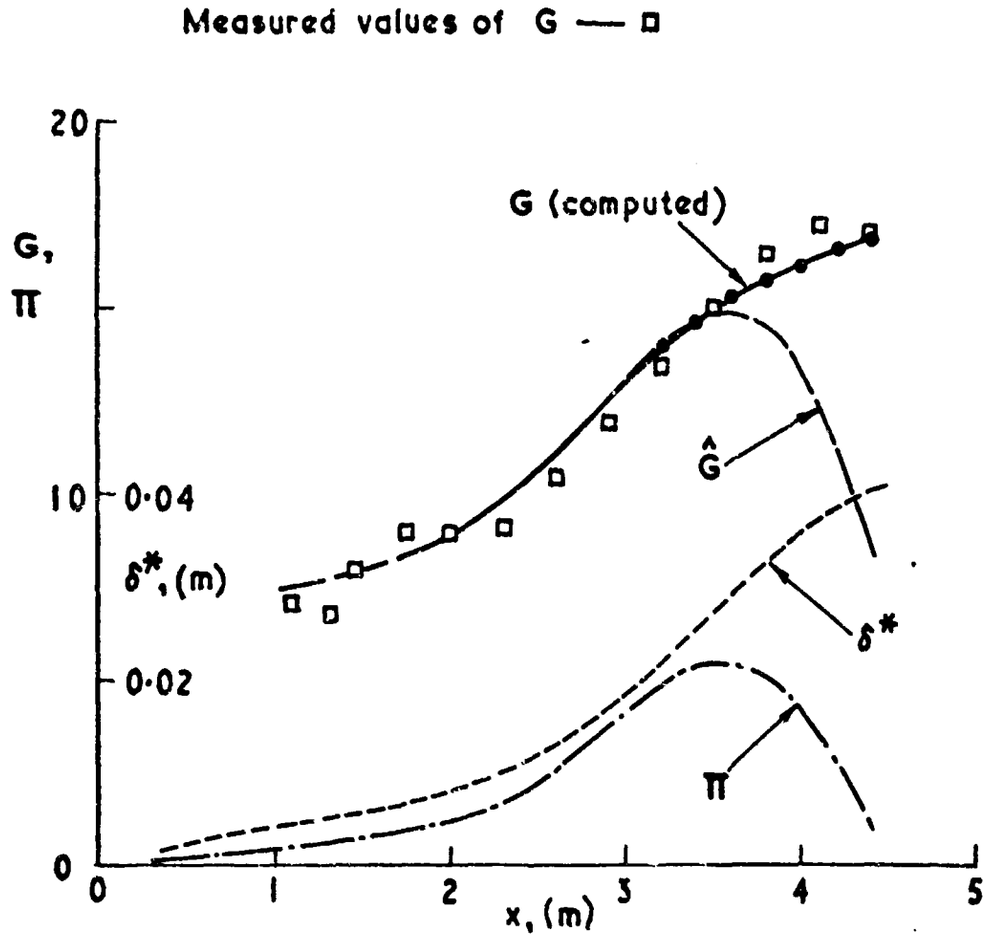

Fig.9 Comparison between new auxiliary equation and experiment: Ludwieg and Tillmann (I), (Ref. 24)

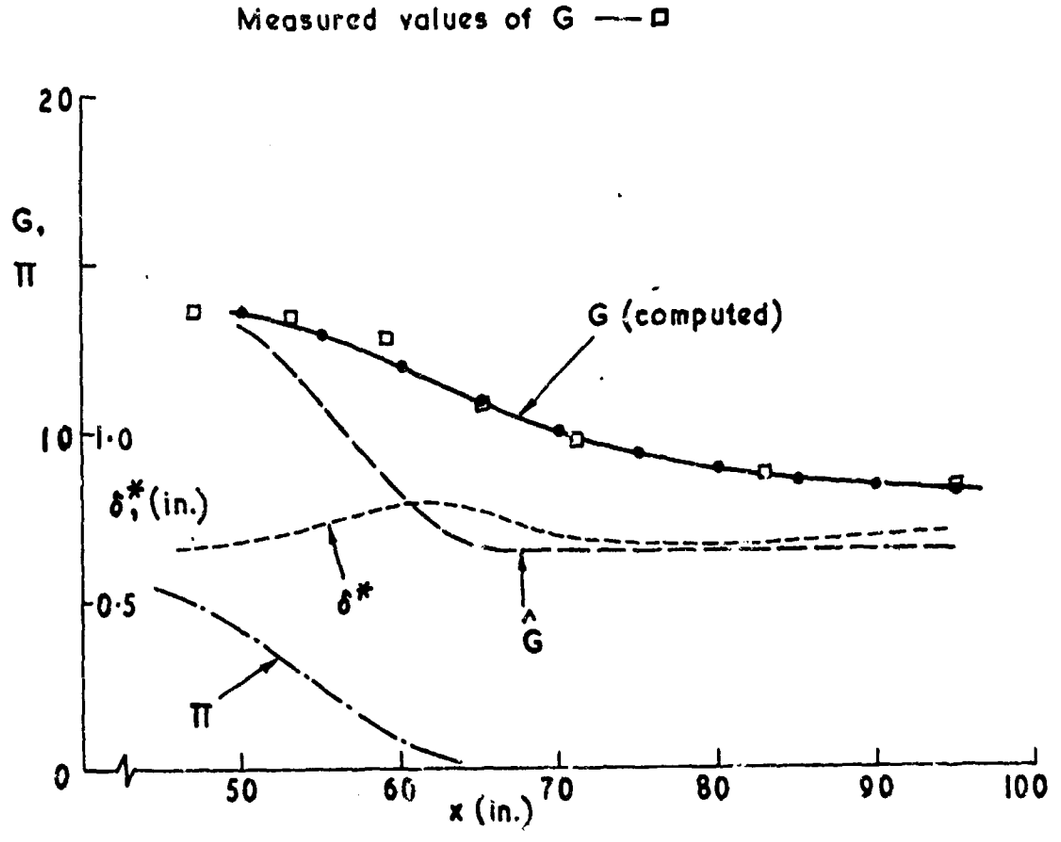

Fig. 10 Comparison between new auxiliary equation and experiment: Bradshaw, (Ref. 18)

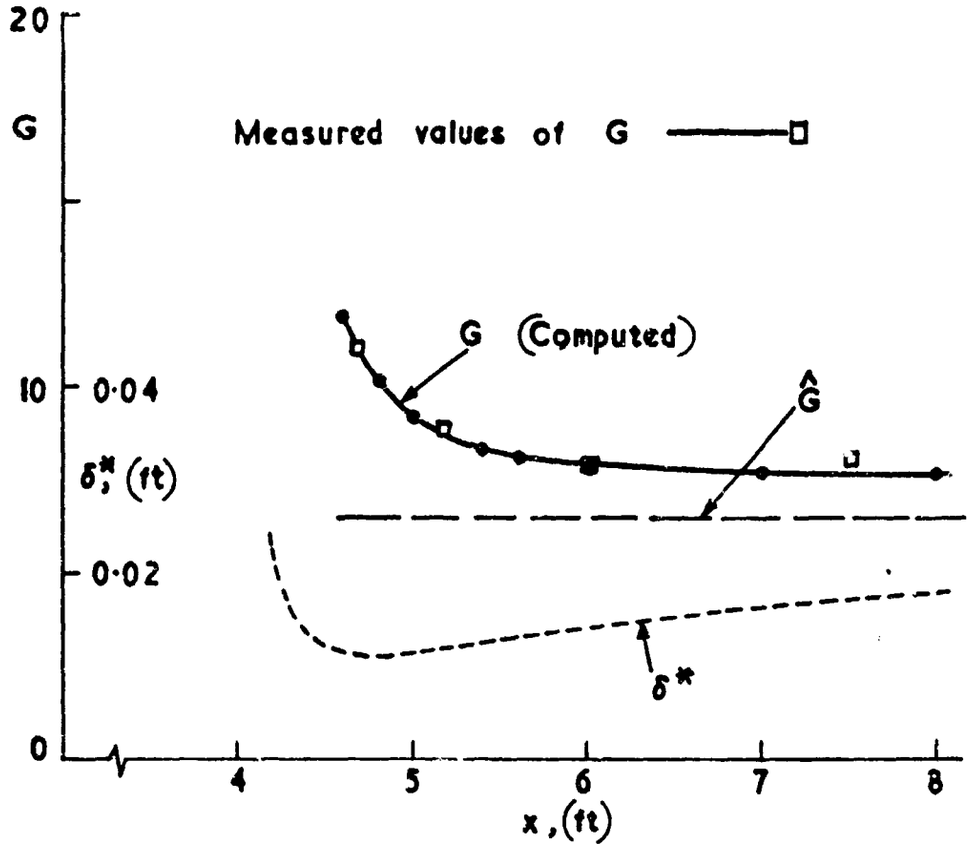

Fig. 11 Comparison between new auxiliary equation and experiment: Klebanoff and Diehl, (Ref. 21)

THE MEAN FLOW IN THE OUTER REGION OF TURBULENT BOUNDARY LAYERS

by

T. Neil Stevenson

Mechanics of Fluids,
The University of Manchester,
Manchester 13, U.K.

SUMMARY

A dimensional analysis is used to indicate the equation for the mean velocity distribution in the outer region of incompressible turbulent boundary layers in terms of a function, F. In the intermediate region this function which occurs in boundary layers in small pressure gradients, at separation and with transpiration is the same as that in zero pressure gradient flow. Experiments in boundary layers in zero pressure gradient, with injection and at separation show that F is virtually a function of y/δ only. The similarity flow in which F is a function of y/δ only is then considered for boundary layers in small pressure gradients.

The calculations involve the functions and constants which occur in zero pressure gradient flow, but no other experimentally determined constants or functions are used.

The theoretical total shear stress variations across boundary layers with injection and at separation are consistent with measured distributions.

SOMMAIRE

On a recours à une analyse dimensionnelle pour formuler l'équation de la distribution moyenne des vitesses dans la région externe de couches limites turbulentes incompressibles, par rapport à une fonction F. Dans la région intermédiaire, cette fonction qui se présente dans les couches limites aux faibles gradients de pression est la même au décollement et avec la transpiration que d'un écoulement à gradient de pression nul. Des expériences effectuées dans des couches limites à gradient de pression nul, avec injection et au décollement, montrent que virtuellement, F est uniquement fonction de y/δ. On considère ensuite l'écoulement similaire dans lequel F est uniquement fonction de y/δ, pour des couches limites aux gradients de pression faible.

Les calculs impliquent les fonctions et constantes qui existent en écoulement à gradient de pression nul, mais il n'est fait usage d'aucune autre constante ou fonction déterminée expérimentalement.

Les variations théoriques totales de l'effort de cisaillement à travers les couches limites avec injection et au décollement sont en accord avec les distributions mesurées.

CONTENTS

LIST OF TABLES

LIST OF FIGURES

NOTATION

B, B_1, B_2, B_3, B_4		functions independent of y, Equations (2.6) to (2.10)
c_f		skin friction parameter, $\tau_w/\frac{1}{2}\rho u_1^2$
D		pressure gradient parameter, $-\frac{\delta}{u_1}\frac{du_1}{dx}$
E		defined by Equation (5.2)
f, f_1, f_3		defined by Equations (A.8), (A.2) and (A.5) respectively
F, F_1, F_3		defined by Equations (3.2), (A.1) and (A.4) respectively
F_2	$=$	$\frac{1}{F_1}\frac{dF_1}{du}$
H		form parameter, δ_1/δ_2
J_1, J_2		velocity profile parameters, Equation (6.3)
K		von Kármán's constant
N	$=$	$\frac{\delta}{D}\frac{dD}{dx}$
p	$=$	$-\frac{u_1}{u_\tau^2}\frac{du_1}{dx}$
P		ratio of static pressure to density
P_2	$=$	$-\frac{\nu}{u_1^2}\frac{du_1}{dx}$
Q, Q_+		dimensionless parameters independent of y, Equations (A.1) and (A.2)
S		function defined by Equation (3.1)
u, v		velocities in x and y directions respectively
u', v'		components of velocity fluctuation
u_τ		friction velocity, $\sqrt{\frac{\tau_w}{\rho}}$
u_2		velocity at $y = \delta_2$

x, y		coordinates along and normal to the wall
δ		boundary layer thickness (as far as possible in the calculations δ has been asumed to be $1.4\ \delta_0$)
δ_0		value of y at which $F = K$
δ_1		displacement thickness
δ_2		momentum thickness
η	=	y/δ
ν		kinematic viscosity
ξ		function of x only, Section 6
ρ		density
τ		total shear stress, $\rho\left(-\overline{u'v'} + \nu\dfrac{\partial u}{\partial y}\right)$
ϕ		defined by Equation (4.6)

Subscripts

w	wall conditions
1	conditions at outer edge of boundary layer

THE MEAN FLOW IN THE OUTER REGION OF TURBULENT BOUNDARY LAYERS

T. Neil Stevenson

1. INTRODUCTION

The approximate theory presented in this paper attempts to correlate the mean velocity in the outer region of incompressible turbulent boundary layers in small pressure gradients, at separation, and with injection or suction through a porous wall.

A dimensional analysis indicates that the outer region depends on a function of the form $f(u_1) - f(u)$ and not necessarily on a velocity defect term, $(u_1 - u)$, which has been used by Clauser[1], Mickley and Smith[2] and Black and Sarnecki[3].

Mickley and Smith[2] found by experiment that the mean velocity in the outer region of turbulent boundary layers with small injection velocities through a porous wall, collapsed onto one curve when $(u_1 - u)/u_\tau^*$ was plotted against y/δ. u_τ^* corresponds to the maximum value of the Reynolds stress which occurs in a particular profile. This is an interesting approach but requires an accurate experimental determination of the Reynolds stress.

Coles[4] introduced a wake function, which represents the departure of the mean velocity profile from the 'law of the wall' velocity profile. The wake function, which is tabulated by Coles, is considered to be independent of the skin friction and pressure gradient. Coles analysed available experimental data and showed that the wake function represented the velocity profiles reasonably well except near separation. Black and Sarnecki[3] were unsuccessful when they tried to use Coles' wake function when there was suction or injection. The present theory correctly predicts that there is no 'wake' in turbulent boundary layers over porous surfaces through which there is a large suction velocity.

Clauser[1], realising that the past history of the boundary layer is very important, managed to adjust the pressure gradient in his experiments so that the mean velocity profiles at different positions along the flow collapsed onto one curve when $(u_1 - u)/u_\tau$ was plotted against y/δ. The present analysis reduces to that of Clauser in a particular case.

The inner region of a turbulent boundary layer adjusts itself to the local wall conditions reasonably quickly whereas the outer region with its slow rates of energy transfer, takes some time to relax to its new form. The theory will not hold during this relaxation period, however it is shown to be quite useful when considering non-equilibrium layers.

In the following sections the inner region solutions will be reviewed before the new approach is introduced.

2. THE INNER REGION

The momentum and continuity equations for the mean flow in a two dimensional turbulent boundary layer are approximately

$$2u\frac{\partial u}{\partial x} + \frac{\partial uv}{\partial y} + \frac{\partial(\overline{u'^2} - \overline{v'^2})}{\partial x} + \frac{\partial \overline{u'v'}}{\partial y} = -\frac{dP}{dx} + \nu\frac{\partial^2 u}{\partial y^2} \tag{2.1}$$

and

$$\frac{\partial u}{\partial x} + \frac{\partial v}{\partial y} = 0 \tag{2.2}$$

where u and v are the mean velocity components in the x and y directions, u' and v' are the components of the velocity fluctuations and $dP/dx(= -u_1 du_1/dx)$ is the pressure gradient. In most cases the term $\partial(\overline{u'^2} - \overline{v'^2})/\partial x$ is small and it will be neglected in the following analysis. We shall assume that $\partial u/\partial x$ and $\partial v/\partial y$ are small compared with $\partial u/\partial y$ in the inner region, the region close to the wall. The momentum and continuity equations therefore simplify to

$$v_w\frac{\partial u}{\partial y} + \frac{\partial \overline{u'v'}}{\partial y} = -\frac{dP}{dx} + \nu\frac{\partial^2 u}{\partial y^2} \tag{2.3}$$

in the inner region. (v_w is the injection velocity normal to a porous wall.) The equation is integrated with respect to y in order to obtain an equation for the shear stress distribution in the inner region:

$$\frac{\tau}{\rho} = \frac{\tau_w}{\rho} + v_w u + \frac{dP}{dx}y \,. \tag{2.4}$$

The total shear stress, τ, is the sum of the viscous shear stress $\mu\partial u/\partial y$ and the Reynolds stress $-\rho\overline{u'v'}$. τ_w is the shear stress at the wall.

The momentum transfer or mixing length hypothesis of Prandtl together with the usual assumption that the mixing length is proportional to the distance from the wall yields the relation between the shear stress and the velocity gradient, $\partial u/\partial y$:

$$\tau = \rho K^2 y^2 \left|\frac{\partial u}{\partial y}\right| \frac{\partial u}{\partial y} \tag{2.5}$$

where K is von Kármán's constant. This equation will not be valid in the region very close to the wall where the viscous shear stress predominates.

The mixing length hypothesis is used by Rubesin[5], Dorrance and Dore[6] and Black and Sarnecki[3] to derive the equations for a turbulent boundary layer with transpiration

through a porous wall. Stratford[7] uses the same hypothesis when considering a turbulent boundary layer with negligible wall shear stress. However Stratford is able to derive the same equation by dimensional arguments.

Equation (2.5) is further substantiated by Townsend[8] who considers regions of turbulent shear flow in which there is equilibrium between the local rates of energy production and dissipation.

Rotta[9] reviews the inner region approximations in detail and shows that the available experimental results verify Equation (2.5).

The total shear stress in Equation (2.4) is eliminated by using Equation (2.5), and the resulting equation,

$$Ky\frac{du}{dy} = \left(u_\tau^2 + v_w u + \frac{dP}{dx}y\right)^{\frac{1}{2}}$$

is integrated with respect to y for the following cases:

(a) When the transpiration velocity is zero,

$$K\frac{u}{u_\tau} = 2(py+1)^{\frac{1}{2}} + \log_e\left|\frac{(py+1)^{\frac{1}{2}}-1}{(py+1)^{\frac{1}{2}}+1}\right| + B_1\left(\frac{p\nu}{u_\tau}\right) \qquad (2.6)$$

where $p = (1/u_\tau^2)(dP/dx)$, and B_1 is independent of y.

(b) When there is no pressure gradient,

$$2\frac{u_\tau}{v_w}\left\{\left(\frac{v_w u}{u_\tau^2}+1\right)^{\frac{1}{2}}-1\right\} = \frac{1}{K}\log_e\frac{yu_\tau}{\nu} + B_2\left(\frac{v_w}{u_\tau}\right) \qquad (2.7)$$

where B_2 is independent of y.

(c) When the blowing velocity and the pressure gradient are zero,

$$\frac{u}{u_\tau} = \frac{1}{K}\log_e\frac{yu_\tau}{\nu} + B \qquad (2.8)$$

where B is a constant. Experiment (Ref. 10) has shown that Equation (2.8), the 'law of the wall', is also valid in small pressure gradients. Equations (2.8) and (2.6) will be compared in Section 5.3. Millikan[11] derived Equation (2.8) by a purely dimensional analysis.

(d) When the skin friction and the transpiration velocity are zero,

$$u = 2y^{\frac{1}{2}}\left(\frac{1}{K^2}\frac{dP}{dx}\right)^{\frac{1}{2}} + B_3\left(\nu\frac{dP}{dx}\right)^{\frac{1}{3}} \qquad (2.9)$$

where B_3 is a constant. Stratford[7] was able to derive this equation by dimensional arguments.

(e) When the skin friction and pressure gradient are zero,

$$\left(\frac{u}{v_w}\right)^{\frac{1}{2}} = \frac{1}{2K}\log_e\frac{yv_w}{\nu} + B_4 \tag{2.10}$$

where B_4 is a constant.

Throughout the derivation of the above equations it has been assumed that the inner region is independent of the conditions at the outer edge of the boundary layer.

3. THE EQUATIONS FOR THE OUTER REGION

The analysis follows that of Millikan[11] but now includes an unknown function of u/u_τ and Q in place of the usual u/u_τ in the zero pressure gradient equation. Q may be a dimensionless pressure gradient or transpiration velocity parameter or a combination of any other relevant parameters.

An overlap or intermediate region is defined as that region in which a solution for the inner region of the form $f_1(u/u_\tau, Q) = yu_\tau/\nu$ and a solution for the outer region of the form $F_1(u/u_\tau, u_1/u_\tau, Q) = y/\delta$ are simultaneously valid.

When the inner region equations were derived in the previous section, the equation which was integrated (Eq.(2.4)) was independent of both ν and δ. It is therefore not surprising that the inner region equations (2.6) to (2.10) are solutions for the intermediate region.

The details of the dimensional analysis are given in the Appendix. It is shown that the equations for the outer region may be written in the form

$$S\left(\frac{y}{\delta}, \frac{u_1}{u_\tau}, Q\right) = f\left(\frac{u}{u_\tau}, Q\right) - \log_e\frac{\delta u_\tau}{\nu} \tag{3.1}$$

and

$$F\left(\frac{y}{\delta}, \frac{u_1}{u_\tau}, Q\right) = S\left(1, \frac{u_1}{u_\tau}, Q\right) - S\left(\frac{y}{\delta}, \frac{u_1}{u_\tau}, Q\right) \tag{3.2}$$

$$= f\left(\frac{u_1}{u_\tau}, Q\right) - f\left(\frac{u}{u_\tau}, Q\right) \tag{3.3}$$

where $S = \log_e y/\delta$ in the intermediate region.

It will be shown that these outer region equations are useful, because experimental results in different turbulent boundary layers, i.e. in pressure gradients, with suction or injection, at separation, may be compared by plotting either $f(u/u_\tau, Q) - \log_e(\delta u_\tau/\nu)$ or $\{f(u_1/u_\tau, Q) - f(u/u_\tau, Q)\}$ against y/δ. The approximate form of the function, f, is known from the solutions in the overlap region which were outlined in the previous section. By plotting experimental results in this way it should be possible to establish the way in which F and S depend on u_1/u_τ and Q.

In the following section the equations for the overlap region will be used to derive specific equations for the outer region which will be compared with experimental results.

4. THE FUNCTIONS S AND F

4.1 Zero pressure gradient

The equations for the outer region are derived by rearranging Equation (2.8) to give

$$\log_e \frac{y}{\delta} = K\left(\frac{u}{u_\tau} - B\right) - \log_e \frac{u_\tau \delta}{\nu} \tag{4.1}$$

in the intermediate region, and by replacing $\log_e y/\delta$ by S to give

$$S = S\left(\frac{y}{\delta}, \frac{u_1}{u_\tau}\right) = K\left(\frac{u}{u_\tau} - B\right) - \log_e \frac{u_\tau \delta}{\nu} \tag{4.2}$$

in the outer region. When $y/\delta = 1$ then

$$S\left(1, \frac{u_1}{u_\tau}\right) = K\left(\frac{u_1}{u_\tau} - B\right) - \log_e \frac{u_\tau \delta}{\nu} \tag{4.3}$$

and therefore

$$S\left(1, \frac{u_1}{u_\tau}\right) - S\left(\frac{y}{\delta}, \frac{u_1}{u_\tau}\right) = K\left(\frac{u_1 - u}{u_\tau}\right) = F\left(\frac{y}{\delta}, \frac{u_1}{u_\tau}\right). \tag{4.4}$$

If experimental results are plotted as y/δ_0 against $(u_1 - u)/u_\tau$, they fall close to a single curve (see Clauser[1] and Townsend[12]). δ_0 is defined as the value of y at which $F = K$. Thus F is virtually independent of u_1/u_τ and Equation (4.4) may be written

$$K\left(\frac{u_1 - u}{u_\tau}\right) = F\left(\frac{y}{\delta}\right). \tag{4.5}$$

This is the accepted velocity defect law equation for the outer region of turbulent boundary layers in zero pressure gradient and with zero transpiration.

It is more difficult to show that S is a function of y/δ only because the equation for S includes the skin friction, the boundary layer thickness and the constants in the law of the wall equation, all of which are difficult to determine. Some experimental results are plotted as S against y/δ in Figure 1. Within the experimental accuracy $S = S(y/\delta)$.

$S(1)$ is related to Coles' constant $\phi(1)$ by the equation

$$S(1) = K(\phi(1) - B) \tag{4.6}$$

Coles[13] has recalculated the majority of the published zero pressure gradient turbulent boundary layer mean flow results and has evaluated the size of the wake component which is related to $\phi(1)$. Coles shows that the wake component and therefore $\phi(1)$ are constant above Reynolds numbers, $R\delta_2 > 3,000$, in equilibrium flows.

4.2 With Transpiration

The equations for the outer region are obtained by rearranging Equation (2.7) to give

$$\log_e \frac{y}{\delta} = 2K \frac{u_\tau}{v_w} \left\{ \left(1 + \frac{v_w u}{u_\tau^2} \right)^{\frac{1}{2}} - 1 \right\} - BK - \log_e \frac{u_\tau \delta}{\nu} \tag{4.7}$$

in the intermediate region and thus

$$S = 2K \frac{u_\tau}{v_w} \left\{ \left(1 + \frac{v_w u}{u_\tau^2} \right)^{\frac{1}{2}} - 1 \right\} - BK - \log_e \frac{u_\tau \delta}{\nu} \tag{4.8}$$

and

$$F = 2K \frac{u_\tau}{v_w} \left\{ \left(1 + \frac{v_w u_1}{u_\tau^2} \right)^{\frac{1}{2}} - \left(1 + \frac{v_w u}{u_\tau^2} \right)^{\frac{1}{2}} \right\} \tag{4.9}$$

in the outer region. Equation (4.9) is the modified velocity defect law with injection (Ref.14). For high blowing velocities u_τ has negligible effect on the outer region and Equation (4.9) reduces to

$$F = 2K \left(\frac{u_1}{v_w} \right)^{\frac{1}{2}} \left(1 - \left(\frac{u}{u_1} \right)^{\frac{1}{2}} \right). \tag{4.10}$$

The experimental results show that the function, F , in Equation (4.9) is virtually independent of v_w/u_τ and u_1/u_τ and is the same function as that in the velocity defect equation. Some of the experimental results reproduced from Reference 14 are presented in Figures 2 and 3.

Some experimental results are plotted as S against y/δ in Figure 4 and, considering the difficulties in evaluating the function S *, the results fall reasonably close to the zero pressure gradient curve.

4.3 At separation

Stratford and Townsend show that the equation for the inner region at separation (Eq.2.9 with $B_3 = 0$) is

$$u = \frac{2}{K} \left(\frac{dP}{dx} \right)^{\frac{1}{2}} y^{\frac{1}{2}} \tag{4.11}$$

---

* B_2 was assumed constant and equal to B .

where dP/dx is the pressure gradient. This equation, which is valid in the intermediate region, is rearranged:

$$\log_e \frac{y}{\delta} = 2\log_e\left(\frac{Ku}{2\delta^{\frac{1}{2}}\left(\frac{dP}{dx}\right)^{\frac{1}{2}}}\right) \tag{4.12}$$

and therefore

$$S = 2\log_e\left(\frac{Ku}{2\delta^{\frac{1}{2}}\left(\frac{dP}{dx}\right)^{\frac{1}{2}}}\right) \tag{4.13}$$

or

$$F = 2\log_e\left(\frac{u_1}{u}\right) \tag{4.14}$$

in the outer region.

Some of the experimental results of Schubauer and Klebanoff[15] and Stratford[16] are plotted as y/δ_0 against $(2/K)\log_e(u_1/u)$ in Figure 5. The results again fall close to the zero pressure gradient velocity defect curve.

In this section the equations for the outer region together with the solutions for the intermediate region, have been compared with experimental results and it has shown that S and F are virtually functions of y/δ only. In the remainder of this paper we shall consider the similarity flow in which $S(y/\delta)$ and $F(y/\delta)$ are universal functions. The resulting equations will then be compared with experiment. The values for $S(y/\delta)$ which are used in the calculations are given in the Table and were evaluated using $F(y/\delta)$ from the velocity defect curve together with a value of 1.05 for $S(1)$.

5. TURBULENT BOUNDARY LAYERS IN A PRESSURE GRADIENT

5.1 From Equation (2.6) the equation for the outer region is

$$K\frac{u}{u_\tau} = 2E + \log_e\left|\frac{E-1}{E+1}\right| + B_1 \tag{5.1}$$

where

$$E = \left(p\delta \exp S\left(\frac{y}{\delta}\right) + 1\right)^{\frac{1}{2}}. \tag{5.2}$$

At the outer edge of the boundary layer

$$K\frac{u_1}{u_\tau} = 2E_1 + \log_e\left|\frac{E_1 - 1}{E_1 + 1}\right| + B_1 \qquad (5.3)$$

where

$$E_1 = (p\delta \exp S_1 + 1)^{\frac{1}{2}} ; \quad S_1 = S(1) \qquad (5.4)$$

Equation (5.1) is subtracted from Equation (5.3) in order to eliminate the unknown function, B_1 , and the equation is then rearranged,

$$\frac{u}{u_1} = 1 - \left\{E_1 - E + \tfrac{1}{2}\log_e\left|\frac{E_1 - 1}{E_1 + 1}\frac{E + 1}{E - 1}\right|\right\}\frac{2}{K}\frac{u_\tau}{u_1} . \qquad (5.5)$$

E may be written in terms of the pressure gradient parameter, $D[= -(\delta/u_1)du_1/dx]$,

$$E = \left\{D\left(\frac{u_1}{u_\tau}\right)^2 \exp S + 1\right\}^{\frac{1}{2}} . \qquad (5.6)$$

Several velocity profiles, u/u_1 against y/δ , which have been calculated from Equation (5.5) for particular values of D , are shown in Figur 5.

5.2 Flows with negligible wall shear stress

When the skin friction is very small Equation (5.6) reduces to

$$\frac{u}{u_1} = 1 - \frac{2D^{\frac{1}{2}}}{K}\left\{\exp\frac{S_1}{2} - \exp\frac{S}{2}\right\} . \qquad (5.7)$$

This equation is more general than that in Section 4.3 where B_3 was assumed to be zero.

In Figures 7, 8 and 9 Equation (5.7) is compared with some reattachment profiles after a separation bubble (McGregor[17]), two separation profiles (Newman[18] and Schubauer and Klebanoff[15]) and some zero skin friction profiles (Stratford[16]). The shape of the experimental profiles are in very good agreement with the theoretical curves, and the theoretical values of D are reasonably close to those in the experiments.

If Equation (5.7) is used to evaluate the displacement thickness, δ_1 , and the momentum thickness, δ_2 , it is found that the form parameter, H , is given by

$$H = \frac{1}{1 - 5.09\,D^{\frac{1}{2}}} = \frac{1}{1 - 1.51\,\frac{\delta_1}{\delta}} . \qquad (5.8)$$

The theoretical curves of H against δ_1/δ are presented in Figure 10 and are compared with some measurements near separation reproduced from Sandborn[23]. The

Equation (5.6) is now rearranged to give

$$\frac{u_1 - u}{u_\tau} = \left(E_1 - E + \tfrac{1}{2} \log_e \left| \frac{E_1 - 1}{E_1 + 1} \frac{E + 1}{E - 1} \right| \right) \frac{2}{K} \qquad (5.11)$$

where $E = (p\delta \exp S + 1)^{\frac{1}{2}}$. This form of equation describes Clauser's equilibrium flow providing $p\delta$ is constant. This pressure gradient condition is the same as that found by Clauser. In Figure 11 it is shown that the curves representing Equation (5.11) are the same shape as the experimental curves. There is a difference between the theoretical and experimental values of $p\delta$ and this needs further investigation.

5.5 Experiments in non-equilibrium boundary layers

Von Doenhoff and Tetervin[20] showed experimentally that curves of u/u_1 against H for particular values of y/δ_2 were almost independent of the skin friction and the pressure gradient. The theoretical velocity profiles of Figure 5 were used to evaluate the displacement and momentum thicknesses to enable curves of u/u_1 against H to be plotted. The curves are compared with the experimental results of von Doenhoff and Tetervin in Figure 14 and with the results of Schubauer and Klebanoff in Figure 15. The present theoretical curves of u_2/u_1 against H are compared with the semi-empirical curves of Ludwieg and Tillmann, and Spence[21] in Figure 16. (u_2 is the value of u at $y = \delta_2$) .

The velocity profiles and the parameters based on the profile shapes, which are predicted by the present analysis compare very well with previous theories and with available experimental results.

The experimental pressure gradient is usually much higher than the theoretical value and it is now suggested that the boundary layer adjusts itself as quickly as possible, trying to attain an energy equilibrium state but usually not succeeding until the separation point is reached. It is only after the boundary layer has separated that it is able to modify the external flow sufficiently to reduce the external pressure gradient and thus achieve an equilibrium state.

6. SHEAR STRESS DISTRIBUTIONS

The inner and outer region equations may be used together with the momentum equation to derive the shear stress distribution across turbulent boundary layers. The momentum Equation (2.1) is integrated from 0 to η to give

$$\frac{\tau}{\rho} = \frac{\tau_w}{\rho} + v_w u + \frac{du_1}{dx} \delta \left\{ 2 \int_0^\eta u d\eta - u\eta - u_1 \eta \right\} +$$

$$+ \frac{d\xi}{dx} \delta \left\{ 2 \int_0^\eta u \frac{\partial(u - u_1)}{\partial \xi} d\eta - u \int_0^\eta \frac{\partial(u - u_1)}{\partial \xi} d\eta \right\} + \frac{d\delta}{dx} \left\{ \int_0^\eta u^2 d\eta - v \int_0^\eta u d\eta \right\} \qquad (6.1)$$

where $\eta = y/\delta$ and ξ is a function of x only. The term $\partial(\overline{u'^2} - \overline{v'^2})/\partial x$ in Equation (2.1) is usually small and it has been neglected in the derivation of the integrated momentum Equation (6.1).

separation criterion derived by Sandborn is also shown in Figure 10. Sandborn assumed the velocity profile at separation to be of the form

$$\frac{u}{u_1} = 1 - \left(1 - \frac{y}{\delta}\right)^m \qquad (5.9)$$

where m is a constant. This equation results in a unique relationship between the momentum, displacement and boundary layer thicknesses. Sandborn shows that Equation (5.9) is a reasonable representation of the velocity profile at separation in Reference 15. This profile has a form parameter, H, of 2.75 and therefore corresponds to the region in which the present $c_f = 0$ curve crosses that of Equation (5.10) (see Fig. 10).

Kutateladze and Leont'ev[19] express the shear stress across a turbulent boundary layer in terms of a cubic parabola which is used together with an equation similar to Equation (2.5) to evaluate the limiting velocity profile at the point of separation. They use Equation (2.5) across the whole of the outer region but include a varying 'mixing length' evaluated at zero pressure gradient. The result is shown in Figure 10 and falls close to the curves predicted by the present analysis but is far from the condition $B_3 = 0$ which corresponds to a value of 2.69 for the form parameter, H.

5.3 A hypothetical equation for the inner region

When $p \to \infty$, Equation (2.6) must reduce to the separation Equation (5.7) and when $p \to 0$ it must reduce to the 'law of the wall' Equation (2.8). If B_3 is zero a simple form for B_1, which satisfies the two limiting conditions is

$$B_1 = KB - 2 + \log_e\left(1 + \frac{4u_\tau}{p\nu}\right). \qquad (5.10)$$

Hypothetical velocity profiles in the inner region may now be evaluated for particular values of c_f and $P_2[= -(\nu/u_1^2)du_1/dx]$. Some of the profiles when $c_f = 0.002$ and 0.0002 are shown in Figures 12 and 13. The higher values of P_2 in the figures corresponds to near separation conditions. The figures are interesting because they show that the inner region profiles with pressure gradient are almost the same as those with zero pressure gradient at the same value of skin friction. This has been shown experimentally by Ludwieg and Tillmann and it is now often accepted that the 'law of the wall' holds in pressure gradients.

This intuitive analysis for the intermediate region in pressure gradients indicates that the equation for the intermediate region, which was used in the derivation of the equations for the outer region, is not necessarily very different from the 'law of the wall' equation.

5.4 The experimental results of Clauser[1]

Clauser measured the mean velocity profiles in turbulent boundary layers subject to two small pressure gradients. The pressure gradients were adjusted so that the mean velocity profiles at different positions along the flow collapsed onto one curve when $u_1 - u/u_\tau$ was plotted against y/δ. The experimental curves are shown in Figure 11.

In the case of boundary layers with injection but no pressure gradient ξ was equated to u_1/u_τ, and B_2 was assumed equal to B. The shear stress across the boundary layer was then evaluated (Ref.14) using Equation (6.1) and the results were found to compare favourably with that reported by Leadon[22].

When there is a pressure gradient but no transpiration it is convenient to let

$$\xi = p\delta = -\frac{u_1}{u_\tau^2}\,\delta\,\frac{du_1}{dx}. \tag{6.2}$$

In the case of a flow with negligible skin friction Equation (6.1) reduces to

$$\frac{\tau}{\rho u_1^2} = D\left\{\eta - 2J_2 + \frac{u}{u_1}J_1\right\} + N\left\{J_2 - J_1 - \frac{u}{u_1}\frac{J_1}{2} + \tfrac{1}{2}\frac{u}{u_1}\eta\right\} + \frac{d\delta}{dx}\left\{J_2 - \frac{u}{u_1}J_1\right\} \tag{6.3}$$

where

$$J_1 = \int_0^\eta \frac{u}{u_1}\,d\eta,\quad J_2 = \int_0^\eta \left(\frac{u}{u_1}\right)^2 d\eta$$

and

$$N = \frac{\delta}{D}\frac{dD}{dx}.$$

A shear stress profile in a flow with zero skin friction and with $N = 0$ and with $D = 0.013$ has been calculated from Equation (6.3) and is shown in Figure 17. Schubauer and Klebanoff's measurements of the shear stress at separation compare quite well with the theoretical shear stress distribution. It must be remembered that the turbulence term $\partial(u'^2 - v'^2)/\partial x$ has not been included in the shear stress calculation and this may have an effect at separation.

The outer region includes the logarithmic overlap region and by comparison with experimental results, the outer region is valid for almost all the boundary layer; all except the region very close to the wall where y/δ is less than about 0.04. In evaluating the integrals the errors involved in neglecting the sublayer are negligible.

7. CONCLUSIONS

A dimensional analysis has been used to indicate the form of the equations for the mean velocity distribution in the outer region of turbulent boundary layers in terms of either a function, F, or a function, S. In the intermediate region these functions, which occur in boundary layers in small pressure gradients, at separation and with transpiration are the same as those in zero pressure gradient flow. Towards the outer edge of the boundary layer the functions may in general differ for the various types of boundary layer. However by comparison with experimental results in boundary layers in zero pressure gradient, with injection and at separation, F appears to be virtually a function of y/δ only and it is the same function as that in the velocity defect law equation.

The velocity profiles in zero pressure gradient, with injection and at separation (providing $B_3 = 0$) can be expressed in terms of F, and the profiles evaluated in this way agree reasonably well with experiment. The velocity profiles in a pressure gradient also require a knowledge of S at the outer edge of the boundary layer. A similarity flow has been considered in which S is assumed to be a function of y/δ only. The resulting family of velocity profiles and the parameters based on the profile shapes are in good agreement with the experimental results. However, before any definite conclusions can be made with regard to the comparison between the theoretical and the experimental pressure gradient parameters, more experiments are required. To improve the analysis it may be necessary to find how $S(1)$ varies in different pressure gradients.

ACKNOWLEDGEMENTS

The author wishes to thank Professor G.M. Lilley and Professor A.D. Young for the many helpful discussions during the course of this work.

REFERENCES

1. Clauser, F.H. — *Turbulent boundary layers in adverse pressure gradients.* Journal of Aeronautical Sciences, 21, 1954, pp.91-108.

2. Mickley, H.S. Smith, K.A. — *Velocity defect law for a transpired turbulent boundary layer.* American Institute of Aeronautics and Astronautics Journal, 1, No.7, 1963, p.1685.

3. Black, T.J. Sarnecki, A.J. — *The turbulent boundary layer with suction and injection.* Aeronautical Research Council, London, No.20, 501, 1958.

4. Coles, D. — *The law of the wake in the turbulent boundary layer.* Journal of Fluid Mechanics, 1, 1956, pp.191-226.

5. Rubesin, M.W. — *An analytical estimation of the effect of transpiration cooling.* National Advisory Committee for Aeronautics, T.N.3341, 1954.

6. Dorrance, W.H. Dore, F.J. — *The effect of mass transfer on the compressible turbulent boundary layer skin friction and heat transfer.* Journal Aeronautical Sciences, 21, 1954, pp.404-410.

7. Stratford, B.S. — *The prediction of separation of the turbulent boundary layer.* Journal of Fluid Mechanics, 5, 1959, pp.1-16.

8. Townsend, A.A. — *Equilibrium layers and wall turbulence.* Journal of Fluid Mechanics, 11, 1961, pp.97-120.

9. Rotta, J.C. — *Turbulent Boundary Layers in Incompressible Flow.* Progress in Aeronautical Sciences, 2, Pergamon Press, London, 1962, pp.1-221.

10. Ludwieg, H. Tillmann, W. — *Investigation of the wall shearing stress in turbulent boundary layers.* National Advisory Committee for Aeronautics, TM.1285, 1949.

11. Millikan, G.B. — *A critical discussion of turbulent flows in channels and circular tubes.* Proceedings of the 5th International Congress for Applied Mechanics, Wiley, 1938, pp.386-392.

12. Townsend, A.A. — *Structure of Turbulent Shear Flow.* Cambridge University Press, 1956.

13. Coles, D. — *The turbulent boundary layer in a compressible fluid.* Rand Corporation, Santa Monica, 1961, p.2417.

14. Stevenson, T.N. — *A modified velocity defect law for turbulent boundary layers with injection.* College of Aeronautics, Cranfield, England. Report Aero. 170, 1963.

15. Schubauer, G.B. Klebanoff, P.S. — *Investigation of separation of the turbulent boundary layer.* National Advisory Committee for Aeronautics, TN.2133, 1951.

16. Stratford, B.S. — *An experimental flow with zero skin friction throughout its region of pressure rise.* Journal of Fluid Mechanics, 5, 1959, pp.17-35.

17. McGregor, I. — *Regions of localised boundary layer separation and their role in the stalling of aerofoils.* Doctor of Philosophy Thesis, 1954. Faculty of Engineering, University of London.

18. Newman, B.G. — *Skin friction in a retarded turbulent boundary layer near separation.* Aeronautical Research Consultative Committee of Australia, Report ACA.53, 1951.

19. Kutateladze, S.S. Leont'ev, A.I. — *Turbulent Boundary Layers in Compressible Gases.* Edward Arnold Ltd., London, 1964.

20. Von Doenhoff, A.E. Tetervin, N. — *Determination of general relations for the behaviour of turbulent boundary layers.* National Advisory Committee for Aeronautics, Report 772, 1943.

21. Duncan, W.J. et alii — *The Mechanics of Fluids.* Edward Arnold Ltd., London, 1960, p.342.

22. Leadon, B.M. Comments on *A sublayer theory for fluid injection.* Journal of Aerospace Science, 28, 1961, pp.826-827.

23. Sandborn, V.A. *An equation for the mean velocity distribution of boundary layers.* National Aeronautics and Space Administration, Memo 2.5.59E, 1959.

TABLE I

The Function $S(y/\delta)$

$S(y/\delta)$	y/δ	$S(y/\delta)$	y/δ
-4.04	0.0174	-1.62	0.19
-3.68	0.0251	-1.35	0.23
-3.22	0.0398	-0.7	0.35
-2.87	0.0575	-0.32	0.43
-2.58	0.0794	+0.175	0.55
-2.30	0.105	0.57	0.67
-2.03	0.138	0.875	0.80
-2.0	0.140	1.05	1.0

APPENDIX

A Dimensional Derivation of the Equations for the Outer Region

The method follows that of Millikan and Rotta but now includes a dimensionless parameter, Q, which is independent of y. Q can be a pressure gradient parameter, a transpiration velocity parameter, a relaxation parameter, etc.

The influence of the kinematic viscosity, ν, is restricted to a very small sublayer region of thickness δ_s. In the outer portion of the boundary layer, $y > \delta_s$, it follows from the processes of turbulent energy dissipation and the diffusion and convection of vorticity that the stress-producing motion is independent of viscosity (see Rotta). The mean flow in the outer region will therefore depend on y, u, u_1, u_τ, Q and δ, so that the dimensional equation for the outer region may be written in the form

$$F_1\left(\frac{u}{u_\tau}, \frac{u_1}{u_\tau}, Q\right) = \frac{y}{\delta}. \tag{A.1}$$

A total shear stress parameter is not included because it is assumed that the shear stress may be evaluated from the momentum equation when the shape of the velocity profile and the conditions near the wall are known. (This implies that the turbulence term $\partial(\overline{u'^2} - \overline{v'^2})/\partial x$ is negligible.) Similarly the inner region is independent of the conditions at the edge of the boundary layer and thus

$$f_1\left(\frac{u}{u_\tau}, Q_+\right) = \frac{yu_\tau}{\nu} \tag{A.2}$$

in the inner region. (Q may be a function of δ and u_1 : Q_+ may be a function of ν).

In Section 2 the momentum equation is solved approximately for the turbulent region close to the wall and it is shown that the velocity gradient is independent of the viscosity, ν, and of the conditions at the edge of the boundary layer, i.e. $\partial u/\partial y$ is independent of ν, u_1 and δ. This region corresponds to an overlap between an inner region in which the total shear stress is independent of the conditions at the edge of the boundary layer, and an outer region in which the shear stress (Reynolds stress) is independent of the viscosity.

If Equations (A.1) and (A.2) are differentiated with respect to y at constant x then

$$\frac{du}{dy}\frac{dF_1}{du} = \frac{1}{\delta} \quad \text{and} \quad \frac{du}{dy}\frac{df_1}{du} = \frac{u_\tau}{\nu} \tag{A.3}$$

or

$$y\frac{du}{dy} = \frac{y/\delta}{dF_1/du} = \frac{\frac{yu_\tau}{\nu}}{df_1/du} = \text{(a function independent of } u_1\text{, } \delta \text{ and } \nu\text{)}$$

in the overlap or intermediate region. Hence

$$\frac{1}{F_1}\frac{dF_1}{du} = \frac{1}{f_1}\frac{df_1}{du} = F_2$$

where F_2 is independent of u_1, δ and ν.

Thus

$$\log_e F_1 = (\int F_2 du) + F_3\left(\frac{u_1}{u_\tau}, Q\right) = \log_e \frac{y}{\delta} \tag{A.4}$$

and

$$\log_e f_1 = (\int F_2 du) + f_3(Q_+) = \log_e \frac{yu_\tau}{\nu}. \tag{A.5}$$

Therefore an 'overlap condition' exists of the form

$$F_3\left(\frac{u_1}{u_\tau}, Q\right) = f_3(Q_+) - \log_e \frac{\delta u_\tau}{\nu}. \tag{A.6}$$

The solutions for the overlap region in the form of Equation (A.4) are derived in Section 4.

The equation for the whole of the outer region may be written in the form:

$$S\left(\frac{y}{\delta}, \frac{u_1}{u_\tau}, Q\right) = (\int F_2 du)_{\text{independent of } u_1, \nu, \delta} + F_3\left(\frac{u_1}{u_\tau}, Q\right)$$

$$= (\int F_2 du) + f_3(Q_+) - \log_e \frac{\delta u_\tau}{\nu} \tag{A.7}$$

or

$$S\left(\frac{y}{\delta}, \frac{u_1}{u_\tau}, Q\right) = f\left(\frac{u}{u_\tau}, Q_+\right) - \log_e \frac{\delta u_\tau}{\nu} \tag{A.8}$$

where $S = \log_e y/\delta$ in the overlap region.

If

$$F\left(\frac{y}{\delta}, \frac{u_1}{u_\tau}, Q\right) = S\left(1, \frac{u_1}{u_\tau}, Q\right) - S\left(\frac{y}{\delta}, \frac{u_1}{u_\tau}, Q\right) \tag{A.9}$$

then

$$F\left(\frac{y}{\delta}, \frac{u_1}{u_\tau}, Q\right) = f\left(\frac{u_1}{u_\tau}, Q_+\right) - f\left(\frac{u}{u_\tau}, Q_+\right). \tag{A.10}$$

Equations (A.8) and (A.10) are used in Section 3.

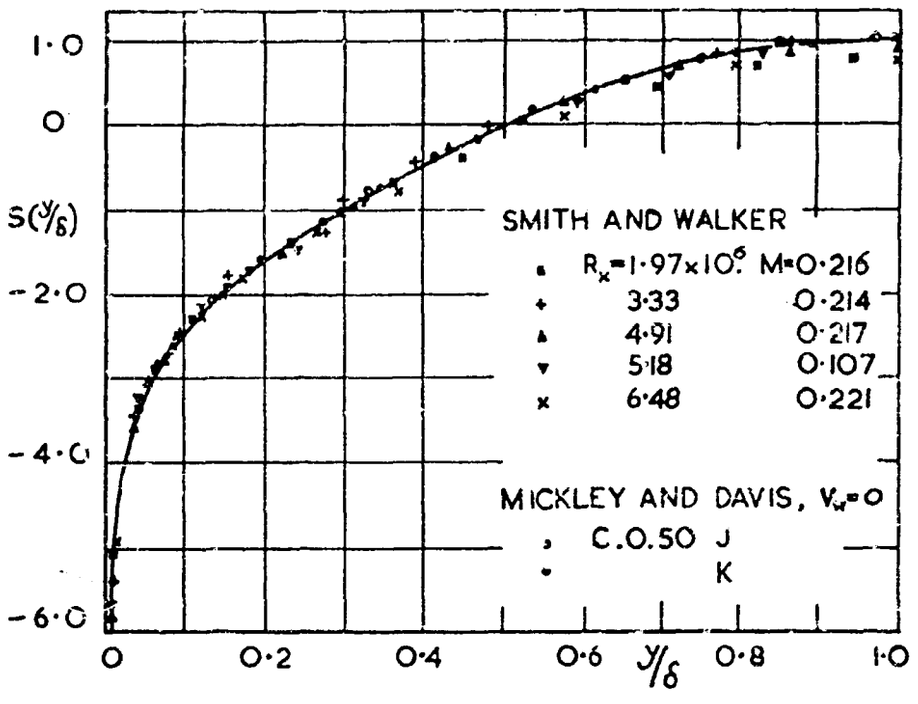

Fig.1 The Function $S(y/\delta)$

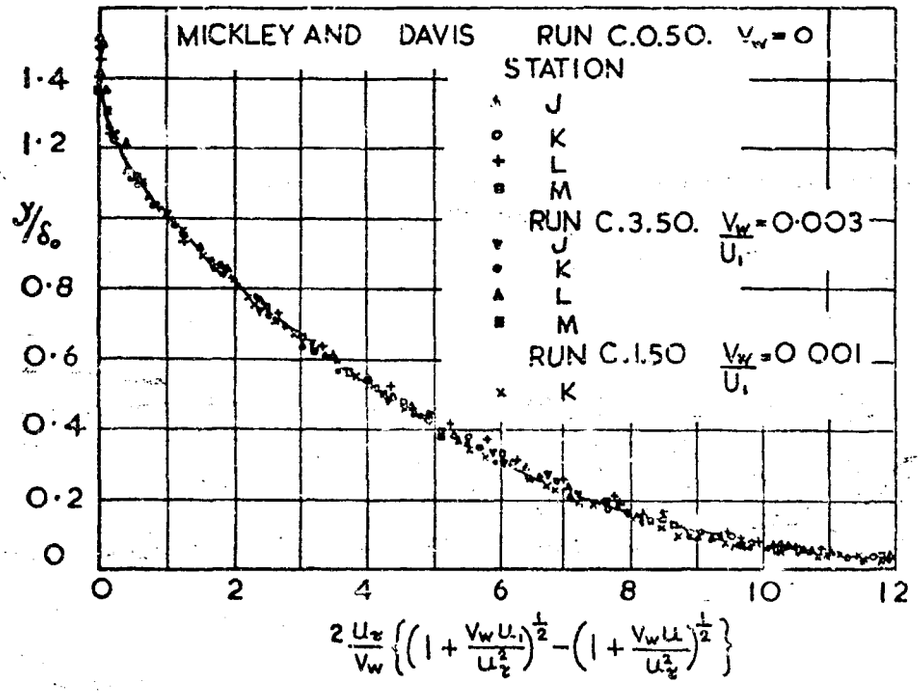

Fig.2 The Outer Region

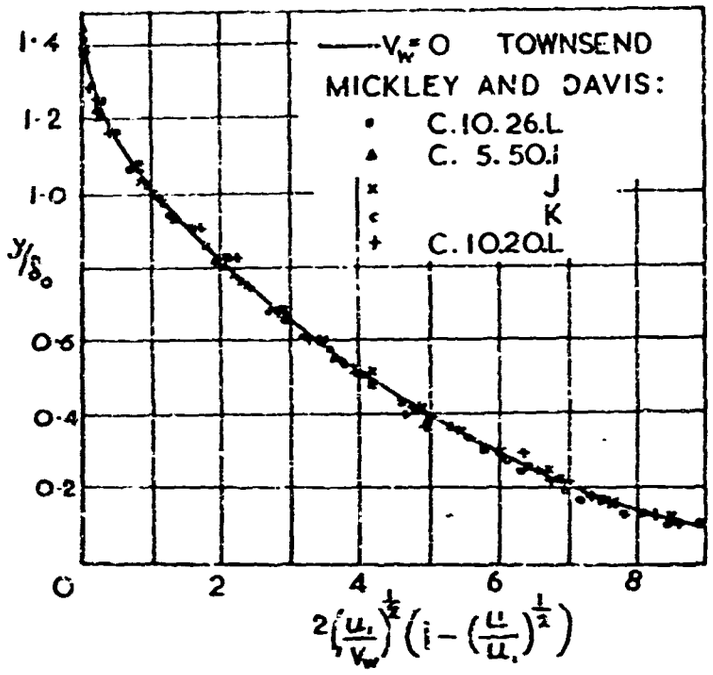

Fig.3 The Outer Region

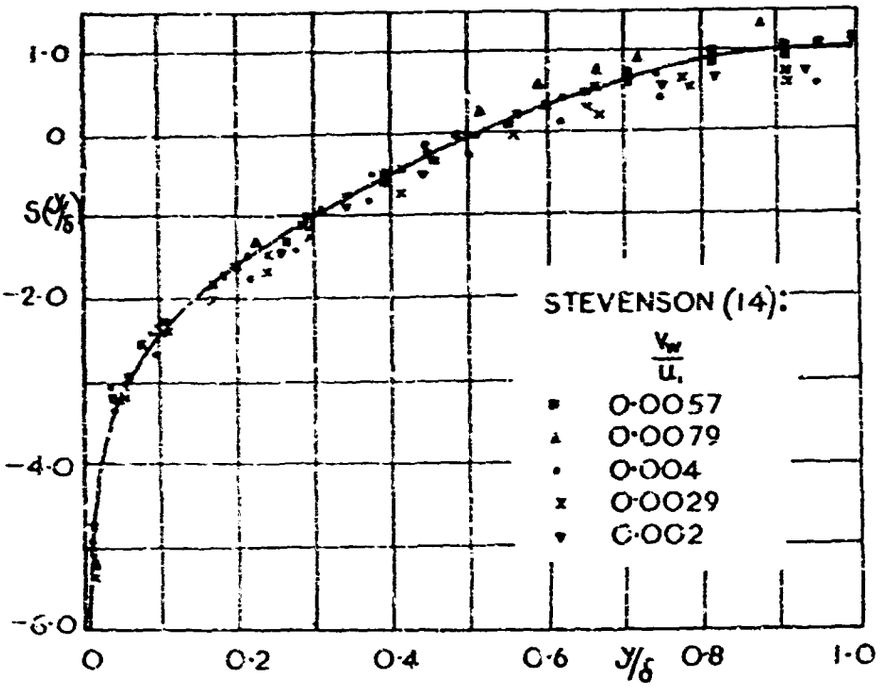

Fig.4 The Function $S(y/\delta)$

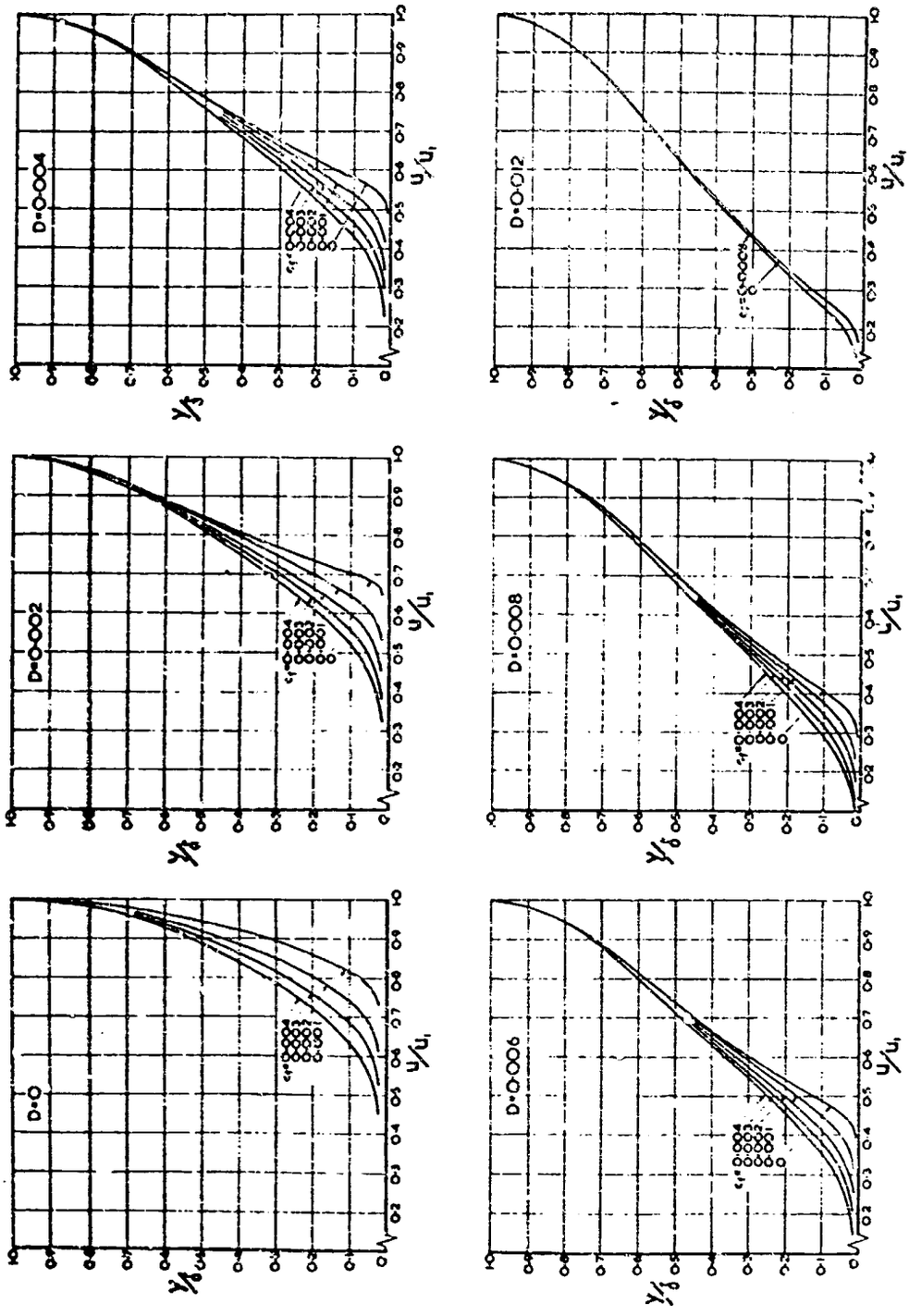

Fig.5 Velocity Profiles in a Pressure Gradient

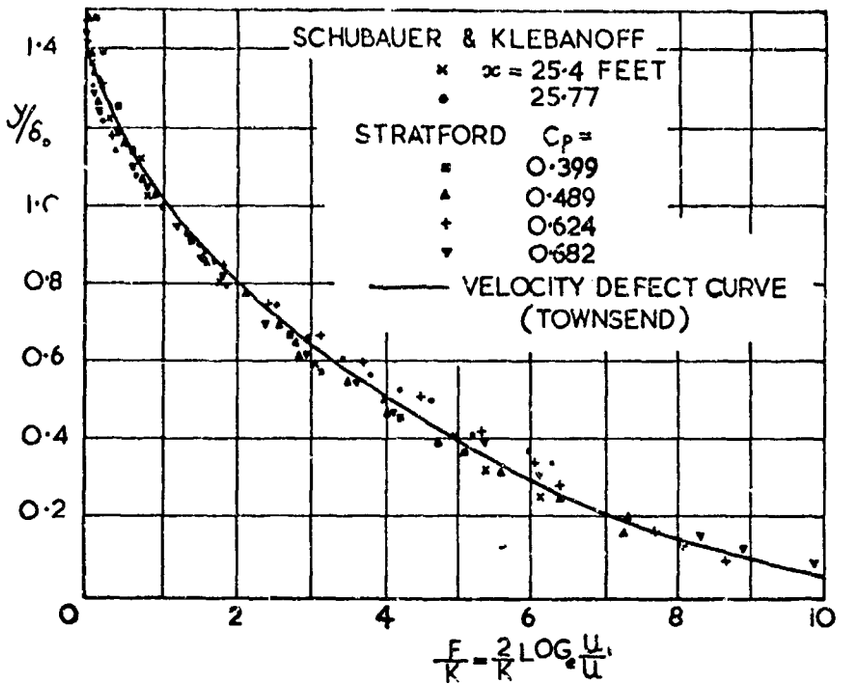

Fig.6 The Outer Region at Separation

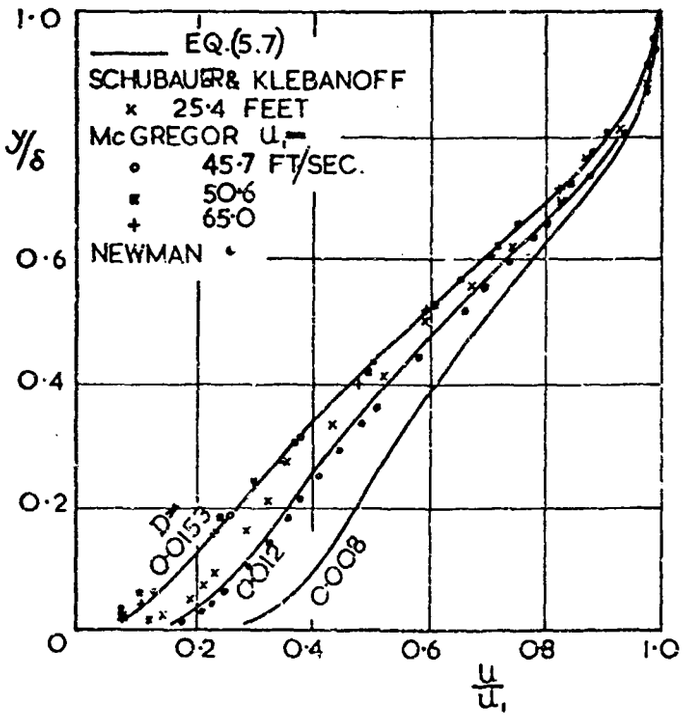

Fig.7 Separation and Reattachment Profiles

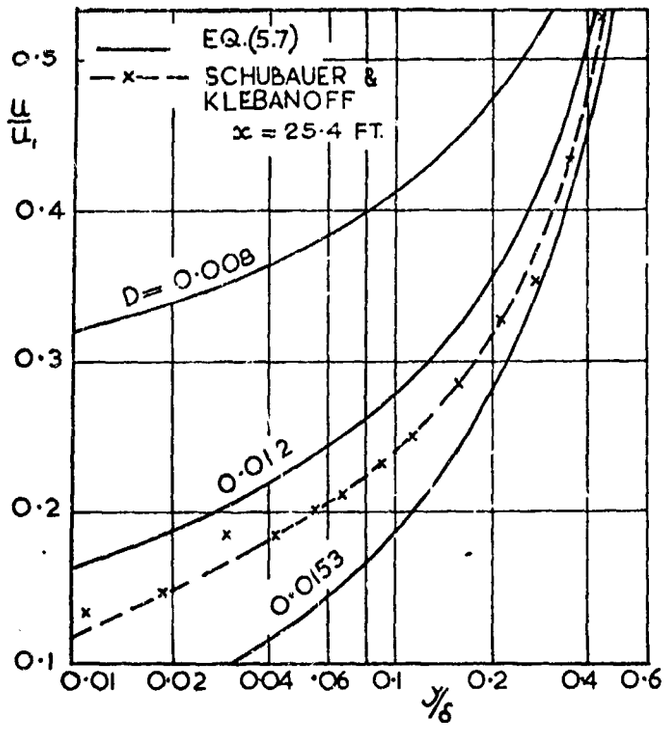

Fig.8 Separation Profiles in the Inner Region

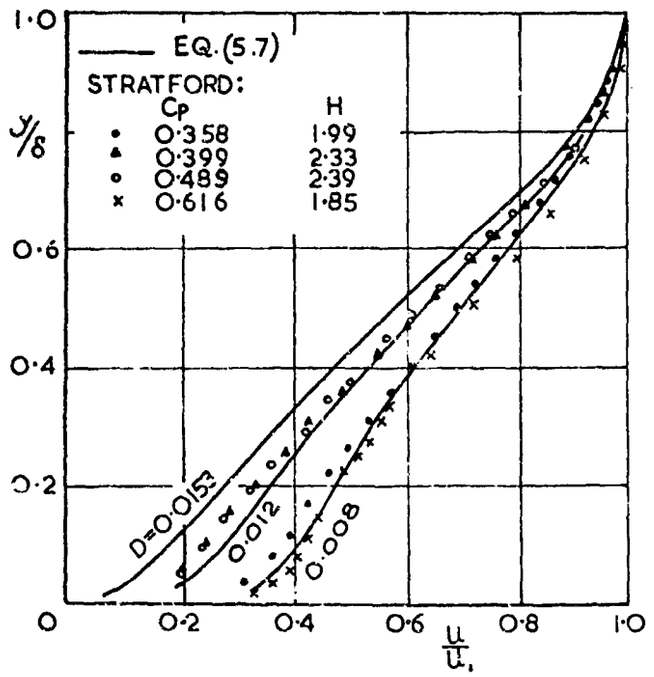

Fig.9 Separation Profiles

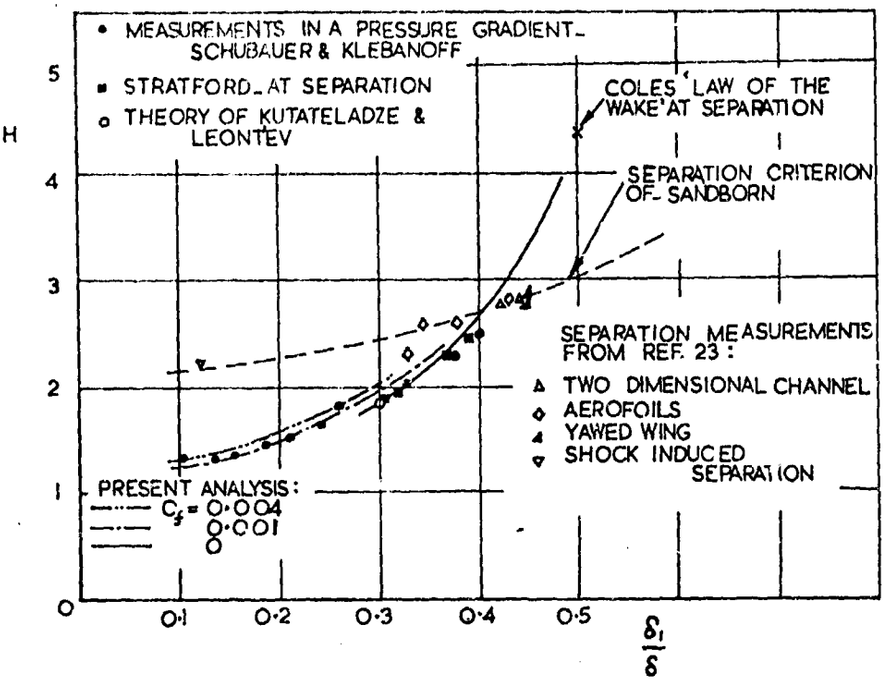

Fig.10 Variation of δ_1/δ with the form Parameter H

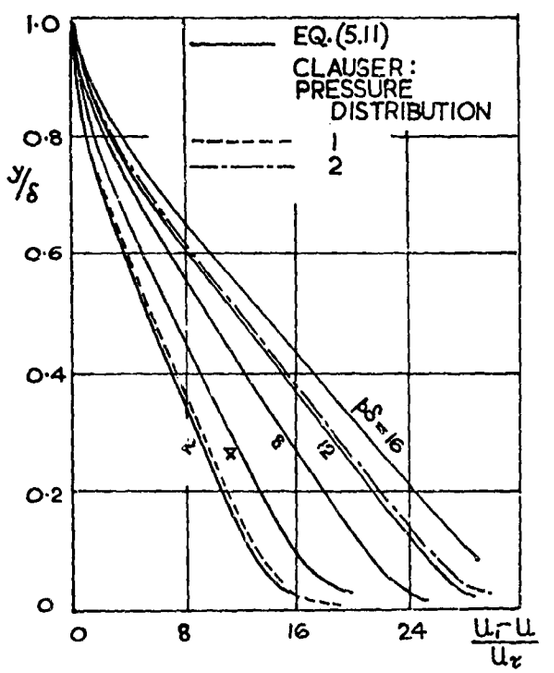

Fig.11 Measurements of Clauser

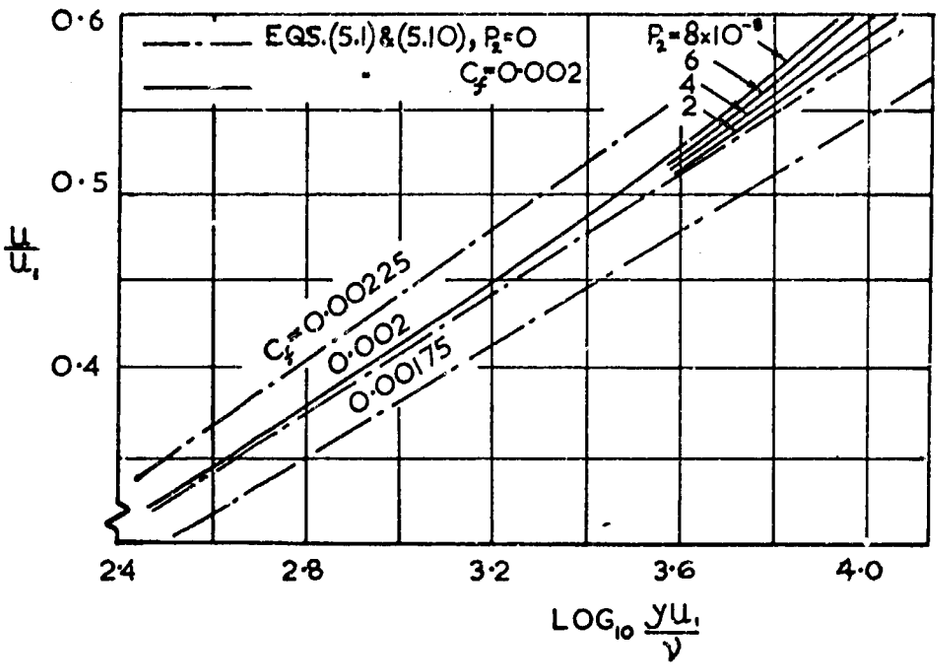

Fig. 12 The Intermediate Region

$$P_2 = -\frac{\nu}{u_1^2}\frac{du_1}{dx}$$

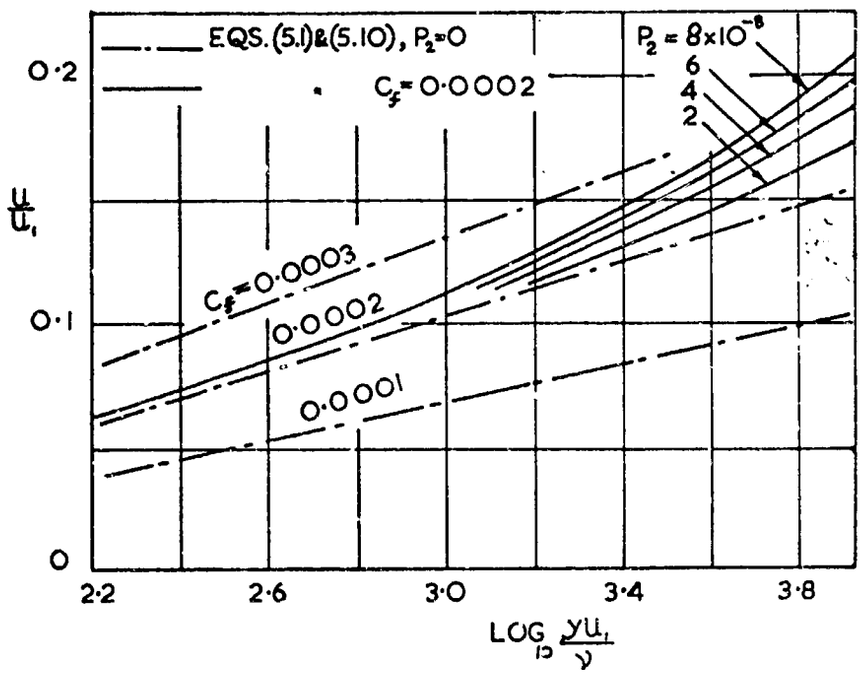

Fig. 13 The Intermediate Region

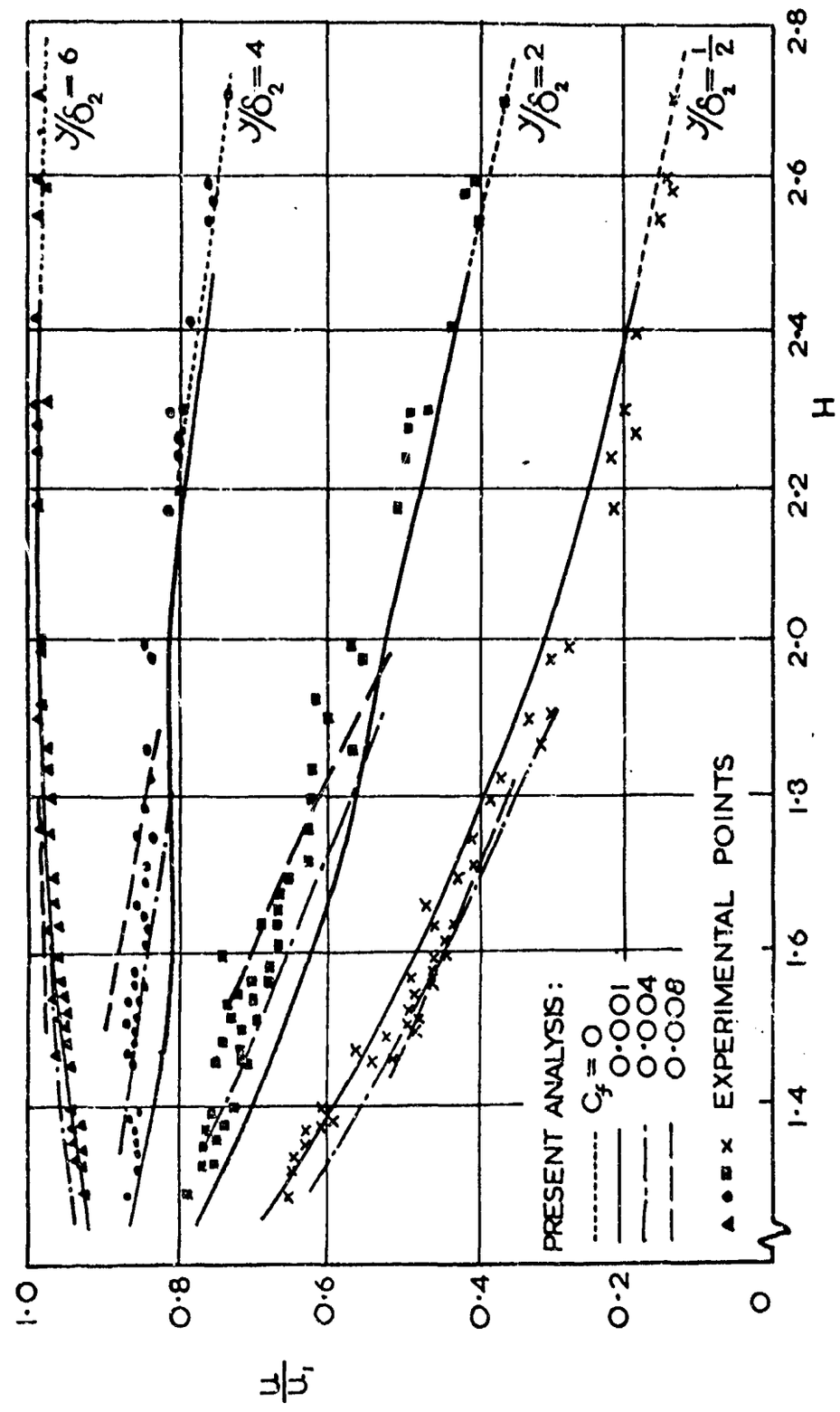

Fig. 14 Von Doenhoff and Tetervin's Measurements

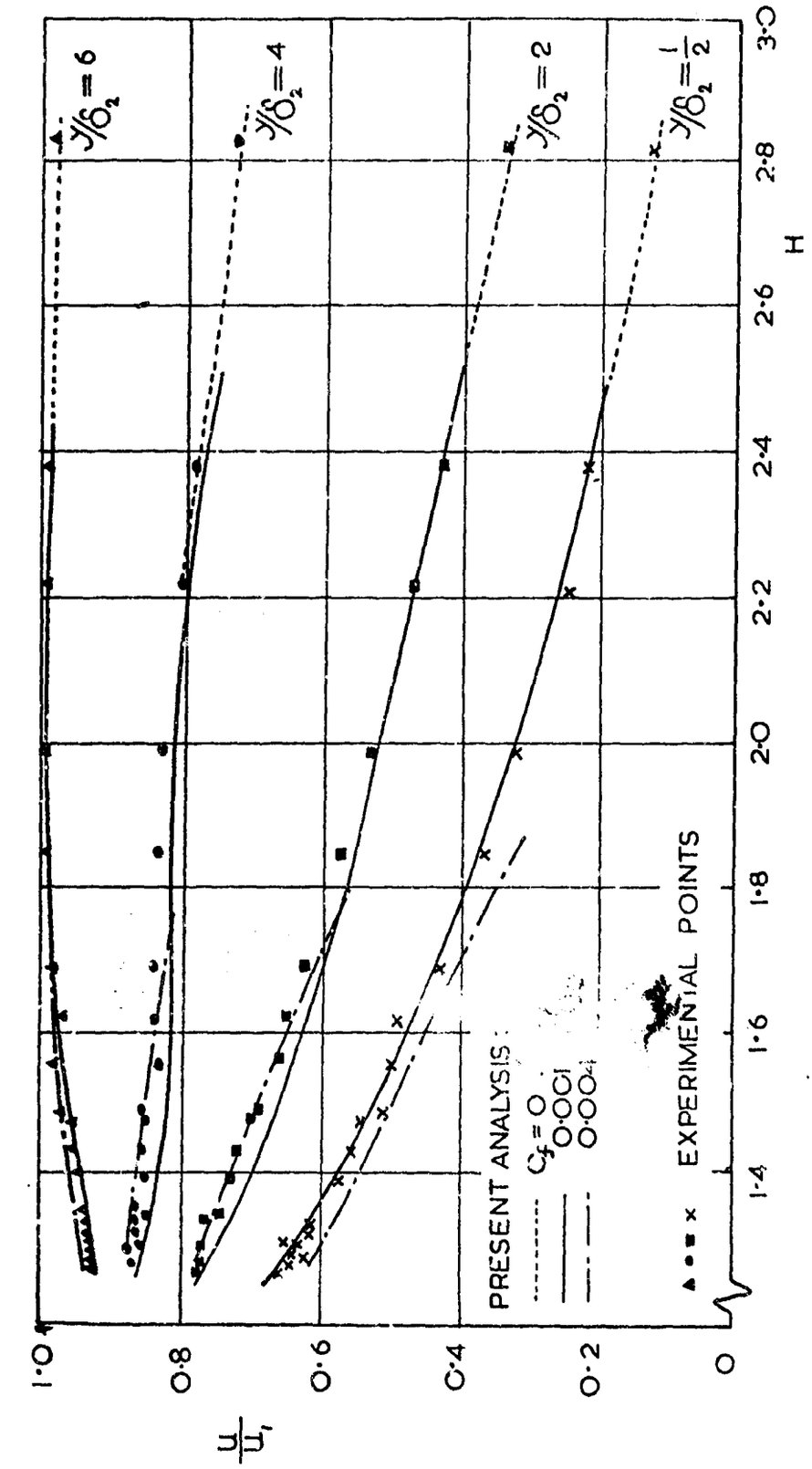

Fig. 15 Schubauer and Klebanoff's Measurements

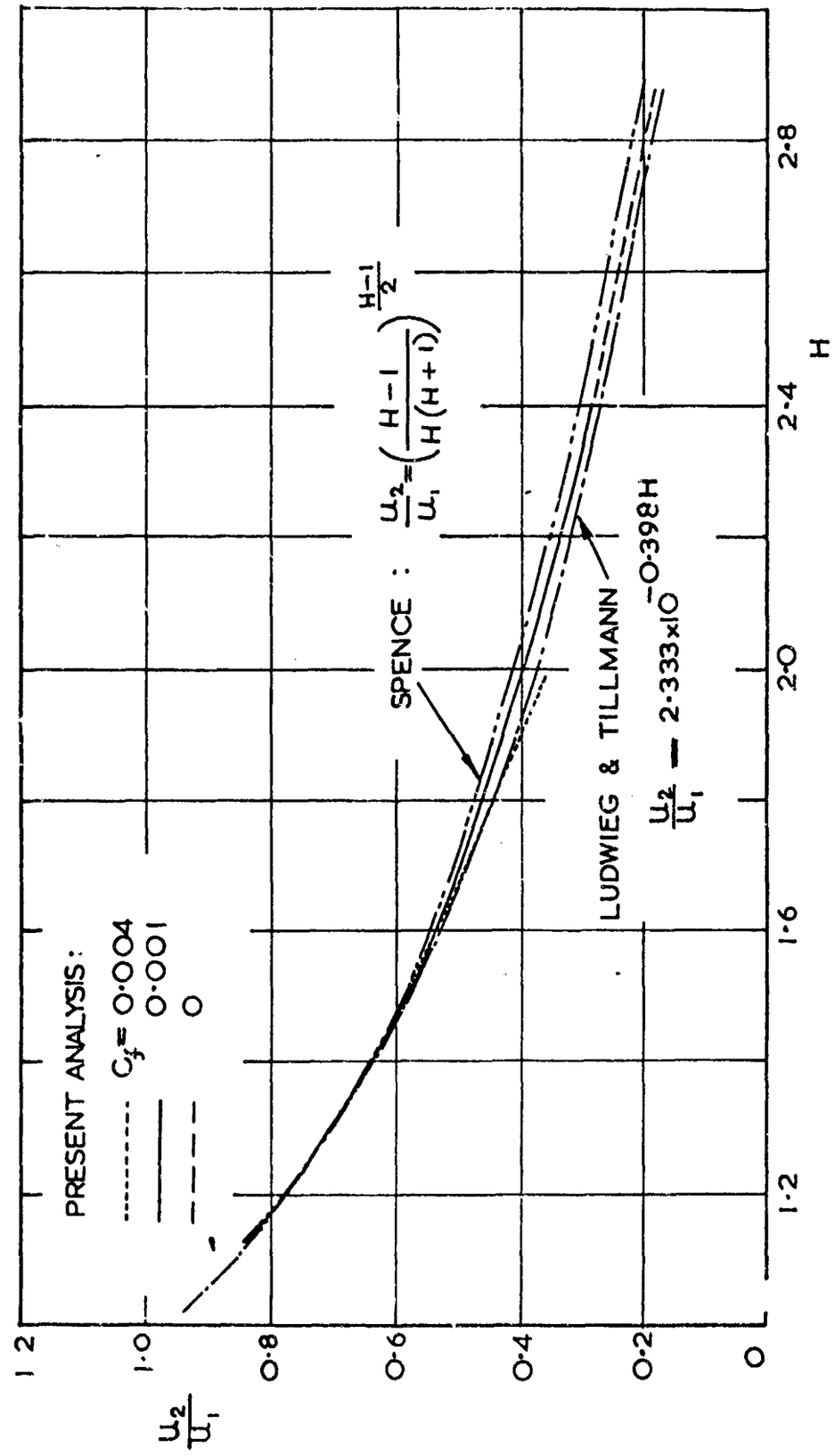

Fig.16 The Parameter u_2/u_1 as a Function of H

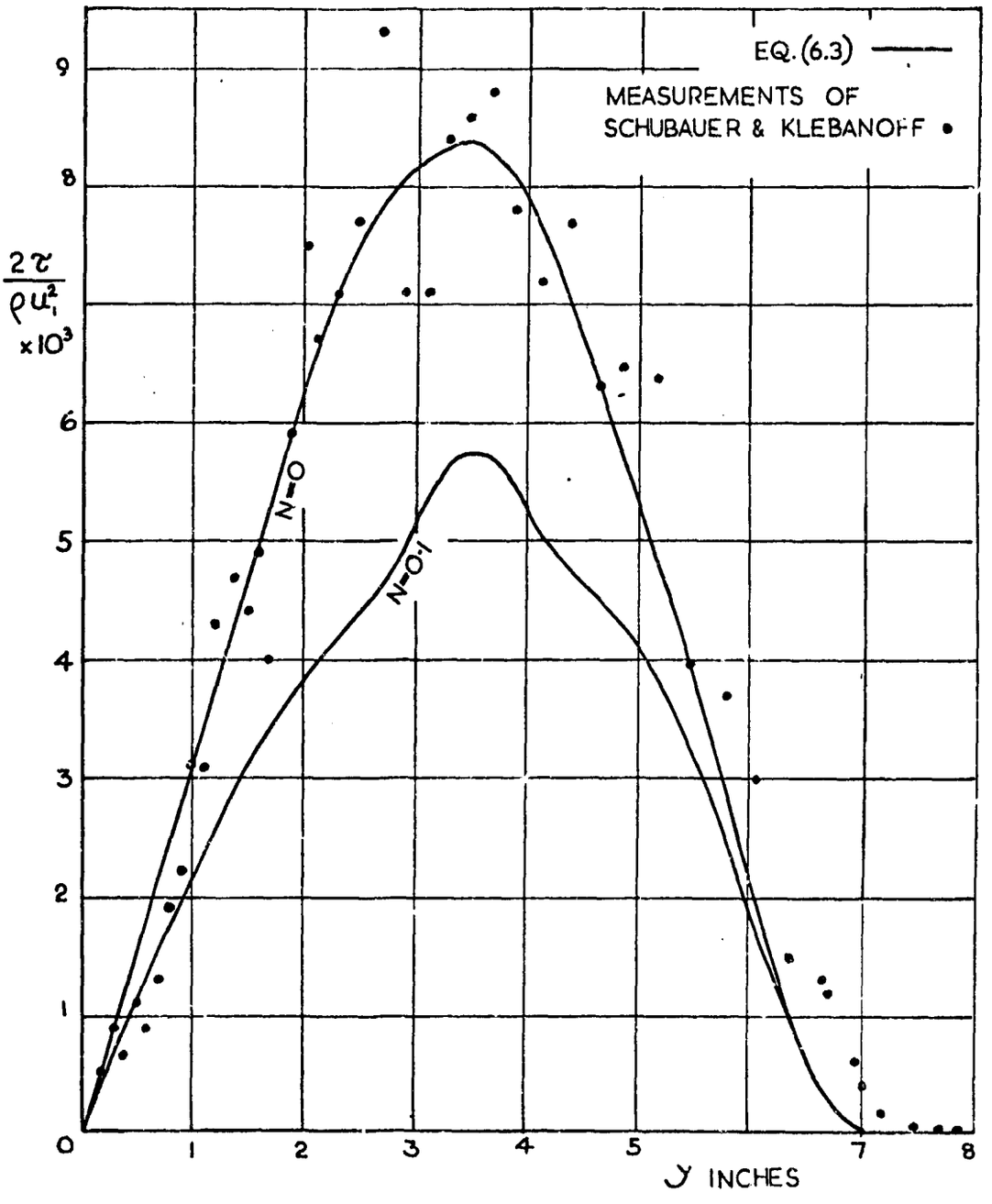

Fig. 17 Shear Stress Distribution at Separation

THE TURBULENT ASYMPTOTIC LAYER

by

H. Tennekes

Research Associate, Department of
Aeronautical Engineering, Technological
University Delft, the Netherlands.

SUMMARY

Some properties of turbulent asymptotic layers in zero pressure gradient with uniform suction, which are equilibrium layers in the sense defined by Clauser, are discussed. A provisional skin friction law for asymptotic layers is given. It is shown that mixing length theory is unable to acccunt for the similarity of the experimental data. The assumption of a constant eddy viscosity in the outer part of asymptotic layers leads to a fair representation of the experimental data. The magnitude of the eddy viscosity of asymptotic layers is only one fifth of the eddy viscosity of turbulent boundary layers on impervious walls.

SOMMAIRE

L'auteur expose certaines propriétés des couches turbulentes asymptotes avec gradient de pression nul et aspiration uniforme, c'est à dire des couches d'équilibre au sens défini par Clauser. Il présente une loi provisoire de frottement du revêtement pour les couches asymptotes, et démontre que la théorie de longueur du mélange ne peut rendre compte de la similitude des données expérimentales. L'hypothèse d'une viscosité de tourbillon constante dans la partie extérieure des couches asymptotes permit de se faire une juste présentation des données expérimentales. Le degré de viscosité de tourbillon des couches asymptotes ne représente qu'un cinquième de la viscosité de tourbillon des couches limites turbulentes le long de parois étanches.

CONTENTS

LIST OF FIGURES

NOTATIONS

$c_f = \frac{\tau_0}{\frac{1}{2}\rho U_\infty^2} = 2\left(\frac{u_*}{U_\infty}\right)^2$. skin friction coefficient

$c_Q = v_0/U_\infty$. suction volume coefficient

d integration constant in Equation (9) (m)

$\bar{U}_1$ mean velocity in boundary layer (m/sec)

U_∞ mainstream velocity (m/sec)

$u_* = (\tau_0/\rho)^{\frac{1}{2}}$. friction velocity (m/sec)

$-\overline{u_1 u_2}$ Reynolds shear stress (m^2/sec^2)

v_0 suction velocity ($v_0 < 0$) (m/sec)

$v^* = x_2 (\partial \bar{U}_1/\partial x_2)$. logarithmic velocity scale (m/sec)

x_1, x_2 Cartesian coordinates, along the surface and normal to the surface (m)

δ boundary layer thickness (m)

$\delta^* = \int_0^\infty \frac{U_\infty - \bar{U}_1}{U_\infty} dx_2$. displacement thickness (m)

$\Delta = U_\infty \delta^*/v^*$. Equation (21) (m)

ν kinematic viscosity (m^2/sec)

$\nu_T = \frac{-\overline{u_1 u_2}}{\partial \bar{U}_1/\partial x_2}$: eddy viscosity, Equation (11) (m^2/sec)

ρ fluid density ($kg\ sec^2/m^4$)

τ_0 wall shear stress (kg/m^2)

THE TURBULENT ASYMPTOTIC LAYER

H. Tennekes

1. INTRODUCTION

Of all incompressible turbulent boundary layers flowing along a flat plate in zero pressure gradient with uniform suction, the asymptotic layer merits special attention. An asymptotic layer is characterized by constant thickness and constant properties in streamwise direction. It will be seen that asymptotic layers are "equilibrium layers" in the sense defined by Clauser[1]. Some properties of this particular class of equilibrium layers will be discussed. The discussion will be based on the similarity laws for sucked and blown turbulent boundary layers given in an earlier paper of the author[2], which contains only a brief outline of the behavior of asymptotic layers.

The similarity laws for sucked turbulent boundary layers mentioned above are based on the concept that turbulent boundary layer flow can be described by a "law of the wall" and a "velocity defect law" which are related through a common velocity scale and a semi-logarithmic velocity profile in the region where these laws overlap. It has been shown[2] that for turbulent boundary layers at moderate suction rates ($0.04 < -v_0/u_\tau < 0.10$ approximately) the two similarity laws are

$$\frac{v_0 \bar{U}_1}{u_\tau^2} = f\left(\frac{v_0 x_2}{\nu}\right). \tag{1}$$

$$\frac{v_0}{u_\tau^2}(\bar{U}_1 - U_0) = F\left(\frac{x_2}{\delta}\right). \tag{2}$$

These laws are called the "limit law of the wall" and the "limit velocity defect law", respectively[2].

If the velocity profiles of asymptotic layers are plotted according to Equation (2), they exhibit similarity, as is shown in Figure 1. Note that δ is taken as the value of x_2 at which $\bar{U}_1 = 0.99\, U_0$. Note also that in the innermost part of the boundary layer Equation (2), which is a defect law, is not supposed to be valid. This accounts for the lack of similarity of the data points for $x_2/\delta < 0.1$. Since the velocity profiles of different asymptotic layers are similar in the appropriate velocity defect law plot, asymptotic layers are equilibrium layers in the sense defined by Clauser[1,2].

It has been shown[2] that the velocity defect law given as Equation (2) is consistent with the equations of motion for the outer part of the boundary layer. It has been shown also[2] that at small suction rates ($-v_0/u_\tau < 0.04$) no asymptotic layers can exist, since the velocity scale would then be no longer proportional to u_τ^2/v_0.

whereas the equations of motion for asymptotic layers admit only a velocity scale proportional to u_τ^2/ν_0 and the related defect law, Equation (2). In the following sections a few other properties of asymptotic layers will be discussed. The material of Sections 2 and 3 is taken from the author's unpublished dissertation[3].

2. A PROVISIONAL SKIN FRICTION LAW

Figure 1 indicates that a major part of the velocity profile of asymptotic layers is semi-logarithmic. The semi-logarithmic part extends almost to the outer edge of the boundary layer. In this respect the asymptotic layer resembles turbulent channel flow. In the latter flow, all streamwise derivatives are also zero. A semi-logarithmic part of the velocity profile is an essential part of the description of turbulent boundary layer flow in terms of separate similarity laws for the flow in the inner layer and the flow in the outer layer[2]. For asymptotic layers, the logarithmic velocity profile may be represented by the following formula:

$$-\frac{v_0}{u_\tau^2}(\bar{U}_1 - U_c) = 0.96 \log_e\left(\frac{x_2}{\delta}\right) - 0.01 . \qquad (3)$$

An experimental investigation of the effects of v_0/u_τ on the velocity profile in the inner layer[3], of which the details cannot be given here, has shown that the logarithmic part of the velocity profile may provisionally be represented by

$$-\frac{v_0\bar{U}_1}{u_\tau^2} = 4.86 \log_e\left(\frac{-v_0 x_2}{\nu}\right) - 11\frac{v_0}{u_\tau} + 8.19 . \qquad (4)$$

Equation (4) is valid for flow at moderate suction rates along smooth surfaces. Since most porous surfaces are not hydrodynamically smooth, care should be observed when applying Equation (4).

Equations (3) and (4) may be combined to yield the following skin friction law for turbulent asymptotic layers:

$$0.86 \log_e\left(\frac{-v_0\delta}{\nu}\right) = 11\frac{v_0}{u_\tau} + 0.38 . \qquad (5)$$

Note that for asymptotic layers $u_\tau^2 = -v_0 U_1$, which follows from the momentum integral equation[2]. Hence, $v_0/u_\tau = -u_\tau/U_1$ and $2c_f = c_f$, so that Equation (5) may be rewritten as

$$11\frac{u_\tau}{U_c} = 11\left(\frac{c_f}{2}\right)^{\frac{1}{2}} = 0.80 - 0.86 \log_e\left(\frac{-v_0\delta}{\nu}\right), \qquad (6)$$

valid only for asymptotic layers flowing along smooth porous walls.

3. THE INADEQUACY OF MIXING LENGTH THEORY

In almost all the current literature on sucked and blown turbulent boundary layers, e.g. References 4, 5, 6, Prandtl's momentum transport version of mixing length theory is used to obtain a prediction of the shape of the velocity profile. The basic hypothesis of momentum transport theory is, for flow near a solid surface[7]

$$-\overline{u_1 u_2} = k^2 x_2^2 \left(\frac{\partial \bar{U}_1}{\partial x_2}\right)^2 . \tag{7}$$

For the flow in the fully turbulent part of an asymptotic layer, the equations of motion reduce to

$$v_0 \bar{U}_1 - v_2 U_0 = -\overline{u_1 u_2} . \tag{8}$$

Substitution of Equation (7) into Equation (8) yields, after integration

$$v_2 \bar{U}_1 - v_0 U_0 = \left\{\frac{v_0}{2k} \log_e \left(\frac{x_2}{d}\right)\right\}^2 . \tag{9}$$

The constant of integration d in Equation (9) remains as yet undetermined. Since a squared logarithm occurs in Equation (9), it is called the "bi-logarithmic law"[3,8].

The bi-logarithmic law provides a sharp contrast with the semi-logarithmic velocity profiles shown in Figure 1 and represented by Equation (3). However, the main objection to Equation (9) is that it cannot account for the observed similarity of the velocity profiles in a plot according to Equation (2). This is shown as follows. Sarnecki[8] states that for asymptotic layers the velocity profile departs only slightly from Equation (9), even near the edge of the boundary layer. If this conjecture, which is used also by Stevenson[4], is accepted, the parameter d should be identified with the boundary layer thickness δ, since according to Equation (9) $\bar{U}_1 = U_1$ at $x_2 = d$. This implies that Equation (9) can be non-dimensionalized as follows:

$$\frac{v_0}{u_\tau^2}(\bar{U}_1 - U_1) = \left\{\frac{v_0}{2ku_\tau} \log_e \left(\frac{x_2}{\delta}\right)\right\}^2 . \tag{10}$$

Equation (10) obviously contradicts the limit velocity defect law, Equation (2), due to the presence of the parameter v_0/u_τ at the right hand side. It can be shown easily[3] that the discrepancy between Equation (2) and (9) is not reconciled when instead of δ another length scale is chosen to non-dimensionalize x_2.

4. THE EDDY VISCOSITY CONCEPT

Since the limit velocity defect law, Equation (2), in first instance does not prescribe a particular shape of the velocity profile, one is tempted to introduce a constant eddy viscosity in order to obtain a formal solution of the equations of motion. This approach has been used successfully for the description of the flow in the outer part of turbulent boundary layers on impervious surfaces[2,5]. For asymptotic layers a similar analysis will be carried out here. Suppose the turbulent shear stress in the outer layer can be represented by

$$-\overline{u_1 u_2} = \nu_T \frac{\partial \bar{U}_1}{\partial x_2} . \tag{11}$$

in which ν_T does not depend on x_2. Substitution of this expression into the equation for the mean flow, Equation (8), and subsequent integration yield

$$\frac{\nu_0}{u_\tau^2} (\bar{U}_e - \bar{U}_1) = C_1 \exp\left(\frac{\nu_e x_2}{\nu_T}\right) . \tag{12}$$

in which C_1 is a so far arbitrary integration constant.

The boundary layer thickness of the velocity profile given in Equation (12) is derived as follows. Assume that δ is the value of x_2 at which $\bar{U}_1 = 0.99\ U_e$. Equation (12) then yields, when u_τ^2 is replaced by $-\nu_e U_e$.

$$0.01 = C_1 \exp \frac{\delta \nu_e}{\nu_T} . \tag{13}$$

This means that

$$\frac{\nu_e \delta}{\nu_T} = C_2 . \tag{14}$$

C_1 and C_2 being related through $C_1 \exp C_2 = 0.01$. By substitution of Equation (14) into Equation (12) one obtains

$$\frac{\nu_e}{u_\tau^2} (\bar{U}_1 - U_e) = C_1 \exp\left(C_2 \frac{x_2}{\delta}\right) . \tag{15}$$

Comparison of this velocity profile with the general expression for the limit defect law shows that C_1 and C_2 should be constants, independent of any parameter. Choosing $C_1 = 0.2$ and $C_2 = -3$, a fair representation of the actual velocity profile is obtained. This conclusion is drawn from Figure 2, which compares the velocity profiles given by Equations (3) and (15). It is therefore very well possible to describe the mean flow in the outer layer of asymptotic layers as if it were caused by a constant eddy viscosity. On the other hand, it is surprising that for asymptotic layers the semi-logarithmic velocity profile in the region of overlap between the similarity laws for the outer layer and the inner layer coincides to a large extent with the velocity profile in the outer layer as described by a constant eddy viscosity.

The magnitude of the eddy viscosity is found by substituting $C_2 = -3$ into Equation (14):

$$\nu_T = -0.33\ \nu_e \delta . \tag{16}$$

For turbulent boundary layers on impermeable walls on the contrary, the eddy viscosity is given by[1]

$$\nu_T = 0.016\ U_e \delta^* . \tag{17}$$

Before attempting an interpretation of these data, Equations (16) and (17) should be rearranged in order to obtain expression which contain the same variables.

If Equations (16) and (17) are to be rewritten in a suitable set of variables, the "logarithmic velocity scale" $(w^*)^{2,3}$ has to be introduced:

$$w^* = x_2 \frac{\partial \bar{U}_1}{\partial x_2} . \tag{18}$$

taken in the semi-logarithmic part of the velocity profile, so that w^* is independent of x_2. For turbulent boundary layers on impervious surfaces

$$w^* = 2.3\, u_\tau . \tag{19}$$

whereas for turbulent boundary layers at moderate suction rates

$$w^* = -9.0\bar{6} \frac{u_\tau^2}{v_0} . \tag{20}$$

Equation (30) can be verified directly by differentiation of Equation (3). Equation (19) is merely the differential form of the well-known velocity profile for unsucked turbulent boundary layers[1].

The logarithmic velocity scale can be used to define a suitable boundary layer thickness:

$$\Delta = \int_{x_2}^{\infty} \frac{U_0 - \bar{U}_1}{w^*} dx_2 = \frac{U_0}{w^*} \int_{x_2}^{\infty} \frac{U_0 - \bar{U}_1}{U_0} dx_2 = \frac{U_0 \delta^*}{w^*} .$$

so that

$$w^* \Delta = U_0 \delta^* . \tag{21}$$

Equation (21) is valid for all turbulent boundary layers in which a logarithmic velocity scale can be defined.

In order to write Equation (16) in a suitable form, the relation between δ and Δ for asymptotic layers is needed. This ratio can be calculated by substitution of Equations (15) and (20) into the definition of Δ given above. The result is ($C_1 = 0.2$, $C_2 = -3$)

$$\delta = 0.9\Delta . \tag{22}$$

Substituting Equation (22) into Equation (16), one obtains for asymptotic layers

$$\nu_T = -0.3\Delta v_0 . \tag{23}$$

Substituting on the other hand Equation (21) into Equation (17), one obtains for turbulent boundary layers on impermeable surfaces

$$\nu_T = 0.016 \Delta w^* . \tag{24}$$

The final step of the "transformation" into suitable variables can be taken by noticing that for turbulent boundary layers at moderate suction rates $v_0 = -0.06\, u_\tau^2/w^*$ and that for unsucked boundary layers $w^* = 5.3\, u_\tau^2/w^*$ (using Eqs. (20) and (19), respectively). Substitution of these expressions into Equations (23) and (24) gives for asymptotic layers

$$\nu_T = 0.018 \frac{\Delta u_\tau^2}{w^*} , \tag{25}$$

and for boundary layers on impervious walls

$$\nu_T = 0.035 \frac{\Delta u_\tau^2}{w^*} . \tag{26}$$

Equations (25) and (26) should be compared with the definition of ν_T given in Equation (11). The velocity gradient $\partial \bar{U}_1/\partial x_2$ is proportional to w^*/Δ, w^* being the velocity scale and Δ a clearly defined boundary layer thickness. The shear stress $-\overline{u_1 u_2}$ is proportional to the wall shear u_τ^2. It may be concluded that the eddy viscosity should be proportional to $u_\tau^2 \Delta / w^*$, so that Equations (25) and (26) are at least dimensionally correct. The eddy viscosity of asymptotic layers can now be compared with the eddy viscosity of unsucked turbulent boundary layers, since both are written in terms of the same variables. It is seen that the eddy viscosity of asymptotic layers (and possibly of all equilibrium layers at moderate suction rates) is only one fifth as large as the eddy viscosity of unsucked turbulent boundary layers.

A final suggestion will now be made concerning the lack of agreement between Equations (25) and (26). If Equation (15) is substituted into Equation (8), one obtains ($C_1 = 0.2$, $C_2 = -3$)

$$\frac{-\overline{u_1 u_2}}{u_\tau^2} = 0.2 \exp\left(-3 \frac{x_2}{\delta}\right) . \tag{27}$$

valid for asymptotic layers only. Close to the wall therefore $-\overline{u_1 u_2} = 0.2\, u_\tau^2$ approximately, i.e. in this context the "representative level of shear stress" is only one fifth of the wall shear. On the other hand, for unsucked boundary layers $-\overline{u_1 u_2} = u_\tau^2$ close to the wall. If not u_τ^2, but $(-\overline{u_1 u_2})_{eff}$ is used in the expressions for the eddy viscosity, Equations (25) and (26) unite, to yield approximately

$$\nu_T = 0.09\, (-\overline{u_1 u_2})_{eff} \frac{\Delta}{w^*} . \tag{28}$$

This expression is obviously provisional. It is not presented as a final result, but rather to indicate a direction in which further progress may be expected.

REFERENCES

1. F.H. Clauser — *The Turbulent Boundary Layer*, Advances in Applied Mechanics, Vol.IV, p.1-51, Academic Press, New York (1956).

2. H. Tennekes — *Similarity Laws for Turbulent Boundary Layers with Suction or Injection*, Journal of Fluid Mechanics, Vol.21 (in the Press), (1965).

3. H. Tennekes — *Similarity Laws for Turbulent Boundary Layers with Suction or Injection*, Dissertation, Delft (1964).

4. H.S. Mickley, R.S. Davis — *Momentum Transfer over a Flat Plate with Blowing*, National Advisory Committee for Aeronautics, Tech. Note 4017 (1957).

5. T.J. Black, A.J. Sarnecki — *The Turbulent Boundary Layer with Suction or Injection*, Aeronautical Research Council, London, 20,501 (FM 2745), (1958).

6. T.N. Stevenson — *Turbulent Boundary Layers with Transpiration*, AIAA Journal, Vol.2, p.1500-1502 (1964).

7. L. Prandtl — *The Mechanics of Viscous Fluids*. W.F. Durand, Aerodynamic Theory, Vol.III, Section G, p.34-208, Springer, Berlin (1935).

8. A.J. Sarnecki — *The Turbulent Boundary Layer on a Permeable Surface*, Dissertation, Cambridge (1959).

9. A.A. Townsend — *Equilibrium Layers and Wall Turbulence*, Journal of Fluid Mechanics, Vol.11, p.97-120 (1961).

10. J.M. Kay — *Boundary Layer Flow with Uniform Suction*, Aeronautical Research Council, London, R & M 2628 (1948).

11. R.A. Dutton — *The Effects of Distributed Suction on the Development of Turbulent Boundary Layers*, Aeronautical Research Council, London, R & M 3155 (1960).

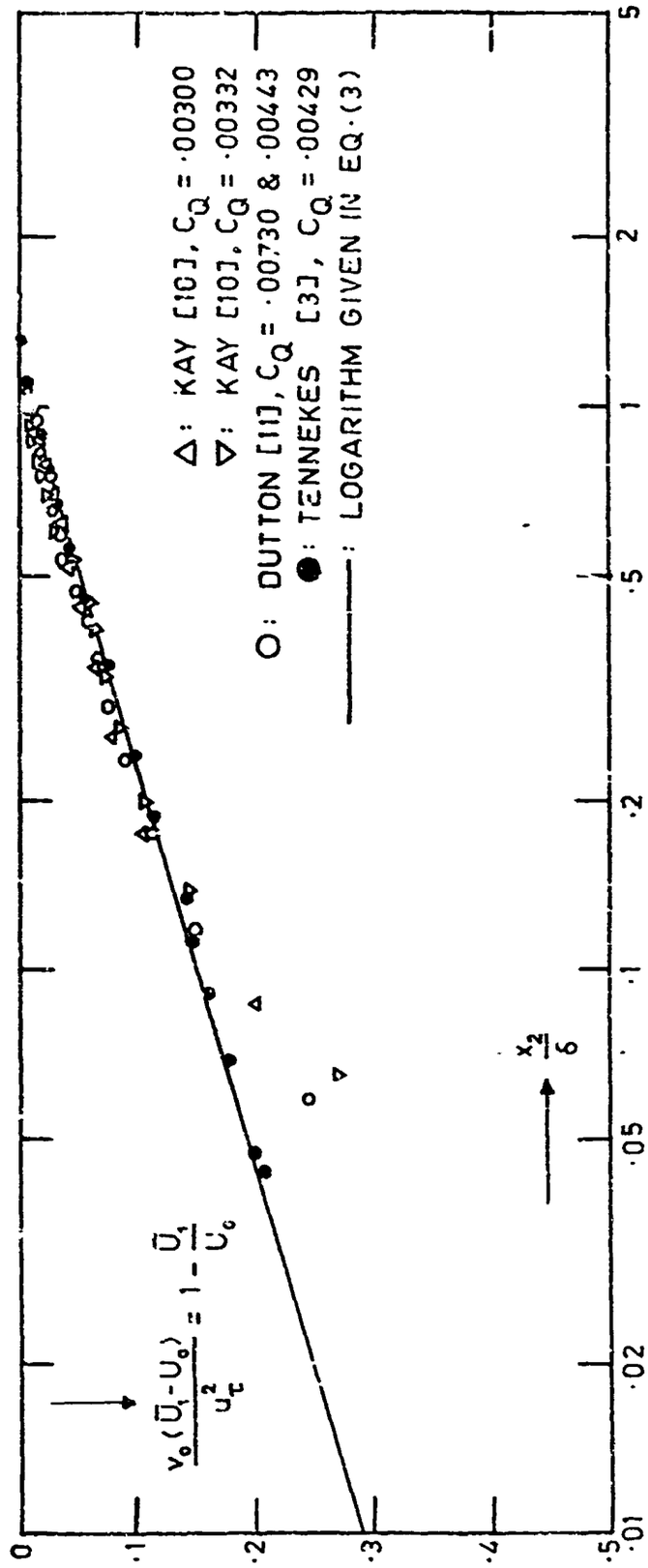

Fig. 1 Velocity profiles of asymptotic layers. Semi-logarithmic plot according to Equation (2)

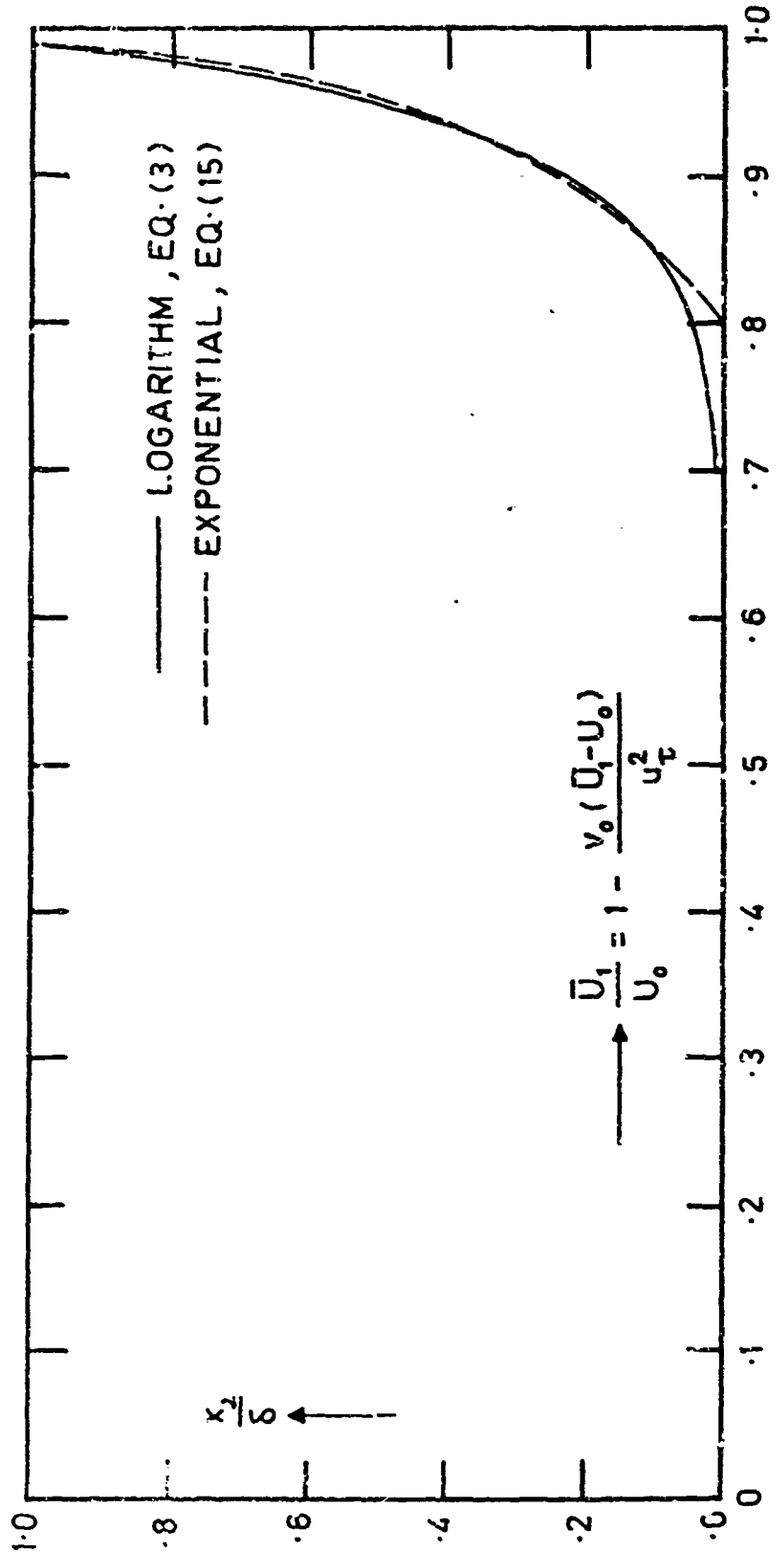

Fig.2 Comparison of the logarithmic velocity profile given by Equation (3) and the exponential velocity profile given by Equation (15)

THE STABILITY OF THE COMPRESSIBLE LAMINAR BOUNDARY LAYER ACCORDING TO A DIRECT NUMERICAL SOLUTION

by

L.M. Mack

Jet Propulsion Laboratory,
California Institute of Technology,
California, U.S.A.

SUMMARY

Two direct numerical methods are used to obtain eigenvalues and eigenfunctions of the complete linearized stability equations and of the inviscid stability equations. For the inviscid equations, new families of amplified solutions are found. The maximum amplification rates and frequencies of these solutions are computed as functions of M_1, the free-stream Mach number, and as functions of wall temperature (cooled wall only) at $M_1 = 5.8$. It is found that one of the new families of solutions is the most unstable and is destabilized by cooling. For finite Reynolds numbers, neutral stability curves are computed, and at a fixed Reynolds number the maximum amplification of disturbances of constant frequency is computed as a function of M_1 and of the wall temperature at $M_1 = 5.8$. The maximum amplification decreases with increasing M_1 at low supersonic Mach numbers, rises to a peak near $M_1 = 5$, and then decreases with further increases in M_1. Cooling the wall is found to have little effect on the maximum amplification.

SOMMAIRE

On utilise deux méthodes numériques directes pour la détermination des valeurs et fonctions propres des équations linéarisées complètes de la stabilité ainsi que des équations de la stabilité sans frottement. Pour les équations sans frottement, on trouve de nouvelles familles de solutions amplifiées. Les taux et fréquences maxima d'amplification de ces solutions sont calculées comme des fonctions de M_1, le nombre de Mach en courant libre, et comme des fonctions de la température pariétale (paroi refroidie seulement), pour $M_1 = 5.8$. On constate que l'une des nouvelles familles de solutions est la plus instable, et se trouve éloignée de la stabilité par le refroidissement. Pour les nombres de Reynolds finis, on calcule les courbes de stabilité neutre et pour un certain nombre de Reynolds l'amplification maximale des perturbations de fréquence constante est calculée comme une fonction de M_1 et de la température pariétale pour $M_1 = 5.8$. L'amplification maximale décroît à mesure que M_1 croît aux faibles nombres de Mach supersoniques, croît ensuite jusqu'à une valeur limite aux alentours de $M_1 = 5$, et décroît de nouveau à mesure que M_1 continue de croître. On constate que le refroidissement de la paroi a une faible influence sur l'amplification maximale.

CONTENTS

LIST OF FIGURES

NOTATION

A	disturbance amplitude
A_1	amplitude of constant-frequency disturbance at start of unstable region
A_J	disturbance amplitude at $R = 100$
c	dimensionless complex wave velocity, $c_r + ic_i$
c_s	phase velocity at generalized inflection point
f	amplitude function of longitudinal velocity fluctuation
F	dimensionless frequency, $\beta^*\nu^*/U^{*2}$
M_1	free-stream Mach number
$\bar{M}$	local Mach number of mean flow relative to phase velocity c_r
n	mode number
p	pressure
Q	typical dependent variable
r	amplitude function of density fluctuation
R_x	free-stream x-Reynolds number, U^*x^*/ν^*
$R = \sqrt{R_x}$	
R_1	Reynolds number at start of unstable region for constant-frequency disturbance
t	time
T	static temperature
T_w	wall temperature
T_r	temperature of insulated wall
u	x-component of velocity
U	free-stream velocity
v	y-component of velocity
x	co-ordinate parallel to free-stream velocity

y	co-ordinate normal to free-stream velocity
Z_i	dependent variable, Equation (6)
α	dimensionless wave number, $(2\pi/\lambda^*)(x^*/R)$
α_{sn}	wave number of inviscid neutral solution with phase velocity c_s, n^{th} mode
α_{in}	wave number of inviscid singular neutral solution ($c_r = 1$), n^{th} mode
β	circular frequency
γ	ratio of specific heats
η	Blasius variable, $(y^*/x^*)R$
η_s	point in boundary layer where $u = c_s$
η_0	point in boundary layer where $u = 1 - 1/M_1$
θ	amplitude function of temperature fluctuation
λ	wave length
ν	free-stream kinematic viscosity coefficient
π	amplitude function of pressure fluctuation
ρ	density
ϕ	amplitude function of normal velocity fluctuation

Superscripts: An asterisk (*) refers to a dimensional quantity; primes (′) to derivatives with respect to η; a tilde (~) to a disturbance quantity.

THE STABILITY OF THE COMPRESSIBLE LAMINAR BOUNDARY LAYER ACCORDING TO A DIRECT NUMERICAL SOLUTION

L.M. Mack

1. INTRODUCTION

The instability of the compressible laminar boundary layer is customarily assumed to play the same role in the transition process at supersonic speeds as it does in low speed flow. However, this assumption has been made without a detailed knowledge of the instability characteristics of the laminar boundary layer over a wide range of Mach numbers and wall temperatures. The results presented in this paper are from an extensive investigation which was carried out in order to remedy this lack of information.

Previous calculations of the stability of the compressible boundary layer[1,2,3] have been hampered by the inadequacies of the asymptotic method. With the capabilities of the present-day computer, the asymptotic method has become obsolete for the production of numerical results. It is now possible to obtain the eigenvalues and eigenfunctions of the linearized stability equations of Lees and Lin[4] directly and without having to neglect any terms. A direct numerical method of solution and a few results were first given by Brown[5,6], originally for the simplified Dunn-Lin equations[7], and later for the complete equations. The method used in this paper was developed independently of Brown's method and is described in detail elsewhere[8].

The compressible boundary layer, unlike the boundary layer at low speeds, is dynamically unstable; i.e., it is unstable to purely inviscid disturbances. This instability, which is slight for low Mach numbers, begins to strongly affect the stability characteristics of the boundary layer along an insulated wall in the Reynolds number range of interest at about $M_1 = 3$. In order to study the inviscid stability separately, a second numerical method was developed to compute the eigenvalues and eigenfunctions of the inviscid stability equations.

The plan of the paper is as follows: In Section 2 a brief description is given of the numerical methods used to produce the results to be presented in the remainder of the paper. Section 3 is devoted to results obtained from the inviscid stability equations. The maximum amplification rate and the frequency with the maximum amplification rate are given as functions of Mach number up to $M_1 = 10$, and as functions of the wall temperature (cooled wall only) at $M_1 = 5.8$. The results obtained at finite Reynolds numbers with the program for the solution of the complete stability equations are given in Section 4. The effects of Mach number on the neutral-stability curve, the maximum over-all amplification of constant-frequency disturbances at a fixed Reynolds number, and the frequency of the disturbance with maximum amplification are all given. The paper concludes with a presentation of the effect of cooling on the amplification characteristics at one Reynolds number at $M_1 = 5.8$.

2. METHODS OF SOLUTION

2.1 Complete Stability Equations

The numerical results of Section 4 are obtained from the linearized two-dimensional stability equations of Lees and Lin[4]. These equations are derived from the Navier-Stokes equations by writing each dependent variable as a steady mean-flow term plus a time-dependent disturbance term, linearizing the resulting equations, and subtracting out the mean-flow equations. Next, the parallel-flow assumption of no x-variation in the mean-flow is applied, and the equations are made dimensionless with respect to free-stream quantities. The independent variable is taken to be

$$\eta = \frac{y^*}{x^*} R \tag{1}$$

the Blasius boundary-layer variable, where

$$R = \sqrt{R_x} \tag{2}$$

and R_x is the free-stream x-Reynolds number. Finally, the five dependent disturbance variables $\tilde{u}$, $\tilde{v}$, $\tilde{p}$, $\tilde{\rho}$, $\tilde{T}$ are written as

$$\tilde{Q}(x,\eta,t) = Q(\eta) \exp[i\alpha(x - ct)] \tag{3}$$

where $Q(\eta)$ is any of the five dimensionless complex amplitude functions f , $\alpha\phi$, π , r , θ for the above five dependent variables, respectively. The dimensionless wave number α is defined by

$$\alpha = \frac{2\pi}{\lambda^*} \frac{x^*}{R} \tag{4}$$

where λ^* is the wave length. An asterisk ($*$) refers to a dimensional quantity. The complex velocity, which is made dimensionless with respect to the free-stream velocity U^* , is

$$c = c_r + ic_i \ . \tag{5}$$

Hence, c_r is the phase velocity of the disturbance in the x-direction, and αc_i is the time rate of amplification. A positive c_i means the disturbance is amplified, and a negative c_i means damping.

$$\left.\begin{aligned} Z_1 &= f \qquad Z_2 = f' \qquad Z_3 = \phi \\ Z_4 &= \frac{\pi}{\gamma M_1^2} \qquad Z_5 = \theta \qquad Z_6 = \theta' \end{aligned}\right\} . \tag{6}$$

The primes refer to differentiation with respect to η . These equations, which are much too lengthy to write out here, are in a convenient form for numerical integration.

The boundary conditions are that the two velocity fluctuations and the temperature fluctuation are zero at the wall, $\eta = 0$, and that all disturbances are bounded at infinity.

$$\left.\begin{array}{lll} \text{at } \eta = 0 & Z_1(0) = 0\,,\ Z_3(0) = 0\,,\ Z_5(0) = 0 \\ \text{as } \eta \to \infty & Z_1\,,\ Z_3\,,\ Z_5 & \text{are bounded} \end{array}\right\}. \tag{7}$$

The temperature boundary condition is appropriate for fluctuations whose frequency is high enough so that the solid material of the wall remains at the wall temperature of the mean boundary layer.

The computer program is written in FORTRAN IV for the IBM 7094 computer. Double-precision arithmetic (16 significant decimal digits) is used for all numerical operations. The numerical method consists of constructing an eigensolution from three linearly independent numerical solutions. These solutions are obtained by first solving the equations with constant coefficients to which the stability equations reduce outside of the boundary layer. From these six solutions, the three which are bounded as $\eta \to \infty$ are selected. The numerical integration of these three solutions from the edge of the boundary layer to $\eta = 0$ yields the needed three linearly independent solutions. An eighth-order Adams-Moulton method with fixed step size is used for the integration. It is possible to perform this integration up to values of αR in the neighborhood of 300, with the exact value dependent upon c. At $\eta = 0$ the three solutions are combined to satisfy the two velocity boundary conditions. The third boundary condition, $Z_5(0) = 0$, can only be satisfied by a non-trivial solution when the parameters α, c, and R form a set of eigenvalues. The eigenvalues are found by one of the three linear search procedures provided in the program. The first of these obtains α and R for a specified c, the second c for specified α and R, and the third c for specified F and R, where

$$F = \frac{\beta^* \nu^*}{U^{*2}} = \frac{\alpha c_r}{R} \tag{8}$$

is the dimensionless frequency. In Equation (8), β^* is the circular frequency and ν^* is the kinematic viscosity coefficient. Once the eigenvalues are known, the eigenfunctions are obtained by combining the three independent solutions at the edge of the boundary layer and integrating the combined solution.

An important quantity in the present investigation is the over-all amplification between two Reynolds numbers of a disturbance of constant frequency. When the amplification at a specific Reynolds number is known for several frequencies, the response of the boundary layer at that Reynolds number to any known disturbance can be computed. The time rate of amplification at a particular x-location in the boundary layer is assumed to be the same as in the parallel flow of the theory. From Equation (3),

$$\frac{1}{A^*}\frac{dA^*}{dt^*} = \alpha^* c_i^*\,. \tag{9}$$

In order to convert the time rate of amplification into a space rate of amplification, the velocity at which the disturbance actually travels through the boundary layer is needed. Although it is customary to use the group velocity for this purpose[9], the phase velocity has been used throughout the present computation for reasons of economy. Also, it was later found that the dispersion (c_r vs α relation) in the boundary layer can be anomalous, and under this circumstance the use of the group velocity is no longer correct. The dimensionless space rate of amplification is, from Equation (9) and with the use of the phase velocity,

$$\frac{1}{A}\frac{dA}{dR} = 2\frac{\alpha c_i}{c_r} . \tag{10}$$

Therefore, the ratio of the amplitude A at Reynolds number R to the amplitude A_1 at Reynolds number R_1 is

$$\frac{A}{A_1} = \exp\left(2\int_{R_1}^{R}\frac{\alpha c_i}{c_r}\,dR\right). \tag{11}$$

The program is used to find $\alpha c_i/c_r$ at several Reynolds numbers for a given frequency, and the integral in Equation (11) is evaluated graphically.

2.2 Inviscid Stability Equations and Boundary-Layer Equations

The inviscid stability equations are obtained from the complete stability equations by taking the limit $R \to \infty$. The resulting equations can be written as a single second-order equation. However, this equation is unsuitable for numerical integration because the term $T - M_1^2(u - c)^2$, which occurs in a denominator, can be zero (u and T are the mean boundary layer velocity and temperature). The two first-order equations,

$$Z_4' = -\frac{i\alpha^2(u - c)}{T} Z_3 \tag{12}$$

$$Z_3' = \frac{u'}{u - c} Z_3 + i\,\frac{[T - M_1^2(u - c)^2]}{u - c} Z_4 \tag{13}$$

which were used by Lees and Lin to show that $[T - M_1^2(u - c)^2] = 0$ is not a true singularity, are free from this difficulty and are the equations selected for the numerical integration.

Equations (12) and (13) have a singularity at the point where $u = c$. In order to avoid both this singularity and the need to expand the solutions in power series about the singularity, the equations are integrated along an indented rectangular contour in the complex η plane. This method has been used successfully by Zaat[10] for the incompressible boundary layer. In accordance with the requirements of the inviscid stability theory[4], the integration contour must pass below the singularity (a result that is also obtained by requiring the inviscid numerical solutions to be the $R \to \infty$ limit of the numerical solutions of the complete equations). The mean boundary-layer quantities u, u' and T are continued onto the indented contour by

means of the first three terms of power-series expansions about the point where $u = c_r$. The derivatives needed in the series coefficients are obtained along with the boundary layer solutions described below.

A sixth-order Adams-Moulton method with the integration step size controlled by specifying the estimated truncation error per step is used to perform the numerical integration. Double-precision arithmetic is not necessary. The integration is carried out from the edge of the boundary layer to the wall, with the bounded solution as $\eta \to \infty$ being used for the initial values. The boundary condition at $\eta = 0$

$$Z_3(0) = 0 \tag{14}$$

is satisfied by using a linear search procedure to find which combinations of the parameters α, c are eigenvalues. When the eigenvalues are known, the eigenfunctions are produced by a final integration.

In order to compute numerical solutions of the stability equations, it is necessary to have mean boundary layer solutions available as input to the two programs described above. These solutions are provided in tabular form from a separate program that yields solutions of the flat-plate boundary layer equations. These solutions are exact within the perfect-gas assumption. The air properties are taken from Reference 11, and the permissible temperature range is from 40°K to 1100°K. The boundary layer equations are integrated in a straightforward manner with the same integration subroutine used for the inviscid equations. The temperature level of the solutions used in this paper is as follows: the free-stream stagnation temperature is 311°K, or the free-stream temperature is 50°K, whichever gives the higher free-stream temperature.

The air properties provided in the two programs for the solution of the stability equations are the same as in the boundary layer program except that the specific heat is constant. The specific-heat ratio is taken equal to 1.4, and the second viscosity coefficient is taken equal to 0.8 of the ordinary viscosity coefficient.

3. INVISCID STABILITY RESULTS

3.1 Neutral Solutions

In their detailed study of the inviscid stability theory, Lees and Lin[4] considered two types of non-supersonic* neutral disturbances. One of these was the sonic neutral solution with the eigenvalues $\alpha = 0$, $c_r = 1 - 1/M_1$. The other was the subsonic neutral solution with the eigenvalues $\alpha = \alpha_s$, $c = c_s$. The phase velocity c_s is equal to the mean velocity at the generalized inflection point, η_s, which is the point in the boundary layer where

$$(u'/T)' = 0 . \tag{15}$$

---

* A disturbance is subsonic, sonic, or supersonic depending upon whether c_r is greater than, equal to, or less than $1 - 1/M_1$.

At $M_1 = 0$, Equation (15) reduces to $u'' = 0$ and r_s is a true inflection point. The existence of an inflection point is the necessary and sufficient condition for the inviscid instability of the incompressible boundary layer. For the compressible boundary layer, Lees and Reshotko[7] have computed α_s as a function of M_1. The fact that the uniqueness proof of Lees and Lin for α_s as a function of c_s and M_1 applies only when $T - M_1^2(u - c)^2 < 0$ led Lees and Reshotko to state that there is some question of the uniqueness of α_s when $T - M_1^2(u - c)^2 > 0$. The physical meaning of this inequality may be seen more easily if the mean flow is viewed relative to the phase velocity. The local Mach number of the relative flow is

$$\bar{M} = M_1 \frac{(c_r - u)}{\sqrt{T}} . \tag{16}$$

Consequently the uniqueness proof is valid only when the mean flow relative to the phase velocity is subsonic throughout the boundary layer.

In the course of the present investigation it became apparent that there must be multiple values of α_s. A systematic search for additional neutral solutions of this type yielded the results shown in Figure 1 for the insulated-wall boundary layer. The dashed curves in this figure are discussed later. The lowest curve, for α_{s1}, is a recalculation of the Lees-Reshotko result. The other nine curves for $\alpha_{sn}(n > 1)$ are the new solutions. With $c_r = c_s$, the free-stream Mach number for which $\bar{M}$ is first equal to unity is $M_1 = 2.2$, and no multiple solutions have been found for $M_1 < 2.2$. A recent theory of Lees[12] confirms that the additional solutions are associated with the existence in the boundary layer of a region of supersonic relative flow. Multiple solutions of this type have also been found by Gill[13] in a study of "top-hat" jets and wakes.

The pressure-fluctuation amplitude functions of the multiple neutral solutions reveal a regularity which suggests that these solutions are a sequence of vibration modes of the boundary layer. The solution for α_{s1}, which can be called the first mode, has no phase change in the pressure fluctuation across the boundary layer. The solution for α_{s2}, the second mode, has a single 180° phase change. The third mode has two 180° phase changes, and so forth. These phase changes can be related to the streamline pattern of the steady flow relative to the phase velocity.

In addition to the neutral solutions with eigenvalues α_{sn}, c_s, another sequence of neutral solutions was found during the investigation. These solutions have the eigenvalues $\alpha = \alpha_{in}$, $c_r = 1$, and, like the additional neutral solutions (α_{sn}, c_s), exist only when there is a supersonic relative-flow region in the boundary layer. There is no neutral solution of this type for the first mode. As each of these solutions is approached from nearby amplified solutions, the ratio of the maximum amplitude to the amplitude at the edge of the boundary layer increases without limit. Consequently, they are called singular neutral solutions. It is not possible to make a direct numerical computation of α_{in}, but since α varies linearly with c_r in the limit $c_r \to 1$ it is possible to obtain a value of α_{in} by extrapolation from the nearby amplified solutions. The few numerical results that are available for α_{in} have been used to draw the two dashed curves in Figure 1. The dashed curves extend to a Mach number near unity because with $c_r = 1$ a supersonic relative-flow region is present at a much lower Mach number than 2.2. The importance of the singular

neutral solutions lies in the fact that, unlike the solutions (α_{sn}, c_s), they exist for all boundary layers in which there is a supersonic relative-flow region.

Besides the subsonic neutral solutions just discussed, supersonic neutral solutions have also been found. Some of these solutions are of a singular nature and serve as limiting solutions for families of amplified and damped supersonic solutions as $c_i \to 0$. Non-singular supersonic neutral solutions which, physically, are undamped outgoing waves have been found for a limited number of cooled-wall boundary layers.

3.2 Amplified Solutions – Insulated-Wall Boundary Layer

Associated with each of the neutral solutions (α_{sn}, c_s), there is a family of amplified and damped solutions which includes the neutral solutions. The eigenvalues of these solutions can be plotted in the manner shown in Figure 2 for the $M_1 = 4.2$ insulated-wall boundary layer. Each point on a curve in Figure 2 represents an inviscid solution, and the points that lie on the axis $c_i = 0$ are the neutral solutions. Two families of amplified solutions appear in Figure 2. The first family connects the sonic neutral solution and the first-mode neutral solution (α_{s1}, c_s). The solutions in this family are referred to as the first-mode amplified solutions. The solutions of the second family, which connect the singular neutral solution $(\alpha_{i2}, 1)$ and the second-mode neutral solution (α_{s2}, c_s), are referred to as the second-mode amplified solutions. The third and higher modes also have amplified solutions which connect $(\alpha_{in}, 1)$ with (α_{sn}, c_s). The amplified first-mode solutions have only a small phase change in the pressure fluctuation in agreement with the behavior of the first-mode neutral solution (α_{s1}, c_s). The amplified second-mode unstable solutions have a considerable phase change, for the most part close to 180°, in agreement with the second-mode neutral solution (α_{s2}, c_s). It is not yet clear how to classify the damped solutions in Figure 2, which include a family of supersonic solutions, and the full understanding of these solutions must await a theoretical investigation into the nature of the amplified and damped solutions of the inviscid equation.

The eigenvalue diagrams at $M_1 = 5.8$, where $\alpha_{i2} < \alpha_{s1}$, are shown in Figure 3. At this Mach number, it is the continuation into the damped region of the family of amplified solutions of the first mode, rather than the second mode as in Figure 2, that leads to the supersonic damped solutions. Further increases in Mach number bring additional changes in the eigenvalue diagrams. In particular, the first and second-mode amplified solutions join at a $c_i > 0$, and the curve that starts at the sonic neutral solution does not regain the neutral axis until it reaches the neutral solution (α_{s2}, c_s).

It has been found that the inviscid relationship between c_r and α is closely preserved at finite Reynolds numbers. Consequently, the statement made earlier that the dispersion in the boundary layer can be anomalous may be verified from the eigenvalue diagrams. It is apparent that as α increases, c_r may either increase or decrease depending upon the family of solutions being followed and the range of α.

With the eigenvalues known, the maximum time rate of amplification and the frequency of the disturbance with the maximum amplification rate (referred to as the most unstable frequency), can be obtained for each mode. This information is provided in Figure 4 as a function of M_1 for the first three modes. In dimensionless form

it is necessary to plot, instead of a frequency alone, the quantity FR, where R is the Reynolds number of the boundary layer profile whose inviscid stability is under consideration. Figure 4 shows that the most unstable mode, at least for $M_1 > 2$, is the second mode. Above $M_1 = 6.5$ the third mode is more unstable than the first mode. The maximum amplification rate of the second mode occurs at $M_1 = 4.6$, and at $M_1 = 10$ has only one-third of its value at $M_1 = 4.6$. At $M_1 = 10$, the most unstable frequency of the second-mode is only 50% higher than for the first mode, but at $M_1 = 3.8$ this frequency is five times as large as the most unstable first-mode frequency.

3.3 Effect of Wall Cooling at $M_1 = 5.8$

One of the most interesting results of the stability theory has always been the prediction of the stabilizing effect of cooling[1]. This prediction follows from an investigation into the influence of wall cooling on the minimum Reynolds number neutral solution, and is based upon the asymptotic theory. Consequently, it is important to use the direct numerical methods to study the effect of cooling on both the inviscid and finite Reynolds number stability characteristics. In this section, the inviscid stability of cooled-wall boundary layers at $M_1 = 5.8$ is considered.

Cooling the wall at a fixed Mach number moves the generalized inflection point η_s in the direction of η_0, the point where $u = 1 - 1/M_1$. When T_w/T_r, the ratio of the wall temperature to the temperature of the insulated wall, is equal to 0.20 at $M_1 = 5.8$, the two points η_s and η_0 coincide. When $T_w/T_r = 0.15$, the point η_s vanishes. With $\eta_s < \eta_0$ or non-existent, the subsonic neutral solutions (α_{sn}, c_s) no longer exist. Consequently, no first-mode amplified solutions are possible since they are bounded by the sonic neutral solution and the neutral solution (α_{s1}, c_s). However, the singular neutral solutions exist regardless of the wall temperature. Further, α_{sn} does not approach α_{in} as $\eta_s \to \eta_0$, and $c_s \to 1 - 1/M_1$ rather than unity. Consequently, the vanishing of the neutral solutions (α_{sn}, c_s) does not imply the stabilization of the higher modes. Indeed it is found that the amplified solutions of the second and higher modes exist at all wall temperatures.

When the wall is cooled so that η_s is near η_0, a neutral supersonic solution is found with a phase velocity slightly less than $1 - 1/M_1$ and a wave number slightly greater than α_{s2}. A family of supersonic amplified solutions with small αc_i is associated with this neutral solution. When the wall is cooled further, so that η_s is less than η_0 or does not exist, the second-mode amplified solutions originating at the singular neutral solution $(\alpha_{i2}, 1)$ join the supersonic amplified solutions at a $c_i > 0$. The latter solutions eventually regain the neutral axis at a singular supersonic neutral solution.

The effect of cooling at $M_1 = 5.8$ on the time rate of amplification and frequency of the most unstable disturbance for the first three modes is shown in Figure 5. As expected, the first mode is completely stabilized by cooling at $T_w/T_r = 0.20$. In contrast, cooling destabilizes both the second and third modes. Associated with the increase in amplification rate is an increase in the most unstable frequency. For the first mode, the most unstable frequency goes to zero as stabilization takes place.

The only other Mach number at which a computation has been made of the effect of cooling on the inviscid stability is $M_1 = 7.6$. At this Mach number, cooling has an

even larger destabilizing effect on the second mode than at $M_1 = 5.8$. For $T_w/T_r = 0.055$, the maximum second-mode amplification rate is increased by 80% and the most unstable frequency is doubled as compared to the insulated-wall values.

4. STABILITY AT FINITE REYNOLDS NUMBERS

4.1 Neutral-Stability Curves for the Insulated-Wall Boundary Layer

It is possible to plot the eigenvalues of the complete stability equations in the same way as was done for the inviscid eigenvalues, but with a separate diagram for each Reynolds number. However, it is customary to represent the eigenvalues by plotting wave number, phase velocity, or frequency as functions of the Reynolds number for constant c_i or αc_i . In such plots, the unstable region is separated from the stable region by a curve of neutral stability ($\alpha c_i = 0$), which serves to define the range of unstable eigenvalues. The present section is devoted to an examination of computations of the neutral-stability curve at $M_1 = 2.2$, and to a study of the effect of Mach number on the neutral stability curve.

The original Lees-Lin theory[4] was applied by Lees[1] to compute neutral-stability curves up to $M_1 = 1.3$. The present author[2] used the Dunn-Lin theory[7] at $M_1 = 1.3$, 1.6 and 2.2, and Lees and Reshotko[3] used an improved asymptotic method, which includes terms neglected by Dunn and Lin, at $M_1 = 2.2$ and 5.6 . The direct numerical method agrees satisfactorily with the asymptotic method at $M_1 = 1.3$ and $M_1 = 1.6$ except in the minimum Reynolds number region, and with the experimental neutral points of Laufer and Vrebalovich[14] at $M_1 = 1.6$. It is at $M_1 = 2.2$ that wide disagreements become apparent.

In Figure 6, three computed neutral-stability curves at $M_1 = 2.2$ are given in the form of frequency vs Reynolds number along with the experimental points. The dashed curve is the result computed from the Dunn-lin theory[2] . The innermost curve is obtained from the complete stability equations by the direct numerical method. There is a large difference between these two neutral curves at all Reynolds numbers. The Lees-Reshotko neutral curve is not shown, but it is in exact agreement with the Dunn-Lin curve on the upper branch, and is slightly-to the right of the Dunn-Lin lower branch.

The third curve in Figure 6 is the neutral-stability curve obtained from the simplified equations of Dunn and Lin by the direct numerical method. This computation tests both the adequacy of these equations and the success of the Dunn-Lin method in solving them. It is apparent from Figure 6 that the asymptotic theory makes a greater numerical error in solving its system of equations than is inherent in the asymptotic equations themselves. The close agreement of the Lees-Reshotko neutral curve with the Dunn-Lin neutral curve also indicates that the source of trouble with the asymptotic method is not to be found in the equations. It is to be concluded that the asymptotic theory is no longer adequate for numerical computations in the Reynolds number range of interest above $M_1 = 1.6$.

The experimental points in Figure 6 lie very close to the upper branch given by the asymptotic theory. On the lower branch, they fall generally along the neutral curve obtained from the complete equations. As a result, the experimental unstable

region is markedly larger than the computed unstable region, and associated with this difference is almost an order of magnitude difference in the experimental and computed amplification rates. The reason for the disagreement between theory and experiment at $M_1 = 2.2$ is not known.

The dependence of the neutral-stability curve upon Mach number is best shown by plotting the eigenvalues against $1/R$ instead of R in order to emphasize the large Reynolds number region. In Figure 7, plots of α vs $1/R$ are given for $M_1 = 1.3$, 2.2, 2.6, 3.0 and 3.8. Only the neutral-stability curve at $M_1 = 1.6$ is similar to the familiar one at $M_1 = 0$. The increasing value of α_{s1} with increasing M_1 enlarges the range of unstable wave numbers as $R \to \infty$, and this enlargement gradually spreads to lower Reynolds numbers as M_1 increases. At $M_1 = 3.8$, this process is complete. The familiar maximum in α at a low Reynolds number has disappeared, and α increases monotonically as the neutral-stability curve is followed from the inviscid sonic neutral point to the inviscid neutral point α_{s1}. The appearance of the neutral-stability curve at $M_1 = 3.8$ is reminiscent of that for the wake, with the difference that the minimum Reynolds number for the wake is much lower. This type of neutral curve implies that the maximum instability occurs as $R \to \infty$. Consequently, the effect of viscosity is only stabilizing, in contrast to the situation at low Mach numbers where, without viscosity, the boundary-layer is either stable or nearly so.

Two neutral-stability curves of α vs R are given in Figure 8 for $M_1 = 4.5$ and $M_1 = 4.8$. These Mach numbers were selected because $\alpha_{12} = \alpha_{s1}$ at $M_1 = 4.6$ (Fig. 1). At $M_1 = 4.5$, where $\alpha_{12} > \alpha_{s1}$, there are two distinct unstable regions and two distinct neutral curves. The lower unstable region corresponds to the inviscid first-mode amplified solutions, and the upper region to the inviscid second-mode unstable solutions. The first-mode neutral curve is similar to the $M_1 = 3.8$ neutral curve. The lower branch approaches $\alpha = 0$ as $R \to \infty$, and the upper branch approaches α_{s1}. The upper branch of the second-mode neutral curve approaches the second-mode neutral solution α_{s2}, and the lower branch presumably approaches the singular neutral solution α_{12}. Because viscosity is only stabilizing, and the second mode has greater inviscid instability than the first mode (Fig. 4), the second-mode unstable region extends to a lower Reynolds number than does the first mode.

At $M_1 = 4.8$, where $\alpha_{12} < \alpha_{s1}$, the two unstable regions have merged into a single large unstable region enclosed by a single neutral-stability curve. This neutral curve extends from the inviscid sonic neutral point to the inviscid second-mode neutral point α_{s2}. A further increase in the Mach number above 4.8 makes the merger of the two unstable regions more complete. Also, it can be expected that the upper branch will tend to α_{s3} when $\alpha_{13} < \alpha_{s2}$ and to α_{s4} when $\alpha_{14} < \alpha_{s3}$.

4.2 Amplification in the Insulated-Wall Boundary Layer

The neutral-stability curves serve to locate the instability regions but do not provide any information concerning the actual growth of disturbances in the boundary layer. The maximum rate of amplification can be obtained at a specified Reynolds number, but of more interest than the rate of amplification is the amplitude of a disturbance of constant frequency as a function of Reynolds number. This type of calculation has been performed by Lees[9] at $M_1 = 0.7$. The relevant equation is Equation (11).

It is found that the ratio of the amplitude at the end of the unstable region to the amplitude at the beginning increases indefinitely as the frequency F decreases. Consequently, any desired amplitude is possible if sufficiently large Reynolds numbers are permitted. A more meaningful computation is to find the variation with frequency of the ratio of the amplitude at a fixed Reynolds number to the amplitude at the start of the unstable region. This computation will yield the value of the maximum amplitude ratio, or amplification, rather than the maximum amplification rate, that is possible at a given Reynolds number, as well as the corresponding frequency. This frequency is referred to as the most unstable frequency. It differs from the inviscid most unstable frequency, as the latter is the frequency with the maximum amplification rate.

A typical result is shown in Figure 9 where the amplitude ratio A/A_1 at $M_1 = 5.8$ is given as a function of frequency for four different Reynolds numbers. When the upper branch of the neutral curve is located upstream of the specified Reynolds number for a particular frequency, the damping downstream of the neutral curve is not considered in computing A/A_1. Hence Figure 9 gives the available amplification at, or upstream of, one of the four Reynolds numbers. The maximum amplification rises from five at $R = 1000$ to 400 at $R = 2500$. At $R = 1500$, the most unstable frequency of 1.1×10^{-4} is amplified 21 times. For the typical wind-tunnel condition of $R_x/in = 10^5$, this frequency is 42,000 cycles/sec. The half frequency, 21,000 cycles/sec, does not pass through the second-mode unstable region and is amplified only 2.3 times.

When the computation of Figure 9 at $R = 1500$ is repeated for several Mach numbers, Figures 10 and 11 can be drawn. These figures give, respectively, the maximum amplification and the most unstable frequency at $R = 1500$ as functions of the Mach number. From $M_1 = 3.6$, where the second-mode unstable region first appears at $R = 1500$, to $M_1 = 4.6$, the merger Mach number*, there are two separate unstable regions and, therefore, two separate curves in the figures. Computed points were available at $M_1 = 0.7$ (Ref.9), 1.3, 2.2, 3.8, 5.8 and 7.0. The amplitude ratios for the second-mode and combined regions between $M_1 = 3.6$ and 5.8, and for the first-mode region between 3.8 and 4.6, have been estimated from the neutral-stability curves and the inviscid amplification rates. The estimated portions of the curves are drawn dashed to emphasize their tentative nature. In order to have a continuous second-mode curve in the vicinity of the merger Mach number, it is necessary to interpret A_1 in the following manner. For $3.6 < M_1 < 4.25$, the most unstable second-mode frequency does not pass through any part of the first-mode unstable region. For $M_1 > 4.25$, this frequency passes through the first-mode region and then a damped region before reaching the second-mode neutral curve. At some Mach number less than the Mach number where the merger of the two unstable regions is completed for this frequency, the initial amplitude at the second-mode neutral curve will equal the initial amplitude at the lower branch of the first-mode neutral curve. Consequently, above this Mach number A_1 is taken to be the amplitude at the first-mode neutral curve rather than the second-mode neutral curve.

As M_1 increases from zero to two, there is a remarkable decrease in the maximum amplification. Indeed, at $M_1 = 2.2$ the boundary layer at $R = 1500$ is almost

---

* $M_1 = 4.6$ is the merger Mach number at infinite Reynolds number. The actual merger Mach number at $R = 1500$ is slightly larger.

stable to the assumed disturbances. The numerical reason for this decrease can be seen by consideration of the maximum space rate of amplification $\alpha c_i/c_r$ of the disturbance with maximum amplification at $R = 1500$. In comparison with $M_1 = 0$, α and c_r at $M_1 = 2.2$ are each decreased by a factor of 5, and c_r is increased by a factor of 2. Consequently, the maximum amplification rate at $M_1 = 2.2$ has only 1/50 of its value at $M_1 = 0$. The decrease is interpreted to mean the virtual disappearance of the viscous instability mechanism that is responsible for the instability of the incompressible boundary layer. The gradual increase in the amplification in the first-mode region between $M_1 = 2.2$ and 4.6 is a consequence of the increasing inviscid instability. This amplification increase is accompanied by more than a four-fold increase in the most unstable frequency.

At $M_1 = 3.9$ the second-mode amplitude ratio is equal to that of the first-mode. However, the most unstable second-mode frequency is almost four times the most unstable first-mode frequency. At the merger Mach number the two frequencies differ by just under a factor of two. The merger Mach number is close to the Mach number at which the second-mode has its maximum inviscid amplification rate (Fig. 4). Therefore, increasing the Mach number can be expected to lead to a decrease in the amplification. The actual decrease in amplification is not as large as would be expected from Figure 4 because the unstable region is enlarged with increasing M_1 as the upper branch of the neutral-stability curve goes, in the limit $R \to \infty$, first to α_{s3} at $M_1 = 6.5$, and then to α_{s4} at some higher Mach number. It is estimated that at $M_1 = 10$, A/A_1 at $R = 1500$ is about 5.

Before any use can be made of the amplification results in interpreting observed transition Reynolds numbers, two points must be kept in mind. First, at $M_1 = 0$ the experiments of Klebanoff, Tidstrom and Sargent[15] have shown that after the linear range of the stability theory two other events precede the first appearance of turbulence. A strongly three-dimensional development of the instability wave is followed by a sudden breakdown in the most amplified portion of the three-dimensional wave. The breakdown can perhaps be explained as a secondary linear instability of the highly distorted time-dependent boundary layer velocity profile[16]. If either of these processes depends upon Mach number in a different way than does the linear stability theory, the variation of the transition Reynolds number with Mach number will not follow the trend of the linear theory. The second point is that the application of the linear theory itself requires the specification of the disturbances present in the boundary layer as to frequency spectrum and amplitude distribution in the flow direction. If a frequency is found to be the most unstable frequency at a certain Reynolds number, but the energy at this frequency is negligible compared to the energy of other frequencies, then the observed dominant frequency will not be the one calculated as the most unstable. The observed frequency spectrum after amplification also depends on whether or not the quantity A_1 appearing in Figures 9 and 10 is a function of x. Figure 9 is the actual frequency spectrum at any of the four Reynolds numbers only if the initial frequency spectrum is flat and A_1 is independent of x.

4.3 Effect of Cooling at $M_1 = 5.8$

The effect of cooling on the inviscid stability at $M_1 = 5.8$ has been discussed in Section 3.3. The conclusion, summarized in Figure 5, was that cooling can completely stabilize the first-mode, but destabilizes the second and higher modes. In

this section, the effect of cooling at $M_1 = 5.8$ on the stability characteristics at finite Reynolds numbers is presented.

Neutral-stability curves, amplification rates, and the over-all amplification of constant frequency disturbances have been computed for $T_w/T_r = 0.65$, 0.25 and 0.05. The effect of cooling on the neutral-stability curve is to uncouple the merged first and second-mode unstable regions, and at the same time to move the first-mode unstable region in the direction of infinite Reynolds number. The second-mode unstable region extends to substantially the same minimum Reynolds number for all wall temperatures but shifts to higher values of α as T_w/T_r decreases.

The maximum amplification rate at a given Reynolds number is given within a few percent by the inviscid theory. The maximum amplification at $R = 1500$ is given in Figure 12 (upper curve) as a function of T_w/T_r, and the most unstable frequency at $R = 1500$ is given in Figure 13. As shown by Figure 12, the maximum amplification is almost independent of the wall temperature. The increase in the amplification rate with decreasing T_w/T_r is compensated for by the narrowing of the unstable region. The most unstable frequency is increased about 75% over its insulated-wall value. The inviscid most unstable frequency doubles over the same temperature range, and at $R = 1500$ averages about 15% less than the frequency of Figure 13. Consequently, provided the Mach number is high enough, the maximum amplification rate and even the most unstable frequency can be obtained satisfactorily from the inviscid theory. However, for the computation of the amplification it is necessary to carry out a finite Reynolds-number calculation.

Figure 12, like Figure 10, gives the actual amplification at $R = 1500$ of a disturbance for which A_1, the initial amplitude, is independent of Reynolds number and frequency. A different type of disturbance is one that is introduced into the boundary layer at some fixed x-position, say at $R = 100$, with an amplitude A_0. For this disturbance, the stabilization of the first-mode by cooling replaces a region of low amplification rate by a damped region in which the damping rate increases with increasing cooling. This change will have a large effect on the observed amplitude of the disturbance at a downstream location. The lower curve in Figure 13 gives the amplitude ratio A/A_0 as a function of T_w/T_r. The most unstable frequency at $R = 1500$ is the same for the localized disturbance as for the uniformly distributed disturbance. Figure 13 shows that the amplitude of the disturbance at $R = 1500$ is less than its initial amplitude for $T_w/T_r < 0.24$. In this special sense, cooling has stabilized the boundary layer.

ACKNOWLEDGMENT

This paper presents the results of one phase of research carried out at the Jet Propulsion Laboratory, California Institute of Technology, under Contract No. NAS7-100, sponsored by the National Aeronautics and Space Administration.

REFERENCES

1. Lees, L. — *The stability of the laminar boundary layer in a compressible fluid.* NACA Rep. No. 876, 1947.

2. Mack, L.M. — *Numerical calculation of the stability of the compressible, laminar boundary layer.* Jet Propulsion Laboratory, California Institute of Technology Rep. No. 20-122, 1960.

3. Lees, L. Reshotko, E. — Journal of Fluid Mechanics, Vol. 12, Part 4, 1962, pp. 555-590.

4. Lees, L. Lin, C.C. — *Investigation of the stability of the laminar boundary layer in a compressible fluid.* NACA TN No. 1115, 1946.

5. Brown, W.B. — In *Boundary Layer and Flow Control* (G.V. Lachmann, ed.), Vol. 2, New York, Macmillan (Pergamon), 1961, pp. 1033-1048.

6. Brown, W.B. — *Exact numerical solution of the complete linearized equations for the stability of compressible boundary layers.* Northrop Aircraft (Norair Div.) Rep. No. NOR-62-15, 1962.

7. Dunn, D.W. Lin, C.C. — Journal Aeronautical Sciences, Vol. 22, 1955, pp. 455-477.

8. Mack, L.M. — In *Methods in Computational Physics* (B. Alder, S. Fernbach, M. Rotenberg, ed.), Vol. 4, New York, Academic Press (in press).

9. Lees, L. — *Instability of laminar flow and transition to turbulence.* Consolidated Vultee Aircraft Rep. No. ZA-7-006, San Diego, 1952.

10. Zaat, J.A. — In *Boundary Layer Research* (H. Görtler, ed.), Berlin, Springer-Verlag, 1958, pp. 127-139.

11. Hilsenrath, J. et alii — *Tables of thermal properties of gases.* Natl. Bur. Std. (U.S.) Circ. No. 564, 1955.

12. Lees, L. — *Stability of laminar boundary layers and wakes at hypersonic speeds.* International Symposium on Fundamental Phenomena in Hypersonic Flow, Buffalo, New York, 1964.

13. Gill, A.E. — *Instabilities of "top-hat" jets and wakes in compressible fluids.* International Symposium on Fundamental Phenomena in Hypersonic Flow, Buffalo, New York, 1964.

14. Laufer, J.
Vrebalovich, T. Journal of Fluid Mechanics, Vol.9, Part 2, 1960, pp.257-294.

15. Klebanoff, P.S.
et alii Journal of Fluid Mechanics, Vol.12, Part 1, 1962, pp.1-34.

16. Greenspan, H.P.
Benney, D.J. Journal of Fluid Mechanics, Vol.15, Part 1, 1963, pp.133-153.

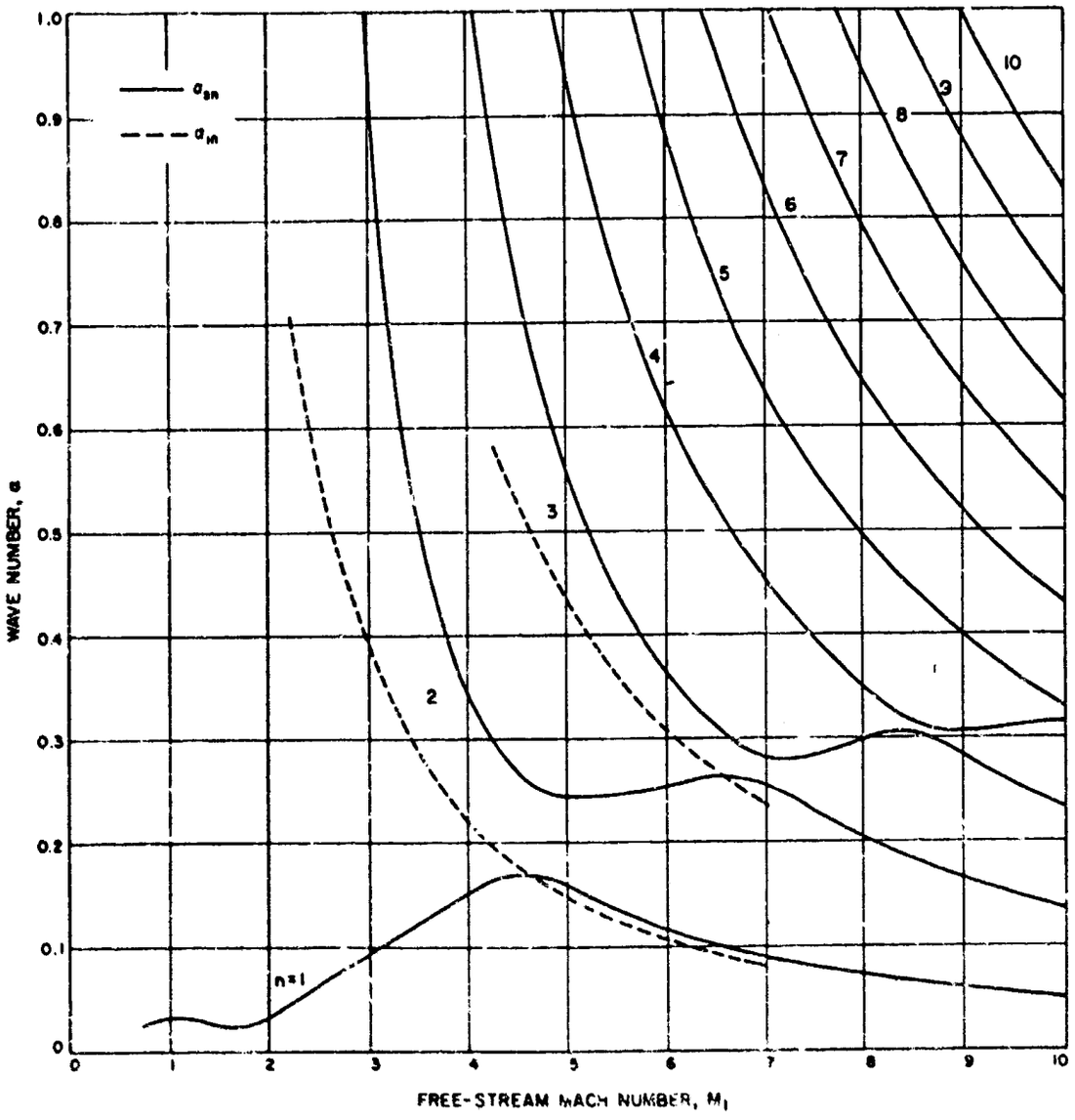

Fig. 1. Wave numbers of inviscid neutral solutions as functions of free-stream Mach number. Insulated-wall boundary layer.

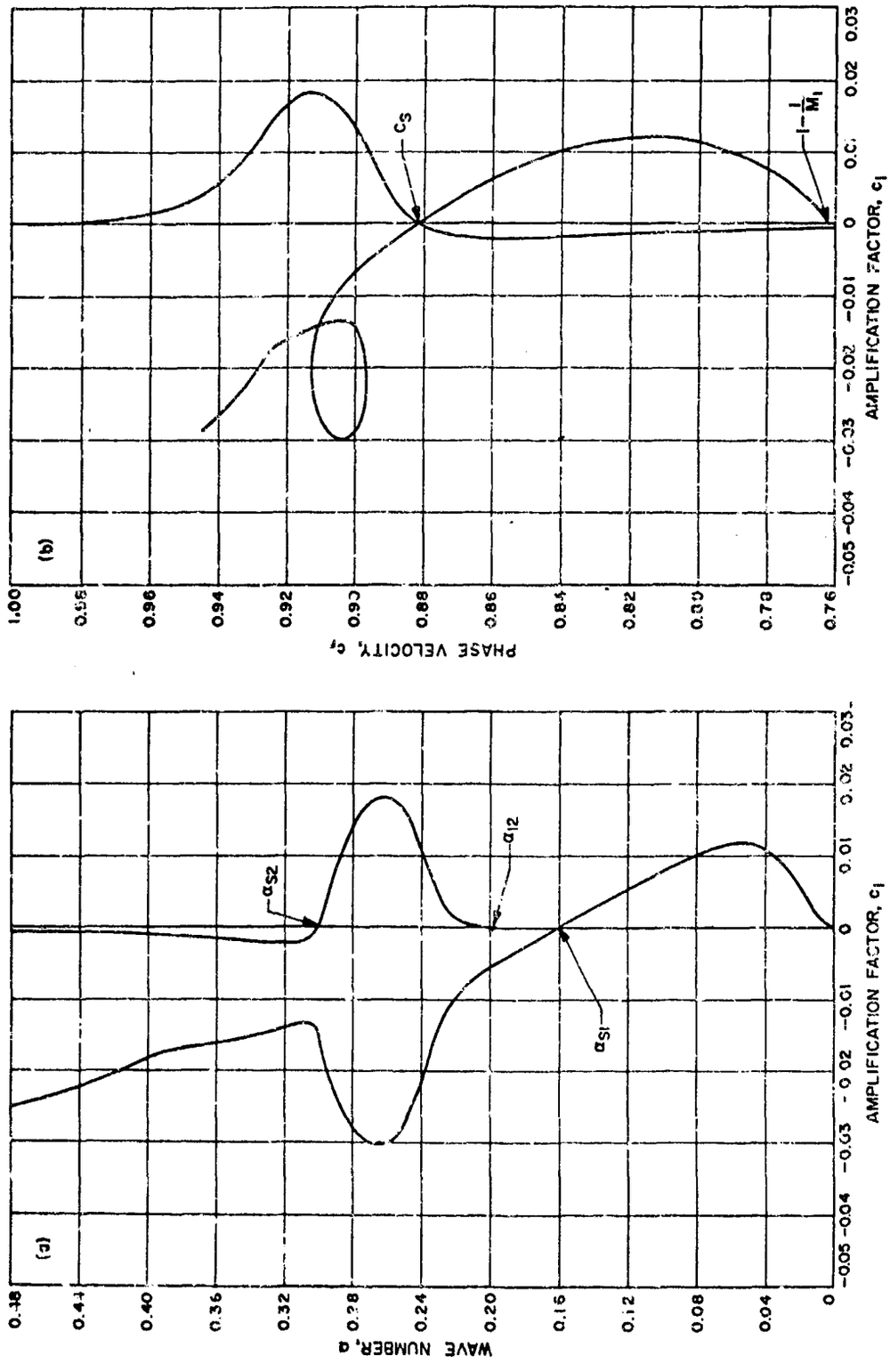

Fig. 2. Inviscid eigenvalues for insulated-wall boundary layer at $M_1 = 4.2$.
(a) α vs c_i. (b) c_r vs c_i.

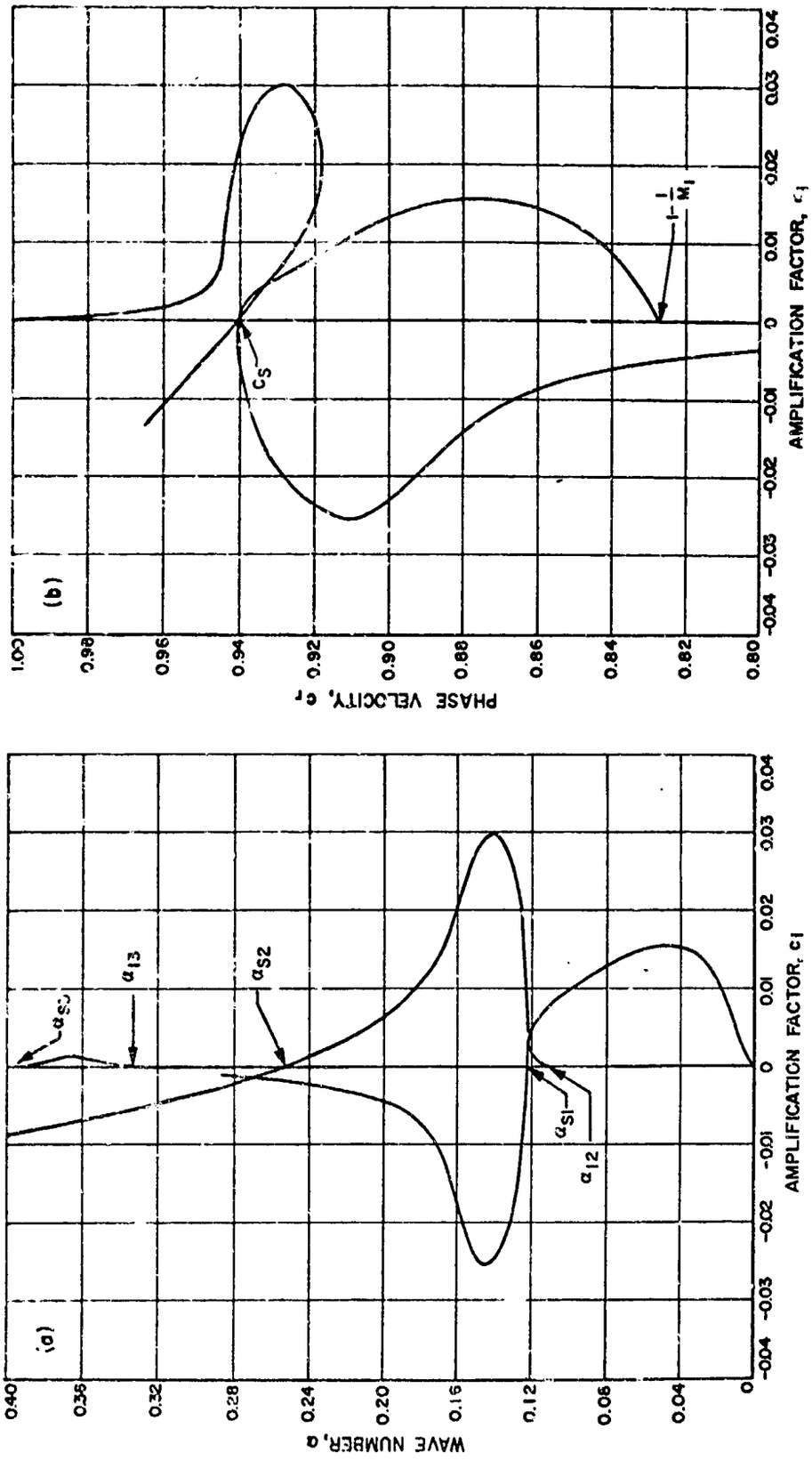

Fig. 3. Inviscid eigenvalues for insulated-wall boundary layer at $M_1 = 5.8$.
(a) α vs c_i, (b) c_r vs c_i.

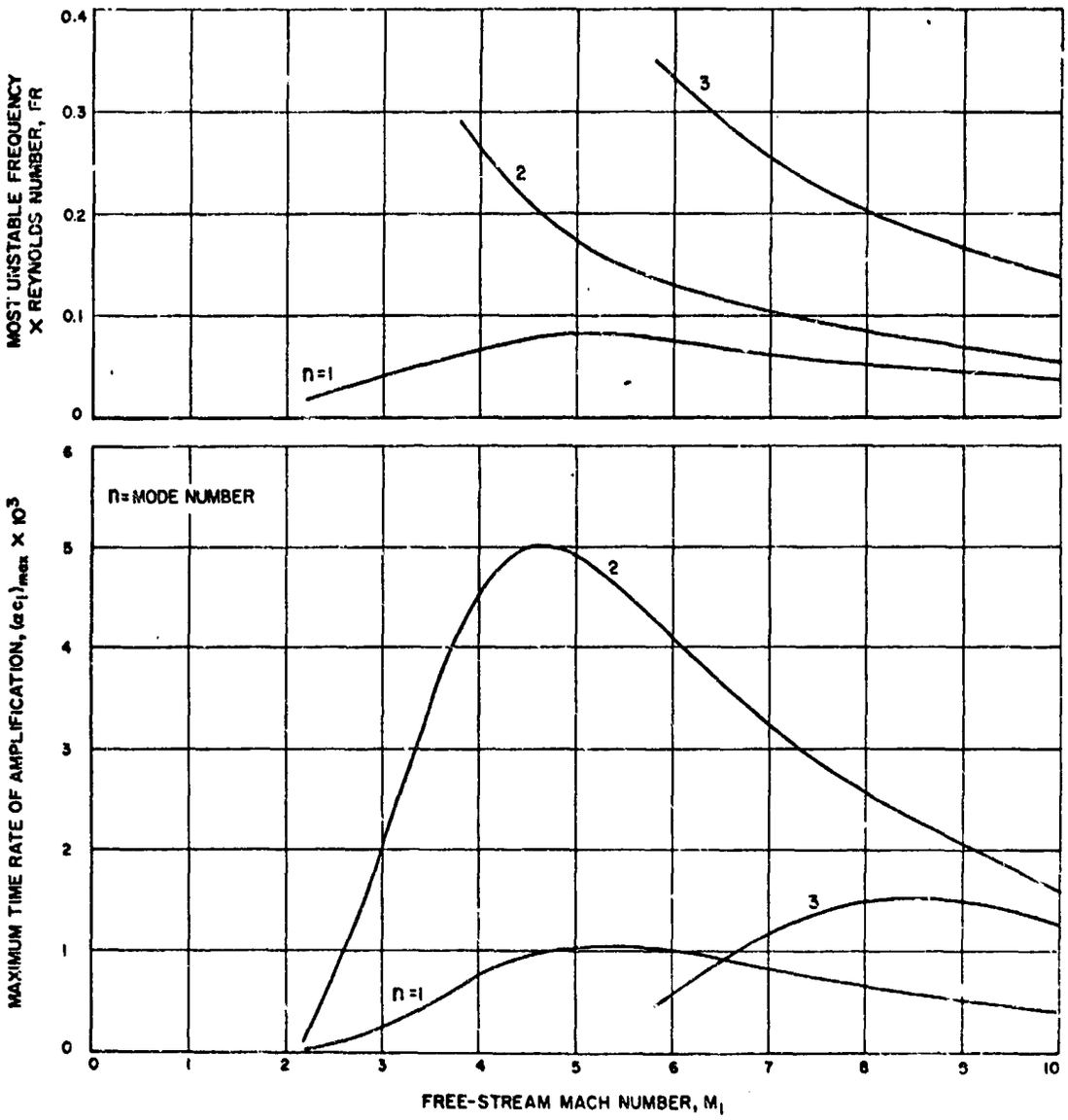

Fig. 4. Effect of free-stream Mach number on amplification rate and frequency of most unstable inviscid disturbance for first three modes.

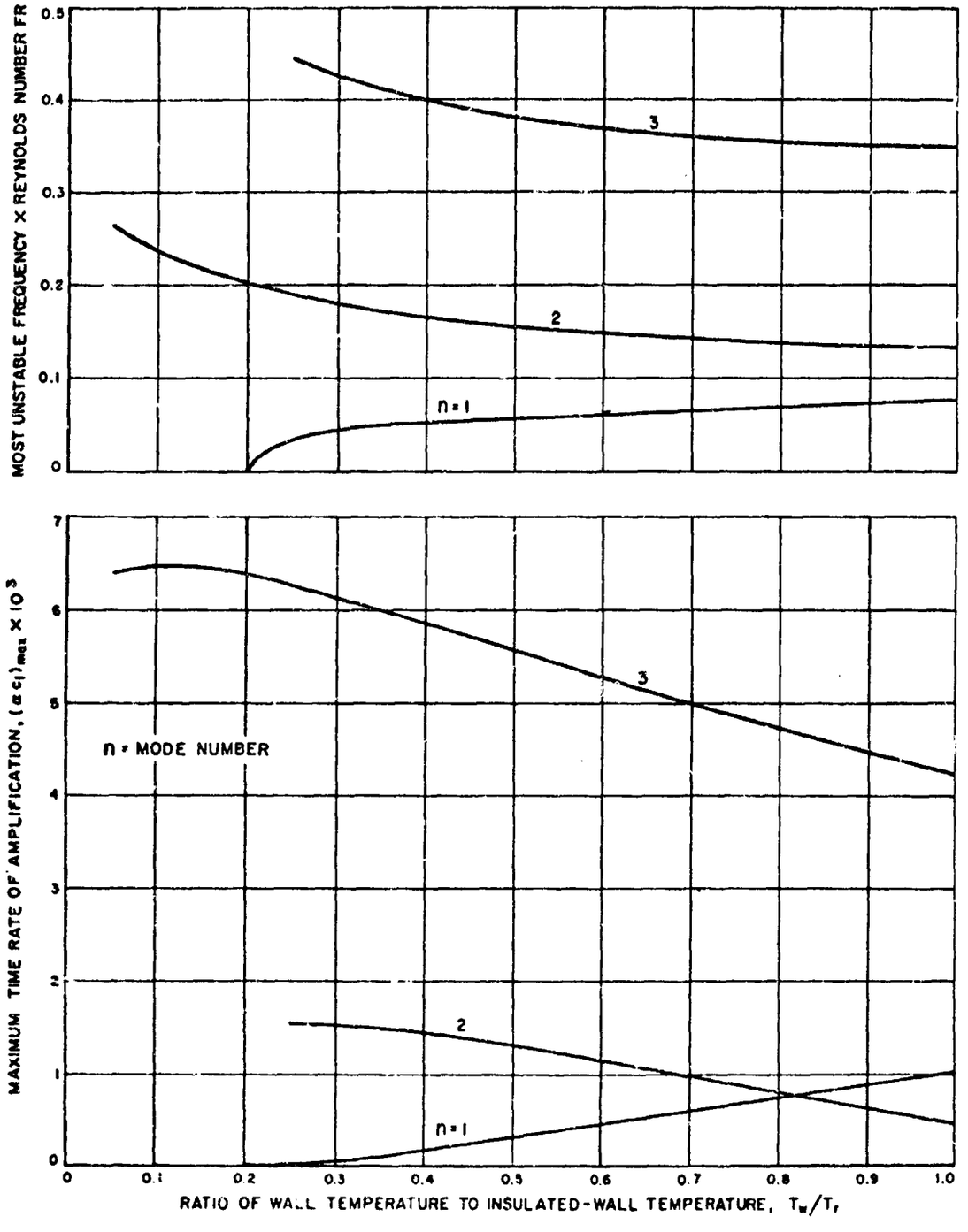

Fig. 5. Effect of cooling at $M_1 = 5.8$ on amplification rate and frequency of most unstable inviscid disturbance for first three modes.

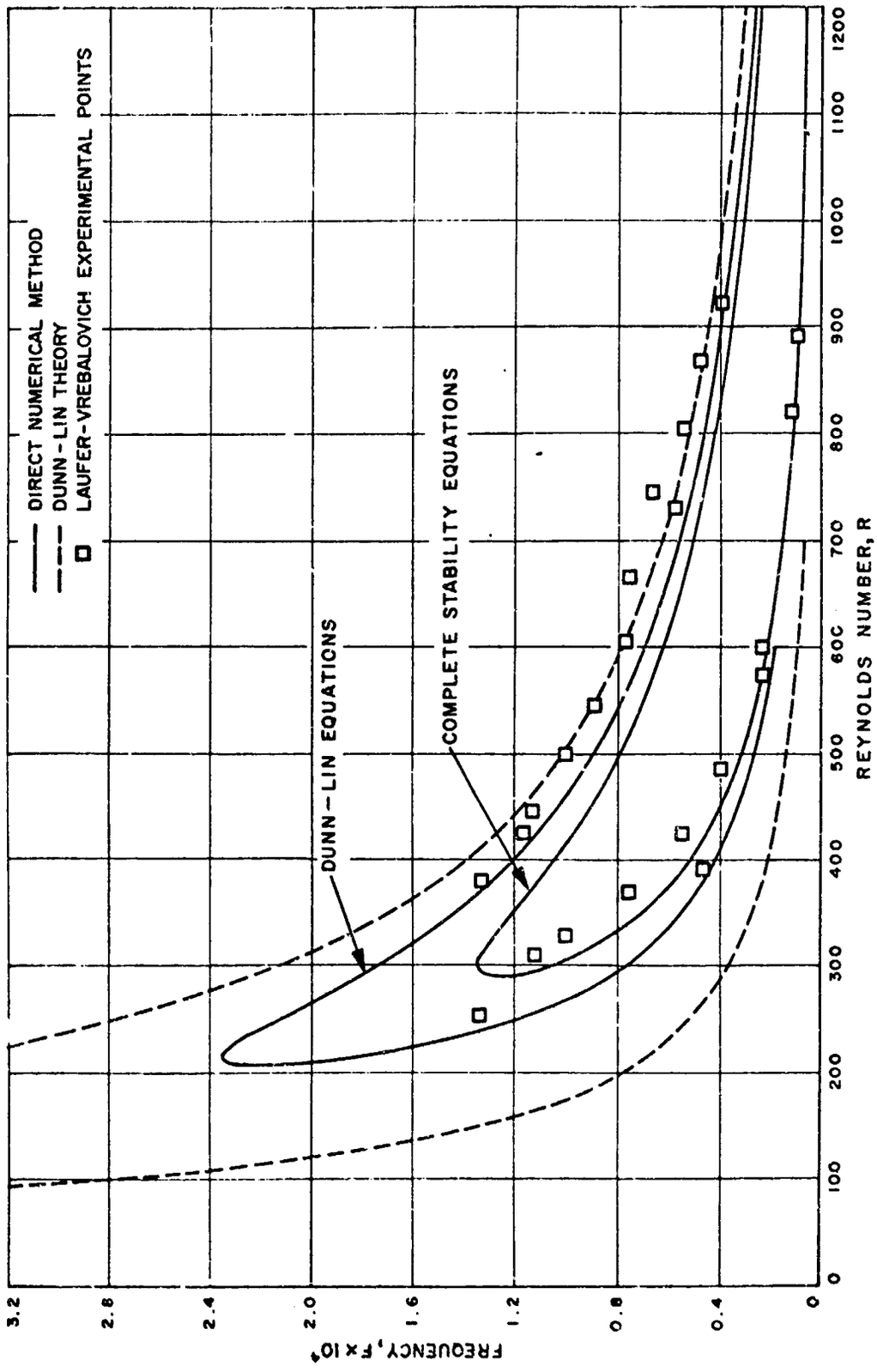

Fig.6. Neutral-stability curves of frequency vs Reynolds number at $M_1 = 2.2$ for insulated-wall boundary layer.

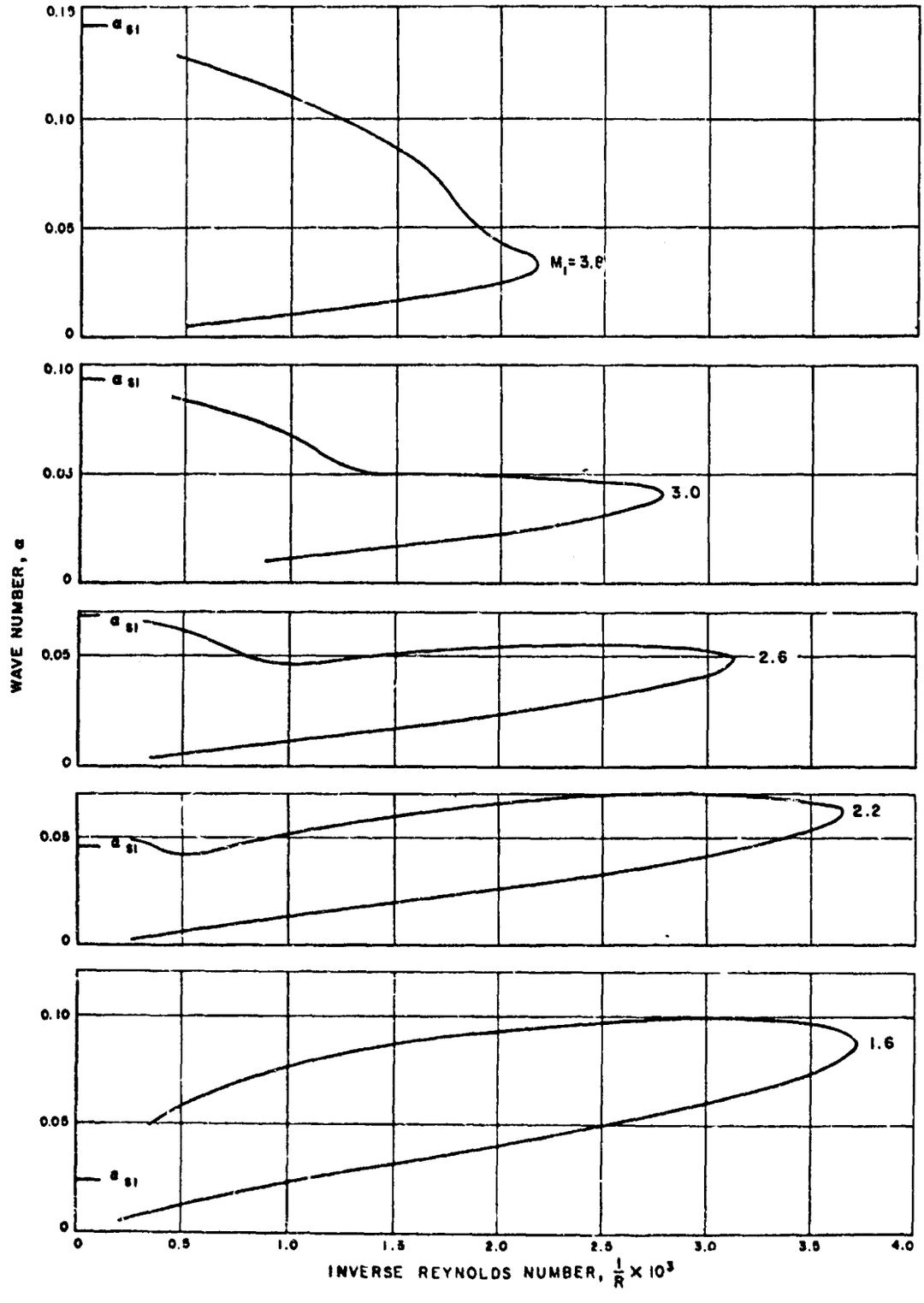

Fig. 7. Effect of free-stream Mach number on neutral-stability curve of insulated-wall boundary layer.

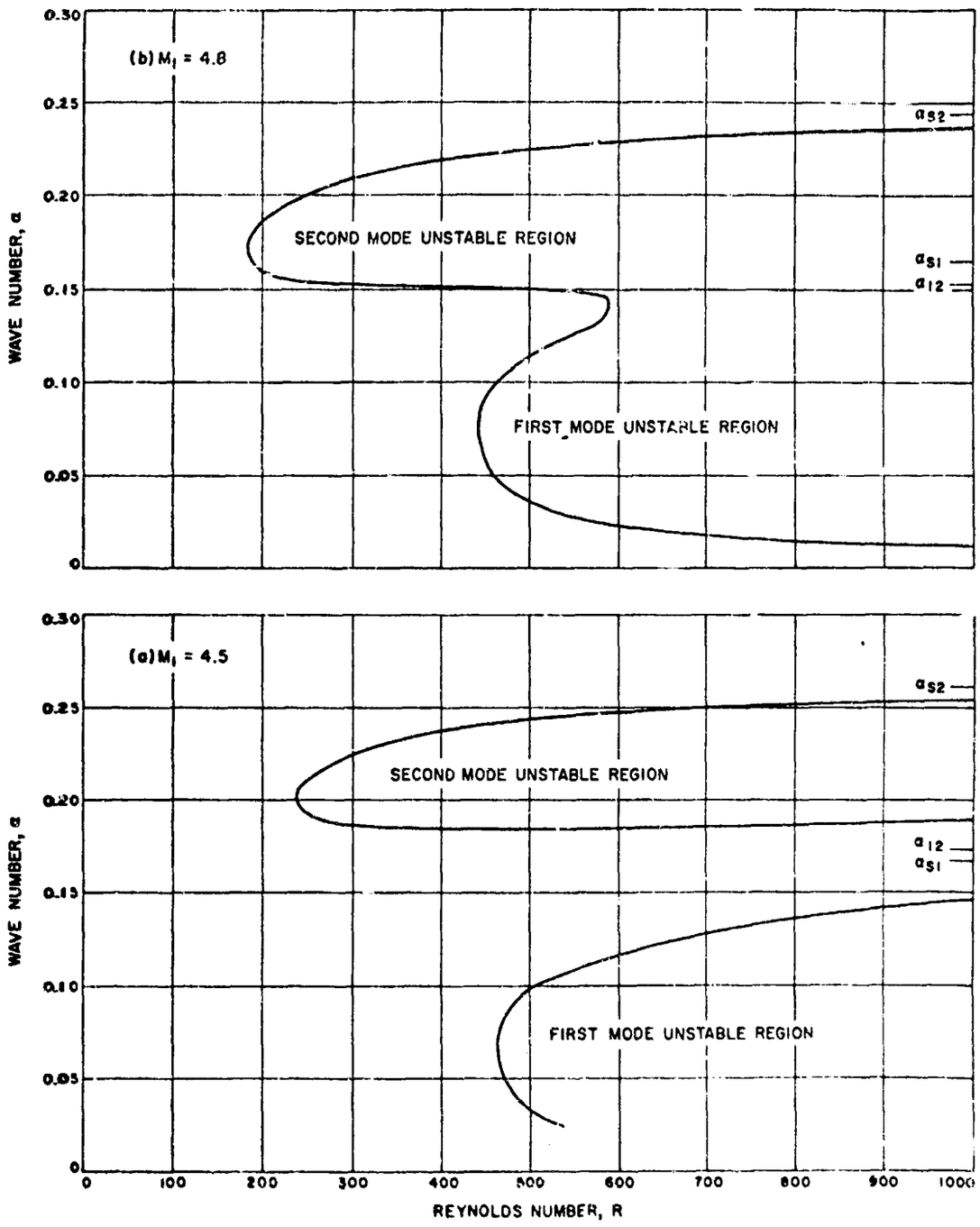

Fig. 8. Neutral-stability curve of wave number vs Reynolds number for insulated-wall boundary layer near Mach number at which $\alpha_{12} = \alpha_{s1}$. (a) $M_1 = 4.5$. (b) $M_1 = 4.8$.

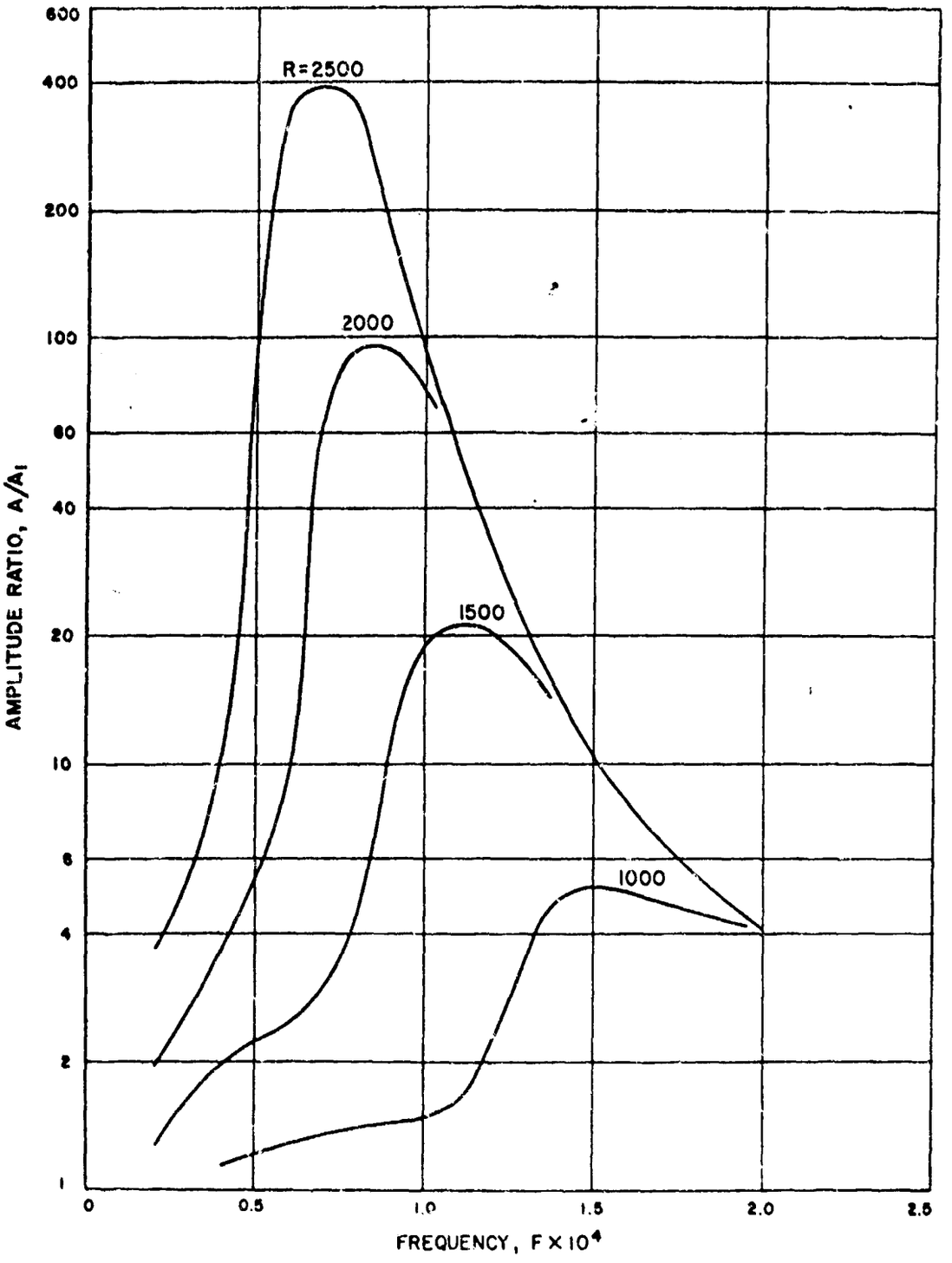

Fig. 9. Frequency response of insulated-wall boundary layer at $M_i = 5.8$.

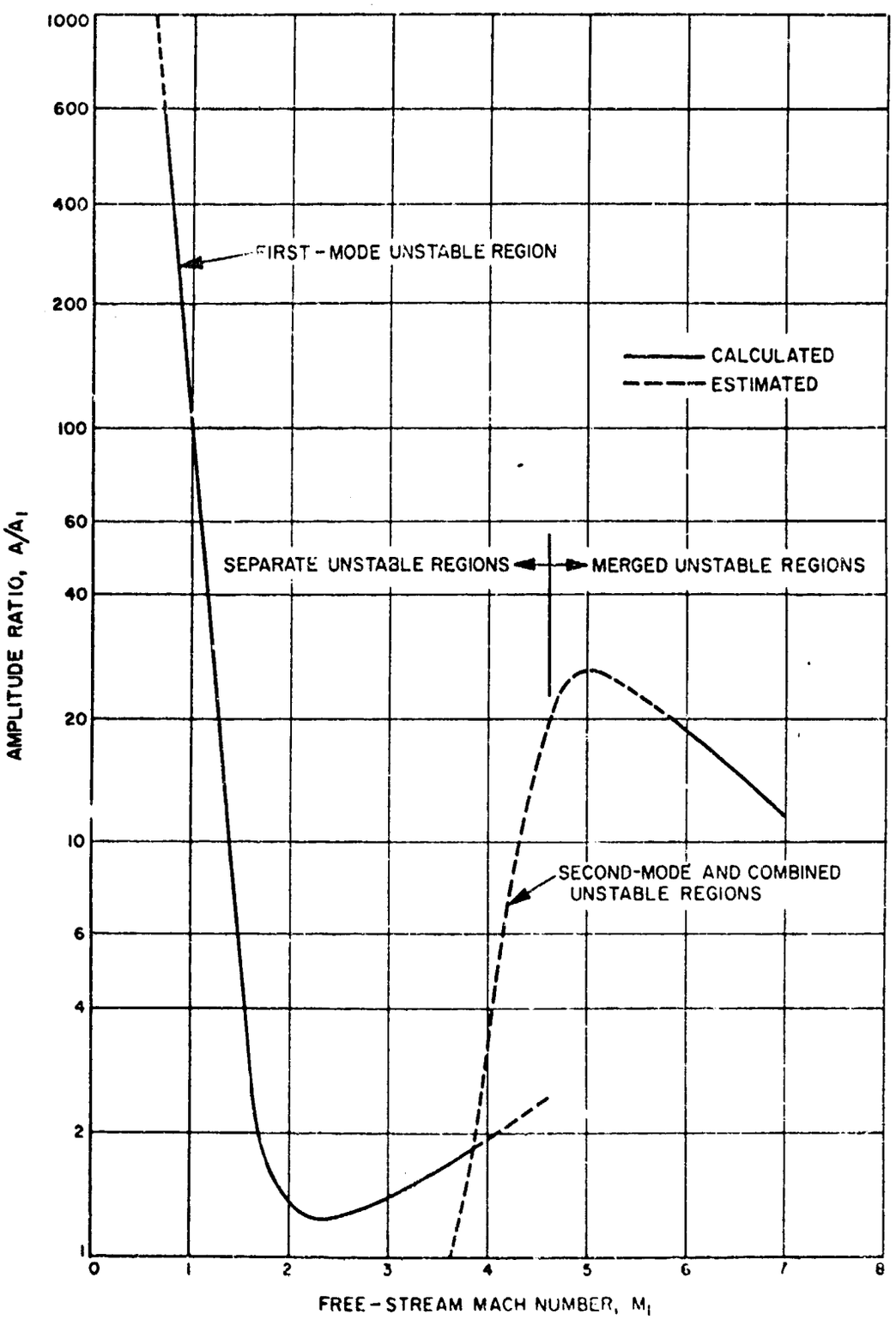

Fig. 10. Amplitude ratio of most unstable disturbance at R = 1500 as a function of free-stream Mach number. Insulated-wall boundary layer.

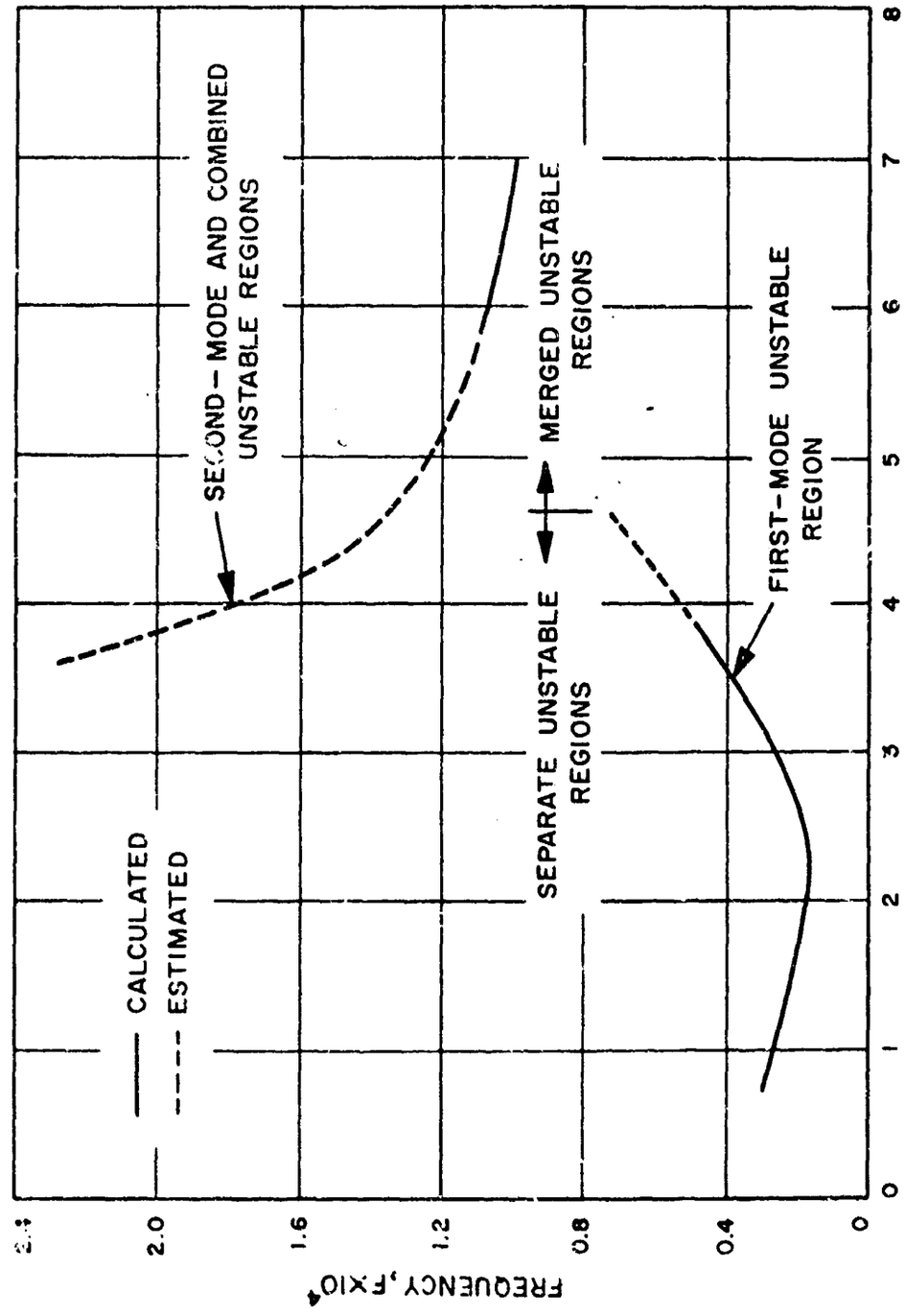

Fig. 11. Frequency of most unstable disturbance at R = 1500 as a function of free-stream Mach number. Insulated-wall boundary layer.

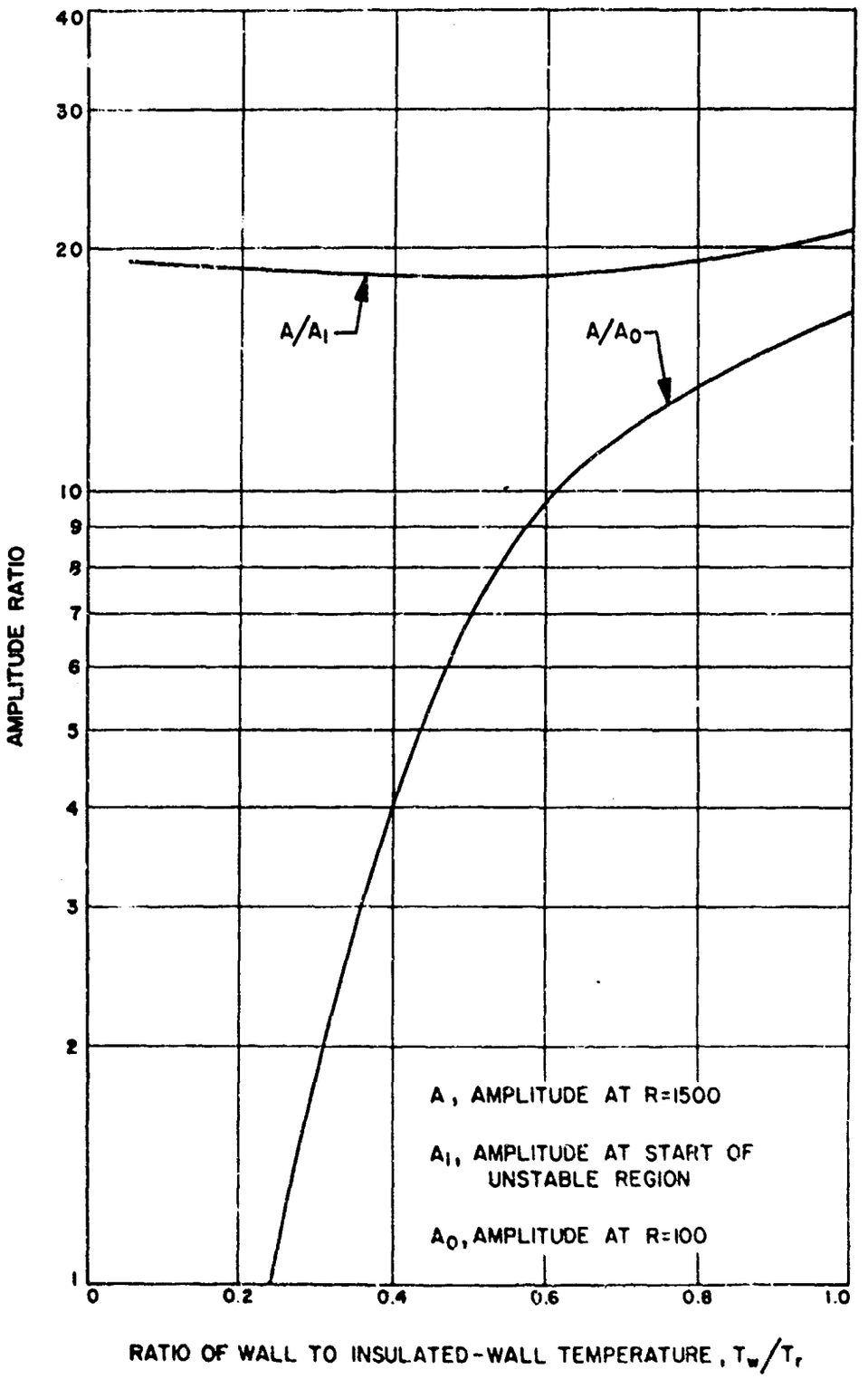

Fig. 12. Effect of cooling at $M_1 = 5.8$ on the amplification at $R = 1500$ of two types of disturbances.

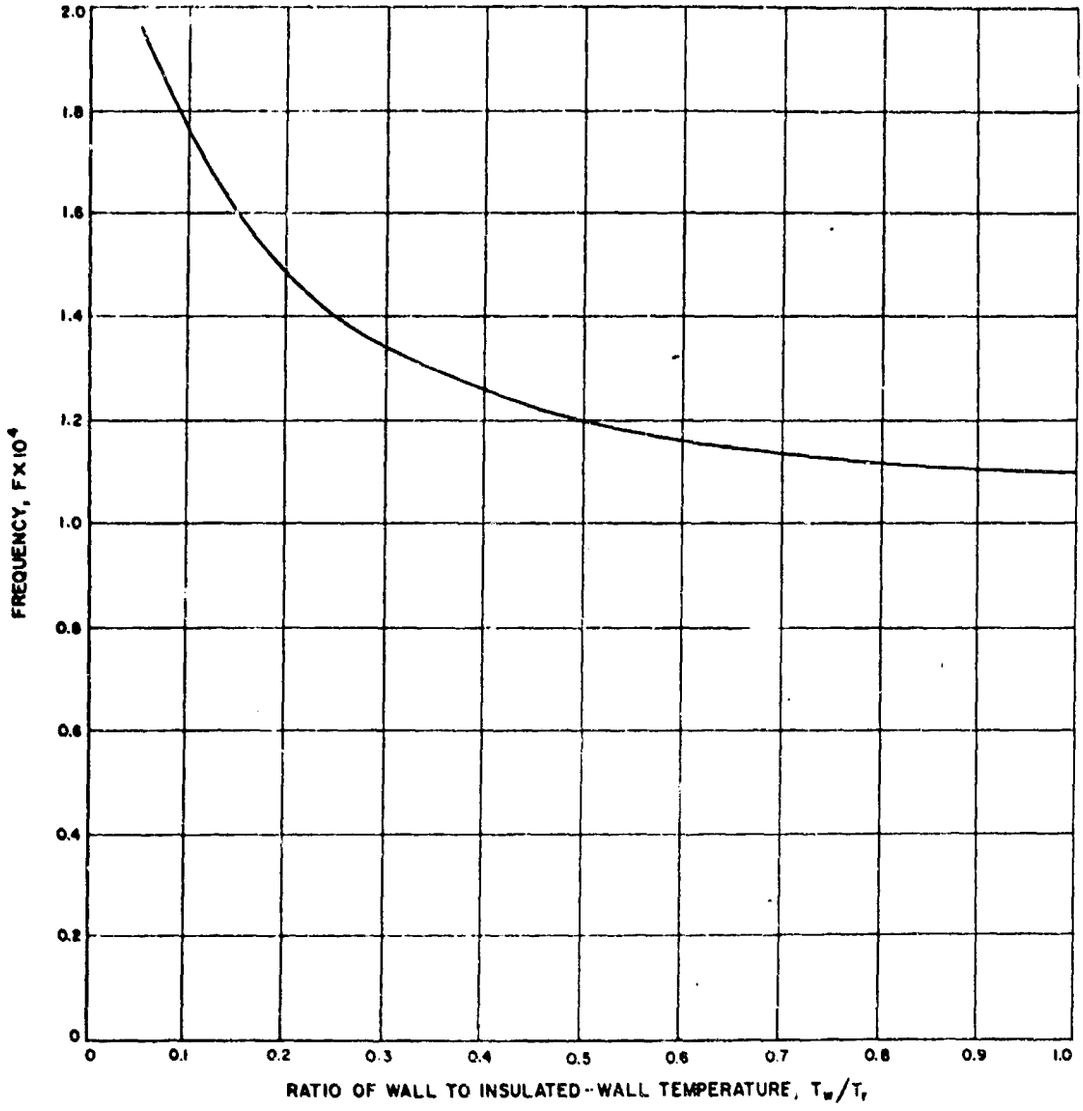

Fig. 13. Effect of cooling at $M_1 = 5.8$ on the most unstable frequency at $R = 1500$.

THE EFFECT OF COMPLIANT WALLS ON BOUNDARY LAYER STABILITY AND TRANSITION

by

Marten T. Landahl* and Richard E. Kaplan†

*Department of Aeronautics and Astronautics
Massachusetts Institute of Technology
Cambridge, Massachusetts, U.S.A.

†Graduate Department of Aerospace Studies
University of Southern California
School of Engineering
Los Angeles, California, U.S.A.

SUMMARY

Recent theoretical progress in the field of boundary layer stability and transition as influenced by a compliant surface is reviewed. The main physical mechanisms involved in boundary layer instability are explained, and it is demonstrated that for any stabilization method to be effective the net dissipation associated with an instability wave must be reduced. Results of extensive numerical calculations show that for certain combinations of compliant surface parameters it is possible to reduce the spatial amplification rates substantially, although the increase in critical Reynolds number usually is small. The main practical difficulty associated with this method of boundary layer stabilization is to find a compliant surface material of low mass density.

The qualitative effects of a wall flexibility on the later non-linear stages of transition are also discussed. It is concluded that the direct effect on the non-linear breakdown process is likely to be small and that the main effect is on the primary wave whose nature may be altered and thus the condition for the appearance of turbulent bursts.

SOMMAIRE

Des récents progrès théoriques réalisés dans le domaine de la stabilité de la couche limite et de la transition grâce à l'introduction d'un plan souple sont passés en revue. Les principaux processus physiques de l'instabilité de la couche limite sont expliqués et l'on démontre qu'une méthode de stabilisation n'est efficace qu'à condition de diminuer la dissipation nette liée à une onde d'instabilité. Les résultats de nombreux calculs numériques montrent que pour certaines combinaisons de paramètres des plans souples il est possible de réduire considérablement les taux d'amplification spatiale quoique l'augmentation du nombre de Reynolds critique soit généralement faible. La principale difficulté pratique liée à cette méthode de stabilisation de la couche limite consiste à trouver un matériau pour le plan souple possédant une faible densité massique.

Les effets qualitatifs de l'élasticité de la paroi sur les stades ultérieurs non linéaires de la transition sont discutés. On conclut que l'effet direct sur le processus de détérioration non linéaire est vraisemblablement restreint et que cet effet s'exerce surtout sur l'onde primaire dont la nature peut se trouver modifiée et être par la suite la condition de l'apparition de poussées de turbulence.

CONTENTS

LIST OF FIGURES

NOTATION

(All variables have been made dimensionless, except as stated, using as references quantities δ, U_∞ and ρ. Dimensional versions are denoted by a star.)

$c = c_r + ic_i$	complex phase speed of disturbance
$c_0 = \sqrt{T/m}$	wave speed on a free membrane
$c_g = \frac{\partial}{\partial\alpha}(\alpha c_r)$	group velocity
c_1	compressional wave speed in viscoelastic material
c_2	shear wave speed
d	damping constant for membrane
d_2	damping constant for viscoelastic material
$\mathfrak{F}$	modified Tietjens function
G	shear modulus
H	depth of viscoelastic layer
k	spring constant of membrane support
m	mass of membrane per unit length
p	pressure
$R = \frac{U_\infty \delta}{\nu}$	Reynolds number, based on boundary layer thickness
T	membrane tension
U(y)	velocity of parallel mean flow
U_∞	free-stream velocity (dimensional)
u, v	perturbation velocity components
Y_{12}	tangential wall admittance
Y_{22}	normal wall admittance

$\alpha = \alpha_r + i\alpha_i$	complex wave number
β_r	frequency of disturbance (dimensional)
β_i	temporal amplification rate (dimensional)
δ	boundary layer thickness (dimensional)
ν	kinematic viscosity (dimensional)
ρ	density of fluid (dimensional)
ρ_2	relative density of viscoelastic solid
$\omega = \alpha c_r = \frac{\beta_r \delta}{U_\infty}$	non-dimensional frequency, based on boundary layer thickness
$\beta_r \nu / U_\infty^2$	non-dimensional frequency based on viscous length scale
$\omega_0 = \sqrt{k/m}$	cut-off frequency of spring-supported membrane

THE EFFECT OF COMPLIANT WALLS ON BOUNDARY LAYER STABILITY AND TRANSITION

Marten T. Landahl and Richard E. Kaplan

1. INTRODUCTION

In recent years a conceptually new idea for boundary layer stabilization has attracted great interest. This idea, introduced by Kramer[1,2], is that the dynamic properties of a boundary layer, and hence its stability and transition characteristics, may be influenced by coupling it hydroelastically to a compliant wall. Kramer's original hypothesis was that by distributing damping over an elastic wall that was tuned to a frequency near that of the most unstable Tollmien-Schlichting wave, it would be possible to add sufficient dissipation to the instability waves that they would become attenuated. On this principle he designed a flexible coating that, in some favorable circumstances, was shown to produce a substantial drag reduction for towed underwater bodies, thus indicating a delayed transition to turbulence. Unfortunately, subsequent attempts to veryify Kramer's findings under more controlled circumstances have been rather unsuccessful, and no conclusive experimental results showing extensive stabilizing effects have as yet been published. On the other hand, theoretical investigations by Benjamin[3], Betchov[4], Landahl[5] and others[6-9] indicate that a substantial stabilizing effect is possible, but that the physical mechanism is rather more intricate than that originally envisaged by Kramer, and that in fact any added dissipation must by itself be destabilizing. Recent extensive numerical calculations by Kaplan[9] give a possible clue to why the experimental findings have, so far, been largely disappointing. It turns out that large stabilizing effects are predicted to occur only for a narrow range of parameters characterizing the flexible wall, and a surface chosen more-or-less at random is most likely to have a negligible or unfavorable effect. There is, of course, also the explanation that the main effect in reality is on the fully developed turbulent boundary layer, a possibility that has been tentatively explored in a recent paper by Benjamin[10].

Apart from the engineering applications, which in light of the investigations carried out so far might not seem too promising on balance, the general field of problems involving a boundary layer or other shear flow in contact with a flexible surface is of great general scientific interest. Such problems appear in a great variety of physical situations as, for example, in wind induced water waves, panel flutter at transonic speeds, flow of blood in arteries, etc. It should also be emphasized that the additional "degree of freedom" introduced by the flexible wall has made it possible to gain further insight into the physical mechanisms causing boundary layer instability; specifically, a completely new explanation of the role of energy dissipation has been arrived at.

The present paper will be primarily concerned with the influence of various types of flexible surfaces on Tollmien-Schlichting stability. Recent progress will be reviewed, in particular regarding the effect on spatial (as opposite to temporal) amplification rates. Some discussion, mostly of qualitative nature, will be given to the effect on secondary instability, i.e., to the later stages of transition.

2. GENERAL FORMULATION OF PROBLEM

The physical problem considered is illustrated in Figure 1. A parallel shear flow of width δ characterized by a velocity distribution $U(y)$ such that $U(y) = U_\infty = 1$ for $y \geq 1$ is bounded by a compliant surface which, when the system is at rest, is located at $y = 0$. The term "compliant surface" should be understood in a very general sense; thus it could be any elastic structure with properties homogenous in x (for example, a membrane or a rubber coating, a water surface, or another shear flow). The problem of the stability of this dynamic system to infinitesimal disturbances may be reduced to the investigation of two-dimensional infinite travelling waves characterized by a stream function $\psi(x,y,t)$ of the form

$$\psi(x,y,t) = \phi(y)\, e^{i\alpha(x-ct)} \tag{1}$$

where α is the wave number and c the phase velocity. The function is governed by the familiar Orr-Sommerfeld equation

$$i\alpha R[(U - c)(\phi'' - \alpha^2\phi) - U''\phi] = \phi'''' - 2\alpha^2\phi'' + \alpha^4\phi\,. \tag{2}$$

The parameters appearing have been made dimensionless using as reference quantities U_∞ and δ. Thus, the Reynolds number R is defined as

$$R = U_\infty\delta/\nu\,. \tag{3}$$

The boundary conditions for the problem are determined from the following physical conditions:

(i) the perturbations vanish far from the boundary;

(ii) the velocity and pressure perturbations at the compliant surface must be compatible with the motion of the surface at the given (α, c).

The first of these gives that

$$\phi, \phi' \to 0 \quad \text{as} \quad y \to \infty\,. \tag{4}$$

We turn next to the boundary conditions at the wall. The dynamic properties of the flexible wall are most conveniently described by its tangential and normal travelling-wave admittances defined as follows:

$$Y_{12}(\alpha, c) = \hat{u}_s/\hat{p}_w \tag{5}$$

$$Y_{22}(\alpha, c) = -\hat{v}_s/\hat{p}_w\,. \tag{6}$$

Here $u_s = \hat{u}_s e^{i\alpha(x-ct)}$ and $v_s = \hat{v}_s e^{i\alpha(x-ct)}$ are the tangential and normal components, respectively, of the surface velocity, and $p_w = \hat{p}_w e^{i\alpha(x-ct)}$ the wall

pressure. The compatibility condition (ii) may be expressed as a matching of Y_{12} and Y_{22} to their corresponding "fluid admittances". Let superscript f denote the admittances of the shear flow considering the streamline along the wall as the flexible surface. Then

$$Y^f_{12} = \frac{u(\eta)}{p_w} \tag{7}$$

$$Y^f_{22} = -\frac{v_i(\eta)}{p_w} \tag{8}$$

where v_i is the vertical velocity of the interface streamline. Now, in linearized approximation

$$u(\eta) = u(0) + \eta U'_w \tag{9}$$

$$v(\eta) = v_i(1 - U_w/c) \tag{10}$$

where subscript w denotes values at the wall ($y = 0$). Normally, U_w would be zero for a solid wall but would be non-zero if the compliant wall consisted of another shear flow. The (dimensionless) fluid pressure at the wall may be obtained from the linearized x-momentum equation. This yields

$$\hat{p}_w = -\frac{i}{\alpha R}(\phi'''_w - \alpha^2\phi'_w) + (c - U_w)\phi'_w + U'_w\phi_w . \tag{11}$$

Upon combining (7) to (11) and expressing u and v in term of ϕ we obtain

$$Y^f_{12} = \frac{\phi'_w}{\hat{p}_w} + \frac{iU'_w}{\alpha c} Y^f_{22} \tag{12}$$

$$Y^f_{22} = i\alpha\phi_w/\hat{p}_w(1 - U_w/c) \tag{13}$$

where $\hat{p}_w$ is given by (11). The second term in (12) results from replacing η by $v_i/(-i\alpha c)$ and expressing v_i in terms of Y^f_{22} and p_w by aid of (8). Having thus expressed the fluid admittances in terms of ϕ and its derivatives at the wall we may now state the boundary conditions at the wall as follows:

$$Y^f_{12} = Y_{12} \tag{14}$$

$$Y^f_{22} = Y_{22} . \tag{15}$$

Here, the left-hand sides are functions of the shear flow only, and the right-hand sides depend only on the properties of the flexible wall. A slight approximation is actually involved in the above derivation in that the induced shear stress is ignored as far as the motion of the compliant boundary is concerned. This is certainly an allowable approximation for fluids of low viscosity.

The four boundary conditions (4), (14) and (15) are homogenous, and non-zero solutions of (2) are thus possible only for certain eigenvalue combinations of the parameters α, c and R. The traditional approach in hydrodynamic stability is to

consider α and R as real and given, and $c = c_r + ic_i$ as complex. Whenever the imaginary part, c_i, is positive, the wave will grow with time (temporal amplification case). However, in most physical situations it is actually more informative to consider R and the (dimensionless) frequency $\omega = \alpha c$ as given real numbers, and $\alpha = \alpha_r + i\alpha_i$ as complex, so that a negative α_i indicates that a disturbance of given frequency will grow in the downstream direction (spatial amplification case). For small amplification rates the temporal and spatial eigenvalues are related by the formulas[11]

$$\omega = \alpha c_r \qquad \alpha_r = \alpha$$

$$\alpha_i = -\frac{\alpha c_i}{c_g} \tag{16}$$

where $c_g = \frac{\partial}{\partial \alpha}(\alpha c_r)$ is the group velocity.

A practical procedure to calculate the eigenvalue is as follows. First, the two of the four linearly independent solutions of (2) satisfying (4) are calculated. From (14) a ratio of the two remaining solutions is next found which is substituted into (15) giving one single eigenvalue relation. This is then solved employing some numerical procedure.

3. DYNAMICS OF THE COMPLIANT WALL

For a realistic evaluation of a flexible surface as a stabilizing device it is desirable to consider simple surface models permitting the variation of mass density, elasticity and damping. Two such models have been extensively studied. One is a stretched membrane of tension $\rho U_\infty^2 T$ over a continuous spring support of spring constant $k\rho U_\infty^2/\delta$. For this one obtains that

$$Y_{22} = -\frac{ic}{m\alpha\left(c_0^2 - c^2 - \frac{icd}{\alpha} + \frac{\omega_0^2}{\alpha^2}\right)} \tag{17}$$

where m is the mass per unit length divided by $\rho\delta$; $c_0 = \sqrt{T/m}$ the propagation speed of free surface waves, divided by U_∞, d the damping constant, divided by $\delta/U_\infty m$; and $\omega_0 = \sqrt{k/m}$ the cut-off frequency divided by δ/U_∞. The tangential admittance of the membrane is zero.

The second model investigated consists of a viscoelastic layer (Voight solid) of thickness $H_* = H\delta$ free to slide without friction on a rigid support. This latter condition was chosen partly to make the results simple, partly to use this surface as a simplified model of dolphin skin which is fairly loosely anchored to the underlying muscle tissue. A viscoelastic solid is characterized by two propagation velocities $c_{1*} = c_1 U_\infty$ and $c_{2*} = c_2 U_\infty$, where c_{1*} is the speed of compression waves and c_{2*} that of shear waves. For materials like rubber and fluids like water one can assume $c_{1*} = \infty$ to a good approximation, and the results for the admittances then simplify to

$$Y_{12} = -c\beta/\gamma \tag{18}$$

$$Y_{12} = -ic(r_2^2 - 1)/\gamma \tag{19}$$

where $r_2^2 = 1 - (c/c_2)^2$

$\beta = (1 + r_2^2)\coth\alpha H - 2r_2 \coth r_2\alpha H$

$\gamma = \rho_s c_2^2[(1 + r_2^2)^2 \coth\alpha H - 4r_2 \coth r_2\alpha H]$

and $c_2 = (G - i\alpha c d_2)/\rho_s$,

$G_\star = \rho_\infty U_\infty^2 G$ being the shear modulus of the material, d_2 a non-dimensional material damping constant, and $\rho_{s\star} = \rho_s \rho$ the material density.

Certain complications arise in the interpretation of the results using the above expressions because the boundary layer thickness was used as a reference length. This quantity varies with Reynolds number and hence with distance along the wall. If one considers the effect of a compliant wall of given constant (dimensional) thickness $H_\star$, then the non-dimensional thickness H should vary like

$$H = H_\star(\delta_0/\delta) = H_\star(R_0/R) \tag{20}$$

where suffix zero denotes a reference quantity. For all the cases considered, H and other parameters involving δ in their non-dimensionalization were varied in this or corresponding manner using as a reference Reynolds number $R_0 = 5000$.

For a lightly damped surface, the normal admittance Y_{22} is mainly imaginary with a negative sign for small wave velocities and with a positive sign for large values of c . Thus its effect is mainly spring-like for small c , and mass-like for large c . The real part is always positive, having a large value at wave velocities near that for free-wave propagation.

4. SIMPLIFIED AEROELASTIC MODEL

It is remarkable that some very important physical features of the hydrodynamic stability problem outlined above may be studied qualitatively without having to consider the difficult mathematical problem of solving the Orr-Sommerfeld problem. This was first brought out by Landahl[5] and further elaborated on by Brooke Benjamin[12]. The simplified model considered is that of a potential flow over a membrane. For such a flow one can easily obtain that

$$Y_{22}^f = -\frac{ic}{(1 - c)^2} \tag{21}$$

Substitution of this into the eigenvalue relation (15) together with (18) (assuming $\omega_0 = 0$ for simplicity) results in a simple quadratic equation for c (considering α as known, i.e. as for the temporal amplification case), which possesses the solutions

$$C_A = (1 + m\alpha)^{-1}[1 + \tfrac{1}{2}imd - (1 - q - imd)^{\frac{1}{2}}] \tag{22}$$

$$C_B = (1 + m\alpha)^{-1}[1 + \tfrac{1}{2}imd + (1 - q - imd)^{\frac{1}{2}}] \tag{23}$$

where $q = (1 - \alpha m c_c^2)(1 + \alpha m) + \tfrac{1}{4}m^2d^2$.

Instability is indicated whenever one of the roots has a positive imaginary part. Three different cases may be distinguished: namely, when $q < 0$, $0 < q < 1$ and $q > 1$. In the first, the wave velocity for the first wave is negative, and both waves are damped. In the second case both waves travel downstream and the slowest one (given by C_A) is unstable with a growth rate approximately proportional to the damping, d. For the third case, finally, the square root will have a large imaginary part and one of the roots thus indicates a violent instability. Following the terminology introduced by Brooke Benjamin[3,12] we will refer to the three fundamentally different waves as Class A, Class B and Class C, respectively. The most interesting one of these is Class A which actually is destabilized by the damping. A physical explanation was arrived at[5] by calculating the total energy level of the dynamic system considered. It was found that for the Class A disturbance this level goes down with increasing amplitude*, whereas for the Class B the level increases, and for the Class C it essentially remains constant. This is illustrated schematically in Figure 2. Since a Class A wave thus is energy deficient, any overall decrease in the energy level caused by dissipation must be compensated for by an increase in the wave amplitude. A Class B wave is stabilized by damping as would be the case for an ordinary mechanical system. Class C instability occurs when the membrane becomes so flexible that there is no wave velocity for which the mechanical restoring force is sufficient to balance the induced hydrodynamic force. For this mode the total energy of the system is constant; there is only a redistribution from the fluid to the wall, and damping thus has a negligible effect.

As pointed out by Brooke Benjamin[12], this three-fold classification will always apply, more or less distinctly, to the instabilities encountered by flexible bodies in a fluid flow. Thus, for example, the violent "frequency coalescence" type flutter so familiar to aeroelasticians is of the Class C variety[13]. The damping-induced Class A type rarely occurs in flutter, but as shown below, will be one of main interest in the present problem.

One can now apply the preceding discussion to the more complicated shear-flow problem at hand simply by replacing the membrane by the boundary layer shear flow, bounded at $y = 1$ by a massless diaphragm of infinite flexibility and at $y = 0$ by the wall (flexible or rigid). Using the asymptotic theory for large R and assuming that c is moderate and small ($\alpha < 1$) so that the variation of the induced pressure across the boundary layer may be neglected, one can show that, to a good approximation,

$$Y_{22}^{b.l.} = Y_{22} + \frac{i\alpha}{U_w'}\,[cU_w'K_1(c) + 1 - \Im(z)] \tag{24}$$

where

$$K_1 = \int_0^1 \frac{dy}{(U - c)^2}$$

* The explanation why this may happen is that there is always a net decrease in the kinetic energy of the stream because of an excess of low-velocity fluid in the wave troughs.

and $\mathfrak{F}$ is the modified Tietjens function of argument $z \simeq c(\alpha R)^{1/3} U_w'^{2/3}$. Here we have assumed for simplicity that the tangential surface admittance Y_{12} is zero. By equating the "boundary layer admittance" $Y_{22}^{b.l.}$ to the "fluid admittance" Y_{22}^{f} given by (21) one obtains essentially the characteristic equation considered by Brooke Benjamin[3] and Landahl[5]. For $Y_{22} = 0$ it reduces to the equation given by Lin[14] for a rigid wall. Of specific interest is the real part Y_{22r} of the boundary layer admittance, because the power transfer per unit length across the diaphragm at $y = 1$ is given by

$$\bar{E} = \tfrac{1}{2}|\hat{p}|^2 Y_{22r}^{b.l.} \quad . \tag{25}$$

Taking the real part of (24) we find that

$$Y_{22r}^{b.l.} = Y_{22r} + \frac{\alpha}{U_w'}\left(\mathfrak{F}_i - \bar{\nabla}\right) \tag{26}$$

where

$$\bar{\nabla}(c) = -\pi c U_w' \frac{U_c''}{U_c'} \quad . \tag{27}$$

The sign of the damping contributed by the shear flow is thus given by the sign of $\mathfrak{F}_i - \bar{\nabla}$. When this quantity is positive for the value of c for which the imaginary parts of the admittances balance (i.e., the pressures in phase with the deformation) there is a net dissipation in the boundary layer, and Class A instability thus occurs. If, on the other hand, $Y_{22r}^{b.l.}$ is less than zero the net damping is negative and the Class A wave is hence stable. The quantity $\mathfrak{F}_i$ is a measure of the difference between energy dissipated by fluid friction and energy extracted from the mean flow due to Reynolds stresses developed in the wall friction layer[15]. It is negative for z less than about 2.3, has a maximum of $\simeq 0.58$ at $z \simeq 3.2$ and tends to zero for $z \to \infty$. Viscosity thus may cause a net negative dissipation, i.e., will be stabilizing, for the lower Reynolds number range. For large Reynolds numbers the net viscous effect in the wall friction layer becomes dissipative, thus tending to cause instability. The quantity $\bar{\nabla}$ basically represents[15] the energy extracted from the mean flow due to the Reynolds stresses in the outer non-viscous part of the boundary layer. For a convex velocity profile it is always positive. If the profile has an inflexion point, $\bar{\nabla}$ will be negative for some range of c, and for sufficiently large Reynolds numbers the net damping will be positive leading to instability.

The discussion makes clear that damping in the flexible wall will generally have a destabilizing effect on the boundary layer. Nevertheless, a compliant surface may be stabilizing on Class A waves if it has large flexibility but low damping. Then the imaginary part of the admittances will balance at a higher wave velocity for which $\bar{\nabla}$ is generally larger, so that the net damping will be reduced and the stability increased. However, an excessive flexibility may invite Class B instability, or even the violent Class C type, and any advantage will then be negated.

It is obvious that the present aeroelastic approach leads to completely different conclusions regarding the role of dissipation than does the familiar Lorentz relation for the "energy balance" (see Lin[14], page 60) which expresses the rate of change of "kinetic energy of the disturbance" as the difference between the rate at which Reynolds stresses convert energy from the mean flow and the rate of viscous

dissipation. It should be remarked that the quantity calculated in this relation is not the actual perturbation in kinetic energy, because this should also include the second-order u-perturbation of the mean flow. Although the Lorentz relation, of course, will be satisfied for the eigensolutions, it gives very limited information for prediction purposes for conditions that are off the eigenconditions. In particular, one may very likely find that a calculation of the "energy balance" for one particular neutrally stable wave would indicate an excess of viscous dissipation over energy production by Reynolds stresses, whereas a corresponding calculation for a slightly amplified wave may show a perfect balance.

The present approach also allows a qualitative evaluation of (probably) all present and future proposed methods of boundary layer stabilization. Boundary layer suction produces a velocity profile that is more convex near the wall, thus causing an increase in $\bar{V}(c)$ (i.e., in the energy converted by Reynolds stresses) with a resulting decrease in the equivalent boundary layer damping and thus the stability. Also, it makes the boundary layer thinner so that the Reynolds number decreases, putting it into a region where the viscosity causes a net negative dissipation. Complete stabilization of Class A instability may be achieved through any means that cause the net dissipation for all waves to become zero or negative. For example, a small amount of viscoelastic additive in a liquid may replace the friction layer near the wall by a thicker elastic layer in which the viscous dissipation is largely cancelled.

5. APPLICATION OF NUMERICAL CALCULATION METHODS

Since the traditional asymptotic methods are apt to be rather inaccurate for the wider range of parameters of interest in the present problem, a numerical calculation method has been developed which allows a rapid and accurate estimate of the stabilizing effects of any particular surface. The method has been described in detail by Kaplan[9], and we will here only outline its general features.

The overall numerical procedure followed is illustrated in Figure 3. Starting from the two exact solutions for $y > 1$ that vanish for $y \to \infty$,

$$\Phi_1 = e^{-\alpha y}, \quad \Phi_2 = e^{-\beta y} \tag{28}$$

where $$\beta = [\alpha^2 + i\alpha R(1-c)]^{\frac{1}{2}}, \quad \mathrm{Re}\{\beta\} > 0$$

the Orr-Sommerfeld Equation (2) is integrated to the wall using a suitable numerical procedure. The matching of tangential admittances (14) then produces the proper combination between Φ_1 and Φ_2 which, upon substitution into the matching condition (15) for the normal admittances, leads to the desired eigenvalue relation. This is solved for c or α, as the case might be, using an iterative scheme.

A special procedure had to be devised to make sure that the two solutions were truly linearly independent at the wall. Due to the large parameter αR appearing in the differential equation (2) the solution Φ_2 grows very rapidly (in an oscillatory manner) as the wall is approached, usually by several orders of magnitude faster than Φ_1. Therefore, if at some stage during the integration of Φ_1 any small

portion of ϕ_3 is introduced due to numerical inaccuracy (this is inevitable due to truncation errors), this portion will grow so much faster than ϕ_1 that it eventually will dominate the solution. Hence, the numerical integration will always produce a solution of the ϕ_3 type, regardless of the initial conditions used. To avoid this, a "purification scheme" was devised which at the end of each integration step $y = y_{n+1}$ removed from ϕ_1 a fraction of the solution ϕ_3 (previously computed and stored) to make the relation

$$\left[(U - c)(\phi_1'' - \alpha^2\phi_1) - U''\phi_1\right]_{y=y_{n+1}} = 0 \tag{29}$$

satisfied (this is recognized as the differential operator in the inviscid Orr-Sommerfeld equation). In this way the initial conditions for ϕ_1 are readjusted at each step to insure that one is always following a slowly growing solution of (2). Hence one is shifting among neighboring solutions at each step to avoid "getting trapped" by ϕ_3. However, one single solution can, if desired, be easily assembled by using the stored "purification coefficients". (For more details about the purification scheme, see Kaplan[9].)

Using a standard Runge-Kutta integration method with 64 steps the computation time on the IBM 7094 required to obtain one set of values for ϕ_1 and ϕ_3 at the wall was approximately 1/2 second. Less than 5 iterations were needed to find an eigenvalue. Originally, the eigenvalue problem for c was programmed assuming a given real value of α. Spatial amplification rates α, for real values of $\omega = \alpha c$, were obtained from the temporal ones, c_i, using the relations (16) and employing a value of the group velocity obtained through numerical differentiation with respect to α. Later more efficient programs have been developed that solve the spatial amplification problem directly, and excellent agreement was obtained with the earlier computed values of α_i. The spatial amplification rate is the more meaningful one for assessing the stabilizing influence of a particular flexible wall because it allows one to calculate how much a disturbance of given frequency will grow in the downstream direction. With a given (dimensional) spatial amplification rate of α_{i*} the total growth of the velocity amplitude between the stations x_0 and x in a flat plate boundary layer is given by the formula

$$\log_e\left(\frac{\hat{u}}{\hat{u}_0}\right) = -\int_{x_c}^{x} \alpha_{i*}\,dx = -\frac{1}{K^2}\int_{R_0^2}^{R^2} \frac{\alpha_{i*}\nu}{U_\infty}\,d(R^2) \tag{30}$$

where the constant K is defined by

$$K = \delta/\sqrt{\nu x/U_\infty} \simeq 6 .$$

The non-dimensional quantity $\alpha_{i*}\nu/U_\infty = \alpha_i/R$ must be determined as a function of R for a fixed value of the non-dimensional frequency $\beta_r\nu/U_\infty^2$. Such a calculated map of α_{i*} for the rigid surface case is shown in Figure 4.

The accuracy of the numerical technique was judged by comparing results for a rigid wall ($Y_{12} = Y_{22} = 0$) with previous calculations, both analytical and numerical, and with the experimental results of Schubauer and Skramstad[16]. As an example of the comparisons with experiments we show in Figure 5 the measured and calculated velocity amplitude variations with x in a point in the boundary layer for various frequencies

of the oscillating ribbon. The excellent agreement gives high confidence in the developed procedure, as well as in the stability theory for parallel shear flows.

Results for the two different kinds of flexible surface models investigated are presented in Figures 6 - 13. Here a selection was made of those combinations of surface parameters that were found to produce a large stabilizing effect and yet be within practical limits. Only results for Class A instabilities will be presented, these being of the main interest in the present context. Figures 6 - 9 gives results for some selected membranes*. In Figure 6 is illustrated the influence of membrane damping on the stability boundary. Clearly, the damping is destabilizing, as the simplified aeroelastic model indeed showed. It is interesting to notice that the curves for the lowest values of the damping apparently are closed indicating only a finite range of unstable Reynolds numbers. For the highest value of the damping, a second region of instability (also of Class A type) was detected for higher frequencies and Reynolds numbers, but an insufficient number of calculated points were available to map this region. Whether instability recurs for higher Reynolds numbers also for the membranes with the lower damping values is presently not clear.

The effect of varying the membrane tension, i.e. c_0 , is illustrated in Figure 7. Generally, the lower value of c_0 , the higher the stabilizing effect, up to the point where the effective free surface wave speed, $\sqrt{c_0^2 + \omega_0^2/\alpha^2}$, becomes too close to the eigenvalue, in which case the real part of Y_{22} grows so large that the net effect eventually becomes destabilizing. This stage was not reached for the membranes considered in Figure 7 because of the fairly stiff spring support used.

The spatial amplification rates for one of the "best" membranes are presented in Figure 8. Such diagrams can be used to construct curves like that given in Figure 9 which shows the spatial amplification rate for a disturbance of given frequency as function of R^2 . According to (30) the total amplification in a boundary layer between two stations x is given by the area under these curves between the corresponding Reynolds numbers. The frequency was chosed to lie near that for most amplified disturbance in both the rigid-wall and the flexible-wall cases. As seen, the decrease in the area under the curves, i.e., of the total amplification, is quite substantial.

Results for the free-sliding viscoelastic layer are shown in Figures 10 - 12. In Figure 10 is demonstrated the influence on the stability boundary of varying the thickness, H , of the layer. The flexibility of the surface increases with increasing H , and hence the stabilizing influence, but the effect of thickness increases beyond $H = 2$ tended to have a minute effect, the reason being that the surface waves in the solid do not penetrate appreciably below this depth.

Spatial amplification rates for one of the more favorable combinations of surface parameters considered are shown in Figure 11. The same qualitative features are observed as for the membrane case, although the stabilizing effect is considerably less than for the best membranes. Thus, the unstable range is decreased and moved to lower wave numbers. Also, there is a marked decrease in amplification rates from the rigid-wall case coupled with a moderate increase in Reynolds number.

---

* The calculations for membranes presented in Reference 9 are in error because a factor of $1/\alpha$ was omitted in the expression for the normal admittance.

The effect of even small changes in the surface parameters on the stabilizing influence is illustrated in Figure 12. The surface considered has half the thickness of the previous one (this difference by itself has only a fairly small effect, as seen from Figure 10), has a somewhat higher shear wave velocity (i.e., is stiffer) and a 20% higher density. A comparison with the results for the rigid wall, Figure 4, shows that little remains of the stabilizing effect.

The main fundamental difference between the membrane and the viscoelastic surface is that the latter has a non-zero tangential admittance. Examination of the expressions (18) and (19) reveals that the tangential motion is appreciable and may for small thicknesses exceed the normal motion. That the simple aeroelastic membrane model nevertheless seems to hold qualitatively also for this surface indicates that the tangential motion is fairly unimportant to the problem. Application of the asymptotic theory shows that the effect of tangential motion is usually mildly destabilizing. This may partly explain why the viscoelastic layers were found, on the whole, less effective than a membrane of comparable compliance.

6. FLEXIBLE SURFACES IN PRESSURE GRADIENT FLOWS

Additional calculations were performed to determine the effectiveness of compliant surfaces in changing the stability boundaries of adverse and favorable pressure gradient flows. Falkner-Skan similarity profiles were used to provide accurate second derivatives for computation. The adverse pressure gradient profiles considered had a Falkner-Skan parameter of $\bar{\beta} = -0.15$.

Calculations were performed for several different membranes. As a length scale the boundary layer thickness of 99.9% free stream velocity was employed. The interpretation of parameters preceeding (20) was not used for these cases of varying free stream velocity.

The results appear very similar to those found previously for the Blasius profile, with the following exception. The surface damping coefficient d had little or no noticeable influence on the stability of the adverse pressure gradient Class A waves. This is interpreted as further verification of the energy deficient character of these disturbances. The total level of dissipation is so high for this flow that a small additional amount of dissipation in the surface causes no discernable influence. The converse is true for favorable pressure gradients.

Figure 13 illustrates this effect. For these calculations the value of d was found to be unimportant and was varied from +0.10 to -0.10 with no variation of stability boundaries. The spatial amplification rates were altered slightly, however, but not nearly as much as in the Blasius case.

7. EFFECTS OF TRANSITION

The main physical mechanisms causing transition of a boundary layer over a rigid flat plate have been clarified and described in recent papers by Benney and Lin[17,18], Klebanoff, et alii[19], Greenspan and Benney[20], and others[21]. Turbulent bursts occur as a secondary localized instability (of presumably Class C type) in regions in the

boundary layer transition zone where the primary instability waves, together with secondary mean motion caused by spanwise irregularities, produce inflexion profiles of large instantaneous shear during the primary oscillation cycle. A pre-requisite for transition is thus a primary wave of sufficiently high amplitude in the presence of a secondary spanwise warping of the mean velocity profile.

The calculations presented above make clear that under favorable circumstances a flexible wall may delay the growth of the primary wave and hence prolong the laminar flow. The main cause is not the increase in critical Reynolds number, which is rather insignificant, but the decrease in spatial amplification rates primarily associated with the increase in the wave length of the most amplified disturbance. However, in addition, one would expect that the secondary flow will be substantially altered and hence the onset of secondary instability. No secondary-flow calculations for a flexible wall similar to those of Benney[18] are as yet available, but it can be speculated that the greater primary-wave lengths encountered for the flexible wall should have a large effect on the spanwise warping. This appears likely because the spanwise separation between the longitudinal vortices appearing in the mean secondary motion should depend on the wave lengths of oblique primary waves (see Benney[22]).

The results for the eigenfunction in the flexible-wall case reveal another possible substantial secondary effect. The strong instantaneous inflexional shear layer in the velocity profile in which turbulent bursts are born is produced by a superposition of the mean profile, made weakly inflexional by the mean secondary streamwise vortices, and the velocity perturbations due to the primary wave. In Figure 14 are compared the u-perturbations for a typical rigid- and flexible-wall case. It is evident that, for the same maximum amplitude, the local shear values produced by the flexible-wall perturbation velocity profile are much smaller than for the rigid-wall case. Hence, a much higher overall amplitude is required to attain the same maximum local shear values. It is interesting to notice that for the flexible membrane the u-perturbation velocity at $y = 0$ is not zero, although it is so at the actual instantaneous position of the membrane. Hence, as pointed out by Brooke Benjamin[3] and further exemplified by Landahl[5], the flexible wall largely cancels the need for a wall friction layer.

Finally, the possibility that wall flexibility may have a direct influence on the secondary instabilities should be considered. It has been hypothesized by Kramer[23] that the outer layer of the dolphin's skin might have such an effect. Greenspan and Benney[20] have shown that many of the important qualitative features of the turbulent bursts could be described by using the linearized stability formulation for a non-viscous flow (viscosity being rather unimportant for violent inflexional instability) applied to a velocity profile consisting of the mean flow with the primary wave superimposed. The calculation is complicated by the fact that the "mean" velocity profile varies with time through the primary cycle, but Benney and Rosenblat[24] have suggested that a convenient way to account for this variation is to use the method of multiple time scales[25] with the "rapid-time" behaviour being determined by the ordinary inviscid stability theory considering the velocity profile as quasi-steady. For the present purpose of determining the qualitative effects of a flexible wall on the secondary instability, it is probably sufficient to perform just the quasi-steady analysis without taking the "slow-time" behaviour into account. In Figure 15 are

presented the results of such calculations based on the instantaneous velocity profile measured by Klebanoff et alii[19] at the onset of turbulent bursts*.

In these calculations the velocity profile was fitted in a fairly crude manner by an exponential function plus an eighth order polynomial as illustrated in the upper portion of Figure 15. The lower portion of the figure shows the calculated results for the non-dimensional temporal amplification rate plotted versus the non-dimensional frequency, both for the rigid wall case and for a sample membrane surface. The non-dimensional frequency for the maximum temporal amplification rate is about 1.3, which is only about 60% of the measured value[19] of $\beta_r \delta / U_\infty = 2.2$. Whether this discrepancy is due to inaccuracies in fitting the velocity profile, or to inadequacy of the quasi-steady quasi-linearized model, or both, has not yet been determined. On the other hand, the calculations give a group velocity of about $0.65\ U_\infty$, which is in good agreement with the measured value of the propagation speed of the turbulent bursts, $0.68\ U_\infty \pm 0.04\ U_\infty$. Nevertheless, the simplified model is probably entirely adequate for the present purpose of estimating the effect of a flexible wall. A membrane was chosen that had been found to give a large effect on the primary wave. As seen from Figure 15, the stabilizing effect on the secondary wave is noticeable, but rather small. From this one would conclude that a flexible wall will only slightly alter the growth rate of the secondary instability, and therefore the direct effect on the turbulent bursts is likely to be small, at least for membranes of moderately small density. A similar conclusion was reached by Benjamin[10] using an even simpler flow model.

8. CONCLUSIONS

From extensive sets of numerical results such as those presented above a fairly complete theoretical picture of the possibilities of a flexible wall as a laminarization device emerges. It has been definitely established that wall compliance in certain cases can have a substantial stabilizing influence on the primary (Tollmien-Schlichting) instability waves. The main effect is a decrease in the spatial amplification rates and in the extent of the unstable region, rather than an increase in the critical Reynolds number which is usually insignificant. Wall compliance also can have an associated influence on the secondary instabilities so that an appreciable total effect in delaying transition is theoretically possible. In order to be effective, the surface should be highly flexible but have low damping. A large compliance could in principle be achieved by tuning the wall to have a characteristic wave velocity slightly above that of the most unstable waves, but then instabilities of Classes B and C may occur and, furthermore, the dissipation will increase, thus producing a destabilizing influence on the energy deficient Class A waves. The calculations show an effective characteristic velocity of about 3/4 of the free stream velocity to be the lower practical limit. In order to achieve a large response one must thus use a light wall, preferably one having an effective mass per unit length not much higher than that of the fluid inside the boundary layer. Obviously, this requirement puts very considerable limitations on the use of compliant walls in practical applications, in particular for airborne vehicles.

---

* The authors are greatly indebted to Dr. L.N. Howard for very valuable assistance in programming these calculations.

From the broader engineering and scientific points of view the studies of compliant wall effects promise to be of great value because of the new and deepened insight into the dynamic characteristics of both laminar and turbulent shear flows that emerges. A compliant wall is likely to be only one of several devices that can substantially alter the flow response to an unsteady disturbance. The use of small quantities of chemical additives seems presently to be the most promising approach.

ACKNOWLEDGEMENT

The authors acknowledge the support of the MIT Computation Center, the USC Computer Sciences Laboratory, and the Western Data Processing Center for the use of their facilities. This work was supported in part by the Office of Naval Research under Contract Nonr-1841(89).

REFERENCES

1. Kramer, M. — *Boundary-Layer Stabilization by Disturbed Damping.* Journal of the Aeronautical Sciences, Vol.24, p.459.

2. Kramer, M. — *Boundary-Layer Stabilization by Disturbed Damping.* J. Amer. Soc. Nav. Eng., Vol.72, p.25.

3. Benjamin, T.B. — *Effects of a Flexible Boundary on Hydrodynamic Stability.* J. Fluid Mech., Vol.9, p.513.

4. Betchov, R. — *Simplified Analysis of Boundary-Layer Oscillations.* J. Ship Res., Vol.4, No.2, p.37.

5. Landahl, M.T. — *On the Stability of a Laminar Incompressible Boundary-Layer Over a Flexible Surface.* J. Fluid Mech., Vol.13, No.4, p.609.

6. Hains, F.D. Price, J.T. — *Effect of a Flexible Wall on the Stability of Poiseuille Flow.* Phys. Fluids, Vol.5, p.365.

7. Nonweiler, T. — *Qualitative Solutions of the Stability Equation for a Boundary-Layer in Contact with Various Forms of Flexible Surfaces.* ARC Report No. 22,670.

8. Boggs, F.W. Tokita, N. — *Theoretical Study of Compliant Coatings to Achieve Drag Reduction on Underwater Vehicles.* U.S. Rubber Company Res. Lab., Wayne, N.J., 1962.

9. **Kaplan, R.E.** — *The Stability of Laminar Incompressible Boundary Layers in the Presence of Compliant Boundaries.* ScD. Thesis, M.I.T., 1964.

10. **Benjamin, T.B.** — *Fluid Flow with Flexible Boundaries.* Paper presented at Eleventh International Congress of Applied Mechanics, Munich, 1964.

11. **Gaster, M.** — *A Note on the Relation between Temporary-Increasing and Spatially-Increasing Disturbances in Hydrodynamic Stability.* J. Fluid Mech., Vol.14, p.222.

12. **Benjamin, T.B.** — *The Threefold Classification of Unstable Disturbances in Flexible Surfaces Bounding Inviscid Flows.* J. Fluid Mech., Vol.16, No.3, p.436.

13. **Landahl, M.T.** — *Graphical Technique for Analyzing Marginally Stable Dynamic Systems.* Journ. Aircraft, Vol.1, No.5, September - October 1964.

14. **Lin, C.C.** — *The Theory of Hydrodynamic Stability.* Cambridge Univ. Press, 1956.

15. **Benjamin, T.B.** — *Shearing Flow Over a Wavy Boundary.* J. Fluid Mech., Vol.6, p.161.

16. **Schubauer, G.B. Skramstad, H.K.** — *Laminar-Boundary-Layer Oscillations and Transition on a Flat Plate.* NACA Report No.909, 1948.

17. **Benney, D.J.** — *On the Secondary Motion Induced by Oscillations.* Phys. Fluids, Vol.3, p.656.

18. **Benney, D.J.** — *A Non-Linear Theory for Oscillations in a Parallel Flow.* J. Fluid Mech., Vol.10, p.209.

19. **Klebanoff, P.S. et alii** — *The Three-Dimensional Nature of Boundary-Layer Instability.* J. Fluid Mech., Vol.12, p.1.

20. **Greenspan, Benney, D.J.** — *On Shear-Layer Instability, Breakdown and Transition.* J. Fluid Mech., Vol.15, p.133.

21. **Kovasznay, L.S.G.** — *A New Look at Transition.* Aeronautics & Astronautics, Pergamon Press, London, 1960, p.161.

22. **Benney, D.J.** — *Finite Amplitude Effects in an Unstable Laminar Boundary Layer.* Phys. Fluids, Vol.7, No.3, March 1964, pp.319-326.

23. **Kramer, M.O.** — *Speculative Consideration on High-Frequency Instability of the Design of Stabilizing Coatings.* Memo. RM-3284-DR, The Rand Corporation, 1962.

24. Benney, D.J.
Rosenblat, S.
Stability of Spatially Varying and Time-Dependent Flows.
Phys. Fluids, Vol.7, p.1384.

25. Kevorkian, J.
Notes in the Summer Institute on Dynamical Astronomy.
Yale University Press, New Haven, Conn. 1962.

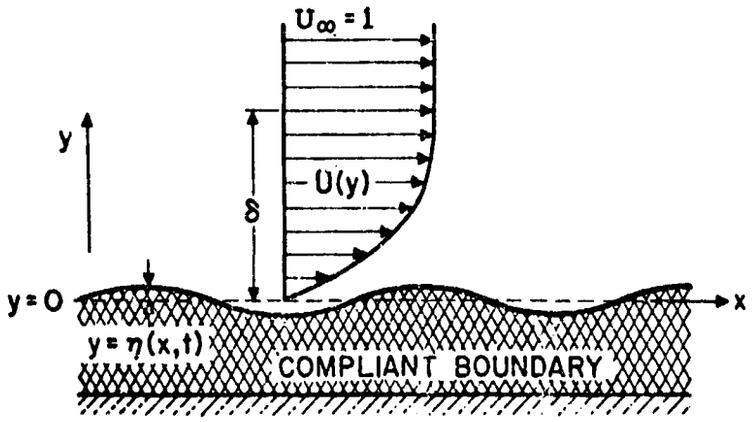

Fig. 1 Boundary layer over a compliant boundary

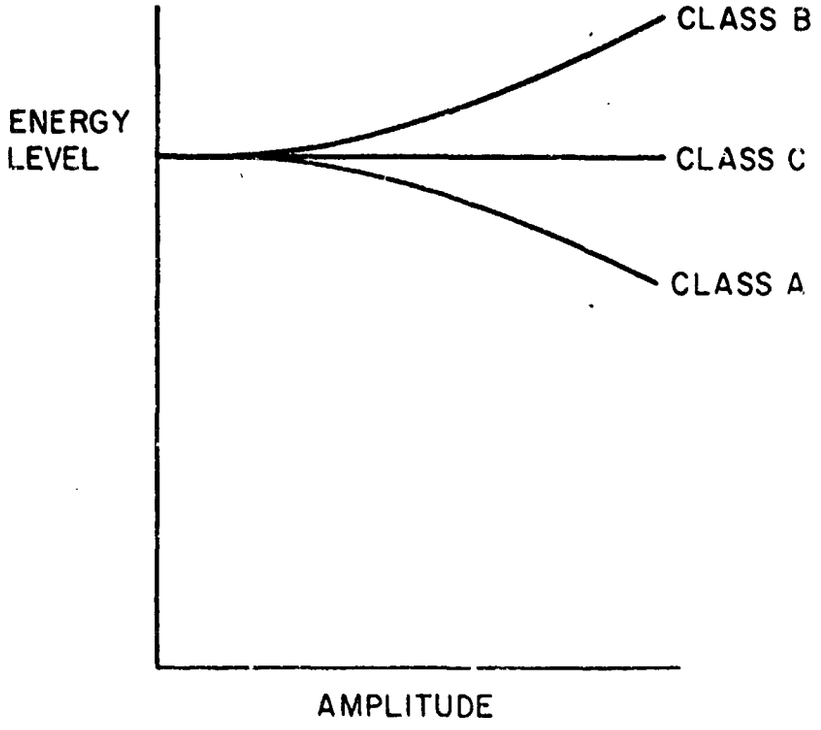

Fig. 2 Variation of the total energy level of the system with amplitude for the three different classes of instability

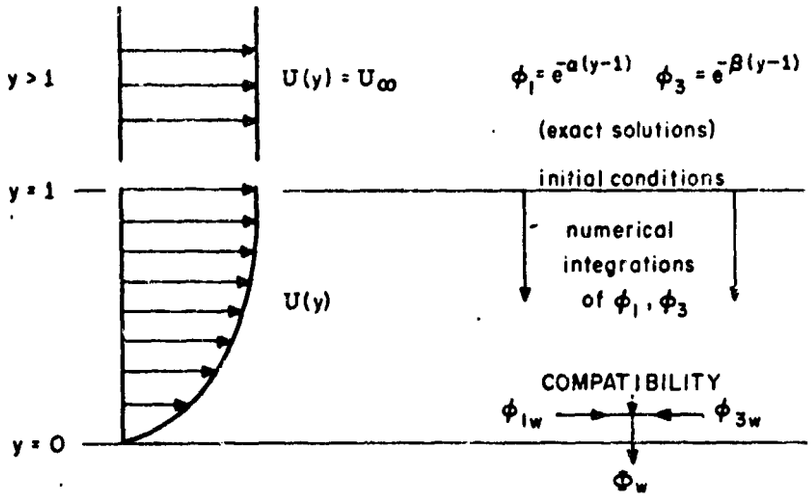

Fig.3 Numerical solution procedure

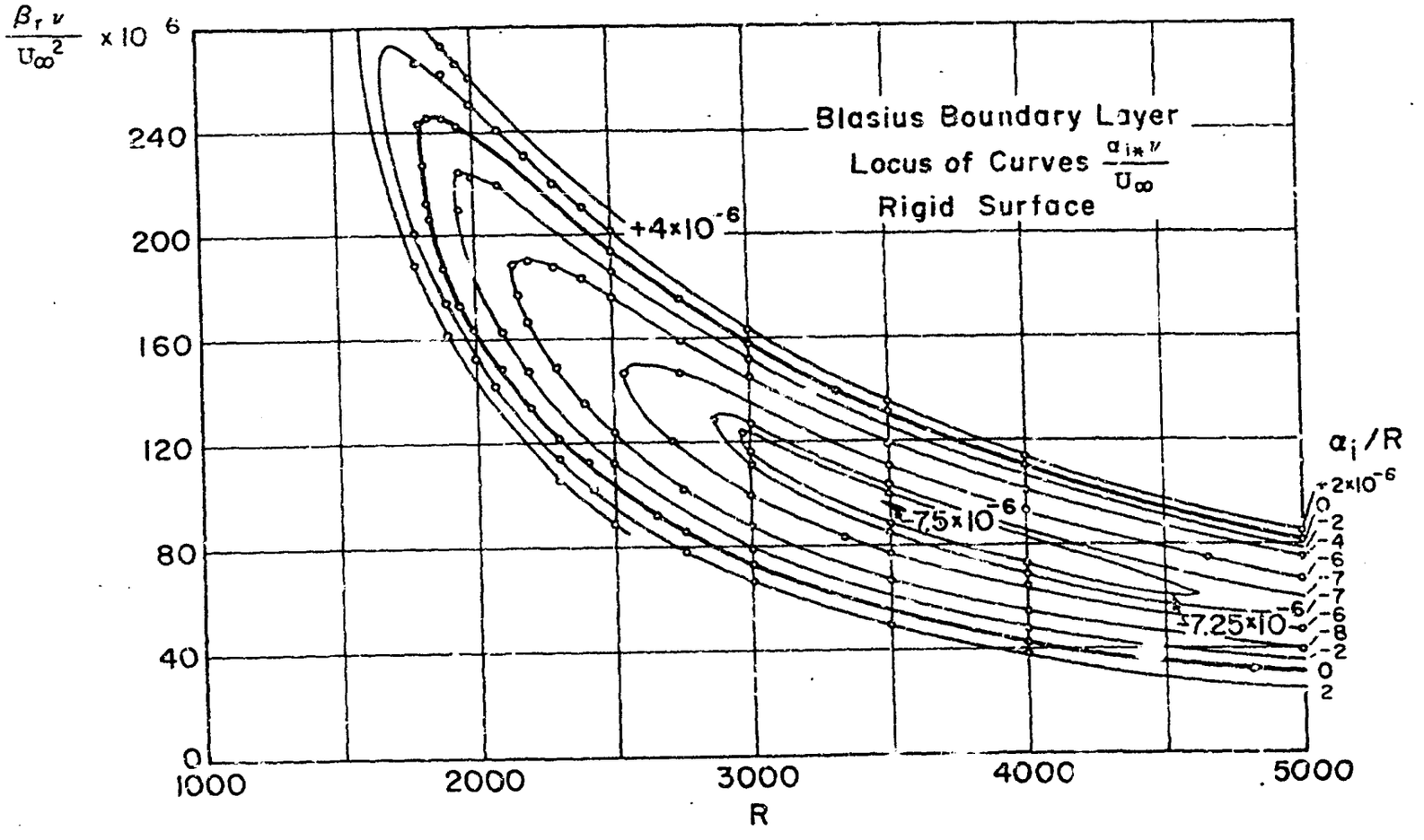

Fig. 4 Spatial amplification rates for the flat plate boundary layer over a rigid surface

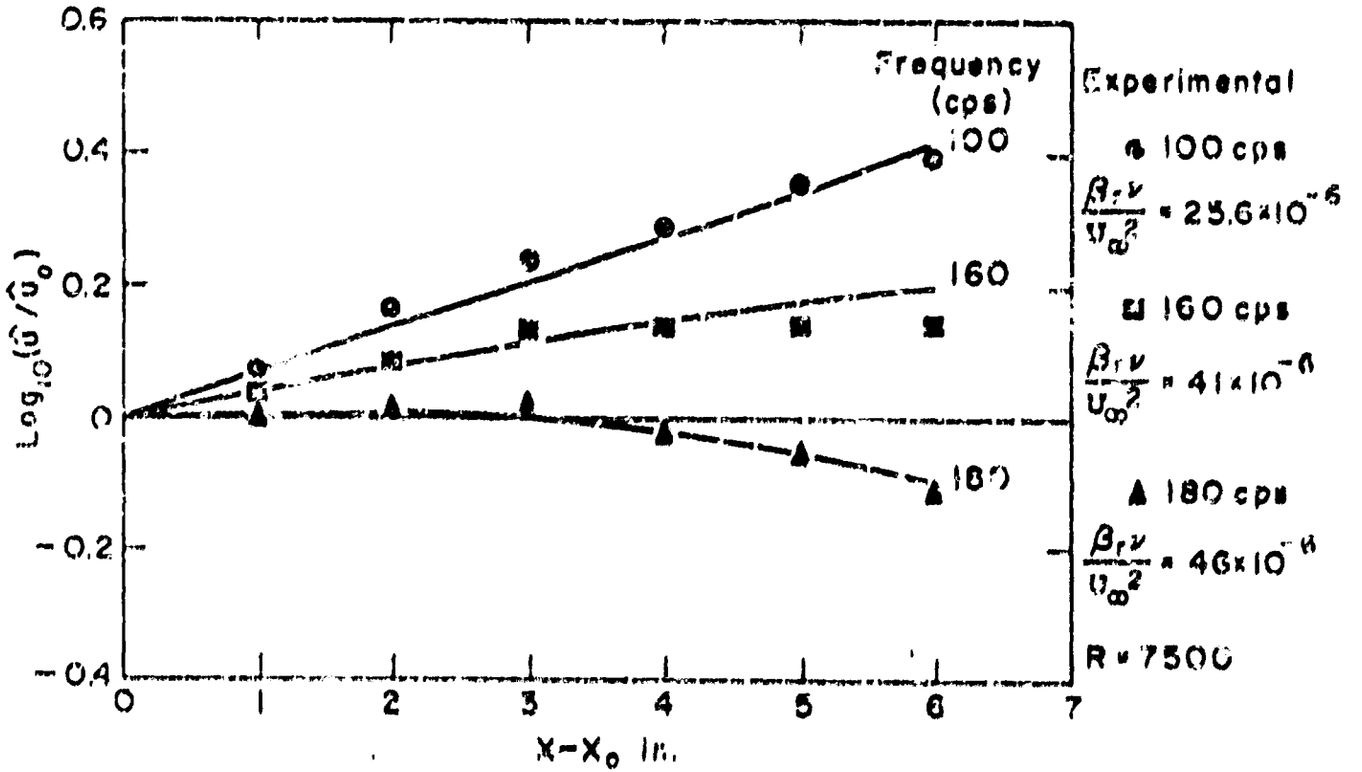

U_∞ = 64 ft/sec
Ribbon 4ft from leading edge of plate
x_o = 2 in. behind ribbon

Ref: Schubauer and Skramstad [1947]

Fig. 5 Comparison of calculated spatial amplification rates with experiments by Schubauer and Skramstad[14]

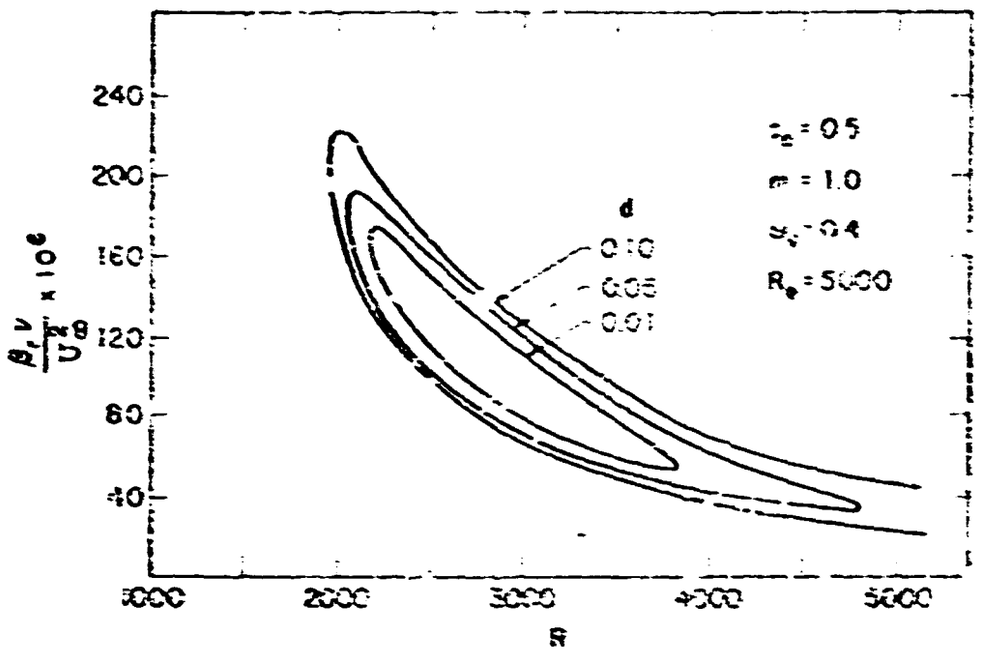

Fig.6 Effect of variation in damping on the stability boundary for the flat plate boundary layer over a membrane. Membrane properties: $m = 1.0$, $c_2 = 0.5$ and $c_1 = 0.4$ at $R_c = 5000$

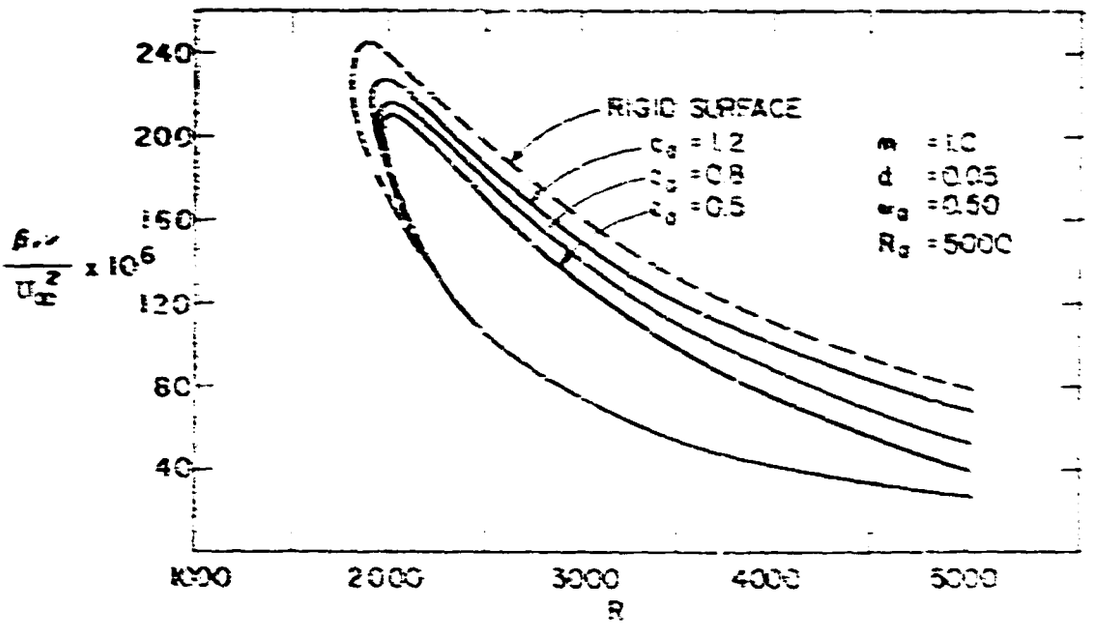

Fig.7 Effect of variation of c_2 on the stability of the flat plate boundary layer over a membrane. $m = 1.0$, $d = 0.05$ and $c_1 = 0.5$ at $R_c = 5000$

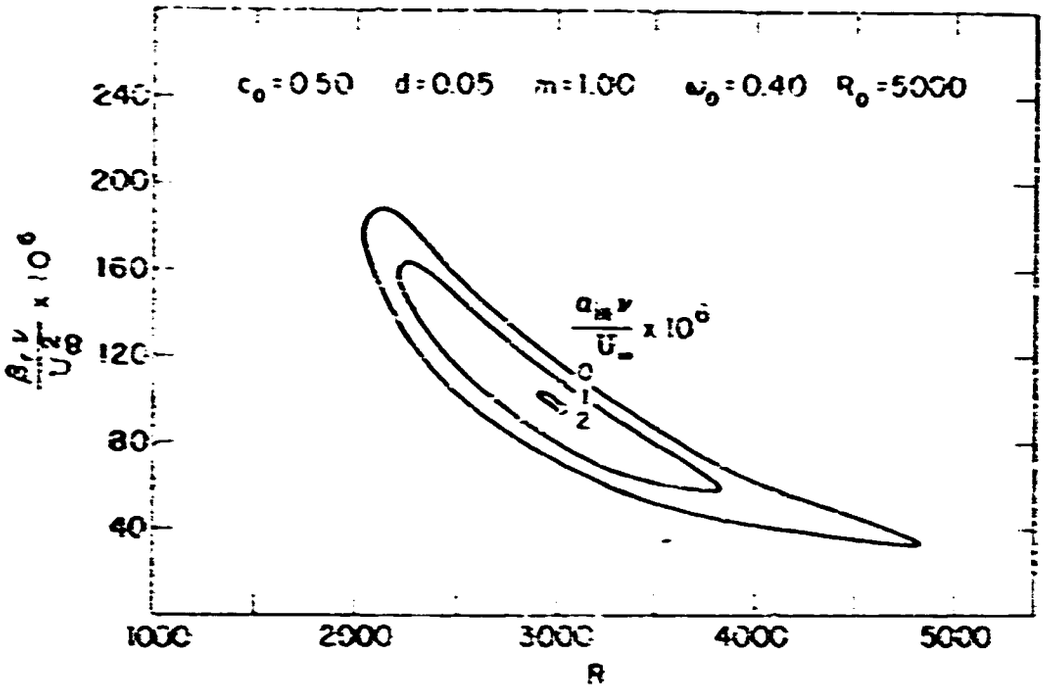

Fig.8 Spatial amplification rates for the boundary layer over a membrane. m = 1.4, c_2 = 0.5, d = 0.05 and ω_2 = 0.4 at R_2 = 5000

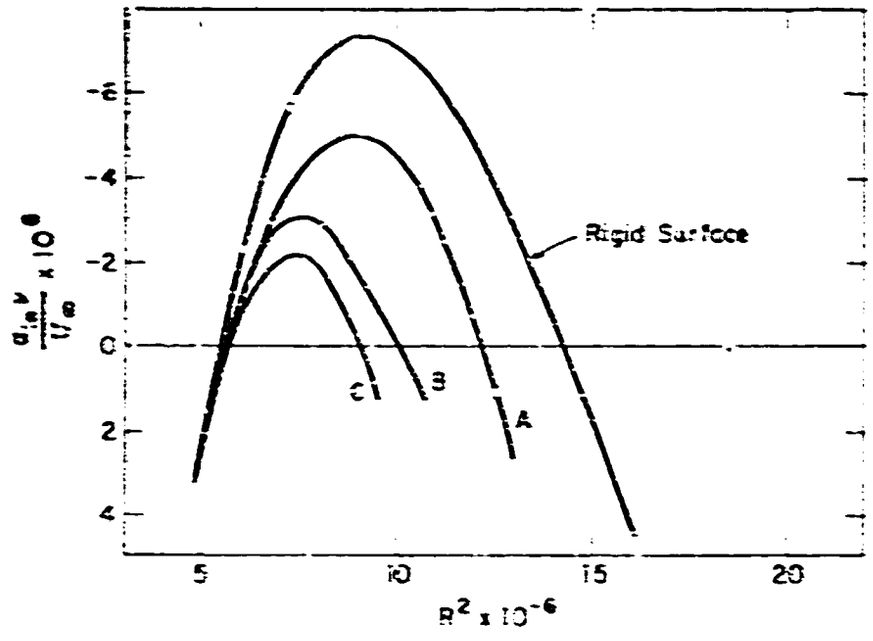

Fig.9 Spatial amplification rates at a given frequency for a boundary layer over three different membranes, all having m = 1.0 and d_2 = 0.05 referred to R_2 = 5000. For A: c_2 = 1.2, ω_2 = 0.5; For B: c_2 = 0.5, ω_2 = 0.5; For C: c_2 = 0.5, ω_2 = 0.4

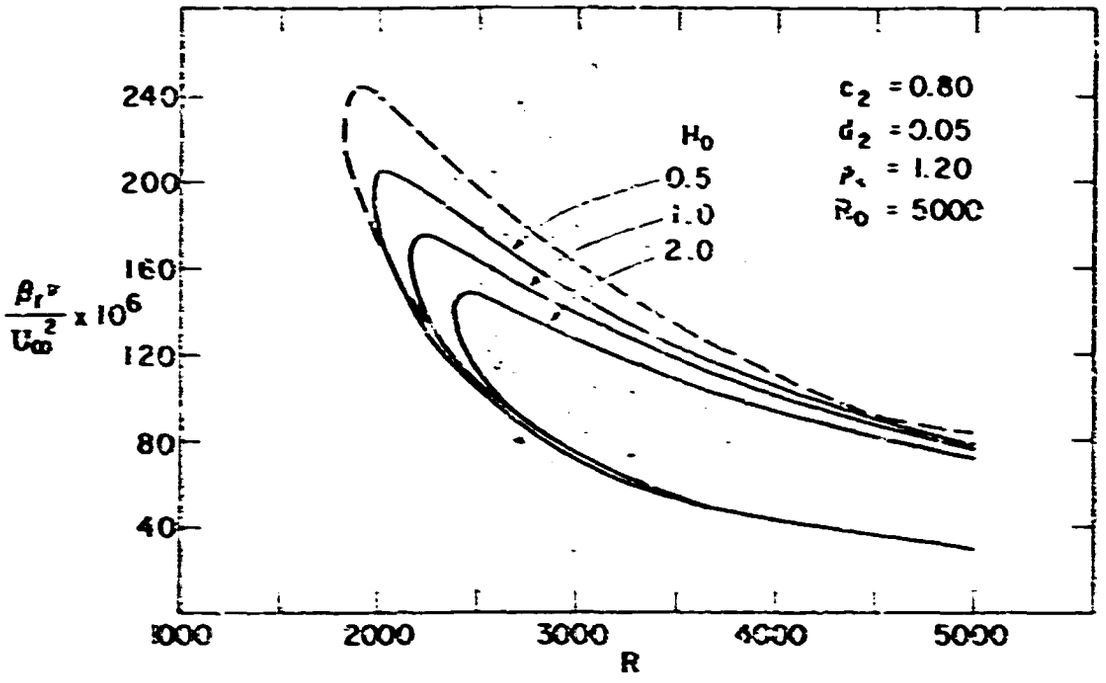

Fig.10 Influence of thickness H of a free-sliding viscoelastic boundary. c_2 = 3.00, d_2 = 0.05, ρ_s = 1.20 at R_1 = 5000

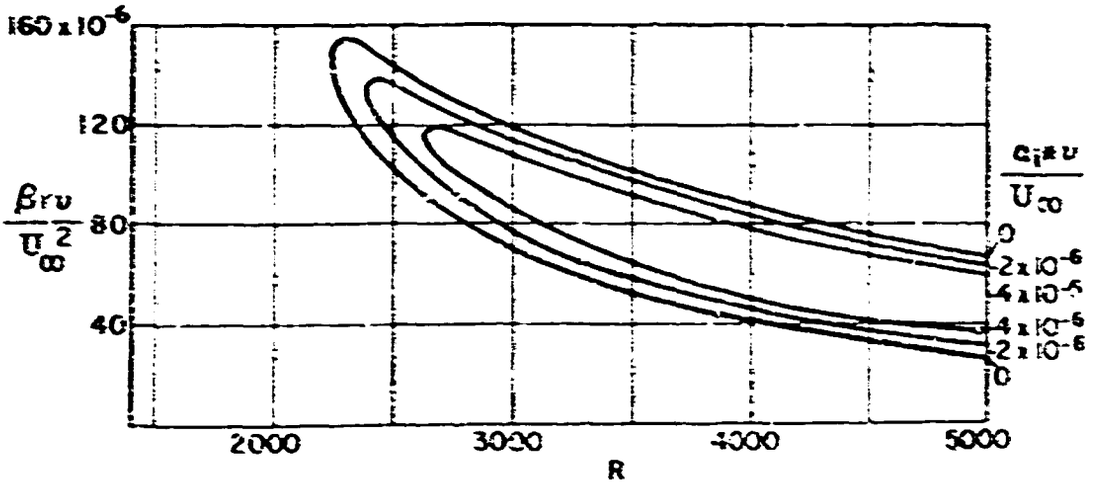

Fig.11 Spatial amplification rates for a viscoelastic layer with H = 2, c_2 = 0.75, ρ_s = 1.0 and d_2 = 0.05 at R_1 = 5000

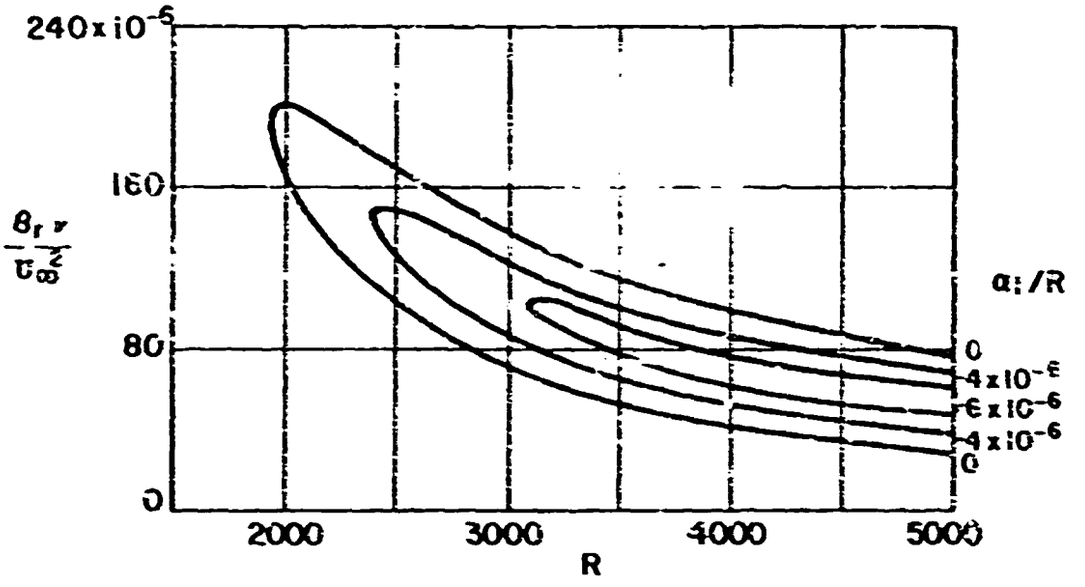

Fig. 12 Spatial amplification rates for a viscoelastic layer with $E = 1.0$, $c_2 = 0.8$, $c_s = 1.2$ and $d_2 = 0.05$ at $R_2 > 5000$

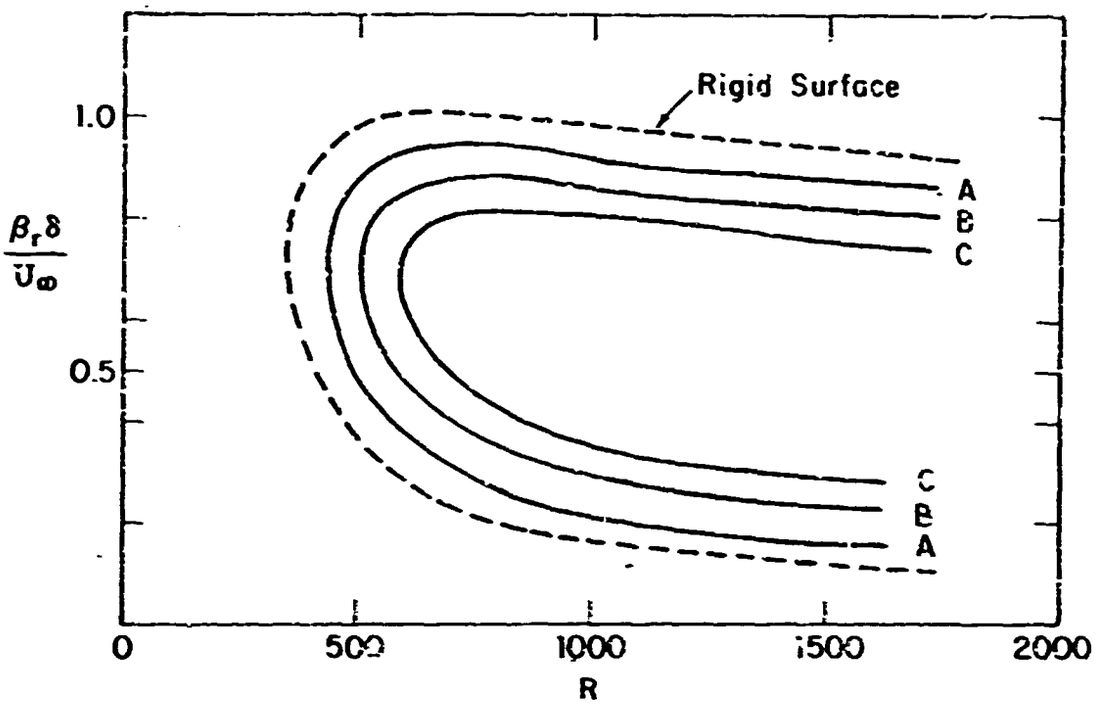

Fig. 13 Stability boundary for a Falkner-Skan similarity profile with $\bar{\beta} = -0.15$ for various membrane surfaces, all with $\alpha = 1.0$, $\omega_c = 0.19$, and d varying between -0.1 and +0.1. A: $c_s = 1.2$; B: $c_s = 1.0$; C: $c_s = 0.96$

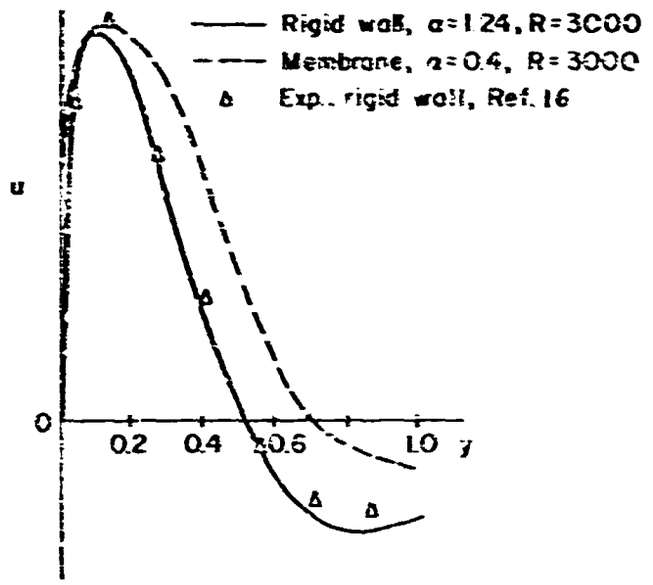

Fig. 14 Perturbation velocity distribution for a typical rigid-wall and a flexible-wall case. The membrane has $\alpha = 2.5$, $c_s = 0.9$, $d = 0.05$ and $\omega_c = 0.1$

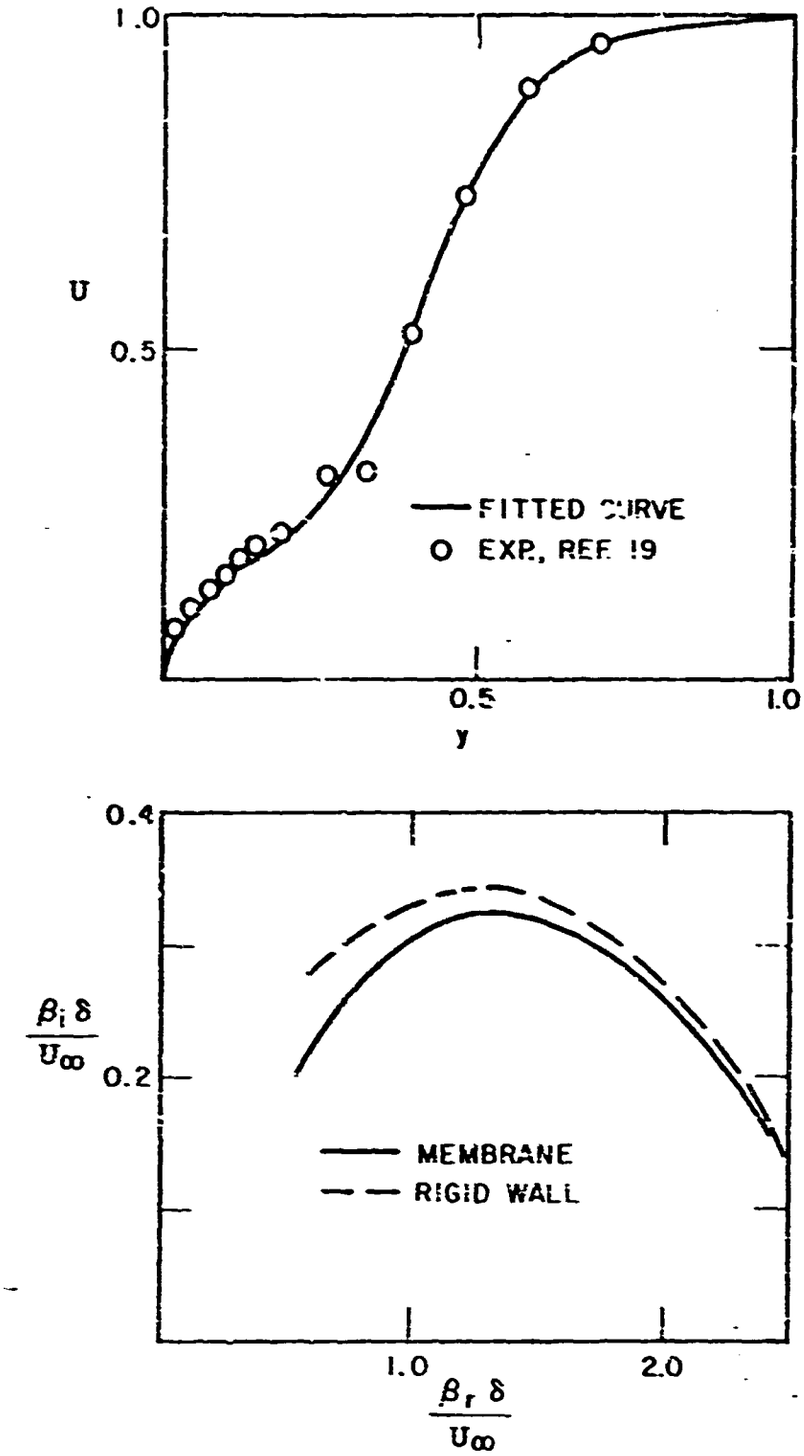

Fig.15 Temporal amplification rates for the secondary instability, both for a rigid and a flexible wall. The membrane chosen has $m = 1.0$, $d = 0.15$, $c_c = 0.5$ $\omega_0 = 0.4$

STREAMWISE VORTICES IN LAMINAR FLOW

by

Jean J. Ginoux

Brussels University and von Kármán Institute for Fluid Mechanics.
Rhode-Saint-Genèse,
Belgium

SUMMARY

It is now generally accepted that one stage of the laminar-turbulent transition process, which followed the region of growing Tollmien-Schlichting waves, is one of developing transverse variations in the boundary layer velocity and wave intensity.

These transverse variations are systematically observed by the author in reattaching supersonic and hypersonic flows, with a wave-length which was a function of the boundary layer thickness and of a characteristic length of the separated zone. They were also observed on supersonic swept back wings.

Refined measurements made at supersonic speeds with small pitot-static probes showed that these variations were caused by one or two rows of counter-rotating streamwise vortices located generally inside the reattaching boundary layers. Very local heat transfer measurements showed that large transverse variations of heat rates existed because of these vortices. Although the mean value of the Stanton number was very near the turbulent value, its local value could be much higher than the latter. This means that aerodynamic heating, in the transition region of a reattaching supersonic boundary layer, can become more severe than expected, even with a fully turbulent flow.

SOMMAIRE

Il est généralement admis à présent qu'un stade du processus de transition de l'état laminaire à l'état turbulent, qui suit celui de l'amplification des ondes de Tollmien-Schlichting, consiste dans le développement de variations transversales de la vitesse et de l'intensité des ondes dans la couche limite.

Ces variations transversales ont été systématiquement observées par l'auteur dans des écoulements super- et hypersoniques recollés; leur longueu. d'onde dépendant de l'épaisseur de la couche limite et d'une dimension caractéristique de la zone décollée. Elles ont également été observées sur des ailes en flèche à vitesse supersonique.

Des mesures très fines effectuées avec des sondes statiques et totales ont montré que ces variations résultaient de la présence d'une ou deux nappes de tourbillons longitudinaux alternés dans les couches limites. Des mesures très localisées ont prouvé l'existence de pointes de transfert de chaleur causées par ces tourbillons. Tandis que le nombre de Stanton moyen restait proche de la valeur turbulente, les valeurs locales de ce nombre étaient nettement plus élevées. Il en résulte que l'échauffement cinétique peut devenir dans la région de transition d'un écoulement supersonique recollé plus sévère que prévu même en supposant un écoulement turbulent établi.

CONTENTS

LIST OF FIGURES

NOTATION

x	streamwise coordinate defined in Figure 1
y	coordinate perpendicular to the surface of the model (see Fig. 1)
z	spanwise coordinate defined in Figure 1
l	position of the pieces of scotch tape (see Fig. 1)
q	heat flux per unit area and unit time
h	heat transfer coefficient
S_t	Stanton number
S_{t_m}	measured Stanton number
S_{t_c}	calculated Stanton number
T_w	wall temperature
T_{wa}	adiabatic wall temperature
t	time
A, B	constants
p_0	stagnation pressure
p_b	base pressure
p_∞	free stream static pressure

STREAMWISE VORTICES IN LAMINAR FLOW

Jean J. Ginoux

1. INTRODUCTION

Earlier investigations made by the author[1,2] have revealed the existence of strong, regular and repeatable three-dimensional perturbations in the boundary layer of two-dimensional laminar reattaching flows. These perturbations were present in various types of separated flows, such as flows over backward and forward facing steps, ramps and cavities, and also in shock wave boundary layer interactions and were observed over a range of Mach numbers from 1.5 to 7.0.

By the use of a sublimation technique, the phenomenon was detected qualitatively in the form of regular striation patterns at the surface of the models. It was also studied quantitatively by transverse, i.e. spanwise, surveys of the boundary layer with small total head probes which indicated rather regular variations of the pitot pressure. The amplitude of these variations was found to be a maximum in the region of transition from laminar to turbulent flow, near mid-height of the boundary layer. The pressure peaks corresponded to the streaks of the striation pattern where the sublimation rate was the largest. Their spacing or wave length was approximately constant for given test conditions and was found to be a function of the boundary layer thickness at separation and of the size of the region of separated flow. The intensity of the flow perturbations was roughly in proportion to the size of very small irregularities of manufacture of the leading edge of the models, although their spacing was not influenced by the size or distribution of these irregularities.

It was concluded from these earlier investigations, that the phenomenon was essentially one of instability in the two-dimensional flow, the main triggering action arising from small irregularities in the leading-edge. This three-dimensional configuration which appears in the process of transition from laminar to turbulent flow has been observed quite systematically at low speeds, in recent years, by other investigators[3-6]. It is generally believed that it involves the presence of counter-rotating streamwise vortices. However, as far as the author is aware, it has never been demonstrated experimentally at supersonic speeds.

The effect of streamwise vortices on flow properties, such as skin friction and heat transfer is not fully known. From the existence of large peaks in the spanwise pitot pressure distributions and the corresponding large sublimation rates of chemicals sprayed on the surface of the model, it is expected that large peaks in skin friction and heat transfer exist locally.

The purpose of the present investigation was first to determine, by refined surveys of reattaching supersonic flows behind backward facing steps, the nature of

the three dimensional configuration of the flow and second to verify, by direct measurement, that large peaks in heat transfer rates were present at flow reattachment.

The research was sponsored by the Air Force Office of Scientific Research, O.A.R., through the European Office, Aerospace Research, United States Air Force, under contracts NRS AF EOAR 63-45 and 64-7.

2. DESCRIPTION OF THE EQUIPMENT

2.1 Wind Tunnel

The experiments were conducted in the VKIFD 16 in x 16 in continuous supersonic wind tunnel S-1 at a Mach number of 2.21. The stagnation temperature was near the ambient temperature. The stagnation pressure was below atmospheric and could be varied from about 100 to 200 mm of mercury absolute, which pressures correspond to free stream Reynolds numbers of 0.5×10^6 and 10^6 respectively, based on a length of 1 ft.

The tunnel is equipped with a conventional optical system using parabolic mirrors and a spark light source.

2.2 Models

A symmetric wedge model with backward facing steps, 8 mm high, was used in this investigation. The model almost completely spanned the working chamber of the tunnel and was fixed to the lower wall of the test section from its rear by two straight supports. A portion of the model, indicated by (A) in Figure 1, was equipped for static pressure and heat transfer measurements. Schlieren photographs showed, as illustrated in Figure 13, that flow reattachment occurred just upstream of the "slider". This portion of the model could be moved along the spanwise direction (z-axis), in the manner of the sliding scale of a slide rule, with a view of measuring the spanwise distribution of static pressure and heat flux, by means of a discrete number of small pressure orifices and heat meters. The slider consisted of a block of insulating material surrounded by a metallic frame.

A few tests were also made by replacing the front part of the model by a flat plate aligned with the rear surface, as shown by the dotted lines in Figure 1.

2.3 Test Techniques

The flow was qualitatively observed at the surface of the models by the use of a sublimation technique. The indicator chosen was acenaphthene, which having a slow response, allowed for the relatively long starting and stopping times of the wind-tunnel. An indication of the surface flow pattern was obtained after one or two hours running time of the tunnel.

Detailed surveys were made with total-head and static probes having an external diameter of 0.8 mm (i.e. 0.03 in). The pitot probe was cylindrical with an internal diameter of 0.6 mm. The static probe was a cone cylinder having one single pressure

orifice, located on its starboard side, 12 diameters behind the nose. The probes were fixed to the surveying mechanism which permitted displacements parallel and perpendicular to the model surface at any streamwise location.

A transient calorimetric technique was used for heat transfer measurements in the reattachment region of the flow. The insulating material (bakelite) of the slider was grooved to hold three copper bars, or heat-meters, 0.5 mm wide, 0.5 mm thick, 30 mm long and 20 mm apart as shown in Figure 1. This particular configuration of the heat meters was suggested by the typical aspect of the striation pattern shown by the sublimation technique (an example being given in Fig.2) and also by the fact that the mean heat transfer rate was found to be approximately constant for $32 < x < 82$ mm in the course of preliminary measurements.

A steel wedge (140 mm span), containing an electric resistance acting as a heater, was mounted above the model, as indicated in Figure 1, and used to heat up the slider, while the tunnel was running, to a temperature of 100°C above its adiabatic value. The wedge could be removed suddenly by a pneumatic device, at such a speed that the time needed to complete the exposure of the copper bars to the airstream was about 50 milliseconds. A Fastax schlieren motion picture of the flow was taken while the heater was being removed and it did not show any unsteadiness as the flow was reattaching on the surface of the model.

The temperature of each of the individual copper bars were measured by means of copper constantan wires having a diameter of 0.1 mm, welded near the extremities of the bars. These temperatures were time recorded on a potentiometric recorder having a 20 in scale, a sensitivity of 1 mV full scale and a response time of 1 sec full scale. Occasionally, the temperatures were also measured using a galvanometric recorder which had a much smaller response time than the potentiometric one; the same results were obtained.

After each measurement, the slider was moved along the spanwise direction by steps of 0.5 mm (0.02 in). In this way, it was possible to get a spanwise distribution of the heat transfer rate, downstream of reattachment for $-35 < z < 35$ mm, where z is the spanwise coordinate defined in Figure 1. The heat flux per unit time through the unit area of the model surface is given by

$$q = ec\rho_m \frac{dT_w}{dt}$$

where e is the thickness of the heat meter, c and ρ_m the specific heat and density of copper, T_w the wall temperature given by the recorder and t the time. The derivative dT_w/dt was determined at time $t = 0$, where the temperature of the heat meter started to drop. The inaccuracy in the measurement of the slope dT_w/dt was responsible for a scatter of the final data of about 5%. The heat transfer coefficient (h) and the Stanton number (S_t) were then computed by

$$h = \frac{q}{T_w - T_{wa}} ; \qquad S_t = \frac{h}{\rho_\infty u_\infty c_p}$$

where the subscript ∞ refers to freestream conditions upstream of the model. T_w is the wall temperature measured at time $t = 0$ and T_{wa} the adiabatic wall

temperature. In a preliminary investigation, T_{wa} was measured on a "thin skin" slider made of araldite and instrumented with thermocouples. It was found that the amplitude of the spanwise variations of T_{wa} was less than 2°C and thus T_{wa} was later assumed to be constant.

3. ON THE EXISTENCE OF STREAMWISE VORTICES

In order to ease the experimental study, the amplitude of the flow perturbations was varied by the use of artifical irregularities at or behind the leading edge of the model. Strips of scotch (cellulose) tape ½ in wide, regularly spaced by ½ in were glued to the surface of the model, at various distances l (see Fig.1) from the leading edge.

As an example, results obtained for $l = 0$ are given below. A sublimation picture of the flow around the model, tested at a stagnation pressure of 100 mmHg absolute, is given in Figure 2(b) and compared with a sublimation picture obtained without the scotch tape (Fig.2(a)). In these figures, the sublimation rate is larger in dark regions than in light ones. It is seen that the strips of tape modified the striation pattern near reattachment (for $30 < x < 80$ mm; where x is defined in Fig.1), inasmuch as a pair of striations were formed by each piece of tape. Further downstream ($x > 100$ mm) the striations rearranged themselves so as to become similar to the pattern obtained in Figure 2(a).

Figure 3 shows the results of spanwise surveys made with the total head probe having its axis at $y = 0.4$ mm, i.e. very close to the wall, and for different distances x downstream of the step. The spanwise locations of the scotch tapes are indicated along the z-axis by shaded areas. It is seen that additional pressure peaks developed as the flow moved downstream, which corresponded to the increase of the number of striations shown in Figure 2(b).

Spanwise surveys made with the pitot probe, at $x = 150$ mm downstream of the step, are shown in Figure 4 for different distances y, in millimeters, of the probe-axis from the wall. These pressure variations are similar to those systematically observed in previous investigations made without tapes[2]. In particular, it is found that they have their maximum amplitude near mid-height of the boundary-layer.

Figure 5 gives the results of two streamwise surveys made with the total head probe for two different values of z, only 4 mm (i.e. 1/6 in) apart. At $z = 0$, the probe was located in between two of the striations formed by the leading edge irregularities; while for $z = -4$ mm, the probe was aligned with one of these striations. The figures indicated give the local boundary layer thickness determined from velocity profiles measured in the boundary layer with the same probe. These results show the drastic spanwise change of the flow properties at reattachment and in particular the spanwise waviness of the outer edge of the boundary layer.

By using the slider, equipped with pressure orifices, it was possible to detect for the first time spanwise variations of static pressure on the model surface in the reattachment zone. The results are given in Figure 6 which shows that large variations of static pressure exist near reattachment, ($x = 32$ mm) associated with each tape, and then become weaker but also more regular further downstream ($x = 82$

Typical results of spanwise surveys made in the boundary layer at $x = 150$ mm with the static probe are given in Figure 7, where the reading of the probe in mmHg absolute is plotted against the spanwise coordinate (z). The measurements were made at different distances (y) from the model surface. It is seen that the nearly periodic pressure variations are characterised by "phase shifts" at certain distances from the wall. Indeed, the pressure peaks observed at $y = 3.5$ mm correspond to pressure troughs at $y = 4.5$ mm and vice-versa. This would indicate, the static probe being sensitive to small cross flow, that a layer of streamwise vortices existed at $3.5 < y < 4.5$ mm. These vortices appeared to be counter-rotating as the mean static pressure was approximately the same at $y = 3.5$ and $y = 4.5$ mm. Knowing that the pressure orifice was on the starboard side of the probe, one could specify the sense of rotation as schematically shown in Figure 7. In the same figure, one can see another phase shift for $0.4 < y < 3.5$ mm, indicating possibly the existence of a second layer of vortices, closer to the wall. Unfortunately, it was not possible to compare the pressure distribution at $y = 0.4$ mm with the wall static pressure as the slider did not cover that region of the flow.

By grouping together some of the above results, one can imagine the idealized vortex distribution shown in Figure 8.

A similar investigation was carried out closer to the reattachment region, i.e. at $x = 52$ mm from the step. However, only one vortex layer was clearly observed as indicated in Figure 9, where the reading of the static probe, in millimeters of mercury, is plotted against the spanwise coordinate. (The drop in static pressure with increasing y, shown by Figures 6 and 9, was caused by the compression wave associated with flow reattachment.) This vortex layer was located in the region $3.5 < y < 4.5$ mm which is much closer to the outer edge of the boundary layer than further downstream (i.e. at $x = 150$ mm).

In some other cases, ($l \neq 0$), the vortices were observed slightly outside of the boundary layer near reattachment. A similar phenomenon was observed by the author on swept back supersonic wings. A sublimation picture of the corresponding flow is shown in Figure 10. In that case, the vortices were definitely detected outside of the boundary layer. However, it was not possible to determine exactly their sense of rotation and further work remains to be done in that particular case.

4. EFFECTS OF STREAMWISE VORTICES ON HEAT TRANSFER

Repeated measurements of the spanwise distribution of the heat transfer coefficients and Stanton number by the transient technique, with scotch tapes at the leading edge ($l = 0$), are given in Figure 11 for a stagnation pressure of 100 mmHg i.e. for a stream Reynolds number of 0.5×10^6 based on a length of one foot. The spanwise locations of the scotch tapes at the leading edge are indicated along the z-axis by shaded areas. The figures shows the existence of large peaks in the heat transfer rate whose locations correspond to those of the pressure peaks previously detected in the boundary layer by the total head probe (Fig. 4).

An attempt was made to compare quantitatively the spanwise distributions of pitot pressure and heat transfer. Because of its small size the probe, when kept in contact with the model surface, was located in the linear region of the boundary

given versus the pressure (p_b) measured at the base of the backward facing step. The base pressure is normalized by the free stream static pressure. Different triggering mechanisms were used to move the transition region from downstream of reattachment to upstream of separation and the base pressure was used here as the parameter indicating the position of transition. Average values of S_t are indicated by large dots in the figure. They are defined by

$$\bar{S}_t = \frac{1}{z_2 - z_1} \int_{z_1}^{z_2} S_t(z)\, dz$$

where $(z_2 - z_1)$ is the portion of the span where $S_t(z)$ was measured. $\bar{S}_t$ is the quantity that would be measured by heat meters much wider than the ones used here. It is seen from Figure 14, that $\bar{S}_t$ increased gradually when reattachment changed from laminar to turbulent. (i.e. when the base pressure decreased), then decreased when the turbulent boundary layer thickened. It is also seen that in the case of laminar reattachment, local S_t-peaks were much larger than in the turbulent case.

It is not surprising therefore that Miller et alii[9] observed regular striation patterns scorched into the stainless steel surface of their flap models during Hotshot wind tunnel tests at high Mach numbers.

5. CONCLUSIONS

The present investigation showed that the three-dimensional perturbations that were previously detected in many types of reattaching supersonic flows consisted of one or two rows of counter-rotating streamwise vortices generally located in the boundary layer.

Very local heat transfer measurements showed that the effect of these vortices was to produce locally very large peaks in the heat rate, much larger than the usually measured turbulent values immediately after transition. It was also found that the flat plate Reynolds analogy was quantitatively correct with streamwise vortices present in the flow.

REFERENCES

1. Ginoux, J.J. — *The Existence of Three-dimensional Perturbations in the Reattachment of a Two-dimensional Supersonic Boundary Layer after Separation.* AGARD Report 272, April 1960.

2. Ginoux, J.J. — *Leading Edge Effect on Separated Supersonic Flows.* Proceedings of ICAS III, Stockholm, August 19[illegible].

3. Klebanoff, Tidstrom — *Evolution of Amplified Waves Leading to Transition in a Boundary Layer with Zero Pressure Gradient.* NASA TN D-195, 1959.

4. Nani, I. — *Some Aspects of Boundary Layer Transition at Subsonic Speeds.* Advances in Aeronautical Sciences, Vol.3, 1962 (ICAS II).

5. Wallis, R.A. — *Boundary Layer Transition at the Leading Edge of Thin Wings and its Effect on General Nose Separation.* Advances in Aeronautical Sciences, Vol.3, 1962 (ICAS II).

6. Rumstadler, P.W. et alii — *An Experimental Investigation of the Flow Structure of the Turbulent Boundary Layer.* Stanford University Report MD-8, June 1963.

7. McCroskey, W.J. — *Effect of a Stepwise Distribution of Heat Transfer on the Supersonic Flow Over a Flat Plate.* VKIFD TN 13, June 1963.

8. Chapman, D. Rubesin, M. — *Temperature and Velocity Profiles in the Compressible Laminar Boundary Layer with Arbitrary Distribution of Surface Temperature.* J.A.S., Vol.16, 1949.

9. Miller, D.S. et alii — *Mach 8 to 22 Studies of Flow Separations due to Deflected Control Surfaces.* AIAA Journal, Vol.2, No.2, February 1964.

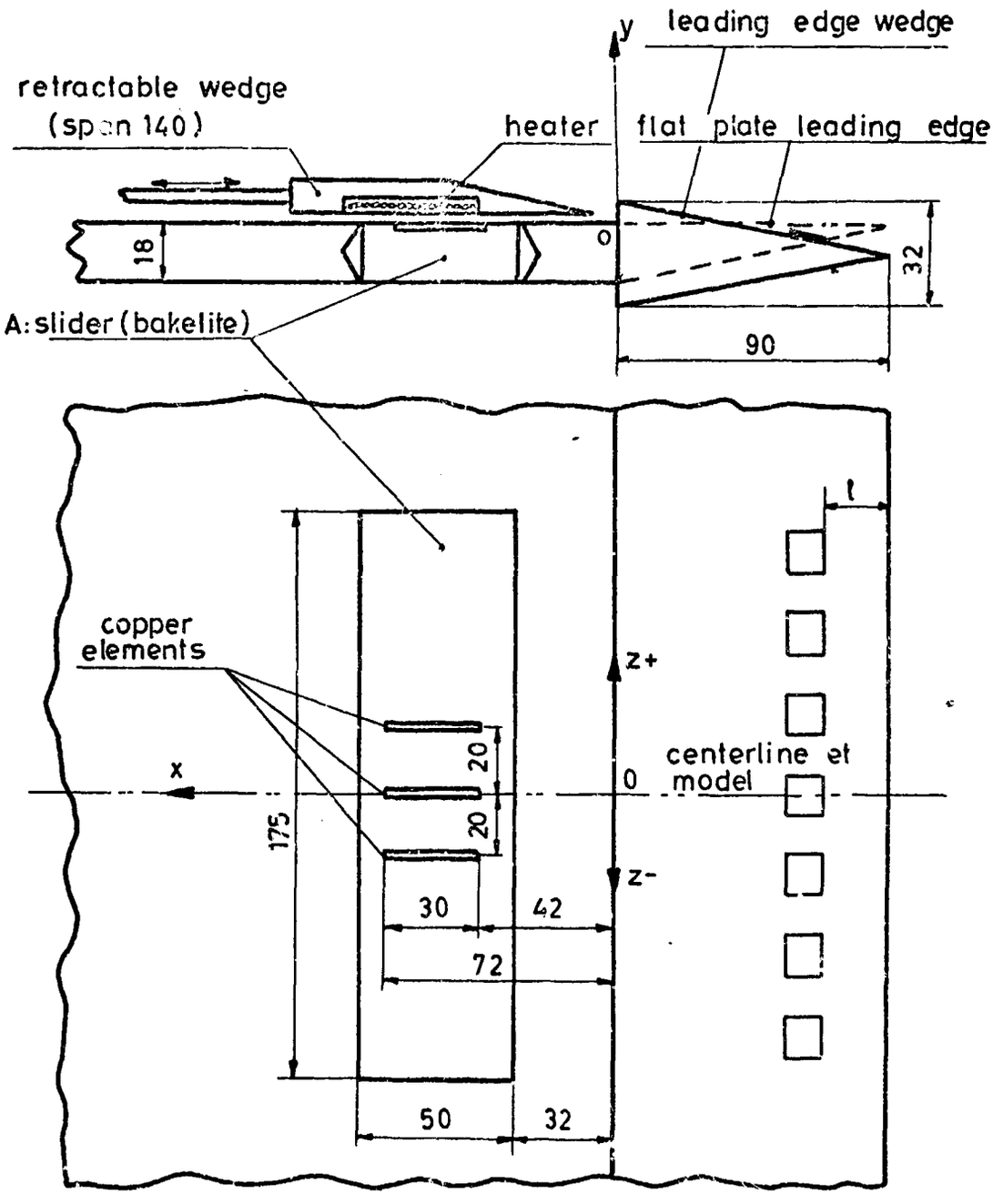

Fig. 1 Model configuration

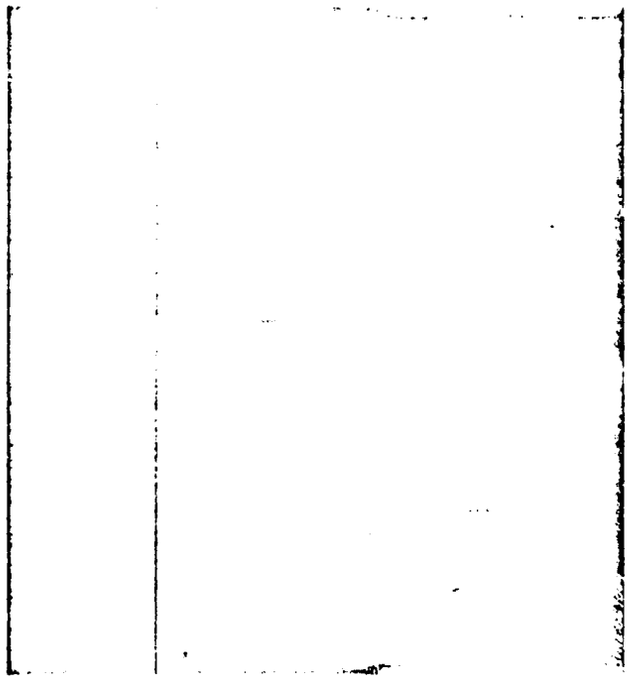

(a) Without the scotch tape

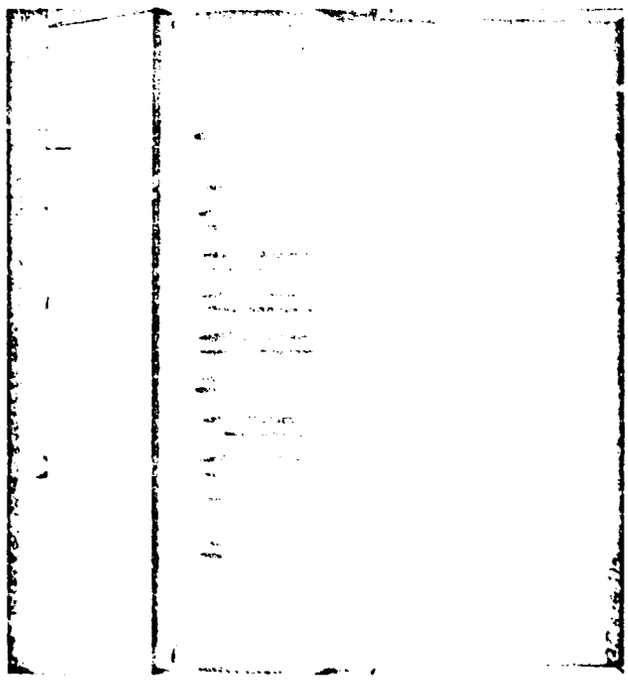

(b) With pieces of scotch tape

Fig. 2 Sublimation pictures with and without pieces of scotch tape at the leading edge

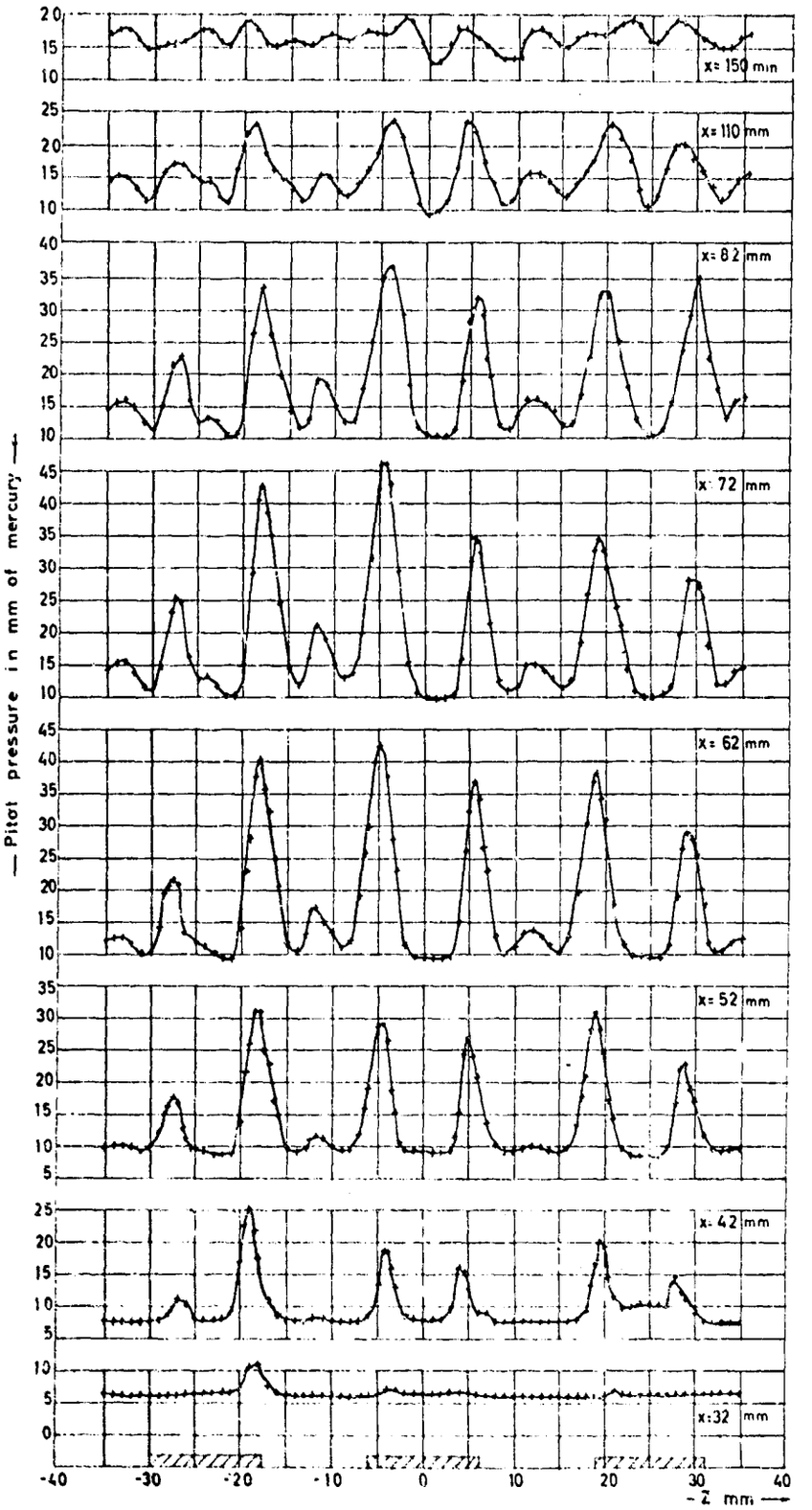

Fig. 3 Spanwise surveys with pitot probe at different x for y = 0.4 mm

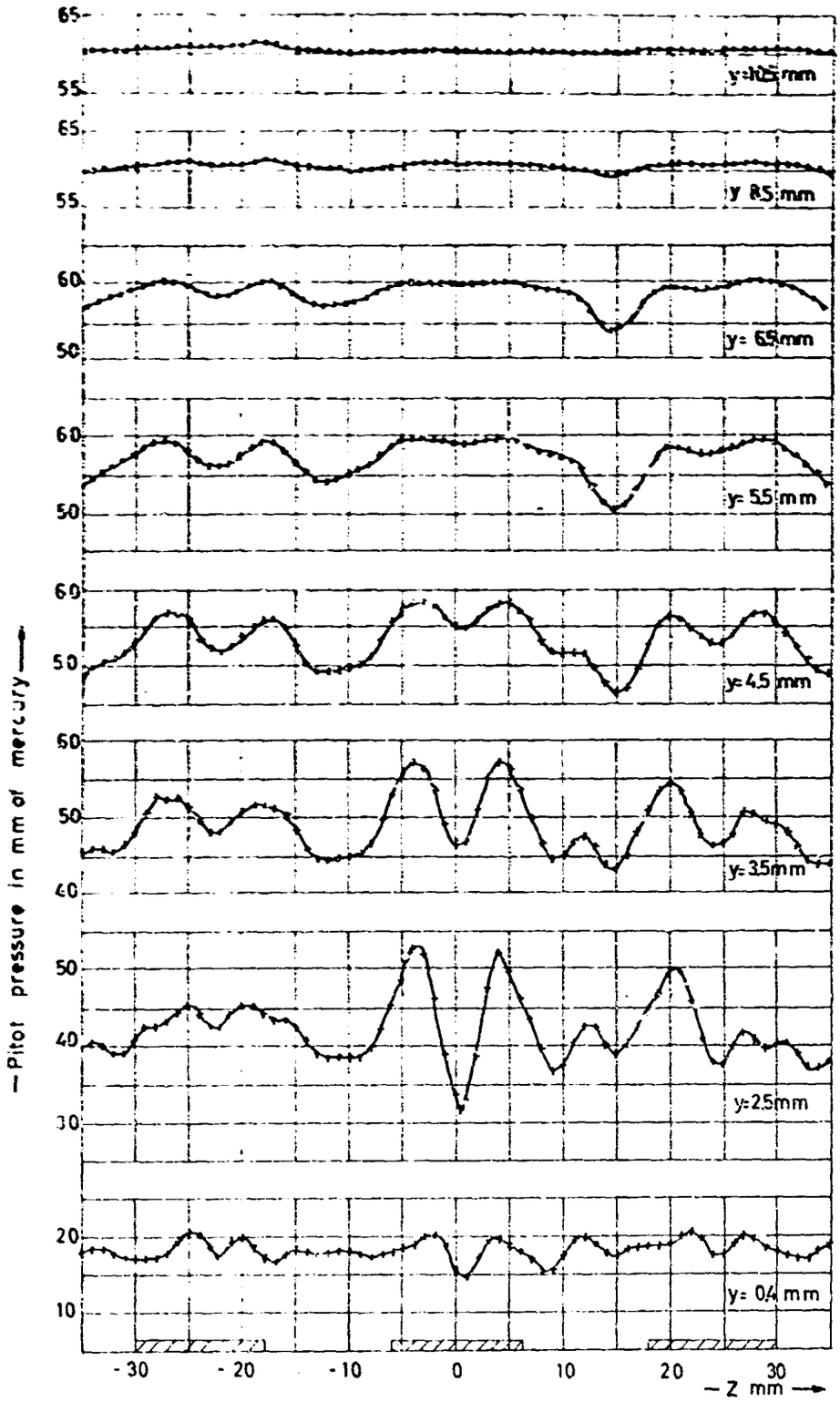

Fig. 4 Spanwise surveys with pitot probe at x = 150 mm for p_0 = 100 mm Hg

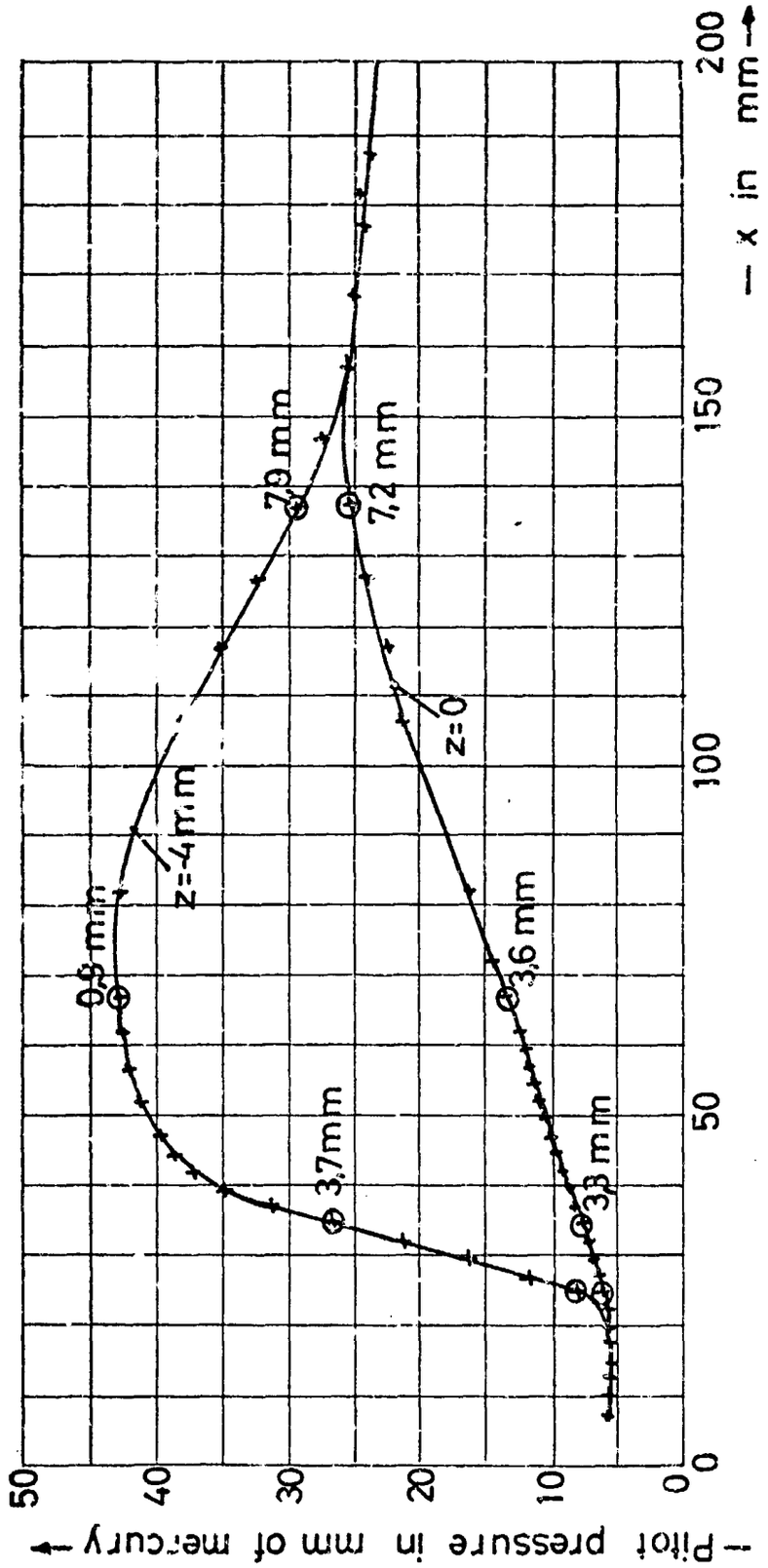

Fig.5 Streamwise variations of pitot pressure (y = 0.4 mm, stagnation pressure = 100 mm Hg)

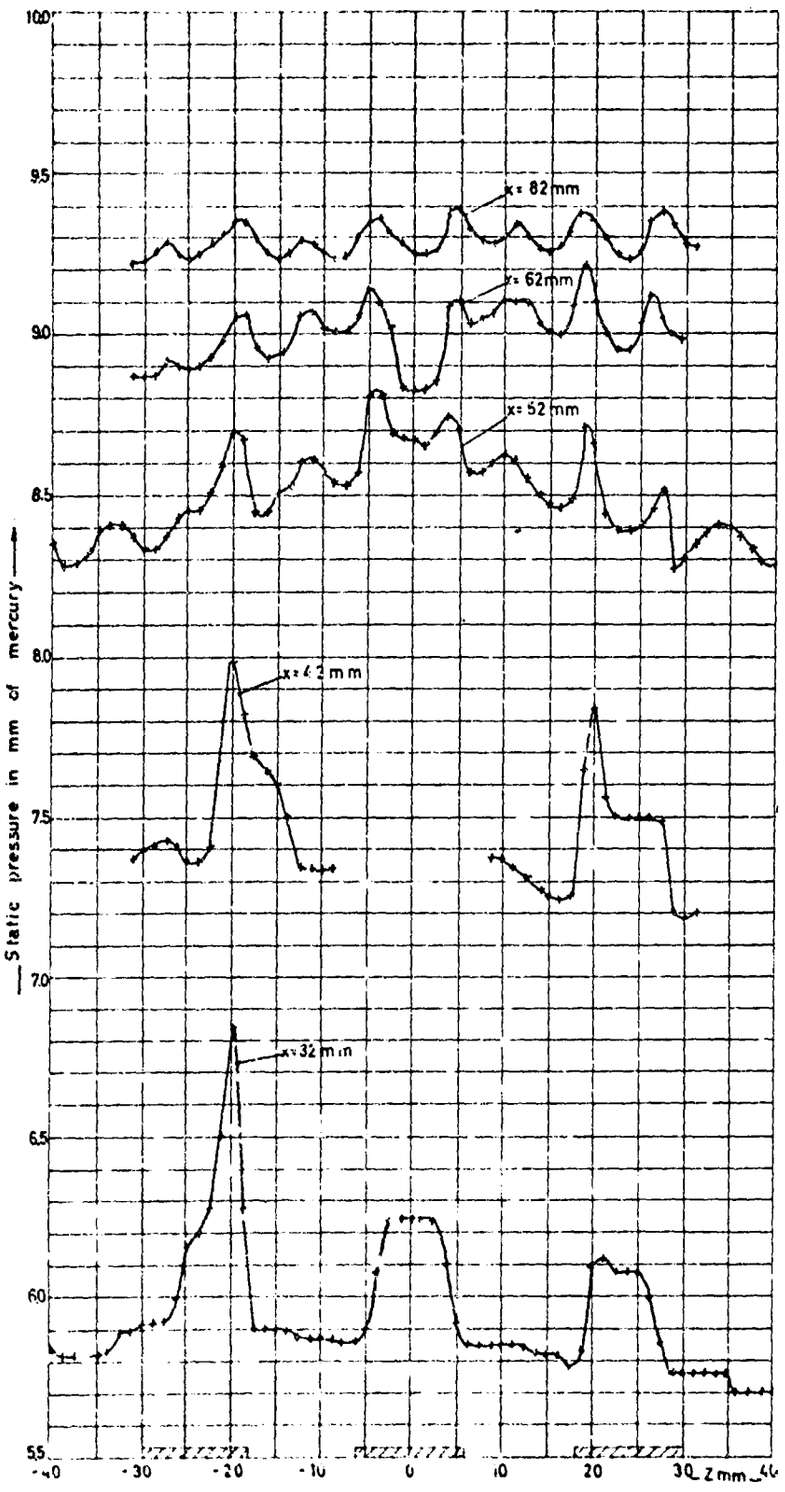

Fig.6 Static pressure measured at the surface of the model (y = 0)

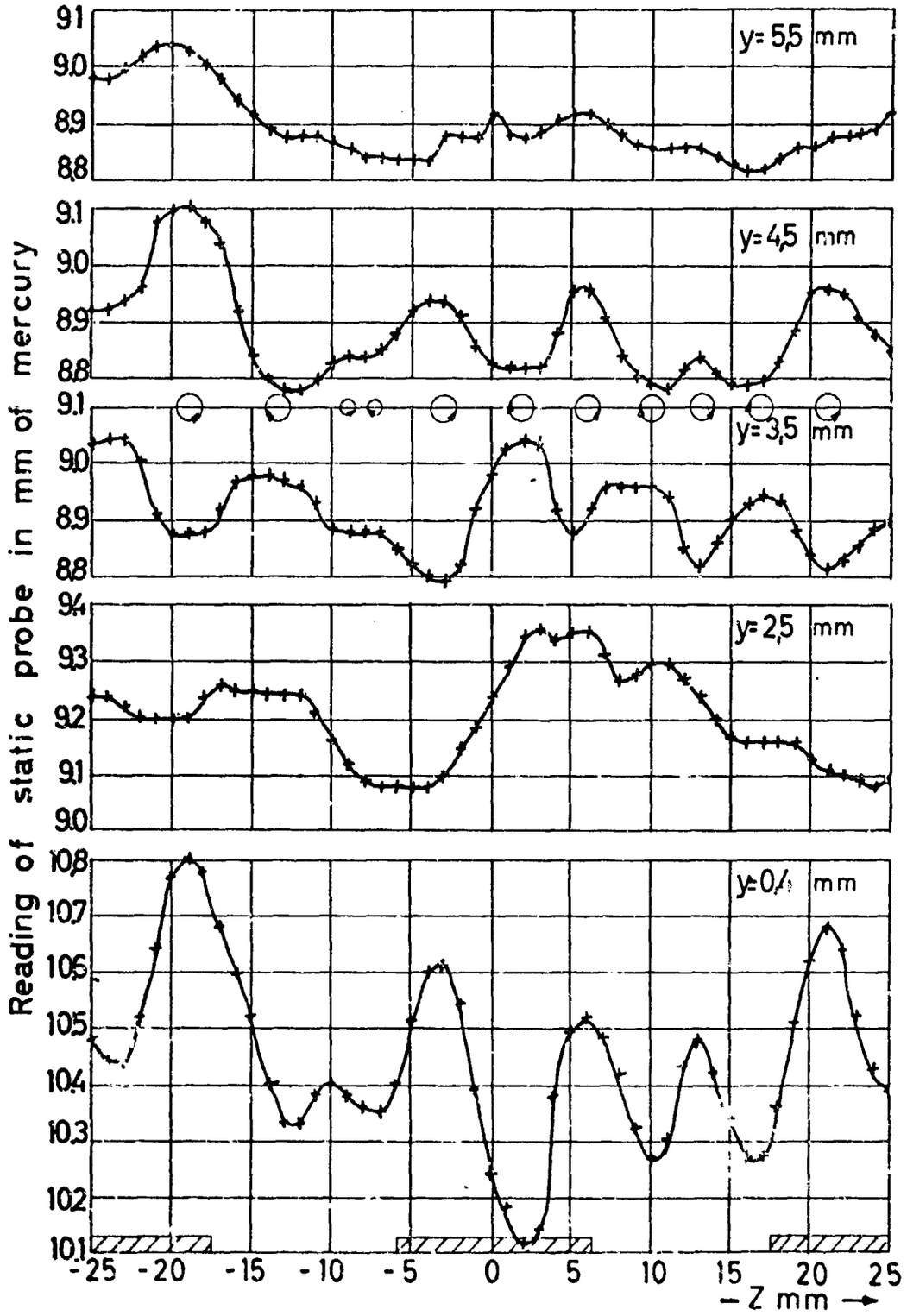

Fig. 7 Spanwise surveys with static probe (x = 150 mm, stagnation pressure 100 mm Hg)

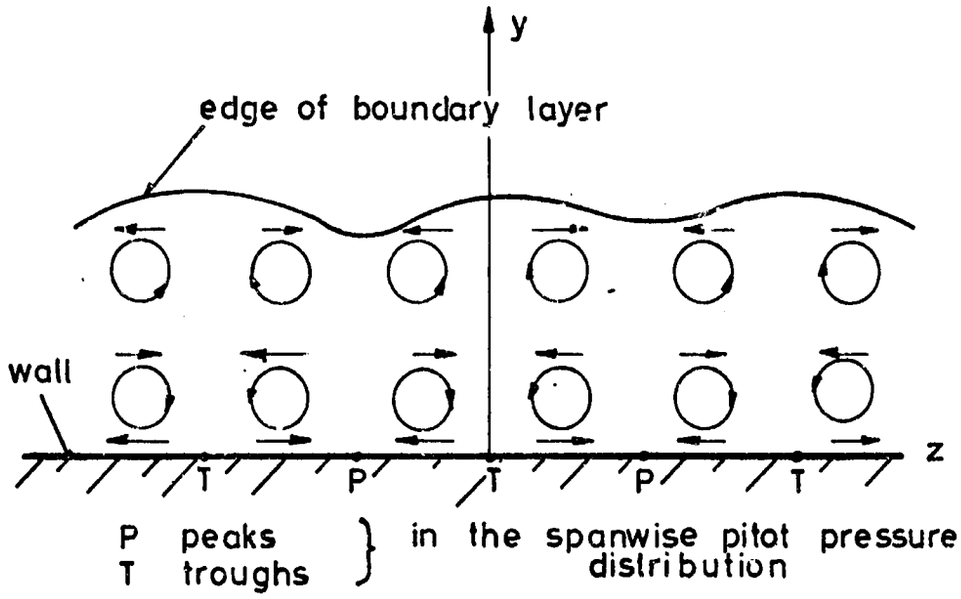

Fig. 8 Vortex distribution in the boundary layer

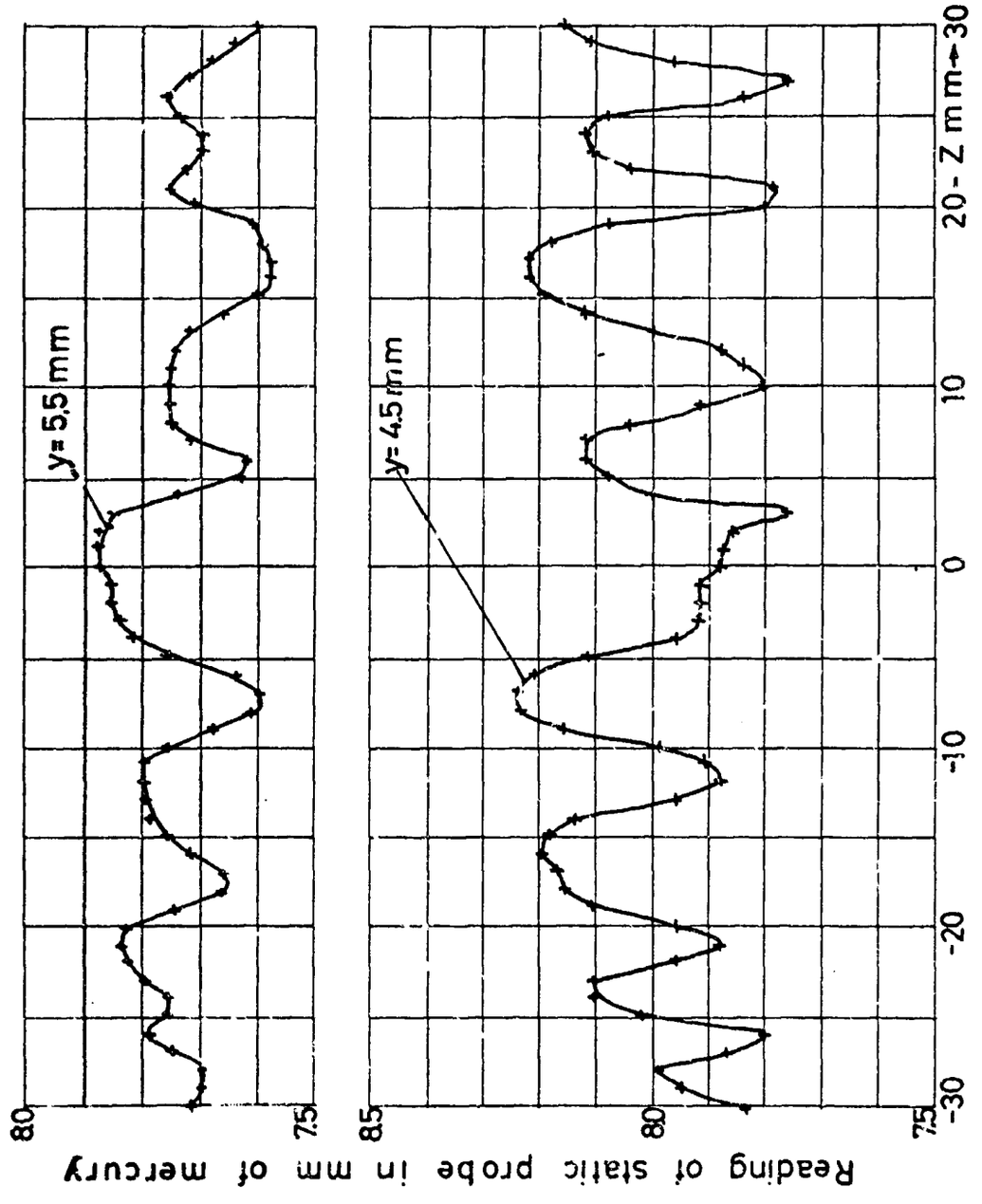

Fig. 9 Spanwise surveys with static probe (x = 52 mm)

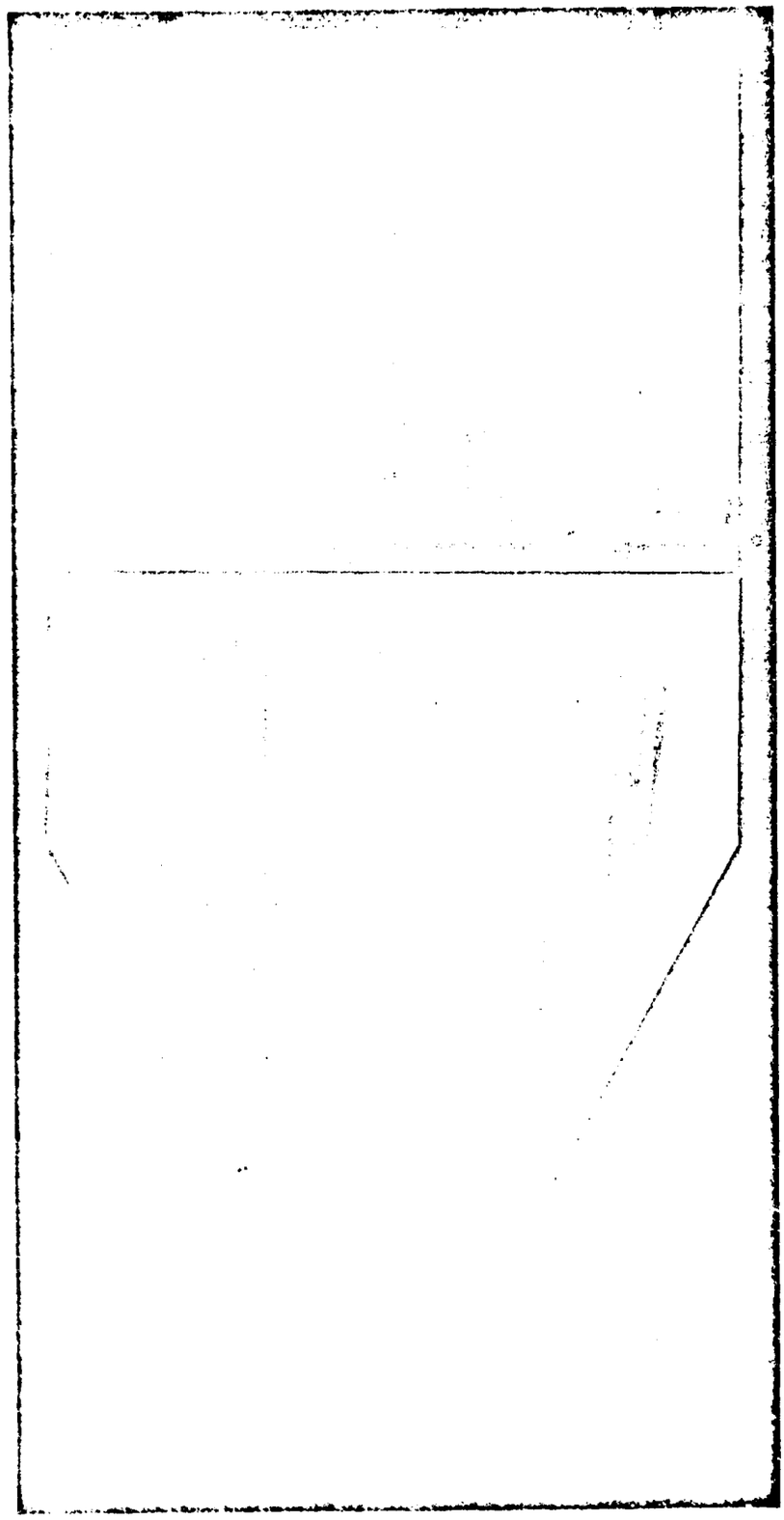

Fig.10 Sublimation picture on swept back wing

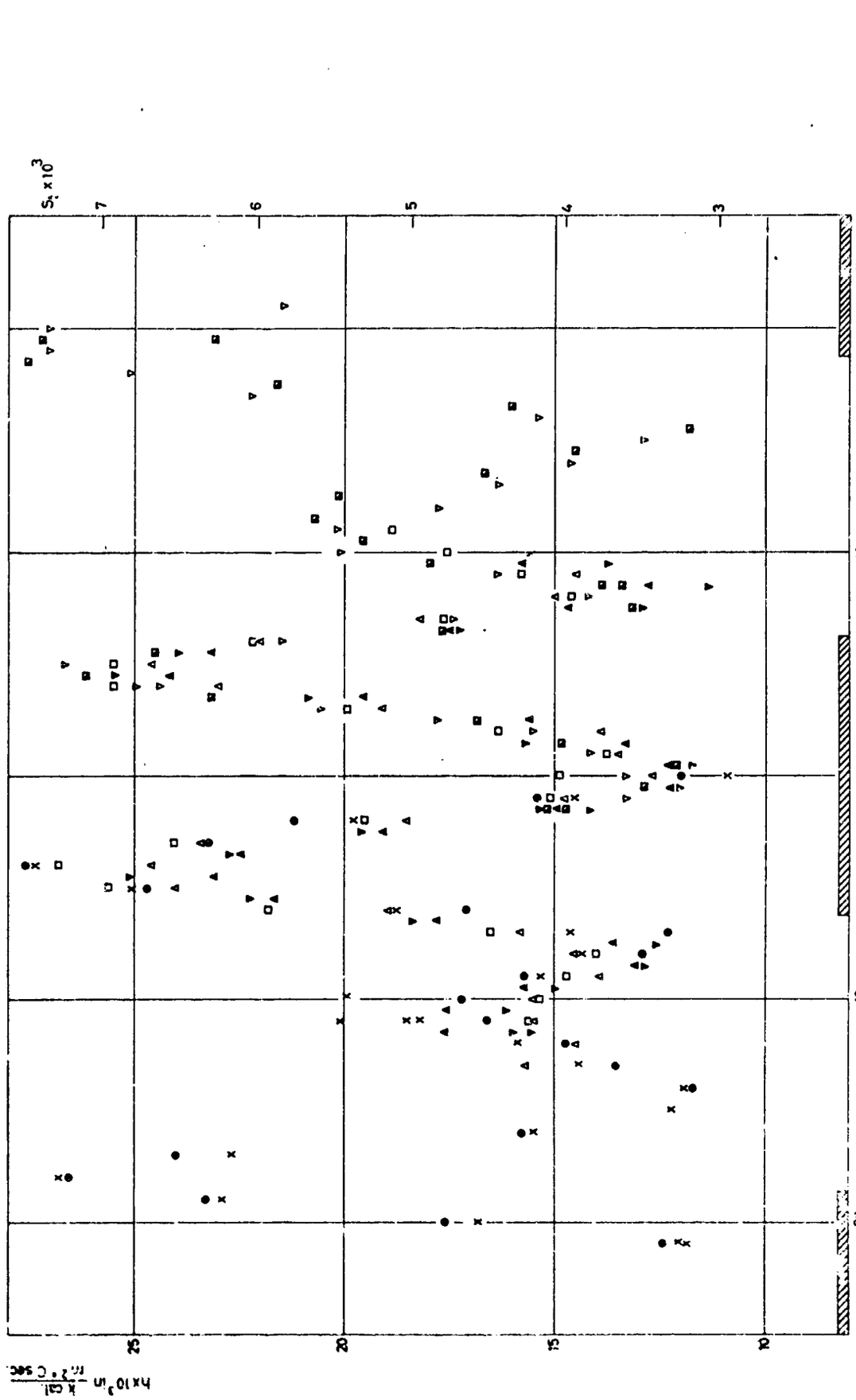

Fig.11 Spanwise distribution of heat transfer with transient technique

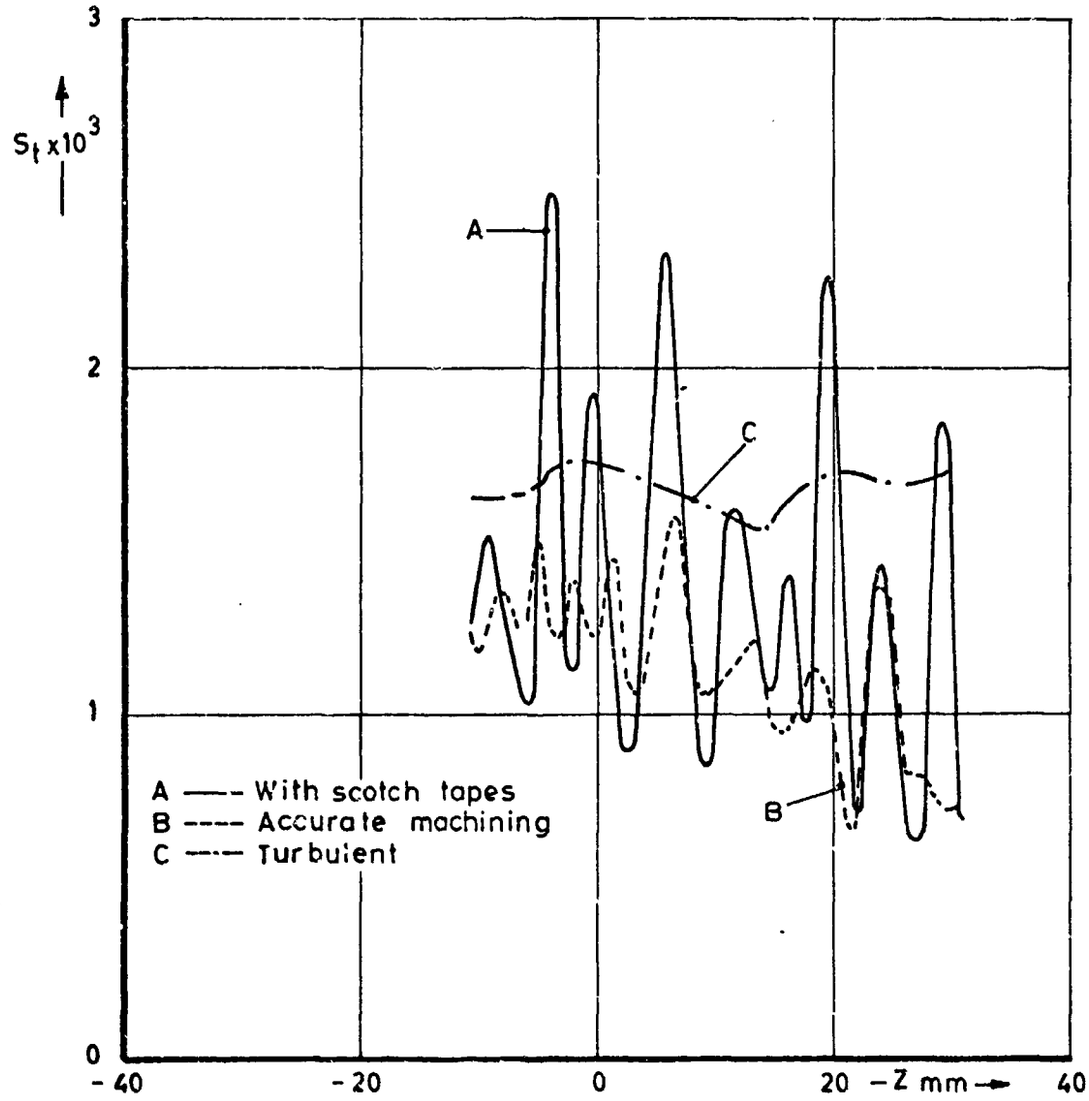

Fig. 12 Comparison between spanwise distributions of S_t

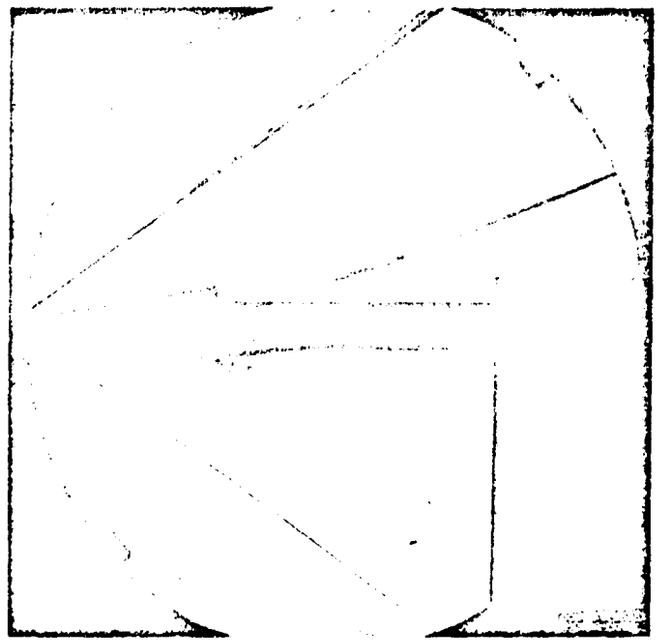

(a) Laminar reattachment

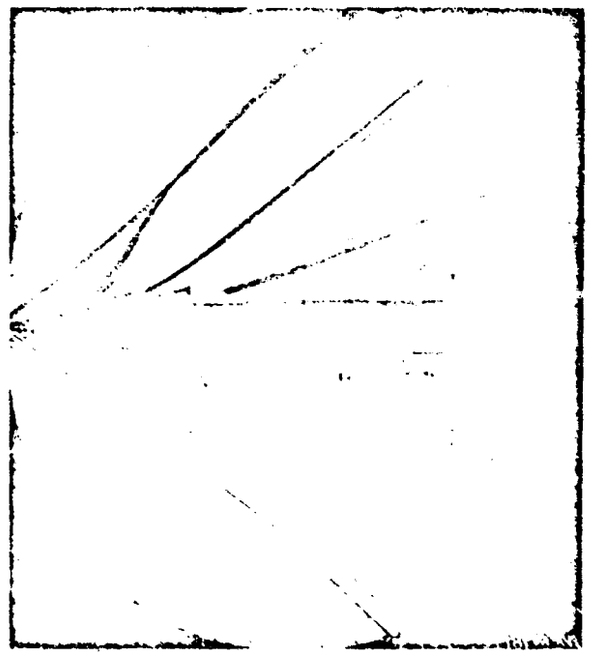

(b) Turbulent reattachment

Fig. 13 Schlieren pictures of the flow for laminar and turbulent reattachments

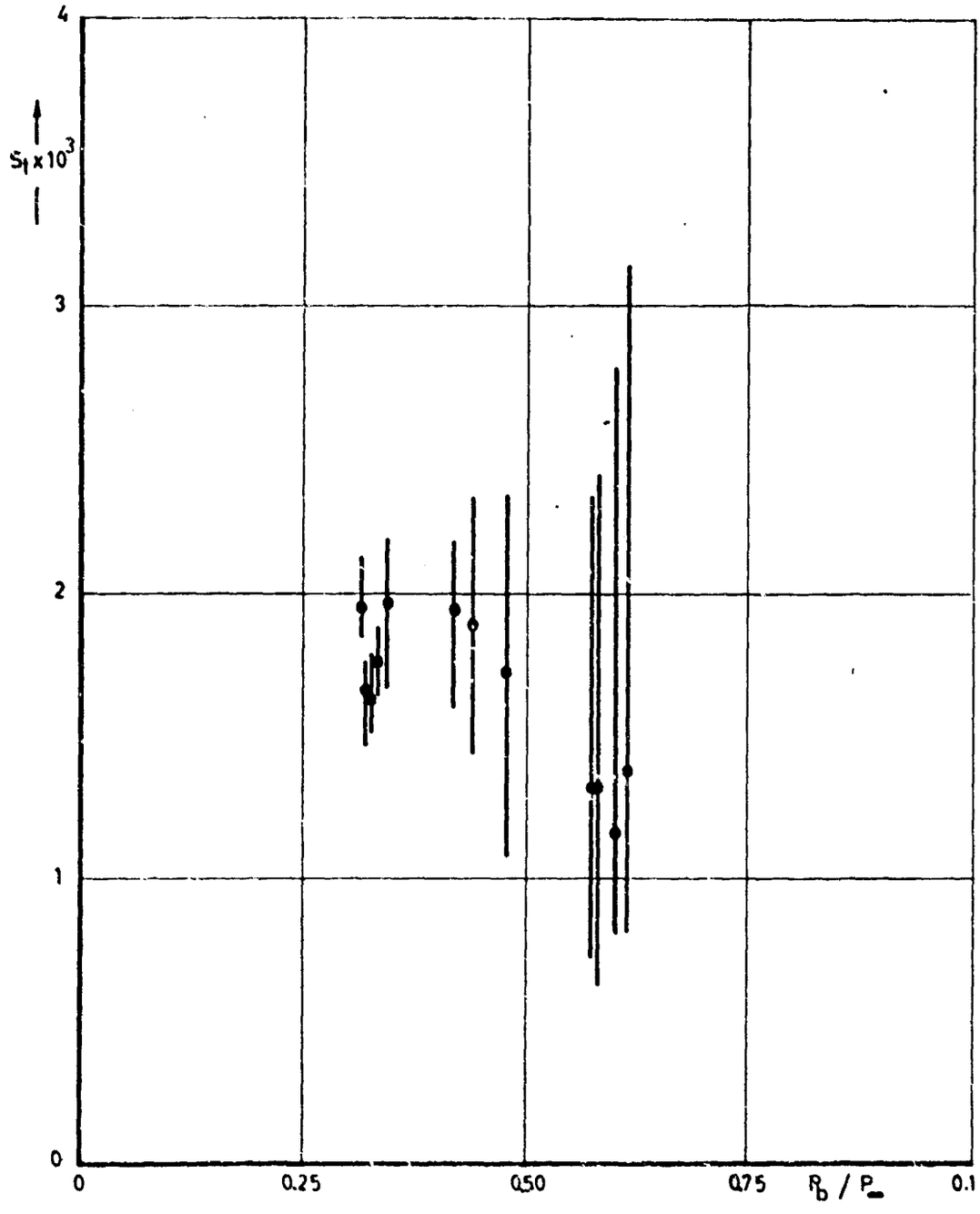

Fig. 14 Influence of the location of transition on heat transfer

HEAT TRANSFER IN LAMINAR BOUNDARY LAYERS WITH OSCILLATING OUTER FLOW

by

K. Gersten

Deutsche Forschungsanstalt,
für Luft- und Raumfahrt,
33 Braunschweig Bienroder Weg, 3,
West Germany.

SUMMARY

Presented is a detailed analysis of a class of laminar two-dimensional time-dependent velocity and thermal boundary layers whose free-stream velocity is given by

$$U(x,t) = cx^m(1 + \epsilon \cos \omega t) ,$$

where ϵ is a small disturbance parameter. The solutions were expanded into power series of the disturbance parameter. The equations for the first and second-order terms have been solved for small values of the frequency ω as well as for large frequency values. These two solutions for low and high frequencies can be matched at intermediate frequencies. The solutions show that the velocity and temperature in the different layers of the boundary layer acquire oscillations which experience phase shifts with respect to the forcing disturbance and to each other. Due to the non-linear terms in the flow equations the fundamental oscillation induces higher harmonics in the boundary layer oscillation and a steady-state part, which is responsible for the alteration of the mean values of skin-friction and heat transfer coefficient by the outer flow oscillation. In the analysis the limiting cases for very low frequency (quasi-steady solution) and very high frequency (solutions after M.J. Lighthill and C.C. Lin respectively) are also included. Numerical results for the flow along a flat plate and for stagnation point flow are given.

SOMMAIRE

On présente une analyse détaillée d'une catégorie de temps laminaire à deux dimensions-vitesse dépendente et couches limites thermiques dont la vitesse de courant libre est donnée par l'expression:

$$U(x,t) = cx^m(1 + \epsilon \cos \omega t) ,$$

dans laquelle ϵ est un paramètre de faible perturbation. Les solutions ont été élargies à des séries de puissances du paramètre de perturbation. Les équations des termes du premier et du second ordre ont été résolues pour de faibles et de fortes valeurs de la fréquence ω. Ces deux solutions pour les basses et hautes fréquences peuvent peut être se correspondre pour les fréquences intermédiaires. Les solutions montrent que la vitesse et la température aux différents niveaux de la couche limite acquièrent des oscillations qui traversent des alternances de phase par rapport à la perturbation contraignante et les unes par rapport aux autres. A cause des termes non linéaires des équations d'écculement, l'oscillation fondamentale produit des harmoniques plus élevées dans l'oscillation de la couche limite ainsi qu'une partie en régime établi, à laquelle est due la modification des valeurs moyennes des coefficients de frottement de surface et de transfert de chaleur par suite de l'oscillation de l'écoulement externe. Les cas extrêmes de très basse fréquence (solution quasi-permanente) et de très haute fréquence (solutions de M.J. Lighthill et C.C. Lin) sont également étudiées. On donnè des résultats numériques pour l'écoulement le long d'une plaque plane et l'écoulement au point d'arrêt.

CONTENTS

LIST OF TABLES

LIST OF FIGURES

NOTATION

x, y	dimensional cartesian coordinates
η	dimensionless coordinate defined by Equation (14)
X	dimensionless frequency parameter defined by Equation (26)
ξ	dimensionless coordinate defined by Equation (20)
η_s	dimensionless coordinate defined by Equation (63)
Y	dimensionless coordinate defined by Equation (73)
α, β	dimensionless coordinates defined by Equations (99) and (73)
δ, δ_s	boundary layer thicknesses defined by Equations (65) and (64) respectively
δ^*	characteristic boundary layer thickness defined by Equation (43)
t	time
ω	frequency
U, V	velocity components in the outer flow
$\bar{U}(x)$	time-independent part of $U = U(x,t)$
u, v	velocity components in the boundary layer
T	temperature
θ	dimensionless temperature in the boundary layer defined by Equation (1a)
u_0, v_0, θ_0	zero-order solutions
$u_{11} = u_{1R}$ $u_{12} = -u_{1J}$ $v_{11} = v_{1R}$ $v_{12} = -v_{1J}$ $\theta_{11} = \theta_{1R}$ $\theta_{12} = -\theta_{1J}$	first-order solutions defined by Equations (6), (7) and (8)
$u_{20}, v_{20}, \theta_{20}$	time-independent second-order solutions defined by Equations (6), (7) and (8)

u_I, v_I, Θ_I	first-order complex solutions defined by Equations (17), (18) and (19)
Δv_∞	v-component at the edge of the boundary layer, defined by Equation (41)
ψ	stream function
$f(\eta)$	dimensionless stream function defined by Equation (15)
$g(\eta)$	dimensionless temperature defined by Equation (15)
$\Phi_I(\xi, \eta)$	complex dimensionless stream function defined by Equation (21)
$\Phi_{II}(X, \eta)$	dimensionless second-order stream function defined by Equation (27)
$\Theta_I(\xi, \eta)$	complex dimensionless temperature function defined by Equation (19)
$\Theta_{II}(X, \eta)$	dimensionless second-order temperature defined by Equation (27)
$\Phi_{In}(\eta)$	functions defined by Equation (45)
$\Phi_{IIn}(\eta)$	functions defined by Equation (50)
$\Theta_{IN}(\eta)$	functions defined by Equation (46)
$\Theta_{IIn}(\eta)$	functions defined by Equation (51)
$\phi_{IPn}(\eta)$	functions defined by Equation (72)
$\phi_{ISn}(Y)$	functions defined by Equation (75)
$\phi_{IIPn}(\eta)$	functions defined by Equation (98)
$\phi_{IISn}(\eta_s)$	functions defined by Equation (98)
$\theta_{IPn}(\eta)$	functions defined by Equation (91)
$\theta_{ISn}(Y)$	functions defined by Equation (91)
$\theta_{IIPn}(\eta)$	functions defined by Equation (101)
$\theta_{IISn}(\eta_S)$	functions defined by Equation (101)
$A_\tau(X), \lambda_\tau(X)$	functions defined by Equation (36)
$A_q(X), \lambda_q(X)$	functions defined by Equation (37)
$A_v(X), \lambda_v(X)$	functions defined by Equation (42)
τ_o	shear stress at the wall

ρ	density
p	pressure
c, m	constants defined by Equation (13)
μ	viscosity
ν	kinematic viscosity
a	thermal diffusivity
ϵ	disturbance parameter defined by Equation (1)
Pr	Prandtl number
Nu	Nusselt number according to Equation (35)

Superscripts:

$\cdot$	differentiation with respect to Y or η_S
$'$	differentiation with respect to η .

Subscripts:

∞	outer flow
W	at the wall
I	first-order solution
II	second-order solution
R, J	real and imaginary part
S	Stokes solution (see Sec. 5)
P	Prandtl solution (see Sec. 5)
$\eta, \eta_S, \xi,$ X, Y, α, β	differentiation with respect to these variables

HEAT TRANSFER IN LAMINAR BOUNDARY LAYERS WITH OSCILLATING OUTER FLOW

K. Gersten

1. INTRODUCTION

The present investigation deals with the solution of the equations for the velocity as well as for the temperature distribution in laminar boundary layers for the case when small periodic perturbations are superimposed on the steady outer flow. In order to determine the effect of the pressure gradient on the laminar heat transfer response, the outer flows are assumed to be of the so-called wedge-type flow with the mean velocity distribution given as $\bar{U}(x) = cx^m$, x denoting the coordinate along the wall and c being a constant. The constant m represents the pressure gradient in the flow. Wedge-type flows are exceptional because they lead to self-similar solutions of the boundary-layer equations. The outer flow is supposed to be disturbed by a simple harmonic oscillation. The first fundamental theoretical investigation on laminar boundary layers with oscillatory disturbances was performed by M.J. Lighthill[15] who used an approximate approach to examine the effect of small harmonic free-stream velocity perturbations on the skin-friction and heat transfer in laminar boundary layers. In this analysis the perturbations were assumed to be small. Therefore the equations for the perturbation fields could be linearized. It turns out that by this procedure the first-order equations predict no change in the net heat transfer rate. The change in the net heat transfer rate is of the second order, as was shown by C.C. Lin[16] for the case of very high frequencies. After these fundamental papers by Lighthill[15] and C.C. Lin[16] a number of theoretical investigations have been undertaken for more general outer flows[7, 11, 14, 21] as well as for stagnation point flow[1, 8, 11, 20, 28] and the flow past a flat plate at zero incidence[5, 6, 9, 10, 13, 19, 25, 27]. With the exception of the paper by P.H. Hill and A.H. Stenning[10], in which Lighthill's approximate method was used, all theoretical studies attempted to find exact solutions of the boundary layer equations. A few experimental investigations[9, 10, 12, 19] on boundary layers in harmonically oscillating outer flow streams show good agreement with the theoretical first-order solutions. General reviews on periodic laminar boundary layers have been given by H. Schlichting[23], K. Stewartson[24], J.T. Stuart[26] and N. Rott[22].

From the results of the mentioned investigations no complete picture of the situation emerges owing to the fact that second-order terms have been computed in a few papers only. Therefore in the following emphasis is laid on the second-order terms which lead to a change in net skin-friction and, especially, in the average rate of heat transfer. In the mathematical analysis a perturbation method is used; it leads to a series expansion for the solutions.

After formulating the mathematical problem for an incompressible fluid in Section 2, the boundary-layer equations of the first and second order perturbation field are given in Section 3. The solutions of the equations can be represented by a series expansion for small frequency parameters $X = (\omega x)/\bar{U}$ and by a series expansion for large frequency parameters, respectively. Both series expansions are expected to match at moderate frequency parameters. In Section 4 solutions for small values of X are given, whereas the solutions for large values of X are given in Section 5. Section 6 contains a discussion of numerical results for the stagnation point flow ($m = 1$) and flow past a flat plate at zero incidence ($m = 0$), respectively. Finally, Section 7 contains a few critical remarks concerning the limits of validity of the given theory.

2. FORMULATION OF THE PROBLEM AND METHOD OF SOLUTION

2.1 Boundary Layer Equations

We now proceed to consider a boundary layer along a wall, Figure 1. The coordinates x and y are measured along the wall and perpendicular to it, respectively. The velocity of the outer flow parallel to the wall has the form

$$U(x,t) = \bar{U}(x)(1 + \epsilon \cos\omega t) \tag{1}$$

where the second term represents the oscillatory perturbation of the steady flow $\bar{U}(x)$. The temperature T_∞ of the outer flow as well as the temperature T_W at the wall are assumed to be constant. We denote the velocity components of velocity in the boundary layer by $u(x,y,t)$ and $v(x,y,t)$, respectively, and introduce the dimensionless temperature

$$\theta(x,y,t) = \frac{T - T_\infty}{T_W - T_\infty}. \tag{1a}$$

The equation for the unsteady incompressible, two-dimensional laminar boundary layers can now be written

$$\frac{\partial u}{\partial x} + \frac{\partial v}{\partial y} = 0 \tag{2}$$

$$\frac{\partial u}{\partial t} + u\frac{\partial u}{\partial x} + v\frac{\partial u}{\partial y} = \nu\frac{\partial^2 u}{\partial y^2} + \bar{U}\frac{d\bar{U}}{dx} + \epsilon\left(\bar{U}\frac{d\bar{U}}{dx} + \bar{U}\frac{d\bar{U}}{dx}\right)\cos\omega t -$$

$$- \epsilon\omega\bar{U}\sin\omega t + \epsilon^2\frac{1}{2}\bar{U}\frac{d\bar{U}}{dx}(1 + \cos 2\omega t) \tag{3}$$

$$\frac{\partial\theta}{\partial t} + u\frac{\partial\theta}{\partial x} + v\frac{\partial\theta}{\partial y} = a\frac{\partial^2\theta}{\partial y^2} \tag{4}$$

taking into account the form of the outer flow field from Equation (1).

The boundary conditions are:

$$\left.\begin{aligned} y = 0: \quad & u = 0, \quad v = 0, \quad \Theta = 1 \\ y = \infty: \quad & u = U(x,t), \quad \Theta = 0. \end{aligned}\right\} \tag{5}$$

Equation (4) for the temperature distribution is linear. Therefore it can be concluded, that an oscillatory disturbance of the outer flow temperature T would only yield an oscillatory perturbation of the temperature distribution in the boundary layer, but could not effect the time-averaged net heat transfer rate. In other words, a change in the net heat transfer rate can occur only as a consequence of a change in the time-averages of the velocity components. From Equation (3) it can be seen that the time-independent term due to the free-stream velocity is

$$\frac{1}{2}\,\epsilon^2\,\bar{U}\,\frac{d\bar{U}}{dx}\,.$$

It might, therefore, be expected that a change in the net heat-transfer rate will be proportional to ϵ^2.

2.2 Series Expansion Method

The form of Equation (3) suggests solutions for $u(x,y,t)$, $v(x,y,t)$ and $\Theta(x,y,t)$ of the following form:

$$u(x,y,t) = u_0(x,y) + \epsilon[u_{11}(x,y)\cos\omega t + u_{12}(x,y)\sin\omega t] + \\ + \epsilon^2[u_{20}(x,y) + u_{21}(x,y)\cos 2\omega t + u_{22}(x,y)\sin 2\omega t] + \epsilon^3[\ldots] + \ldots, \tag{6}$$

$$v(x,y,t) = v_0(x,t) + \epsilon[v_{11}(x,y)\cos\omega t + v_{12}(x,y)\sin\omega t] + \\ + \epsilon^2[v_{20}(x,y) + v_{21}(x,y)\cos 2\omega t + v_{22}(x,y)\sin 2\omega t] + \epsilon^3[\ldots] + \ldots, \tag{7}$$

$$\Theta(x,y,t) = \Theta_0(x,y) + \epsilon[\Theta_{11}(x,y)\cos\omega t + \Theta_{12}(x,y)\sin\omega t] + \\ + \epsilon^2[\Theta_{20}(x,y) + \Theta_{21}(x,y)\cos 2\omega t + \Theta_{22}(x,y)\sin 2\omega t] + \epsilon^3[\ldots] + \ldots . \tag{8}$$

The above forms are now substituted into Equations (2), (3) and (4) and in each of them the terms are arranged in ascending powers of ϵ. Since ϵ is arbitrary, the coefficients of ϵ^n must vanish singly, and we are led to the following set of equations:

<u>zero-order</u>, steady-state equations:

$$\left.\begin{aligned} \frac{\partial u_0}{\partial x} + \frac{\partial v_0}{\partial y} &= 0, \\ u_0\frac{\partial u_0}{\partial x} + v_0\frac{\partial u_0}{\partial y} &= \nu\frac{\partial^2 u_0}{\partial y^2} + \bar{U}\frac{d\bar{U}}{dx}, \\ u_0\frac{\partial \Theta_0}{\partial x} + v_0\frac{\partial \Theta_0}{\partial y} &= a\frac{\partial^2 \Theta_0}{\partial y^2}. \end{aligned}\right\} \tag{9}$$

with the boundary conditions

$$y = 0: \quad u_c = 0, \quad v_0 = 0, \quad \Theta_0 = 1$$

$$y = \infty: \quad u_0 = \bar{U}(x), \quad \Theta_0 = 0.$$

first-order equations:
terms with $\cos\omega t$

$$\left.\begin{aligned}
&\frac{\partial u_{11}}{\partial x} + \frac{\partial v_{11}}{\partial y} = 0, \\
&\omega u_{12} + u_{11}\frac{\partial u_0}{\partial x} + u_0\frac{\partial u_{11}}{\partial x} + v_{11}\frac{\partial u_0}{\partial y} + v_0\frac{\partial v_{11}}{\partial y} = \nu\frac{\partial^2 u_{11}}{\partial y^2} + 2\bar{U}\frac{d\bar{U}}{dx} \\
&\omega\Theta_{12} + u_{11}\frac{\partial\Theta_0}{\partial x} + u_0\frac{\partial\Theta_{11}}{\partial x} + v_{11}\frac{\partial\Theta_0}{\partial y} + v_0\frac{\partial\Theta_{11}}{\partial y} = a\frac{\partial^2\Theta_{11}}{\partial y^2}
\end{aligned}\right\} \qquad (10)$$

terms with $\sin\omega t$

$$\left.\begin{aligned}
&\frac{\partial u_{12}}{\partial x} + \frac{\partial v_{12}}{\partial y} = 0, \\
&-\omega u_{11} + u_{12}\frac{\partial u_0}{\partial x} + u_0\frac{\partial u_{12}}{\partial x} + v_{12}\frac{\partial u_0}{\partial y} + v_0\frac{\partial v_{12}}{\partial y} = \nu\frac{\partial^2 u_{12}}{\partial y^2} - \omega\bar{U}, \\
&-\omega\Theta_{11} + u_{12}\frac{\partial\Theta_0}{\partial x} + u_0\frac{\partial\Theta_{12}}{\partial x} + v_{12}\frac{\partial\Theta_0}{\partial y} + v_0\frac{\partial\Theta_{12}}{\partial y} = a\frac{\partial^2\Theta_{12}}{\partial y^2}
\end{aligned}\right\} \qquad (11)$$

with boundary conditions:

$$y = 0: \quad u_{11} = 0, \quad v_{11} = 0, \quad u_{12} = 0, \quad v_{12} = 0, \quad \Theta_{11} = 0, \quad \Theta_{12} = 0$$

$$y = \infty: \quad u_{11} = \bar{U}(x), \quad u_{12} = 0, \quad \Theta_{11} = 0, \quad \Theta_{12} = 0.$$

second-order equations:
time-independent terms

$$\left.\begin{aligned}
&\frac{\partial u_{20}}{\partial x} + \frac{\partial v_{20}}{\partial y} = 0, \\
&u_0\frac{\partial u_{20}}{\partial x} + u_{20}\frac{\partial u_0}{\partial x} + v_0\frac{\partial u_{20}}{\partial y} + v_{20}\frac{\partial u_0}{\partial y} = \nu\frac{\partial^2 u_{20}}{\partial y^2} + \frac{1}{2}\bar{U}\frac{d\bar{U}}{dx} - \\
&\qquad - \frac{1}{2}\left(u_{11}\frac{\partial u_{11}}{\partial x} + u_{12}\frac{\partial u_{12}}{\partial x} + v_{11}\frac{\partial u_{11}}{\partial y} + v_{12}\frac{\partial u_{12}}{\partial y}\right),
\end{aligned}\right\} \qquad (12)$$

$$u_0 \frac{\partial \theta_{20}}{\partial x} + u_{20} \frac{\partial \theta_0}{\partial x} + v_0 \frac{\partial \theta_0}{\partial y} + v_{20} \frac{\partial \theta_0}{\partial y} = a \frac{\partial^2 \theta_{20}}{\partial y^2} - \left| - \frac{1}{2} \left(u_{11} \frac{\partial \theta_{11}}{\partial x} + u_{12} \frac{\partial \theta_{12}}{\partial x} + v_{11} \frac{\partial \theta_{11}}{\partial y} + v_{12} \frac{\partial \theta_{12}}{\partial y} \right) \right| \tag{12}$$

with the boundary conditions:

$$y = 0: \quad u_{20} = 0, \quad v_{20} = 0, \quad \theta_{20} = 0$$

$$y = \infty: \quad u_{20} = 0, \quad v_{20} = 0, \quad \theta_{20} = 0.$$

Similar sets of equations result from multiplying $\cos 2\omega t$ and $\sin 2\omega t$. Owing to the nonlinearity of the velocity Equation (3) combinations of first- and second-order terms will also appear. This leads to equivalent sets of third-order equations and so on. In other words an infinite number of sets of equations for all powers of ϵ is generated. Consequently the series expansions Equations (6), (7) and (8) of the solutions are only physically meaningful if the series converge. A general statement about the convergence of these series is not now available. But from the results, which we will present later in the analysis, it will be possible to make inferences which will be discussed in Section 7. It seems plausible that this series expansion is justified on condition that ϵ is a very small parameter.

In this investigation only the first-order equations and the time-independent second-order equations are considered. The latter are assumed to give the essential part of the change in the net heat-transfer rate provoked by oscillations in the outer flow. The difference between the exact change and that given only by the second-order term will be of the order of ϵ^4, which is negligible for small values of ϵ.

3. BOUNDARY LAYER EQUATIONS

3.1 Zero-Order (Steady-State) Equations

We now consider the flow past a wedge, i.e. an outer flow velocity distribution of the form

$$\bar{U}(x) = cx^m . \tag{13}$$

In this case, Equations (9) lead to self-similar solutions[23], that is to solutions which depend on one single spatial variable only, namely on the similarity variable

$$\eta = y\sqrt{\frac{\bar{U}}{\nu x}} = y\sqrt{\frac{c}{\nu}}\, x^{(m-1)/2} . \tag{14}$$

We now introduce two functions $f(\eta)$ and $g(\eta)$ of the new variable η by the definitions:

$$\left.\begin{aligned} \psi_0(x,y) &= \sqrt{\nu x \bar{U}(x)}\, f(\eta) \\ u_0(x,y) &= \frac{\partial \psi_0}{\partial y} = \bar{U}(x) \cdot f'(\eta) = c x^m f'(\eta) \\ v_0(x,y) &= -\frac{\partial \psi_0}{\partial x} = -\frac{1}{2}\sqrt{c\nu}\, x^{(m-1)/2}\,[(m+1)f(\eta) + (m-1)\eta f'(\eta)] \\ \Theta_0(x,y) &= g(\eta)\ . \end{aligned}\right\} \tag{15}$$

When this is done, the partial differential equations (9) reduce to the following ordinary differential equations

$$\left.\begin{aligned} f''' + \frac{m+1}{2} f f'' + m(1 - f'^2) &= 0 \\ \frac{1}{Pr} g'' + \frac{m+1}{2} f g' &= 0 \end{aligned}\right\} \tag{16}$$

with the boundary conditions

$$\eta = 0: \quad f = 0, \quad f' = 0, \quad g = 1$$

$$\eta = \infty: \quad f' = 1, \quad g = 0.$$

Here $Pr = \nu/\alpha$ is the Prandtl number. For gases it is of the order of 1 ($Pr = 0.7$ approximately in air). Equations (16) are well known equations for the steady-state problem (in the absence of the disturbance in the outer flow), and their solutions are well-known [15].

3.2 First-Order Equations

It is possible to combine the two sets of Equations (10) and (11) by introducing complex functions in the following way:

$$u_I = u_{IR} + i u_{IJ} = u_{11} - i u_{12} \tag{17}$$

$$v_I = v_{IR} + i v_{IJ} = v_{11} - i v_{12} \tag{18}$$

$$\Theta_I = \Theta_{IR} + i\Theta_{IJ} = \Theta_{11} - i\Theta_{12} \tag{19}$$

Introducing the similarity variable η from Equation (14) and a new variable defined as

$$\xi = \frac{i\omega x}{\bar{U}(x)} = \frac{i\omega}{c} x^{1-m} \tag{20}$$

together with the definitions

$$\left.\begin{aligned}
\psi_I(x,y) &= \sqrt{\nu x \bar{U}(x)}\ \Phi_I(\xi,\eta)\ , \\
u_I(x,y) &= \frac{\partial \psi_I}{\partial y} = \bar{U}(x)\Phi_{I\eta}(\xi,\eta) = cx^m \Phi_{I\eta}(\xi,\eta)\ , \\
v_I(x,y) &= -\frac{\partial \psi_I}{\partial x} = -\frac{1}{2}\sqrt{c\nu}\, x^{(m-1)/2}\,[(m+1)\Phi_I + (m-1)\eta\Phi_{I\eta} + 2(1-m)\xi\Phi_{I\xi}]\ , \\
\Theta_I(x,y) &= \Theta_I(\xi,\eta)
\end{aligned}\right\} \quad (21)$$

we obtain the following working equations:

$$\Phi_{I\eta\eta\eta} + \frac{m+1}{2} f\Phi_{I\eta\eta} - (\xi + 2mf')\Phi_{I\eta} +$$

$$+\frac{m+1}{2} f'\Phi_I - (1-m)f'\xi\Phi_{I\xi\eta} + (1-m)f''\xi\Phi_{I\xi} + 2m + \xi = 0\ , \quad (22)$$

$$\frac{1}{Pr}\Theta_{I\eta\eta} + \frac{m+1}{2} f\Theta_{I\eta} - \xi\Theta_I - (1-m)f'\xi\Theta_{I\xi} =$$

$$-\frac{1}{2} g'[(m+1)\Phi_I + 2(1-m)\xi\Phi_{I\xi}] \quad (23)$$

with the boundary conditions:

$$\left.\begin{aligned}
\eta = 0: \quad & \Phi_I = 0\ , \quad \Phi_{I\xi} = 0\ , \quad \Phi_{I\eta} = 0\ , \quad \Theta_I = 0 \\
\eta = \infty: \quad & \Phi_{I\eta} = 1\ , \quad \Theta_I = 0\ .
\end{aligned}\right\} \quad (24)$$

Equations (22) and (23) admit the following solutions:

$$\left.\begin{aligned}
\Phi_I(\xi,\eta) &= \Phi_{IR}(X,\eta) + i\Phi_{IJ}(X,\eta) \\
\Theta_I(\xi,\eta) &= \Theta_{IR}(X,\eta) + i\Theta_{IJ}(X,\eta)
\end{aligned}\right\} \quad (25)$$

where

$$X = \frac{\omega x}{\bar{U}(x)} \quad (26)$$

is the dimensionless frequency parameter.

3.3 Second-Order (Time-Independent) Equations

By analogy with Equations (21) and (26) we make the following assumptions for the second-order time-independent terms of velocities and temperature:

$$\left.\begin{aligned}
\psi_{20}(x,y) &= \sqrt{c\nu}\, x^{(m+1)/2}\, \Phi_{II}(X,\eta) \\
u_{20}(x,y) &= c x^{m} \Phi_{II\eta}(X,\eta) \\
v_{20}(x,y) &= -\tfrac{1}{2}\sqrt{c\nu}\, x^{(m-1)/2}\, [(m+1)\Phi_{II} + (m-1)\eta\Phi_{II\eta} + 2(1-m)X\Phi_{IIX}] \\
\Theta_{20}(x,y) &= \Theta_{II}(X,\eta)\ .
\end{aligned}\right\} \tag{27}$$

Substituting these expressions into Equation (12), we get:

$$\Phi_{II\eta\eta\eta} + \frac{m+1}{2} f\Phi_{II\eta\eta} - 2mf'\Phi_{II\eta} - (1-m)f'X\Phi_{II\eta X} + (1-m)f''X\Phi_{IIX} + \frac{m+1}{2} f''\Phi_{II}$$

$$= \tfrac{1}{2}\{m\Phi^2_{IR\eta} + (1-m)X\Phi_{IR\eta}\cdot\Phi_{IRX\eta} + m\Phi^2_{IJ\eta} + (1-m)X\Phi_{IJ\eta}\cdot\Phi_{IJX\eta} - m\} -$$

$$- \tfrac{1}{2}\{(m+1)\Phi_{IR}\Phi_{IR\eta\eta\eta} + 2(1-m)X\Phi_{IRX}\Phi_{IR\eta\eta} + (m+1)\Phi_{IJ}\Phi_{IJ\eta\eta} + 2(1-m)X\Phi_{IJX}\Phi_{IJ\eta\eta}\}\ . \tag{28}$$

The temperature function $\Theta_{II}(X,\eta)$ must satisfy the following equation:

$$\frac{1}{Pr}\Theta_{II\eta\eta} + \frac{m+1}{2} f\Theta_{II\eta} - (1-m)f'X\Theta_{IIX} = -\frac{1+m}{2} g'\Phi_{II} -$$

$$- (1-m)g'X\Phi_{IIX} + \tfrac{1}{2}\{(1-m)X(\Phi_{IR\eta}\Theta_{IkX} + \Phi_{IJ\eta}\Theta_{IJX}) -$$

$$- \frac{m+1}{2}(\Phi_{IR}\Theta_{IR\eta} + \Phi_{IJ}\Theta_{IJ\eta}) - (1-m)X(\Phi_{IRX}\Theta_{IR\eta} + \Phi_{IJX}\cdot\Theta_{IJ\eta})\}\ . \tag{29}$$

The boundary conditions for Φ_{II} and Θ_{II} are

$$\eta = 0: \quad \Phi_{II} = 0\ , \quad \Phi_{II\eta} = 0\ , \quad \Phi_{IIX} = 0\ , \quad \Theta_{II} = 0$$

$$\eta = \infty: \quad \Phi_{II\eta} = 0\ , \quad \Theta_{II} = 0\ .$$

3.4 Velocity and Temperature Field

Summarizing the preceding results for the velocity as well as for the temperature distributions, we obtain the following formulae:

$$u(x,y,t) = \tilde{U}(x)\{f'(\eta) + \epsilon[\Phi_{IR\eta}(\eta,X)\cos\omega t - \Phi_{IJ\eta}(\eta,X)\sin\omega t] +$$

$$+ \epsilon^2\Phi_{II\eta}(\eta,X) + \ldots\}\ , \tag{30}$$

$$v(x,y,t) = -\tfrac{1}{2}\sqrt{c\nu}\, x^{(m-1)/2} \{(m+1)f(\eta) + (m-1)\eta f'(\eta) +$$
$$+ \epsilon[(m+1)\Phi_{IR}(\eta,X) + (m-1)\eta\Phi_{IR\eta}(\eta,X) + 2(1-m)X\Phi_{IRX}(\eta,X)]\cos\omega t -$$
$$- \epsilon[(m+1)\Phi_{IJ}(\eta,X) + (m-1)\eta\Phi_{IJ\eta}(\eta,X) + 2(1-m)X\Phi_{IJX}(\eta,X)]\sin\omega t +$$
$$+ \epsilon^2[(m+1)\Phi_{II}(\eta,X) + (m-1)\eta\Phi_{II\eta}(\eta,X) + 2(1-m)X\Phi_{IIX}(\eta,X)] + \ldots \} \tag{31}$$

$$\Theta(x,\eta,t) = g(\tau) + \epsilon[\Theta_{IR}(\eta,X)\cos\omega t - \Theta_{IJ}(\eta,X)\sin\omega t] + \epsilon^2\Theta_{II}(\eta,X) + \ldots \tag{32}$$

From the derivatives at the wall we obtain for the wall shear stress:

$$\frac{\tau_0(x,t)}{\mu\bar{U}\sqrt{\frac{\bar{U}}{\nu x}}} = f''(0) + \epsilon[\Phi_{IR\eta\eta}(0,X)\cos\omega t - \Phi_{IJ\eta\eta}(0,X)\sin\omega t] + \epsilon^2\Phi_{II\eta\eta}(0,X) + \ldots \tag{33}$$

and the heat transfer rate:

$$\frac{Nu}{\sqrt{\frac{\bar{U}x}{\nu}}} = -\{g'(0) + \epsilon[\Theta_{IR\eta}(0,X)\cos\omega t - \Theta_{IJ\eta}(0,X)\sin\omega t] + \epsilon^2\Theta_{II\eta}(0,X) + \ldots \tag{34}$$

where

$$Nu = \frac{q\cdot x}{k(T_W - T_\infty)} = -\frac{x}{T_W - T_\infty}\left(\frac{\partial T}{\partial y}\right)_{y=0} = -x\left(\frac{\partial\Theta}{\partial y}\right)_{y=0} \tag{35}$$

is the Nusselt number for the local heat transfer rate $q(x,t)$. The Equations (33) and (34) can also be written in the following way:

$$\frac{\tau_0(x,t)}{\mu\bar{U}\sqrt{\frac{\bar{U}}{\nu x}}} = f''(0) + \epsilon A_\tau(X)\cos[\omega t + \lambda_\tau(X)] + \epsilon^2\Phi_{II\eta\eta}(0,X) \tag{36}$$

$$\frac{Nu}{\sqrt{\frac{\bar{U}x}{\nu}}} = -\{g'(0) + \epsilon A_q(X)\cos[\omega t + \lambda_q(X)] + \epsilon^2\Theta_{II\eta\eta}(0,X) + \ldots\} \tag{37}$$

where

$$A_\tau(X) = \sqrt{\Phi^2_{IR\eta\eta}(0,X) + \Phi^2_{IJ\eta\eta}(0,X)} \tag{38}$$

and

$$\tan\lambda_\tau(X) = \frac{\Phi_{IJ\eta\eta}(0,X)}{\Phi_{IR\eta\eta}(0,X)} \tag{39}$$

with analogous expressions for A_q and λ_q.

It might be worth mentioning that the velocity component v does not merge into the outer flow velocity component

$$V(x,t) = -m\sqrt{c\nu}\, x^{(m-1)/2}\, \eta(1 + \epsilon\cos\omega t) \,. \tag{40}$$

There exists a certain effect on the v-component of the velocity at the outer edge from the boundary layer flow, which is

$$\begin{aligned}\Delta v_\infty(x,t) = v_\infty - V = -\tfrac{1}{2}\sqrt{c\nu}\, x^{(m-1)/2} \{&(m+1)f + (m-1)\eta f' - 2m\eta + \\ &+ \epsilon[(m+1)\Phi_{IR} + (m-1)\eta\Phi_{IR\eta} + 2(1-m)X\Phi_{IRX} - 2m\eta]\cos\omega t - \\ &- \epsilon[(m+1)\Phi_{IJ} + (m-1)\eta\Phi_{IJ\eta} + 2(1-m)X\Phi_{IJX}]\sin\omega t + \\ &+ \epsilon^2[(m+1)\Phi_{IJ} + (m-1)\eta\Phi_{II\eta} + 2(1-m)X\Phi_{IIX}] + \ldots\}_{\eta=\infty}\end{aligned} \tag{41}$$

and can also be written in the following form:

$$\begin{aligned}\frac{\Delta v_\infty}{\bar{U}\sqrt{\frac{\nu}{\bar{U}x}}} = &\left(m\eta - \frac{m-1}{2}\eta f' - \frac{m+1}{2} f\right)_{\eta=\infty} + \epsilon A_v(X)\cos[\omega t + \lambda_v(X)] - \\ &- \epsilon^2\left[\frac{m+1}{2}\Phi_{II} + \frac{m-1}{2}\eta\Phi_{II\eta} + (1-m)X\Phi_{IIX}\right]_{\eta=\infty} .\end{aligned} \tag{42}$$

It can be shown that this velocity at the outer edge of the boundary is related to the value of the displacement thickness δ^* in steady-state boundary layers:

$$\delta^*(x,t) = x\frac{\Delta v_\infty(x,t)}{U(x,t)} \tag{43}$$

where

$$\delta^*(x,t) = \int_0^\infty \left(1 - \frac{u(x,y,t)}{U(x,t)}\right) dy \,. \tag{44}$$

For unsteady boundary layers, however, this quantity loses its meaning as a displacement thickness; this was shown by F.K. Moore[18].

4. SOLUTIONS FOR SMALL VALUES OF FREQUENCY PARAMETER

Since we are unable to obtain complete solutions of Equations (22), (23), (28) and (29), we propose to establish series expansions in terms of the frequency parameter X separately for small and for large values of it. These two expansions are supposed to join smoothly in the intermediate frequency range and thus to represent the required solution over the whole frequency range. This section will consider the series expansion of the solution for small values of the frequency parameter, both for the first-order and for the second-order equations.

4.1 First-Order Equations

We seek solutions of the first-order Equations (22) and (23) in the following form:

$$\Phi_I(\xi,\eta) = \sum_{n=0}^{\infty} \xi^n \Phi_{In}(\eta) \,. \tag{45}$$

$$\Theta_I(\xi,\eta) = \sum_{n=0}^{\infty} \xi^n \Theta_{In}(\eta) \,. \tag{46}$$

Substitution into Equations (22) and (23) leads to the following sets of linear equations:

$$\Phi_{In}''' + \frac{m+1}{2} f\Phi_{In}'' - [2m + n(1-m)] f'\Phi_{In}' + \left[\frac{m+1}{2} + n(1-m)\right] f''\Phi_{In} = \Phi_{In-1}' + r_n$$

$$\frac{1}{Pr}\Theta_{In}'' + \frac{m+1}{2} f\Theta_{In}' + n(m-1) f'\Theta_{In} = \Theta_{In-1} - \left[\frac{m+1}{2} + n(1-m)\right] g'\Phi_{In}$$

with

$$\left.\begin{aligned} \eta = 0: \quad & \Phi_{In} = 0\,, \quad \Phi_{In}' = 0\,, \quad \Theta_{In} = 0 \\ \eta = \infty: \quad & \Phi_{In}' = 0\,, \quad \Theta_{In} = 0 \end{aligned}\right\} \tag{47}$$

where $r_0 = -2m$, $r_1 = -1$, $r_n = 0$ for $n > 1$,

$$\Phi_{In-1} = 0 \quad \text{for } n = 0\,, \quad \Theta_{In-1} = 0 \quad \text{for } n = 0\,.$$

There exist very simple so-called quasi-steady solutions, i.e. solutions of the zero-order-equations:

$$\Phi_{I0}(\eta) = \tfrac{1}{2}[f(\eta) + \eta f'(\eta)] \tag{48}$$

$$\Theta_{I0}(\eta) = \tfrac{1}{2}\eta g'(\eta) \tag{49}$$

where $f(\eta)$ and $g(\eta)$ are the solutions of Equations (16).

4.2 Second-Order Equations

We seek series expansions in powers of $X = \omega x/\bar{U}$ for the solutions of the equations (28) and (29), respectively. It can be seen by inspection, that all terms with odd powers of X will vanish. We assume, therefore, solutions of this form:

$$\Phi_{II}(X,\eta) = \Phi_{II0}(\eta) - X^2\Phi_{II2}(\eta) + X^4\Phi_{II4}(\eta) - + \ldots \tag{50}$$

$$\Theta_{II}(X,\eta) = \Theta_{II0}(\eta) - X^2\Theta_{II2}(\eta) - X^4\Theta_{II4}(\eta) - + \ldots \tag{51}$$

If we substitute these series into Equations (28) and (29) and collect terms, we obtain the following sets of ordinary, linear differential equations:

$$\Phi''_{II0} + \frac{m+1}{2} f\Phi''_{II0} - 2mf'\Phi'_{II0} + \frac{m+1}{2} f''\Phi_{II0} = \frac{1}{2}\left[m\Phi'^{2}_{I0} - \frac{m+1}{2}\Phi_{I0}\Phi''_{I0} - m\right] \tag{52}$$

$$\frac{1}{Pr}\Theta''_{II0} + \frac{m+1}{2} f\Theta'_{II0} = -\frac{m+1}{2}\left[g'\Phi_{II0} + \tfrac{1}{2}\Phi_{I0}\Theta'_{I0}\right]; \tag{53}$$

$$\Phi'''_{II2} + \frac{m+1}{2} f\Phi''_{II2} - 2f'\Phi'_{II2} + \frac{5-3m}{2} f''\Phi_{II2} =$$

$$-\frac{1}{2}\left[\Phi'^{2}_{I1} - \frac{3-m}{2}\Phi_{I1}\Phi''_{I1} - 2\Phi'_{I0}\Phi'_{I2} + \frac{1+m}{2}\Phi_{I0}\Phi''_{I2} + \frac{5-3m}{2}\Phi''_{I0}\Phi_{I2}\right] \tag{54}$$

$$\frac{1}{Pr}\Theta''_{II2} + \frac{m+1}{2} f\Theta'_{II2} - 2(1-m)f\Theta_{II2} = -\frac{1}{2}\left[(5-3m)g'\Phi_{II2} - 2(1-m)\Phi'_{I0}\Theta_{I2} +\right.$$

$$\left. + (1-m)\Phi'_{I1}\Theta_{I1} + \frac{m+1}{2}\Phi_{I0}\Theta'_{I2} + \frac{5-3m}{2}\Phi_{I2}\Theta'_{I0} - \frac{3-m}{2}\Phi_{I1}\Theta'_{I1}\right]; \tag{55}$$

$$\Phi'''_{II4} + \frac{m+1}{2} f\Phi''_{II4} + (2m-4)f\Phi'_{II4} + \frac{9-7m}{2} f''\Phi''_{II4} =$$

$$\frac{1}{2}\left[(2-m(\Phi'^{2}_{I2} + 2(2-m)\Phi'_{I0}\Phi'_{I4} + 2(m-2)\Phi'_{I1}\Phi'_{I3} - \frac{1+m}{2}\Phi_{I0}\Phi''_{I4} + \frac{3m-5}{2}\Phi_{I2}\Phi''_{I2} +\right.$$

$$\left. + \frac{7m-9}{2}\Phi''_{I0}\Phi_{I4} - \frac{m-3}{2}\Phi_{I1}\Phi_{I3} - \frac{5m-7}{2}\Phi''_{I1}\Phi_{I3}\right] \tag{56}$$

$$\frac{1}{Pr}\Theta''_{II4} + \frac{m+1}{2} f\Theta'_{II4} - 4(1-m)f'\Theta_{II4} =$$

$$\frac{1}{2}\left[(7m-9)g'\Phi_{II4} + 2(1-m)\Phi'_{I2}\Theta_{I2} + 4(1-m)\Phi'_{I0}\Theta_{I4} - 3(1-m)\Phi'_{I1}\Theta_{I3} + (1-m)\Phi'_{I3}\Theta_{I1} +\right.$$

$$\left. + \frac{7m-9}{2}\Phi_{I4}\Theta'_{I0} + \frac{3m-5}{2}\Phi_{I2}\Theta'_{I2} - \frac{1+m}{2}\Phi_{I0}\Theta'_{I4} + \frac{7-5m}{2}\Phi_{I3}\Theta'_{I1} + \frac{3-m}{2}\Phi_{I1}\Theta'_{I3}\right]. \tag{57}$$

The scheme can be continued for ascending powers of the frequency parameter X, but we will confine ourselves to the preceding terms. In this manner the largest neglected term will be of the order of X^6. For all equations the boundary conditions are given by:

$$\left.\begin{aligned} \eta = 0: \quad & \Phi_{IIn} = 0, \quad \Phi'_{IIn} = 0, \quad \Theta_{IIn} = 0 \\ \eta = \infty: \quad & \Phi'_{IIn} = 0, \quad \Theta_{IIn} = 0. \end{aligned}\right\} \tag{58}$$

Quasi-steady solutions for Equations (52) and (53) can be easily given - they are

$$\left.\begin{aligned} \Phi_{II0} &= \tfrac{1}{16}(\eta^2 f'' + \eta f' - f) \\ \Theta_{II0} &= \tfrac{1}{16}(\eta^2 g'' - \eta g). \end{aligned}\right\} \tag{59}$$

4.3 Convergence of the Series

In order to justify the series expansions postulated in Equations (45), (46), (50), (51), it is necessary to show that these series converge, at least for a certain interval of small values of X. S.H. Lam and N. Rott[14] were able to prove, that the series expansion of the solution of the general equation (22) converges for all values of ξ, and that this is a unique solution of the problem. It is expected that an analogous proof of the convergence for the other series expansions might hold, but the details of this scheme have not been worked out. In the special case of flow along a flat plate at zero incidence S. Gilbellato[5,6] showed, that the series Equations (45) and (46) converge absolutely for arbitrary values of ξ

5. SOLUTIONS FOR LARGE VALUES OF THE FREQUENCY PARAMETER

5.1 Concept of the inner ('Stokes') Boundary Layer

In order to understand the response of the flow in the boundary layer, especially with respect to high-frequency oscillations in the outer flow, we will first consider the simple case, when the outer flow has the following form:

$$\bar{U}(x,t) = \epsilon c \cos\omega t. \tag{60}$$

This leads us at once to the well-known exact solution of the full Navier-Stokes-equation, which was first given by G.G. Stokes[23]:

$$u(y,t) = \epsilon c\left[\cos\omega t - e^{-\sqrt{\frac{\omega}{2\nu}}\,y}\cos\left(\omega t - \sqrt{\frac{\omega}{2\nu}}\,y\right)\right] \tag{61}$$

or

$$u(\eta_S, t) = \epsilon c[\cos\omega t - e^{-\eta S}\cos(\omega t - \eta_S) \tag{62}$$

where

$$\eta_S = \eta\sqrt{\frac{\omega}{2\nu}} = \frac{y}{\sqrt{\frac{2\nu}{\omega}}} = \frac{y}{\delta_S} \tag{63}$$

represents a dimensionless distance from the wall and

$$\delta_S = \sqrt{\frac{2\nu}{\omega}} \tag{64}$$

plays the role of a boundary layer thickness. In the case of an incompressible fluid the problem is equivalent to the flow near an oscillating flat plate in a fluid at rest. In the literature this is referred to as 'Stokes' (second) problem. From Equation (64) it follows that for increasing values of frequency ω, the thickness of the 'Stokes-layer' decreases and becomes very small ultimately.

If the flow equations were linear we could immediately obtain a complete solution to our problem of a boundary layer with an oscillatory disturbance in the outer flow, at least in the case of the flat plate (m = 0), by a linear superposition of the steady-state solution and the oscillatory 'Stokes'-solution. It should be noted that the boundary layer thicknesses are different in the two solutions. The boundary layer thickness in the Stokes problem is given by Equation (64), whereas that for the steady-state solution is

$$\delta = \sqrt{\frac{\nu x}{\bar{U}(x)}} \,. \tag{65}$$

The ratio of these thicknesses

$$\frac{\delta_S}{\delta} = \sqrt{\frac{2\bar{U}}{\omega x}} = \sqrt{\frac{2}{X}} \tag{66}$$

becomes very small for high frequencies; in other words, for large values of the frequency parameter X the 'Stokes'-layer is much thinner than the original boundary layer, as shown schematically, in Figure 2.

Owing to the non-linear character of the flow equation, there will occur an interaction between the Stokes solution and the original boundary-layer solution leading to a much more complicated solution than would be the case with a linear problem. Nevertheless, we may expect that even in the non-linear problem the essential part of the solution for high frequencies will be of the Stokes type. We, therefore, represent the required solution as a sum of two parts in the following way:

$$\begin{aligned} \Phi &= \Phi_S + \Phi_P \\ \Theta &= \Theta_S + \Theta_P \,. \end{aligned} \tag{67}$$

Here Φ_S and Θ_S are functions of the Stokes type and vary only in the small Stokes-layer, (S-layer), whereas Φ_P and Θ_P represent the interaction between the Stokes flow fields and the original steady-state boundary layer; we shall refer to the latter as to the Prandtl-layer (P-layer), see also Figure 2. The necessity of splitting the solution for high frequencies into two parts has been mentioned by W.E. Gibson[7] and by S.H. Lam and N. Rott[14]. Owing to the postulated form of the solution, Equation (67), the flow equations and the temperature equations were also split into two equations, respectively; it is noted that, in general, the equations

remain coupled. The coupling of these two solutions is evidenced by the boundary conditions at the wall, which have to be satisfied by the composite solution, but not by each of the two constituent parts of the solutions separately. In the following the mathematical procedure will be described in detail separately for the first-order equations and second-order equations, respectively.

5.2 First-Order Equations

5.2.1 *Velocity Field*

The substitution of

$$\Phi_I = \Phi_{IS} + \Phi_{IP} \tag{68}$$

into Equation (22) and the assumption, that only the Prandtl solution Φ_{IP} merges with the outer flow oscillation, whereas the Stokes solution Φ_{IS} vanishes outside the Stokes layer, lead to the following two equations:

$$\Phi_{IP\eta\eta\eta} + \frac{m+1}{2} f\Phi_{IP\eta\eta} - (\xi + 2mf')\Phi_{IP\eta} + \frac{m+1}{2} f''\Phi_{IP} -$$

$$- (1-m)f'\xi\Phi_{IP\xi\eta} + (1-m)f''\xi\Phi_{IP\xi} = -2m - \xi \tag{69}$$

and

$$\Phi_{IS\eta\eta\eta} + \frac{m+1}{2} f\Phi_{IS\eta\eta} - (\xi + 2mf')\Phi_{IS\eta} + \frac{m+1}{2} f''\Phi_{IS} -$$

$$- (1-m)f'\xi\Phi_{IS\xi\eta} + (1-m)f''\xi\Phi_{IS\xi} = 0 \tag{70}$$

with the boundary conditions

$$\left.\begin{aligned} \eta = 0: \quad & \Phi_{IS} + \Phi_{IP} = 0, \quad \Phi_{IS\eta} + \Phi_{IP\eta} = 0 \\ \eta = \infty: \quad & \Phi_{IS\eta} = 0, \quad \Phi_{IP\eta} = 1. \end{aligned}\right\} \tag{71}$$

In this way Equations (69) and (70) satisfy the boundary conditions at the outer edge of the boundary layer. In order to find the solutions of Equation (69) for large values of the frequency parameter, we change the variable ξ to $\beta = 1/\sqrt{\xi}$.

Substituting a series in powers of β for the solutions

$$\Phi_{IP} = \eta + \sum_{n=0}^{\infty} \beta^{n+1} \Phi_{IPn}(\eta) \tag{72}$$

into Equation (69), we obtain a set of equations for the functions $\Phi_{IPn}(\eta)$.

If we change the variables in Equation (70) from ξ and η to β and Y according to:

$$\beta = \frac{1}{\sqrt{\xi}}, \qquad Y = \sqrt{\xi}\,\eta \tag{73}$$

and if we represent the function f in the form of a power series

$$f = A_2 \frac{\eta^2}{2!} - m\frac{\eta^3}{3!} + \frac{3m-1}{2} A_2^2 \frac{\eta^5}{5!} + \ldots, \tag{74}$$

an equivalent series can be assumed for the function Φ_{IS}, namely

$$\Phi_{IS} = \sum_{n=0}^{\infty} \beta^{n+1} \phi_{ISn}(Y) . \tag{75}$$

Upon substituting into Equation (70), we obtain the successive equations for the functions $\phi_{ISn}(Y)$, which can be easily solved.

Now the composite solutions can be written in the form of sums of the partial solutions $\phi_{IPn}(\eta)$ and $\phi_{ISn}(Y)$, i.e.

$$\Phi_I = \eta + \sum_{n=0}^{\infty} \beta^{n+1} \phi_{ISn}(Y) + \sum_{n=0}^{\infty} \beta^{n+1} \phi_{IPn}(\eta) , \tag{76}$$

$$\Phi_{I\eta} = 1 + \sum_{n=0}^{\infty} \beta^{n} \dot{\phi}_{ISn}(Y) + \sum_{n=0}^{\infty} \beta^{n+1} \phi'_{IPn}(\eta) , \tag{77}$$

$$\Phi_{I\eta\eta} = -\sum_{n=0}^{\infty} \beta^{n-1} \ddot{\phi}_{ISn}(Y) + \sum_{n=0}^{\infty} \beta^{n+1} \phi''_{IPn}(\eta) , \tag{78}$$

$$\Phi_{I\xi} = -\frac{1}{2}\sum_{n=0}^{\infty} (n+1)\beta^{n+3} (\phi_{ISn} + \phi_{IPn}) + \frac{1}{2} Y \sum_{n=0}^{\infty} \beta^{n+3} \dot{\phi}_{ISn} . \tag{79}$$

The boundary conditions Equation (71) allow us to establish boundary conditions for the functions $\phi_{IS}(Y)$ and $\phi_{IP}(\eta)$, which are as follows:

$$\left.\begin{aligned} &\phi_{ISn}(0) + \phi_{IPn}(0) = 0 , \qquad n = 0,1,2 \ldots, \\ &\dot{\phi}_{IS0}(0) + 1 = 0 , \\ &\dot{\phi}_{ISn}(0) + \phi'_{IPn-1}(0) = 0 \qquad n = 1,2 \ldots \end{aligned}\right\} \tag{80}$$

Since $Y = (1+i)\eta_S$ and $\beta = \frac{1}{\sqrt{iX}} = \frac{1}{\sqrt{X}}\frac{1-i}{\sqrt{2}}$ are complex variables, the function Φ_I and its derivatives are complex functions. Separating into real and imaginary parts, we obtain:

$$\Phi_{IR} = \frac{2\eta_S}{\sqrt{2X}} - \frac{1}{\sqrt{2X}} + \frac{1}{\sqrt{2X}} e^{-\eta_S}(\cos\eta_S - \sin\eta_S) + O(X^{-1}) \tag{81}$$

$$\Phi_{II} = + \frac{1}{\sqrt{2X}} + \frac{1}{\sqrt{2X}} e^{-\eta_S}(-\cos\eta_S - \sin\eta_S) + O(X^{-1}) \tag{82}$$

$$\Phi_{IR\eta} = 1 - e^{-\eta_S}\cos\eta_S + O(X^{-1}) \tag{83}$$

$$\Phi_{II\eta} = e^{-\eta_S}\sin\eta_S + O(X^{-1}) \tag{84}$$

$$\Phi_{IR\eta\eta} = \sqrt{\frac{X}{2}}\, e^{-\eta_S}(\cos\eta_S + \sin\eta_S) + O(X^{-\frac{1}{2}}) \tag{85}$$

$$\Phi_{II\eta\eta} = \sqrt{\frac{X}{2}}\, e^{-\eta_S}(\cos\eta_S - \sin\eta_S) + O(X^{-\frac{1}{2}}) \tag{86}$$

$$X\Phi_{IRX} = -\frac{1}{2\sqrt{2X}}\left[e^{-\eta_S}(\cos\eta_S - \sin\eta_S + 2\eta_S\cos\eta_S) - 1\right] + O(X^{-\frac{1}{2}}) \tag{87}$$

$$X\Phi_{IIX} = -\frac{1}{2\sqrt{2X}}\left[e^{-\eta_S}(-\cos\eta_S - \sin\eta_S - 2\eta_S\sin\eta_S) + 1\right] + O(X^{-\frac{1}{2}}) \tag{88}$$

$$X\Phi_{IR\eta X} = \tfrac{1}{2}\eta_S\, e^{-\eta_S}(\cos\eta_S + \sin\eta_S) + O(X^{-\frac{1}{2}}) \tag{89}$$

$$X\Phi_{II\eta X} = \tfrac{1}{2}\eta_S\, e^{-\eta_S}(\cos\eta_S - \sin\eta_S) + O(X^{-\frac{1}{2}}) \,. \tag{90}$$

The preceding asymptotic solution for Φ_I is valid for large values of the frequency parameter and is identical with Lighthill's well known solution[15]. It turns out that this solution is independent of the function $\bar{U}(x)$. Furthermore it is also identical with the solution which C.C. Lin[16] obtained as a result of the application of his theory for high frequencies. Since C.C. Lin did not assume a series solution in powers of ϵ, it can be concluded that this solution is the exact solution for the disturbance. In other words, for high frequencies the disturbance is proportional to ϵ, and all higher harmonics, i.e. $\epsilon^2\cos 2\omega t$, $\epsilon^2\sin 2\omega t$, $\epsilon^4\cos 4\omega t$, $\epsilon^4\sin 4\omega t$ + ..., are of a smaller order with respect to the frequency parameter X. This will have the consequence that the second-order solution, found from the series expansion method, will give the same result for high frequencies as the exact non-linear theory by C.C. Lin, see Section 7.

5.2.2 *Temperature Field*

In order to solve Equation (23) for the temperature field θ_I, we proceed in the same way as before. We again represent the solution as a sum of two terms

$$\theta_I = \theta_{IS} + \theta_{IP} = \sum_{n=0}^{\infty} \beta^{n+3}\, \theta_{ISn}(Y) + \sum_{n=0}^{\infty} \beta^{n+2}\, \theta_{IPn}(\eta) \tag{91}$$

where the functions $\theta_{ISn}(Y)$ and $\theta_{IPn}(\eta)$ satisfy simple differential equations and the following boundary conditions:

$$\left.\begin{aligned} \theta_{IP0}(0) &= 0\,, \\ \theta_{IPn}(0) + \theta_{ISn-1}(0) &= 0\,, \qquad n = 1,2,3,\ \ldots. \end{aligned}\right\} \tag{92}$$

Separation of the solution into real and imaginary part gives

Pr ≠ 1 :

$$\theta_{IR} = \frac{1}{\sqrt{2}} X^{-\frac{3}{2}} \left\{ m g' + \frac{B_1 \,Pr}{1-Pr}\left(m - \frac{1-m}{1-Pr}\right) e^{-\eta_S}(\cos\eta_S + \sin\eta_S) - \right.$$

$$- \frac{B_1 \,Pr}{1-Pr}(1-m)\eta_S\, e^{-\eta_S}\sin\eta_S - \frac{B_1}{1-Pr}\left[m + (m+1)\frac{Pr}{1-Pr}\right] \cdot$$

$$\left. e^{-\sqrt{Pr}\,\eta_S}(\cos\sqrt{Pr}\,\eta_S + \sin\sqrt{Pr}\,\eta_S)\right\} + O(X^{-2})\,, \tag{93}$$

$$\theta_{IJ} = -\frac{m+1}{2}\eta g' X^{-1} + \frac{1}{\sqrt{2}} X^{-\frac{3}{2}} \left\{ m g' + \frac{B_1 \,Pr}{1-Pr}\left(m - \frac{1-m}{1-Pr}\right) e^{-\eta_S}(\cos\eta_S - \sin\eta_S) - \right.$$

$$\frac{-B_1 \,Pr}{1-Pr}(1-m)\eta_S e^{-\eta_S}\cos\eta_S - \frac{B_1}{1-Pr}\left[m + (m-1)\frac{Pr}{1-Pr}\right] \cdot$$

$$\left. e^{-\sqrt{Pr}\,\eta_S}(\cos\sqrt{Pr}\,\eta_S + \sin\sqrt{Pr}\,\eta_S)\right\} + O\left(X^{-\frac{5}{2}}\right)\,; \tag{94}$$

Pr = 1 :

$$\theta_{IR} = \frac{1}{\sqrt{2}} X^{-\frac{3}{2}} \left\{ m g' - \frac{B_1}{4} e^{-\eta_S}\left[4m(\cos\eta_S + \sin\eta_S) + \right.\right.$$

$$\left.\left. + (5m-1)\eta_S \sin\eta_S - (1-m)\eta_S^2(\sin\eta_S - \cos\eta_S)\right]\right\} + O(X^{-2}) \tag{95}$$

$$\Theta_{IJ} = -\frac{m+1}{2}\eta g' X^{-1} +$$

$$+\frac{1}{\sqrt{2}} X^{-\frac{3}{2}} \left\{ mg' - \frac{B_1}{4} e^{-\eta_S} \left[4m(\cos\eta_S - \sin\eta_S) + (5m-1)\eta_S \cos\eta_S - \right.\right.$$

$$\left.\left. - (1-m)\eta_S^2(\cos\eta_S + \sin\eta_S) \right] \right\} + O\left(X^{-\frac{5}{2}}\right) . \qquad (96)$$

The solution for $Pr \neq 1$ (Eqns. (93), (94)) agrees with the solution found by Lighthill[15], except that in Lighthill's solution the function $g'(\eta)$ is replaced by its value B_1 at the wall. This, however, has the consequence that in Lighthill's solution the function η is not compensated by the function $g'(\eta)$ in the combination $\eta g'(\eta)$ for $\eta \to \infty$. Therefore, Lighthill's temperature distribution tends to infinity for $\eta \to \infty$ instead of tending to zero: by contrast, the solution given in Equation (94) satisfies the proper condition at infinity.

5.3 Second-Order Equations

We consider the solution $\Phi_{II}(X,\eta)$ of Equation (28) for large values of the frequency parameter. The first-order functions on the right hand side are now known from the results found in Section 5.2.1 (from Eqns. (76) to (90)). After substituting these functions into Equation (28) we obtain:

$$\Phi_{II\eta\eta\eta} + \frac{m+1}{2} f\Phi_{II\eta\eta} - 2mf'\Phi_{II\eta} - (1-m)f'X\Phi_{IIX\eta} + (1-m)f'\eta\Phi_{IIX} + \frac{m+1}{2} f''\Phi_{II} =$$

$$-\frac{1}{2} m \left\{ e^{-\eta_S} \left[(2+\eta_S)\cos\eta_S - (1-\eta_S)\sin\eta_S \right] - e^{-2\eta_S} \right\} + O(X^{-1}) . \qquad (97)$$

The solution is once again represented as the sum

$$\Phi_{II} = \Phi_{IIS} + \Phi_{IIP} = \sum_{n=0}^{\infty} \alpha^{n+3} \phi_{IISn}(\eta_S) + \sum_{n=0}^{\infty} \alpha^{n+2} \phi_{IIPn}(\eta) \qquad (98)$$

where

$$\alpha = \sqrt{\frac{2}{X}} \qquad (99)$$

is a new variable, chosen to be analogous to the complex variable β in the first-order solution.

The functions $\phi_{IPn}(\eta)$ and $\phi_{IISn}(\eta_S)$ again satisfy simple differential equations and the following boundary conditions

$$\left.\begin{aligned} &\phi_{IIP0}(0) = 0 , \\ &\phi_{IIPn}(0) + \phi_{IISn-1}(0) = 0 , \qquad n = 1,2 \ldots , \\ &\phi'_{IIPn}(0) + \dot{\phi}_{IISn}(0) = 0 , \qquad n = 0,1,2 \ldots . \end{aligned}\right\} \tag{100}$$

The analogous second-order solution for the temperature field is:

$$\Theta_{II} = \sum_{n=0}^{\infty} \alpha^{n+5} \theta_{IISn}(\eta_S) + \sum_{n=0}^{\infty} \alpha^{n+2} \theta_{IIPn}(\eta) . \tag{101}$$

6. NUMERICAL RESULTS

6.1 Stagnation Point Flow, m = 1

We only consider the functions $\Phi_{I\eta\eta}(0,X)$, $\Phi_I(\infty,X)$, $\Theta_{I\eta}(0,X)$, $\Phi_{II\eta\eta}(0,X)$, $\Phi_{II}(\infty,X)$ and $\Theta_{II\eta}(0,X)$, which are important for the shear stress at the wall, the heat transfer and displacement thickness, respectively, according to Equations (33), (34) and (41). All coefficients of their series for small values of X and for large values of X are collected in Table I and Table 2, respectively. The functions themselves have been plotted in Figures 3 to 8.

The results in Figure 4 for the shear stress oscillations are typical for problems involving oscillations. The amplitude A_τ of the oscillating shear stress at the wall starts with its quasi-steady values at $X = 0$ and increases to infinity for $X \to \infty$. The phase shift λ_τ between the shear stress oscillation and the outer flow velocity oscillation starts from zero for $X = 0$ and increases monotonically to the asymptotic value of $+ 45^0$ at very high frequencies. In other words, the phase of the shear stress oscillations leads the fluctuations in the stream velocity. The physical meaning of this fact is that the velocity in the boundary layer reacts much faster to the outer flow pressure gradient than the outer flow velocity. To the outer flow velocity there corresponds the following pressure gradient:

$$-\frac{1}{\delta}\frac{\partial p}{\partial x} = c^2 x + \epsilon c(\cos\omega t - \omega \sin\omega t) . \tag{102}$$

For large values of the frequency the phase of the pressure fluctuation leads the outer flow velocity fluctuation by 90^0.

The heat transfer fluctuation (Fig.6) shows a completely different characteristic. With increasing frequency the amplitude A_q decreases and tends to zero whereas the phase shift λ_q tends to -90^0, which means that for very high frequencies the phase of the heat transfer fluctuations lags behind that of the outer flow velocity by 90^0.

It can be seen from Equation (42) that the value Δv_∞ is finite and has a time-independent as well as an oscillating part (Fig.8). For very high frequencies the phase of the fluctuating part lags *behind* the phase of the outer flow velocity $U(x,t)$ by 45°. The boundary layer thickness fluctuates with a constant amplitude, i.e. one which is independent of x. In Figure 9 the different oscillatory functions are compared for large frequency values.

The second-order time-independent parts $\Phi''_{II}(0,X)$, $\Theta'_{II}(0,X)$, $\Phi_{II}(\infty,X)$ (Figs.10 to 12) show a tendency to decrease to zero when the frequency increases. In the limit of extremely high frequencies there is no effect on the net shear stress and net heat transfer. The same is valid for the displacement thickness. In the range of small frequencies the shear stress is increased whereas the heat transfer decreases. The maximum effects appear at $X = 0$, i.e. in the quasi-steady case. For this case we have:

$$\frac{\tau_0}{\mu\bar{U}\sqrt{\frac{\bar{U}}{\nu\nu}}} = 1.2326\left(1 + \frac{3}{16}\epsilon^2\right), \qquad \frac{\Delta v_\infty}{\bar{U}\sqrt{\frac{\nu}{Ux}}} = 0.6482\left(1 - \frac{1}{16}\epsilon^2\right)$$

$$\frac{Nu}{\sqrt{\frac{\bar{U}x}{\nu}}} = 0.4959\left(1 - \frac{1}{16}\epsilon^2\right), \qquad Pr = 0.7 \tag{103}$$

6.2 Flow Past a Flat Plate, m = 0

The problem is more complicated than that of a stagnation point flow, because the frequency parameter $X = (\omega x/\bar{U})$ is now variable. Since several authors calculated some of the functions Φ_{In} and Θ_{In}, respectively, for comparison the most important initial derivatives of these functions have been collected from different sources in Tables 3 and 4. The final results are the coefficients of the series expansion given in Table 5. All coefficients in the series for large values of X have been collected in Table 6. The values at the wall ($\eta = 0$) of the functions $\Phi_{IR\eta\eta}$, $\Phi_{IJ\eta\eta}$, $\Theta_{IJ\eta}$, $\Theta_{IR\eta}$, $\Phi_{II\eta\eta}$, $\Theta_{II\eta}$, which give the shear stress at the wall and the heat transfer, respectively, have been plotted in Figures 13 to 18.

The results are, in general, very similar to those for the stagnation point flow. The only essential difference is the behavior of the functions for large values of X. In the flat plate case the functions tend to zero much more rapidly when $X \to \infty$ than was the case in the stagnation-point flow. The effect of the outer flow disturbance on the temperature fluctuations as well as on the net shear stress and net heat transfer is very small for high frequencies. The only exception is the shearing stress fluctuation, whose amplitude still tends to infinity when the frequency increases. This means that even for small values of ϵ the shearing stress will vanish and even turn negative within each fluctuation period if the frequency is high enough. The negative shearing stress at the wall is associated with reverse flow and may lead to a certain kind of separation of the flow and the subsequent formation of vortices or bubbles. If this were the case, the boundary layer equations would cease to govern the process. The fact that the fluctuating disturbance of the steady-state wall shear stress becomes infinitely large does not violate the assumptions made in the series-expansion analysis, because for very large frequencies the radius of

convergence for ϵ becomes infinite, as will be shown in Section 7. The maximum effect of the disturbance on the net shear stress and heat transfer again appear at small values of X. In the limit $X \to 0$ (quasi-steady case) we obtain

$$\frac{\tau_0}{\mu U \sqrt{\frac{U}{\nu x}}} = 0.3321 \left(1 + \frac{3}{16}\epsilon^2\right) \tag{104}$$

$$\frac{Nu}{\sqrt{\frac{Ux}{\nu}}} = -B_1 \left(1 - \frac{1}{16}\epsilon^2\right) \tag{105}$$

where the values of B_1 depend on Prandtl number. The form of Equations (104) and (105) shows clearly that the Reynolds analogy ceases to apply, even in the particular case when $Pr = 1$.

7. LIMITS OF VALIDITY OF THEORY

It is now useful to discuss briefly the fundamental assumptions on which the analysis of this paper was based. This will provide an indication about the limits of the validity of the theory.

(a) *Boundary Layer Concept*

By using the boundary layer equations the fundamental assumptions of boundary layer theory have been implied. This means, that the v-component of the velocity is assumed to be small in comparison with the mean stream velocity, that the pressure gradient perpendicular to the wall is zero and that the wall curvature is negligible. If the boundary layer thickness were to become very large, the boundary layer concept would break down. This is especially the case near or behind a point of separation. Since in our analysis zero or even negative wall shear stresses can occur, reverse flow and local 'separation' render the application of the boundary layer concept at least questionable. On the other hand, in experimental studies with free streams involving outer disturbances, flow separation has been observed[2, 3]; it was even suggested that separation provides the essential mechanism for an increase in heat transfer. If this is the case, it must be realized that the phenomen could not be treated theoretically in a simple way, if at all. It might be mentioned, however, that in the case of the stagnation point flow the boundary layer equations are identical with the Navier-Stokes equations. Therefore, no limitations with respect to the boundary layer concept exist as far as stagnation-point-flow is concerned.

(b) *Series Expansion Method*

In the analysis it was assumed that the flow field as well as the temperature field can be represented by series in powers of the parameter ϵ which multiplies the amplitude of the disturbance. This assumption is only justified if these series converge. No general statement about convergence can be made at present, but from a few results which have been found in special cases, it seems plausible, that at least for small values of ϵ, convergence is assured. An outer flow described by

$U(x,t) = cx + \epsilon \cos\omega t$ lead to an exact solution for all values of ϵ. In this particular case the series consist of one term only, and the radius of convergence is infinite. For an outer flow considered here statements of the convergence can be made for the limiting cases of very low and very high frequency. In the case when $\omega = 0$, the outer flow assumes the simple form

$$U(x) = \bar{U}(1 + \epsilon) \qquad (106)$$

which is independent of time. If we use the well-known results for the wall shear stress and the Nusselt number in steady-state flow $U(x)$, we get

$$\frac{\tau_0}{\mu\bar{U}\sqrt{\frac{\bar{U}}{\nu x}}} = f''(0)(1 + \epsilon)^{\frac{3}{2}}, \qquad \frac{Nu}{\sqrt{\frac{\bar{U}x}{\nu}}} = -g'(0)(1 + \epsilon)^{\frac{1}{2}}. \qquad (107)$$

Expansions into binominal series will converge for $\epsilon \lesssim 1$ and will lead to the quasi-steady solution. In the case of flat-plate ($m = 0$) flow, F.K. Moore and S. Ostrach[17] demonstrated that the radius of convergence ($\epsilon \lesssim 1$) is not restricted to the point $X = (\omega x/\bar{U}) = 0$ itself, but can be extended to the solution at least up to the terms of order X^2. In Section 5 it was found that the first-order solution for high frequency is the complete unsteady part of the solution, because terms proportional to $\epsilon^2 \cos 2\omega t$, $\epsilon^2 \sin 2\omega t$, $\epsilon^4 \cos 4\omega t$, $\epsilon^4 \sin 4\omega t$ were all of a smaller order of magnitude with respect to the reciprocal frequency parameter. Therefore, the second-order solution would give the exact solution for the change in net wall shear stress and heat transfer in this limiting case of high frequency. By comparing the theory of C.C. Lin[16], which is valid for high frequencies and is not based on any assumptions regarding the disturbance amplitude ϵ, with our analysis, one can easily show that C.C. Lin's final equation for Φ would have the same right-hand side and the same highest order term on the left-hand side. In Lin's theory the Equation is, however, non-linear. The method of solving will be the same, namely by splitting up the solution in a Stokes part and a Prandtl part (see also W.E. Gibson[7]). For the Stokes part only the first term of the left-hand side is important. Therefore these two Stokes equations will be identical in Lin's theory as well as in our series expansion method. This has the consequence that the solutions for the shear stress and the heat transfer are identical too. Since in Lin's theory ϵ is not restricted, the radius of convergence is infinite for the limit of high frequencies. In the intermediate range of frequencies it can be assumed that the radius of convergence increases monotonically from $\epsilon = 1$ $(X \to 0)$ to $\epsilon = \infty$ $(X \to \infty)$. At least for values of ϵ which are very small compared with unity, the application of the series expansion method is always justified.

8. CONCLUSIONS

1. The report analyses the two-dimensional, unsteady, laminar, incompressible boundary layer which exists on a wall when the external, free-stream velocity is of the form

$$U(x,t) = cx^m (1 + \epsilon \cos\omega t).$$

The solutions are presented as series expansions in powers of the parameter ϵ, and the first and second-order terms in the solution are calculated.

2. The first-order terms are oscillatory and retain the frequency of the disturbance but display a shift in phase within the boundary layer. The second-order terms consist of parts oscillating with double the frequency and of time-independent parts, which give a change in net wall shear stress and heat transfer.

3. The solutions are presented as series expansions in terms of the frequency parameter

$$X = \frac{\omega x}{\bar{U}}$$

separately for small and for large values of it; these join smoothly in the intermediate frequency range. The limiting cases $X \to 0$ (quasi-steady solution) and $X \to \infty$ (Stokes-type solution lead to comparatively simple solutions.

4. Numerical results are presented for flow near a stagnation point and for flow along a flat plate. The first-order terms display different characteristics for the wall shear stress and the heat transfer rate. The amplitude of the shear stress increases without bound with increasing values of the frequency parameter, whereas the heat transfer-rate amplitude decreases and tends to zero for $X \to \infty$. The phase shift for shear stress and heat transfer rate starts at zero for $X = 0$ and increases to 45° for shear stress and decreases to -90° for heat transfer. The second-order time-independent terms start at the value of the quasi-steady solution, which is positive for the shear-stress (increase in friction) and negative for the heat transfer (decrease in heat transfer) and tend to zero for $X \to \infty$. The curves tend to zero much faster for flat plate flow than for stagnation flow.

5. A brief discussion of the fundamental assumptions used in the mathematical analysis gives some information about the limits of the validity of the theory.

6. The paper is a short version of a more comprehensive investigation of this subject[4].

ACKNOWLEDGEMENT

The work described in the paper was done during 1963, while the author was visiting Associate Professor at Brown University, Providence, R.I. U.S.A. It was made possible owing to the financial assistance provided by the Aerospace Research Laboratories of the Office of Aerospace Research, U.S. Air Force, as part of a program of research under the technical supervision of Dr. M. Scherberg through Contract AF 33(615) - 1263. The author is deeply indebted to Professor Kestin for his kind hospitality and for many stimulating discussions and valuable suggestions concerning this investigation.

REFERENCES

1. **Arduini, C.** — *Strato Limite Incompressibile Laminare Nell'Intorno del Punto di Ristagno di un Cilindro Indefinito Oscillante.* L'Aerotecnica 41, 1961, pp.341-346.

2. **Bayley, F.J. et alii** — *The Effect of Flow Pulsations on Heat Transfer by Forced Convection from a Flat Plate.* International Developments in Heat Transfer 1961, International Heat Transfer Conference, Boulder, Colorado, Part II, p.499-509.

3. **Feiler, Ch.E. Yeager, E.B.** — *Effect of Large-Amplitude Oscillations on Heat Transfer.* NASA TR R-142, 1962,

4. **Gersten, K.** — *Unsteady Laminar Velocity and Thermal Boundary Layers for Wedge Type Flows with Oscillatory Disturbances.* Brown University, Division of Engineering, Report AF 1263/1, 1964.

5. **Gibellato, S.** — *Strato Limite Attorno ad Una Lastra Piana Investita da un Fluido Incompressibile Clotato di una Velocita che e somma di ura Parte Constante e di una Parte Alternata.* Atti Della Accademia Delle Scienze di Torino 89 1954-1955, p.180-192, and Vol.90 1955-1956, p.13-24.

6. **Gibellato, S.** — *Strato Limite Termico Attorno a una Lastra Piana Investita da una Corrente Lievemente Pulsante di Fluido Incompressibile.* Atti Accademia delle Scienze di Torino, 91, 1956-1957, p.152-170.

7. **Gibson, W.E.** — *Unsteady Laminar Boundary Layers.* Ph.D.-Thesis at M.I.T. Department of Mathematics, 1957.

8. **Glauert, M.B.** — *The Laminar Boundary Layer on Oscillating Plates and Cylinders.* Journal of Fluid Mechanics, Vol.1, 1956, p.97-110.

9. **Gosh, A.** — *Contribution a l'Etude de la Couche Limite Laminaire Instationnaire.* Publications Scientifiques et Techniques du Ministère de l'Air. No.381, 1961.

10. **Hill, P.G. Stenning, A.H.** — *Laminar Boundary Layers in Oscillatory Flow.* Trans. ASME 82D (Journal of Basic Engineering), 1960, p.593-608.

11. **Hori, E.** — *Unsteady Boundary Layers* (4 Reports), Bulletin of JSME, Vol.4 1961, p.664-671; Vol.5, 1962, p.57-64; Vol.5, 1962, p.64-72; Vol.5, 1962, p.461-470.

12. Hori, E. — *Experiments on the Boundary Layer of an Oscillating Circular Cylinder.* Bulletin of JSME Vol.6, 1963, p.201-209.

13. Kestin, J. et alii — *On Boundary Layers Associated with Oscillating Streams.* Applied Scientific Research A, Vol.10, 1961, p.1-22.

14. Lam, S.H. Rott, N. — *Theory of Linearized Time Dependent Boundary Layers.* Technical Note of Cornell University, Graduate School of Aero. Engineering AFOSR TN-60-1100, 1960. See also: 'Matching' problems in the theory of the time-dependent boundary layer. Proceeding 10th International Congress Applied Mechanics, Stresa, 1960, 239-240.

15. Lighthill, M.J. — *The Response of Laminar Skin Friction and Heat Transfer to Fluctuations in the Stream Velocity.* Proceedings Royal Society A, Vol.224, 1954, p.1-23.

16. Lin, C.C. — *Motion in the Boundary Layer with a Rapidly Oscillating External Flow.* Proceeding 9th International Congress Applied Mechanics, Brussels, 1957, Vol.4, p.155-167.

17. Moore, F.K. Ostrach, S. — *Average Properties of Compressible Laminar Layer on Flat Plate with Unsteady Flight Velocity.* NACA-TR 1325, 1957, see also NACA TN 2471, 1951 and TN 3569, 1955.

18. Moore, F.K. — *Aerodynamic Effects of Boundary Layer Unsteadiness.* Proceedings 6th Anglo-American Aeronautical Conference, Folkestone, 1957, p.439-471.

19. Nickerson, R.J. — *The Effect of Free-Stream Oscillation on the Laminar Boundary Layers on a Flat Plate.* ScD-thesis at M.I.T. Department of Mechanical Engineering 1957. Also: WADC TR 57-481, ASTIA Document No.AD 210477, 1958.

20. Rott, N. — *Unsteady Viscous Flow in the Vicinity of a Stagnation Point.* Quarterly Journal of Mechanics and Applied Mathematics, Vol.13, 1956, p.444-451.

21. Rott, N. Rosenzweig, M.L. — *On the Response of the Laminar Boundary Layer to Small Fluctuations of the Free-Stream Velocity.* Journal of the Aeronautical Space Sciences, Vol.27, 1960, p.741-747, 787.

22. Rott, N. — *Theory of Time-Dependent Laminar Flows.* High Speed Aerodynamics and Jet Propulsion, Vol.VI (Editor: F.K. Moore), Princeton, 1964.

23. Schlichting, H. — *Boundary Layer Theory.* Translated by J. Kestin, 4th Edition, McGraw-Hill 1960.

24. Stewartson, K. — *The Theory of Unsteady Laminar Boundary Layers.* Adv. Applied Mechanics, VI 1960, p.1-37.

25. Stuart, J.T. *A Solution of the Navier-Stokes and Energy Equations Illustrating the Response of Skin Friction and Temperature of an Infinite Plate Thermometer to Fluctuations in the Stream Velocity.* Proceedings Royal Society A, 231 1955, p.116-130.

26. Stuart, J.T. *Unsteady Boundary Layers.* In: *Laminar Boundary Layers.* Edited by L. Rosenhead, Clarendon Press, Oxford, Press 1963, p.349-408.

27. Watson, J. *A Solution of the Navier-Stokes-Equations, Illustrating the Response of a Laminar Boundary Layer to a Given Change in the External Stream Velocity.* Quarterly Journal of Mechanics and Applied Mathematics 11, 1958, p.302-325.

28. Watson, J. *The Two-Dimensional Lam nar Flow Near the Stagnation Point of a Cylinder which has an Arbitrary Transverse Motion.* Quarterly Journal of Mechanics and Applied Mathematics 12, 1959, p.175-190.

Table 2

Stagnation Flow (m = 1). Coefficients of the Series Expansions for Large Values X (Pr = 0.7)

	$X^{\frac{1}{2}}$	X^{0}	$X^{-\frac{1}{2}}$	X^{-1}	$X^{-\frac{3}{2}}$	X^{-2}
$\Phi''_{IR}(0)$	0.7071	0	1.4142	0	-0.3094	
$\Phi''_{IJ}(0)$	0.7071	0	-1.4142	1.0785	-0.3094	0
$\Phi_{IR}(\infty)$	0	η	-0.7071	0	+2.1213	-3.7333
$\Phi_{IJ}(\infty)$	0	0	0.7071	-1.9437	+2.1213	0
$\Theta'_{IR}(0)$	0	0	0	0	0	+0.5400
$\Theta'_{IJ}(0)$	0	0	0	0.2700	0	0
$\Phi''_{II}(0)$	0	0	0.3536	0		
$\Phi_{II}(\infty)$	0	0	0	-0.6084		
$\Theta'_{II}(0)$	0	0	0	0.1496		

Table 2

Stagnation Flow (n = 1). Coefficients of the Series Expansions for Large Values X (Pr = 0.7)

	X^1	X^0	X^{-1}	X^{-2}	$X^{-\frac{3}{2}}$	X^{-3}
$\Phi^r_{12}(0)$	0.7071	0	-1.1142	0	-0.3064	
$\Phi^r_{13}(0)$	0.7071	0	-1.4142	1.0735	-0.3094	0
$\Phi_{12}(\infty)$	0	0	-0.7071	0	-1.1213	-3.7333
$\Phi_{13}(\infty)$	0	0	0.7071	-1.9437	-2.1213	0
$\Theta^r_{12}(0)$	0	0	0	0	0	+0.5400
$\Theta^r_{13}(0)$	0	0	0	0.2700	0	0
$\Phi^r_{11}(0)$	0	0	0.3536	0		
$\Phi_{11}(\infty)$	0	0	0	-0.5994		
$\Theta^r_{11}(0)$	0	0	0	0.1436		

Table 3

Flat Plate Flow (m = 0). Comparison of the initial Values of the Flow Solutions, Found by Different Authors

$\Phi''_{I_1}(0)$	=	0.8485	F.K. Moore[18]
		0.8485	N. Rott, M.L. Rosenzweig[21]
		0.8485	S.H. Lam, N. Rott[14]
		0.8485	R.I. Nickerson[19]
		0.8488	C.R. Illingsworth (Journal of Fluid Mechanics Vol.3, 1958)
		0.859	A Gosh[9]
		0.838	S. Gibellato[5]
$\Phi''_{I_2}(0)$	=	-0.4696	F.J. Moore[18]
		-0.4697	S.H. Lam, N. Rott[14]
		-0.4697	R.I. Nickerson[19]
		-0.468	A. Gosh[9]
		-0.465	S. Gibellato[5]
$\Phi''_{I_3}(0)$	=	0.3677	R.I. Nickerson[19]
		0.3677	S.H. Lam, N. Rott[14]
		0.386	A. Gosh[9]
$\Phi''_{I_4}(0)$	=	-0.2695	R.I. Nickerson[19]
		-0.2695	S.H. Lam, N. Rott[14]
		-0.282	A. Gosh[9]
$\Phi''_{I_5}(0)$	=	0.1739	R.I. Nickerson[19]
		0.1769	S.H. Lam, N. Rott[14]
		0.18	A. Gosh[9]

Table 4

Flat Plate Flow (m = 0). Comparison of the Initial Values of the Temperature Solutions, Found by Different Authors for Pr = 0.7, Pr = 0.72 and Pr = 1.0

Pr = 1.0	Pr = 0.72	Pr = 0.70
$g_0'(0) = -0.3321$ (Reynolds Analogy)	$g_0'(0) = -0.2956$ (Moore[18])	$g_0'(0) = -0.2927$ (Nickerson[19])
$\Theta_{I0}'(0) = -0.1660$	$\Theta_{I0}'(0) = -0.1478$	$\Theta_{I0}'(0) = -0.1464$
$\Theta_{I1}'(0) = 0.0271$ $\Theta_{I1}'(0) = 0.0265$ (Gibellato[6])	$\Theta_{I1}'(0) = 0.0205$ (Ostrach[18]) $\Theta_{I1}'(0) = 0.0205$ (Illingworth, Journal of Fluid Mechanics Vol.3 1958)	$\Theta_{I1}'(0) = 0.0199$ (Nickerson[19]) $\Theta_{I1}'(0) = 0.0195$ (Gibellato[6])
$\Theta_{I2}'(0) = 0.1470$ $\Theta_{I2}'(0) = 0.145$ (Gibellato[6])	$\Theta_{I2}'(0) = 0.1251$ (Ostrach[18])	$\Theta_{I2}'(0) = 0.1234$ $\Theta_{I2}'(0) = 0.125$ (Gibellato[6])
$\Theta_{I3}'(0) = -0.2303$		$\Theta_{I3}'(0) = -0.1846$
$\Theta_{I4}'(0) = 0.2176$		$\Theta_{I4}'(0) = 0.1695$
$\Theta_{I5}'(0) = -0.1597$		$\Theta_{I5}'(0) = -0.1221$
$\Theta_{II0}'(0) = 0.0208$	$\Theta_{II0}'(0) = 0.0185$	$\Theta_{II0}'(0) = 0.0183$
$\Theta_{II2}'(0) = -0.1441$	$\Theta_{II2}'(0) = -0.1223$	$\Theta_{II2}'(0) = -0.1204$
$\Theta_{II4}'(0) = -0.2068$		$\Theta_{II4}'(0) = -0.1642$

Table 5

Flat Plate Flow ($m_1 = 0$). Coefficients of the Series Expansions for Small Values X. (Pr = 0.7, 0.72 and Pr = 1.0)

		X^0	X	X^2	X^3	X^4	X^5
$\Phi_{IR\eta\eta}(0)$		0.4981	0	0.4697	0	-0.2695	0
$\Phi_{IJ\eta\eta}(0)$		0	0.8485	0	-0.3677	0	0.1769
$\Phi_{IR}(\infty)$		η - 0.8604	0	1.1947	0	-0.7744	0
$\Phi_{IJ}(\infty)$		0	1.0284	0	-1.0577	0	0.4931
$\Theta_{IR\eta}(0)$	Pr = 0.7	-0.1464	0	-0.1234	0	0.1695	0
	Pr = 0.72	-0.1478		-0.1251			
	Pr = 1.0	-0.1660		-0.1470		0.2176	
$\Theta_{IJ\eta}(0)$	Pr = 0.7	0	0.0199	0	+0.1846	0	-0.1221
	Pr = 0.72		0.0205				
	Pr = 1.0		0.0271		0.2303		-0.1597
$\Phi_{II\eta\eta}(0)$		0.0623	0	-0.2168	0	0.1946	0
$\Phi_{II}(\infty)$		0.1076	0	-1.1103	0	0.8721	0
$\Theta_{II\eta}(0)$	Pr = 0.7	0.0183	0	0.1204	0	-0.1642	0
	Pr = 0.72	0.0185		0.1223			
	Pr = 1.0	0.0208		0.1441		-0.2068	

Table 6

Flat Plate Flow ($\alpha = 0$). Coefficients of the Series Expansions for Large Values X. (Pr = 0.7, 0.72 and Pr = 1.0)

		$X^{\frac{1}{2}}$	X^{0}	$X^{-\frac{1}{2}}$	X^{-1}	$X^{-\frac{3}{2}}$	X^{-2}	$X^{-\frac{5}{2}}$
$\Phi_{IIwww}(\theta)$		0.7071	0	0	0	0	0	0.00585
$\Phi_{IIwww}(\theta)$		0.7071	0	0	-0.1038	0	0	-0.00585
$\Phi_{II}(\infty)$		0	0	-0.7071	0	0	+0.2586	0
$\Phi_{II}(\infty)$		0	0	-0.7071	-0.8604	0	0	0
$\theta_{IIwww}(\theta)$	Pr = 0.7 Pr = 0.72 Pr = 1.0	0	0	0	0	0	0	+0.1584
$\theta_{IIwww}(\theta)$	Pr = 0.7 Pr = 0.72 Pr = 1.0	0	0	0	+0.1168 +0.1167 +0.1254	0	0	-0.1584
$\Phi_{IIwww}(\theta)$		0	0	0	0	0		
$\Phi_{II}(\infty)$		0	0	0	0	0		
$\theta_{IIwww}(\theta)$	Pr = 0.7 Pr = 0.72 Pr = 1.0	0	0	0	0	0		

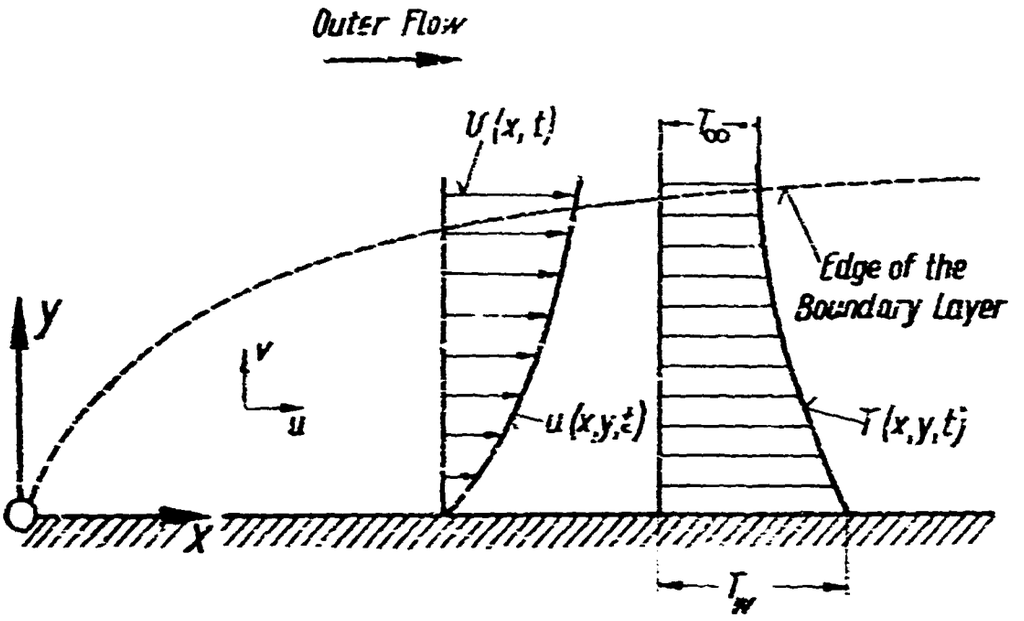

Fig.1 Sketch of boundary layer on a wall

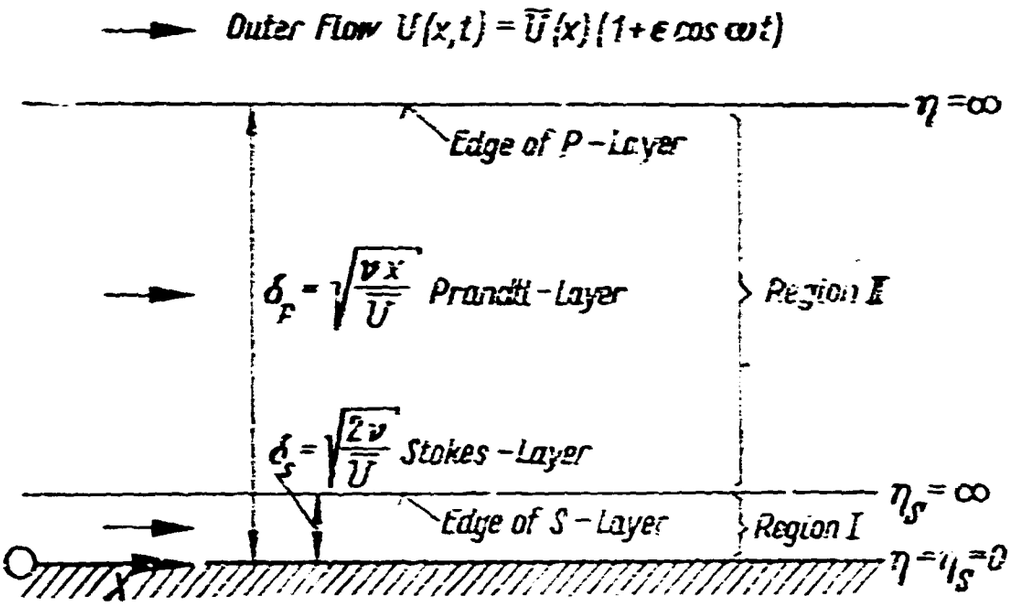

Fig.2 Stokes layer in the boundary layer

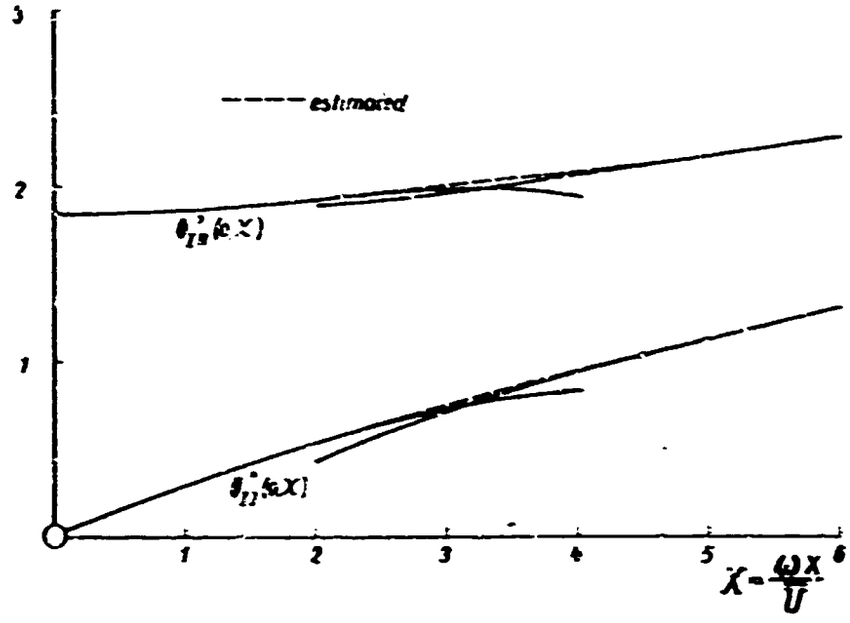

Fig.3 Stagnation flow (n = 1). First-order flow, solution $\Phi_1''(0,X)$. Real and imaginary part

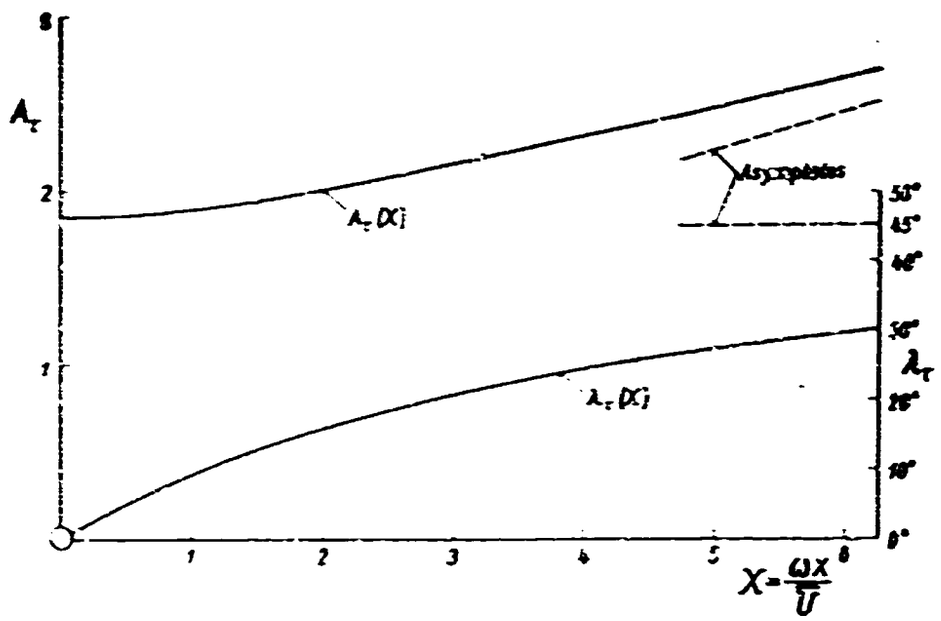

Fig.4 Stagnation flow (n = 1). First-order flow solution. Amplitude $A_\tau(X)$ and phase shift $\lambda_\tau(X)$

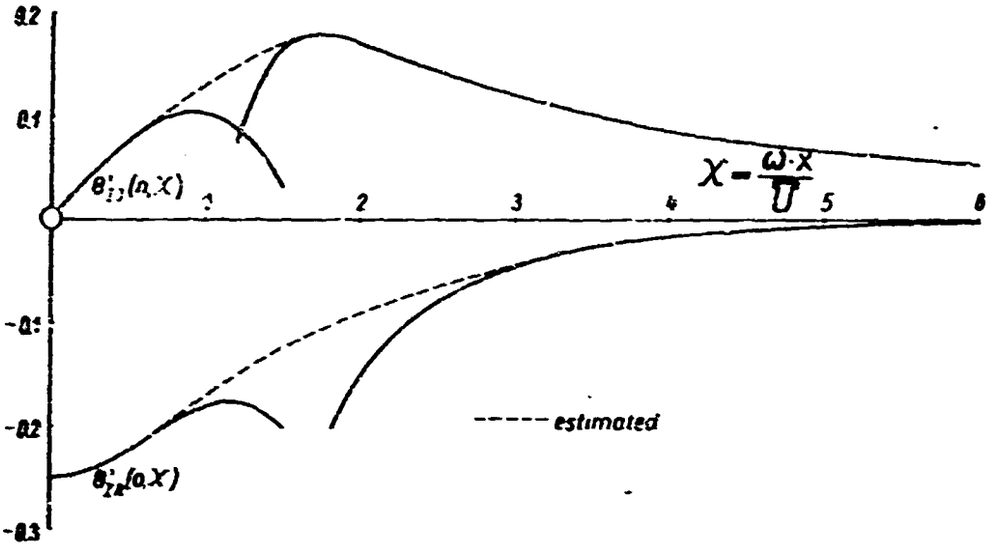

Fig.5 Stagnation flow (n = 1). First-order temperature solution $\vartheta_I'(0,X)$ for Pr = 0.7 . Real and imaginary part

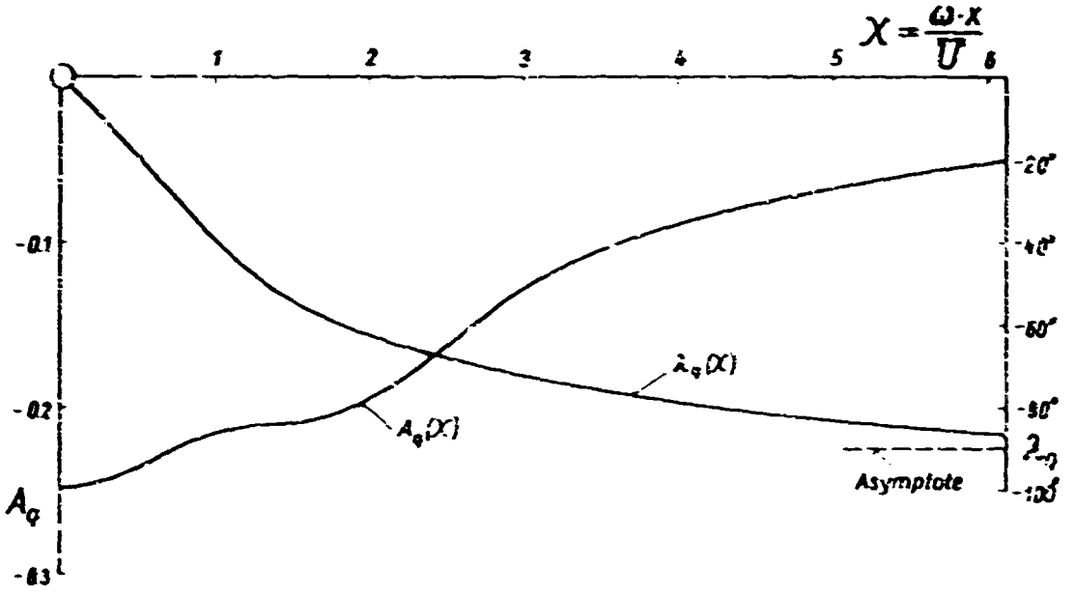

Fig.6 Stagnation flow (n = 1). First-order temperature solution for Pr = 0.7 . Amplitude $A_Q(X)$ and phase shift $\lambda_Q(X)$

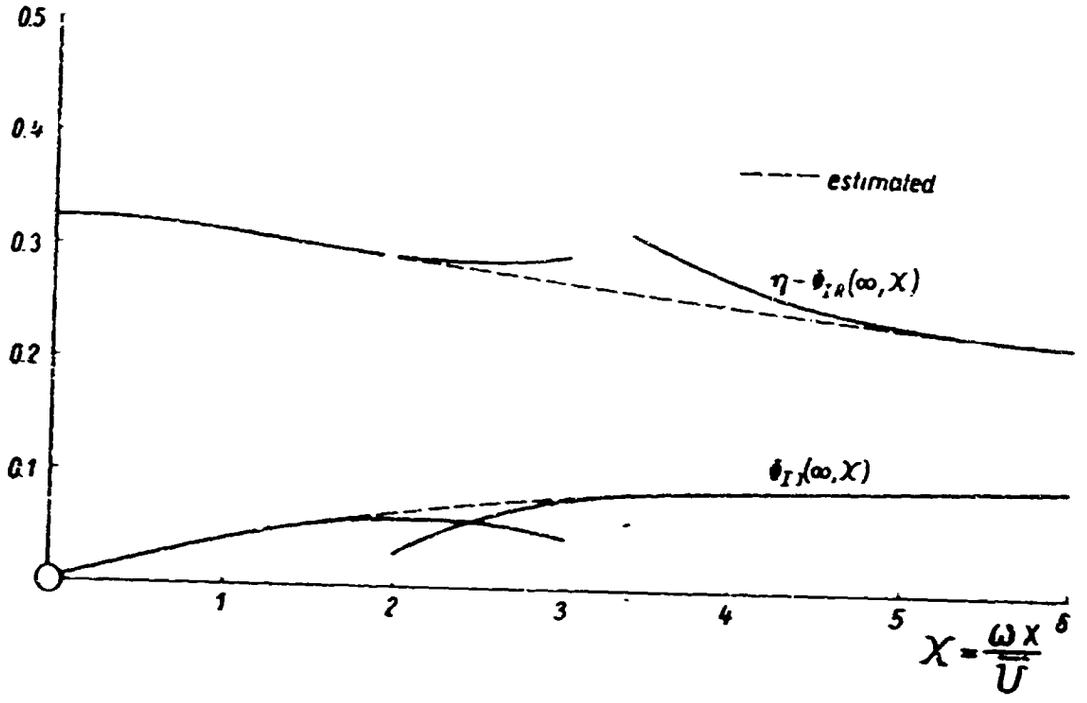

Fig.7 Stagnation flow (m = 1). First-order flow solution $\Phi_I(\infty, X)$. Real and imaginary part

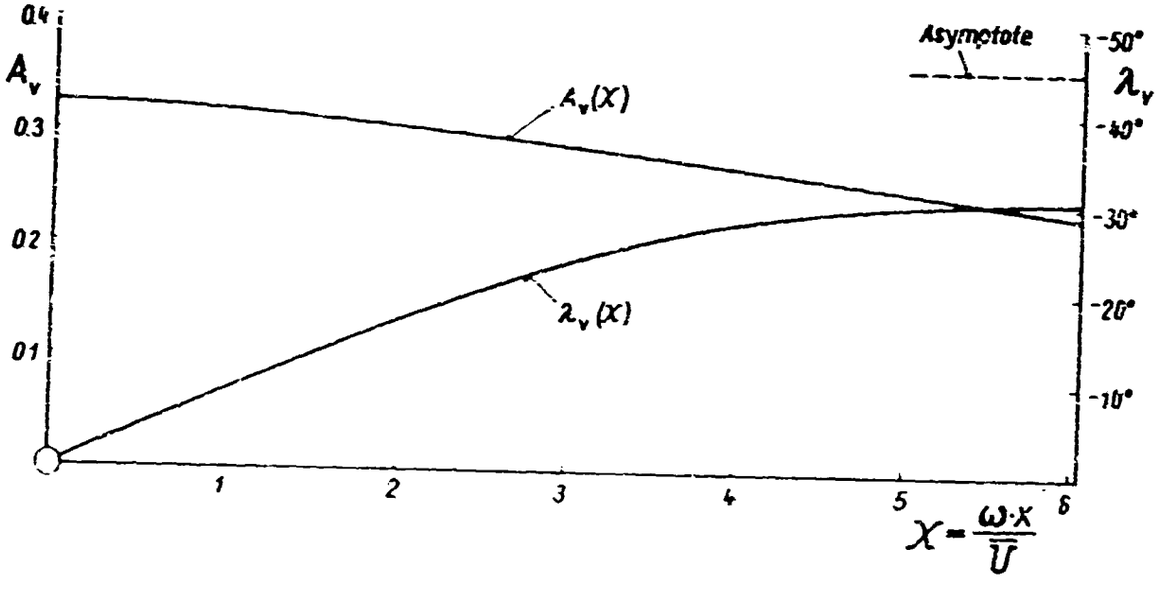

Fig.8 Stagnation flow (m = 1). First-order flow solution. Amplitude $A_v(X)$ and phase shift $\lambda_v(X)$

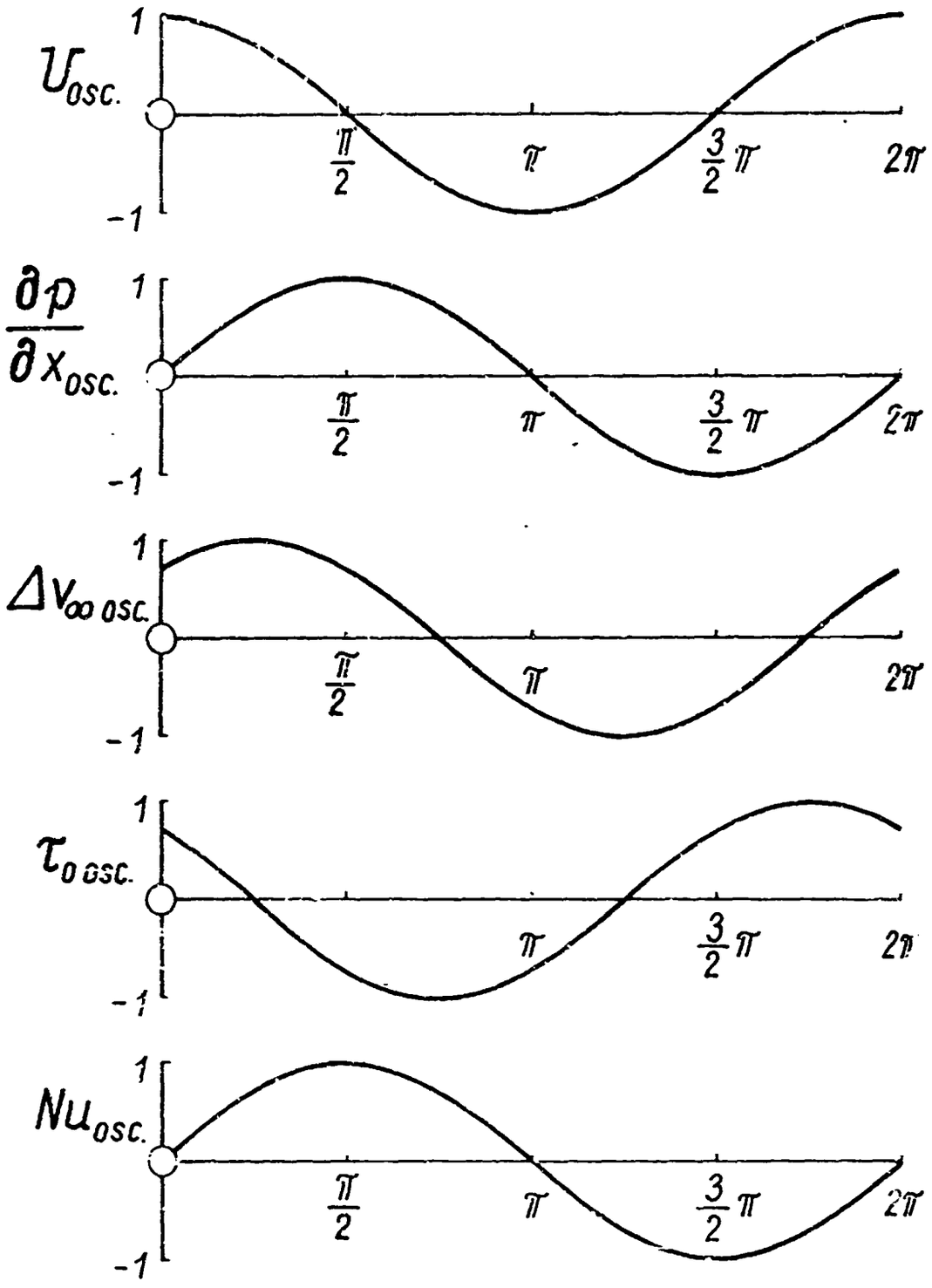

Fig.9 Comparison of the oscillatory parts of the characteristic values of flow and temperature field at very high frequency parameter ($X \to \infty$)

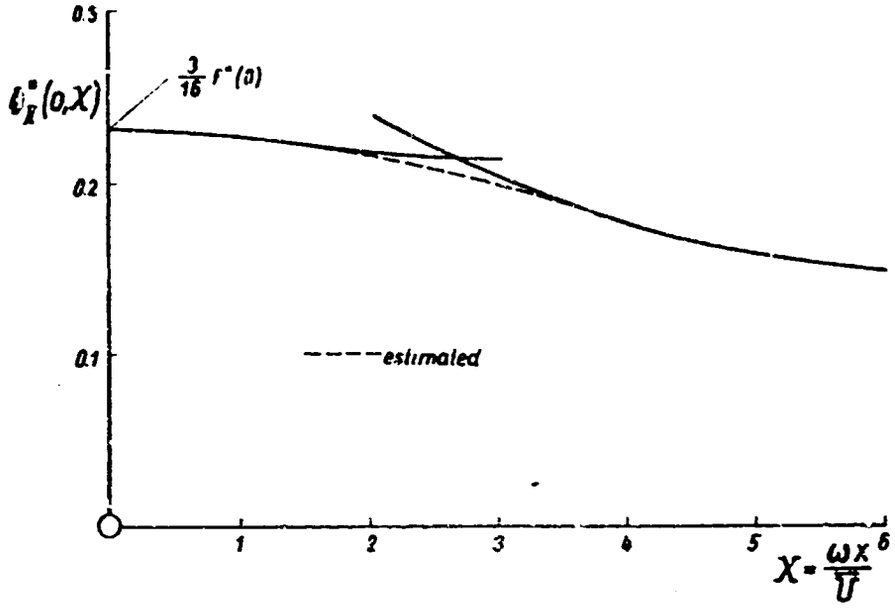

Fig.10 Stagnation flow (m = 1). Second-order flow solution $\Phi_I''(0,X)$

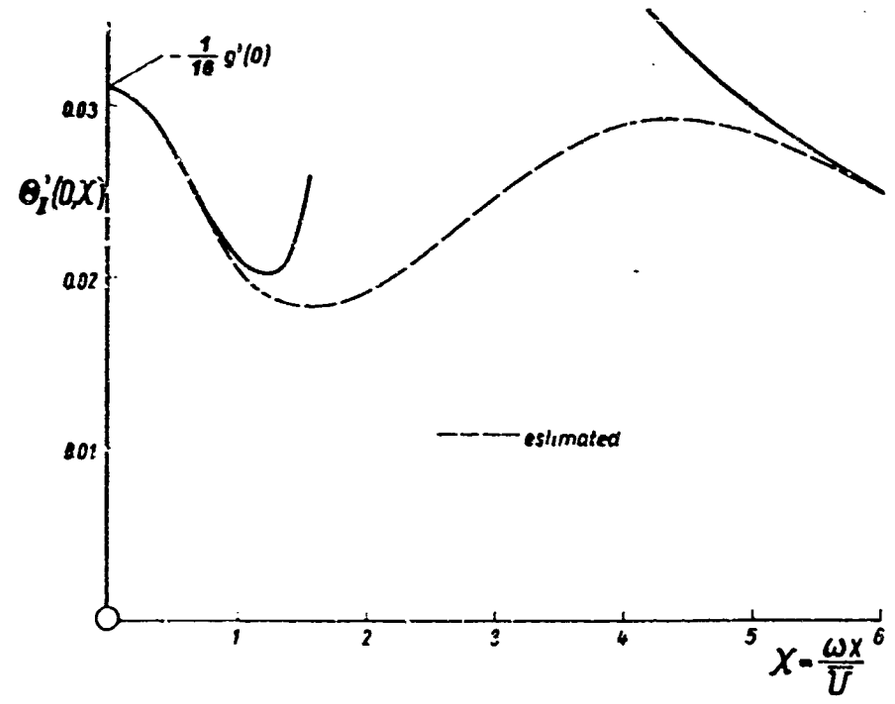

Fig.11 Stagnation flow (m = 1). Second-order temperature solution $\Theta_{II}^{i}(0,X)$ for Pr = 0.7

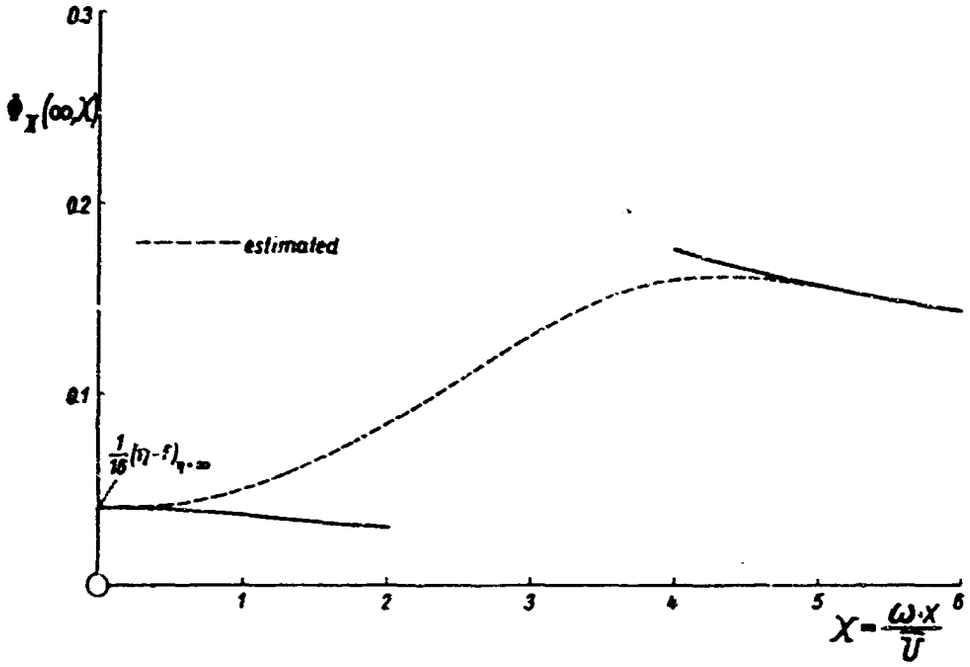

Fig.12 Stagnation flow (m = 1). Second-order flow solution $\Phi_{II}(\infty,X)$

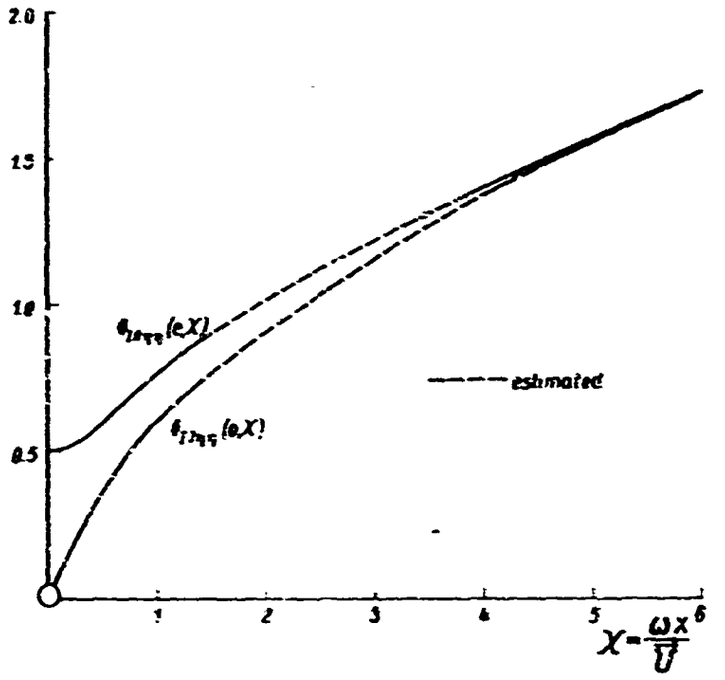

Fig.13 Flat plate flow (m = 0). First-order flow solution $\Phi_{I\eta\eta}(0,X)$. Real and imaginary part

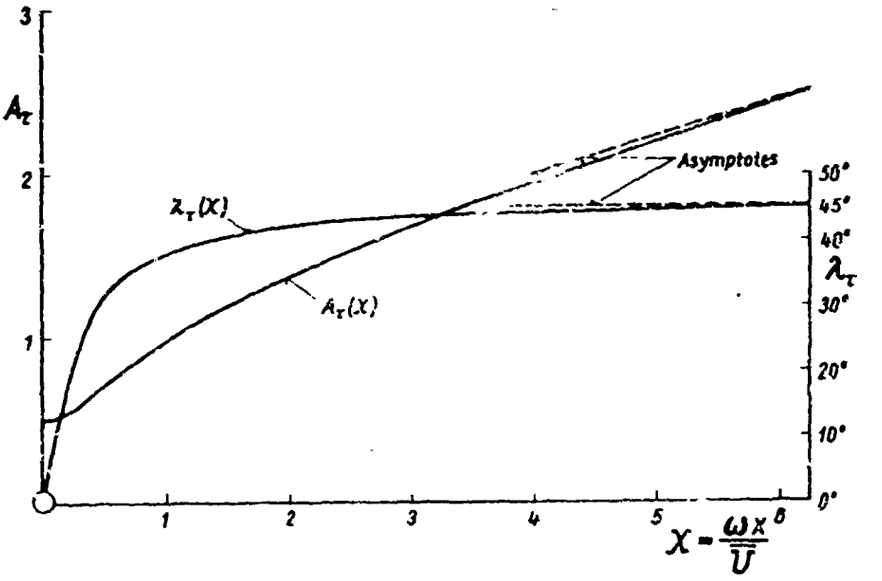

Fig.14 Flat plate flow (m = 0). First-order flow solution. Amplitude $A_\tau(X)$ and phase shift $\lambda_\tau(X)$

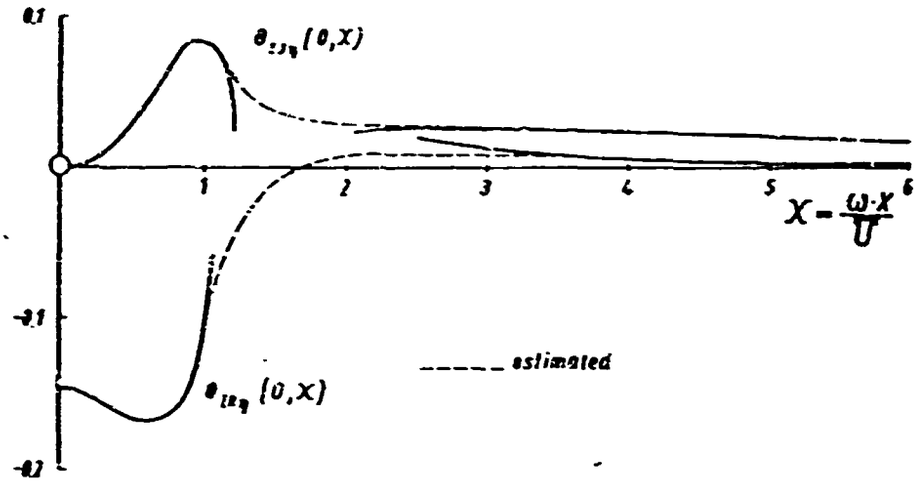

Fig. 15 Flat plate flow (m = 0). First-order temperature solution $\theta_{I\eta}(0,X)$ for Pr = 0.7 . Real and imaginary part

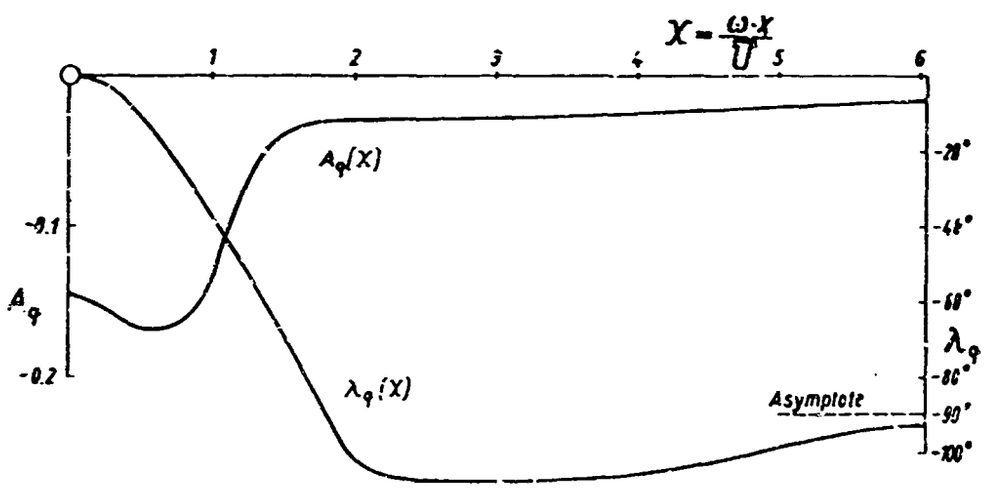

Fig. 16 Flat plate flow (m = 0). First-order temperature solution for Pr = 0.7. Amplitude $A_q(X)$ and phase shift $\lambda_q(X)$

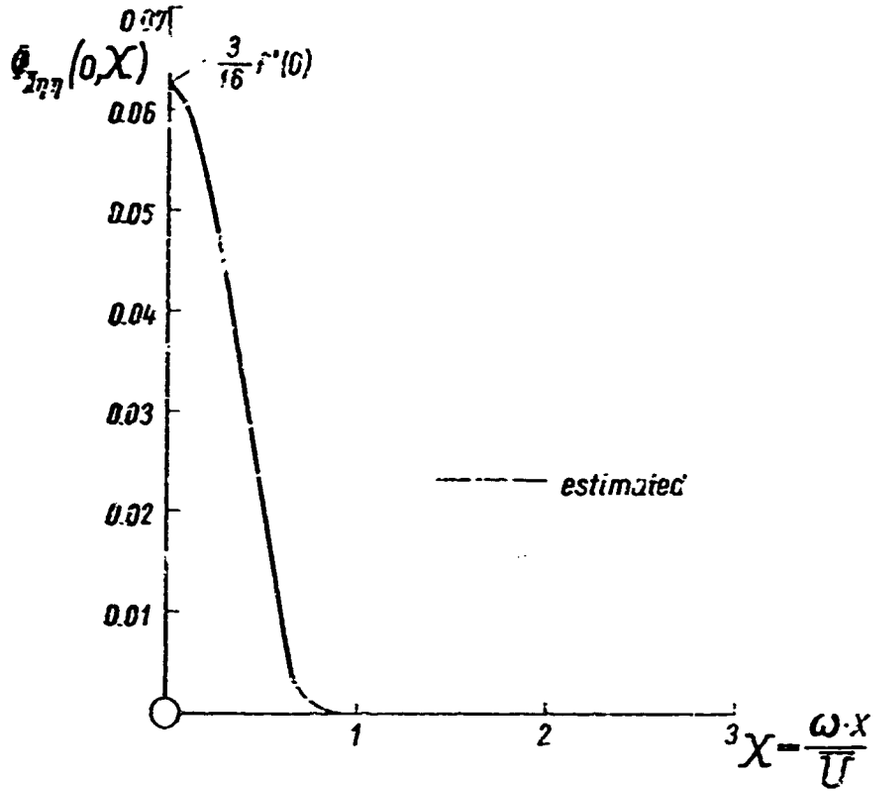

Fig. 17 Flat plate flow (m = 0). Second-order flow solution $\Phi_{II\eta\eta}(0,X)$

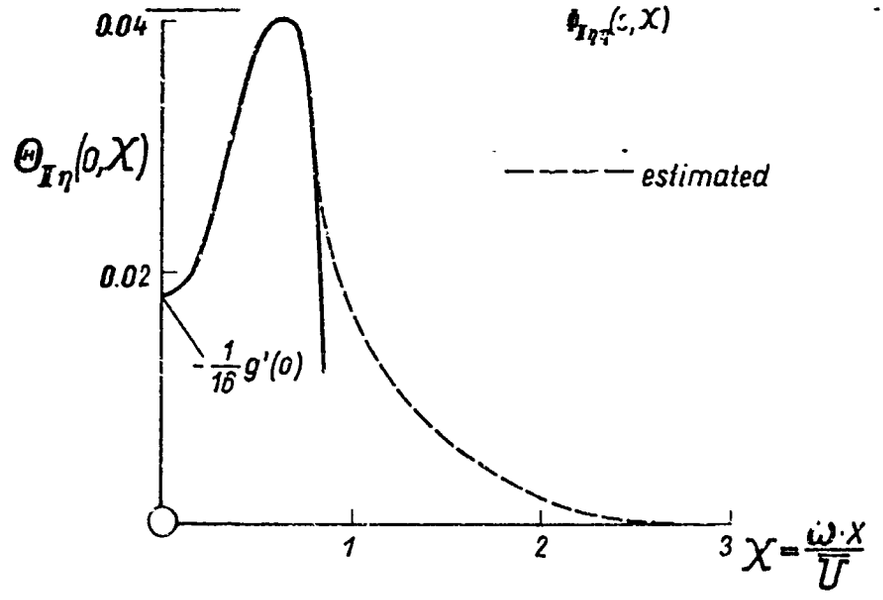

Fig. 18 Flat plate flow (m = 0). Second-order temperature solution $\Theta_{II\eta}(0,X)$ for Pr = 0.7

TRANSITION REVERSAL ON A FLAT PLATE AT HYPERSONIC SPEEDS

by

B.E. Richards and J.L. Stollery

Aeronautics Department,
Imperial College,
London, U.K.

SUMMARY

The variation of transition Reynolds number with wall temperature has been studied experimentally using a sharp-edged smooth flat plate. Early measurements were made at Mach numbers of 7.5 and 10 in a conical flow. More recently some experimental data at M = 8.2 have been obtained in a more uniform stream. These more recent data are reported in this note.

The transition region was determined from focussed shadowgraph pictures and checked by taking heat transfer rate measurements along the plate and pitot pressure traverses through the boundary layer.

Indications are that for a given unit Reynolds number, plate geometry and Mach number it is possible for the transition point to first move back, then advance and finally again recede as the wall temperature is reduced. This pattern of movement supports the theoretical prediction of Reshotko (1963).

SOMMAIRE

Les variations du nombre de Reynolds dans la zone de la transition, en fonction de la température des parois, ont été étudiées expérimentalement à l'aide d'une plaque plane, lisse et aux bords tranchants. On a d'abord effectué des mesures, dans un écoulement conique, à Mach 7,5 et 10. Plus récemment, on a obtenu dans un écoulement plus uniforme, des données expérimentales pour Mach 8,2, données qui sont exposées au cours de cette communication.

La zone de transition a été déterminée à l'aide d'images strioscopiques convergentes et vérifiée par des mesures du taux de transfert de chaleur le long de la plaque et par des prises de pression génératrice indiquée à travers la couche limite.

Il apparaît que, pour un nombre de Reynolds, une géométrie de plaque et un nombre de Mach donnés, le point de transition peut tout d'abord reculer, puis avancer, pour finalement reculer à nouveau au fur et à mesure que la température des parois diminue. Ce schéma de mouvement vient confirmer les prédictions théoriques de Reshotko (1963).

CONTENTS

LIST OF FIGURES

NOTATION

C^*	coefficient in $\frac{\mu^*}{\mu_\infty} = C^* \frac{T^*}{T_\infty}$
C_F	average skin friction coefficient
C_f	local skin friction coefficient
C_p	specific heat
M	Mach number
p_0	pitot pressure lb/in^2
Pr	Prandtl number
$\dot{q}$	heat transfer rate B.Th.U/ft^2 sec
Re_x	Reynolds number at $x - \frac{\rho_\infty u_\infty x}{\mu_\infty}$
Re_t	transition Reynolds number $- \frac{\rho_\infty u_\infty x_t}{\mu_\infty}$
$Re_{min,crit}$	minimum critical Reynolds number
t	time
T	temperature
T^*	reference temperature
T_0	total temperature
T_r	recovery temperature
T_w	wall temperature
u	velocity component parallel to flat plate surface
x	distance from leading edge
x_t	distance of transition point from leading edge as indicated by shadowgraph
x_v	distance from virtual origin of turbulent boundary layer
y	vertical co-ordinate measured from flat plate surface

γ	ratio of specific heats
δ	boundary layer thickness taken at $\frac{u}{u_\infty} = 0.99$
μ	viscosity
ρ	density

Subscripts

∞	local conditions at outer edge of boundary layer, assumed equal to freestream conditions
T*	based on reference temperature conditions

Superscript

*	denotes parameter evaluated at reference temperature T*

TRANSITION REVERSAL ON A FLAT PLATE AT HYPERSONIC SPEEDS

B.E. Richards and J.L. Stollery

1. INTRODUCTION

Jack, Wisniewski and Diaconis (1957) obtained the first experimental indication of transition reversal on a cone at a Mach number of 3.1. They found that starting with a wall temperature about one quarter of the recovery temperature the transition point on the cone moved unexpectedly back as the wall temperature increased. Only at the higher wall temperatures did the transition point "reverse" its direction and exhibit the expected upstream movement with heating.

In a later paper Wisniewski and Jack (1961) report data at $M = 3.8$ in which there are two "reversals', see Figure 6. The latter data and some more recent results of Lyons et alii (1964) at $M = 5$ give some support to the theoretical predictions of Reshotko (1963). Reshotko completed the extension of the Tollmien-Schlichting instability theory to compressible flat plate boundary layers, taking into account both temperature and velocity fluctuations and applying the appropriate boundary conditions. He found that there were two loops in the plot of wall temperature against Mach number (Fig.7(a)) within which the compressible laminar boundary layer was completely stable to small disturbances. From this result Reshotko conjectures that the "double reversal" pattern of transition point movement with wall temperature at a given Mach number (Fig.7(b) and (c)) is likely at supersonic and hypersonic Mach numbers. More recently Lees (1964) has reported some numerical solutions of the complete small disturbance equations, obtained by Dr. Leslie Mack of Jet Propulsion Laboratory, which indicate that an even more complex variation of transition point position is possible.

The complete absence of data at Mach numbers greater than 5 encouraged the authors to attempt measurements of transition position on a highly cooled flat plate at Mach numbers between 7 and 10 using the gun tunnel. Preliminary tests, using a conical nozzle, at $M = 10$ and 7.5 showed that at the lower Mach number with a unit Re of 8.9×10^5 per in and $T_w/T_r = 0.51$ natural transition occurred at $Re_x = 5.3 \times 10^6$. At the higher Mach number the unit Reynolds number available was only 5.0×10^5 per in and the boundary layer remained laminar over the entire plate length. It was recognised that an intermittent tunnel employing a shock compression heater was not the ideal facility for this type of investigation but the experimental simplicity of obtaining constant temperature wall conditions at hypersonic speeds in the range $0.50 > T_w/T_r > 0.05$ keeping every other parameter constant suggested that the transition reversal pattern should be qualitatively correct. Hence a detailed investigation was made at $M = 8.2$ using a contoured nozzle to provide a more uniform stream with no axial pressure gradient in the test section.

2. APPARATUS

2.1 The Gun Tunnel

The Imperial College gun tunnel has been described by Stollery et alii (1960) and by Needham (1963). Briefly it is a blow down tunnel with a shock compression heater. The shock is generated by compressed air driving a free light piston down a 20 ft long barrel filled with the test gas (air) All tests were made using a driver pressure of 2615 lb/in^2. The barrel pressure was varied between 15 and 100 lb/in^2 to change the recovery temperature (T_r) and hence the unit Reynolds number.

The 7½ in exit diameter contoured nozzle gave a parallel flow with a 6 in useful core. An open jet test section was used and the useful tunnel running time was around 40 milliseconds. Other details of these and earlier conditions are given in the table below.

Mach number	7.5 -	8.2
Type of nozzle	Conical	Contoured
Reynolds number per inch	$3 \times 10^5 - 8.9 \times 10^5$	$2.5 \times 10^5 - 7.1 \times 10^5$
Reservoir temperature °K	1290 - 665	1230 - 665
Reservoir pressure lb/in^2	1580	1580
Static pressure lb/in^2	0.254	0.138
Recovery temperature °K	1030 - 535	1030 - 535
Mach number gradient	7.5 to 8.2 over 8 in	none
Static pressure gradient	0.254 - 0.138 over 8 in	none

2.2 Model Details

The flat plate models are shown in Figure 1. Both models were pedestal mounted at zero incidence in the open jet test section below the centre line. Side curtains extending below the model were fitted as shown in Figure 1(c) to prevent disturbances from the lower surface influencing conditions on the upper test surface.

2.2.1 *The Heat Transfer Model (A) - Figure 1(a)*

This model was a 5 in span 11.5 in chord flat plate with a leading edge thickness of approximately 0.001 in. Forty thin film platinum resistance gauges at ¼ in intervals were baked on a Pyrex plate let into the model, as shown in Figure 1(a). At the ends of each gauge a 0.020 in hole, drilled ultrasonically, allowed the lead wires to be taken away under the Pyrex plate. In order that localised high resistances on the gauge are not formed, due to painting the platinum round sharp corners, the holes were radiussed into the upper surface of the Pyrex by means of an etching process using hydrofluoric acid. Each countersunk volume and hole was filled with silver paint, in order to connect the platinum gauges with the lead wires, leaving the top surface with no projections.

Eight pairs of gauges were distributed along chordwise lines ¾ in on either side of the centre line to check the two dimensional nature of the flow. No provision was made for cooling this model since its purpose was to check the photographic method of determining the transition point.

2.2.2 *The Cold Wall Model (B) – Figure 1(b)*

The second model, a 5 in span 14.25 in chord flat plate, had a leading edge thickness of 0.0006 in ± 0.0002 as measured by a short-focus microscope on a Société Genevoise Universal Measuring Machine. The test surface had a finish of 16 micro-inches centre line average value and carried no surface instrumentation. The surface finish was measured with a Rank Taylor-Hobson Talysurf and the reading of a centre line average value is the average height above and below a mean line taken over a distance of 0.03 in.

The model was constructed with cooling passages (see Fig.1(c)) through which liquid nitrogen was gravity-fed until the desired wall temperature was reached. A fixed restriction in the inlet pipe limited the flow of nitrogen and prevented "blow back". Seven copper-constantan thermocouples were mounted close to the model surface and distributed as shown in the figure. It was found that for a nitrogen throughput of approximately 0.5 lb/min the model cooled steadily and uniformly at a rate of approximately 20°C/min. The temperatures at the seven measuring stations were so similar after steady conditions had been reached that in many later tests only one central thermocouple was read. For a fine temperature control the nitrogen flow was replaced by an atmospheric air flow from a compressed air line.

2.3 Instrumentation

2.3.1 *Heat Transfer*

The heat transfer equipment was fully described by Holden (1963). The resistance change of any five gauges can be measured during one run. The signals are usually fed to analogue networks of the type designed by Meyer (1960) and modified by Holden to accept a 50 ms* running time. The heat transfer rate histories were displayed on Tetronix 502 oscilloscopes and recorded by Land Polaroid cameras.

2.3.2 *Pitot Pressure Measurements*

Pitot traverses taken through both laminar and turbulent boundary layers were made with flattened probes 0.016 in deep and 0.075 in wide. Two similar probes, ½ in apart and at differing heights above the plate were mounted immediately behind the trailing edge of model A for the turbulent boundary layer, and a specially constructed short flat plate for the laminar boundary layer. Each probe projected forward a distance of 0.85 in, and were connected to unbonded strain gauge pressure transducers (Solartron type NT4-313-30) located in the pedestal mount to keep the response time down. The pressure records were photographed in the same way as the heat transfer rate traces.

---

* milliseconds

2.3.3 *The Measurement of Wall Temperature*

The voltage of the copper-constantan thermocouple was measured using a Cambridge Portable Potentiometer. The standard temperature-resistance calibration curve for this type of thermocouple being checked periodically by cooling the whole model to the accurately known boiling point temperature of liquid nitrogen at atmospheric pressure. Wall temperature readings were normally taken after allowing at least two minutes for the model to "settle". Since the test section pressure was reduced to 0.3 mmHg before cooling the model, only a minute trace of frost was formed and no significant heat transfer by convection was possible. Heat conduction from the pedestal mount to the model was reduced by an insulating Bakelite gasket.

2.3.4 *The Shadowgraph System*

The knife edge of the conventional single pass schlieren system was removed to give a focussed shadowgraph picture. The spherical mirrors were of 10 ft focal length arranged to give a magnification if 0.8. Photographs were taken in a darkened room using Ilford fast blue-sensitive plates (type XK) with a spark source of 10 μsec duration.

3. RESULTS AND DISCUSSION

3.1 Measurements of the Location of the Transition Region

Conventional focussed shadowgraph pictures of the flow over a flat plate will pick out the greatest rate of change of density gradient ($d^2\rho/dy^2$) in the laminar boundary layer as a thin, sharp black line lying just above the plate surface. It was noticed that at some distance downstream this line begins to thin, loses its sharpness and finally becomes so diffuse that it is unrecognisable against the grey background, see Figure 2(c). Earlier investigators, notably Lee (1952) and Bertram (1957), have shown that this behaviour is indicative of transition. The theoretical justification for this assumption is shown in Figure 2(a) by the sketches of the $d^2\rho/dy^2$ profiles through the laminar and turbulent boundary layers prepared using the calculations of Van Driest (1951 and 1952) with $M = 8$ and $T_w/T_0 = 4$. For a laminar layer the maximum value of $d^2\rho/dy^2$ occurs at about 0.95δ in contrast to the turbulent layer which has a very small change of density gradient in this region, the maximum changes occurring close to the wall.

In order to understand the shadowgraph pictures more fully some heat transfer rate records were taken simultaneously. The comparison between the photographic and heat transfer "definitions" of transition region (Fig.3) shows that the boundary layer is fully turbulent when the shadowgraph line finally disappears. The point of disappearance was used in this report to define transition.

3.2 Heat Transfer Results

Natural transition occurred at $M = 8.2$ for all three unit-Reynolds-number test conditions. The distinct changes of heat transfer rate distribution along the wall, dq/dx negative for laminar or turbulent flow and positive in the transition region, made the three zones easy to define, see Figure 4.

The individual heat transfer records of $\dot{q}$ vs. t also gave some indication of transition by nature of their unsteadiness. Within the laminar zone the traces were fairly smooth but throughout the transition region irregular upward spikes were observed. These may be indicative of turbulence spots or bursts as reported by Schubauer and Skramstad (1948) at low speeds, and more recently by Nagamatsu and Sheer (1964) at hypersonic speeds. The spikes gradually disappeared within the turbulent zone and the gauges furthest downstream recorded smooth traces, similar in shape to those situated in the laminar region.

Theoretical estimates of the heat transfer rate distribution are also shown in Figure 4. The reference enthalpy methods of Eckert (1955) and Sommer and Short (1955) were used for the laminar and turbulent boundary layers respectively. For the turbulent case the Kármán-Schoenherr equations were used to determine the skin-friction coefficient as indicated by Peterson (1963). The virtual origin was chosen empirically at a point half way along the transition region as defined by the heat transfer records. Details of the various calculations are given in the Appendix. Agreement between "theory" and experiment is good. In the case of the turbulent boundary layer the position and extent of transition have to be found before the "theory" can be applied. Measurements taken within the transition region confirm the results of Holloway and Sterrett (1964) who found a sensibly linear increase of $\dot{q}$ with x .

3.3 Pitot Pressure Measurements

Further proof of the nature of the boundary layer was provided by pitot traverses made well within the laminar and turbulent regions defined by Figure 4. Results are shown in Figures 5(a) and 5(b).

Pitot pressure records taken at stations between 80 and 90% of the laminar boundary layer thickness showed some unsteadiness. Since at $y \simeq 0.9\delta$ the pitot pressure gradient (dp_0/dy) is a maximum then disturbances from any source (including those introduced by the presence of the probe) are likely to cause more noticeable fluctuations at this station. These fluctuations might possibly be associated with the critical layer predicted by stability theory and found experimentally at $M = 8.0$ by Potter and Whitfield (1960) to lie near the edge of the layer. Nagamatsu (1964) found that turbulence bursts propagated with a velocity equal to 90% of the free-stream value under his test conditions of $M = 8$, $T_w = 290^\circ K$, $T_r \simeq 1300^\circ K$. This suggests that the critical layer is approximately 0.9δ from the surface.

The measured uncorrected laminar data compare favourably with the theoretical profile of Van Driest (1952). The turbulent data are similar to other experimental values measured in continuous tunnels (see Fig.5) but in this case the agreement with theory is poor. The turbulent profile was measured at $x = 10.7$ in ($Re_x = 6.7 \times 10^6$) and heat transfer rates were recorded at the same time. The values of $\dot{q}$ upstream of the probe were unchanged by the presence of the probe.

3.4 Transition Reversal

Initial tests were carried out using flat plates at room temperature only. It was possible to alter the wall to recovery temperature ratio but only at the expense of changing the unit Reynolds number. Since both of these parameters are very

influential it was necessary to separate them. This was done by changing T_w as described in paragraph 2.2.2.

Figure 6 shows the results of the recent tests at $M = 8.2$ as plots of transition Reynolds number against T_w/T_r for three values of unit Reynolds number. Varying only the plate surface temperature, each of the three graphs exhibits transition reversal and re-reversal as the plate temperature is reduced. This trend supports the conjecture of Reshotko (Fig.7(c)) and so lends some weight to the hypothesis that the pattern of transition at hypersonic speeds is predictable by the Tollmien-Schlichting instability theory. It will be noticed that the results indicate two regions of greater stability and that the upper region is very narrow. At the highest unit Reynolds number there was some suggestion of a third band of increased stability, see Figure 7(c) series 1 data. During the series 1 tests the leading edge was damaged slightly by diaphragm particles striking and chipping the edge. When the edge was restored the series 2 data were obtained. The scatter of the other readings is due entirely to difficulties in "reading" the photographs.

3.5 The Effect of Unit Reynolds Number

Bertram (1957) noted the generally strong increase of transition Reynolds number with unit Reynolds number and attributed this trend to the effect of leading-edge thickness. More recently Whitfield and Potter (1964) have shown that even for zero bluntness a unit Reynolds number effect is present and they have managed to separate the two effects, one due to the bluntness Reynolds number, the other due to unit Reynolds number. In the present tests the plate geometry was fixed and so both the above Reynolds numbers were changed simultaneously. The Reynolds number based on leading-edge thickness was varied between 225 and 430. According to Whitfield and Potter such a change at constant unit Reynolds number would have moved the transition point 0.3 in. This is negligible compared with the measured shift of 3 in and no attempt has been made to correct for this small bluntness effect.

Cross plotting from the dotted mean lines through the data of Figure 6 the effect of unit Reynolds number at a fixed wall temperature ratio can be found as shown in Figure 8. For the lower wall temperatures the curves in Figure 8 are very steep due to the close proximity of the first stable band (Fig.6). However, at $T_w/T_r = 0.5$ the unit Reynolds number effect is similar to that of other investigators.

3.6 Other Factors Affecting the Position of the Transition Point

Luxton (1964) has recently reviewed the many factors affecting transition and re-stated the importance of roughness. Potter and Whitfield (1961) suggested that some transition reversal data could be explained by wall cooling reducing the boundary layer thickness and so increasing the effective roughness. The idea is that rough elements, which under low heat transfer conditions are too small to promote transition, could have a strong influence if the wall was highly cooled. The roughness "model" they propose requires that the roughness element must be a considerable fraction of the displacement thickness. These conditions could only be satisfied in the present tests by roughness very close to the leading edge since the surface finish was good to ± 16 μin. In addition there is present some just observable and un-measured frost. Even if roughness is the cause of transition reversal it is difficult to see how it could be connected with the subsequent re-reversal phenomenon.

The free stream turbulence level is known to affect transition and though this level is as yet unmeasured in the gun tunnel it is thought to be high. Comparison between different sets of transition data is almost impossible since so many parameters are important. If the present data are extrapolated (heroically) to adiabatic wall conditions and compared with the Whitfield and Potter (1964) data at $M = 8$ and similar unit Re, then their measured transition Reynolds numbers are about four times greater.

4. CONCLUSIONS

An experimental investigation has been carried out in the Imperial College gun tunnel at a Mach number of 8.2 in order to determine the separate effects of wall temperature and unit Reynolds number on boundary layer transition. Analysis of the experimental results and a comparison with other theoretical and experimental data have led to the following conclusions:

Heat transfer rate measurements have confirmed that the transition region on a flat cold wall at $M = 8.2$ can be satisfactorily determined from focussed shadowgraph pictures.

The variation of transition Reynolds number with wall temperature at $M = 8.2$ is similar to the theoretical pattern suggested by Reshotko (1963) and similar to some of the experimental data obtained at lower Mach numbers.

Transition appears to be a gradual process occurring over a large region between laminar and turbulent boundary layers.

The strong variation of transition Reynolds number with unit Reynolds number is similar to that found by other investigators.

ACKNOWLEDGMENTS

The authors wish to thank Dr. J.K. Harvey and Mr. D.A. Needham for many helpful discussions and to acknowledge the care with which the Departmental Workshop manufactured the experimental apparatus.

REFERENCES

Banner, L.T.
Williams, M.J.
Boundary Layer Measurements in the ARL Hypersonic Tunnel Conical Nozzle. ARL (Australia), Aerodynamics Note 215 (1963).

Bertram, M.H.
Exploratory Investigation of Boundary Layer Transition on a Hollow Cylinder at a Mach number of 6.9. NACA Report 1313 (1957).

Eckert, E.R.G.
Engineering Relations for Skin Friction and Heat Transfer to Surfaces in High Velocity Flow. J. Ae. Sc., Vol.22, No.8, (1955) pp.585-587.

Holden, M.H.
Heat Transfer in Separated Flow. Ph. D. Thesis, Imperial College, University of London (1963).

Holloway, P.F.
Sterrett, J.R.
Effect of Controlled Surface Roughness on Boundary Layer Transition and Heat Transfer at Mach numbers of 4.8 and 6.0. NASA TN D-2054 (1964).

Jack, J.R.
et alii
Effects of Extreme Surface Cooling on Boundary Layer Transition. NASA TN 4094 (1957).

Laufer, J.
Vrebalovich, T.
Stability of a Supersonic Laminar Boundary Layer on a Flat Plate. JPL Report No.20-116 (1958).

Lee, J.D.
The Influence of High Adverse Pressure Gradients on Boundary Layers in Supersonic Flow. UTIA Report No.21 (1952).

Lees, L.
Stability of Laminar Boundary Layers and Wakes at Hypersonic Speeds. International Symposium on Fundamental Phenomena in Hypersonic Flow, Buffalo (1964). To be published by Cornell University Press.

Luxton, R.E.
Transition in the Compressible Boundary Layer – Review and Consideration of the Effects of Roughness and Heat Transfer. Unpublished Note, University of Sydney (1964).

Lyons, W.C.
et alii
Hypersonic Drag, Wake and Stability Data for Cones and Spheres. AIAA Preprint No. 64-[illegible] (1964).

Meyer, R.F.
A Heat Flux Meter for Use with Thin Film Surface Thermometers. NRCC Report LR-279 (1960).

Nagamatsu, H.T.
Sheer, R.E. Jr.
Boundary Layer Transition on a Highly Cooled 10° Cone in Hypersonic Flows. General Electric Research Lab. Report No.64-RL-(3622C), (1964).

Needham, D.A. — *Progress Report on the Imperial College Hypersonic Gun Tunnel.* I.C. Aero. Dept. Report No.118 (1963).

Peterson, J.B. — *A Comparison of Experimental and Theoretical Results for the Compressible Turbulent Boundary Layer Skin Friction with Zero Pressure Gradient.* NASA TN D-1795 (1963).

Potter, J.L.; Whitfield, J.D. — *Effects of Unit Reynolds Number, Nose Bluntness, and Roughness on Boundary Layer Transition.* AEDC-TR-60-5 (1960).

Potter, J.L.; Whitfield, J.D. — *The Relations between Wall Temperature and the Effect of Roughness on Boundary Layer Transition.* J. Ae. Sc., Vol.28, No.8, (1961), p.663.

Reshotko, E. — *Transition Reversal and Tollmien-Schlichting Instability.* Physics of Fluids, Vol.6, No.3, (1963), pp.335-342.

Schubauer, G.B.; Skramstad, H.K. — *Laminar Boundary Layer Oscillations and Transition on a Flat Plate.* NACA TR 909 (1948).

Sommer, S.C.; Short, B.J. — *Free Flight Measurements of Turbulent Boundary Layer Skin Friction in the Presence of Severe Aerodynamic Heating at Mach Numbers from 2.8 to 7.0.* NACA TN 3391 (1955).

Stollery, J.L. et alii — *The Imperial College Gun Tunnel.* J. Roy. Aero. Soc., Vol.64, No.1, (1960), p.24.

Van Driest, E.R. — *Turbulent Boundary Layer in Compressible Fluids.* J. Ae. Sc., Vol.18, No.3, (1951), pp.145-160.

Van Driest, E.R. — *Investigation of Laminar Boundary Layer in Compressible Fluids using the Crocco Method.* NACA TN 2597 (1952).

Whitfield, J.D.; Potter, J.L. — *The Influence of Slight Leading Edge Bluntness on Boundary Layer Transition at a Mach Number of Eight.* AEDC-TDR-64-18, (1964).

Wisniewski, R.J.; Jack, J.R. — *Recent Studies on the Effect of Cooling on Boundary-Layer Transition at Mach 4.* J. Ae. Sc., Vol.28, No.3, (1961), p.250.

APPENDIX

Heat Transfer Equations used for Comparison with Experiment

LAMINAR

Eckert's reference temperature is defined by

$$\frac{T^*}{T_\infty} = 1 + 0.0392\, M^2 + 0.5\left(\frac{T_w}{T_\infty} - 1\right)$$

and the heat transfer rate calculated from

$$\dot{q} = \rho_\infty u_\infty C_p \frac{0.332}{(Re_x)^{1/2}(Pr^*)^{2/3}}\left(\frac{\rho^*\mu^*}{\rho_\infty \mu_\infty}\right)$$

TURBULENT

For the case of turbulent boundary layers, the skin friction was determined by the Sommer and Short T^* method indicated by Peterson (1963), i.e.

$$\frac{T^*}{T_\infty} = 1 + 0.035\, M^2 + 0.45\left(\frac{T_w}{T_\infty} - 1\right)$$

The Kármán-Schoenherr equations were used to determine the local skin friction coefficient at this reference condition. These have been plotted by Peterson (1963) from the following equations.

$$\frac{0.242}{\sqrt{C_{F,T^*}}} = \log_{10}\left(Re_{x_v}, T^*\right)\left(C_{F,T^*}\right)$$

$$\frac{C_{f,T^*}}{C_{F,T^*}} = \frac{1}{1 + 3.59\sqrt{C_{F,T^*}}}; \quad C_f = \frac{C_{f,T^*}}{T^*/T_\infty}$$

The heat transfer rate is given by

$$\dot{q} = \rho_\infty u_\infty C_p \frac{C_f}{2}(Pr^*)^{-2/3}$$

In this paper the virtual origin, x_v, was taken to be at a position half way along the transition region, as indicated by experimental heat transfer results.

TRANSITIONAL

A simple semi-empirical method of predicting the heat transfer during the transition region, similar to that used by Holloway and Sterrett (1964), was used. A linear increase of heat transfer from the end of the laminar region is assumed. This method assumes the positions of the beginning and end of transition.

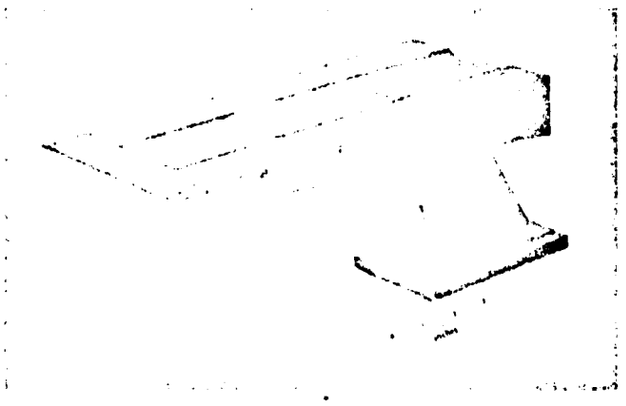

Fig.1(a) Heat transfer model - Model A

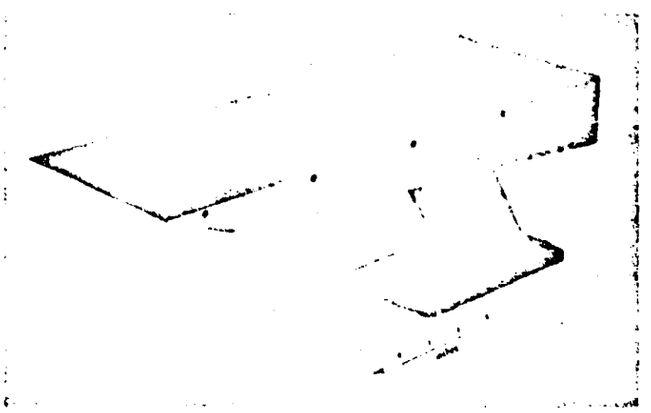

Fig.1(b) Cold wall model - Model B

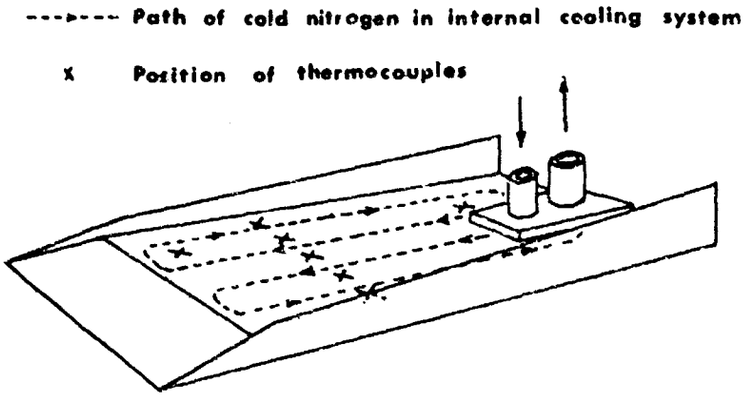

Fig.1(c) Cold wall model as positioned in working section

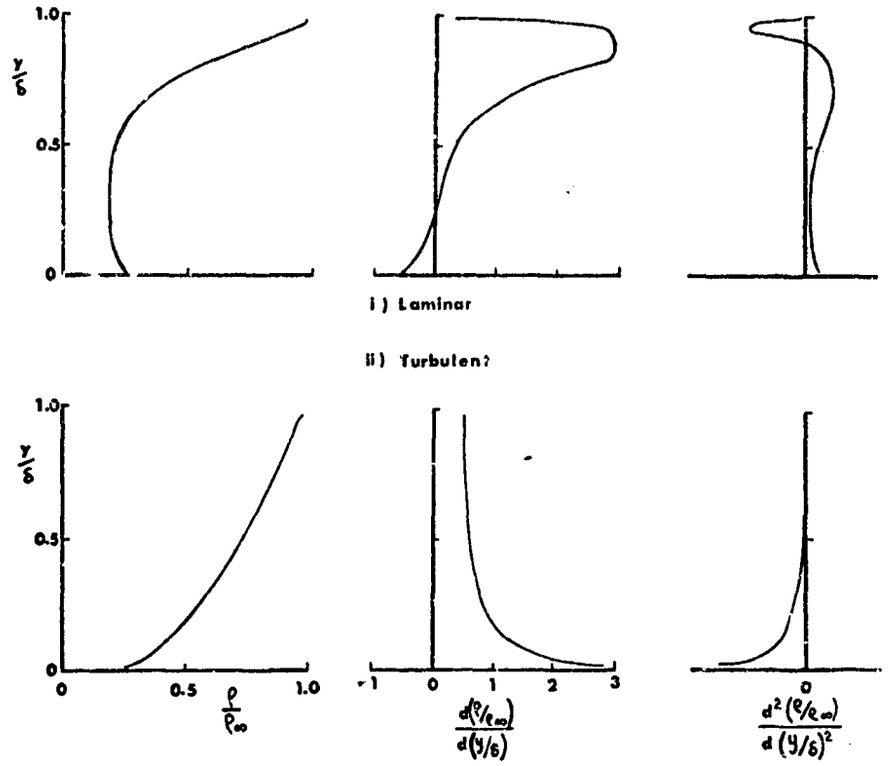

Fig. 2(a) Density profiles through laminar and turbulent boundary layers at hypersonic speeds

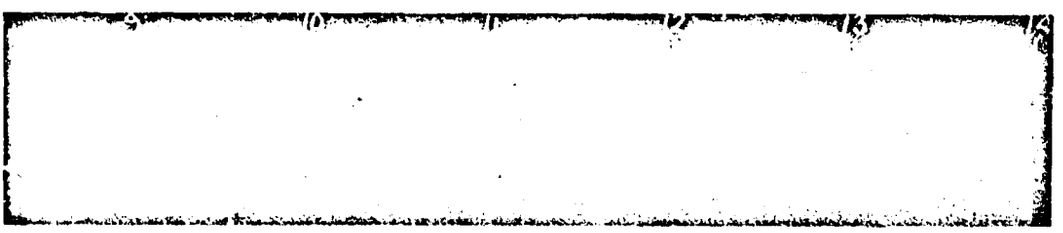

Fig. 2(b) Typical shadowgraph picture of laminar boundary layer
$m = 8.2$, $Re/in = 7.12 \times 10^5$, $T_w/T_r = 0.132$

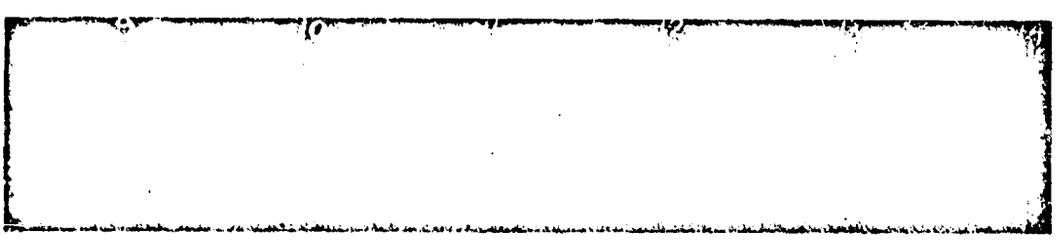

Fig. 2(c) Typical shadowgraph picture of turbulent boundary layer
$m = 8.2$, $Re/in = 7.12 \times 10^5$, $T_w/T_r = 0.280$, $x_t = 10.5$ in

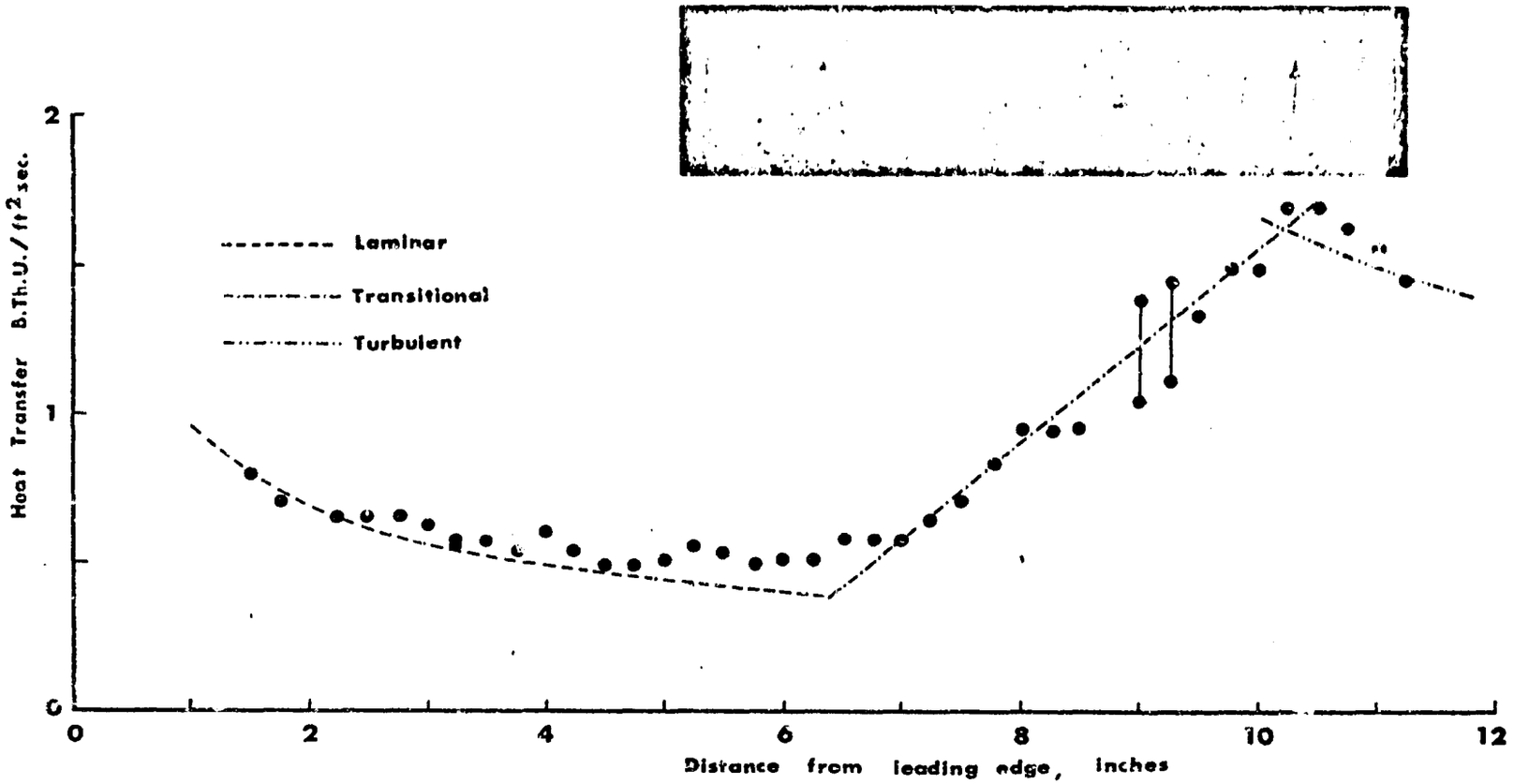

Fig.3 Comparison of heat transfer rates with shadowgraph of a typical transition observation

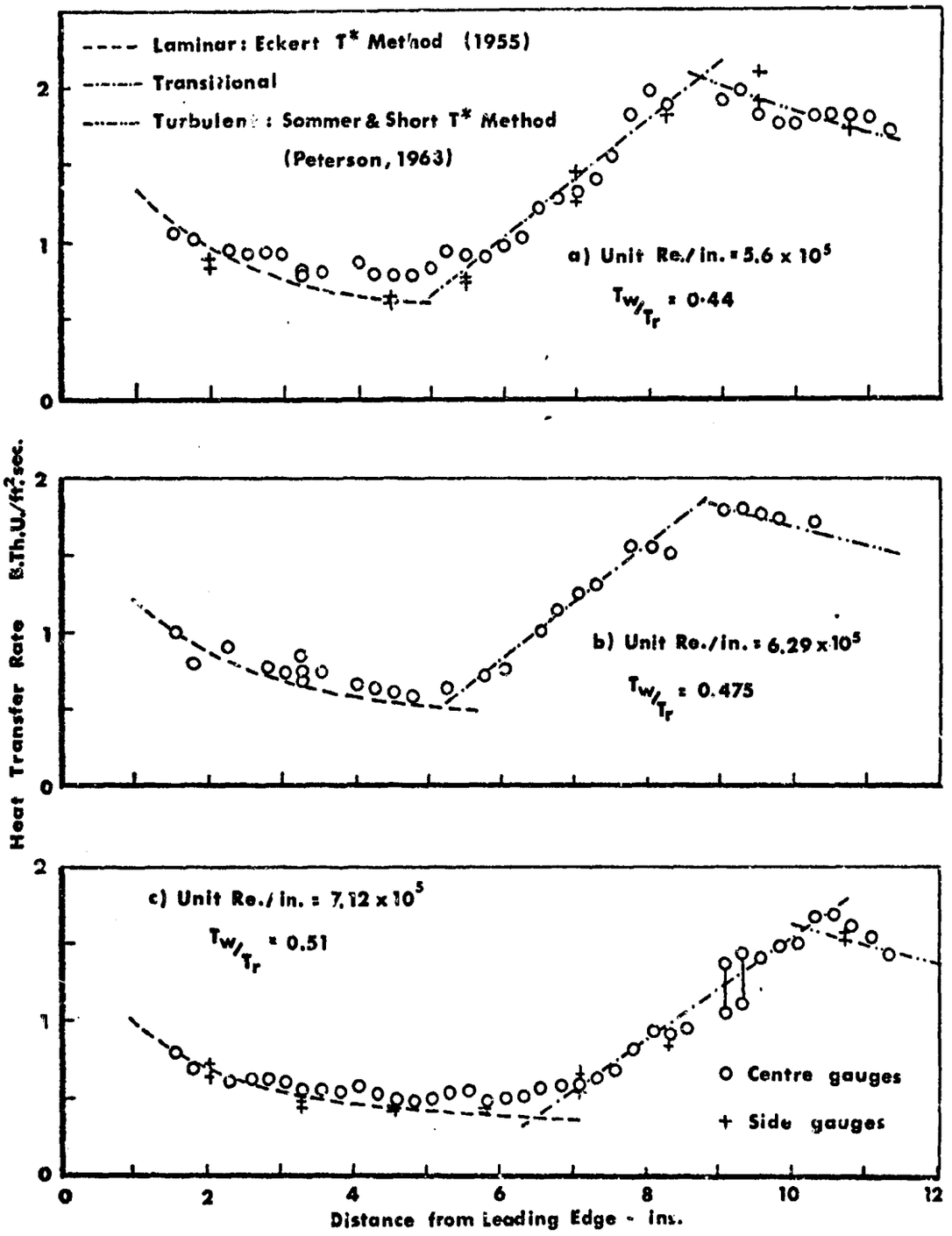

Fig. 4 Heat transfer rate along flat plate during transition M = 8.2, T_w = 290°K

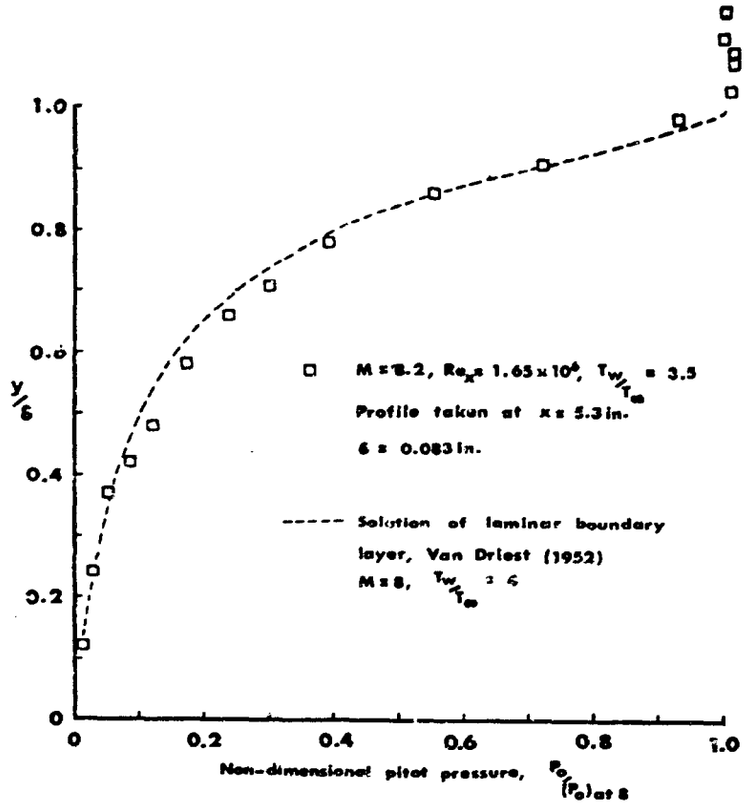

Fig.5(a) Pitot pressure profile through laminar boundary layer

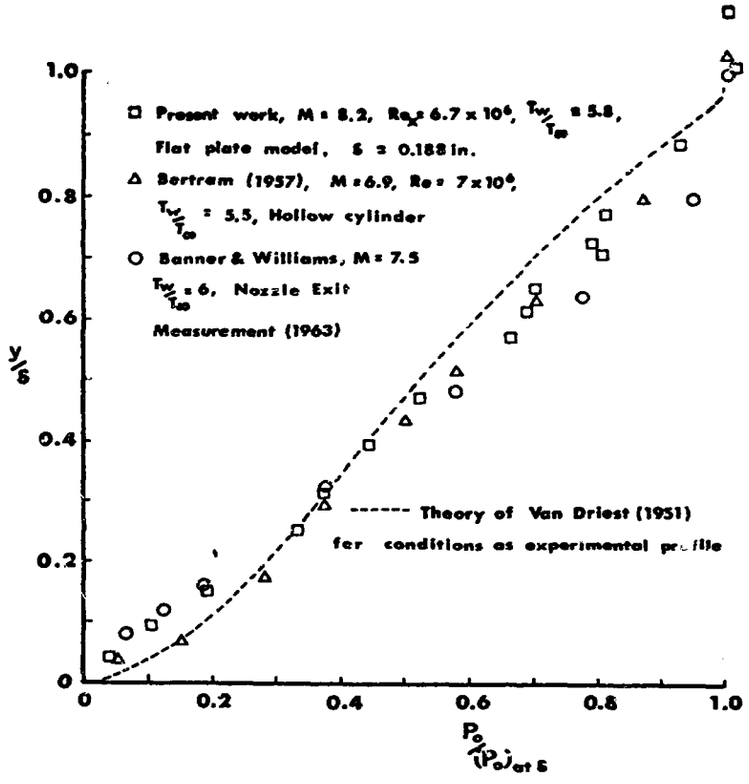

Fig.5(b) Pitot pressure profile through hypersonic turbulent boundary layer

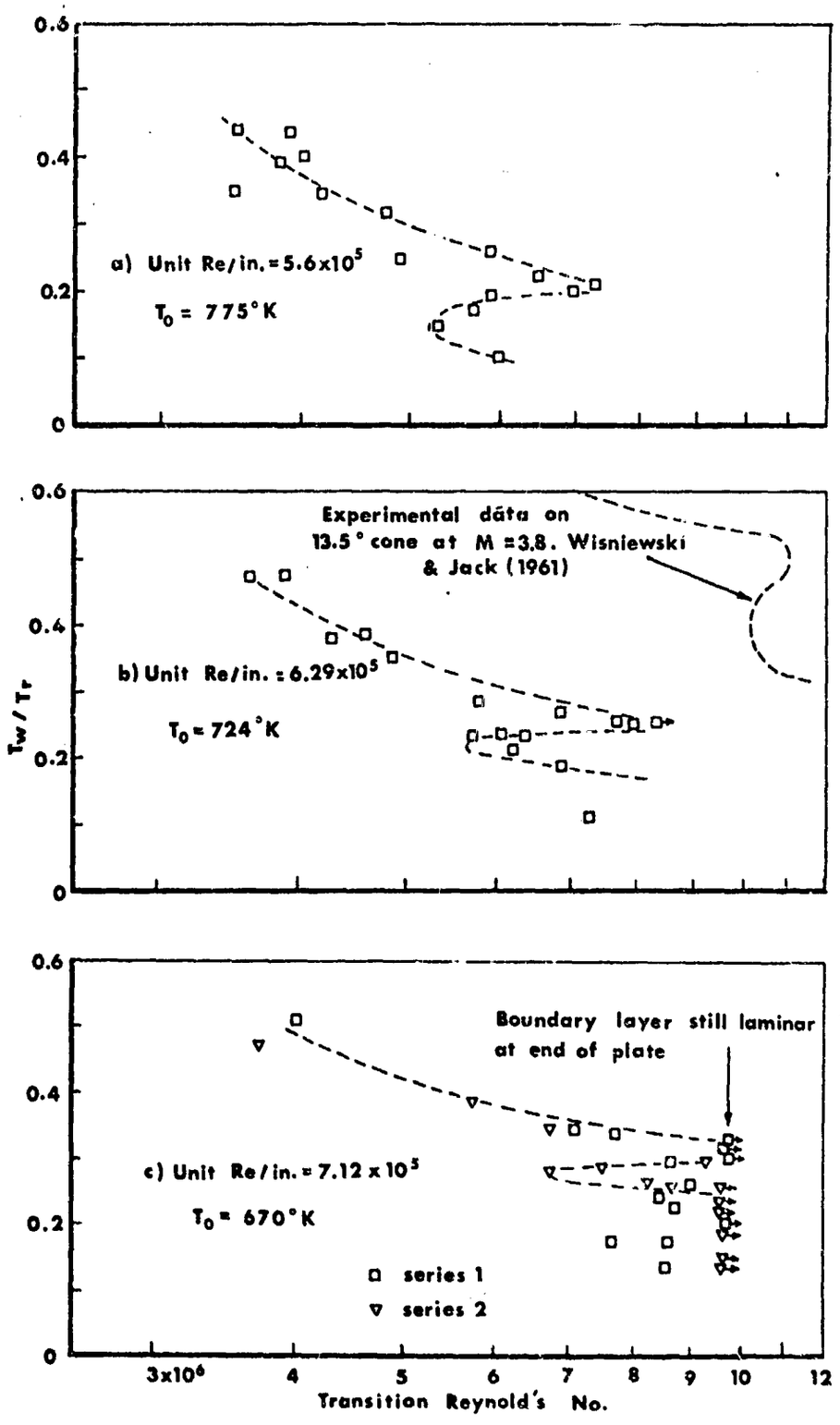

Fig.6 Effect of wall temperature on transition M = 8.2

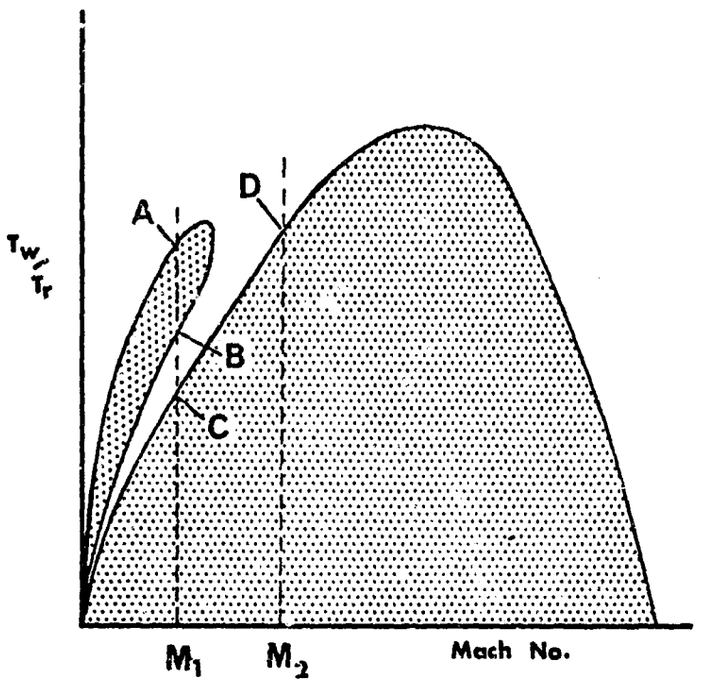

(a)

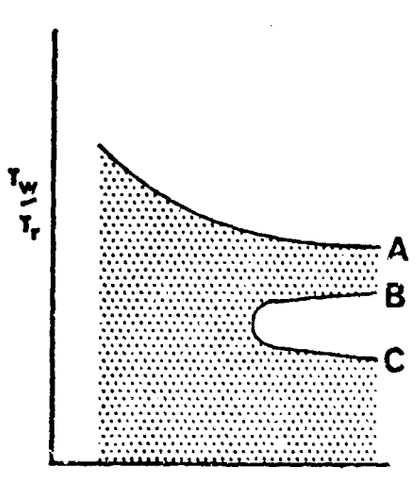

(b) at M_1

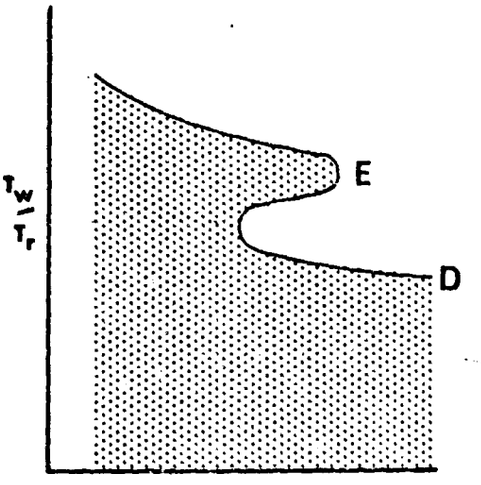

(c) at M_2

Fig. 7 Estimated variation of minimum critical Reynolds number at two different Mach numbers. (Shaded area represent regions of complete stability.) Diagram from Reshotko (1963)

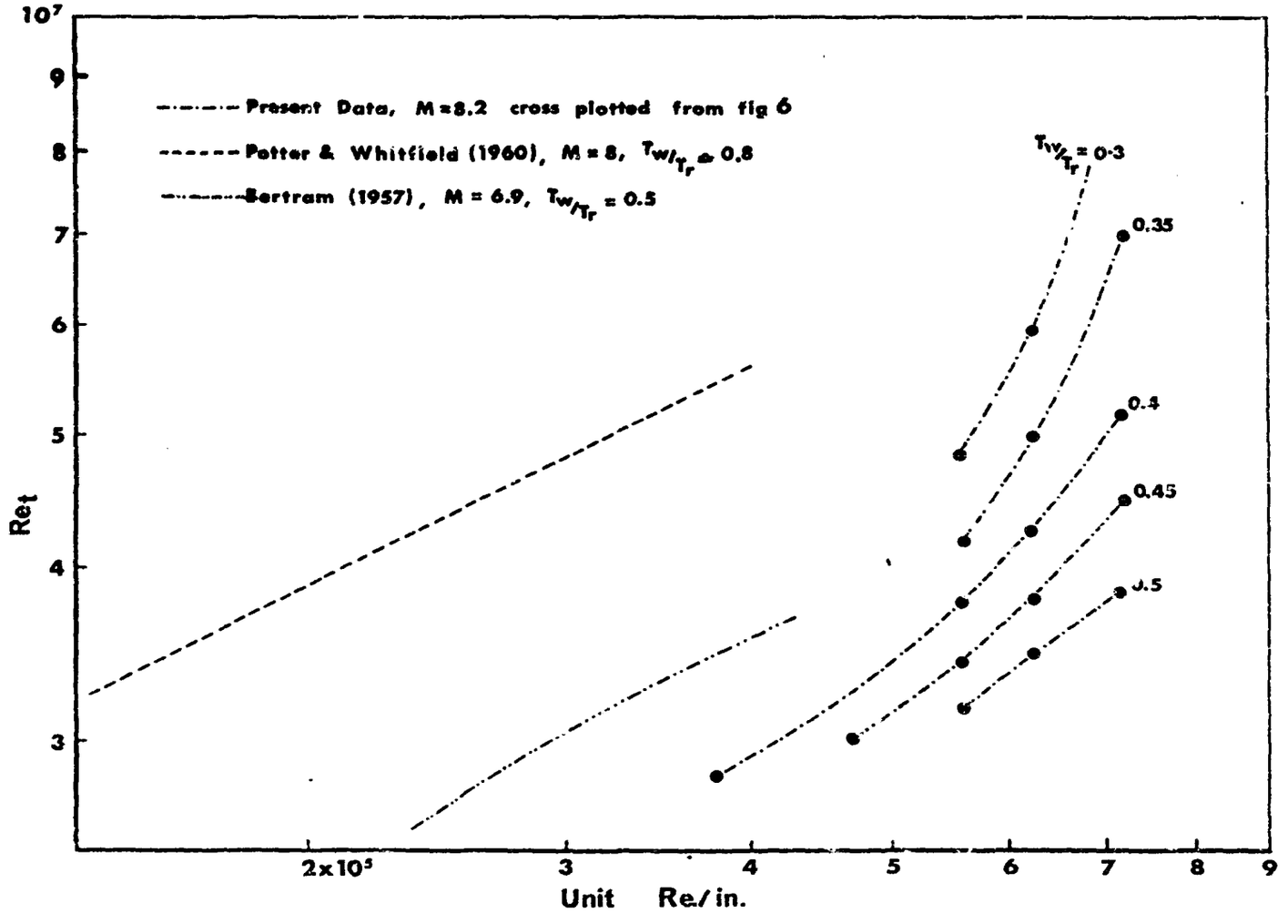

Fig.8 Unit Reynolds number effect on transition Reynolds number

BOUNDARY-LAYER DISTURBANCE BY ISOLATED PROTUBERANCES OF VARIABLE HEIGHT ON A CYLINDER NOSE

by

E. Dobbinga

Department of Aeronautical Engineering,
Delft Technical University, Netherlands.

SUMMARY

The report describes measurements at low speeds of the transition of a boundary-layer in a favourable pressure-gradient, as affected by isolated protuberances.

The roughness elements were installed on the cylindrical nose of a two-dimensional streamline body. The height of the protuberances could be varied continously and, by rotating the cylindrical nose, also the distance between the protuberance and the stagnation point could be changed.

This preliminary report gives a general picture of the behaviour of four types of roughness elements. The character of the disturbance changes markedly if the critical height of protuberances increases beyond a crucial value which is smaller than the boundary-layer thickness. The effect of protuberances appears in general to be very sensitive to the shape of the top.

SOMMAIRE

L'auteur expose comment certaines mesures effectuées à de faibles vitesses de transition d'une couche limite, dans un gradient de pression favorable, sont affectées par des protubérances isolées.

Les rugosités constituant ces protubérances ont été disposées sur la tête cylindrique d'un corps profilé bi-dimensionnel. Au cours de l'expérience on pouvait faire varier continuellement la hauteur de ces protubérances ainsi que la distance les séparant du point d'impact, cette dernière variation étant obtenue en faisant effectuer un mouvement de rotation à la tête cylindrique.

Ce rapport préliminaire donne un aperçu général du comportement de quatre types de rugosités. La nature de la perturbation varie de façon marquée si la hauteur critique des protubérances dépasse une valeur cruciale, inférieure à l'épaisseur de la couche limite. L'effet des protubérances semble, en règle générale, être étroitement lié à la forme du sommet du corps.

CONTENTS

LIST OF FIGURES

NOTATION

d		diameter of a protruding roughness element
D		diameter of the big cylinder (the cylindrical nose-piece of the streamline model); $D = 400$ mm
k		height of a protuberance; diameter of a two-dimensional wire
p_{to}		undisturbed total pressure
p_w		pressure on the centre of the tunnel side wall (see Fig. 1)
q		reference dynamic pressure = $(p_{to} - p_w)$ kgf/m^2
R_k	=	$u_k . k/\nu$
U		velocity outside the boundary layer (m/sec)
u		velocity at a distance y from the surface of the big cylinder
u_k		the value of u for $y = k$
z		coordinate in vertical direction, parallel to the axis of the big cylinder
		$z = 0$ is the measuring plane at the height of the centre of the test section
φ		angular position on the big cylinder, measured from the stagnation point; positive in the direction of the hot wire; (degrees)
φ_k		value of φ for a roughness element
$\varphi_{\text{hot wire}}$		$= 57.3^\circ$
ν		kinematic viscosity = 14×10^{-6} m^2/sec (mean value)

BOUNDARY-LAYER DISTURBANCE BY ISOLATED PROTUBERANCES OF VARIABLE HEIGHT ON A CYLINDER NOSE

E. Dobbinga

1. INTRODUCTION

In descriptions of the disturbing effect of roughness elements in a laminar boundary-layer often use is being made of a Reynolds number R_k as characteristic parameter. This parameter has the drawback, however, that the critical value of R_k is not the same for particles of different shape. As an example reference can be made to Figure 2 of a report by Braslow[1].

The measurements, described below have been planned to furnish some more information about the influence of the particle shape on the disturbing power. The investigation has been arranged so that use could be made of an existing model. This model had been used for an investigation of the influence of roughness particles of fixed shape on the flow around an airofoil nose in the neighbourhood of the stagnation point*.

From (unpublished) results of this work the velocity distribution and the calculated boundary-layer profiles have been derived (Figs.3 and 4). The only addition to the model has been a mechanism which permitted the height of the roughness elements to be changed during the tests. Originally it was intended to measure only at one wind speed and with roughness elements at only one position on the model nose in order to get a comparison of the critical dimensions of different particles under identical flow conditions. The appearence of unexpected phenomena, however, led to a change in the program, the new aim being to obtain first a general impression about the behaviour of roughness particles in the stagnation flow. This preliminary report gives a survey of some results.

2. THE DISPOSITION IN THE WIND TUNNEL

The experiments have been made in the 4 x 6 ft low-turbulence wind tunnel of the Aeronautical Department of Delft Technical University. A sketch of the situation is given in Figure 1.

The model consists of a steel cylinder (400 mm diameter), a wooden tail downstream of the cylinder and an interchangeable roughness element on the cylinder.

The cylinder is attached to the turntables in top and bottom of the test section. By rotating the cylinder a roughness element could be moved from the stagnation point

* The idea to use a model of this type is due to Mr. J.L. van Ingen of the Aeronautical Department, who also supervised the early measurements.

to any other position in the boundary-layer along the frontpart of the cylinder. The angle of rotation measured from the stagnation point is denoted by φ_k . The influence of the roughness element on the boundary-layer has been measured with a hot wire (0.003 mm thick, 12Ω). This instrument was fixed to the tunnel sidewall; in all the tests the hot wire was kept in the same position: in the middle of the tunnel height and 57.3° from the stagnation point. The distance between the wire and the cylinder surface was such that the velocity at the wire in the undisturbed laminar boundary-layer was about 0.9 times the speed outside the boundary layer. The wire was kept at a constant temperature; the output was fed into an oscilloscope.

3. THE ROUGHNESS ELEMENTS

Two types of disturbing elements have been tested:

(a) three-dimensional elements, consisting of the top part of thin cylindrical elements protruding from the surface of the big cylinder.

(b) two-dimensional wires.

(a) The height of the three-dimensional elements could be varied during the tests by means of the displacement mechanism sketched in Figure 2. The cylindrical part of the roughness element is soldered in a piston. By means of a spring this piston is pressed inward against the ball-point of a displacement screw with 1 mm pitch. This screw could be rotated from outside the tunnel by means of a pulley and a string.

A 10-turn potentiometer connected to a digital voltmeter and driven by the displacement screw could measure a displacement up to 10 mm. Displacements could be given (according to the voltmeter) in steps of 0.001 mm. In this respect it may be noted that in some cases marked repeatable changes in flow characteristics have been observed while changing the height k by not more than one micron. The protruding end of the cylindrical roughness element passed through a brass plug. For each roughness diameter a separate plug, fitting to this diameter, and a separate piston were available. After each assembly of the displacement mechanism in the big cylinder, the roughness element was retracted and the outer surface of the brass plug was worked flush with the steel cylinder. A direct calibration of the voltmeter giving the height of the protuberance was obtained by comparing the position of the top of the roughness element with that of the surface of the steel cylinder in the immediate surroundings of the element. The frame of the micrometer used for this purpose carried three fixed points which could be pressed against the cylinder surface. In each case readings have been taken at many different values of the roughness height k .

Furthermore each roughness element has been photographed by means of a simple long "camera" which allowed a 15 times enlarged photograph to be taken directly on photographic paper. The comparison of the picture of the roughness element with that of a permanent calibration wire gave a check on the dimensions of the element.

In some cases only the photographic method has been used, e.g. for very sharp cones (not discussed in this report), and for disturbing elements entering into the boundary-layer from outside.

About the accuracy of the values of k measured during the experiments it can be said that the error in the absolute value of k in a certain run may have been of the order of 0.01 mm; in the important range of k between 0 and 0.3 mm the errors in the differences between different values of k in the same run are probably (much) smaller than 0.01 mm.

(b) Two-dimensional wires. For comparison a number of wires have been tested. As indicated in Figure 1 these wires were installed at an angle of about 6° with the direction of the cylinder axis. This made it possible to pull the wires firmly against the cylinder surface by means of a tightening screw. Only the 0.2 mm and the 0.395 mm wires were real solid steel wires the thicker wires: 0.305; 0.41; 0.80; 1.22 and 2.23 mm diameter, consisted in reality of 200 mm long pieces of stainless steel tube which were pulled against the surface by means of a thin wire going through the tubes. In all normal runs the middle of the tubes was placed at the centre of the tunnel height ($z = 0$).

4. THE MEASUREMENTS

The reference dynamic pressure q is defined as the difference between the undisturbed total pressure and the pressure on the centre o one of the test section side walls (see Fig.1).

During each run the value of q has been kept constant: it could be measured by means of a Betz-type water manometer. Most of the data have been taken at $q = 120$ kgf/m^2, in these cases no deviations larger than 0.2% have occurred. Some additional data have been obtained for $q = 30$ kgf/m^2, in those cases deviations up to to 1% have been tolerated.

The largest difference in Reynolds number due to variations of barometric pressure and air temperature has been about 1.5%. As mentioned in the introduction, some data about the velocity field around the cylinder (derived from earlier work) have been presented in Figures 3 and 4.

The two methods which have been employed during the measurements are the following:

(a) The height k of the roughness element was adjusted at a certain value and φ_k was varied by rotating the big cylinder. Values of φ_k at which the first turbulent spot was detected by the hot wire and φ_k at which the flow appeared to be just completely turbulent have been determined.

(b) For the lower values of k it appeared to be more practical to set φ_k at a certain fixed value and to vary k until the first spot appeared and until full turbulence was just established according to the picture on the oscilloscope. For two-dimensional wires of course, only method (a) could be used.

5. RESULTS; DISCUSSION

The investigation had the character of a reconnaissance. Only some general results will be presented here. The character of the disturbing effect of protruding cylindrical roughness elements of varying height is shown in the Figures 5, 6 and 7 for roughness

diameters d of 0.2; 0.4 and 3.0 mm respectively. These elements had flat tops and a relatively sharp edge.

Figure 8 gives the measured data for two-dimensional wires. An explanation of the symbols used can be found in the list of notations. For orientation, in each figure also the values of δ^* and δ (for u/U = 0.999) as derived from earlier work, have been indicated.

The figures show that, if the roughness element is placed at high values of φ_k where U is large, an increase of the height k gives a "normal" sequence of effects. At low values of k the boundary layer stays laminar at the station of the hot wire. If k becomes larger than a certain critical value, turbulent spots are detected and if a second critical value is passed the flow around the hot wire becomes completely turbulent. At high values of φ_k the width of the region with spots increases with the width of the roughness element; it is largest for the two-dimensional wires.

For smaller values of φ_k (smaller values of U) the critical values of k increase. However, only in the case of the two-dimensional wires (Fig.8) does this seem to go on more or less continuously. For the protruding elements a change in flow picture occurs at a "crucial" value of k. At $q = 120\ kgf/m^2$, this crucial value is about 0.3 to 0.4 mm or about half the boundary-layer thickness. For the thin 0.2 mm element (Fig.5) the "crucial value" of k is somewhat higher than for the thick 3 mm element but the differences are small.

The change in flow pattern is most pronounced in the case of the thin 0.2 mm roughness element (Fig.5).

For $k < 0.395$ mm the transition between the laminar and the turbulent regimes is extremely sharp; in some cases only a change in k of a few microns was sufficient to give a complete transition. For k larger than 0.395 mm, however, in the $\varphi_k - k$ diagram an extensive regime exists in which turbulent spots appear and in which a gradual transition occurs. The change in sharpness of the transition has been indicated in the figures by means of different symbols. Filled symbols correspond to very sharp transitions; open symbols have been used if the uncertainty in φ_k is of the order of say 0.2 degrees. Symbols with broken contours refer to vague or very vague transition boundaries with uncertainties in φ_k of one or more degrees.

In the case of the 0.2 mm diameter protuberance (Fig.5) the disturbing power of the element goes down if k becomes larger than the "crucial value". If for instance, at the station $\varphi_k = 24^o$, the height k is increased, the boundary layer at $\varphi = 57.3^o$ will be fully turbulent for k between 0.34 and 0.39 mm and laminar again for $k > 0.4$ mm.

For roughness elements with larger diameters and smaller value of $k_{crucial}/d$ the changes in flow pattern are less pronounced; in the case of the wires no sudden change has been observed (Fig.8).

For the 3 mm and also for the 0.4 mm diameter protruding element, a part of the region between the fully turbulent and the fully laminar regions in the $\varphi_k - k$ graph has a special character; it is called a "mixed region" (Fig.7). When one passes through this mixed region, several areas of laminar (or quasi laminar) flow, fully

turbulent flow and regions with spots or regions with periodic motions may be passed successively. Often there is some hysteresis, but in some cases the different fully turbulent regions, some of which may be as narrow as a few microns, are stable in that respect that one can "find them again". These mixed regions have not been explored extensively; the situation is rather confusing there.

The "crucial" value of k of about 0.35 mm (for $q = 120$ kgf/m^2) appears also to be critical for disturbances coming from outside the boundary layer. To investigate this, a special disturbing element has been used consisting of a 0.1 mm steel wire running from a piston of the displacement mechanism inside the big cylinder to the tunnel side wall (to the point S in Fig. 1); this wire was kept taught by means of a weight outside the test section. Around the wire, a 200 mm long piece of stainless steel tube, having 0.41 mm outside diameter, was attached. If the piston was retracted, one end of this tube could be pulled against the cylinder surface. Measurements have been made with this "roughness element" at station $\varphi_k = 30^\circ$ only ($q = 120$ kgf/m^2). As long as the distance k between the near end of the 0.41 mm tube and the cylinder surface was larger than 0.4 mm no influence on the boundary-layer could be detected at the hot wire station, the boundary layer being completely laminar. For k smaller than 0.4 mm irregular bursts of turbulence were seen on the oscilloscope.

From the Figures 5 and 6 it can be seen that at least for these particular runs the critical values of k measured for the 0.4 mm diameter roughness element are larger than the corresponding values for the 0.2 mm element at the same stations φ_k. This queer result has been checked by runs with different roughness elements of the same diameters 0.2; 0.4 and 3 mm. The $\varphi_k - k$ curves obtained in the check-runs showed the same general character as the curves given in the Figures 5, 6 and 7. However, in the level of critical values of k in the lower branch of the curves (at high values of φ_k) shifts of a few hundredths of a millimeter and in one case (for the 0.4 mm roughness) even up to 0.05 mm have been observed. The rather confusing data have not yet been analysed. It is not quite clear what effect is responsible for the shifts in the critical value of k. Additional tests with some elements with rounded tops showed that the critical value of k can be extremely sensitive to the shape of the top of the roughness element. Also thought has been given to the question whether the flow conditions around the cylinder nose have been identical during all the measurements. There is no evidence that changes in the flow have occurred. While the value of $q = p_{t_0} - p_w$ has been kept constant during the measurements, often a watchful eye has also been kept on the value of the pressure drop in the contraction of the wind tunnel and no alarming changes in this pressure drop have been observed. Moreover as an extra check the 0.2 mm two-dimensional wire has been measured several times during the course of the experiments and in each case at $q = 120$ kgf/m^2 the first "spots" appeared at the same value of φ_k : 31.8° plus or minus 0.1°.

This however, is not an absolute proof that the flowfield around the cylinder has been the same in all test: during the experiments with the rotating cylinder no pressure distributions around this cylinder have been measured.

It is felt that before a comparison of the values of the critical height of different roughness elements can be presented some additional checks should be made. For this reason no further analysis of the data is given in the present paper.

8. CONCLUSIONS

1. A "crucial" value of the critical height of protruding roughness elements exists beyond which a marked change in the disturbing effect of the elements occurs.

2. In the present experiments this crucial height was not much dependent on the diameter of the protruding particles. The larger the width of the protuberance the less marked the change in flowcharacteristics appeared to be.

3. The critical height of roughness elements is strongly affected by the shape of the top. In this respect it can be mentioned that at large values of φ_k the critical value of the diameter of two-dimensional wires which have a rounded "top", is larger than the critical value of k of the 3 mm diameter protuberance.

ACKNOWLEDGEMENTS

The author wishes to thank Mr. D.M. Passchier who made the boundary-layer calculations, Mr. Amano for help during the measurements and Mr. M.H.W. van Heuven and Mr. H.J. Moore who patiently and capably took care of the technical preparations.

REFERENCE

1. **Braslow**, A.L. *Review of the effect of distributed surface roughness on boundary-layer transition*, AGARD Report 254, April 1960.

Symbols in the Figures 5 – 8:

Triangles: first turbulent spots at station $\varphi = 57.3^\circ$

Circles: boundary of region of complete turbulence at station $\varphi = 57.3^\circ$

Filled symbols: sharp transition

Open symbols: less sharp (uncertainty $\sim 0.2^\circ$ in φ_k)

Symbols with broken contours: vague or very vague, (uncertainty up to several degrees in φ_k)

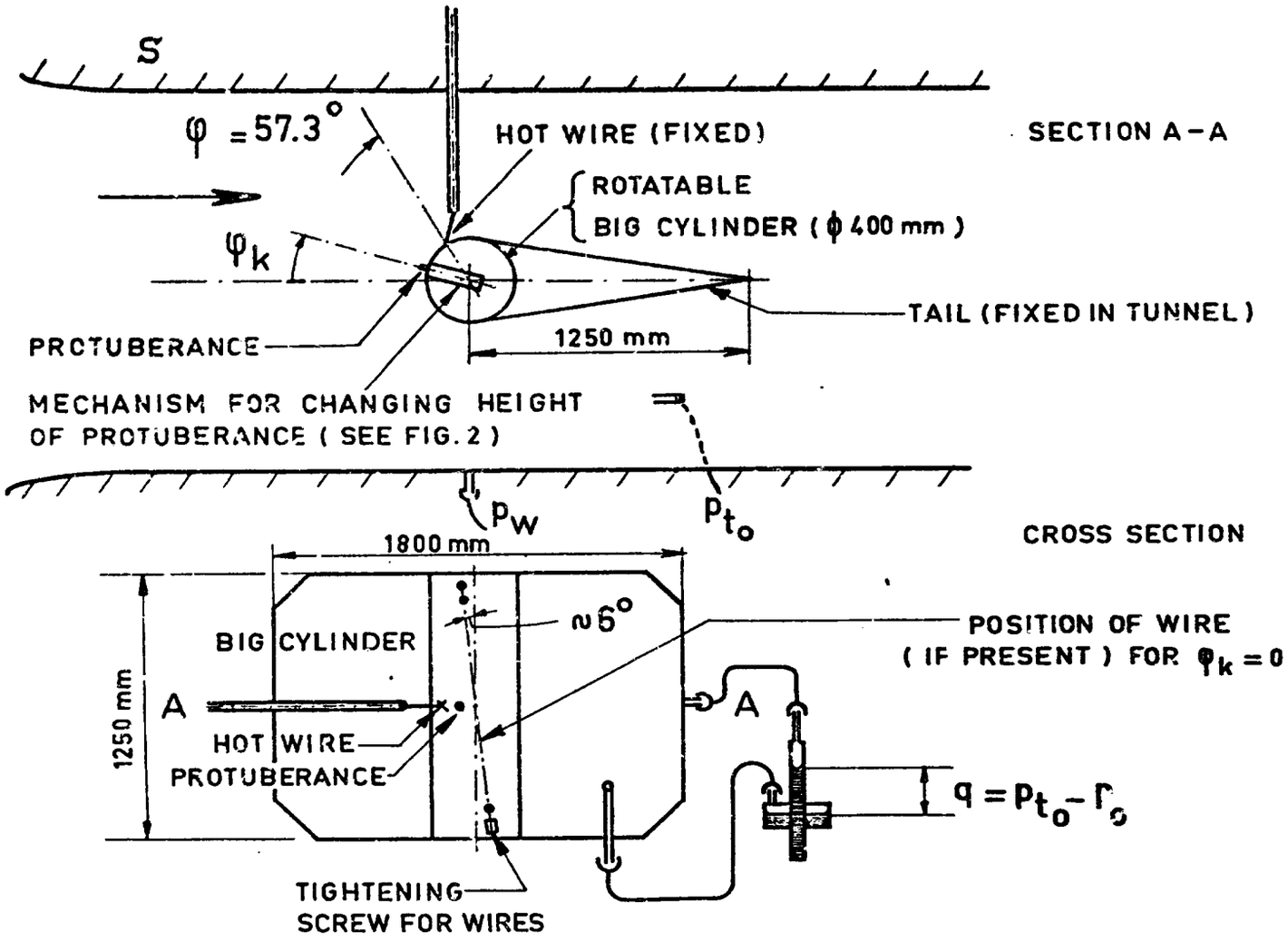

Fig. 1 Disposition in the wind tunnel

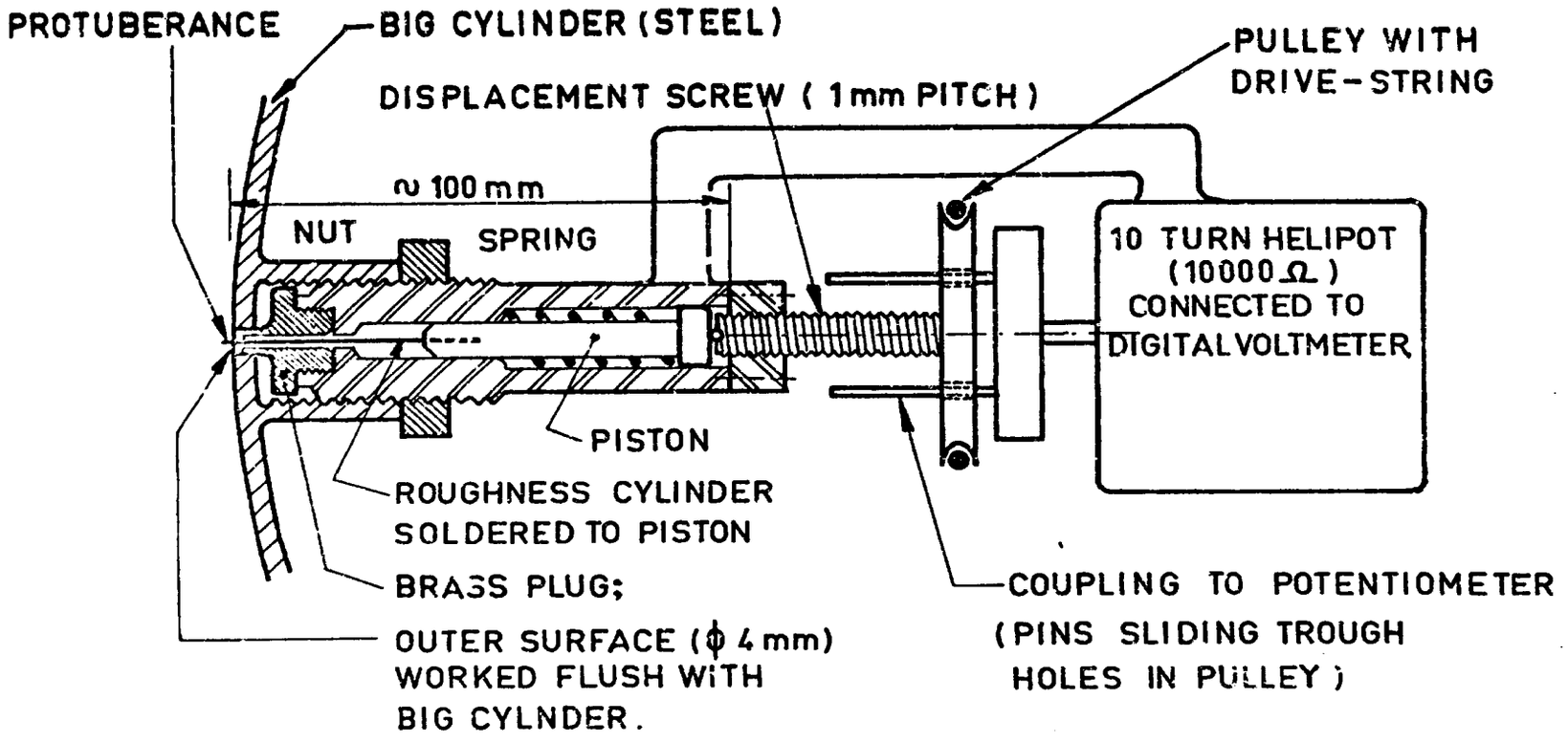

Fig. 2 The mechanism for changing the height of the protuberances

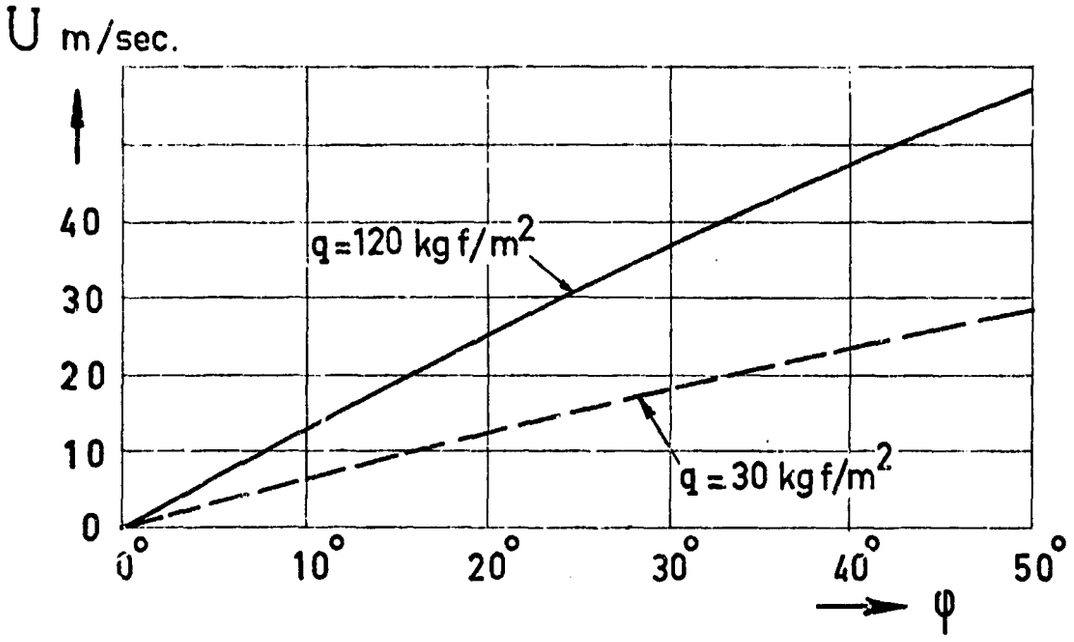

Fig. 3 The distribution of the velocity U outside the boundary-layer

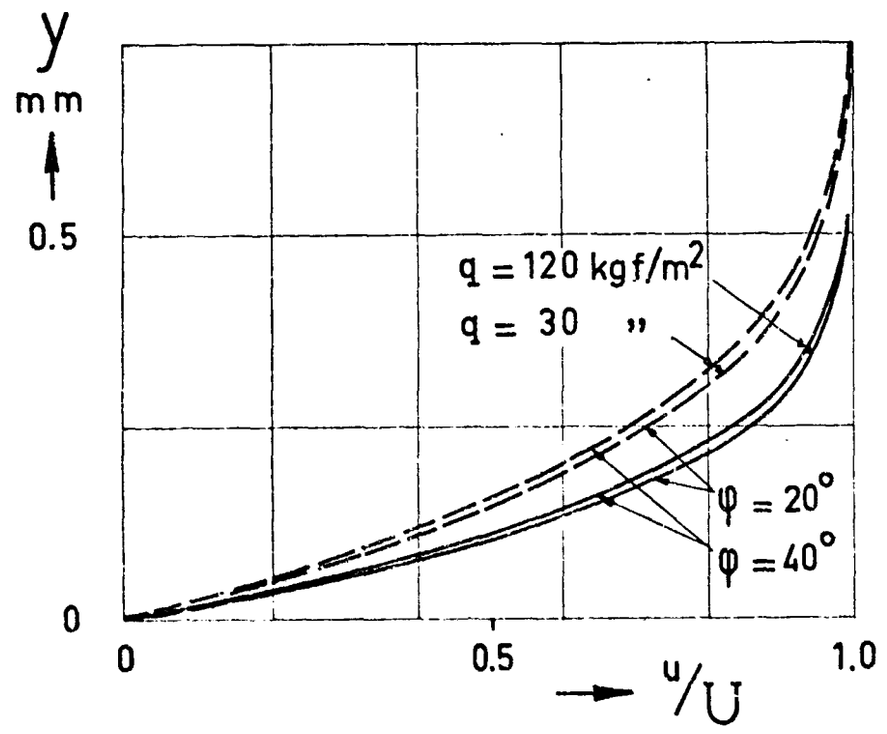

Fig. 4 Velocity profiles of the laminar boundary-layer

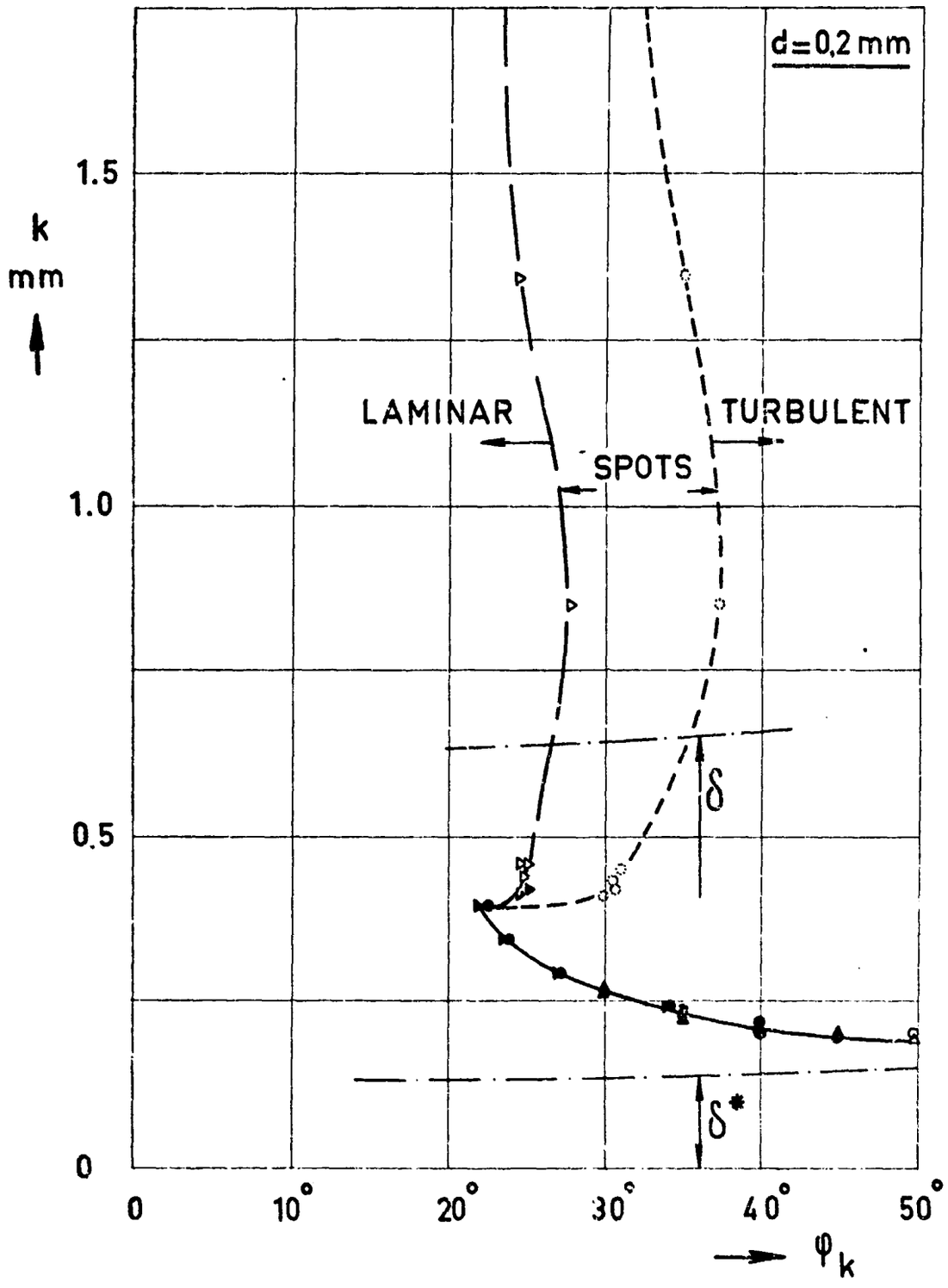

Fig. 5 The effect on the boundary-layer at station $\varphi = 57.3^{\circ}$ caused by a protuberance of 0.2 mm diameter and height k ($q = 120$ kgf/m^2)

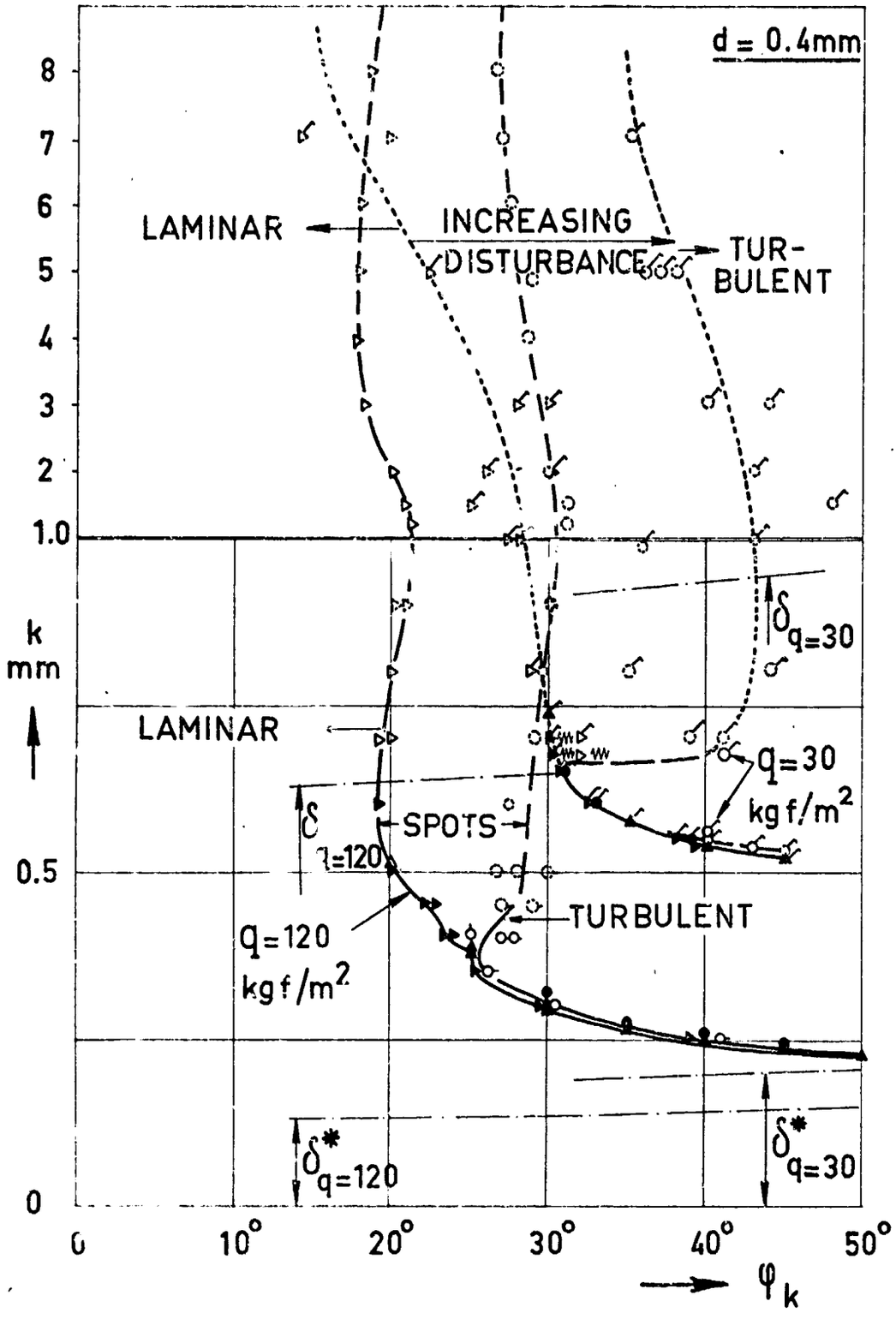

Fig.6 The effect on the boundary-layer at station $\varphi = 57.3^{\circ}$ caused by a protuberance of 0.4 mm diameter and height k

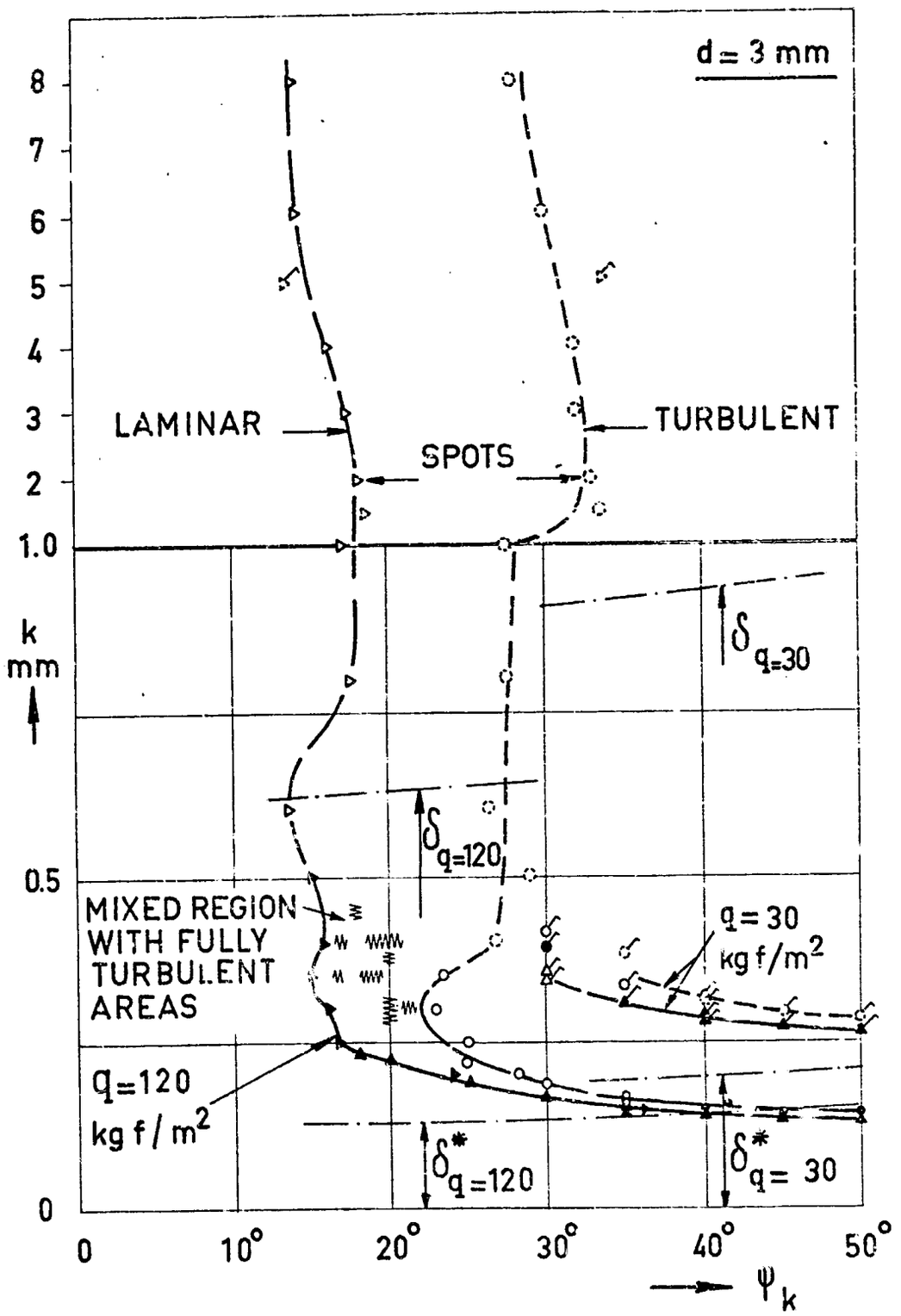

Fig. 7 The effect on the boundary-layer at station $\varphi = 57.3^\circ$ caused by a protuberance of 3.0 mm diameter and height k

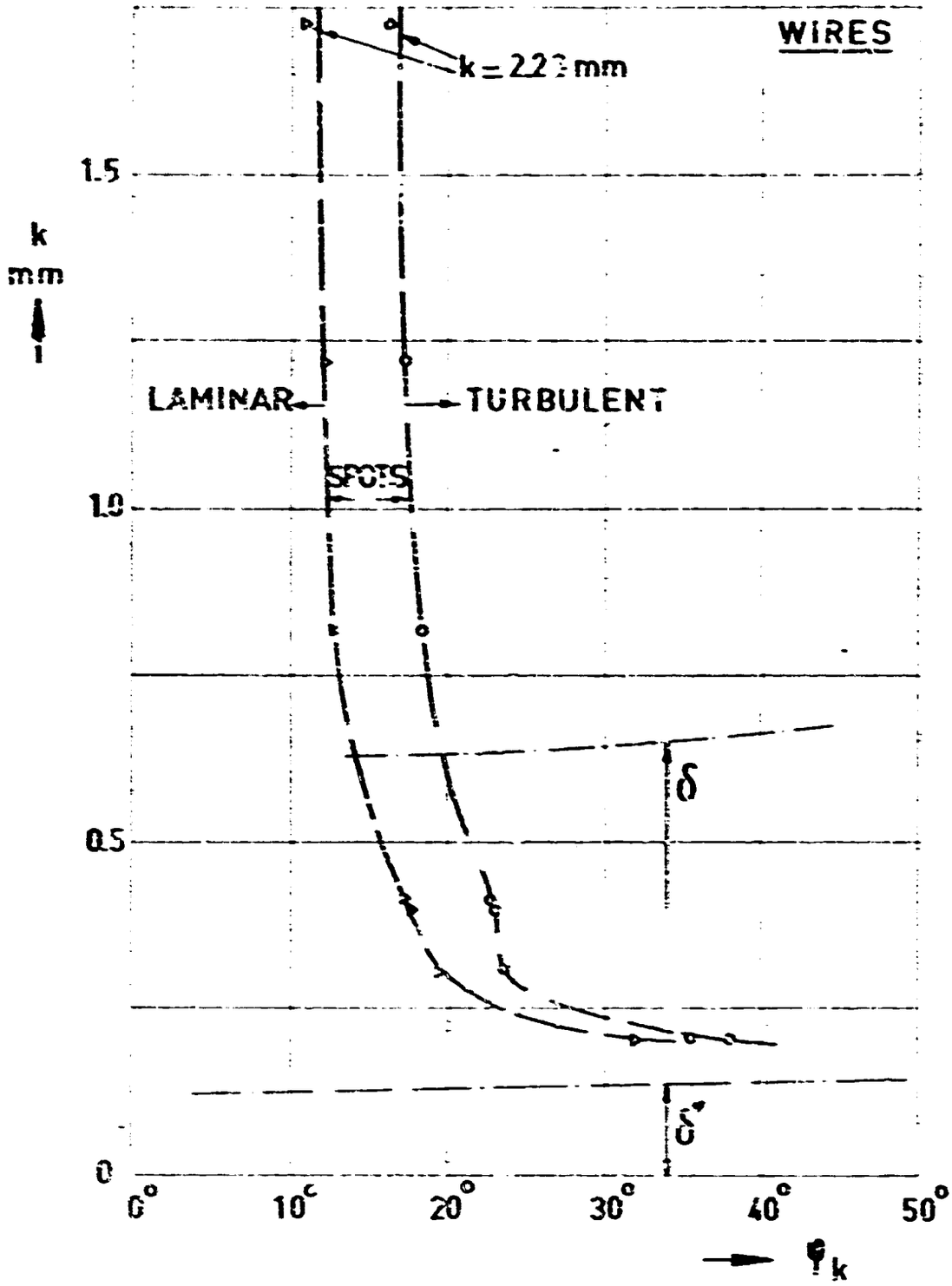

Fig 8 The effect on the boundary-layer at station $\varphi = 57.3^\circ$ caused by two-dimensional wires (k = diameter) ($q = 130$ kgf/m^2)

SOME PROBLEMS OF FLOW LAMINARIZATION ON A SLENDER DELTA WING

by

N. Gregory and E.M. Love

Aerodynamics Division,
National Physical Laboratory,
Teddington, Middlesex, U.K.

SUMMARY

The problems are discussed in the light of an experimental investigation made in a low-speed wind tunnel on the effect of distributed suction on the state of the boundary layer on a slender delta wing of aspect ratio 1 with sharp leading edges. Laminar flow at high Reynolds numbers can be maintained on the upper surface with suction at negative angles of incidence where the flow is attached throughout, and at high positive angles of incidence in areas between the secondary attachment lines and some way outboard of them. Secondary separation is preceded by strong cross flow and insufficient suction was available either to eliminate separation or to avoid transition. At other incidences wedges of turbulence appear and ways of eliminating them need to be found. The phenomenon of transverse turbulent contamination associated with any excrescences near the apex and midspan remains a difficulty.

SOMMAIRE

Ces problèmes sont discutés à la lumière de recherches expérimentales, effectuées dans une soufflerie à faible vitesse, sur l'influence de la répartition de l'aspiration sur l'état de la couche limite d'une aile delta mince dont l'allongement est de 1 pour des bords d'attaque tranchants. L'écoulement laminaire peut être maintenu sur la surface supérieure aux nombres de Mach élevés par l'aspiration sous une incidence négative là où l'écoulement est attaché de manière continue et sous une forte incidence positive dans les régions situées entre les lignes d'attache secondaires et quelque peu en dehors de celles-ci. Le décollement secondaire est précédé par un fort écoulement transversal et l'aspiration a été insuffisante pour supprimer le décollement ou éviter la transition. Aux autres incidences il apparaît des pointes de turbulence qu'il faut trouver le moyen de supprimer. Le phénomène de la contamination turbulente transversale lié à des excroissances au voisinage de la pointe et à mi-longueur constitue une difficulté à résoudre.

CONTENTS

LIST OF TABLES

LIST OF FIGURES

NOTATION

c		porous-surfaced chord
s		local semi-span
x		chordwise distance from apex
y		spanwise distance from centre-line
v_0		suction inflow velocity
U_0		undisturbed velocity
U_1		local velocity
α		incidence
ν		kinematic viscosity
C_p		pressure coefficient
R_c	=	$U_0 c/\nu$, chord Reynolds number
$U_0 x/\nu$	=	$\frac{x}{c} R_c$
R_x	=	$U_1 x/\nu$, local Reynolds number
R_{x_T}		local Reynolds number at transition
R_θ	=	$U_1 \theta/\nu$, boundary layer Reynolds number based on momentum thickness

SOME PROBLEMS OF FLOW LAMINARIZATION ON A SLENDER DELTA WING

N. Gregory and E.M. Love

1. INTRODUCTION

Although supersonic aircraft have an additional contribution to their drag – the wave drag – which is missing in subsonic aircraft, progress in design has so reduced wave drag that the skin friction drag of Mach 2 aircraft designs has again become an important portion of the total drag. A possible figure is 40%. The payload of such an aircraft is a smaller proportion of the all-up-weight than is the case subsonically, and is also a much smaller proportion of the weight of fuel carried. These points have been well brought out by Courtney[1]. A supersonic aircraft, therefore, particularly stands to benefit from any fuel economy resulting from a drag reduction due to laminarization.

A first step in the direction of discovering whether it is possible to laminarize a slender delta aircraft has been taken in the experimental work described below, in which distributed suction has been applied over the upper surface of a slender delta wing with sharp leading edges at low speeds in the 13 ft × 9 ft wind tunnel of the National Physical Laboratory. This initial experiment was undertaken at low speeds as a matter of convenience though it may well be economically important for laminar flow to be effective at subsonic as well as at supersonic cruising speeds. It was hoped to ascertain what difficulties were associated with the slender planform and its especial flow régimes, and to discover which forms of instability needed to be suppressed. Following a discussion of the results of this experiment, their application to a supersonic aircraft is considered.

2. POROUS DELTA WING

The slender delta wing was designed to be of straight conical form for a length of 6½ ft with bi-convex circular arc transverse sections 12% thick. Over this length the upper surface was formed from 0.074 in thick porous sintered stainless steel sheet, apart from 3 in at the apex which was solid. Aft of the 6½ ft porous chord a further 25 in of impermeable fibreglass fairing brought the wing back to a thin unswept trailing edge. The leading edge sweep angle was 76° giving an aspect ratio of 1. The detail design and construction of the model was carried out by Messrs. Handley Page Ltd. A general arrangement drawing of the model is shown in Figure 1 and this model is shown installed in the NPL 13 ft × 9 ft wind tunnel in Figure 2.

The porous sheet could not be obtained in one piece so it was necessary to accept two straight joins as indicated in Figure 1. The surface waviness was small along radial lines from the apex (Table I) but was much greater across the diagonal joint,

and near the edge of the model where the correct transverse curvature was not maintained. Where the waviness of the diagonal joint was found to affect slightly the transition position and suction requirements, the measurements were confined to the starboard side of the wing which was virtually free from joints.

The porous surface was divided by the supporting splines into a large centre compartment extending over ±50% of the semi-span and three narrow compartments on either side, from 50% to 60%, 60% to 75% and 75% to 100% of the semi-span. The three narrow compartments on either side of the model were connected together in pairs and the four distinct suction areas are referred to as the Centre, Inner, Middle and Outer compartments.

The permeability of the basic porous sheet was everywhere less than 130% of a mean figure, but about 12% by area was more than 30% below the mean. This area was effectively visualised by spraying the wing with naphthalene and applying a uniform mean suction inflow rate of 0.06 ft/sec to all four compartments. The bulk of the naphthalene sublimed in 20 minutes, but after half an hour of suction, there were still regions of heavy coating as shown in Figure 3. This delineates the areas of low permeability in the basic porous sheet, and also shows regions of low flow near the edges and apex due to the tapering off the depth of the compartments. It also shows some places where the adhesive used to bond and seal the porous sheet to the radial splines had spread. The oblique view that was necessary in order to photograph the entire upper surface of the wing has resulted in pronounced distortion of the chordwise perspective as shown. This particular oblique view has been used throughout the rest of the paper for all photographs and diagrams of the upper surface of the wing.

The permeability of the wing was measured separately for each compartment. The pressure differential required to produce 0.12 ft/sec mean inflow rate into each compartment was shown below, and the flow rate was

Compartment	*Centre*	*Inner*	*Middle*	*Outer*
Suction, in water gauge	75	82	100	133

roughly proportional to pressure difference. The original specification for the porous sheet demanded 0.12 ft/sec for only 28 in water gauge and as the available pumping system gave about 100 in of water gauge, the suction flow rates were very limited. It was decided to test the wing in this condition to avoid further long delays awaiting a replacement sheet.

The nominally sharp leading edge of the wing has a thickness which lay between extremes of 0.012 in and 0.018 in.

An impermeable covering of 0.0005 in thick Melinex sheet was sucked down on the upper surface to allow oil-flow techniques to be used to visualize the surface flow streamlines on the impermeable wing. Transition was indicated at low speeds by the sublimation of naphthalene sprayed on to the wing. This technique was used mainly on the impermeable covered wing: it was also used directly on the porous surface, with and without suction, but was not very satisfactory. At higher speeds, hot-film anemometry

was used, thin platinum films being plated on the leading chisel-edges of thin glass slips taped to the surface. Comparison between the two techniques was complicated by the fact that the transition front indicated by the sublimation technique showed a large forward movement with increasing time of exposure to the wind because the area of intermittent turbulence was extensive in the stream direction owing to the weakness of the pressure gradients, as on a flat plate.

The flow observations were restricted to the upper surface, but both positive and negative angles of incidence were used. Pressure distributions, however, were taken at $\frac{1}{3}$ and $\frac{2}{3}$ of the porous chord and along the centre line of the model (midspan) on both upper and lower surfaces.

3. MEASUREMENTS WITHOUT SUCTION

3.1 Pressure Distribution

The chordwise pressure distribution along the centre line of the impermeable wing is shown in Figure 4 for R_c equal to 7.5×10^6, the highest test Reynolds number, and the spanwise pressure distribution at $\frac{1}{3}$ of the porous-surface chord, c, is shown in Figure 5. The chordwise pressure distribution suggests an induced camber due partly to slight distortion of the model near the apex and partly to the interference from the mounting struts and suction pipes under the wing. The transverse pressure distribution at $\frac{2}{3}$ chord therefore differs in its peak values from that at $\frac{1}{3}$ chord, and has been omitted. The results given in this paper will be referred to geometric incidence, but it will be appreciated that corresponding transition positions and regimes of flow would be found on an uncambered delta wing free from support interference at somewhat different incidences from those encountered here.

A further departure from conicality was noticed in the transverse pressure distributions and is shown in Figure 6 which illustrates the pressures at 16^0 incidence at a number of wind speeds. The pressure recovery between the minimum pressure and the point where the pressure rise ceases is much less at the two lower speeds than at the top speed. This is because (as was shown by hot films), at 20 and 60 ft/sec wind speeds the separation is a laminar one, is transitional at 120 ft/sec, and is the separation of a fully turbulent boundary layer only at 180 ft/sec. The additional pressure rise sustainable by a turbulent boundary layer results in an outward movement of the secondary separation line. This point is discussed further in the next section.

Approximate indications of the secondary attachment position and of secondary separation have been obtained from Figure 5 and the corresponding pressure distributions at other speeds, by noting the spanwise locations at which the pressure fall commences and the pressure rise ceases. These positions are indicated in Figure 7 which also shows the position of minimum pressure. The state of the boundary layer at the approximate separation position, as indicated by hot films, is marked L (laminar), I (intermittent) or T (turbulent) on Figure 7. Good agreement was obtained with oil-flow observations when the flow was laminar. When turbulent, however, oil-flow suggested separation a few percent of the semi-span inboard of the limit of pressure rise.

3.2. Transition

Observations taken over the range of incidencies $-5^0 < \alpha < +18^0$ showed four different régimes of boundary-layer flow, of which the second was an intermediate state between the first and third and was enhanced by the induced camber effect.

First Régime, $\alpha < -1\frac{1}{2}^0$

In this régime the entire leading edge was at a negative angle of attack to the oncoming flow. In the absence of effective camber the régime should range from zero incidence. At $R_c = 2.5 \times 10^6$ the flow was laminar over most of the chord, the onset of intermittently turbulent flow being indicated by the dotted lines in Figure 8.

The transition region was extensive because of the favourable pressure gradient, and on the centre line, hot-film probes at 0.67c and 0.96c showed that transition was quite insensitive to incidence and yielded local Reynolds numbers R_{x_T} of $2.1\text{–}2.9 \times 10^6$ for first turbulent bursts to $3.6\text{–}4.0 \times 10^6$ for fully turbulent flow as shown in Table II. These can be compared with values of R_{x_T} of $1.5\text{–}1.7 \times 10^6$ obtained in a flat plate at zero incidence in the same tunnel.

Away from the centre line, wedges of turbulent flow were present, as can be seen in Figure 8, and from their mid-semi-span location are referred to hereafter as 'inboard' wedges. These wedges appeared at local Reynolds numbers between 1.6 and 2.6×10^6 and gave fully turbulent flow at about 2.5 to 3.6×10^6 as shown in Table III. At a given incidence, these inboard wedges appeared at a roughly constant percentage of the semi-span independent of their chordwise origin, but when incidence and windspeed were both varied so as to maintain the origin of the inboard wedge at a fixed chordwise location, the spanwise origin moved further outboard with increasingly negative incidence. Once formed, however, the wedges ran in the mainstream direction. It was checked that these wedges of turbulent flow would have intersected on the centre line further aft than the transition points indicated in Table II. The reasons for these wedges of turbulent flow are still obscure.

Second Régime, $-1\frac{1}{2}^0 < \alpha < 3^0$

Here, the forward portion of the leading edge was at a negative angle of attack to the local flow, but the angle changes to a positive one further aft. Laminar flow is obtained over the front of the wing, but is terminated by the intersection of wedges of turbulent flow originating part way along the leading edge (Figure 8) where the attached flow first gives way to a small separation bubble. These wedges of turbulent flow are subsequently referred to as 'edge' wedges. Their position is principally determined by the effective incidence variations along the leading edge, rather than by Reynolds number, since an increase in the latter causes the origin of the separation bubble to move forward but a small amount, before attached flow conditions are reached.

It should be mentioned that at wind speeds up to 80 ft/sec, striations were present in the sublimation pattern inboard of the edge turbulent wedges. These striations, indicating stationary streamwise vortices in the boundary layer, originated along the leading edge over 4 or 5 inches distance upstream of the point of laminar flow breakdown and were visible for some 7 to 8 inches in the chordwise direction.

Oil-flow technique showed that (in the particular case of 0° incidence at 80 ft/sec) the $\frac{1}{10}$ in long separation bubble, from which the edge wedges of turbulent flow started, persisted along the leading edge for about a foot but then ceased to re-attach and rolled up so that secondary attachment and separation lines radiated from this point, just as happens at much higher incidences at the apex. However, at the rear of the porous surface both attachment and separation remained within an inch or two of the leading edge. The flow inboard of this secondary attachment remained turbulent.

At zero and -1° incidence, hot films at 0.33c revealed transition conditions which were constant over a considerable spanwise extent inboard of the edge wedges of turbulent flow. The transition Reynolds numbers, Table IV, are appreciably less than those of Table II and are also less than those for positions further aft (at lower speeds) where laminar flow is terminated by the intersection of wedges at values of $R_{x_T} \times 10^{-6}$ which may rise as high as 3.0 to 4.0. It is possible that an indiscernible roughness or imperfection at the apex, or indeed the apex itself, was responsible for these low transition Reynolds numbers. This is suggested by a single streak observed in the sublimation pattern at 60 ft/sec at incidences between 1° and 4° coming straight from the apex, although at these wind speeds the vortex pair thus indicated did not interfere with the interesting wedge transition pattern. However, the whole second régime may not be of great practical importance for a wing without any geometric or induced camber.

Third Régime $4^\circ < \alpha < 12^\circ$

This incidence range is characterised by the rolling up of the leading edge shear layer with the occurrence of a fresh secondary attachement line whose position moves inboard with increase of incidence (Figure 7) and reaches the vicinity of the centre line at an incidence not far above 12°.

The transition pattern changes markedly with both incidence and Reynolds number. At a fixed wind speed of 60 ft/sec, (R_c equal to 2.5×10^6) the effect of incidence is shown by Figures 9 to 11. Inboard of the secondary attachment line the flow is laminar except where contaminated by a pair of wedges of turbulent flow. At 4° incidence these wedges originate from the apex but owing to the small local Reynolds number do not at first spread very rapidly. Further aft, the fully turbulent core of these wedges spreads at a semi-angle of about 7° and since the attachment line is spreading at 8.8° semi-angle, there is a narrow region of intermittently turbulent flow, but no laminar flow. It is probable that these wedges are the edge wedges of the second régime starting inboard of a closed separation bubble very near the apex. The shear layer ceases to re-attach and rolls up a very short distance from the apex, thus creating secondary attachment lines, and causing the wedges to appear between them. At 6° incidence the situation is similar, but the fully turbulent core of the wedge does not occur until about 0.55 chord back from the apex. At this incidence the attachment lines are diverging at less than the spread angle of the fully turbulent core of the wedge, so that at this and higher incidences these wedges eventually reach the attachment line and contaminate the flow outboard of attachment. At 8° (Figure 10) and 10° the twin wedges start intermittently at about 0.55c and the flow upstream of this point is laminar. It is noteworthy that apart from the 4° case, the wedges always seem to be about ±0.25 s from the centre line at the point where they are first detected, though their chordwise origin varies with both incidence and Reynolds number. This is illustrated by Tables V and VI. At 12° the wedges do not

appear, either because attachment has moved inboard of the ±0.25 semi-span position, or because the rolling up of the leading edge shear layer continues right to the apex. From $-1\frac{1}{2}$ to 12° incidence therefore, laminar flow on the centre line is terminated by the intersection of turbulent edges.

Outboard of attachment the flow near the apex is laminar (at 60 ft/sec) at 8° and above where the inboard wedges of turbulent flow do not spread across the flow attachment line. When the flow eventually becomes turbulent further away from the apex the flow can stand a larger pressure rise before separation, which therefore moves further outboard. A kink occurs in the separation line as is visualised by the oil-flow technique, Figures 12 and 13. This phenomenon is discussed quantitatively in the next section.

Fourth Régime $\alpha > 12^{\circ}$

As the twin attachment lines approach one another and completely coalesce into a single centre-line attachment, the troublesome turbulent wedges of the last section are eliminated. Transition of the flow between about ±0.5s now re-appears free from spanwise contamination and is spread (Table VII) over a local Reynolds number region between, roughly, $2.5\text{-}3 \times 10^6$ to $3.5\text{-}4 \times 10^6$, values that agree very well with those recorded in Table I for negative incidences.

The kink in the separation line, like the other transition phenomena, is spread over an appreciable chordwise extent as can be seen from oil-flow photographs, Figures 12, 13. It does not show up in the sublimation photographs, such as Figure 14 for 16° incidence, except for a very slight wave in the sublimation boundary which indicates the change from laminar separation near the apex to transition to turbulent flow further aft. It so happens that these phenomena occur at much the same spanwise position. The turbulent separation is not indicated by sublimation. The locally streamwise boundary layer vortices which can be seen in Figure 14 cannot be used as a guide to the kink in the separation line since they are found upstream of laminar separation as well as upstream of transition. They do however indicate that this transition when it occurs results from an instability of the cross flow in the boundary layer.

The change in the type of separation results in its outward shift by about 0.05 semi-span at 8° (0.75 → 0.8s), increasing to 0.17 semi-span at 18° (0.65 → 0.82s): the position of turbulent separation is relatively insensitive to incidence. The local Reynolds number at which the kink in the separation line occurs is about 2.2×10^6 and is also relatively insensitive to incidence, though it increases slightly with increasing wind speed, Table VIII.

These observations are in broad agreement with those of Lawford[2] for a very much smaller convex-surfaced model.

4. MEASUREMENTS WITH SUCTION

4.1 Transition

The effect of suction on transition can now be considered in the light of the qualitative description of the flow over the impermeable wing given in the preceeding section.

The low permeability of the porous surface limited the mean inflow rate, $v_0/U_0 \times 10^4$, at 180 ft/sec windspeed (R_c equal to 7.5×10^6) tc 5.5 out to 75% of the semi-span and to 4 between 75% and the leading edge. Although these ratios could be raised by lowing the wind speed, this would not have helped since the Reynolds number and the need for suction would also have been reduced by this artifice.

First Régime, $\alpha < -1\frac{1}{2}^\circ$

As the flow was essentially streamwise, various uniform inflow rates were applied over the whole upper surface, and the maximum wind speeds were determined at which the flow at various semi-span locations at 0.67 and 0.96 chord were kept free from first bursts of turbulent flow. The relation between the inflow velocity ratio v_0/U_0 and the Reynolds number U_0x/ν, for a range of semi-span positions is shown in Figure 15a and b for -5° and $-1\frac{1}{2}^\circ$ incidence. Results for intermediate incidences also lie between these two sets of graphs.

It should be noted in Figure 15 that at the same Reynolds number the suction velocity ratio required is greater at 0.67c than at 0.96c. This follows the trend seen in Tables II, III, V and VII where without suction, the greater wind speeds (and also tunnel turbulence levels) result in slightly smaller critical transition Reynolds numbers. This trend is also reinforced by the increasingly favourable pressure gradients found at the rear of the model, Figure 4. An additional factor in the case of suction is evident from Figure 3 which suggests that at a given mean inflow rate, the local inflow towards the rear of the model is slightly in excess of the inflow further forward.

The inboard wedges of turbulent flow shown in Figure 8 and Table III are eliminated by applying a considerably greater inflow rate than is necessary to maintain laminar flow closer to the centre-line. At $-1\frac{1}{2}^\circ$ and -2°, however, the flow rate required on the centre line itself is greater than that necessary at spanwise stations on either side. This is the extra suction required to cope with the particular disturbances which gave rise to the low transition Reynolds numbers of Table IV. Despite these features, the variation of suction inflow velocity ratio required to give laminar flow along the centre line with change of incidence appears to be a gradual process, Figure 16.

Second Regime, $-1\frac{1}{2} \leqslant \alpha \leqslant 3^\circ$

The principal feature of this régime is the intersecting wedges of turbulent flow originating at some joint along the edge where the flow first separates. The available suction has no effect on the origin of these turbulent wedges, and only reduced slightly the wedge spreading angle so that only a few percent chord of extra laminar flow can be gained by suction. The onset of the edge wedge can be seen in the suction results for $-1\frac{1}{2}^\circ$ incidence, with hot-film gauge at x/c equal to 0.96 and y/s equal to 0.92 shown in Figure 15(b). At -1° and a high wind speed so that centre-line transition was ahead of the interaction of the edge wedges, and was due to the disturbance indicated by Table IV, the high suction rate of $v_0/U_0 \times 10^4$ equal to 3.3 was required at a local Reynolds number of 2.5×10^6, compared with 0.6 required out to 0.33s on either side of the centre line.

Third Régime, $4^\circ < \alpha < 12^\circ$

Without suction, inboard wedges of turbulent flow occur at a Reynolds number which varies both with incidence and chordwise position (Tables V and VI). Suction (within that available) was only able to delay the occurrence of these wedges by a limited amount, as is instanced for 8° incidence in Figure 15c.

The flow necessary to maintain laminar flow outboard of 0.5s is discussed in the next section.

Fourth Régime, $\alpha > 12^\circ$

Over the inboard half of the wing, transition without suction was due to the normal instability of two-dimensional flow. A small inflow rate is consequently able to maintain laminar flow, Figure 15(d), (e), and this rate does not vary significantly with the spanwise location.

Further outboard, difficulty was experienced in using hot films to indicate transition where this was due to secondary flow instability as it was initiated by the appearance of high frequency turbulence rather than by a large increase in the amplitude of the disturbance. In order to obtain results, hot wires were used instead, as they had a better high frequency response. It was found that the application suction only over the narrow compartments outboard of 0.5s was ineffective. Extra suction eliminated turbulence when applied uniformly over the whole surface, and yield the results shown in Figure 15(d) and (e). Still further increase eliminated altogether any signs of cross-flow vortices. The lack of results at high Reynolds numbers is due to the limitation on suction flow rather than any fundamental difficulty such as occurred in the other régimes.

4.2 Pressure Distribution

The available inflow was even more inadequate to eliminate secondary separation, to do which Oberdorffer[3] and Moore[4] had measured inflow rates in the region of $(v_0/U_0)\sqrt{U_0 x/\nu}$ between 30 and 60 for a slender delta wing with a thick biconvex cross-section with leading-edge angle in the cross-flow plane of 88°. By dropping the wind speed, suction flow rates $(v_0/U_0)\sqrt{U_0 x/\nu}$ up to 1.9 were obtained on the present wing. Transverse pressure distributions are shown in Figure 17. The suction flow rates quoted were the maximum attainable at the given wind speed and are for the centre and middle compartments. The flow into the inner compartment was about 19% lower, and into the outer compartment about 37% lower than the figures quoted. Judged by the movement of the position of cessation of pressure rise, the flow rate $(v_0/U_0)\sqrt{U_0 x/\nu}$ of 1.9 used at the lowest wind speed moved laminar separation outboard by about 0.13 semi-span, the lower rate of 1.1 had a much smaller effect, and at the highest wind speed where the flow was turbulent without suction, the available suction did not prevent transition due to secondary flow instability and had no beneficial effect on the subsequent turbulent separation.

5. DISCUSSION

5.1 Present Experimental Results

An attempt is made in Figure 18 to summarise schematically the results discussed in detail in the preceding two sections. The variation with incidence of the spanwise position of the various types of flow is shown and mean values are listed for the local Reynolds numbers $U_1 x/\nu$ for the onset of transition in each portion of the flow. The unattached numbers are the values of $v_0/U_0 \times 10^4$, the suction quantity necessary to maintain laminar flow at a Reynolds number of $U_0 x/\nu$ of 6×10^6.

Wedges of turbulent flow are found in Régimes II and III which are not prevented by the application of distributed suction, and the flow outboard of secondary separation is always turbulent. It is desirable to find out whether the inboard and edge wedges are peculiar to the present sharp edged wing. It should also be established whether by eliminating the effective camber of the present wing the edge wedge can be eliminated or the incidence range over which it occurs can be reduced. A modification that it is intended to investigate is a small radius rounding of the leading edge to give attached flow at incidence near zero, but this would introduce the likelihood of spanwise contamination along the leading edge at high Reynolds numbers which would require further arrangements of localised slot suction for control. It is also desirable to confirm whether the inboard wedges of Régimes I and III are associated with the flow at the apex as is thought to be the case, and hence to discover whether they can be eliminated by modification of the apex, such as apex rounding, distributed suction at the apex, or by suction at a full-span slit just aft of the apex. These turbulent wedges appear over such a large incidence range of the present slender delta, covering the likely range of cruising lift coefficients, as to render the present slender delta design unsuitable for laminarization until ways of eliminating these wedges have been found.

The maximum test Reynolds number of 8×10^6 was insufficient to allow scale effect on suction quantity to be assessed owing to the considerable run of natural laminar boundary layer in the presence of favourable pressure gradients. Suction was applied uniformly from the apex, and all the curves of Figure 15 show an increase in suction with Reynolds number $U_0 x/\nu$ from zero at $U_0 x/\nu$ equal to about 2×10^6. If constant values of R_θ, the boundary layer Reynolds number were to be found far enough downstream, and these were independent of Reynolds number and of tunnel turbulence level, constant values v_0/U_0 would be required. The only signs of this occurring are in the regions of straight forward wedge-free flow, along the centre line at negative incidences, and immediately outboard of attachment at high positive incidences, but asymptotic values of v_0/U_0 cannot be determined. Any further experimental work should be extended to higher Reynolds numbers, and it would also be desirable to measure drag. It is encouraging to note that at a chord Reynolds number of 6×10^6 even the best results obtained from earlier work on two-dimensional and 30° swept laminar flow aerofoil experiments[5] have required suction quantities $v_0/U_0 \times 10^4$ as high as 4. Thus, if the rapid rise of suction quantity with increase of Reynolds number, which is required to prevent the turbulent wedges from occurring, can be avoided, the suction demands for a slender delta wing may not prove excessive.

Looking further ahead, two practical problems particularly require investigation. The conditions at a wing-body junction when the wing has separated flow must be

examined. And slit design and geometry have to be determined for practical surfaces which would be effective for boundary-layer flow in the various directions which might occur over a suitable incidence range.

5.2 Laminarization of a Supersonic Slender Delta

The various types of attached, seperated and mixed flows that can be found around highly swept leading edges in supersonic flight are discussed by Stanbrook and Squire[6], who give criteria for the occurrence of various types of flow. When separated flow occurs at the leading edge the vortex lies further inboard than at low speeds[7]. This suggests that it would be more worthwhile to suck sufficiently to maintain the flow laminar against cross-flow instability as the extent of flow affected would be much larger than in the incompressible case. It is not clear, however, whether it would be easy to do so, as the vortex is closer to the upper surface, which might possibly result in boundary layer transition due to turbulence in the external flow. In the present experiment, laminar flow was not obtained until about 3° incidence, but at the lower incidences it is thought that the turbulent boundary-layer under the vortex was due to contamination from upstream near the apex rather than the mechanism just suggested. The necessity for tests at full-scale Mach number is obvious.

Another possibility is attached flow at the swept leading edge, with a weak oblique shock wave further aft which deflects the flow into the streamwise direction, or if strong enough, causes boundary-layer separation and an inboard rolled-up vortex sheet. The latter flow would be similar in principle to that investigation here, but the attached flow deflected by the shock would develop a cross flow and experimental research is required to see whether transition could be prevented by boundary layer control.

Further complications would arise from the flow over wings with curved leading edges. Separated flow could occur outboard of attached flow, with the possibility, as in the present tests, of turbulent contamination originating at the start of the flow region which of itself might be compatible with laminar flow inboard of secondary separation further away from the apex. Conversely, with an ogee shape in which the sweep of the leading edge is reduced outboard, a free vortex might leave the leading edge and cross the wing, with an outboard region of attached supersonic flow.

In view of these numerous types of flow which might occur, much more experimental work is required, particularly at full-scale Mach number, before it will be clear whether it is possible to achieve laminar flow supersonically on a slender delta aircraft.

5.3 Turbulent Contamination

The problem of turbulent contamination is encountered on a slender delta wing in a slightly different form from the spanwise leading-edge contamination problem on wings of lower sweep angle. If the leading edge were rounded, the phenomenon would occur as on a wing of lower sweep, but this would not matter if the flow subsequently separated close to its initial attachment. On the other hand, if the flow remained attached, then the measures developed for swept wings would again be required.

The transverse pressure gradients at the inboard secondary attachment are so small compared with those at a leading edge of small radius of curvature that the stability

of the flow along such an attachment line is probably not greatly different from that of two-dimensional boundary-layer flow, and small amounts of suction inflow should keep the flow laminar. If an isolated excrescence were present, however, the results are equally as serious as at the leading edge of a swept wing. For at incidences where one or two inboard attachment lines occur on the upper surface, the flow directions are such that, coupled with the natural spread of turbulence perpendicular to the local flow, turbulence from an isolated excrescence on or near an attachment line eventually spreads to the secondary separation position on both sides of the centre-line of the wing. This is illustrated by Figure 19 which shows for 12° incidence, considerable areas of the present wing for which a single excrescence would contaminate over 50% of the possible laminar area. For the sake of this calculation it has been assumed that distributed suction would maintain the flow laminar as far outboard as 80% of the semi-span, where the previous turbulent separation would become a laminar separation.

The situation is not a great deal better at zero incidence with parallel flow over the wing surface. Just because the wing is of low aspect ratio with leading edges diverging from the apex at an angle less than half as much again as the spread angle of the turbulent wedge, an excrescence at the apex would contaminate just over 70% of the laminar area. Contours for the rest of the wing are shown in Figure 20.

If substantial drag reductions are to be guaranteed on a slender delta, it will therefore be necessary to fit a number of transverse slots over some or all of the span in the upper surface, over at least the first half of the chord. These slots will have to be able to remove the whole turbulent boundary layer if contamination has occurred, without undue duct loss, and not to upset laminar flow if no suction is required. Alternatively, a means would be required for cleaning the aircraft surface in flight so as to be able to guarantee the absence of excrescences.

6. CONCLUSIONS

Wind tunnel tests at low speeds on a slender delta wing with a sharp leading edge and a wholly porous upper surface have revealed that distributed suction can only maintain laminar flow at negative angles of incidence and at high positive angles of incidence where the secondary attachment lines occur inboard of 25% semi-span. In these latter conditions laminar flow obtained from the centre line to about 60% of the semi-span, outboard of which insufficient suction was available to avoid transition due to strong cross-flow which preceded secondary separation. At other incidences, wedges of turbulent flow were present which were not eliminated by suction. These wedges either originated on the leading edge at the point where attached flow first gave way to a bubble of separation, or appeared to be caused by disturbances due to the apex acting as a roughness. Further tests will be carried out with the leading edge and the apex rounded to establish whether these troublesome turbulent wedges are peculiar to a sharp-edged model.

To establish finally the economy of laminarisation of a slender delta layout required further experimental work. This must be extended to a higher Reynolds number in order to ascertain the effects on suction quantity, and to the full-scale Mach number in order to ascertain the effects of compressibility: future experiments must also measure drag.

A further problem concerns the serious effects of turbulent contamination on wings of low aspect ratio. Methods must be found for ensuring that a slender delta wing does not lose a substantial proportion of its laminar flow owing to the presence of a single isolated excrescence on the front part of the wing.

ACKNOWLEDGMENTS

Acknowledgments are due to Miss S.P. [illegible] for assistance with the experimental work and to Mr. P.E.C. Hounsfield of Messrs. Handley Page Ltd. for his interest and cooperation in the manufacture of the model.

The work described in this paper forms part of the research programme carried out by the Aerodynamics Division of the National Physical Laboratory for the Ministry of Aviation and is published with the permission of the Director, National Physical Laboratory.

REFERENCES

1. Courtney, A.L. — *Some Considerations Affecting the Design and Operation of Supersonic Civil Transports.* Journ. Roy. Aero Soc., Vol.68, 598, September 1964.

2. Lanford, J.A. — *Low-Speed Wind Tunnel Experiments on a Series of Sharp-Edged Delta Wings. Part II. Surface Flow Patterns and Boundary Layer Transition Measurements.* R.A.E. Tech. Note Aero 2954, ARC 26032, March 1964.

3. Oberdorffer, E. — *The Influence of the Secondary Separation in the Flow Round a Slender Delta Wing With Leading Edge Separation.* Thesis, Training Centre for Experimental Aerodynamics, Brussels, 1961.

4. Moore, D.G. — *Low Speed Tests Using Suction on a Slender Delta With Leading Edge Separation.* Thesis, Training Centre For Experimental Aerodynamics Brussels, June 1962.

5. Lachmann, G.V. (ed) — *Boundary Layer and Flow Control: Its Principles and Application.* Vol.II, pp.945 and 1023, Pergamon Press. 1961.

6. Stanbrook, A. Squire, L.C. — *Possible Types of Flow at Swept Leading Edges.* The Aeronautical Quarterly, Vol.15 (1) 72, February 1964.

7. Gaudet, L. Winter, K.G. — *Preliminary Measurements of the Flow Field on the Lee-Side of a Delta Wing of Unit Aspect Ratio At a Mach Number of 2.6 and an Incidence of 15°.* RAE Tech Note Aero 2787, ARC 23,510, September 1961.

Table I

Waviness measured on a 3 in gauge length

	General limit	*Across diagonal joint*	*Close to leading edge*
Radial traverse	± 0.002 in	± 0.008 in ± 0.012 in	
Transverse traverse	± 0.005 in	± 0.010 in	± 0.010 in near apex

Table II

Centre-line transition at incidences, $-5^{\circ} < \alpha < -1\frac{1}{2}^{\circ}$

	First burst		*Fully turbulent*	
x/c	0.67	0.96	0.67	0.96
U_{∞} ft/sec	75-80	65/70	130	95
$R_{L_T} \times 10^6$	2.1-2.2	2.[illegible]-2.94	3.6	4.9

Table III

Inboard turbulent wedges at incidences, $-5^{\circ} \leqslant \alpha \leqslant -1\frac{1}{2}^{\circ}$

	First bursts							
x/c	0.67				0.96			
α°	-5	-3	-2	$-1\frac{1}{2}$	-5	-3	-2	$-1\frac{1}{2}$
U_0 ft/sec	60	60	70	70	55	55	60	-
$R_{x_T} \times 10^{-6}$	1.64	1.66	1.96	1.97	2.3	2.3	2.6	
Spanwise position, $\frac{y}{s}$	0.50(?)	0.50	0.50	0.50	0.40 -0.75	0.58 -0.75	0.33	
	Fully turbulent							
x/c	0.67				0.96			
α°	-5	-3	-2	$-1\frac{1}{2}$	-5	-3	-2	$-1\frac{1}{2}$
U_0 ft/sec	90	93	107	108	68	72	78	75
$R_{x_T} \times 10^{-6}$	2.5	2.6	3.0	3.3	2.8	3.0	3.3	3.6
Spanwise position, $\frac{y}{s}$	0.58 -0.75	0.50 -0.67	0.50	0.50	0.58 -0.75	0.58	0.41	0.33

Table IV

Central transition at incidences, $-1^{\circ} \leqslant \alpha \leqslant 0^{\circ}$ at 0.33 chord

	First bursts		*Fully turbulent*	
α°	-1	0	-1	0
U_0 ft/sec	85	65	170	85
Spanwise extent, $\frac{y}{s}$	± 0.33	± 0.5	± 0.33	± 0.6
$R_{x_T} \times 10^{-6}$	1.3	0.9	2.3	1.2

Table V

Scale effect on inboard wedges at 8° incidence

	First bursts			*Fully turbulent*			*By sublimation*	
U_0 ft/sec	60	30-50	45	110	85	65	80	120
Chordwise origin, $\frac{x}{c}$	0.33	0.67	0.96	0.33	0.67	0.96	0.55	0.35
$R_{x_T} \times 10^{-6}$	0.9	0.9-1.5	1.9	1.6	2.5	2.74	1.93	1.85

Table VI

Incidence and scale effect on inboard wedges.

Conditions at which fully turbulent wedges originate at 0.33 chord.

Incidence	4°	6°	8°	10°
U_0 ft/sec	25-50	85	85-110	120-145
$R_{x_T} \times 10^{-6}$	0.35-0.70	1.2	1.2-1.6	1.6-2.1

Table VII

Transition on inner half of wing at incidences, $\alpha \geq 12^0$

Where two values of U_c, x/c or R_{x_T} are given, the left hand value indicates first bursts and the right hand value fully turbulent conditions.

α^0	U_0 ft/sec	x/c	$R_{x_T} \times 10^{-6}$
12	140-165(?)	0.33	2 14-2.52(?)
	85-115	0.67	2.59-3.51
	80	0.66-0.95	2.43-3.52
	60	0.90->1	2.51-
14	98-118	0.67	3.03-3.64
	68-83	0.96	3.07-3.74
16	180-200(?)	0.33	2.85-3.17(?)
	102-115	0.67	3.16-3.55
	68-85	0.96	3.10-3.87
18	100-120	0.67	3 21-3.84
	-85	0.96	-3.92
	80	0.89-1.0	3.06-3.84

Table VIII

Change in type of secondary separation

α^0	U_0 ft/sec	*Technique*	x/c	$C_{p_{sepn}}$	$R_x \times 10^{-6}$
6	60	S	0.76	-0.41	2.26
7	60	S	0.72	-0.46	2.17
8	60	S	0.71	-0.51	2.17
10	60	S	0.67	-0.62	2.12
12	60	S	0.65	-0.72	2.12
	80	S	0.60	-0.74	2.63
	80	O	0.50-0.60	-0.74	2.19-2.63
	120	O Port	0.40-0.43	-0.75	2.64-2.83
		O Stbd	0.38-0.43	-0.75	2.50-2.83
	180	O	0.23-0.28	-0.75	2.27-2.76
14	60	S	0.65	-0.89	2.06
16	60	S	0.55	-1.02	1.95
18	80	S	0.3-0.4	-1.19	1.48-1.97
		O Port	0.3-0.44	-1.19	1.48-2.16
		O Stbd	0.4-0.50	-1.19	1.97-2.46

S = sublimation
O = oil flow

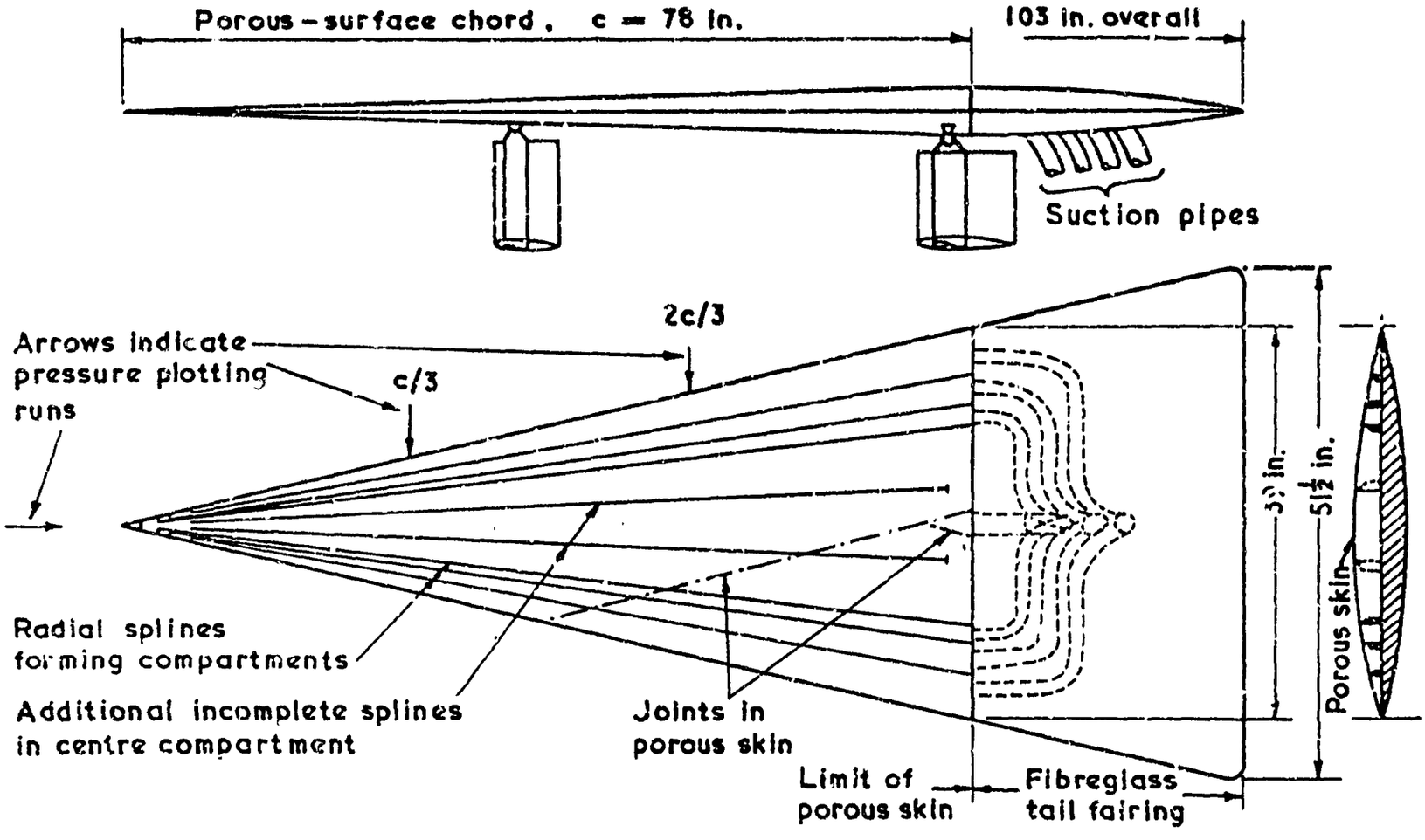

Fig. 1 General arrangement of porous delta wing

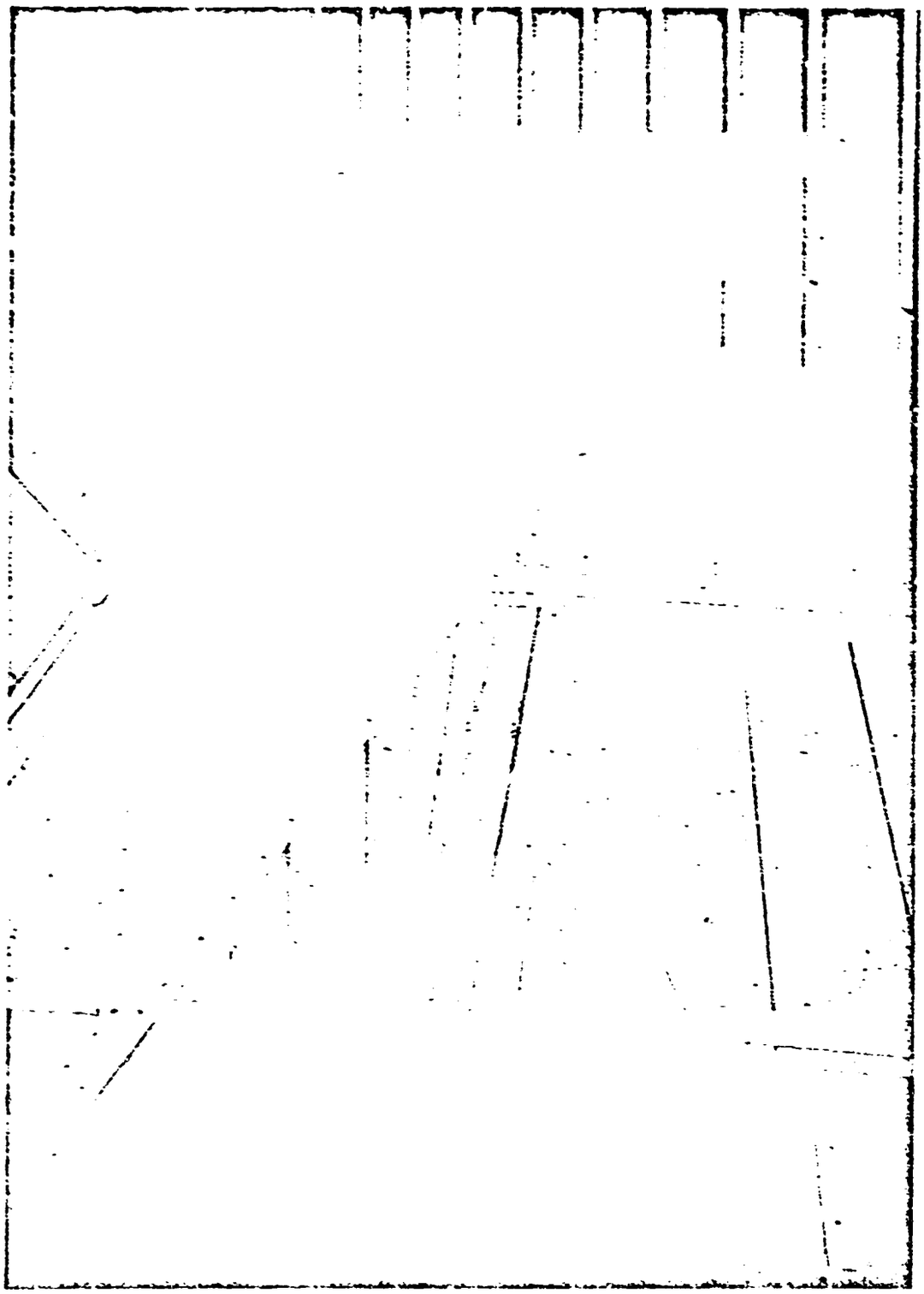

Fig. 2 Porous delta wing installed in 13 ft × 9 ft wind tunnel

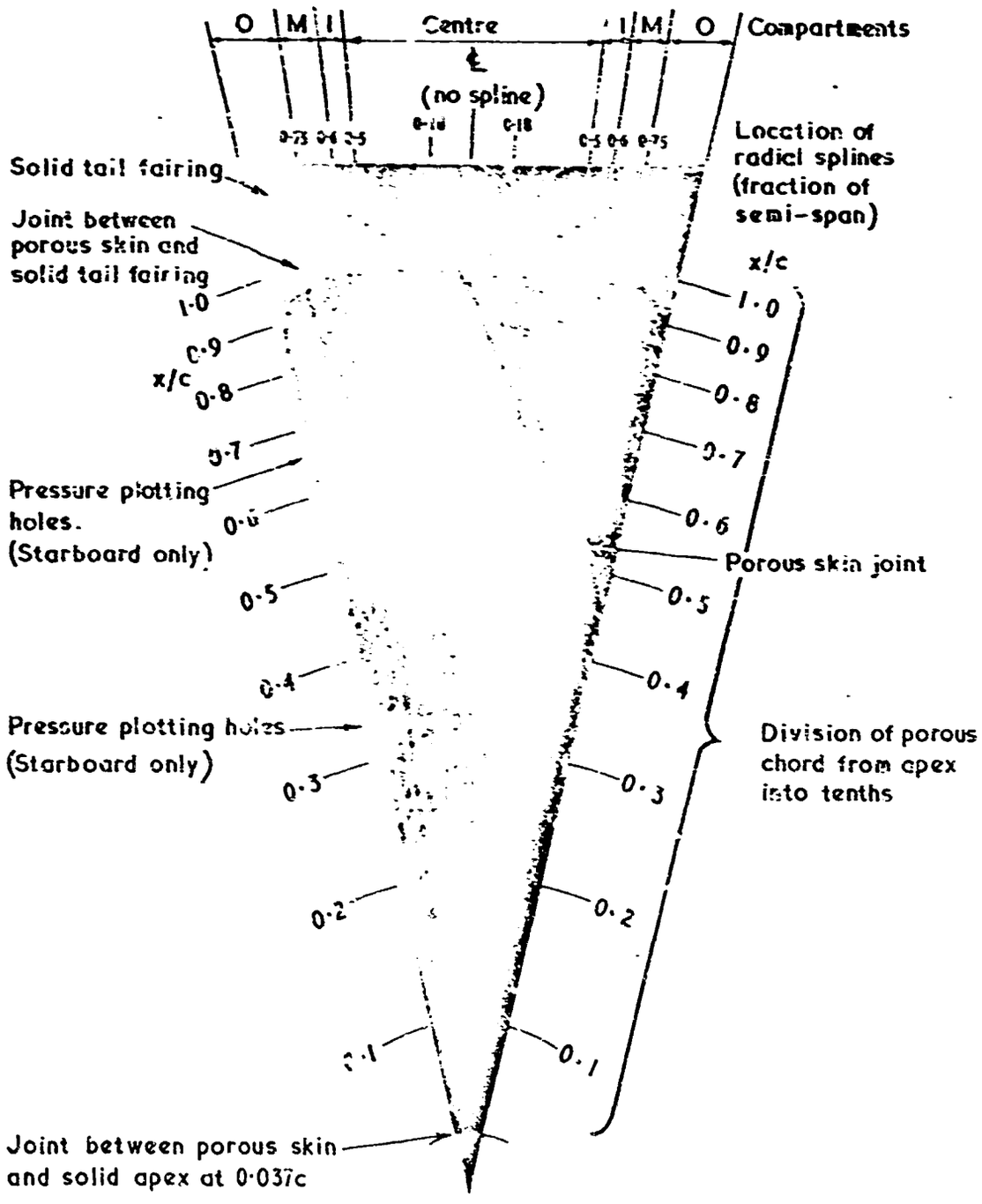

Fig.3 Oblique view of upper surface showing naphthalene remaining after spraying and sucking air through porous surface at a mean speed of 0.06 ft/sec for half an hour, tunnel off.

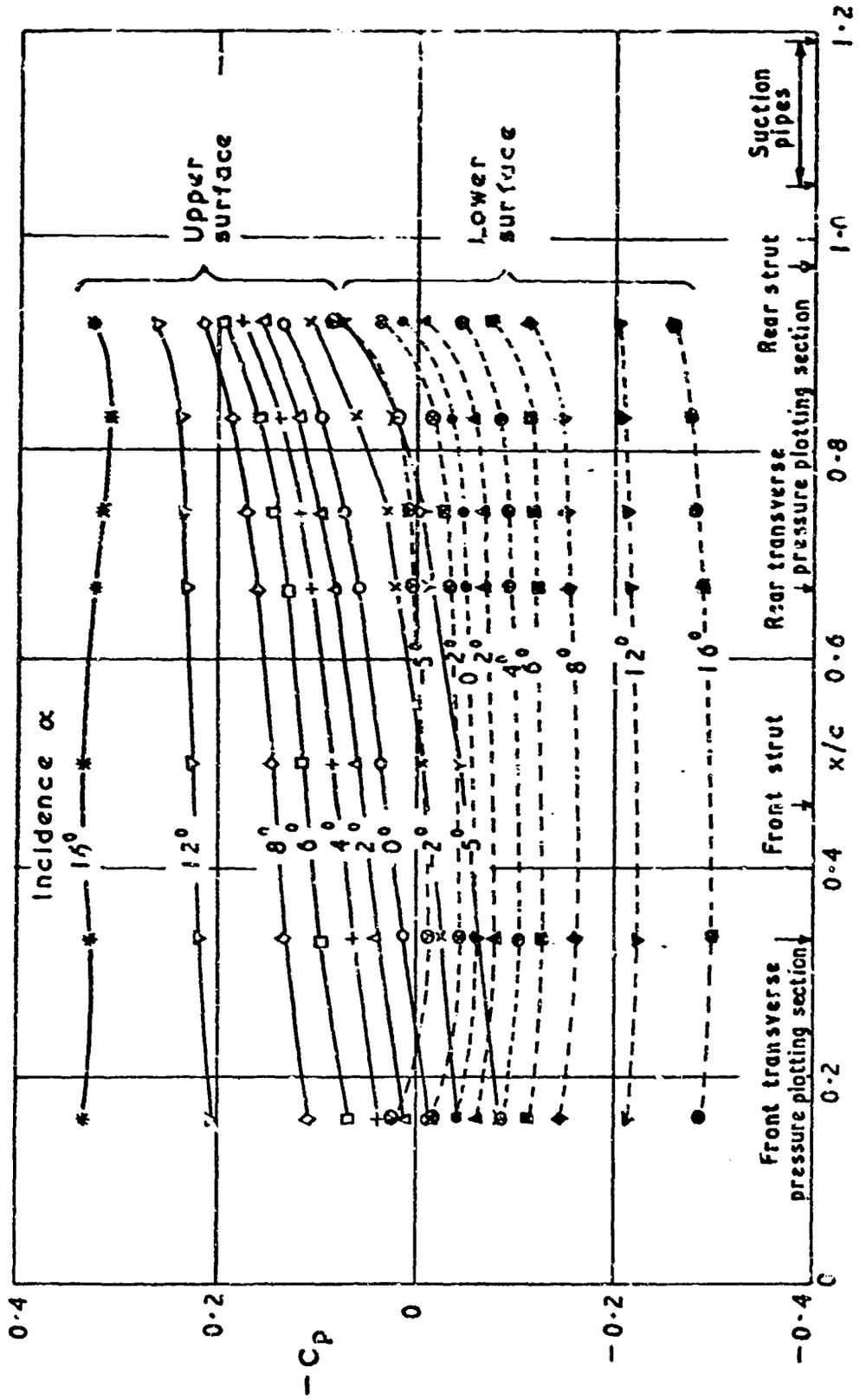

Fig. 4 Centre-line pressure distribution on impermeable wing $R_c = 7.5 \times 10^6$

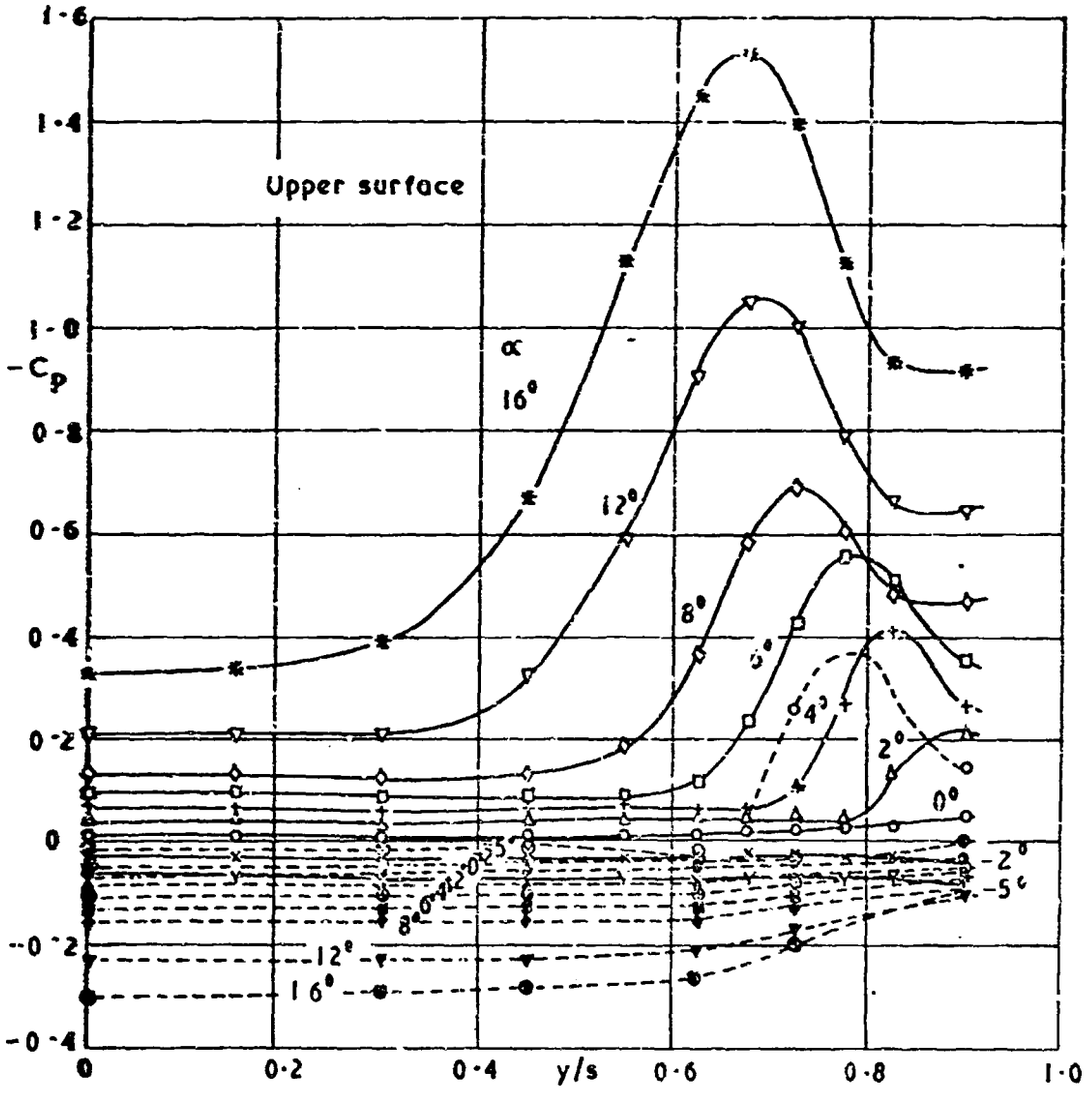

Fig. 5 Transverse pressure distribution on impermeable wing at $\frac{1}{3}$ porous-surface chord.

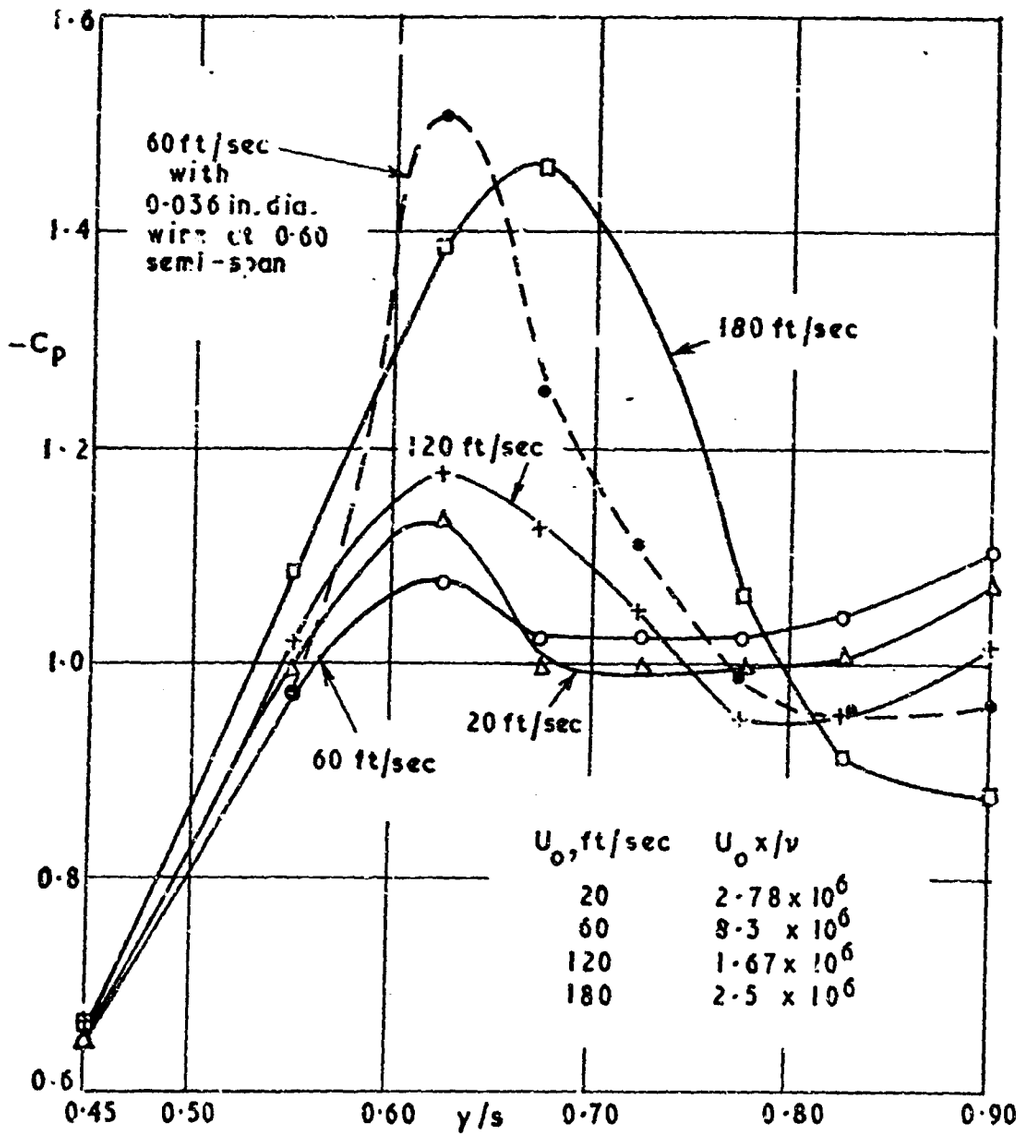

Fig. 6 Scale effect on upper surface transverse pressure distribution at $\frac{1}{3}$ porous-surface chord at 16° incidence

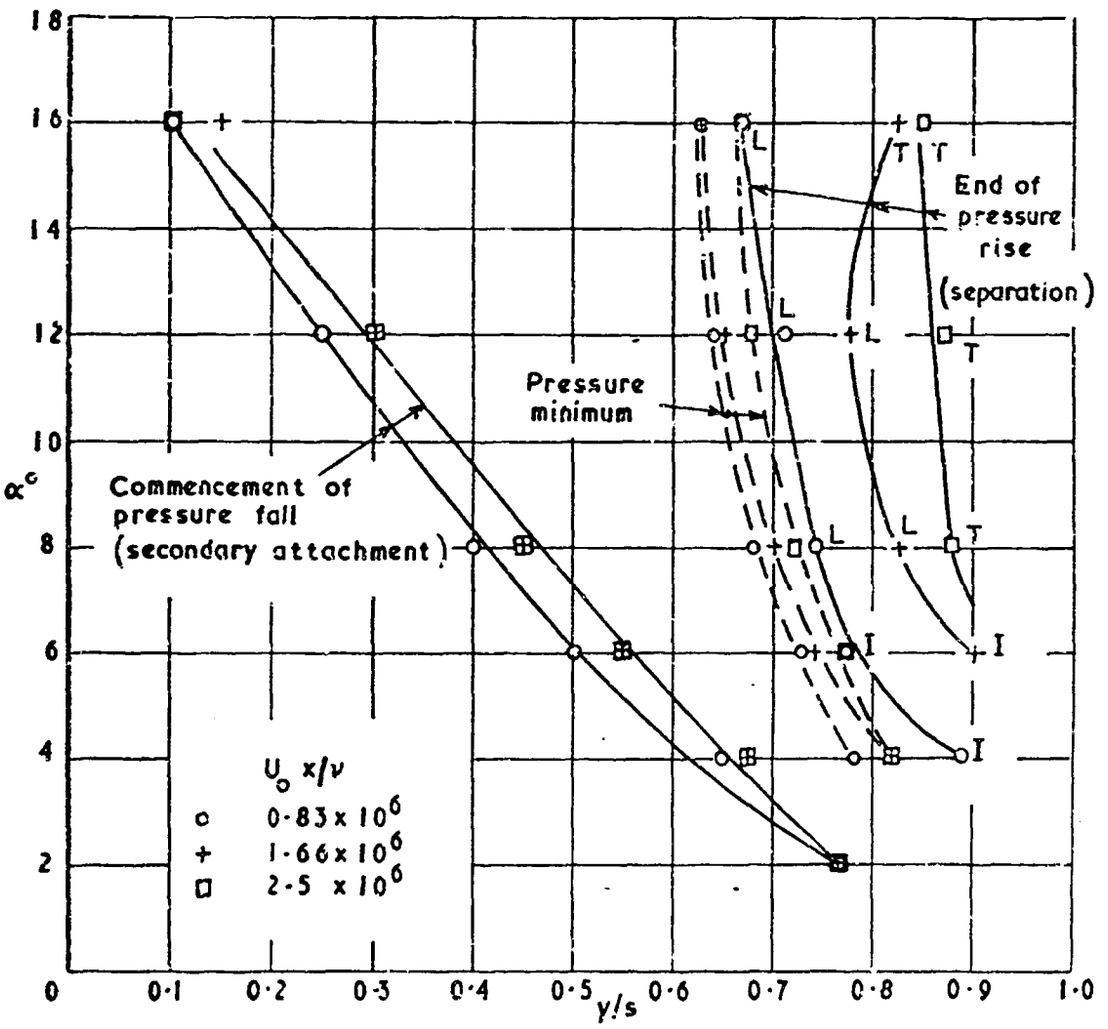

Fig. 7 Variation with incidence and Reynolds number of the spanwise location of the commencement of pressure fall, pressure minimum, and end of pressure rise at $\frac{1}{3}$ porous-surface chord

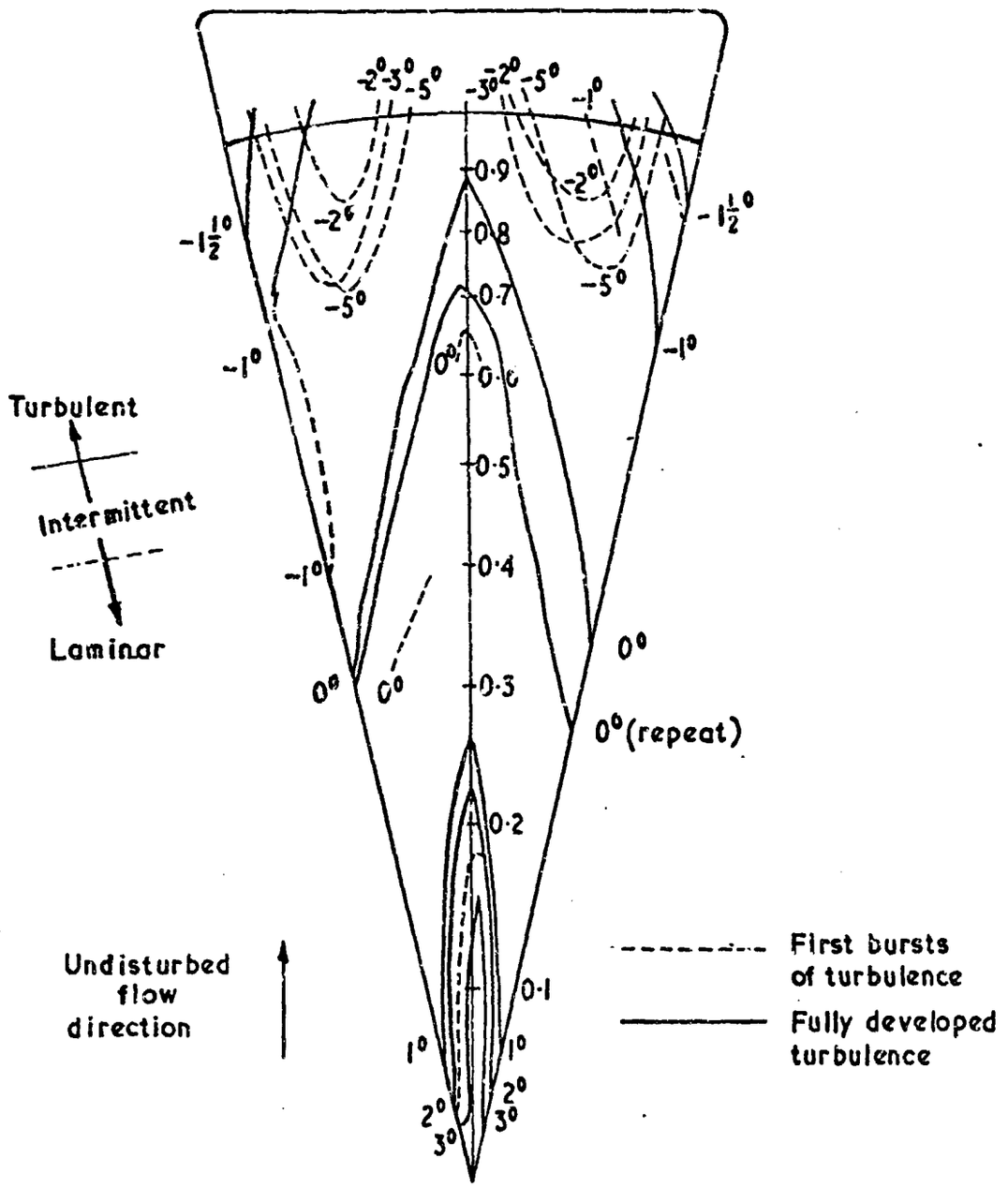

Fig.8 Variation of transition front with incidence in range $-5^{\circ} \leq \alpha \leq 3^{\circ}$ at a wind-speed of 60 ft/sec. $R_c = 2.5 \times 10^6$. Synthesis from naphthalene and hot film measurements on impermeable wing

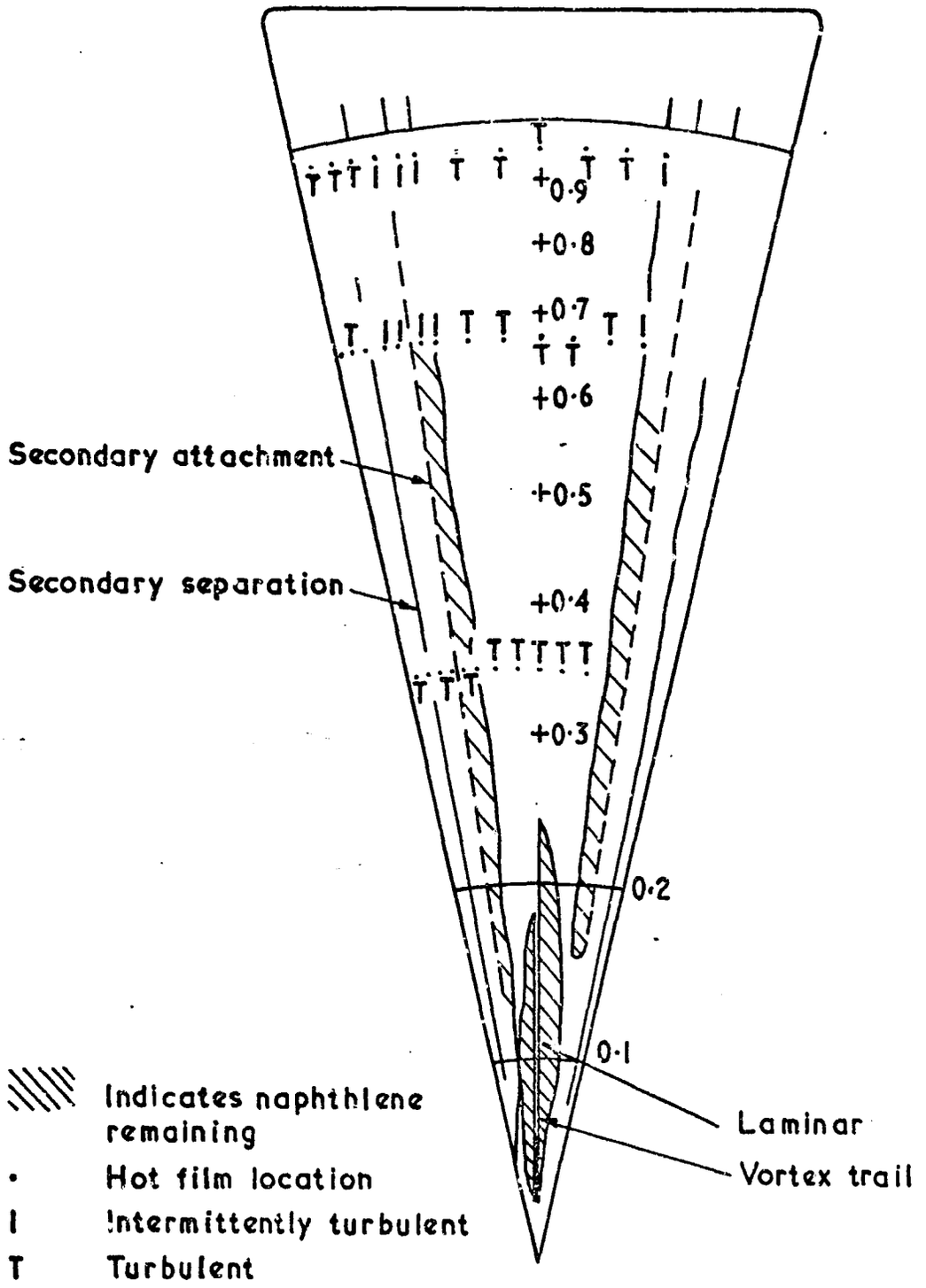

Fig.9 Transition pattern at 4^{o} incidence and 60 ft/sec windspeed $R_c = 2.5 \times 10^6$

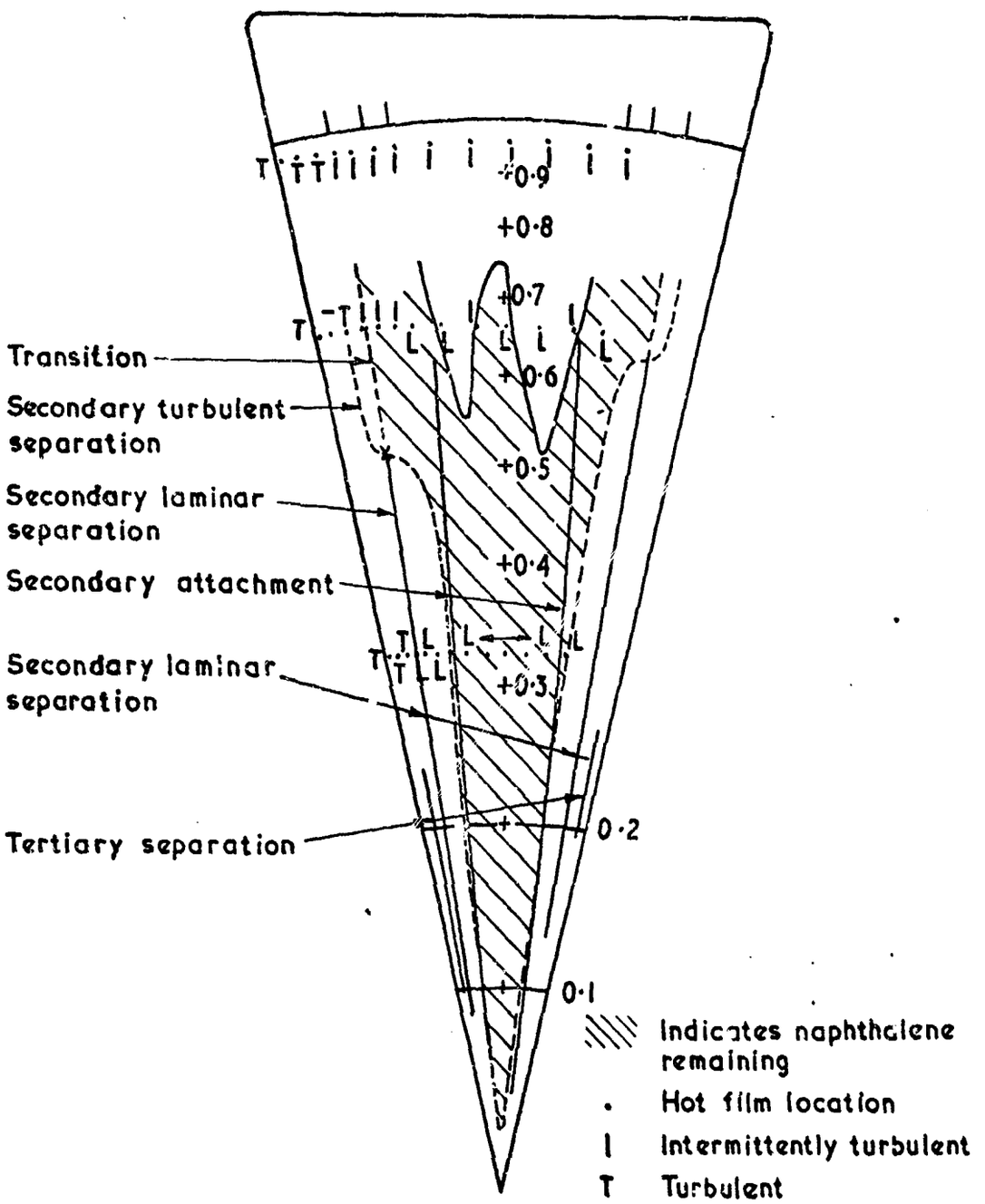

Fig. 10 Transition pattern at 8° incidence and 60 ft/sec windspeed $R_c = 2.5\ 10^6$

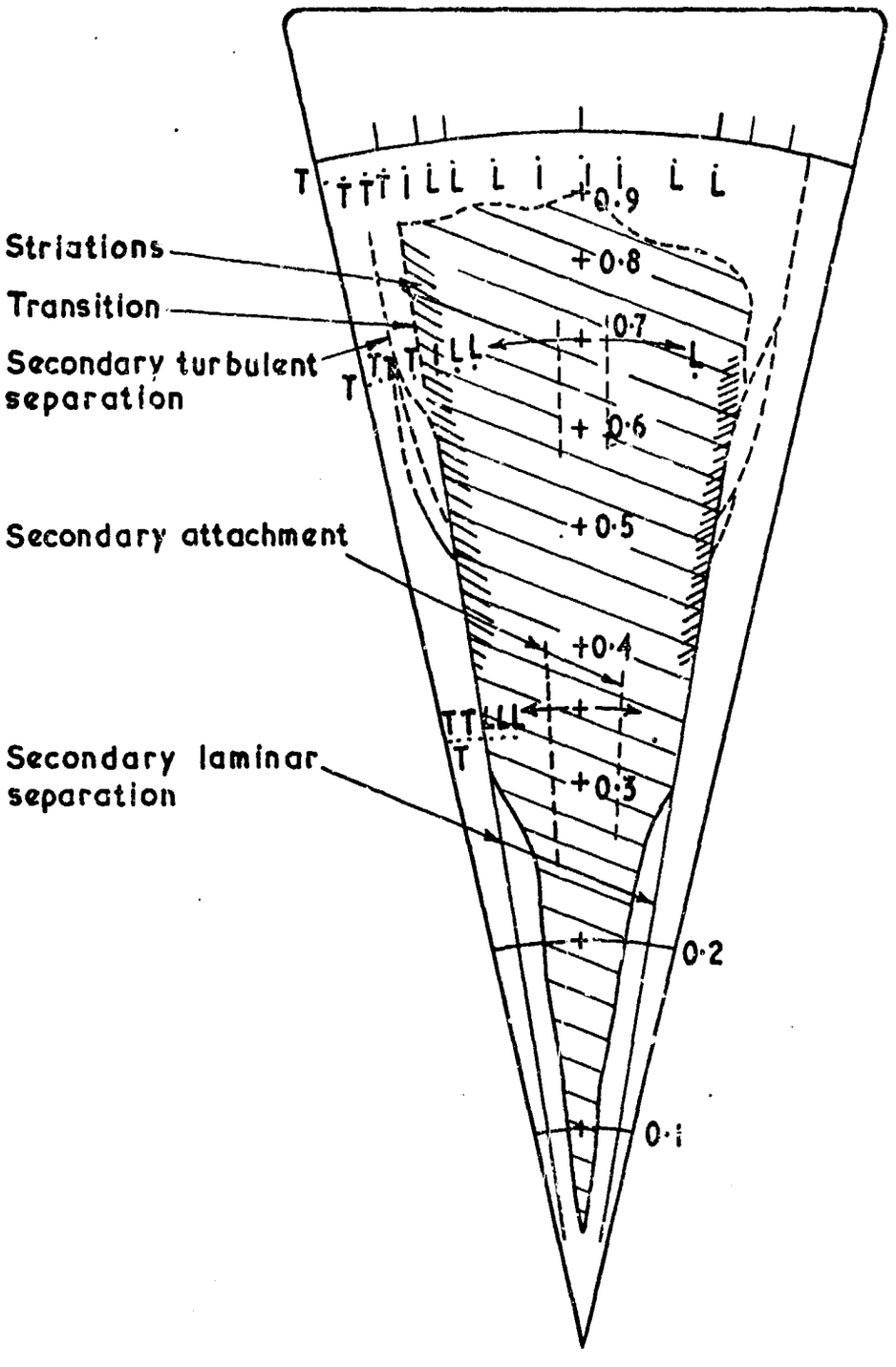

Fig. 11 Transition pattern at 12° incidence and 60 ft/sec windspeed $R_c = 2.5 \times 10^6$

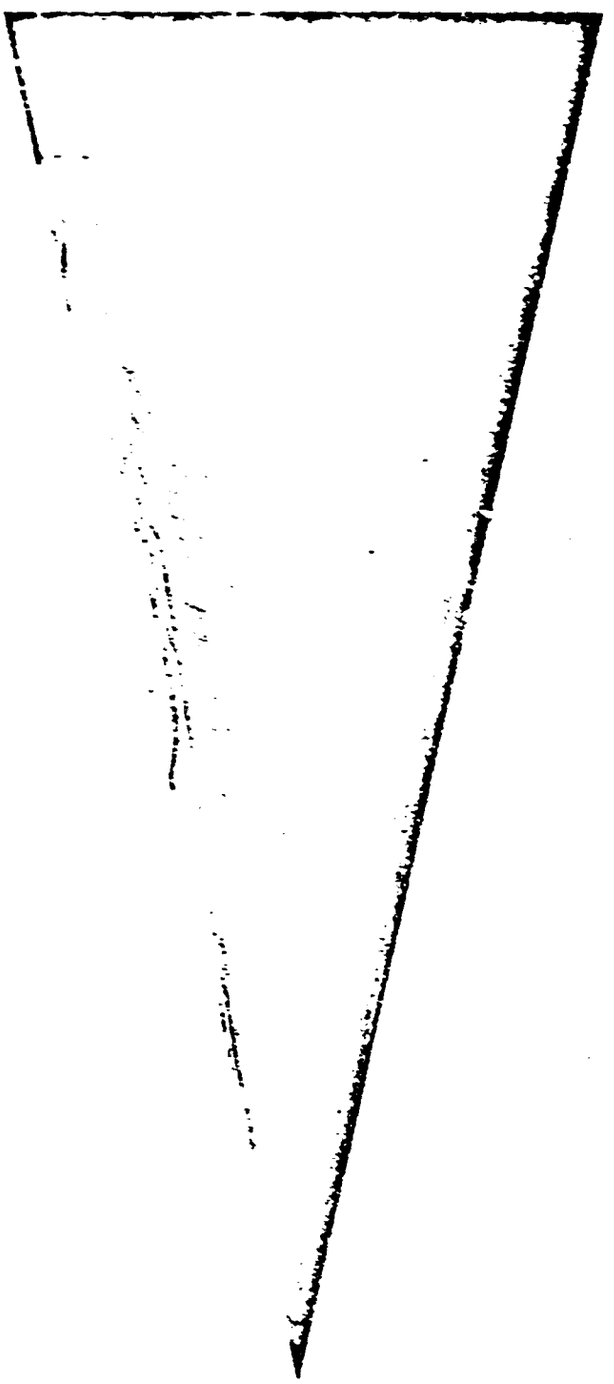

Fig. 12 Surface oil-flow pattern at 12° incidence and 80 ft/sec windspeed
$R_c = 3.2 \times 10^6$

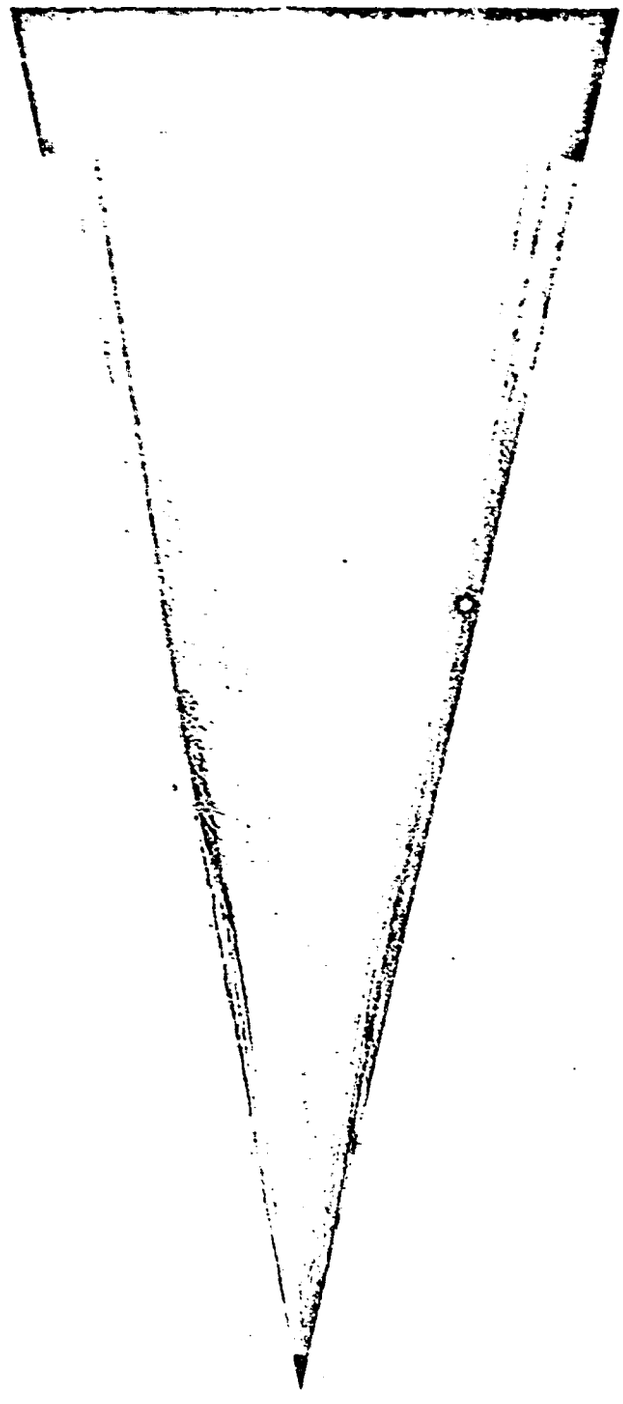

Fig. 13 Surface oil-flow pattern at 12^{0} incidence and 180 ft/sec windspeed
$R_c = 7.5 \times 10^6$

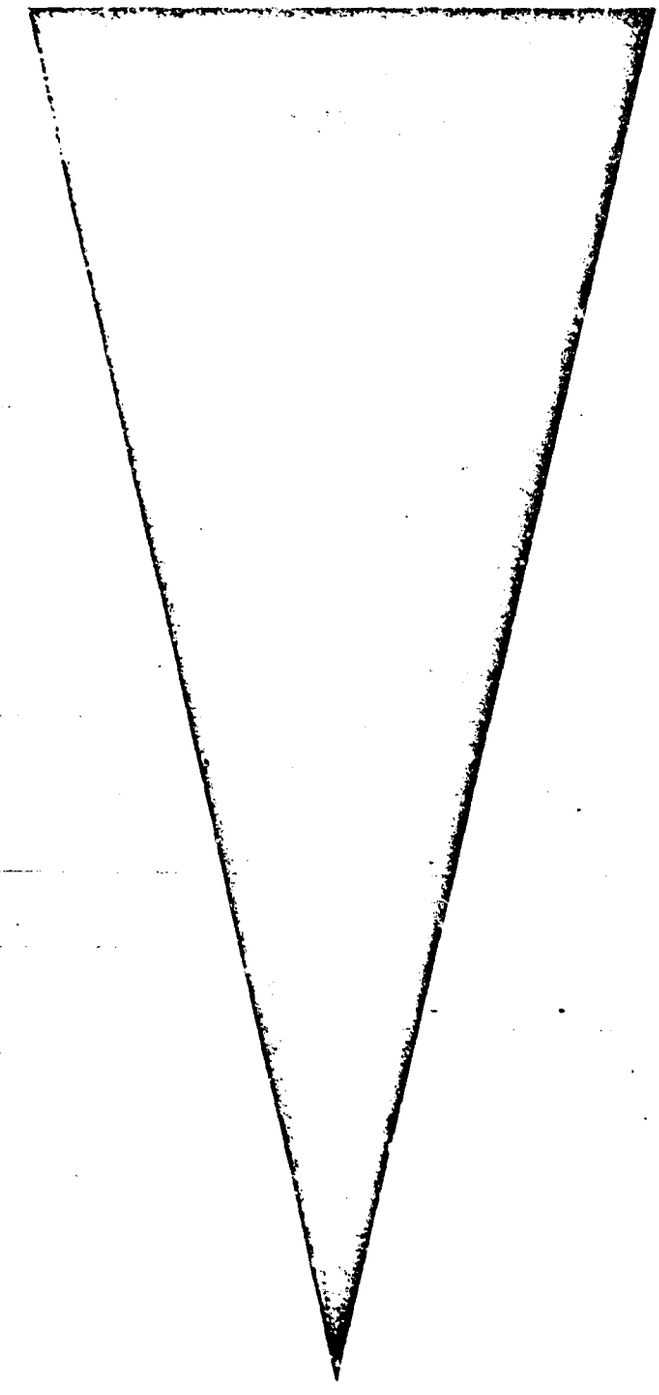

Fig. 14 Sublimation pattern at 16° incidence and 60 ft/sec windspeed $R_c = 2.5 \times 10^6$

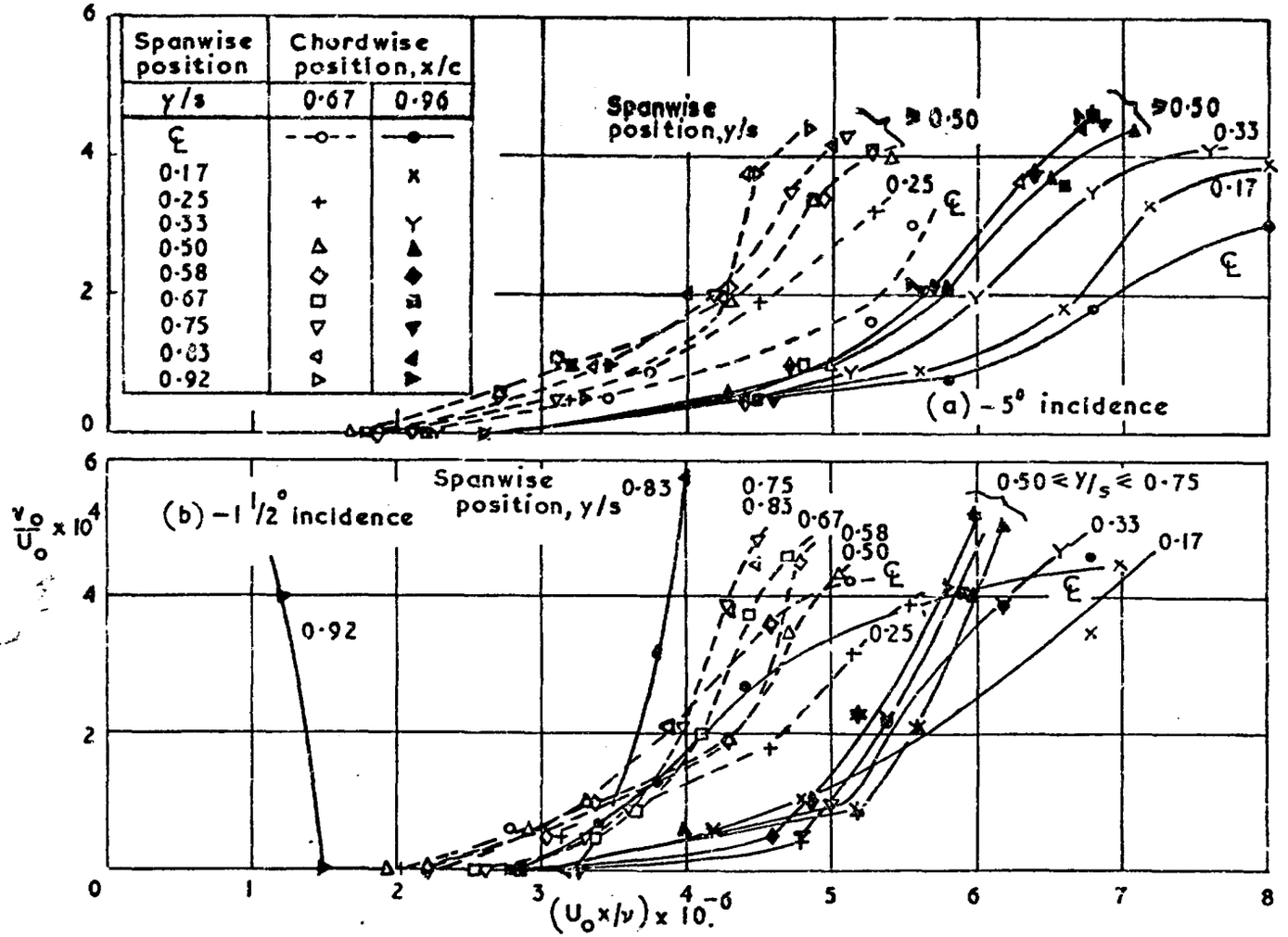

Fig. 15 Variation of inflow velocity ratio to maintain laminar flow with Reynolds number (a) -5° incidence (b) $-1\frac{1}{2}^{o}$ incidence

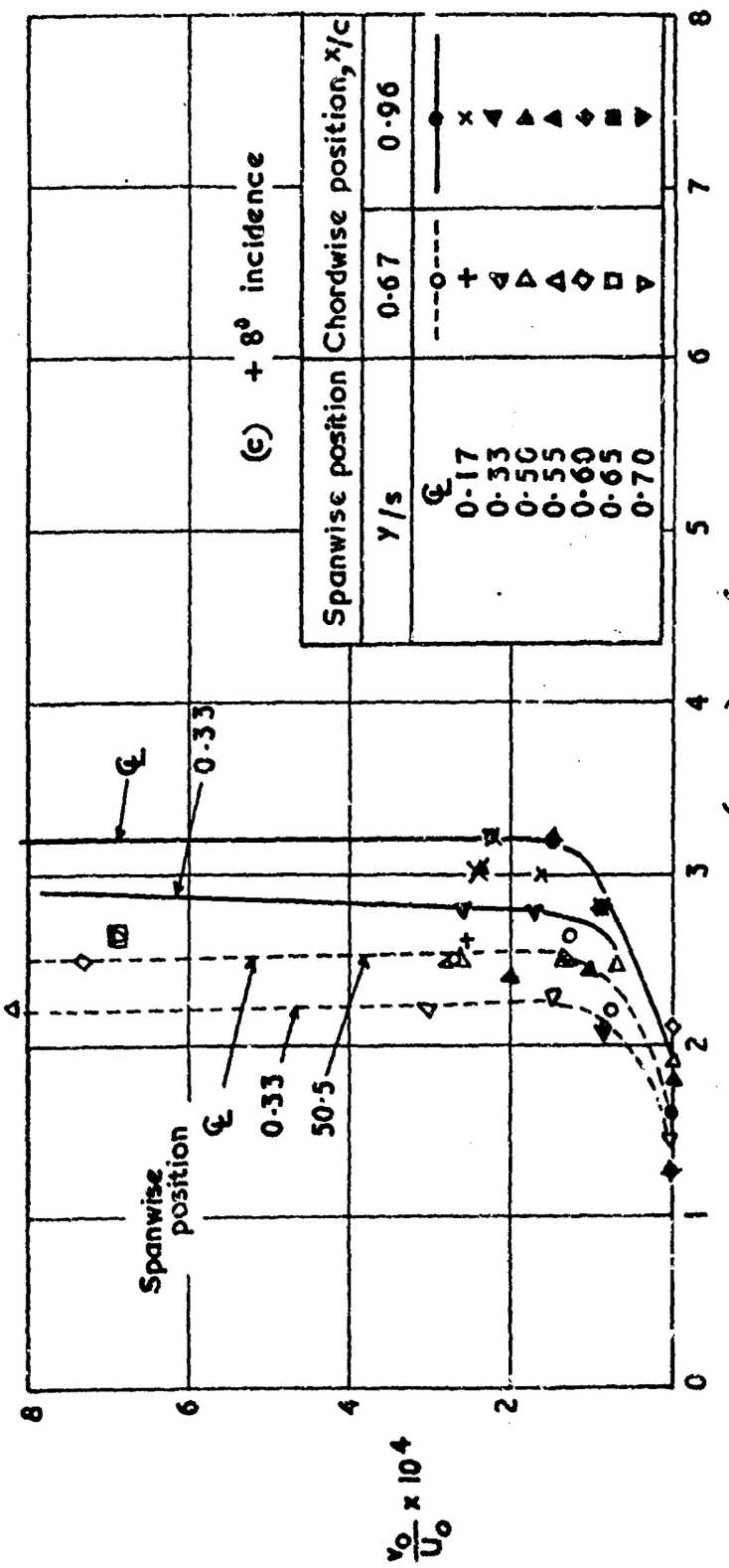

Fig. 15 cont. (c) + 8° incidence

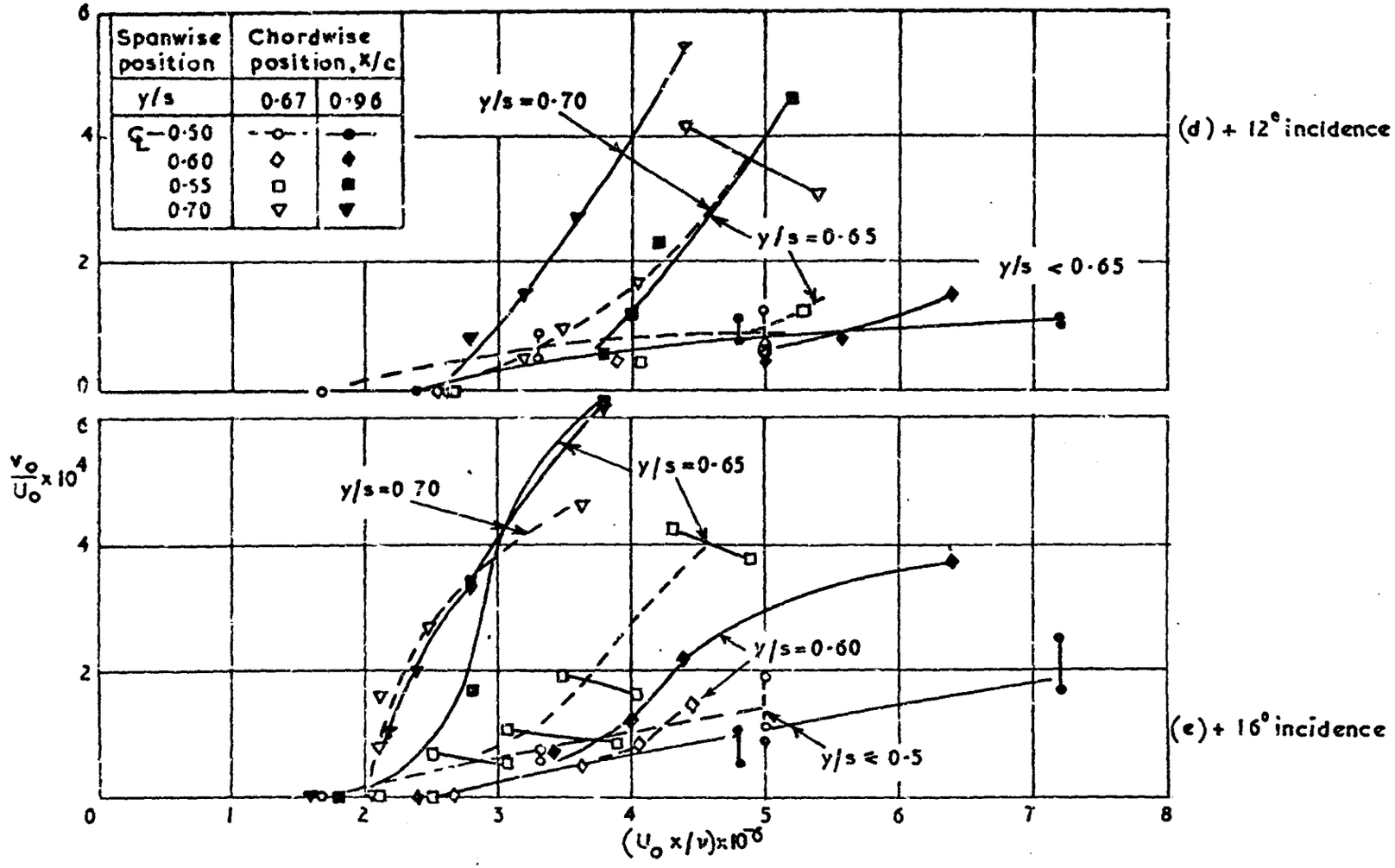

Fig.15 cont. (d) + 12° incidence (e) + 16° incidence

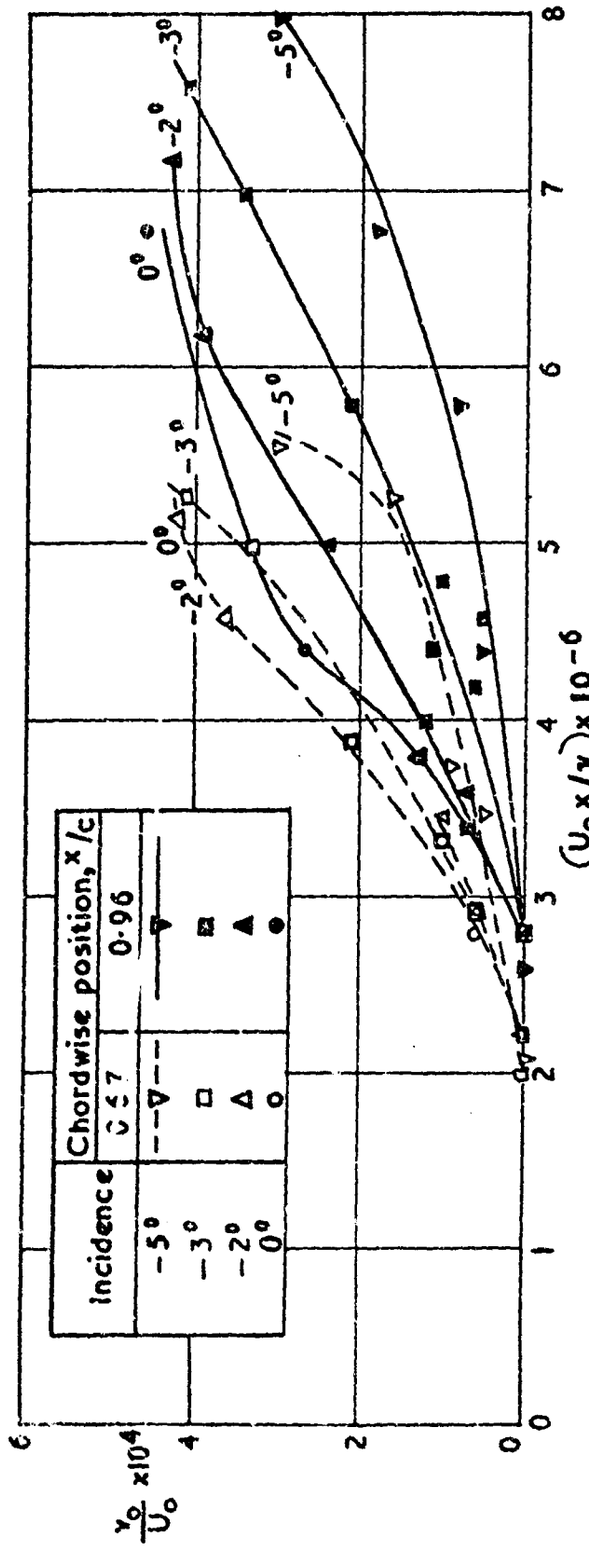

Fig. 16 Variation of inflow velocity ratio to maintain laminar flow along centre-line with Reynolds number and incidence

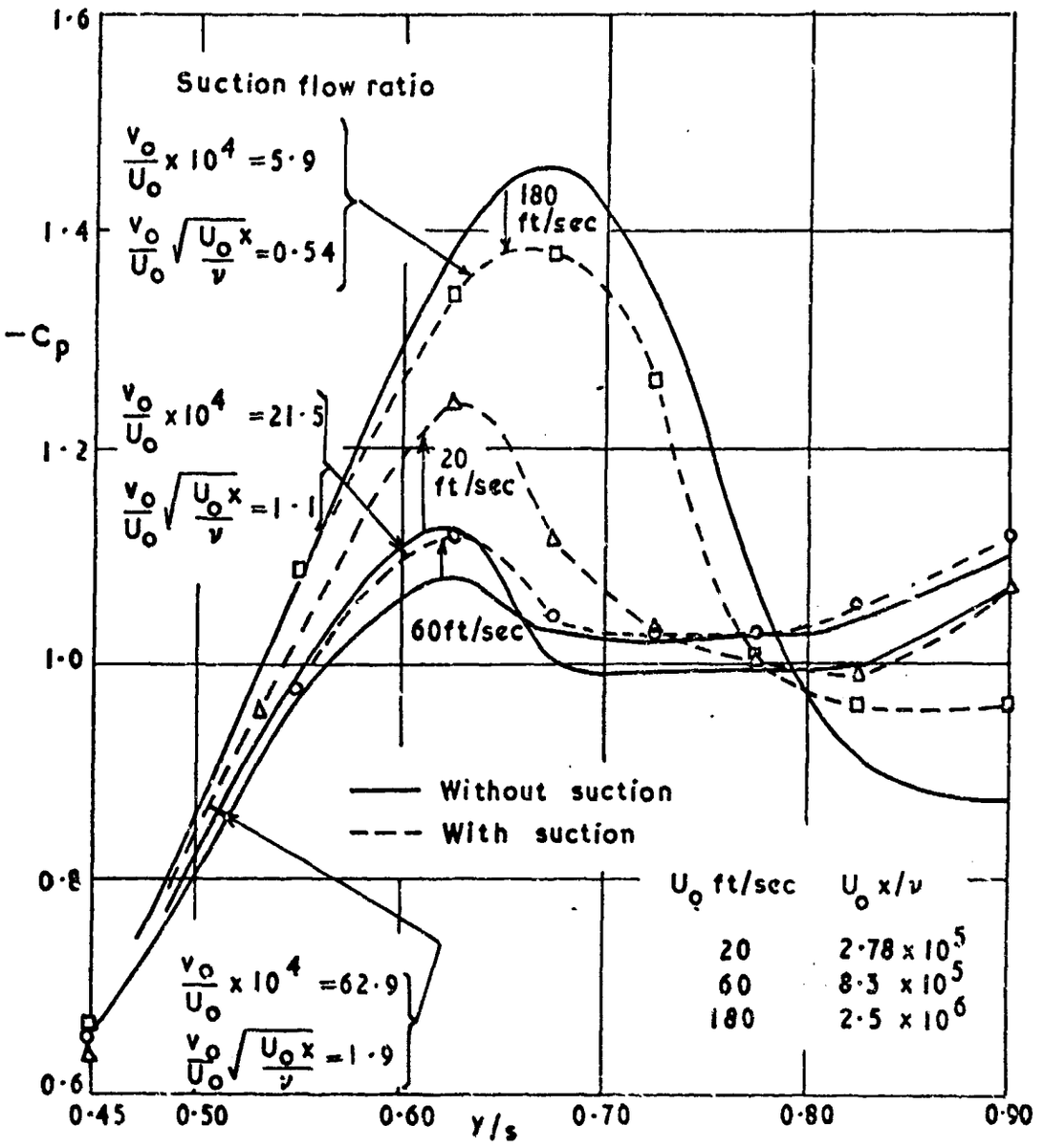

Fig. 17 Effect of distributed suction on upper surface transverse pressure distribution at $\frac{1}{3}$ porous-surface chord and 16° incidence

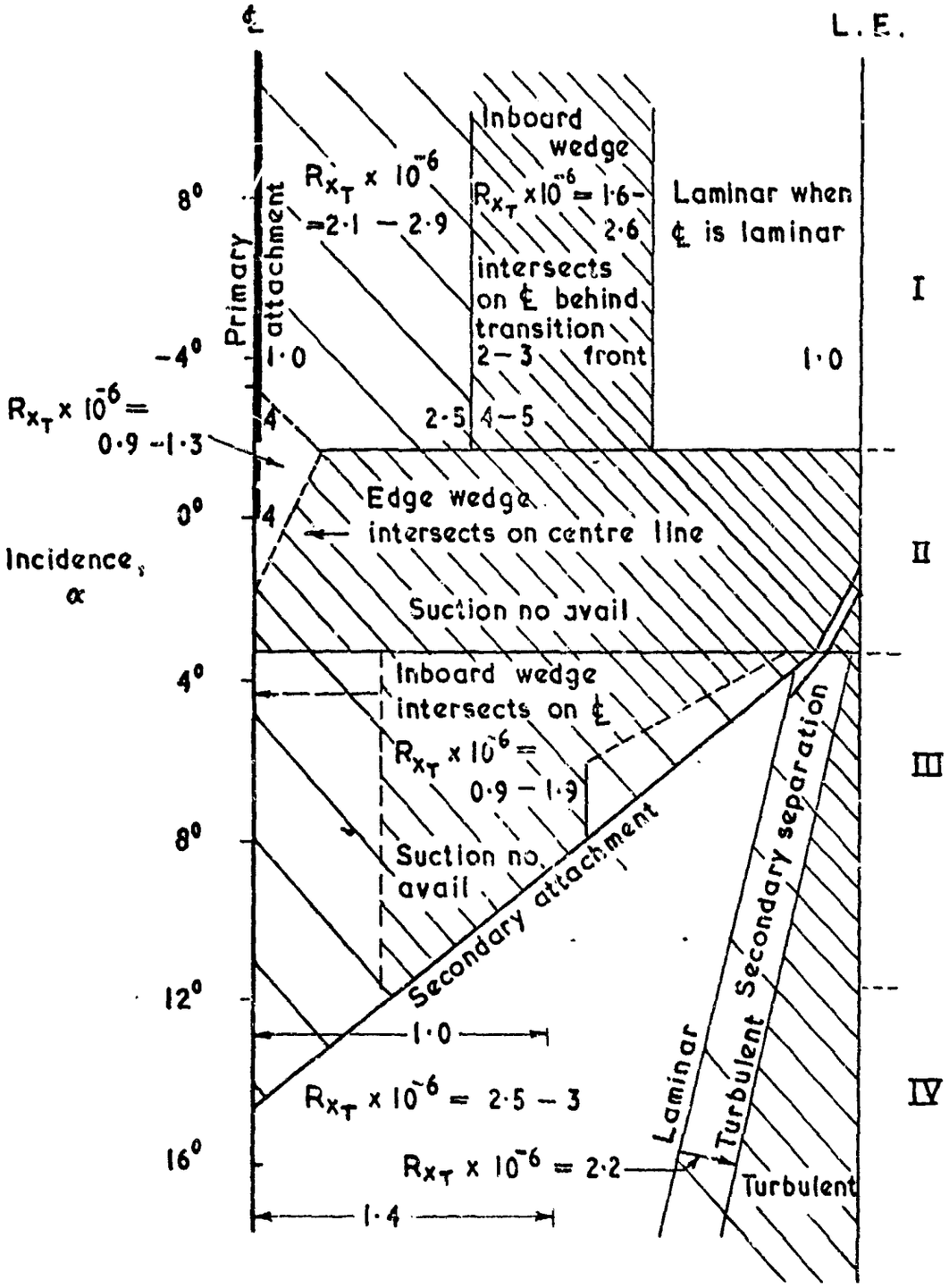

Fig. 18 Diagram showing approximate transition Reynolds numbers in various regimes of flow, and approximate suction quantities, $v_0/U_0 \times 10^4$, required to give laminar flow at $U_0 x/\nu$ equal to 6×10^6.

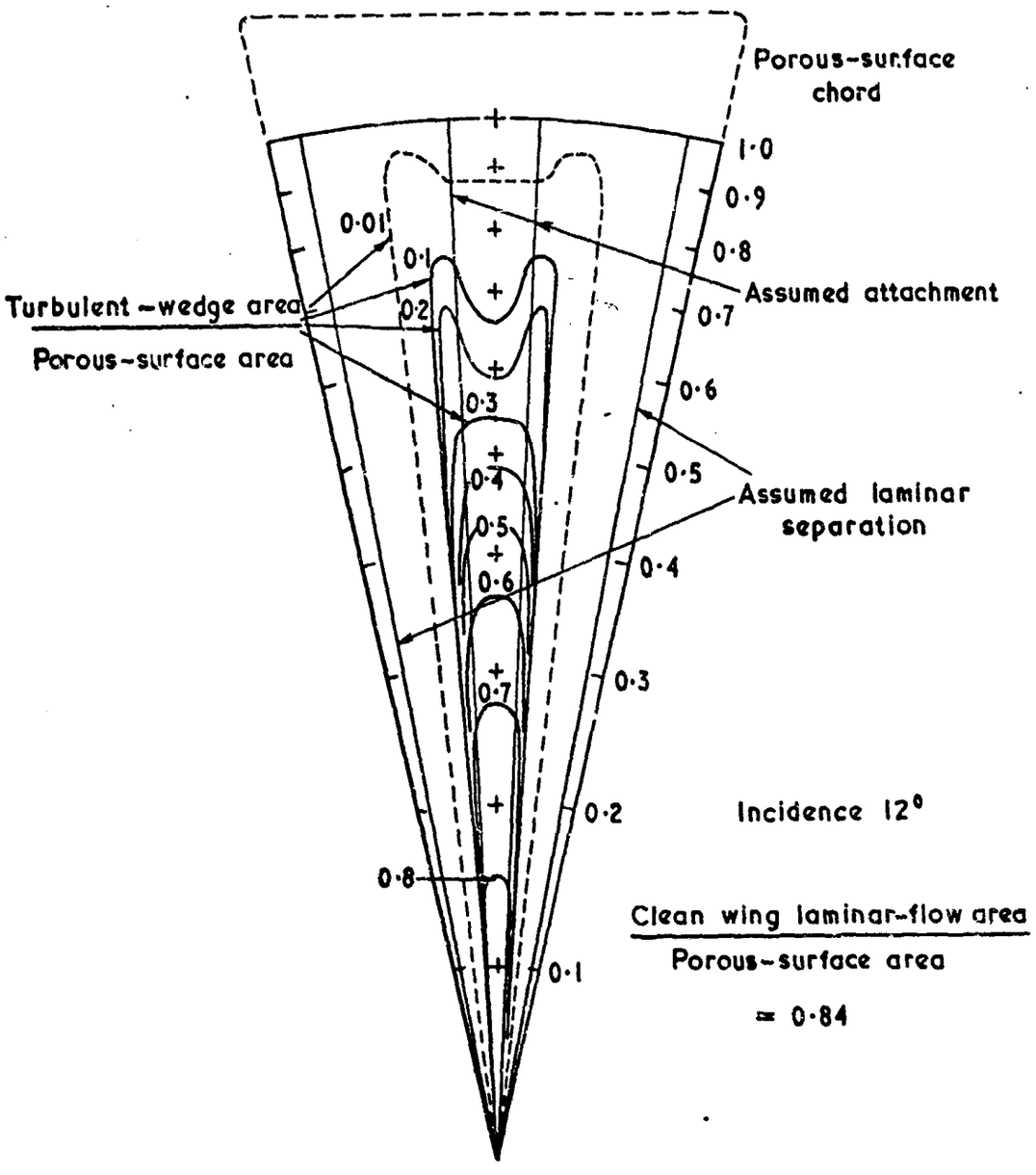

Fig. 19 Contours showing location of a single excrescence on the upper surface of the wing at 12° incidence to produce a given ratio:- area of turbulent flow due to excrescence/porous-surface area

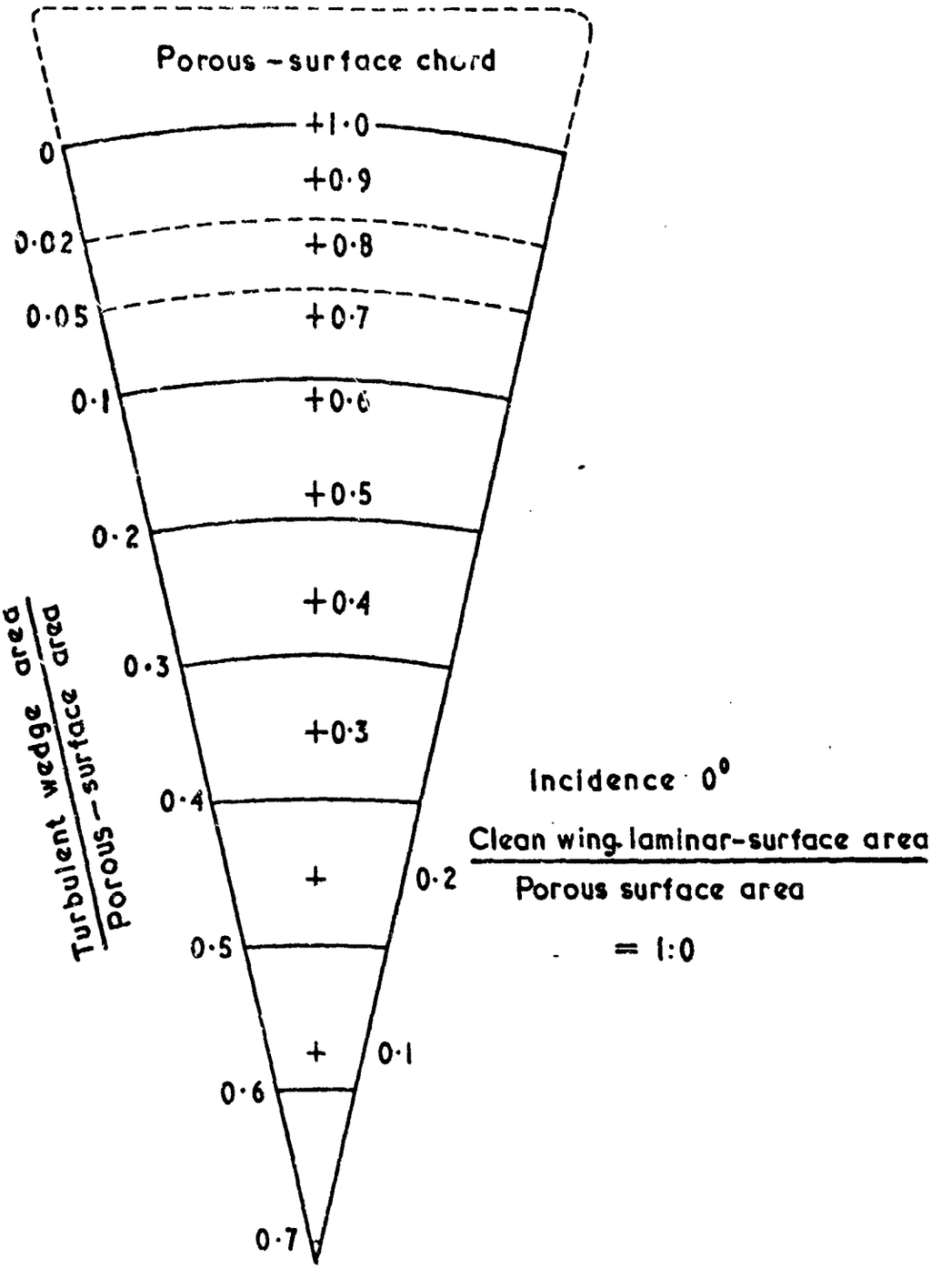

Fig. 20 Contours showing location of a single excrescence on the upper surface of the wing at effectively zero incidence (giving parallel flow) to produce a given ratio: area of turbulent flow due to excrescence/porous-surface area

DISTRIBUTION

Copies of AGARD publications may be obtained in the various countries at the addresses given below.

On peut se procurer des exemplaires des publications de l'AGARD aux adresses suivantes.

BELGIUM BELGIQUE	Centre National d'Etudes et de Recherches Aéronautiques 11, rue d'Egmont, Bruxelles
CANADA	Director of Scientific Information Service Defence Research Board Department of National Defence 'A' Building, Ottawa, Ontario
DENMARK DANEMARK	Danish Defence Research Board Østerbrogades Kaserne, Copenhagen, Ø
FRANCE	O.N.E.R.A. (Direction) 25, Av. de la Division Leclerc Châtillon-sous-Bagneux (Seine)
GERMANY ALLEMAGNE	Zentralistelle für Luftfahrtdokumentation und Information 8 Munchen 27 Maria-Theresia-Str. 21 Attn: Dr. H.J. Rautenberg
GREECE GRECE	Greek National Defence General Staff B.JSG, Athens
ICELAND ISLANDE	Director of Aviation c/o Flugrad, Reykjavik
ITALY ITALIE	Ufficio del Delegato Nazionale all'AGARD Ministero Difesa – Aeronautica Roma
LUXEMBURG LUXEMBOURG	Obtainable through Belgium
NETHERLANDS PAYS BAS	Netherlands Delegation to AGARD Michiel de Ruyterweg 10, Delft